ASSESSMENT METHODOLOGY FOR DIAGONALLY CRACKED REINFORCED CONCRETE DECK GIRDERS

Final Report

SPR 350
SR 500-091

RESEARCH

Oregon Department of Transportation

ASSESSMENT METHODOLOGY FOR DIAGONALLY CRACKED REINFORCED CONCRETE DECK GIRDERS

Final Report

SPR 350
SR 500-091

by

Christopher Higgins,
Thomas H. Miller, David V. Rosowsky, Solomon C. Yim,
Tanarat Potisuk, Theresa K. Daniels, Brian S. Nicholas, Melissa J. Robelo,
Ae-Young Lee and Richard W. Forrest
Structural Engineering Group
Department of Civil, Construction and Environmental Engineering
Oregon State University
202 Apperson Hall
Corvallis, OR 97331

for
Oregon Department of Transportation
Research Unit
200 Hawthorne Ave. SE -- Suite B-240
Salem, OR 97301-5192

and
Federal Highway Administration
400 Seventh Street SW
Washington, DC 20590

October 2004

Technical Report Documentation Page

1. Report No.	2. Government Accession No.	3. Recipient's Catalog No.
FHWA-OR-RD-05-04		

4. Title and Subtitle	5. Report Date
ASSESSMENT METHODOLOGY FOR DIAGONALLY CRACKED REINFORCED CONCRETE DECK GIRDERS	October 2004
	6. Performing Organization Code

7. Author(s)	8. Performing Organization Report No.
Christopher Higgins, Thomas H. Miller, David V. Rosowsky, Solomon C. Yim, Tanarat Potisuk, Theresa K. Daniels, Brian S. Nicholas, Melissa J. Robelo, Ae-Young Lee and Richard W. Forrest Structural Engineering Group Department of Civil, Construction and Environmental Engineering Oregon State University 202 Apperson Hall Corvallis, OR 97331	

9. Performing Organization Name and Address	10. Work Unit No. (TRAIS)
Oregon Department of Transportation Research Group 200 Hawthorne SE, Suite B-240 Salem, Oregon 97301-5192	
	11. Contract or Grant No. SPR 350, SR 500-091

12. Sponsoring Agency Name and Address			13. Type of Report and Period Covered
Oregon Department of Transportation Research Unit 200 Hawthorne SE, Suite B-240 Salem, Oregon 97301-5192	and	Federal Highway Administration 400 Seventh Street SW Washington, DC 20590	Final Report
			14. Sponsoring Agency Code

15. Supplementary Notes

16. Abstract

This report details the results of a research program conducted to estimate the capacity and remaining life of 1950's vintage conventionally reinforced concrete deck girder (RCDG) bridges with diagonal cracks. The investigation encompassed field testing, laboratory testing, and analysis to develop a reliability based assessment methodology. Background, findings, and conclusions from each of these components are provided in individual sections of this report. Current limitations are described, including the impact of skew, temperature and shrinkage effects on capacity, as well as serious stem-flange interface cracking. There are also limitations in predicting the capacity of bent caps. Finally, recommendations are made for implementing the assessment methodology.

17. Key Words	18. Distribution Statement
Reinforced concrete, deck-girder bridges, diagonal cracking, shear, reliability assessment, laboratory testing, field testing, analysis, modified compression field theory	Copies available from NTIS, and online at http://www.odot.state.or.us/tddresearch

19. Security Classification (of this report)	20. Security Classification (of this page)	21. No. of Pages	22. Price
Unclassified	Unclassified	340 + appendices	

Technical Report Form DOT F 1700.7 (8-72) Reproduction of completed page authorized Printed on recycled paper

SI* (MODERN METRIC) CONVERSION FACTORS

APPROXIMATE CONVERSIONS TO SI UNITS

Symbol	When You Know	Multiply By	To Find	Symbol
		LENGTH		
In	inches	25.4	Millimeters	mm
Ft	feet	0.305	Meters	m
Yd	yards	0.914	Meters	m
Mi	miles	1.61	Kilometers	km
		AREA		
In^2	square inches	645.2	Millimeters squared	mm^2
ft^2	square feet	0.093	Meters squared	m^2
Yd^2	square yards	0.836	Meters squared	m^2
Ac	acres	0.405	Hectares	ha
Mi^2	square miles	2.59	Kilometers squared	km^2
		VOLUME		
fl oz	fluid ounces	29.57	Milliliters	mL
Gal	gallons	3.785	Liters	L
ft^3	cubic feet	0.028	Meters cubed	m^3
Yd^3	cubic yards	0.765	Meters cubed	m^3
NOTE: Volumes greater than 1000 L shall be shown in m^3.				
		MASS		
Oz	ounces	28.35	Grams	g
Lb	pounds	0.454	Kilograms	kg
T	short tons (2000 lb)	0.907	Megagrams	Mg
		TEMPERATURE (exact)		
°F	Fahrenheit temperature	5(F-32)/9	Celsius temperature	°C

APPROXIMATE CONVERSIONS FROM SI UNITS

Symbol	When You Know	Multiply By	To Find	Symbol
		LENGTH		
mm	millimeters	0.039	inches	in
m	meters	3.28	feet	ft
m	meters	1.09	yards	yd
km	kilometers	0.621	miles	mi
		AREA		
mm^2	millimeters squared	0.0016	square inches	in^2
m^2	meters squared	10.764	square feet	ft^2
ha	hectares	2.47	acres	ac
km^2	kilometers squared	0.386	square miles	mi^2
		VOLUME		
mL	milliliters	0.034	fluid ounces	fl oz
L	liters	0.264	gallons	gal
m^3	meters cubed	35.315	cubic feet	ft^3
m^3	meters cubed	1.308	cubic yards	yd^3
		MASS		
g	grams	0.035	ounces	oz
kg	kilograms	2.205	pounds	lb
Mg	megagrams	1.102	short tons (2000 lb)	T
		TEMPERATURE (exact)		
°C	Celsius temperature	1.8C + 32	Fahrenheit	°F

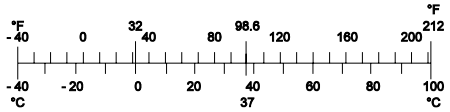

* SI is the symbol for the International System of Measurement

(4-7-94 jbp)

ACKNOWLEDGEMENTS

The authors would like to thank Messrs. Steven M. Soltesz, Steven C. Lovejoy, and David F. Fifer of the Oregon Department of Transportation for their valuable assistance with the many research tasks. The authors would also like to thank Mr. William J. Farrow III for his contributions to the initial laboratory setup and testing. In addition, the authors would like to thank Drs. Colin Brown and Michael Collins for their interest and helpful suggestions. The authors would like to thank the Technical Advisory Committee members Messrs. Craig L. Shike, Stephen T. Burgess, Richard L. Groff, Bert H. Hartman, Steven C. Lovejoy, and Raymond Mabey of ODOT and Mr. Bruce Johnson. Finally, the authors would like to thank Messrs. Alan R. Kirk and McGregor Lynde of ODOT for preparing the report for publication.

DISCLAIMER

This document is disseminated under the sponsorship of the Oregon Department of Transportation and the United States Department of Transportation in the interest of information exchange. The State of Oregon and the United States Government assume no liability of its contents or use thereof.

The contents of this report reflect the views of the author(s) who are solely responsible for the facts and accuracy of the data presented herein. The contents do not necessarily reflect the official policies of the Oregon Department of Transportation or the United States Department of Transportation.

The State of Oregon and the United States Government do not endorse products of manufacturers. Trademarks or manufacturers' names appear herein only because they are considered essential to the object of this document.

This report does not constitute a standard, specification, or regulation.

ASSESSMENT METHODOLOGY FOR DIAGONALLY CRACKED REINFORCED CONCRETE DECK GIRDERS

TABLE OF CONTENTS

EXECUTIVE SUMMARY xvii

1.0 INTRODUCTION 1

2.0 FIELD TESTING 5

3.0 LABORATORY TESTING 121

4.0 ANALYSIS OF SHEAR CAPACITY FOR VINTAGE RC GIRDERS AND BENT CAPS 205

5.0 RELIABILITY BASED ASSESSMENT METHODOLOGY 273

6.0 REFERENCES 325

APPENDICES

APPENDIX A1: SHOP DRAWINGS
APPENDIX A2: MATERIALS PROPERTIES
APPENDIX A3: CRACK MAP
APPENDIX A4: EXPERIMENTAL DATA
APPENDIX A5: FORCE DEFLECTION
APPENDIX A6: HIGH-CYCLE FATIGUE

APPENDIX B: MOVING LOAD REPORT

APPENDIX C1: LIVE LOAD EFFECTS ON A THREE-SPAN CONTINUOUS BRIDGE
APPENDIX C2: RATING VEHICLES AND RATING VEHICLE ASSESSMENT
APPENDIX C3: MCKENZIE RIVER BRIDGE CROSS SECTIONS
APPENDIX C4: SUMMARY OF ANALYSIS METHODOLOGY AND FIELD DATA COLLECTION

EXECUTIVE SUMMARY

This report details the results of a research program conducted to estimate the capacity and remaining life of 1950's vintage conventionally reinforced concrete deck girder (RCDG) bridges with diagonal cracks. The investigation encompassed field testing, laboratory testing, and analysis to develop a reliability based assessment methodology. Background, findings, and conclusions from each of these components are provided in individual sections of this report and are summarized here.

Field Tests

The response of three in-service bridges was monitored under ambient traffic conditions as well as controlled loading. For select girders, the stress ranges in the steel shear stirrups (the vertical steel reinforcement) and the deformation of diagonal cracks were measured while under vehicle loading. Load distribution and impact factors, key values for structural analysis, were developed from the data. Comparing the calculated factors with American Association of Highway Transportation Officials (AASHTO) design factors showed that AASHTO load distribution factors are conservative, but the AASHTO impact factor is representative of actual bridge response. Field measurements also showed that the repetitive stress cycles produced in the shear stirrups due to traffic is unlikely to cause metal fatigue (high cycle fatigue, HCF) of the stirrups.

Laboratory Tests

Laboratory tests were conducted on 44 large-scale girder elements designed to represent as near as possible 1950's construction practice. Various steel reinforcement configurations were tested to determine the effect of typical vintage beam characteristics on load capacity. Bending conditions were varied to reproduce girder behavior at different positions in a bridge. Loading protocols included incrementally increasing load amplitudes, repeated loading up to two million cycles, and a moving load along the length of the girders. The following are the key results:

- Adequate anchorage of flexural steel reinforcement (the horizontal steel reinforcement) so that the steel bars did not slip in the concrete was crucial to achieve higher ultimate capacity. If the flexural steel terminates before the end of the girder, which was a common practice in the 1950s, diagonal cracks are likely to extend into the beam from this area, and the crack will not be as well constrained to carry load resulting in decreased ultimate load capacity.

- Initial crack damage may not necessarily contribute to the final failure mode if loading conditions change so as to create a new critical region.

- Crack width alone may not indicate the level of previous damage to the beam. Tightly spaced stirrups exhibited relatively small crack width at failure while widely spaced stirrups exhibited large and wider cracks at failure.

- Cyclic loading to cause stress in the specimen stirrups equivalent to the single highest stress measured during field testing verified that HCF of the steel is unlikely.

- Cyclic loading was applied to cause progressive permanent deformation of the shear stirrups (low cycle fatigue, LCF), bond deterioration between the stirrups and concrete, increased crack width, stirrup fracture, and ultimately element failure. However, specimens were able to sustain large numbers of LCF cycles; consequently, traffic loading is unlikely to produce the LCF failures observed in the laboratory on actual bridges.

- Though metal fracture of the stirrups due to HCF was shown to be inconsequential, fatigue of the bond between the concrete and the stirrups was also investigated. Debonding could produce less constraint at diagonal crack locations and reduced capacity. However, specimens fabricated with fully debonded stirrups exhibited only slightly reduced capacity than otherwise similar specimens with bonded stirrups.

- Conventional laboratory load testing uses stationary loading points, though bridges are exposed to loads moving along the length of the girders. A set of moving load tests produced similar capacity measurements as comparable stationary tests, verifying that the stationary tests reflect the behavior of in-service girders.

Analysis

Five analysis methods were compared for estimating the shear capacity of the laboratory specimens: ACI method; *Response 2000*™, a specialty analysis program; AASHTO Modified Compression Field Theory (MCFT); Strut-and-Tie Method; and finite element method. Over the range of variables considered, AASHTO-MCFT and *Response 2000*™, which both rely on MCFT, reasonably estimated the capacity of the specimens, including cases with very wide diagonal cracks and substantial previous damage. *Response 2000*™ provided the best correlation with experimental results, while AASHTO-MCFT produced slightly conservative capacity estimations.

Curves to predict LCF life were developed based on beam stresses and observed cumulative damage after repeated cycles. Separate curves were made for girder sections of varying stirrup spacing; however, additional characterization of beam behavior during LCF may provide a generalized prediction tool of LCF life.

For bridge elements with small aspect ratios such as bent caps, AASHTO-MCFT and *Response 2000*™ predicted low capacity compared with load effects. In the analytical methods, the estimated shear capacity of the bent caps was limited by the treatment of the steel capacity and anchorage of the flexural steel at the bent column locations. More refined methods and models are required to better predict the capacity of bent caps.

Reliability Assessment

A reliability assessment methodology was developed to allow transportation personnel to rationally establish load restrictions, prioritize bridges for replacement or repair, and identify specific segments of bridges requiring repair. The methodology integrated the analysis from the

field and laboratory testing with Oregon-specific truck loading, generated from weigh-in-motion (WIM) data. A technique was developed for calculating a reliability index (β) for each critical section of a girder by comparing the maximum operating forces in the section with the estimated capacity of the section and incorporating the inherent variability of the capacity estimate. The girder location with the smallest reliability index controls the capacity of the bridge.

After applying the reliability assessment methodology to a set of bridges to calibrate β, a minimum β can be selected for Oregon's RCDG bridges that represents an acceptable level of risk. A LCF evaluation is included in the assessment to determine whether cumulative damage from cyclic loading is a factor. After applying the assessment method to a series of bridges, the LCF evaluation may be eliminated if experience shows that LCF is clearly inconsequential.

Current limitations are described, including the impact of skew, temperature and shrinkage effects on capacity, as well as serious stem-flange interface cracking. There are also limitations in predicting the capacity of bent caps. Finally, recommendations are made for implementing the assessment methodology.

ASSESSMENT METHODOLOGY FOR DIAGONALLY CRACKED REINFORCED CONCRETE DECK GIRDERS

1.0 INTRODUCTION.....1

1.1 BACKGROUND 1
1.2 OBJECTIVES 2
1.3 RESEARCH APPROACH 2

1.0 INTRODUCTION

There are over 500 conventionally reinforced concrete (CRC) cast-in-place bridges in the Oregon Department of Transportation inventory that are identified as exhibiting diagonal cracking. Of these cracked bridges, 220 are along the I-5 and I-84 corridors. The majority of these bridges was built between the years 1947 and 1962 and classified structurally as reinforced concrete deck-girder (RCDG) bridges. Uncertainties regarding the capacity and remaining life of these bridges has resulted in unplanned bridge replacements, weight restrictions resulting in significant detours, as well as costly emergency repairs, additional inspections, and monitoring. The problem has further impacted local municipal and county agencies, which own and have responsibility for a large number of RCDG bridges in the State. In response to the uncertainties and the scope of the problem, a research program was undertaken to assess the capacity and predict the remaining life of RCDG bridges.

1.1 BACKGROUND

Large numbers of conventionally reinforced concrete (CRC) bridges remain in the national bridge inventory that are lightly reinforced for shear. One of the most common types is the slab-girder bridge used widely during the highway expansion of the late 1940's through the early 1960's. Bridges of this type have girders cast integrally with the slab and may be single span or continuous over multiple supports.

Early AASHTO (American Association of State Highway and Transportation Officials) provisions (*AASHO 1944, 1949, 1953, 1957, 1961, 1965*) for shear design of CRC bridges used allowable stress design and relied on the concrete to carry a prescribed working stress at service load levels. Reinforcing steel was used to provide supplemental shear resistance when required, and the permissible stirrup stress increased from 16 ksi in 1949 (*AASHO 1949*) to 20 ksi in 1953 (*AASHO 1953*). The magnitude of working stress permitted for the concrete in shear was $0.02f'_c$ for unanchored longitudinal bars and $0.03f'_c$ for anchored longitudinal bars (*AASHO 1941, 1944, 1953, 1957, 1961, 1965, and 1969*).

During the late 1940's, research on bond strength for deformed reinforcing bars resulted in increased allowable bond stress in the 1953 AASHO Specification thereby reducing requirements for anchorages. The new deformed bars meeting ASTM A305-50T were used to provide anchorage (and therefore permit use of higher allowable concrete shear stress in design) in locations that would previously have required flexural bars to be bent across the web or terminated by a hook in a compression region (*Siess 1960*).

The combined effects of higher allowable concrete shear stress (permitted with less well anchored flexural bars terminated in tension regions) and the increased allowable stirrup stress changes made in the Specifications in the late 1940's and early 1950's may help to explain the diagonal cracking observed in 1950's vintage RCDG bridges.

Shear design provisions in the AASHTO specifications for CRC bridges have evolved over time to reflect the latest experimental research, behavior theories, analysis methods, and service performance. Following the collapse of two separate warehouses at Air Force bases in Ohio and Georgia in 1955 and 1956, significant experimental research work was undertaken to improve the understanding of shear behavior. This research indicated that previous design provisions overestimated the concrete contribution to shear capacity and the permissible concrete stresses were reduced in the early 1960's to $1.1\sqrt{f'_c}$ (*ACI 1963*). As a consequence, designers in the 1950's relied on a larger allowable concrete stress than would be permitted today; and these early designs would have smaller cross-sectional dimensions, smaller sized stirrups or more widely spaced shear reinforcement, and reduced requirements for flexural bond stresses. It is interesting to note that the service level truck load model H20-S16-44 has not changed and remains the current HS20-44 truck used in the 17th Edition of the Standard Specification (*AASHTO 2002*). While the load model has not changed, it is clear that actual truck load magnitudes and the volume of truck traffic have increased over time.

Many CRC slab-girder bridges are reaching the end of their originally intended design lives and the combined effects of over-estimation of allowable stresses for shear at design, increasing service load magnitudes and volume, as well as shrinkage and temperature effects, may contribute to diagonal tension cracking in these bridges. Due to the relatively light shear reinforcement, diagonal cracks may not be well constrained and therefore become quite wide.

Inspections of approximately 1800 vintage CRC slab-girder bridges in Oregon by Oregon Department of Transportation personnel revealed over 500 with varying levels of diagonal cracking. Crack widths over 0.1 in. were observed. These findings resulted in load postings, monitoring, emergency shoring, repairs, and unscheduled bridge replacements. The large numbers of bridges and their widespread distribution across the state prompted a research study to investigate the remaining capacity and life of diagonally cracked RCDC bridges.

1.2 OBJECTIVES

The objectives of this research were to: (1) assess field performance of typical RCDG bridges with diagonal cracks under in-service load and controlled loading conditions; (2) develop models that will enable ODOT engineers to estimate the life of RCDG bridge girders with diagonal cracks; and (3) develop new or modify existing analysis methods to predict remaining capacity of shear-cracked RC girders.

1.3 RESEARCH APPROACH

To address the research objectives, an integrated approach was taken to develop a reliability-based assessment technique. Research components included the following:

- collection of data describing vehicle loads in the State and prediction of the corresponding load effects;
- inspection, instrumentation, and controlled testing of in-service RCDG bridges;

- tests of large-scale laboratory specimens were conducted to evaluate strength and fatigue performance for a variety of loading conditions and specimen parameters;
- analyses for capacity using a range of available methods; and
- development of techniques to estimate service-level prediction for fatigue evaluation.

Employing all of these elements, an assessment methodology that makes use of reliability concepts was developed. The research tasks and findings are described and the assessment methodology is applied to a bridge in the ODOT inventory as detailed below.

ASSESSMENT METHODOLOGY FOR DIAGONALLY CRACKED REINFORCED CONCRETE DECK GIRDERS

2.0 FIELD TESTING.....5

2.1 SPORES BRIDGE, I-5 NORTHBOUND OVER MCKENZIE RIVER (BRIDGE NUMBER 08175N) 5
2.1.1 Crack Identification and Mapping 6
2.1.2 Instrumentation 17
2.1.3 Testing Method 20
2.2 JASPER BRIDGE, OVER MIDDLE FORK OF WILLAMETTE RIVER (BRIDGE NUMBER 04117A) 34
2.2.1 Description of Tested Spans 34
2.2.2 Crack Mapping and Instrumentation 38
2.2.3 Testing Method 47
2.3 15 MILE CREEK BRIDGE, I84 EAST AND WESTBOUND, THE DALLES, OR (BRIDGE NUMBER 308A) 78
2.3.1 Description of Tested Spans 78
2.3.2 Crack Mapping and Instrumentation 82
2.3.3 Testing Method 88
2.4 AMBIENT TRAFFIC INDUCED STIRRUP STRESS 101
2.5 DYNAMIC INFLUENCE/IMPACT 106
2.6 LOAD DISTRIBUTION 108
2.7 COMBINED DEAD AND LIVE LOAD STRESS IN STIRRUPS 118
2.8 STIRRUPS STRESS DISTRIBUTIONS ACROSS A SINGLE CRACK 118
2.9 CONCLUSIONS.....118

List of Figures

Figure 2.1a: Design drawing for McKenzie River Bridge 6
Figure 2.1b: Design drawing for McKenzie River Bridge 7
Figure 2.1c: Design drawing for McKenzie River Bridge 8
Figure 2.2: Portion of McKenzie River Bridge selected for field investigation 9
Figure 2.3: ODOT crack comparator used to measure crack widths 10
Figure 2.4: Laser distance meter used to locate cracks and stirrups relative to support locations 10
Figure 2.5: Rebar locator used to identify embedded stirrups 11
Figure 2.6a: McKenzie bridge crack and instrument locations on span 8 12
Figure 2.6b: McKenzie bridge crack and instrument locations on span 9 13
Figure 2.6c: McKenzie bridge crack and instrument locations on span 10 14
Figure 2.6d: McKenzie bridge crack and instrument locations on span 11 15
Figure 2.6e: McKenzie bridge crack and instrument locations on bent caps 16
Figure 2.7: Concrete removed to expose stirrup and attach strain gage 17
Figure 2.8: Example instrumented location with strain gage and LVDT on McKenzie River Bridge 18
Figure 2.9: Schematic of sensor locations on McKenzie River Bridge 19
Figure 2.10: Truck classification based on triggered video at McKenzie River Bridge 21
Figure 2.11: Cargo type based on triggered video at McKenzie River Bridge 21
Figure 2.12a: Test truck with trailer for McKenzie River Bridge 22
Figure 2.12b: Truck with trailer axle spacing and weights for tests on McKenzie River Bridge 22
Figure 2.13: Truck lane positions on McKenzie River Bridge 23
Figure 2.14a: Stirrup stress response for test truck on north-bound fog line at 5 mph 24
Figure 2.14b: Stirrup stress response for test truck in north-bound truck lane at 5 mph 24
Figure 2.14c: Stirrup stress response for test truck in north-bound passing lane at 5 mph 25
Figure 2.14d: Stirrup stress response for test truck in north-bound truck lane at 55 mph 25
Figure 2.14e: Stirrup stress response for test truck in north-bound passing lane at 55 mph 26
Figure 2.14f: Stirrup stress response for test truck in north-bound truck lane at 64 mph 26
Figure 2.14g: Stirrup stress response for test truck in north-bound passing lane at 60 mph 27
Figure 2.14h: Stirrup stress response test truck with trailer on north-bound fog lane at 5 mph 27
Figure 2.14i: Stirrup stress response for test truck with trailer in north-bound truck lane at 5 mph 28
Figure 2.14j: Stirrup stress response for test truck with trailer in north-bound passing lane at 5 mph 28
Figure 2.14k: Stirrup stress response for test truck with trailer in north-bound truck lane at 54 mph 29
Figure 2.14l: Stirrup stress response test truck with trailer in north-bound passing lane at 55 mph 29
Figure 2.15a: Crack displacement-Stirrup stress response for test truck on north-bound fog line at 5 mph 30
Figure 2.15b: Crack displacement-Stirrup stress response for test truck in north-bound truck lane at 5 mph 30
Figure 2.15c: Crack displacement-Stirrup stress response for test truck in north-bound passing lane at 5 mph 31
Figure 2.15d: Crack displacement-Stirrup stress response for test truck with trailer on north-bound fog line at 5 mph 31
Figure 2.15e: Crack displacement-Stirrup stress response for test truck with trailer in north-bound truck lane at 5 mph 32
Figure 2.15f: Crack displacement-Stirrup stress response for test truck with trailer in north-bound passing lane at 5 mph 32
Figure 2.16a: Design drawings for Jasper Bridge 35
Figure 2.16b: Design drawings for Jasper Bridge 36
Figure 2.16c: Design drawings for Jasper Bridge 37
Figure 2.17: Portion of Jasper Bridge selected for field investigation 38
Figure 2.18a: Jasper Bridge crack and instrument locations on span 4 39
Figure 2.18b: Jasper Bridge crack and instrument locations on span 5 40
Figure 2.18c: Jasper Bridge crack and instrument locations on span 6 41
Figure 2.18d: Jasper Bridge crack and instrument locations on span 7 42
Figure 2.18e - Jasper Bridge crack and instrument locations on span 8 43
Figure 2.18f: Jasper Bridge crack and instrument locations on span 9 44

Figure 2.18g: Jasper Bridge crack and instrument locations on bent caps 45
Figure 2.19: Schematic of sensor locations on Jasper Bridge 46
Figure 2.20: Classification of vehicle configuration based on video data from Jasper Bridge 47
Figure 2.21: Classification of cargo type based on video data from Jasper Bridge 48
Figure 2.22a: Test truck used on Jasper Bridge 49
Figure 2.22b: Truck axle spacing and weights for tests on Jasper Bridge 49
Figure 2.23: Truck position relative to girders for tests on Jasper Bridge 50
Figure 2.24a: Stirrup stress response for test truck heading northbound on curb at 3 mph 51
Figure 2.24b: Stirrup stress response for test truck heading northbound centered over first interior girder at 3 mph 51
Figure 2.24c: Stirrup stress response for test truck heading northbound centered over second interior girder at 3 mph 52
Figure 2.24d: Stirrup stress response for test truck heading southbound on curb at 3 mph 52
Figure 2.24e: Stirrup stress response for test truck heading southbound centered over first interior girder at 3 mph 53
Figure 2.24f: Stirrup stress response for test truck heading southbound centered over second interior girder at 3 mph 53
Figure 2.24g: Stirrup stress response for test truck in northbound lane at 5 mph 54
Figure 2.24h: Stirrup stress response for test truck in southbound lane at 5 mph 54
Figure 2.24i: Stirrup stress response for test truck in northbound lane at 34 mph 55
Figure 2.24j: Stirrup stress response for test truck in southbound lane at 32 mph 55
Figure 2.25a: Crack displacement-Stirrup stress response for test truck in northbound lane at 5 mph 56
Figure 2.25b: Crack displacement-Stirrup stress response for test truck in northbound lane at 5 mph 56
Figure 2.26: Static positioning of test truck along curb for Jasper Bridge 58
Figure 2.27: Static positioning locations for test truck on Jasper Bridge 59
Figure 2.28: Axle weights and spacing for series of trucks crossing the Jasper Bridge 62
Figure 2.29a: Truck photograph and stress history produced for Truck #1 March 20, 2003 64
Figure 2.29b: Truck photograph and stress history produced for Truck #2 (note that first rear axle is not on roadway) 65
Figure 2.29c: Truck photograph and stress history produced for Truck #3 66
Figure 2.29d: Truck photograph and stress history produced for Truck #4 67
Figure 2.29e: Truck photograph and stress history produced for Truck #5 68
Figure 2.29f: Truck photograph and stress history produced for Truck #6 69
Figure 2.29g: Truck photograph and stress history produced for Truck #7 70
Figure 2.29h: Truck photograph and stress history produced for Truck #8 on April 1, 2003 71
Figure 2.29i: Truck photograph and stress history produced for Truck #9 72
Figure 2.29j: Truck photograph and stress history produced for Truck #10 73
Figure 2.29k: Truck photograph and stress history produced for Truck #11 74
Figure 2.30a: Maximum stirrup stress produced for each known truck gross vehicle weight crossing Jasper Bridge 76
Figure 2.30b: Maximum stirrup stress produced for the maximum tandem weight on each known truck crossing Jasper Bridge 77
Figure 2.30c: Maximum stirrup stress produced for the axle weight within an 11 ft length on each known truck crossing Jasper Bridge 77
Figure 2.31a: Design drawings for 15 Mile Creek Bridge 79
Figure 2.31b: Design drawings for 15 Mile Creek Bridge 80
Figure 2.31c: Design drawings for 15 Mile Creek Bridge 81
Figure 2.32: Portion of 15 Mile Creek Bridge selected for field investigation 82
Figure 2.33a: 15 Mile Creek Bridge crack, stirrup, and instrumentation locations on span 5 eastbound 83
Figure 2.33b: 15 Mile Creek Bridge crack, stirrup, and instrumentation locations on span 4 eastbound 84
Figure 2.33c: 15 Mile Creek Bridge crack, stirrup, and instrumentation locations on span 5 westbound 85
Figure 2.33d: 15 Mile Creek Bridge crack, stirrup, and instrumentation locations on span 4 westbound 86
Figure 2.33e: 15 Mile Creek Bridge crack, stirrup, and instrumentation locations on bent caps 87
Figure 2.34: Schematic locations of instrumentation on 15 Mile Creek Bridge 88
Figure 2.35a: Test truck used on 15 Mile Creek Bridge 89
Figure 2.35b: Axle weights and spacing for test truck used on 15 Mile Creek Bridge 90

Figure 2.36: Test truck lane location relative to girder positions on 15 Mile Creek Bridge 90
Figure 2.37a: Stirrup stress response for test truck in east-bound truck lane at 5 mph 91
Figure 2.37b: Stirrup stress response for test truck in east-bound passing lane at 5 mph..... 91
Figure 2.37c: Stirrup stress response for test truck in east-bound truck lane at 55 mph 92
Figure 2.37d: Stirrup stress response for test truck in east-bound passing lane at 55 mph..... 92
Figure 2.37e: Stirrup stress response for test truck in east-bound truck lane at 65 mph 93
Figure 2.37f: Stirrup stress response for test truck in east-bound passing lane at 65 mph 93
Figure 2.37g: Stirrup stress response for test truck in west-bound truck lane at 5 mph 94
Figure 2.37h: Stirrup stress response for test truck in west-bound passing lane at 5 mph..... 94
Figure 2.37i: Stirrup stress response for test truck in west-bound truck lane at 55 mph 95
Figure 2.37j: Stirrup stress response for test truck in west-bound passing lane at 55 mph..... 95
Figure 2.37k: Stirrup stress response for test truck in west-bound truck lane at 65 mph 96
Figure 2.37l: Stirrup stress response for test truck in west-bound passing lane at 65 mph..... 96
Figure 2.38a: Crack displacement-Stirrup stress response for test truck in east-bound truck lane at 5 mph..... 97
Figure 2.38b: Crack displacement-Stirrup stress response for test truck in east-bound passing lane at 5 mph..... 97
Figure 2.38c: Crack displacement-Stirrup stress response for test truck in west-bound truck lane at 5 mph..... 98
Figure 2.38d: Crack displacement-Stirrup stress response for test truck in west-bound passing lane at 5 mph..... 98
Figure 2.39a: S-N response for all instrumented locations on McKenzie River Bridge for period of 8.15 days..... 101
Figure 2.39b: S-N response for all instrumented locations on Jasper Bridge for period of 11.9 days 102
Figure 2.39c: S-N response for all instrumented locations on 15 Mile Creek Bridge for period of 8.1 days... 102
Figure 2.40: Fatigue behavior of reinforcing steel (*MacGregor 1997*) 106
Figure 2.41: Impact coefficients for all three field study bridges 107

List of Tables

Table 2.1: Maximum and minimum stresses and stress ranges at instrumented locations for test truck (with and without trailer) on McKenzie River Bridge 33
Table 2.2a: Stresses at instrumented locations for slow speed tests of ODOT truck moving over Jasper Bridge 57
Table 2.2b: Maximum stress at instrumented locations for traveling speed tests of ODOT truck moving over Jasper Bridge 57
Table 2.3a: Stresses at instrumented locations when ODOT truck oriented northbound against the north curb and stationary with steering axle over bents for Jasper Bridge 60
Table 2.3b: Stresses at instrumented locations when ODOT truck oriented southbound against the north curb and stationary with steering axle over bents for Jasper Bridge 60
Table 2.3c: Stresses at instrumented locations when ODOT truck oriented northbound against the south curb and stationary with steering axle over bents for Jasper Bridge 60
Table 2.3d: Stresses at instrumented locations when ODOT truck oriented southbound against the south curb and stationary with steering axle over bents for Jasper Bridge 60
Table 2.4: Truck and axle weights from field measured trucks on Jasper Bridge 63
Table 2.5a: Maximum stresses for real trucks on Jasper Bridge 75
Table 2.5b: Minimum stresses for real trucks on Jasper Bridge 75
Table 2.5c: Stress ranges for real trucks on Jasper Bridge 75
Table 2.6a: Maximum and minimum stresses and stress ranges at instrumented locations for test truck westbound on 15 Mile Creek Bridge 99
Table 2.6b: Maximum and minimum stresses and stress ranges at instrumented locations for test truck eastbound on 15 Mile Creek Bridge 100
Table 2.7a: Equivalent constant amplitude stress range for instrumented locations on McKenzie bridge 103
Table 2.7b: Equivalent constant amplitude stress range for instrumented locations on Jasper Bridge 104
Table 2.7c: Equivalent constant amplitude stress range for instrumented locations on 15 Mile Creek Bridge 105
Table 2.8: - Statistical analysis of impact coefficients 108
Table 2.9a: Girder distribution for ODOT truck and truck and trailer traveling at crawl speed and located in different lane positions on McKenzie River Bridge (Note: TT is truck with trailer see Figure F12b) 110
Table 2.9b: Girder distribution for real trucks traveling northbound on Jasper Bridge 111
Table 2.9c: Girder distribution for ODOT truck traveling at crawl speed and located in different lane positions on Jasper Bridge 112
Table 2.9d: Girder distribution for static truck position #2 on Jasper Bridge 113
Table 2.9e: Girder distribution for ODOT truck traveling at crawl speed and located in different lane positions on 15 Mile Creek Bridge 114
Table 2.10: Wheel load distribution factor by lever rule (AASHTO Standard Specification) 116
Table 2.11: Lane load distribution by AASHTO LRFD Specification 116
Table 2.12: Load distribution factors for controlling cases by AASHTO LRFD Specification and Standard Specifications 117

2.0 FIELD TESTING

Four bridges were investigated during the field testing portion of the research program. These bridges were: Willamette River Bridge on OR 219 near Newberg, OR; Spores Bridge on northbound I-5 over the McKenzie River; Jasper Bridge over the Middle Fork of the Willamette River near Jasper, OR; and 15 Mile Creek Bridge consisting of both east and westbound I-84 east of The Dalles, OR. Data and results from the Willamette River Bridge are detailed in a separate report (*Higgins, et al. 2004*). Spores Bridge, Jasper Bridge, and 15 Mile Creek Bridge are described below.

2.1 SPORES BRIDGE, I-5 NORTHBOUND OVER MCKENZIE RIVER (BRIDGE NUMBER 08175N)

Spores Bridge crosses the McKenzie River on Interstate 5 in Lane County at the Linn County line. The bridge consists of 11 spans (Figures 2.1a-c): four (4) reinforced concrete deck girder approach spans at each end, and three (3) reinforced concrete box-girder main spans. The bridge was constructed in 1960. The south approach spans of the northbound lane of Spores Bridge, shown in Figure 2.2, were selected for testing due to ease of accessibility and no need for traffic control. The names McKenzie River Bridge and Spores Bridge are used interchangeably in this report.

The south approach spans are each 50 ft long from centerline of supports. The south-most span is a simple span, followed by a 3-span continuous portion. The spans support a roadway width of 30 ft, and have a total width of 35 ft - 2 in.. There are four girder lines in each of the spans, with diaphragms 9 in. x 46 in. located at the quarter points. The girders are 14.5 in. x 48 in. uniform and prismatic along the simple span. In the continuous spans, the girders are 13 in. x 48 in. over the middle half of the spans, but the web widths taper to become wider 20 in. x 48 in. at continuous support locations. Bent caps are 16.5 in. x 75 in. and supported on 20 in. square columns. The reinforced concrete deck is 6 in. thick. The specified concrete compression strength was 3300 psi and the reinforcing steel consisted of intermediate grade (nominally 40 ksi yield stress) deformed round bars.

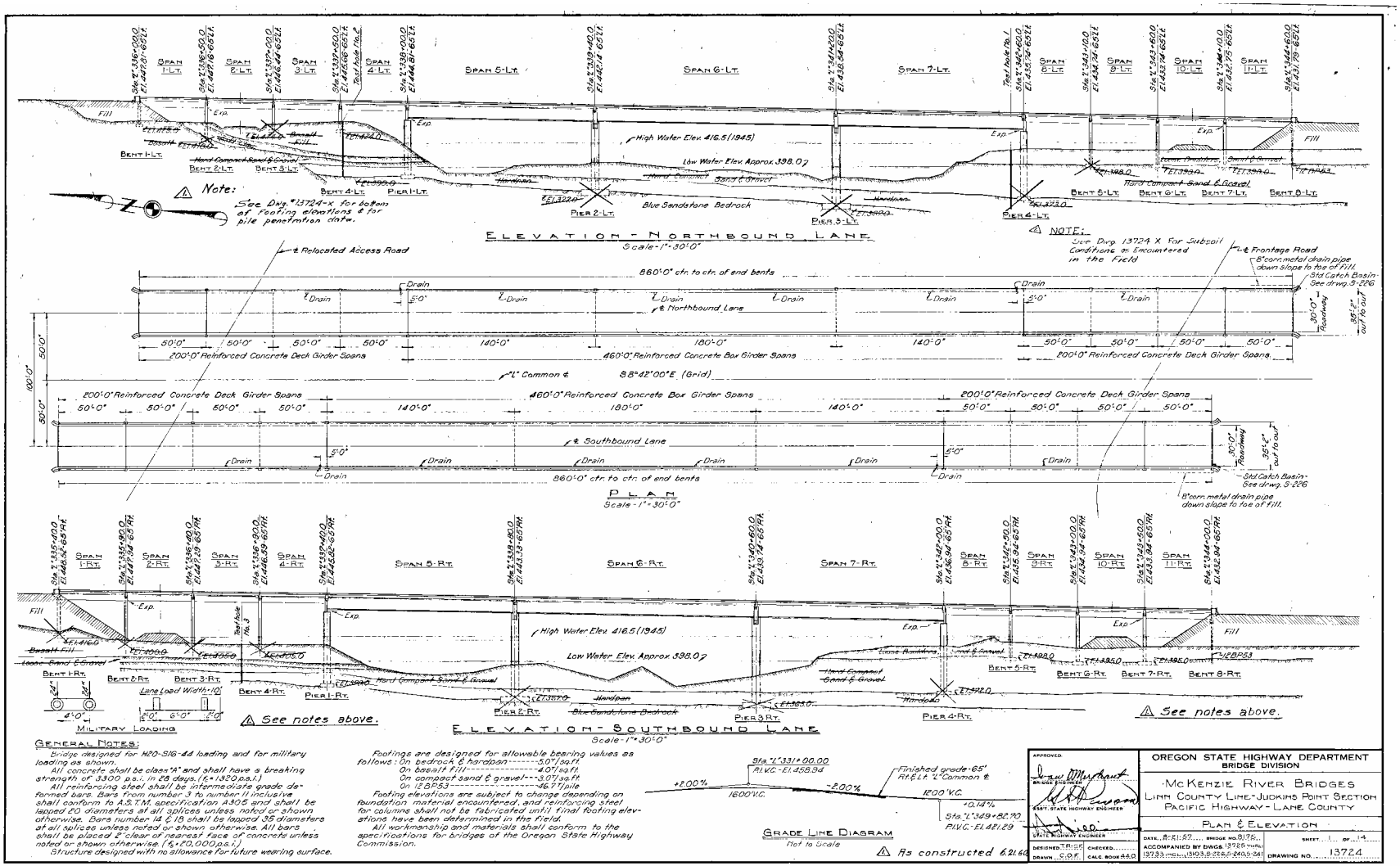

Figure 2.1a: Design drawing for McKenzie River Bridge

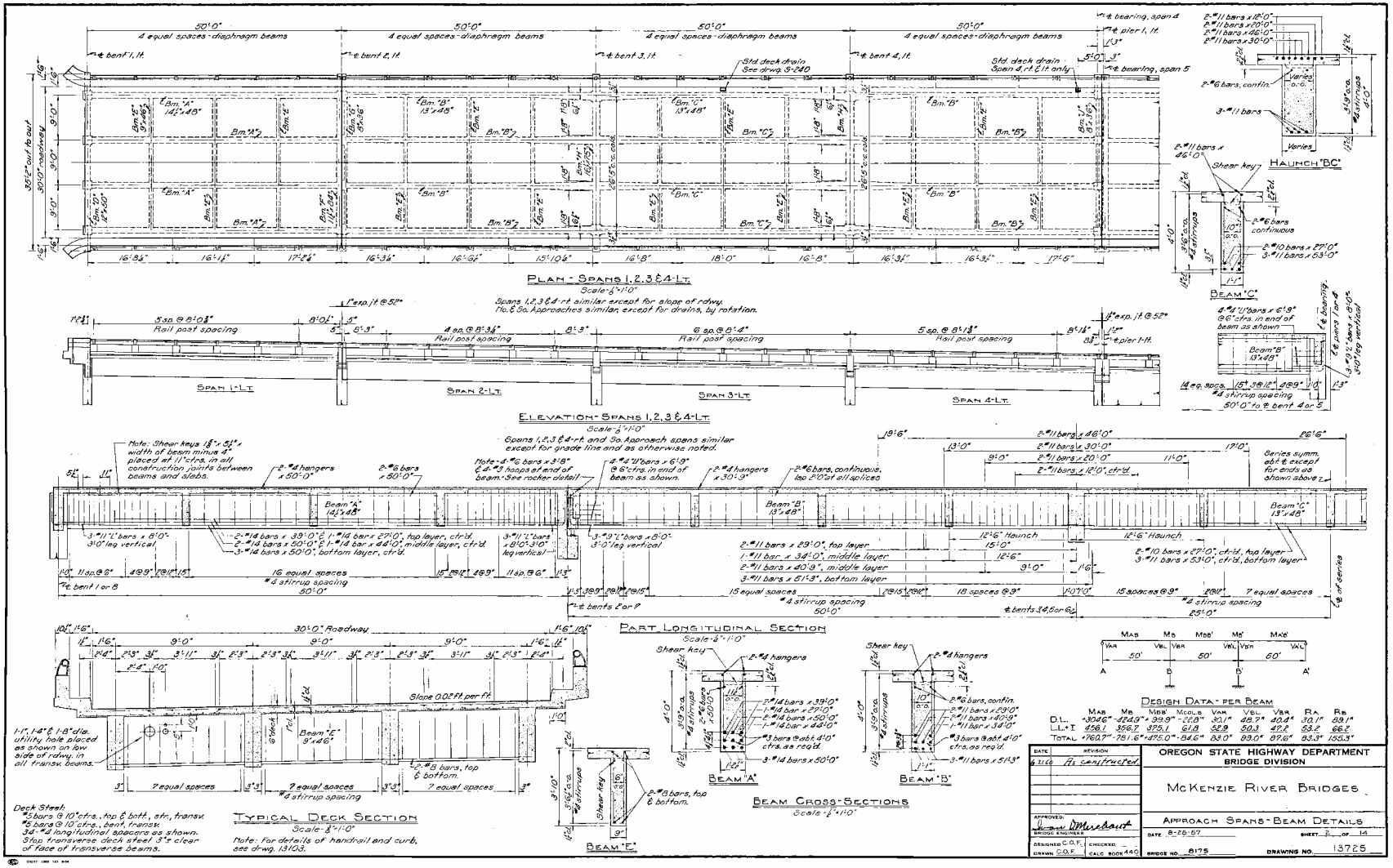

Figure 2.1b: Design drawing for McKenzie River Bridge

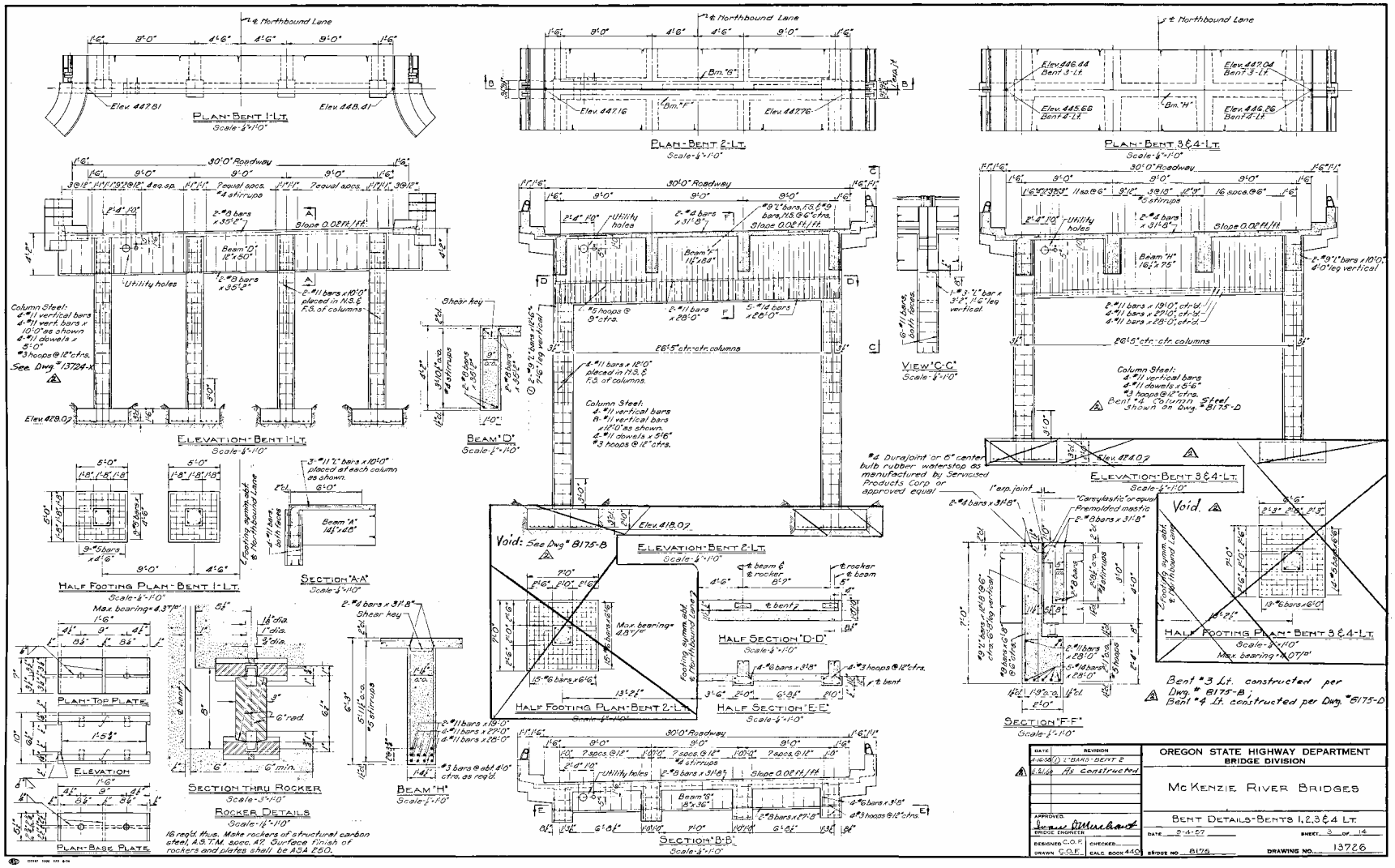

Figure 2.1c: Design drawing for McKenzie River Bridge

Figure 2.2: Portion of McKenzie River Bridge selected for field investigation

2.1.1 Crack Identification and Mapping

All bent caps and longitudinal deck girders were inspected to determine the extent of diagonal tension and flexural cracking. Crack widths were measured using an ODOT crack comparator, as shown in Figure 2.3. The location of each crack having a width of 0.008 in. or larger was measured and recorded using a Leica Disto Pro[4] hand-held laser distance meter, as shown in Figure 2.4.

Locations of stirrups were identified using a Proceq Profometer 3 rebar locator, as shown in Figure 2.5, and recorded using the laser distance meter. Stirrup locations and the extents and widths of existing diagonal cracks on the face of each structural element are shown in Figures 2.6a-e.

Diagonal tension cracks were observed in bent caps, interior girders and exterior girders. In general, cracking of the exterior girders was found to be more severe than cracking of the interior girders, with wider and more numerous cracks in the exterior girders compared to adjacent interior girders.

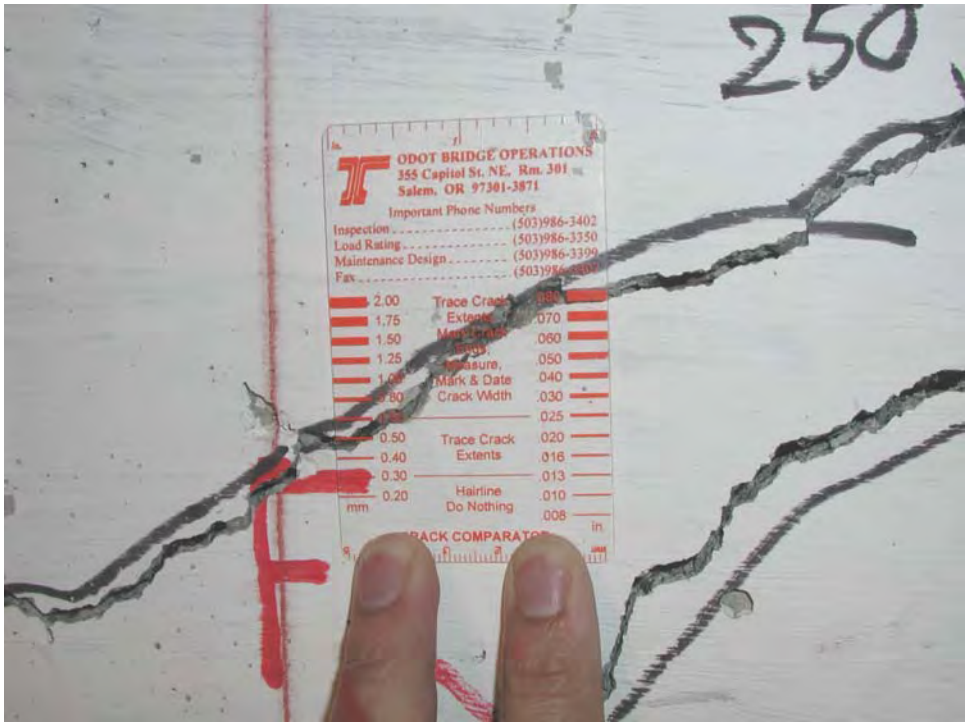

Figure 2.3: ODOT crack comparator used to measure crack widths

Figure 2.4: Laser distance meter used to locate cracks and stirrups relative to support locations

Figure 2.5: Rebar locator used to identify embedded stirrups

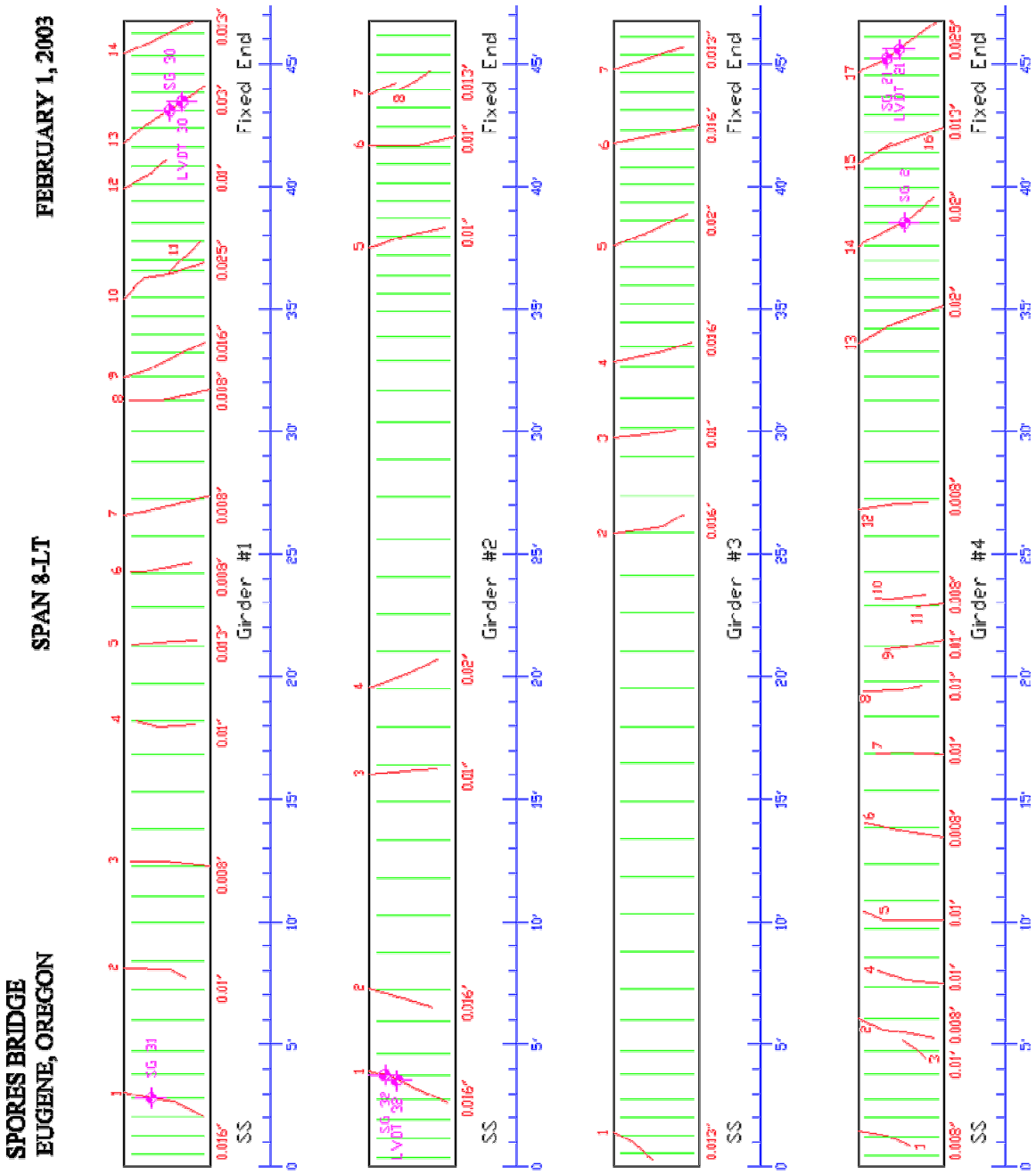

Figure 2.6a: McKenzie bridge crack and instrument locations on span 8

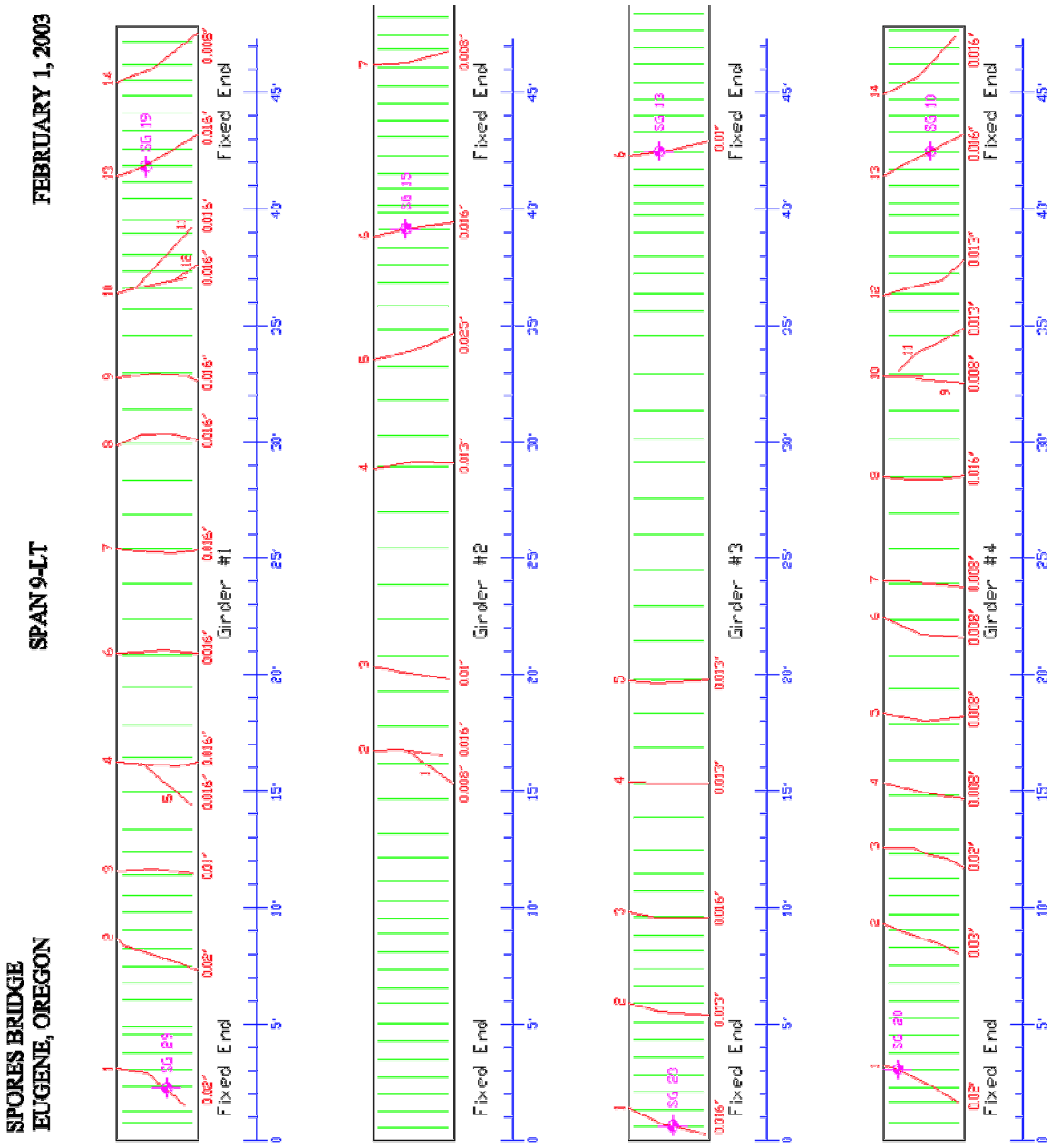

Figure 2.6b: McKenzie bridge crack and instrument locations on span 9

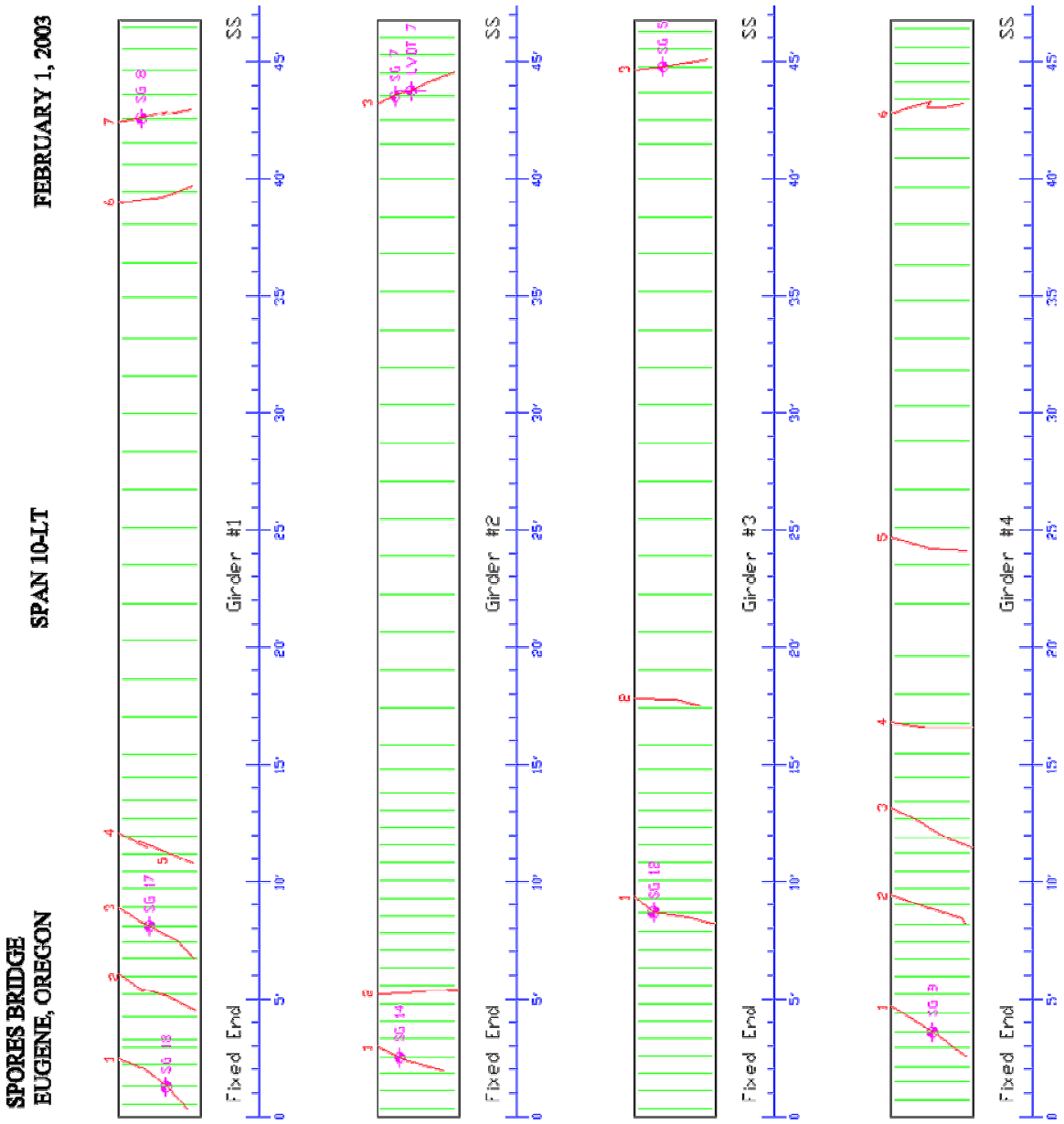

Figure 2.6c: McKenzie bridge crack and instrument locations on span 10

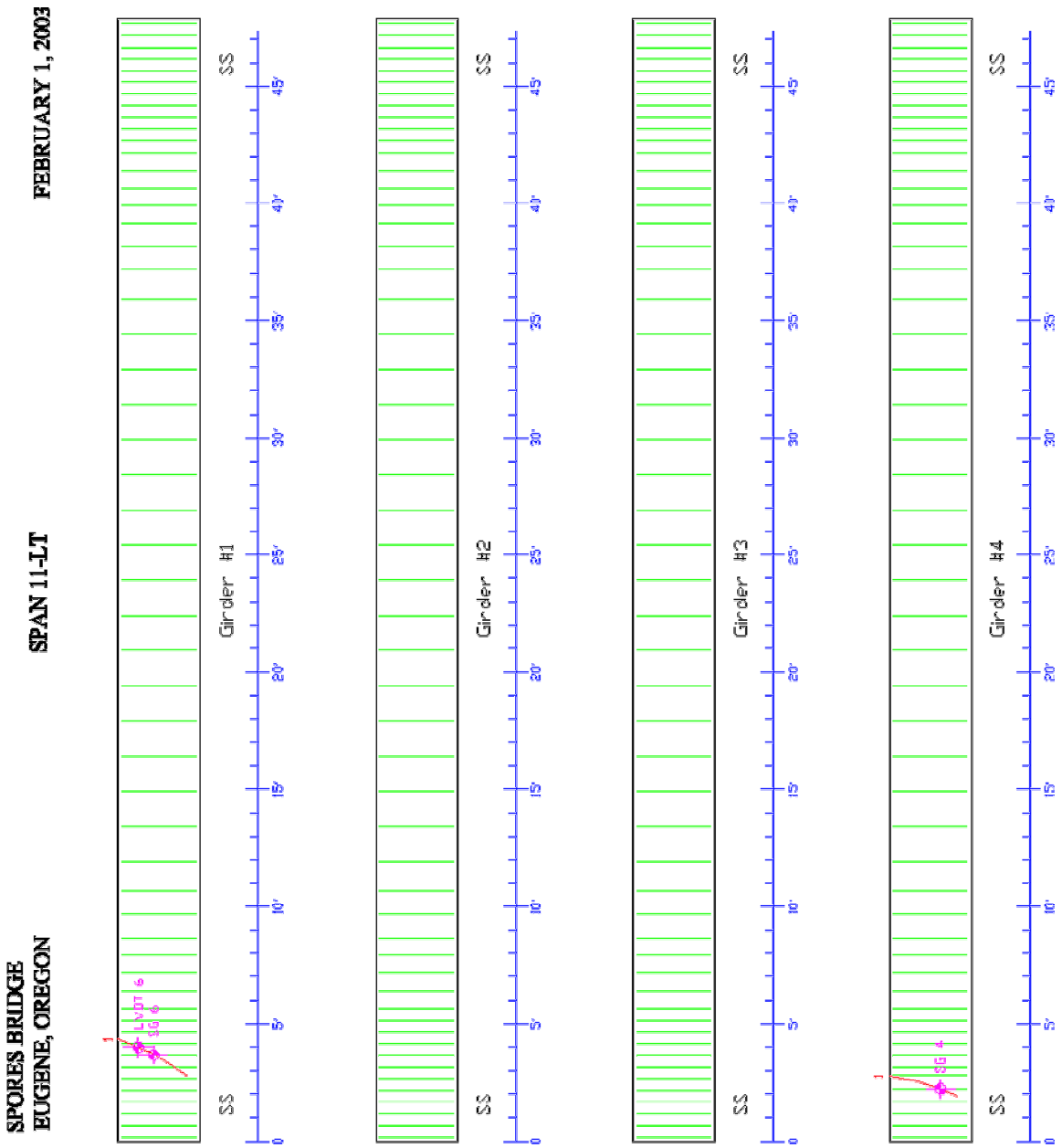

Figure 2.6d: McKenzie bridge crack and instrument locations on span 11

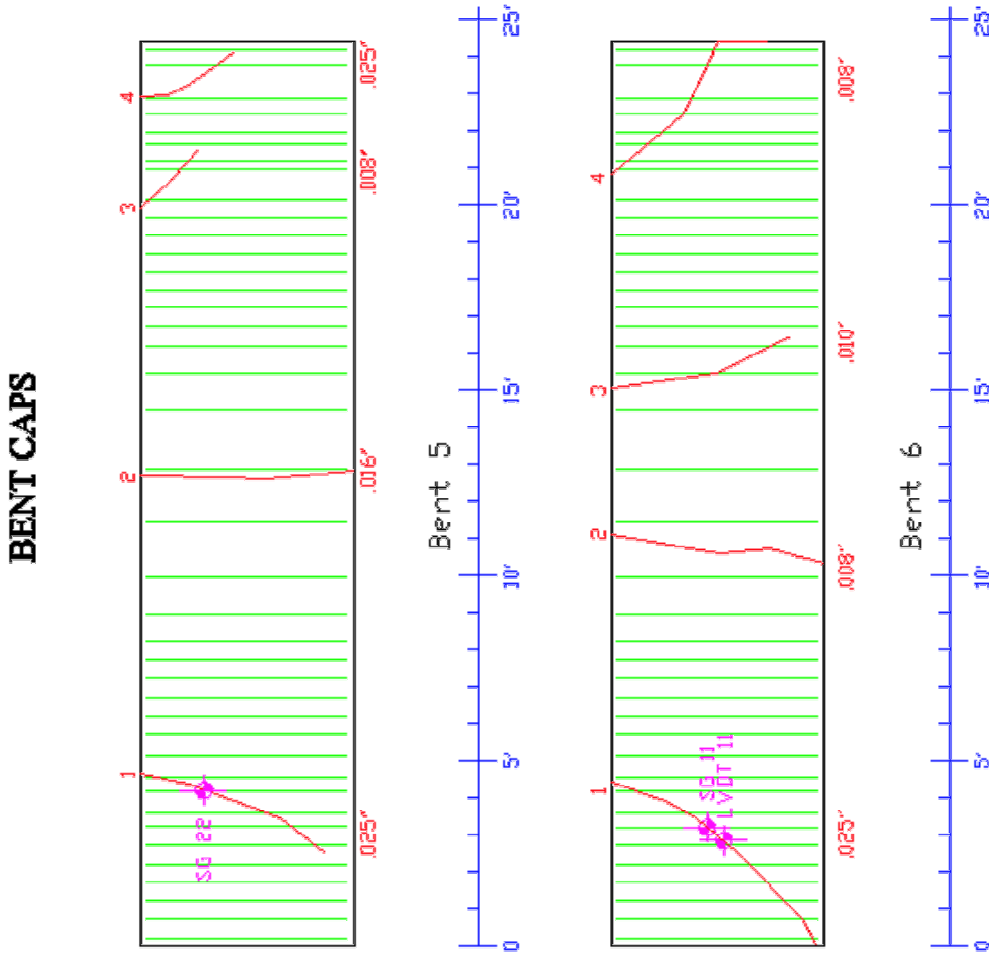

Figure 2.6e: McKenzie bridge crack and instrument locations on bent caps

2.1.2 Instrumentation

After inspection, strain gages and displacement transducers were installed at selected diagonal crack locations. Instrumentation locations were chosen for regions that experience relatively high live-load shear forces and for relatively wide diagonal cracks. Preference was given to diagonal cracks that crossed stirrups at approximately mid-height of the girder web. Strain gages were used to measure the stress carried by stirrups across diagonal cracks and linear position sensors were used to measure crack displacement during traffic loading. Strain gages were installed by chipping into the concrete and exposing the embedded stirrup at the crack location. The actual amount of concrete removed depended on the concrete cover, but typical concrete removal provided an exposed stirrup length of approximately 4 in. overall, centered about the crack, as shown in Figure 2.7.

Figure 2.7: Concrete removed to expose stirrup and attach strain gage

The width of the excavation was approximately 3 in. permitting preparation of the rebar surface for bonding strain gages on the stirrup leg. The deformation pattern was generally not removed to install the strain gage unless the vertical rib was located on the outside face. The chosen strain gage size (Measurements Group strain gage EA-06-062AQ-350, with a gage length of 1/16 in.) permitted installation within the deformation pattern of the stirrups. This strain gage is a bondable type gage with a 350 ohm resistance.

Position sensors were surface mounted at selected strain gage locations across a diagonal crack. A typical installation of a strain gage and position sensor is shown in Figure 2.8. Strain gages were installed in 24 different locations on the bridge. Crack displacement sensors were also installed at six (6) of these locations. Instrumented locations are illustrated schematically in Figure 2.9 and precise locations are shown in Figures 2.6a-e.

Figure 2.8: Example instrumented location with strain gage and LVDT on McKenzie River Bridge

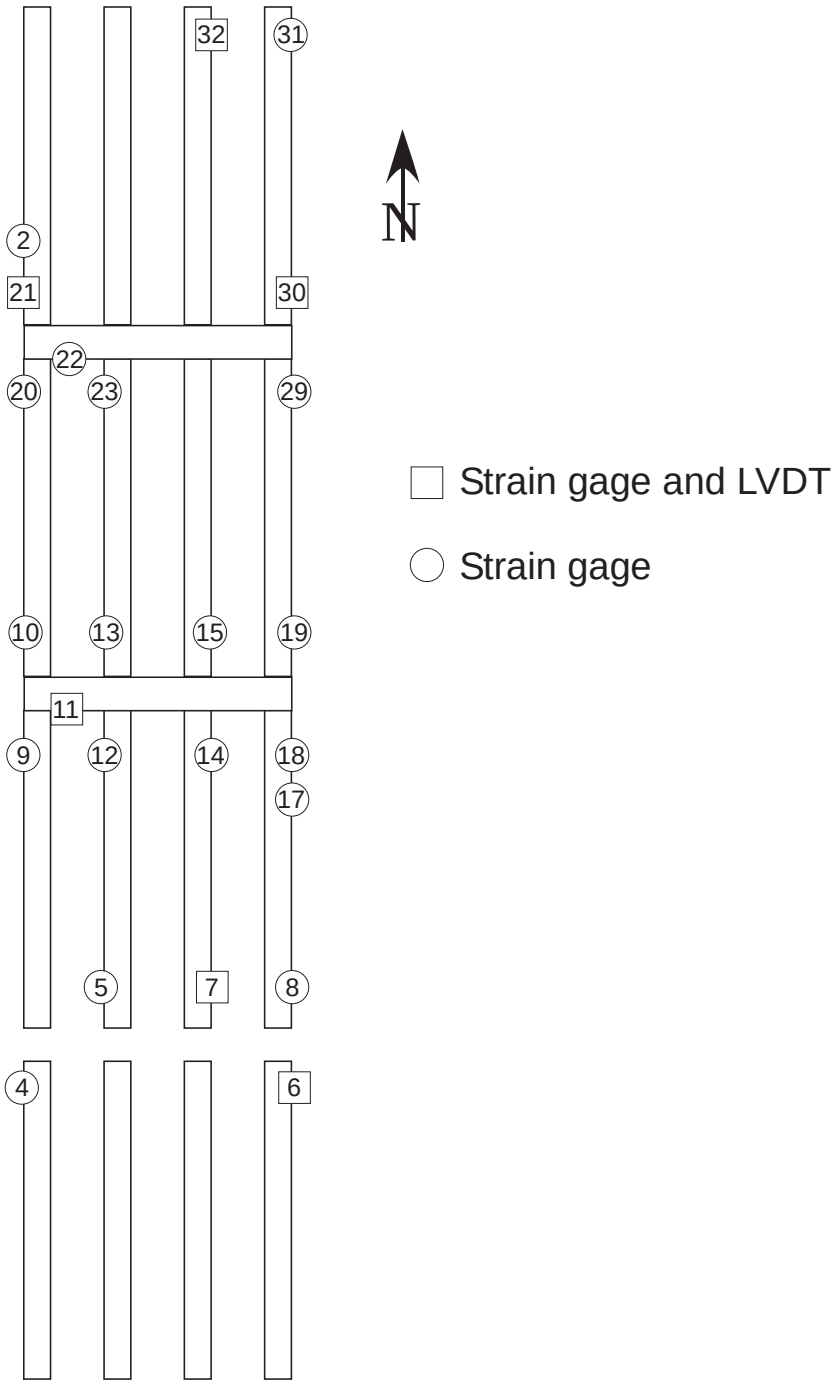

Figure 2.9: Schematic of sensor locations on McKenzie River Bridge

The strain gages and position sensors were connected to a Campbell Scientific CR9000 data logger. This is a high-speed, multi-channel, 16-bit digital data acquisition system. In order to reduce noise and prevent aliasing in the data, both analog and digital filters were employed. During the ambient monitoring period, data were sampled at 100 Hz. A digital high-pass filter

was utilized with a cut-off frequency of 40 Hz. The system recorded sensor readings and converted signals into corresponding rebar stresses and crack displacements.

Data from sensors were archived for retrieval and post-processing. The data acquisition system also included a digital video camera capable of capturing high-resolution images of traffic crossing the bridge.

2.1.3 Testing Method

Two series of live load data were collected: response under ambient traffic loading and response under controlled truck loading. The stirrup reinforcing stresses and crack displacements generated by normal traffic flow were recorded over a period of 8 calendar days in February and March, 2003.

The system also recorded individual event histories when stress thresholds exceeded 5.5 ksi at sensor location CH_7 or 2.0 ksi at location CH_21. For each trigger event, data were recorded for three seconds prior to and following the trigger. During these events, a video image of the corresponding vehicle was produced. These video images, taken during daylight hours (which enabled identification of the vehicle configurations) were used to determine a vehicle type and the axle configurations during larger stress events.

The observed vehicle configurations are summarized in Figure 2.10 according to ODOT vehicle classification charts and in Figure 2.11 according to the type of cargo carried by the vehicle. The most common axle configuration observed was the 3S2 and the most frequently observed cargo type was approximately evenly divided between carrier box and forest products (including log and chip trucks as well as those caring finished wood products).

Controlled truck tests were conducted using a heavily loaded ODOT maintenance truck, as shown in Figure 2.12a. Tests were conducted using the truck with trailer combination, as well as with the truck alone. The axle weights and spacing were determined before the test and are shown in Figure 2.12b. Traffic was temporarily slowed with the use of a rolling roadblock so that the control truck would be the only vehicle on the bridge during data collection.

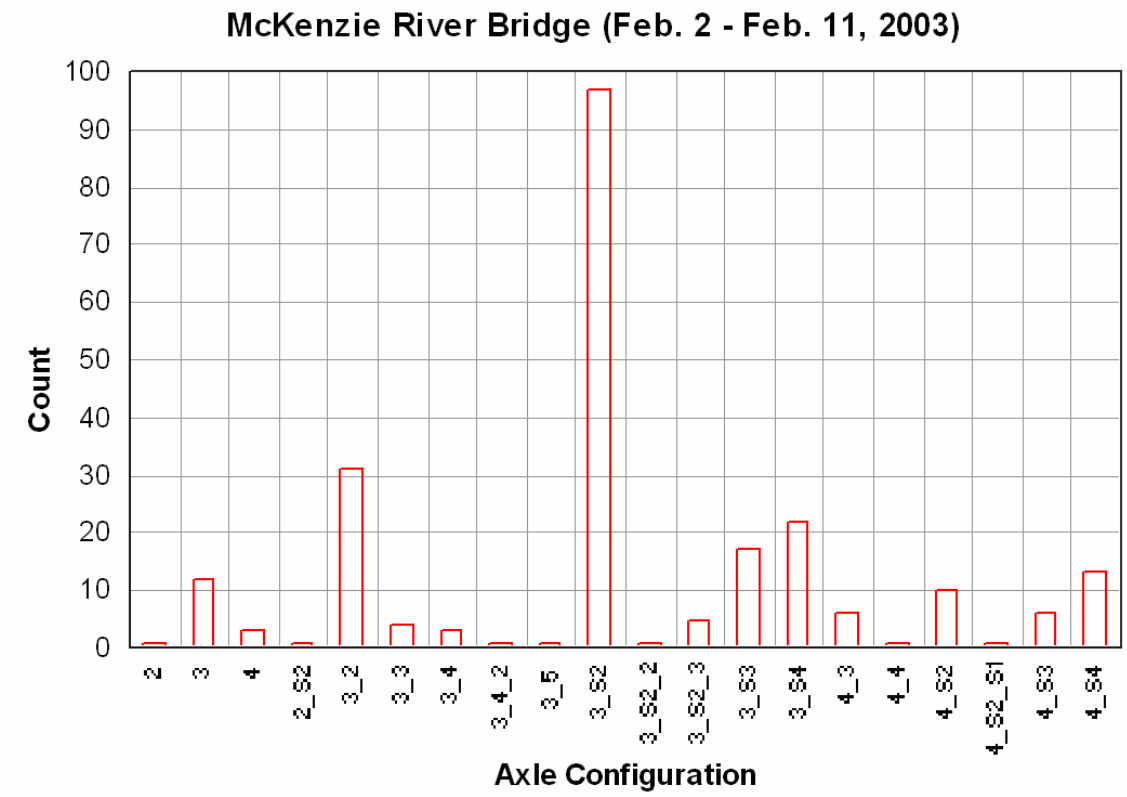

Figure 2.10: Truck classification based on triggered video at McKenzie River Bridge

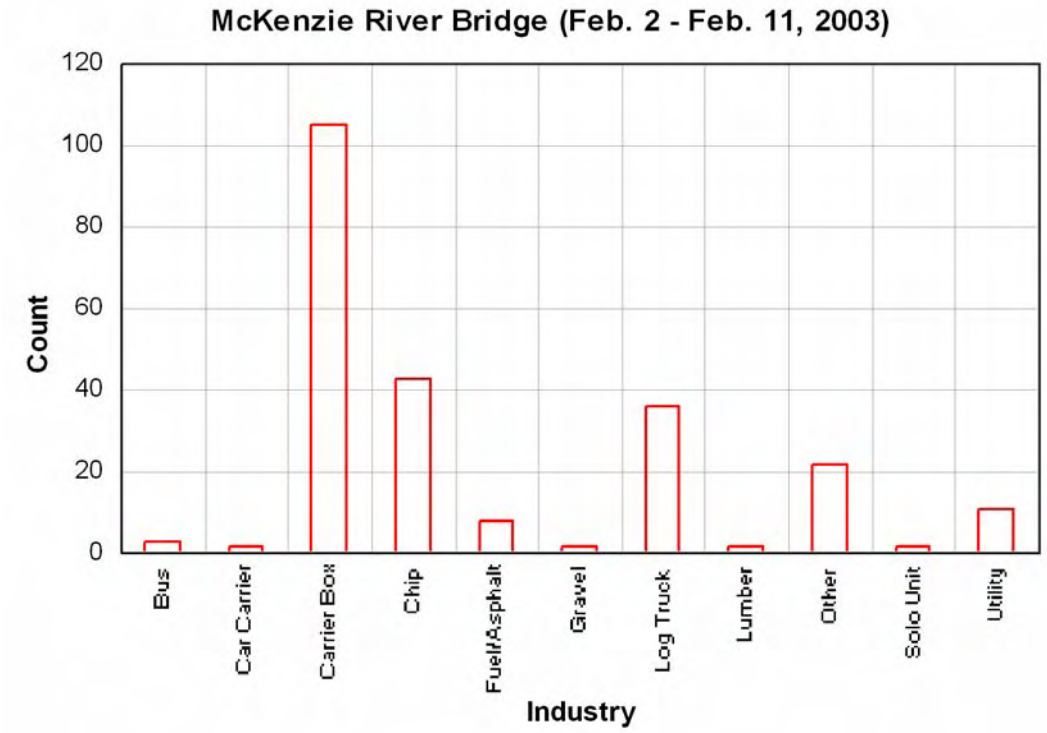

Figure 2.11: Cargo type based on triggered video at McKenzie River Bridge

Figure 2.12a: Test truck with trailer for McKenzie River Bridge

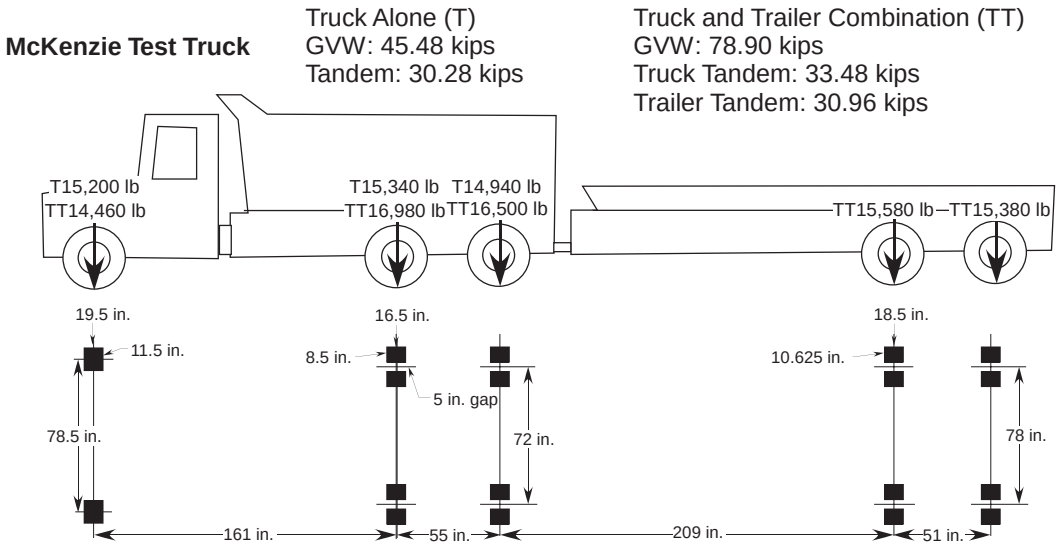

Figure 2.12b: Truck with trailer axle spacing and weights for tests on McKenzie River Bridge

The control truck passed over the bridge at several designated speeds and lane positions. Test speeds varied from 5 mph to 65 mph. Lane locations included placing the truck in the truck lane, in the passing lane, and the passenger side tires located on the fog line. Lane positions and the corresponding truck positions relative to the girder locations are illustrated in Figure 2.13.

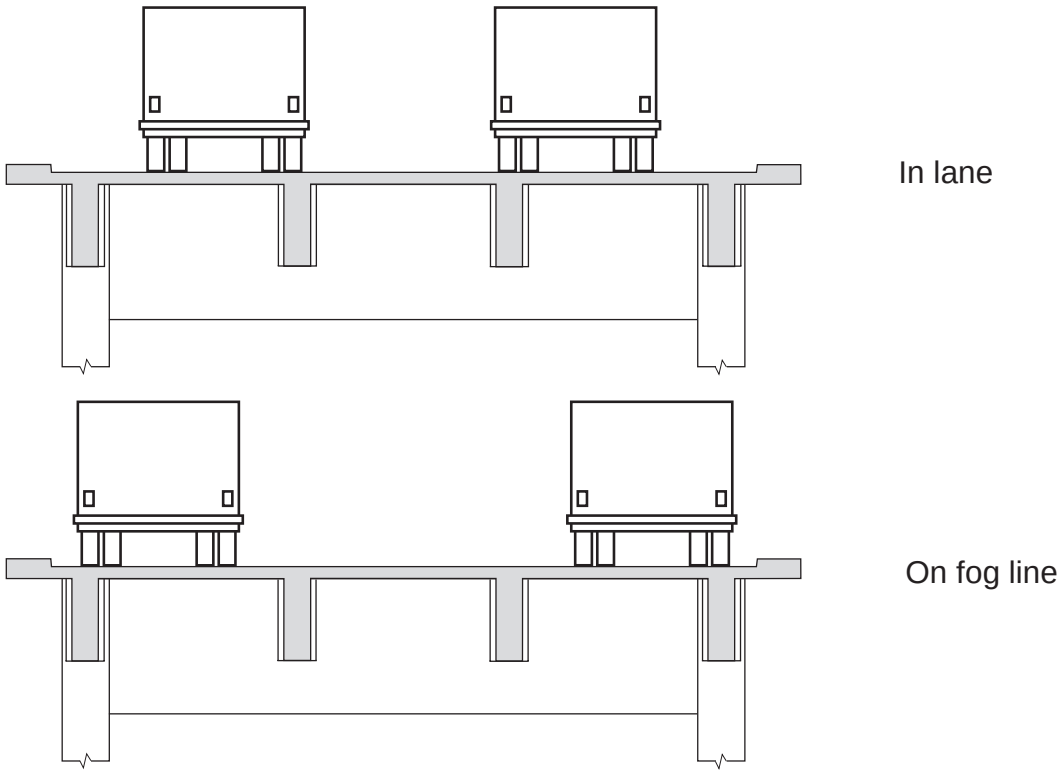

Figure 2.13: Truck lane positions on McKenzie River Bridge

During each pass of the control truck, stirrup stresses and crack deflections were recorded for each instrumented location. Stirrup stress histories for each of the test runs are shown in Figures 2.14a-l and the crack motions are shown in Figures 2.15a-f. Peak values and stress ranges are summarized in Table 2.1.

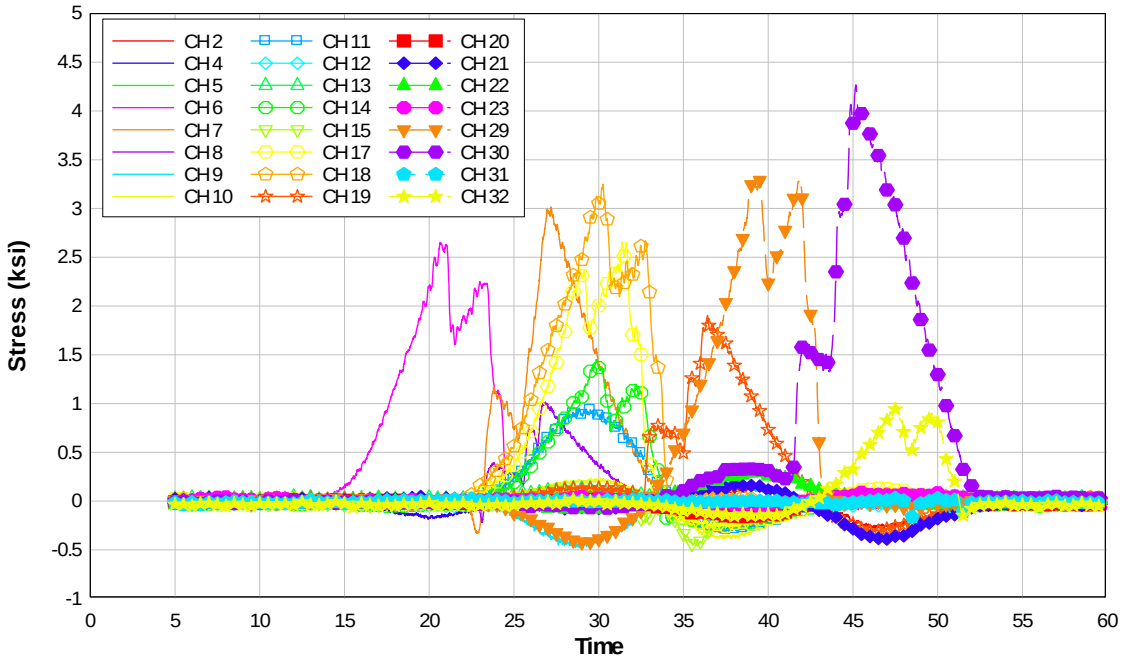

Figure 2.14a: Stirrup stress response for test truck on north-bound fog line at 5 mph

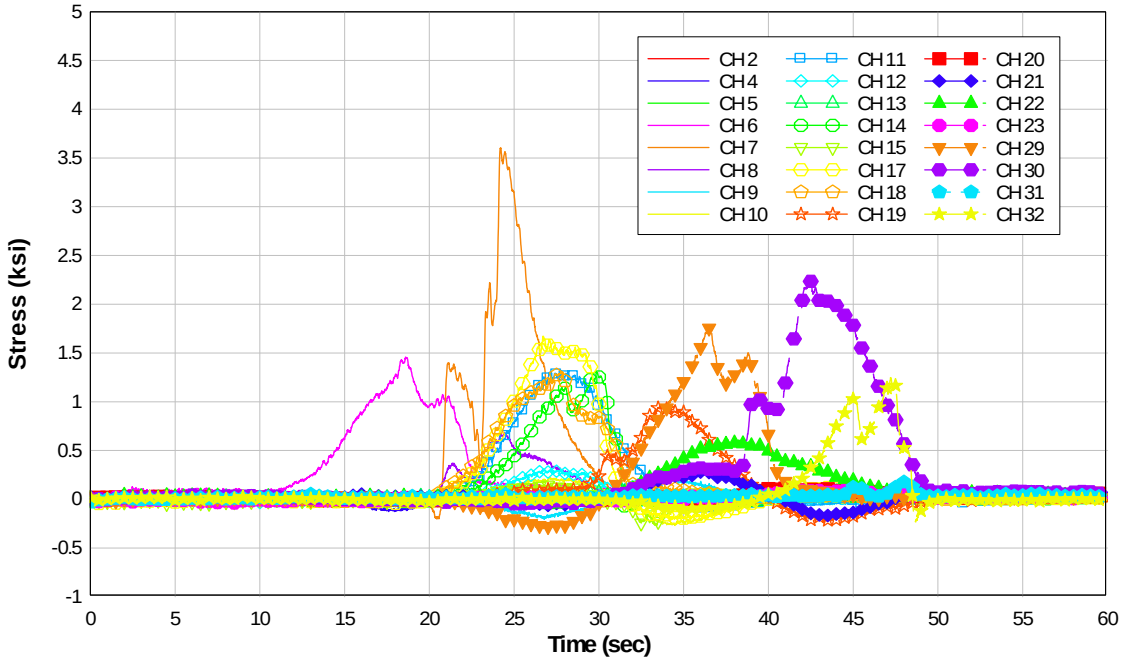

Figure 2.14b: Stirrup stress response for test truck in north-bound truck lane at 5 mph

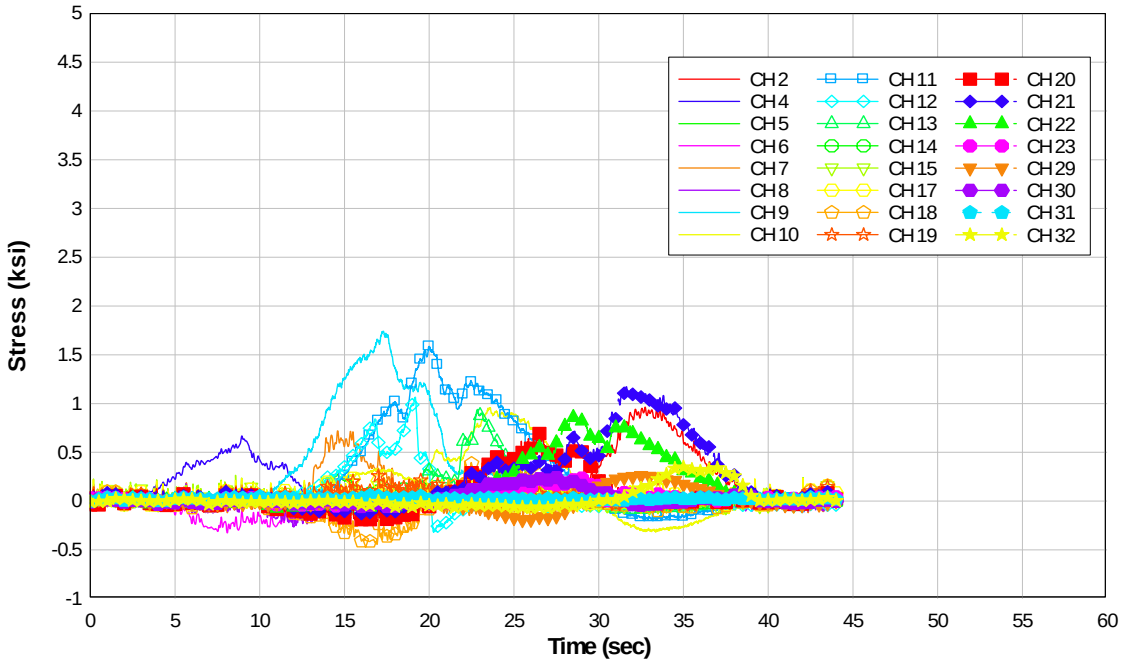

Figure 2.14c: Stirrup stress response for test truck in north-bound passing lane at 5 mph

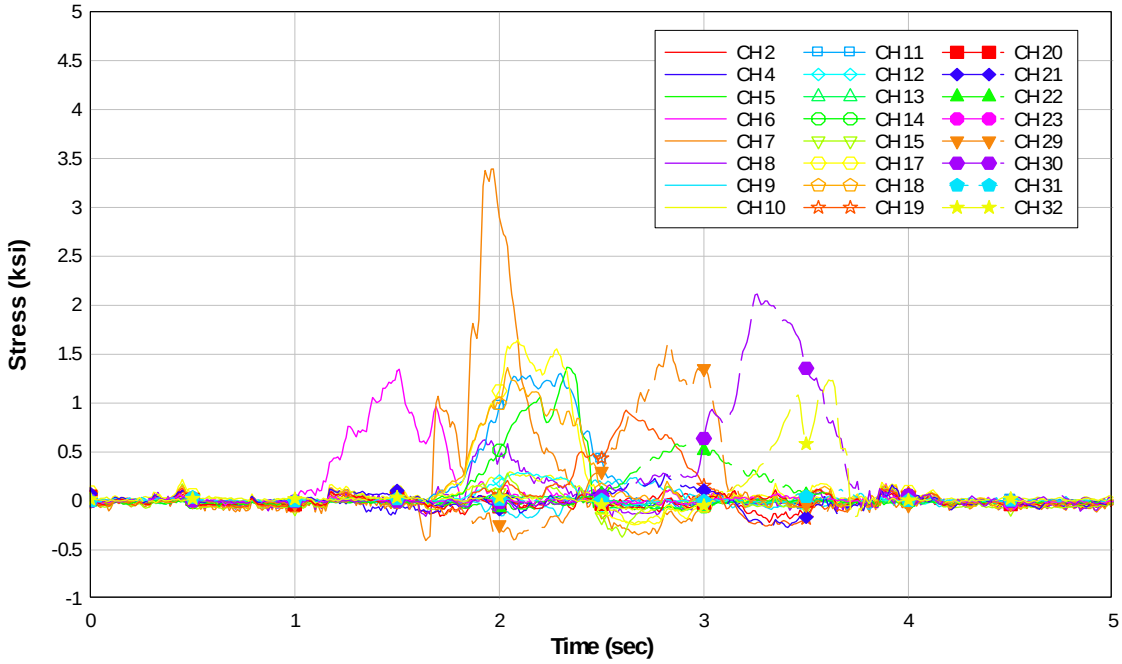

Figure 2.14d: Stirrup stress response for test truck in north-bound truck lane at 55 mph

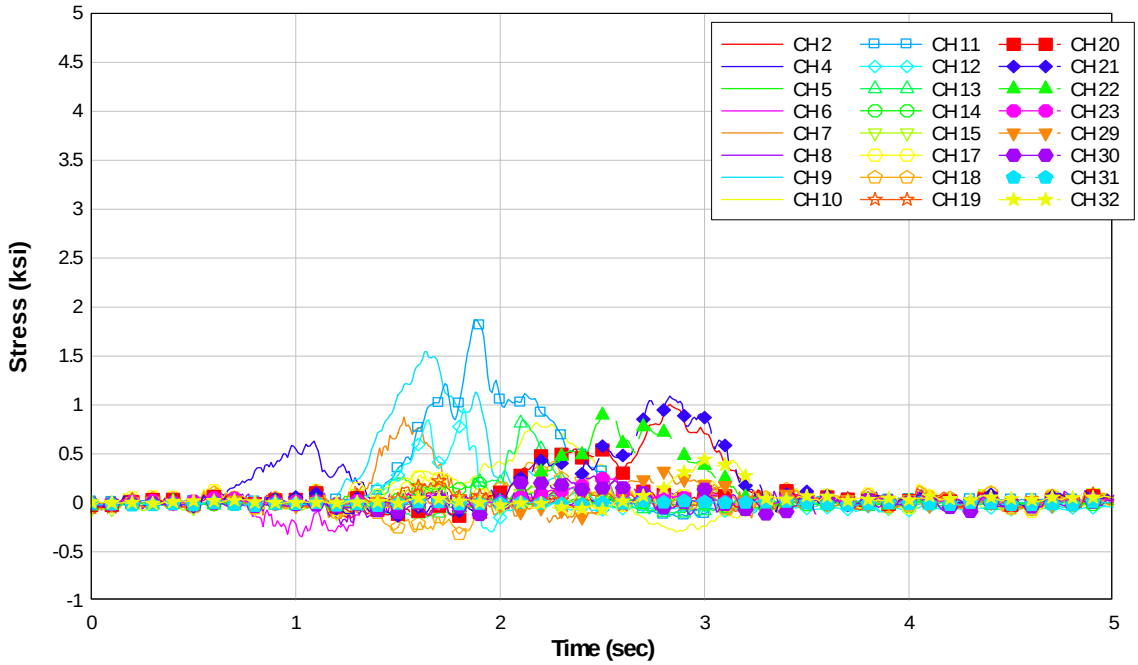

Figure 2.14e: Stirrup stress response for test truck in north-bound passing lane at 55 mph

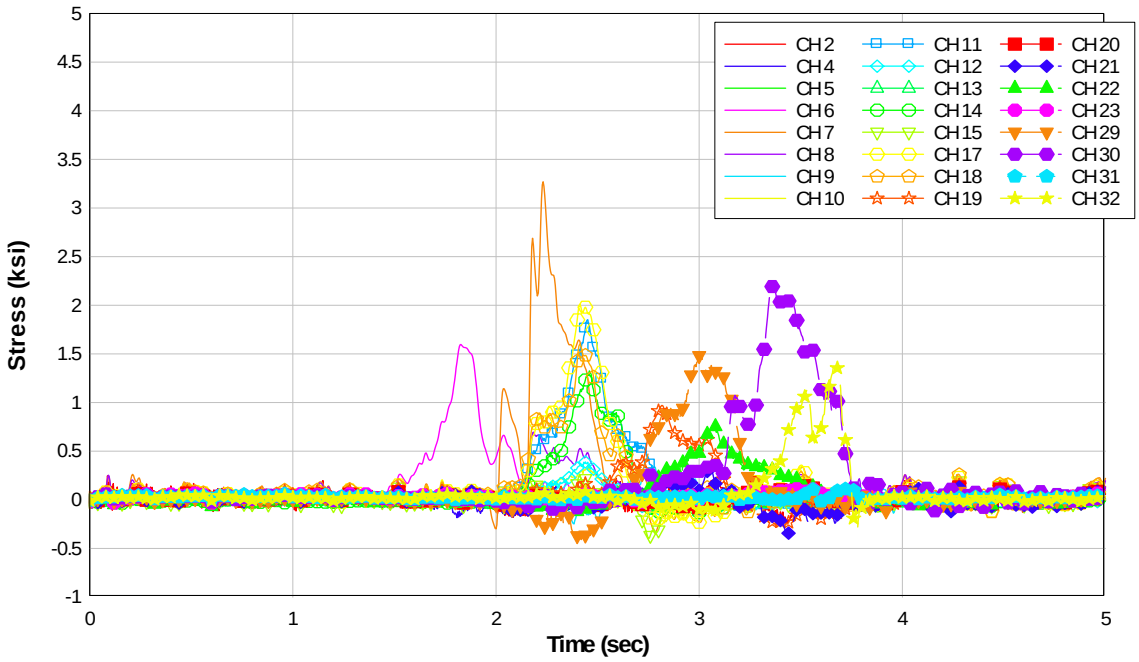

Figure 2.14f: Stirrup stress response for test truck in north-bound truck lane at 64 mph

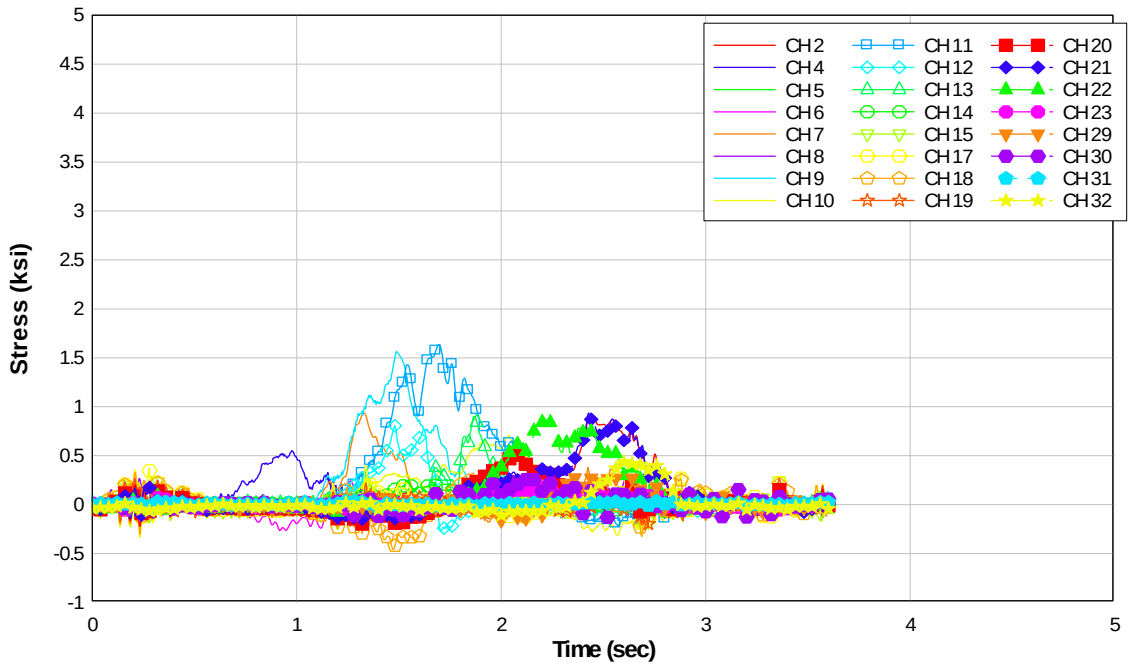

Figure 2.14g: Stirrup stress response for test truck in north-bound passing lane at 60 mph

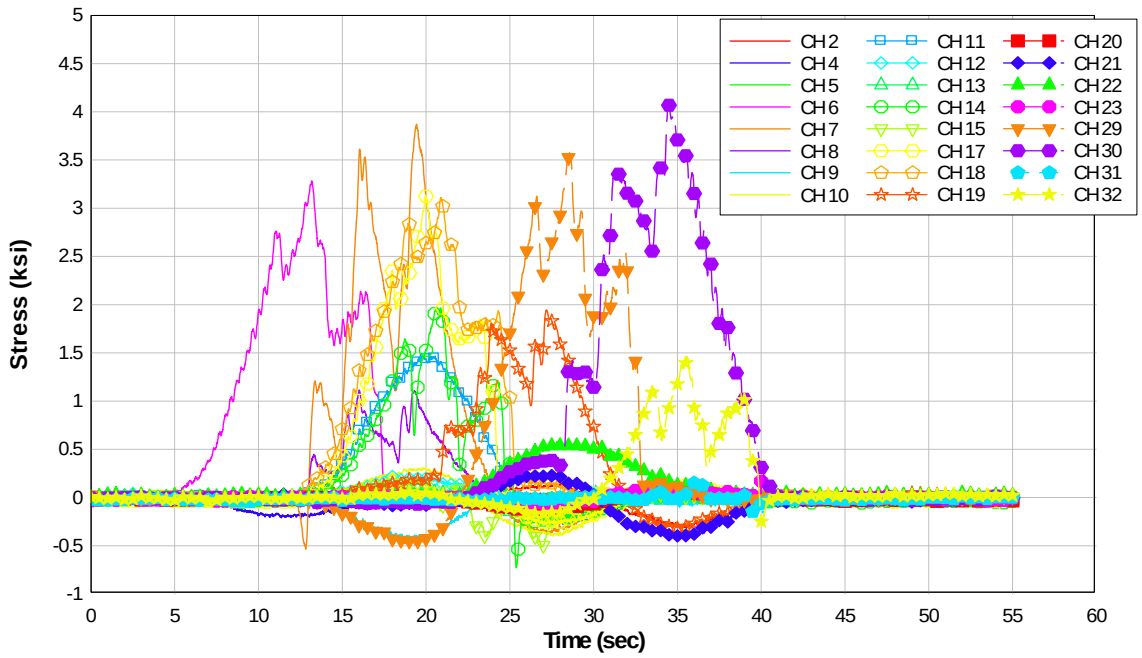

Figure 2.14h: Stirrup stress response test truck with trailer on north-bound fog lane at 5 mph

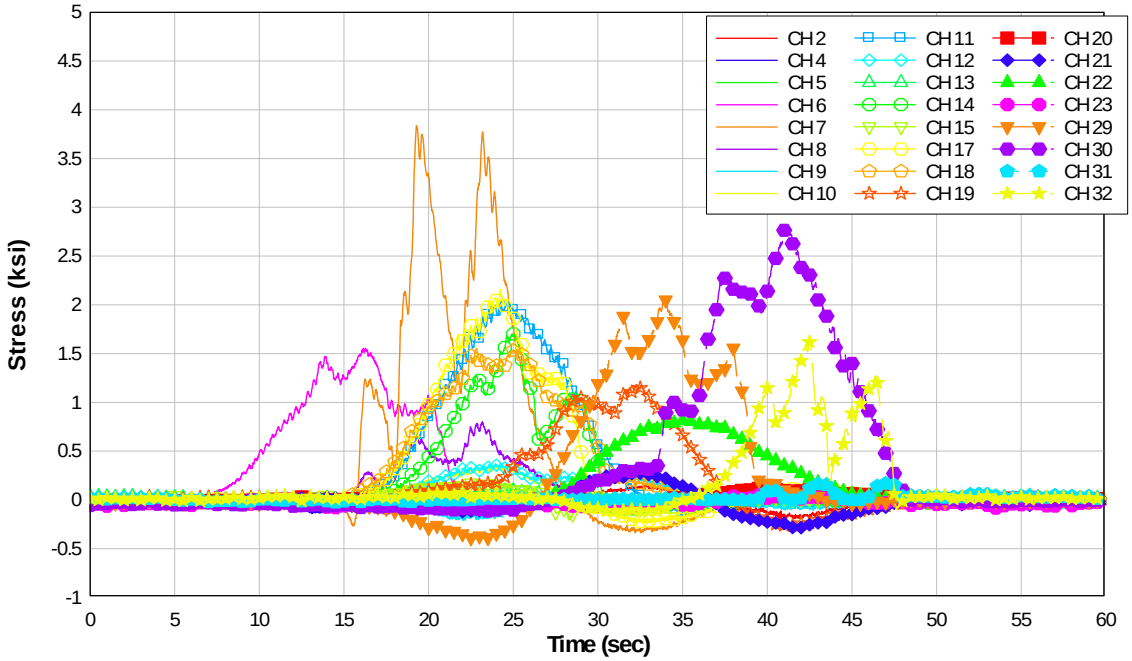

Figure 2.14i: Stirrup stress response for test truck with trailer in north-bound truck lane at 5 mph

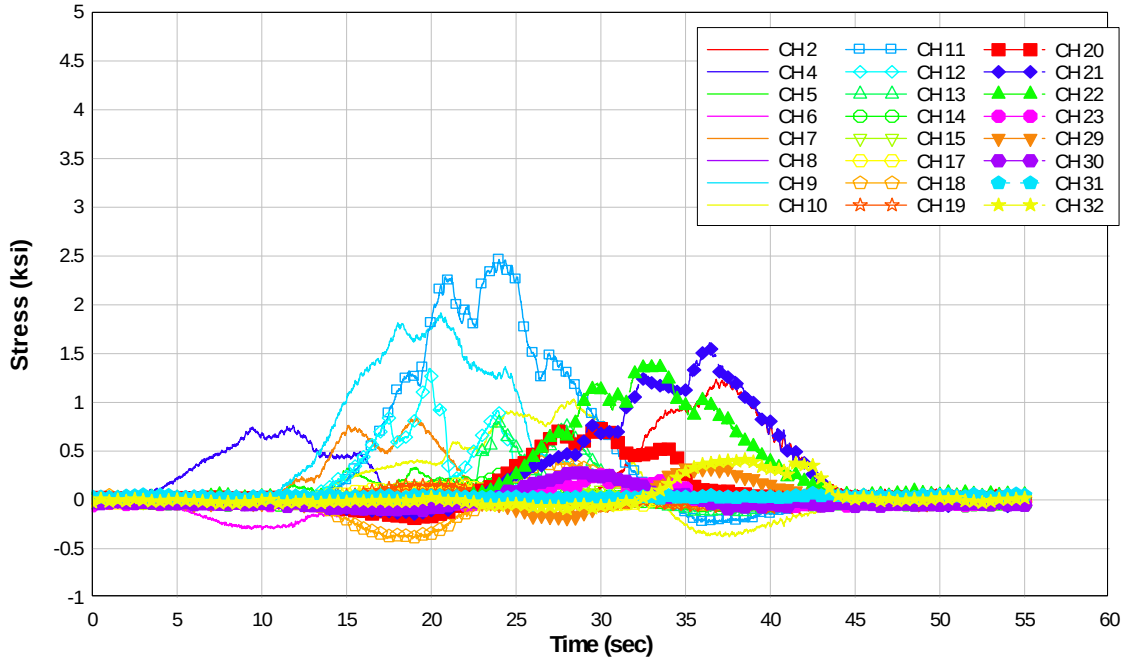

Figure 2.14j: Stirrup stress response for test truck with trailer in north-bound passing lane at 5 mph

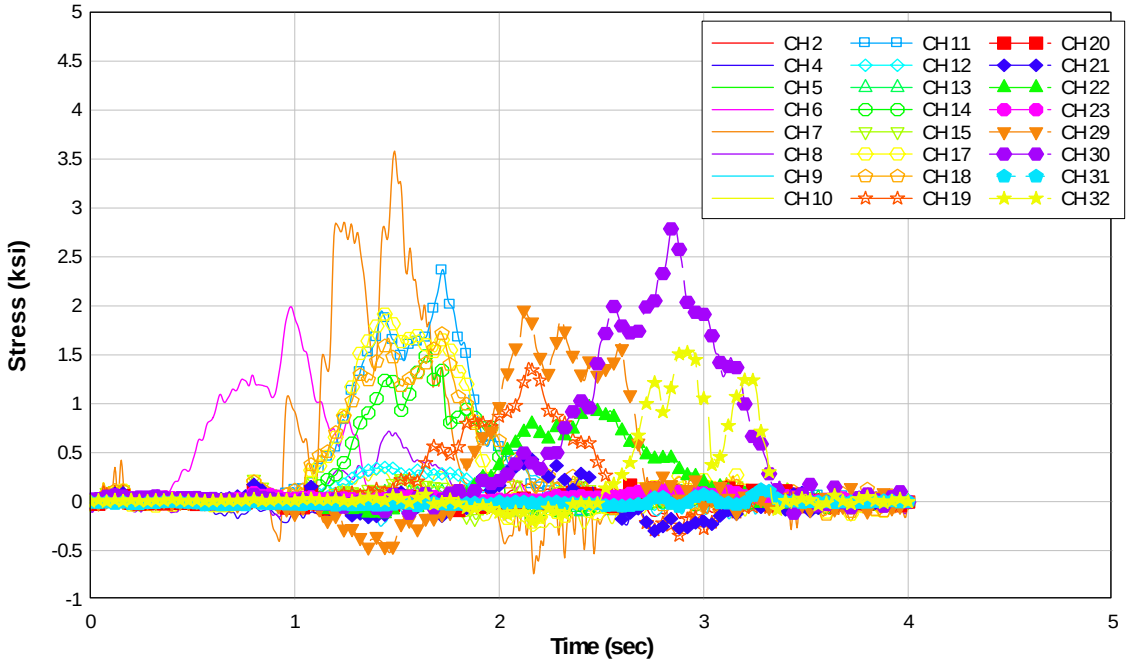

Figure 2.14k: Stirrup stress response for test truck with trailer in north-bound truck lane at 54 mph

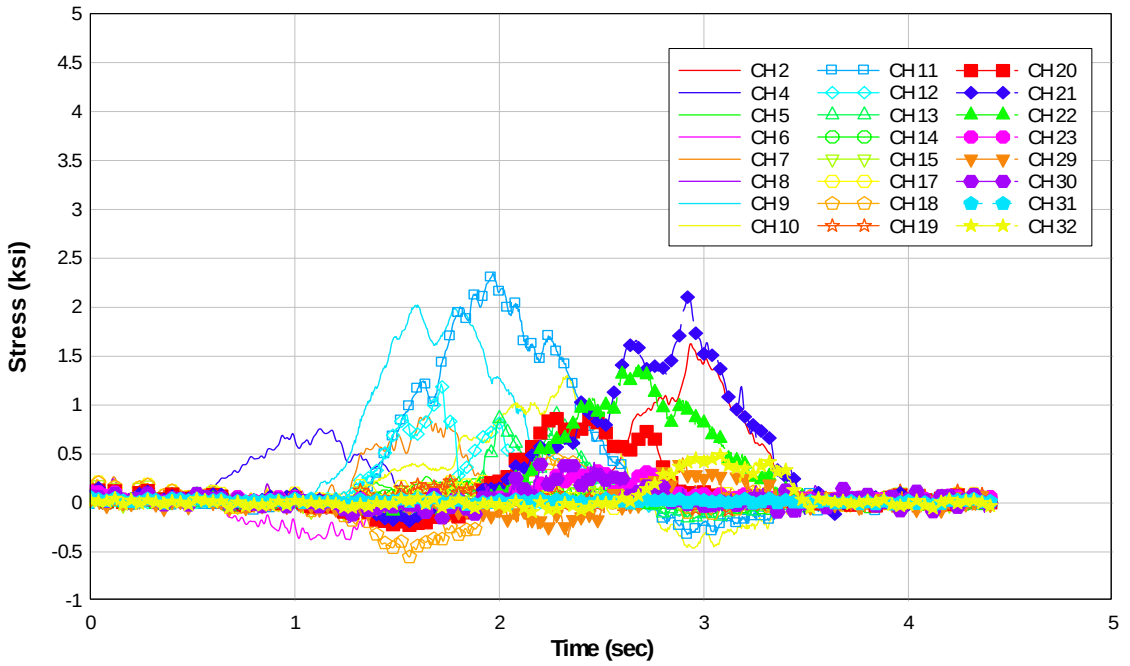

Figure 2.14l: Stirrup stress response test truck with trailer in north-bound passing lane at 55 mph

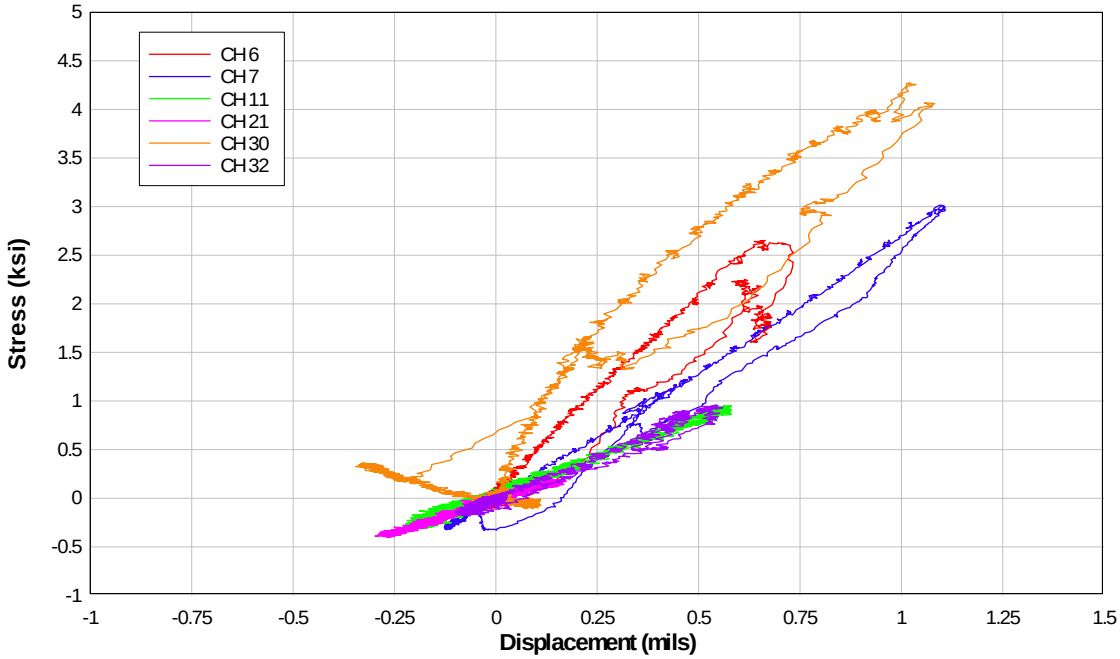

Figure 2.15a: Crack displacement-Stirrup stress response for test truck on north-bound fog line at 5 mph

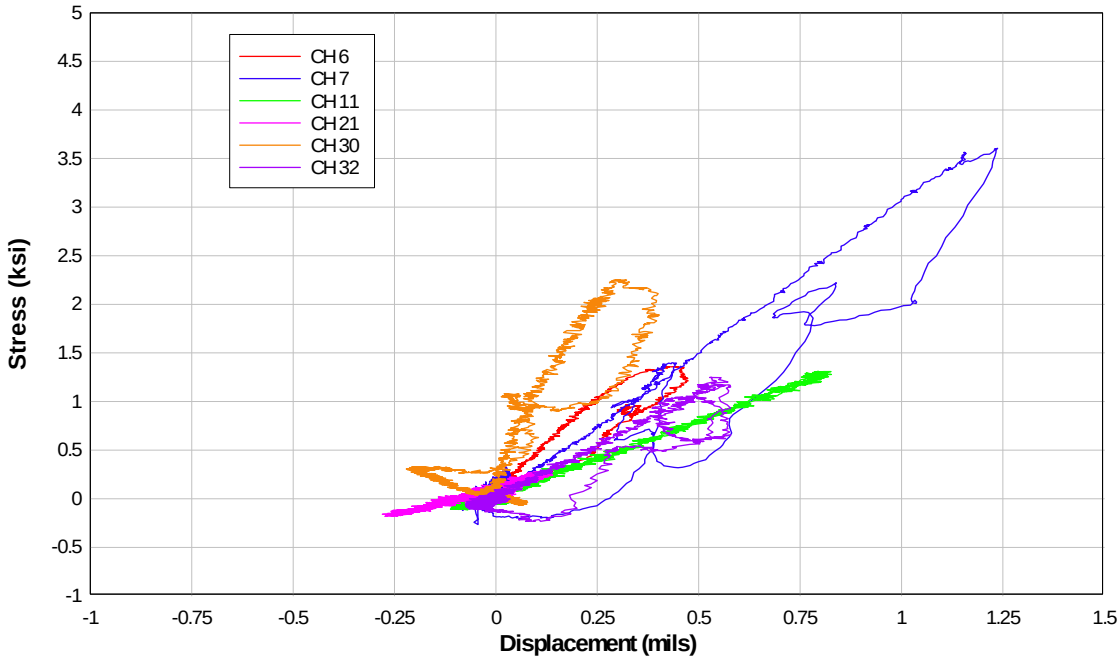

Figure 2.15b: Crack displacement-Stirrup stress response for test truck in north-bound truck lane at 5 mph

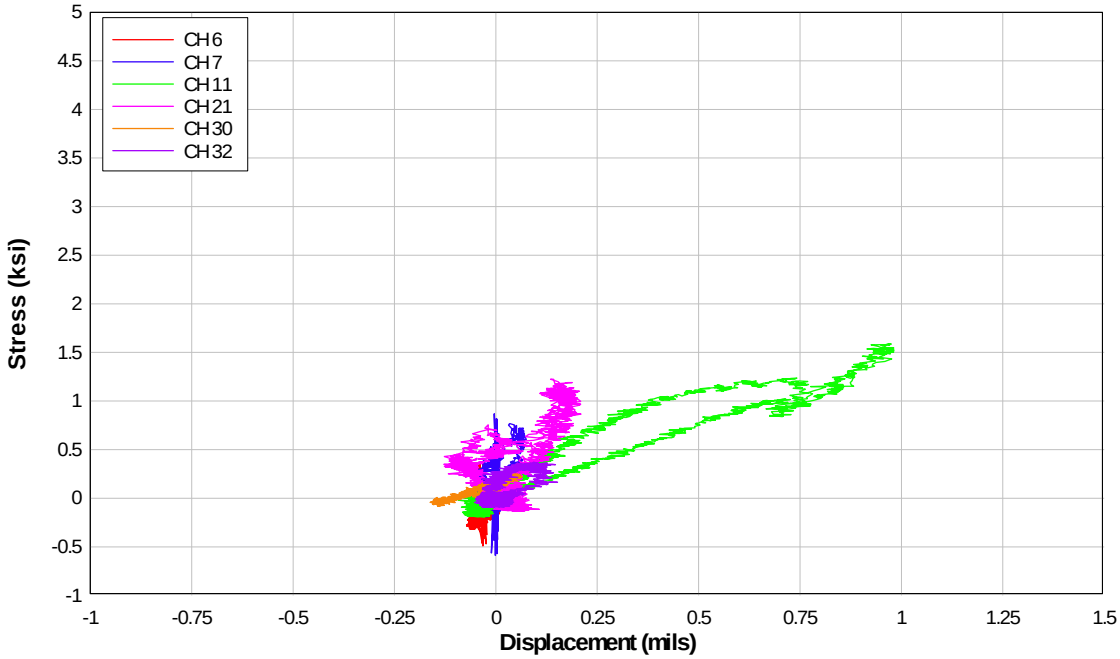

Figure 2.15c: Crack displacement-Stirrup stress response for test truck in north-bound passing lane at 5 mph

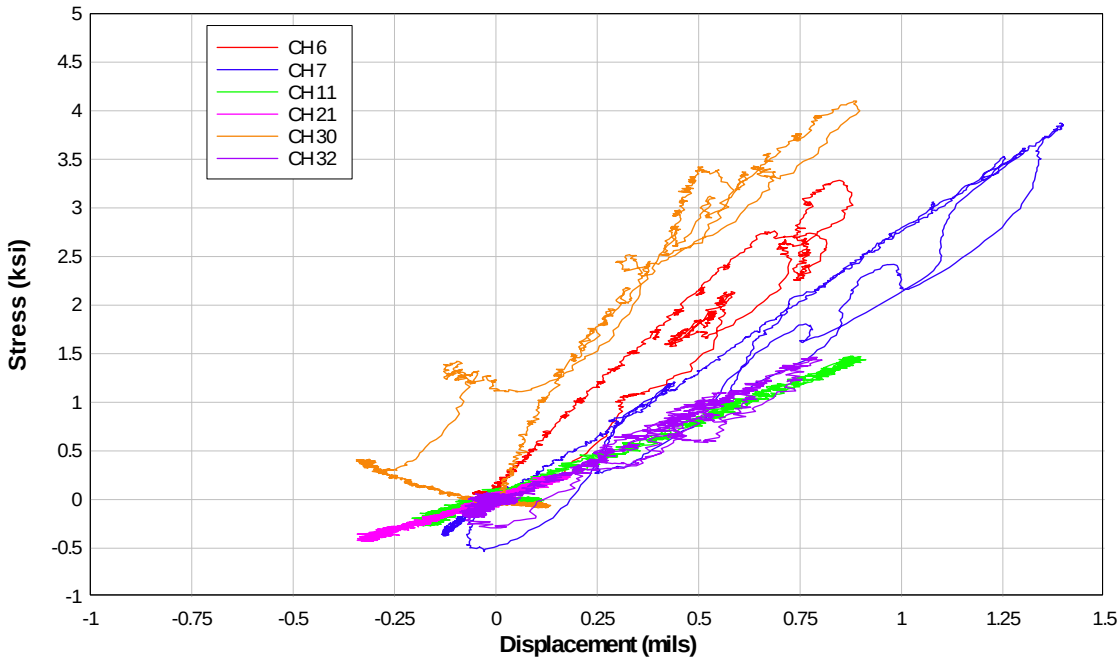

Figure 2.15d: Crack displacement-Stirrup stress response for test truck with trailer on north-bound fog line at 5 mph

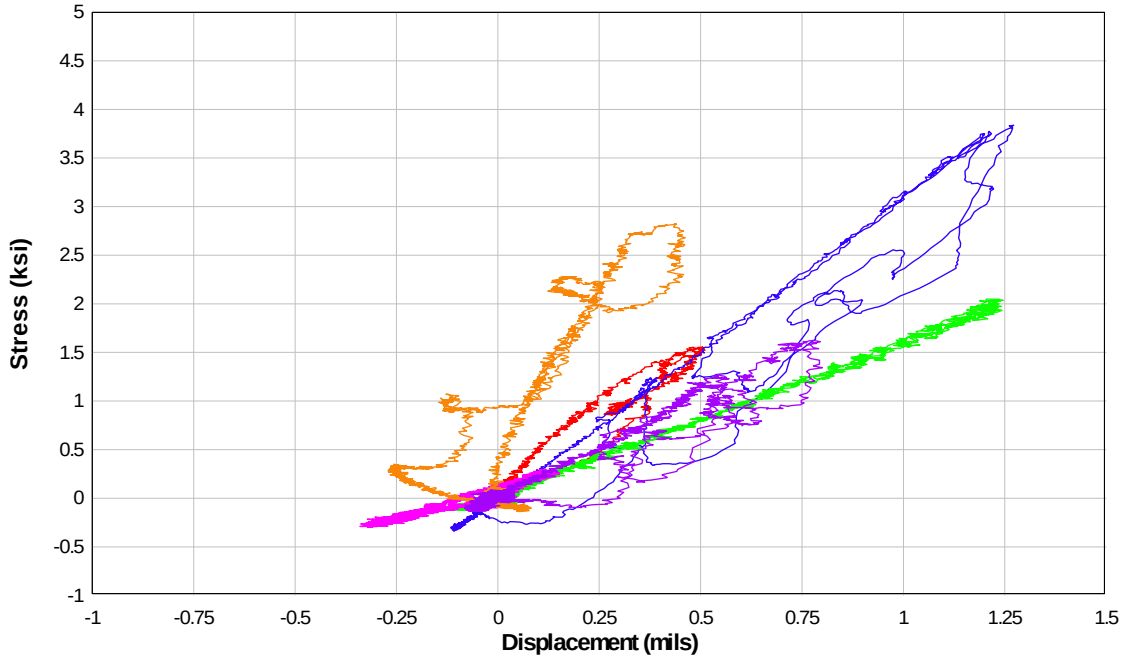

Figure 2.15e: Crack displacement-Stirrup stress response for test truck with trailer in north-bound truck lane at 5 mph

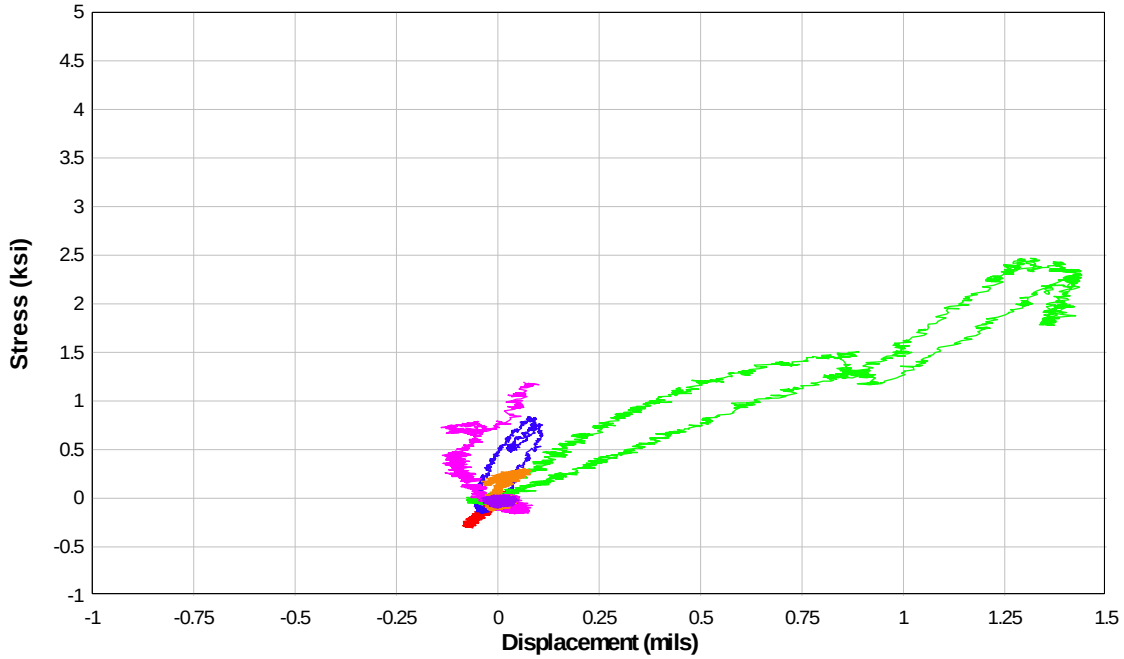

Figure 2.15f: Crack displacement-Stirrup stress response for test truck with trailer in north-bound passing lane at 5 mph

Table 2.1: Maximum and minimum stresses and stress ranges at instrumented locations for test truck (with and without trailer) on McKenzie River Bridge

Maximum Stress

Test Truck Configuration	Speed (mph)	Lane Position	CH_2 (ksi)	CH_4 (ksi)	CH_5 (ksi)	CH_6 (ksi)	CH_7 (ksi)	CH_8 (ksi)	CH_9 (ksi)	CH_10 (ksi)	CH_11 (ksi)	CH_12 (ksi)	CH_13 (ksi)	CH_14 (ksi)	CH_15 (ksi)	CH_17 (ksi)	CH_18 (ksi)	CH_19 (ksi)	CH_20 (ksi)	CH_21 (ksi)	CH_22 (ksi)	CH_23 (ksi)	CH_29 (ksi)	CH_30 (ksi)	CH_31 (ksi)	CH_32 (ksi)
Truck	5	Fog	0.15	0.07	0.01	2.65	3.01	1.02	0.23	0.24	0.95	0.11	0.14	1.45	0.14	2.66	3.25	1.90	0.05	0.19	0.31	0.10	3.30	4.27	0.06	0.96
Truck	5	Truck	0.04	0.07	0.05	1.46	3.60	0.68	0.23	0.22	1.31	0.31	0.08	1.30	0.15	1.67	1.31	0.97	0.13	0.28	0.61	0.11	1.77	2.25	0.18	1.25
Truck	5	Passing	0.96	0.67	0.28	0.18	0.72	0.18	1.74	0.96	1.59	1.07	0.94	0.15	0.27	0.29	0.41	0.30	0.73	1.19	0.88	0.28	0.27	0.25	0.06	0.37
Truck and Trailer	5	Fog	0.15	0.04	0.08	3.28	3.87	1.12	0.26	0.31	1.47	0.23	0.11	1.97	0.17	3.14	3.11	1.95	0.09	0.25	0.58	0.17	3.58	4.10	0.18	1.46
Truck and Trailer	5	Truck	0.15	0.06	0.05	1.55	3.84	0.80	0.28	0.35	2.05	0.37	0.11	1.70	0.18	2.16	1.56	1.18	0.12	0.29	0.83	0.07	2.10	2.82	0.21	1.62
Truck and Trailer	5	Passing	1.24	0.76	0.33	0.07	0.84	0.05	1.92	1.03	2.47	1.35	0.81	0.27	0.15	0.18	0.40	0.18	0.75	1.61	1.40	0.29	0.36	0.30	0.08	0.43
Truck	55	Truck	0.12	0.07	0.05	1.35	3.39	0.63	0.24	0.30	1.30	0.29	0.06	1.37	0.29	1.65	1.36	0.93	0.14	0.27	0.58	0.08	1.63	2.12	0.12	1.24
Truck	64	Truck	0.25	0.18	0.12	1.60	3.27	0.70	0.35	0.35	1.85	0.39	0.09	1.33	0.25	2.01	1.60	0.97	0.19	0.32	0.76	0.16	1.49	2.20	0.13	1.37
Truck	55	Passing	1.01	0.63	0.26	0.17	0.88	0.15	1.55	0.82	1.87	0.97	0.85	0.22	0.19	0.29	0.42	0.22	0.60	1.09	0.92	0.26	0.35	0.29	0.02	0.45
Truck	60	Passing	0.91	0.55	0.32	0.25	0.94	0.28	1.57	0.71	1.64	0.81	0.90	0.25	0.33	0.40	0.33	0.27	0.51	0.94	0.89	0.22	0.38	0.30	0.06	0.46
Truck and Trailer	54	Truck	0.20	0.13	0.02	1.99	3.58	0.72	0.38	0.33	2.37	0.37	0.12	1.50	0.27	1.93	1.74	1.42	0.21	0.47	0.96	0.14	1.97	2.87	0.13	1.54
Truck and Trailer	55	Passing	1.63	0.76	0.27	0.16	0.89	0.27	2.02	1.30	2.35	1.22	0.91	0.24	0.21	0.25	0.51	0.26	0.92	2.12	1.39	0.38	0.46	0.42	0.07	0.50

Minimum Stress

Test Truck Configuration	Speed (mph)	Lane Position	CH_2 (ksi)	CH_4 (ksi)	CH_5 (ksi)	CH_6 (ksi)	CH_7 (ksi)	CH_8 (ksi)	CH_9 (ksi)	CH_10 (ksi)	CH_11 (ksi)	CH_12 (ksi)	CH_13 (ksi)	CH_14 (ksi)	CH_15 (ksi)	CH_17 (ksi)	CH_18 (ksi)	CH_19 (ksi)	CH_20 (ksi)	CH_21 (ksi)	CH_22 (ksi)	CH_23 (ksi)	CH_29 (ksi)	CH_30 (ksi)	CH_31 (ksi)	CH_32 (ksi)
Truck	5	Fog	-0.27	-0.19	-0.08	-0.10	-0.33	-0.22	-0.48	-0.38	-0.31	-0.11	-0.15	-0.26	-0.46	-0.27	-0.04	-0.32	-0.19	-0.40	-0.10	-0.07	-0.44	-0.10	-0.20	-0.18
Truck	5	Truck	-0.03	-0.13	-0.04	-0.03	-0.20	-0.02	-0.21	-0.27	-0.11	-0.05	-0.05	-0.07	-0.27	-0.21	-0.04	-0.22	-0.04	-0.18	-0.07	-0.06	-0.30	-0.07	-0.04	-0.23
Truck	5	Passing	-0.18	-0.05	-0.13	-0.33	-0.18	-0.26	-0.08	-0.32	-0.19	-0.32	-0.15	-0.05	-0.11	-0.08	-0.44	-0.08	-0.21	-0.13	-0.09	-0.06	-0.20	-0.08	-0.01	-0.09
Truck and Trailer	5	Fog	-0.32	-0.21	-0.02	-0.01	-0.53	-0.13	-0.44	-0.40	-0.27	-0.07	-0.20	-0.73	-0.51	-0.28	-0.05	-0.33	-0.14	-0.43	-0.07	-0.09	-0.50	-0.09	-0.17	-0.29
Truck and Trailer	5	Truck	-0.21	-0.14	-0.05	-0.04	-0.34	-0.10	-0.21	-0.23	-0.13	-0.07	-0.08	-0.11	-0.21	-0.23	-0.04	-0.27	-0.06	-0.30	-0.11	-0.10	-0.41	-0.14	-0.03	-0.14
Truck and Trailer	5	Passing	-0.04	-0.02	-0.04	-0.30	-0.15	-0.09	-0.08	-0.38	-0.24	-0.07	-0.18	-0.08	-0.04	-0.07	-0.40	-0.09	-0.20	-0.16	-0.04	-0.09	-0.20	-0.13	-0.02	-0.10
Truck	55	Truck	-0.22	-0.14	-0.04	-0.07	-0.40	-0.16	-0.17	-0.23	-0.09	-0.07	-0.09	-0.10	-0.37	-0.24	-0.08	-0.25	-0.11	-0.30	-0.09	-0.05	-0.40	-0.11	-0.02	-0.17
Truck	64	Truck	-0.24	-0.18	-0.06	-0.07	-0.34	-0.13	-0.25	-0.24	-0.12	-0.11	-0.10	-0.13	-0.40	-0.24	-0.16	-0.25	-0.09	-0.35	-0.14	-0.05	-0.41	-0.15	-0.04	-0.29
Truck	55	Passing	-0.16	-0.05	-0.09	-0.35	-0.16	-0.22	-0.15	-0.30	-0.14	-0.29	-0.15	-0.06	-0.12	-0.13	-0.32	-0.09	-0.15	-0.14	-0.06	-0.04	-0.22	-0.14	-0.03	-0.07
Truck	60	Passing	-0.13	-0.09	-0.14	-0.26	-0.15	-0.19	-0.10	-0.31	-0.22	-0.27	-0.12	-0.09	-0.26	-0.34	-0.46	-0.22	-0.23	-0.20	-0.10	-0.08	-0.18	-0.13	-0.03	-0.11
Truck and Trailer	54	Truck	-0.17	-0.21	-0.07	-0.05	-0.74	-0.18	-0.25	-0.30	-0.14	-0.07	-0.12	-0.17	-0.18	-0.26	-0.17	-0.35	-0.14	-0.30	-0.12	-0.01	-0.52	-0.14	-0.05	-0.20
Truck and Trailer	55	Passing	-0.16	-0.02	-0.09	-0.38	-0.09	-0.20	-0.14	-0.46	-0.32	-0.04	-0.18	-0.08	-0.11	-0.08	-0.55	-0.09	-0.26	-0.19	-0.11	-0.08	-0.35	-0.15	-0.04	-0.12

Stress Range

Test Truck Configuration	Speed (mph)	Lane Position	CH_2 (ksi)	CH_4 (ksi)	CH_5 (ksi)	CH_6 (ksi)	CH_7 (ksi)	CH_8 (ksi)	CH_9 (ksi)	CH_10 (ksi)	CH_11 (ksi)	CH_12 (ksi)	CH_13 (ksi)	CH_14 (ksi)	CH_15 (ksi)	CH_17 (ksi)	CH_18 (ksi)	CH_19 (ksi)	CH_20 (ksi)	CH_21 (ksi)	CH_22 (ksi)	CH_23 (ksi)	CH_29 (ksi)	CH_30 (ksi)	CH_31 (ksi)	CH_32 (ksi)
Truck	5	Fog	0.42	0.25	0.09	2.75	3.35	1.23	0.71	0.62	1.26	0.22	0.29	1.71	0.60	2.93	3.29	2.23	0.24	0.59	0.41	0.17	3.75	4.37	0.25	1.14
Truck	5	Truck	0.07	0.20	0.09	1.49	3.81	0.71	0.44	0.49	1.42	0.35	0.13	1.38	0.42	1.88	1.36	1.20	0.17	0.46	0.68	0.17	2.08	2.32	0.21	1.48
Truck	5	Passing	1.14	0.72	0.41	0.50	0.90	0.44	1.82	1.27	1.78	1.39	1.09	0.20	0.37	0.37	0.85	0.38	0.94	1.31	0.97	0.35	0.48	0.33	0.07	0.46
Truck and Trailer	5	Fog	0.47	0.25	0.10	3.30	4.40	1.25	0.70	0.71	1.74	0.30	0.30	2.70	0.69	3.42	3.16	2.28	0.23	0.68	0.65	0.26	4.07	4.18	0.35	1.76
Truck and Trailer	5	Truck	0.36	0.20	0.10	1.60	4.17	0.90	0.49	0.58	2.18	0.44	0.19	1.81	0.39	2.39	1.60	1.45	0.19	0.59	0.94	0.17	2.51	2.96	0.24	1.76
Truck and Trailer	5	Passing	1.28	0.78	0.37	0.37	0.99	0.14	2.00	1.41	2.70	1.42	0.99	0.34	0.19	0.25	0.79	0.26	0.95	1.77	1.43	0.37	0.57	0.43	0.09	0.53
Truck	55	Truck	0.33	0.21	0.09	1.42	3.80	0.79	0.41	0.53	1.40	0.36	0.15	1.46	0.66	1.89	1.44	1.18	0.25	0.57	0.67	0.13	2.03	2.22	0.15	1.41
Truck	64	Truck	0.49	0.36	0.17	1.67	3.61	0.82	0.60	0.59	1.98	0.50	0.19	1.46	0.65	2.25	1.76	1.22	0.28	0.67	0.90	0.22	1.90	2.35	0.16	1.66
Truck	55	Passing	1.16	0.68	0.35	0.52	1.03	0.38	1.70	1.12	2.01	1.26	1.00	0.28	0.31	0.42	0.74	0.31	0.74	1.23	0.98	0.29	0.56	0.43	0.06	0.52
Truck	60	Passing	1.04	0.65	0.45	0.51	1.08	0.47	1.66	1.02	1.86	1.08	1.02	0.34	0.59	0.74	0.79	0.49	0.74	1.14	0.99	0.30	0.56	0.43	0.09	0.57
Truck and Trailer	54	Truck	0.37	0.35	0.09	2.05	4.32	0.91	0.63	0.64	2.51	0.44	0.24	1.66	0.45	2.19	1.91	1.77	0.36	0.77	1.09	0.15	2.49	3.01	0.18	1.75
Truck and Trailer	55	Passing	1.79	0.78	0.36	0.54	0.98	0.48	2.16	1.77	2.67	1.26	1.08	0.32	0.32	0.33	1.06	0.35	1.18	2.30	1.49	0.47	0.81	0.57	0.11	0.62

2.2 JASPER BRIDGE, OVER MIDDLE FORK OF WILLAMETTE RIVER (BRIDGE NUMBER 04117A)

The Jasper Bridge is located near Jasper, Oregon and crosses the middle fork of the Willamette River on Highway 222. The bridge consists of 9 spans (Figures 2.16a-c): a single span reinforced concrete deck girder northeast approach span, two steel truss main spans, and six reinforced concrete deck girder southwest approach spans. The bridge was designed in 1950.

2.2.1 Description of Tested Spans

The southwest approach spans, shown in Figure 2.17, were selected as test spans because of their ease of accessibility from the ground. The approach span lengths from the southeast are as follows: 48 ft, 60 ft, and 48 ft, with simple supports at Pier 3 and Bents 4 and 7, forming two 3-span continuous sections. The spans have a roadway width of 26 ft, and a total width of 29 ft-9 in.

Four girders support the 6.5 in. thick reinforced concrete deck, with diaphragms 10 in. x 41 in. located at the quarter points of each span. The girder widths are constant at 13.5 in. but the overall girder height varies from 42 in. at midspan to 63 in. at the continuous support locations. Bent caps are 16 in. x 68 in. and supported by 24 in. square columns. The specified concrete compression strength was 3300 psi and the reinforcing steel consisted of intermediate grade (nominally 40 ksi yield stress) deformed square bars.

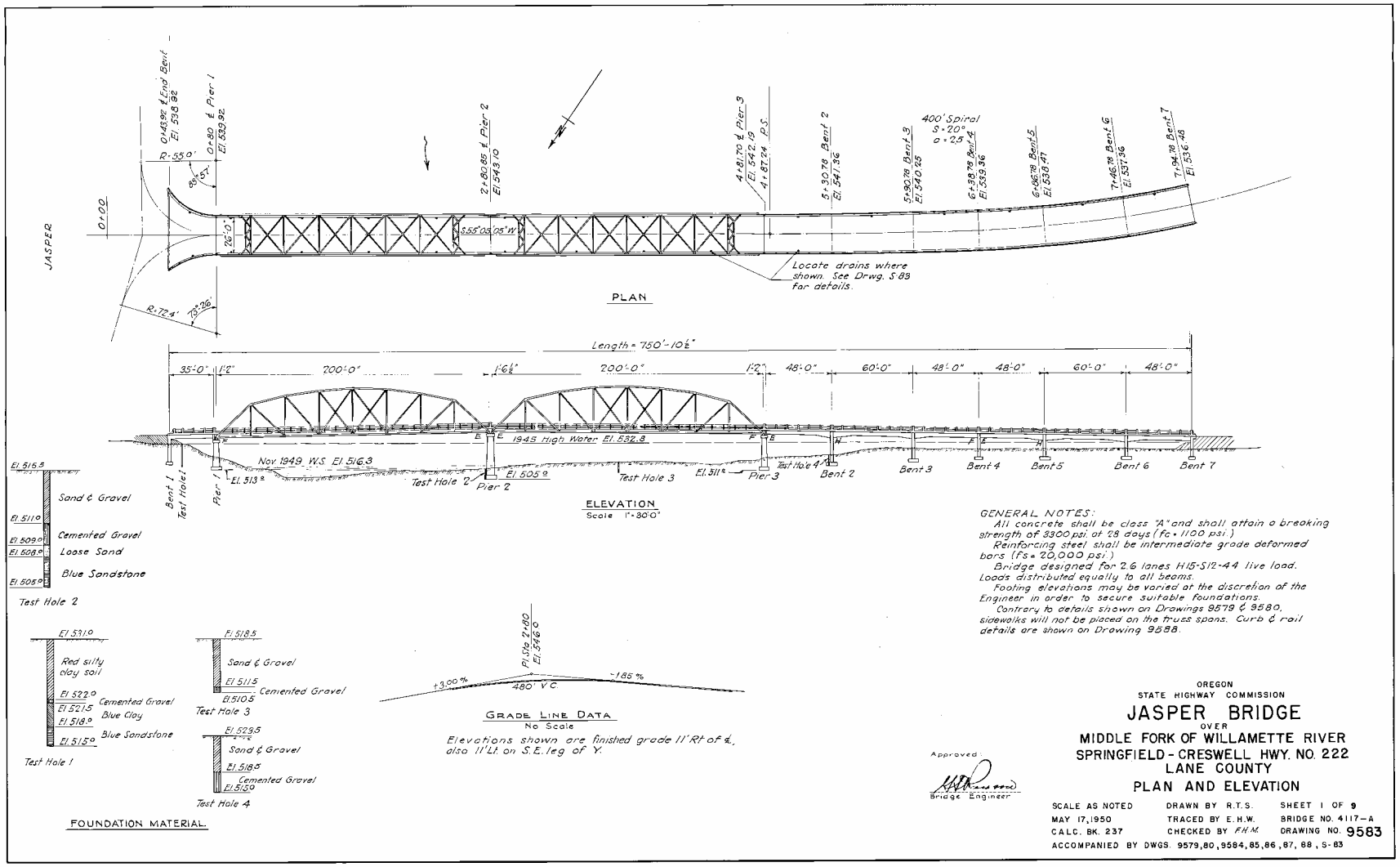

Figure 2.16a: Design drawings for Jasper Bridge

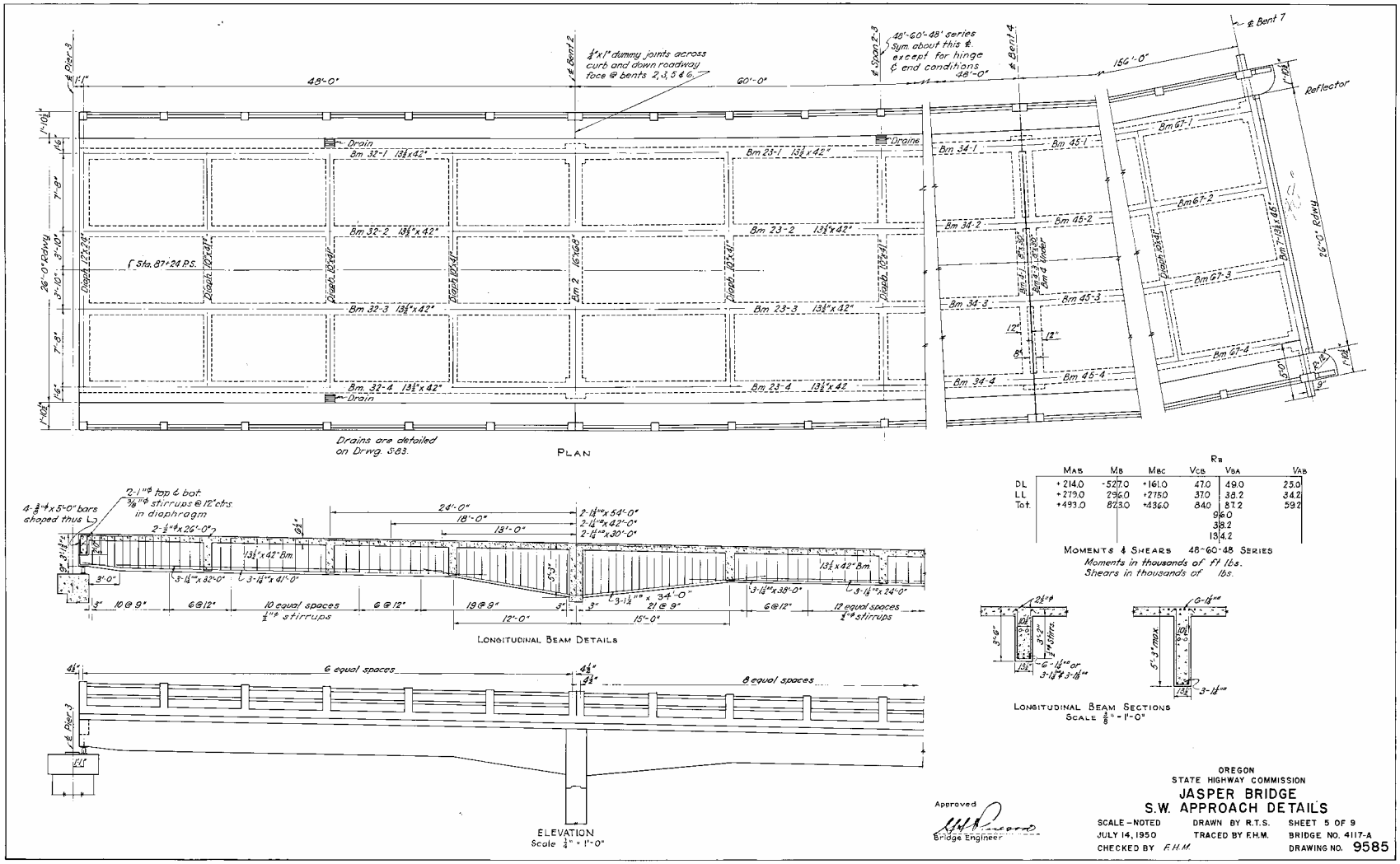

Figure 2.16b: Design drawings for Jasper Bridge

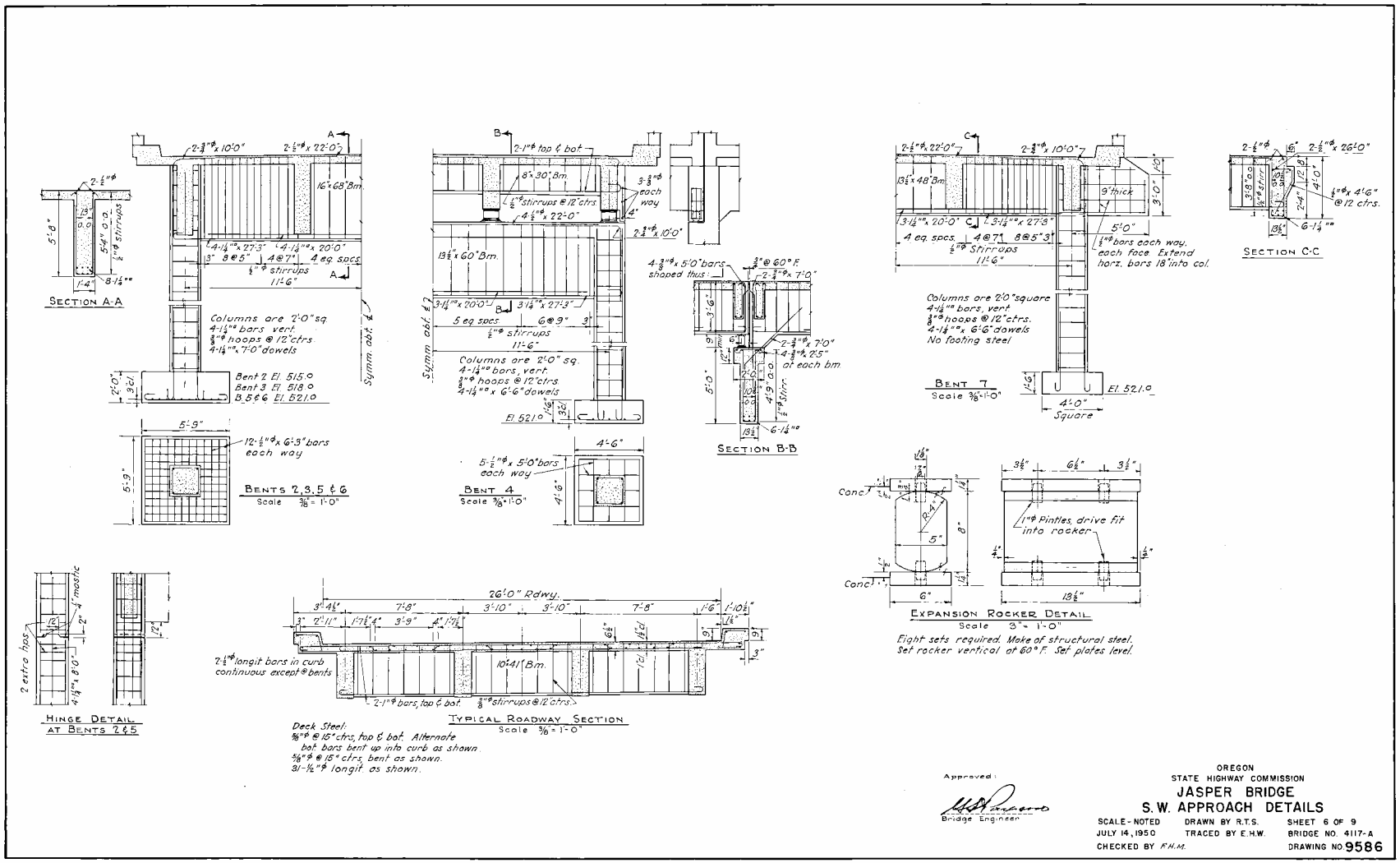

Figure 2.16c: Design drawings for Jasper Bridge

Figure 2.17: Portion of Jasper Bridge selected for field investigation

2.2.2 Crack Mapping and Instrumentation

The crack mapping and instrumentation techniques corresponded closely with those for the McKenzie Bridge as described above. Diagonal-tension crack patterns for the girders and bent caps are shown in Figures 2.18a-g. Twenty-seven (27) locations were selected for instrumentation. At four of these locations, strain gages were installed on opposite stirrup legs crossing a diagonal crack to compare the stirrup stress at the interior and exterior face of the girder.

Two locations were identified where multiple stirrups cross a diagonal crack. At these locations, two stirrups were instrumented to measure the profile of stirrup stresses along the length of the crack. Single stirrup legs were instrumented at the other eighteen locations. Position sensors were installed at four locations to assess crack displacements. Instrumentation locations and channel numbers are identified schematically in Figure 2.19.

Data were again collected using a Campbell Scientific CR9000 data acquisition system. During the ambient monitoring period, data were sampled at 100 Hz. A digital high-pass filter was utilized with a cut-off frequency of 40 Hz. A digital camera was triggered by response events to identify sources of larger stirrup stress cycles. The data acquisition system converted sensor readings into corresponding stresses and displacements, and stored the data for later retrieval and analysis.

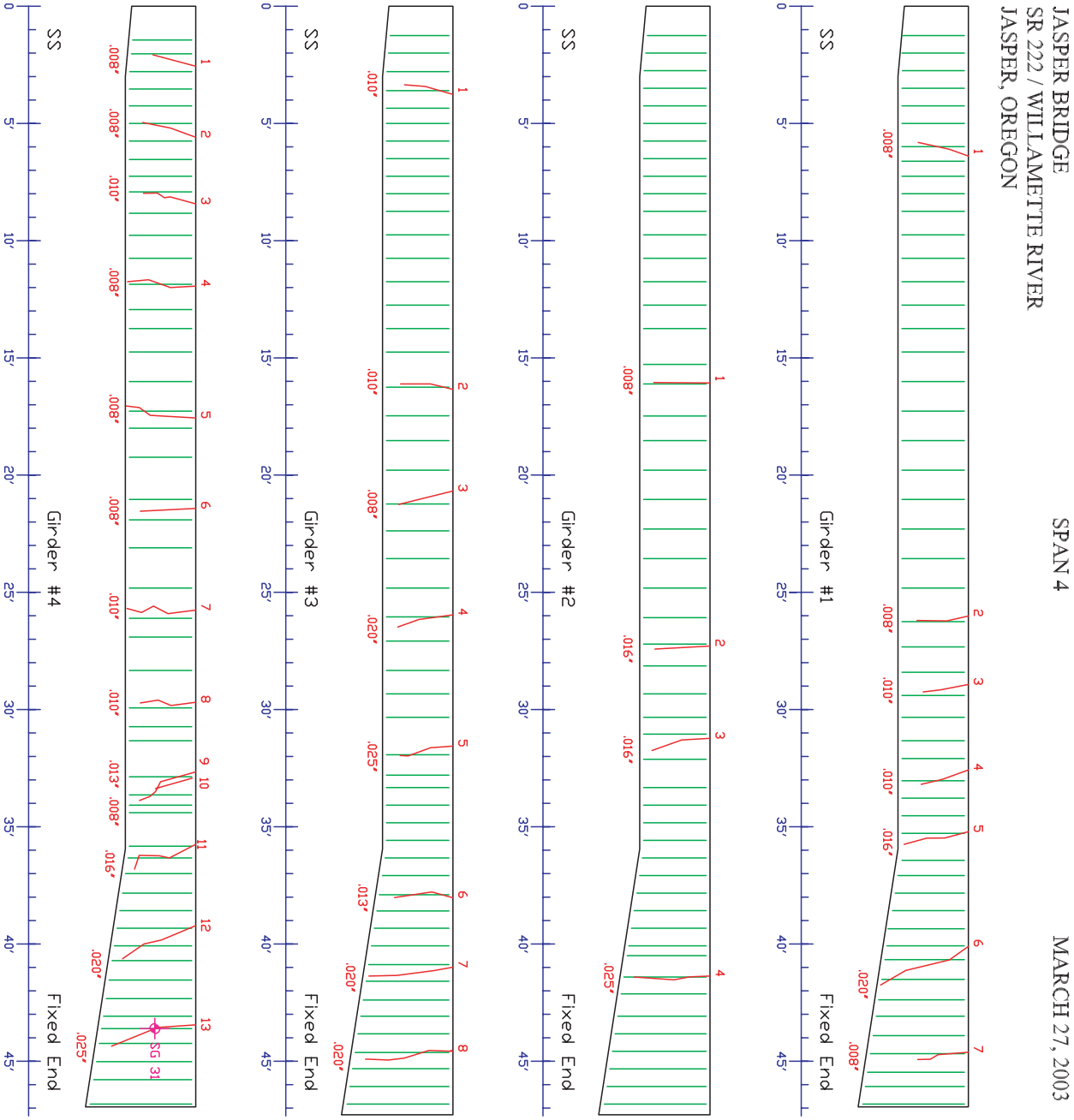

Figure 2.18a: Jasper Bridge crack and instrument locations on span 4

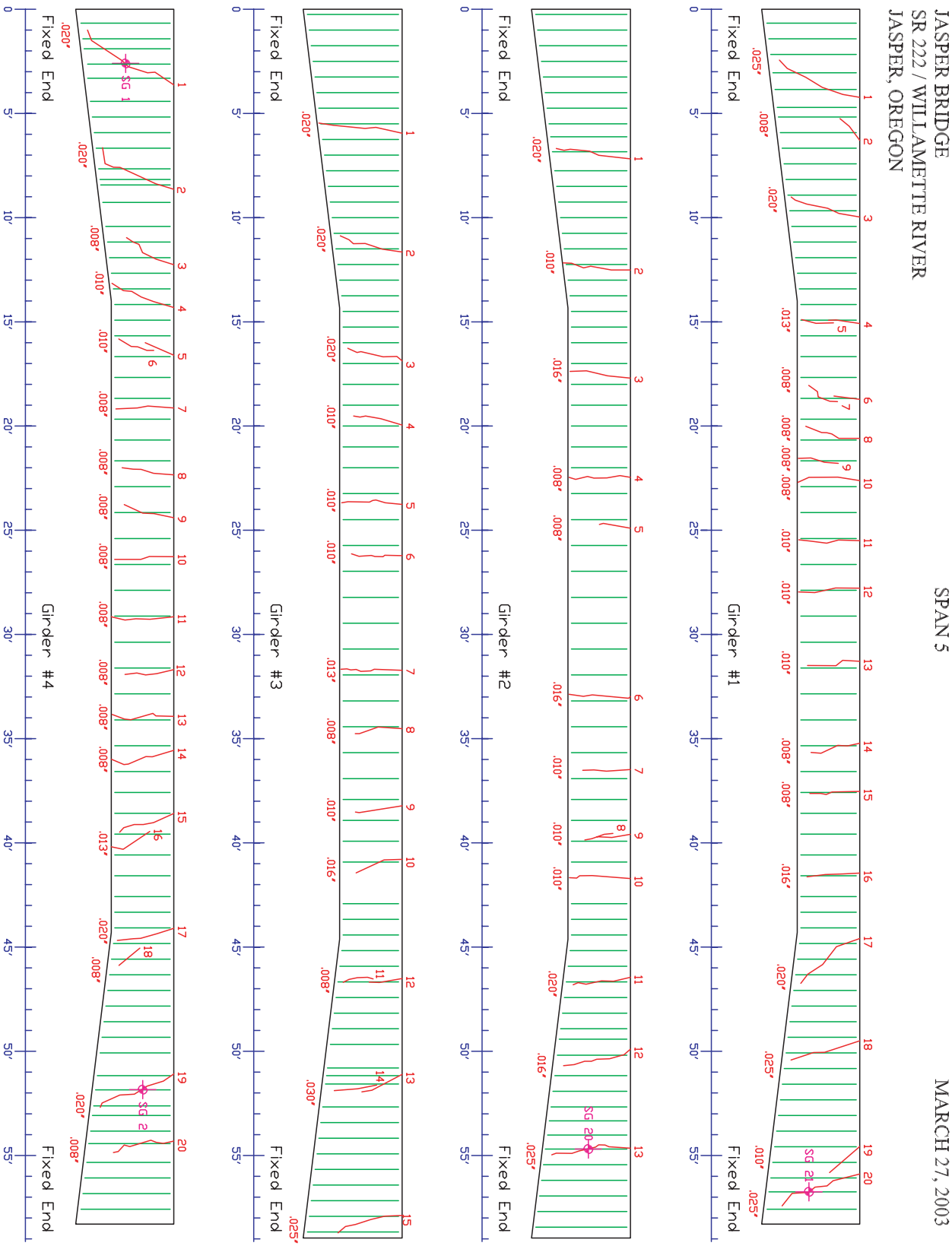

Figure 2.18b: Jasper Bridge crack and instrument locations on span 5

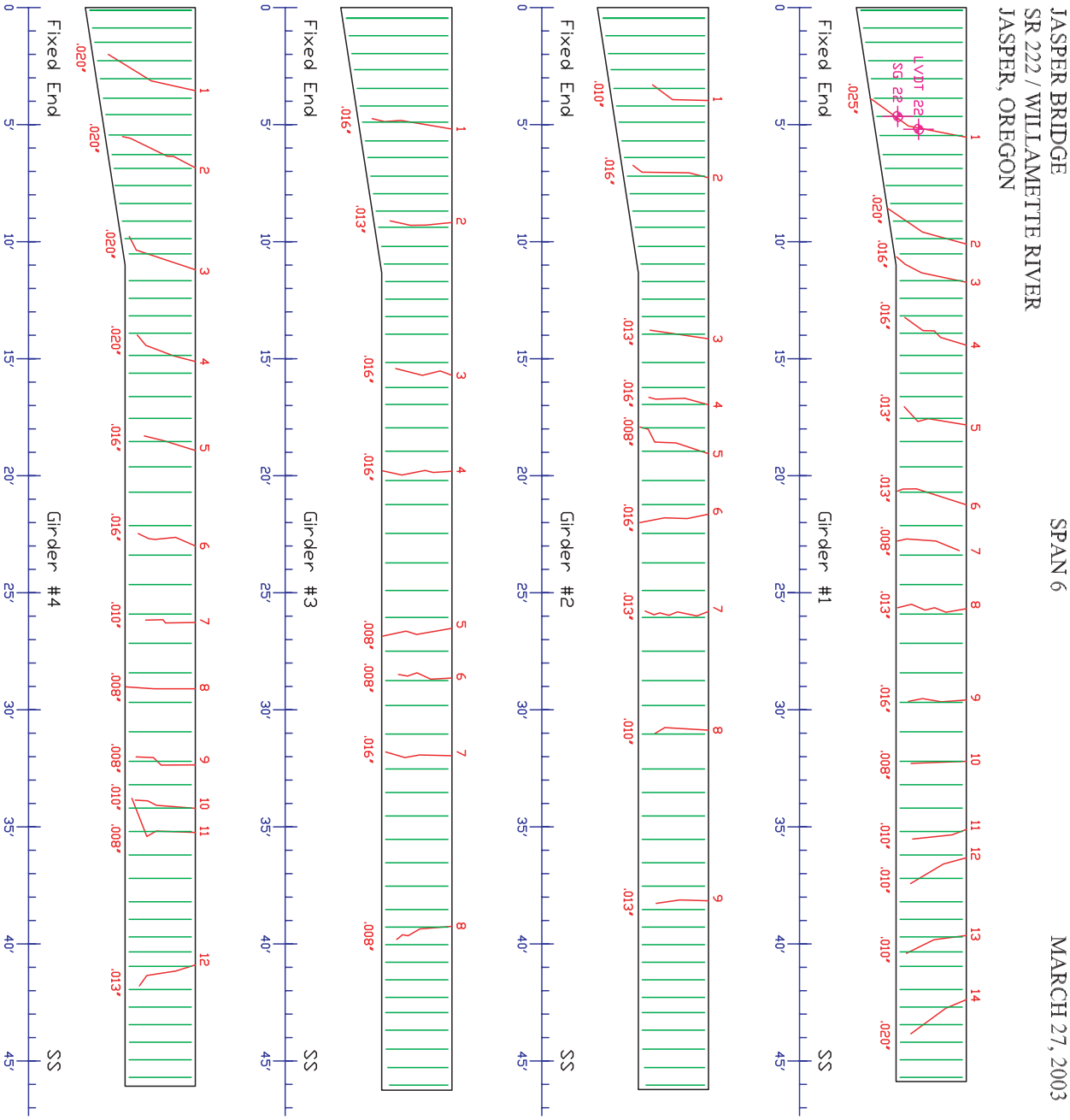

Figure 2.18c: Jasper Bridge crack and instrument locations on span 6

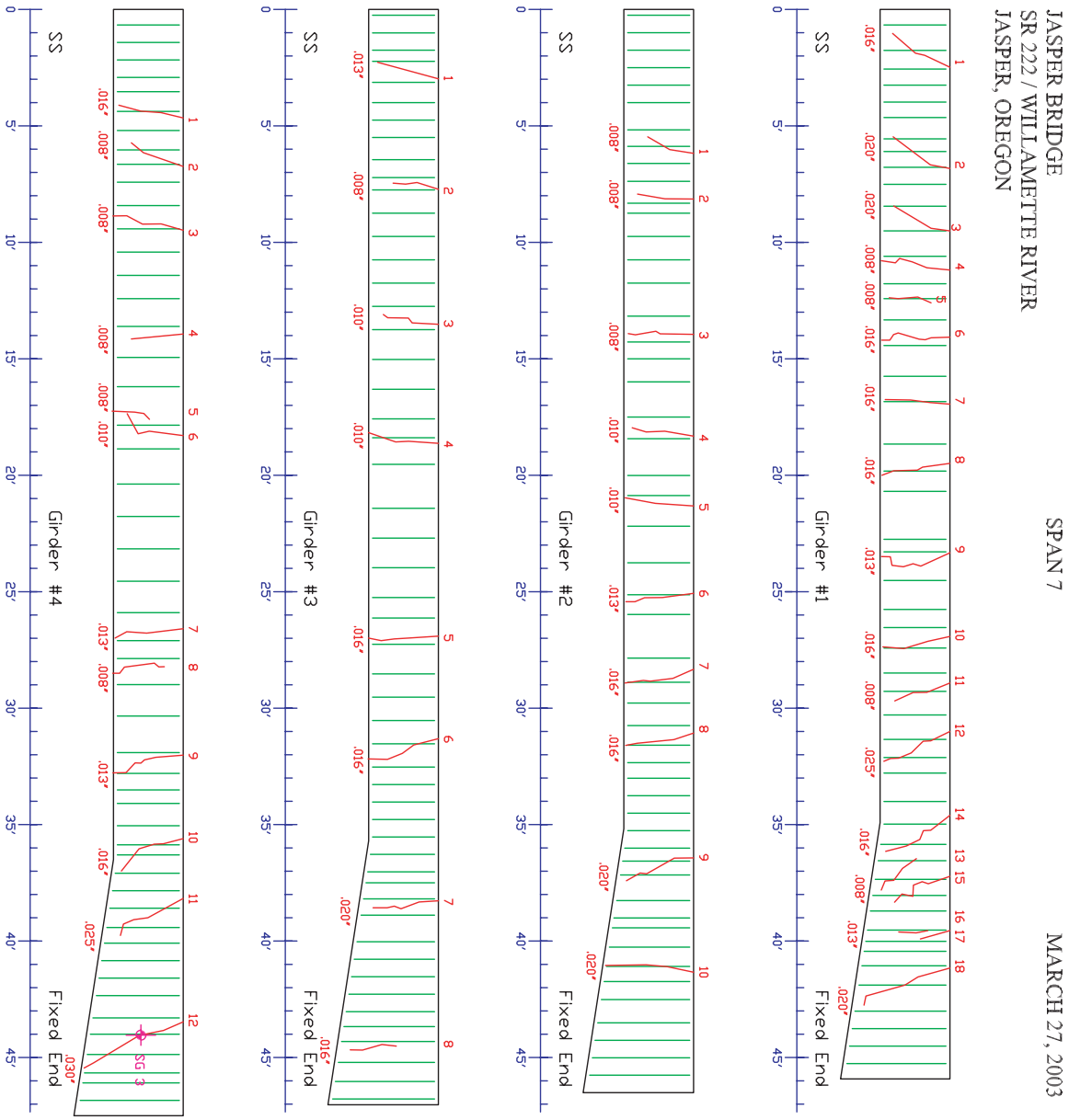

Figure 2.18d: Jasper Bridge crack and instrument locations on span 7

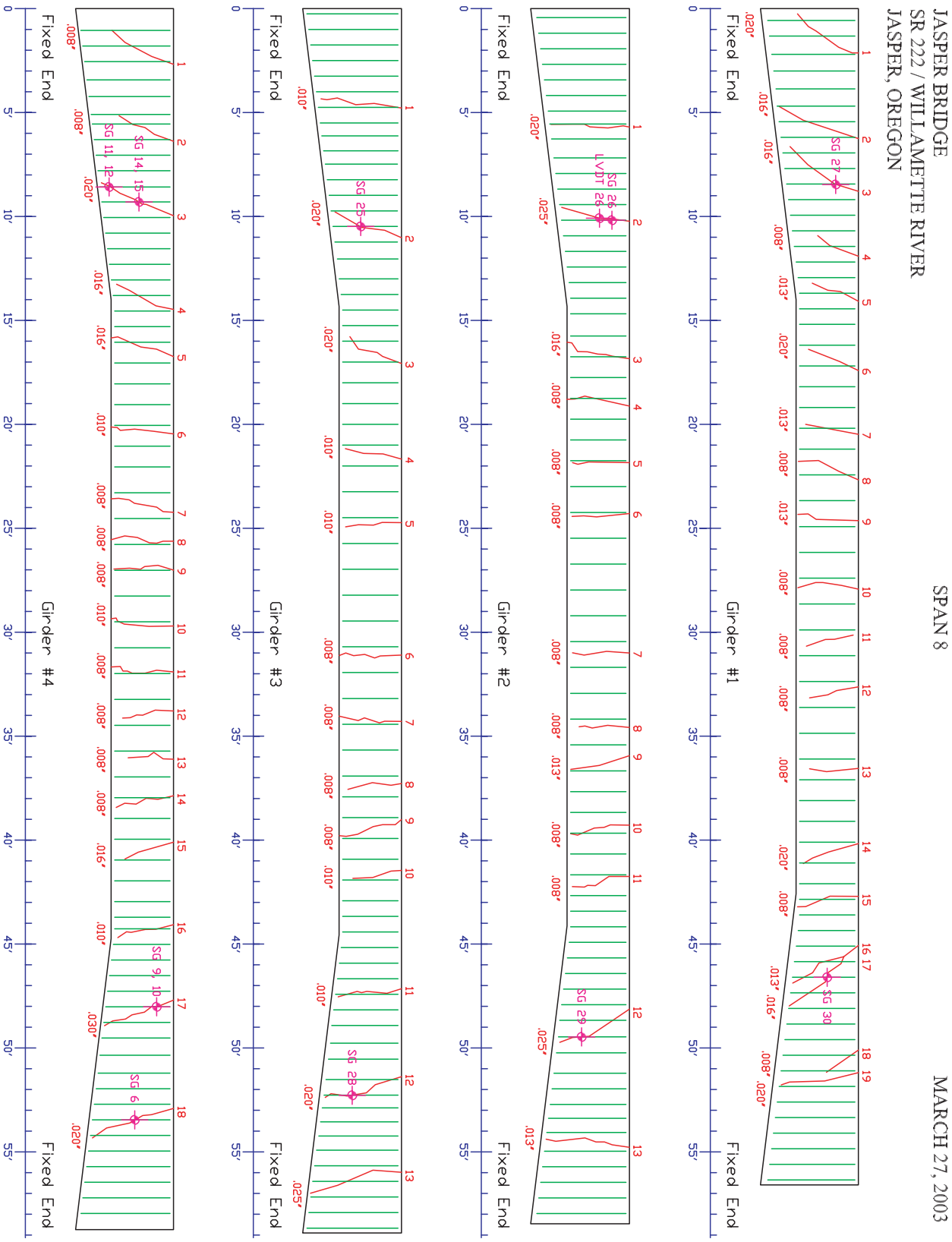

Figure 2.18e - Jasper Bridge crack and instrument locations on span 8

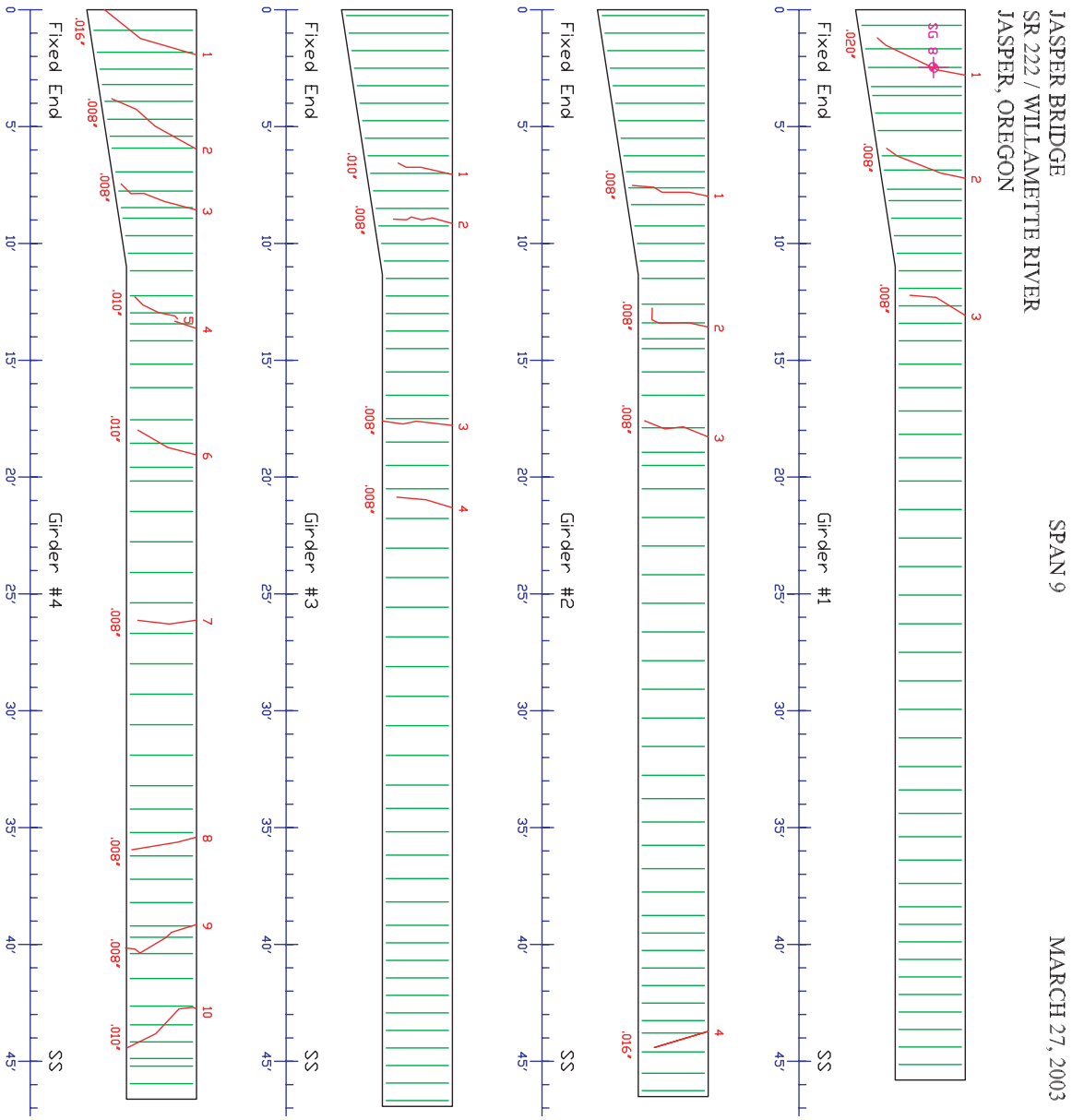

Figure 2.18f: Jasper Bridge crack and instrument locations on span 9

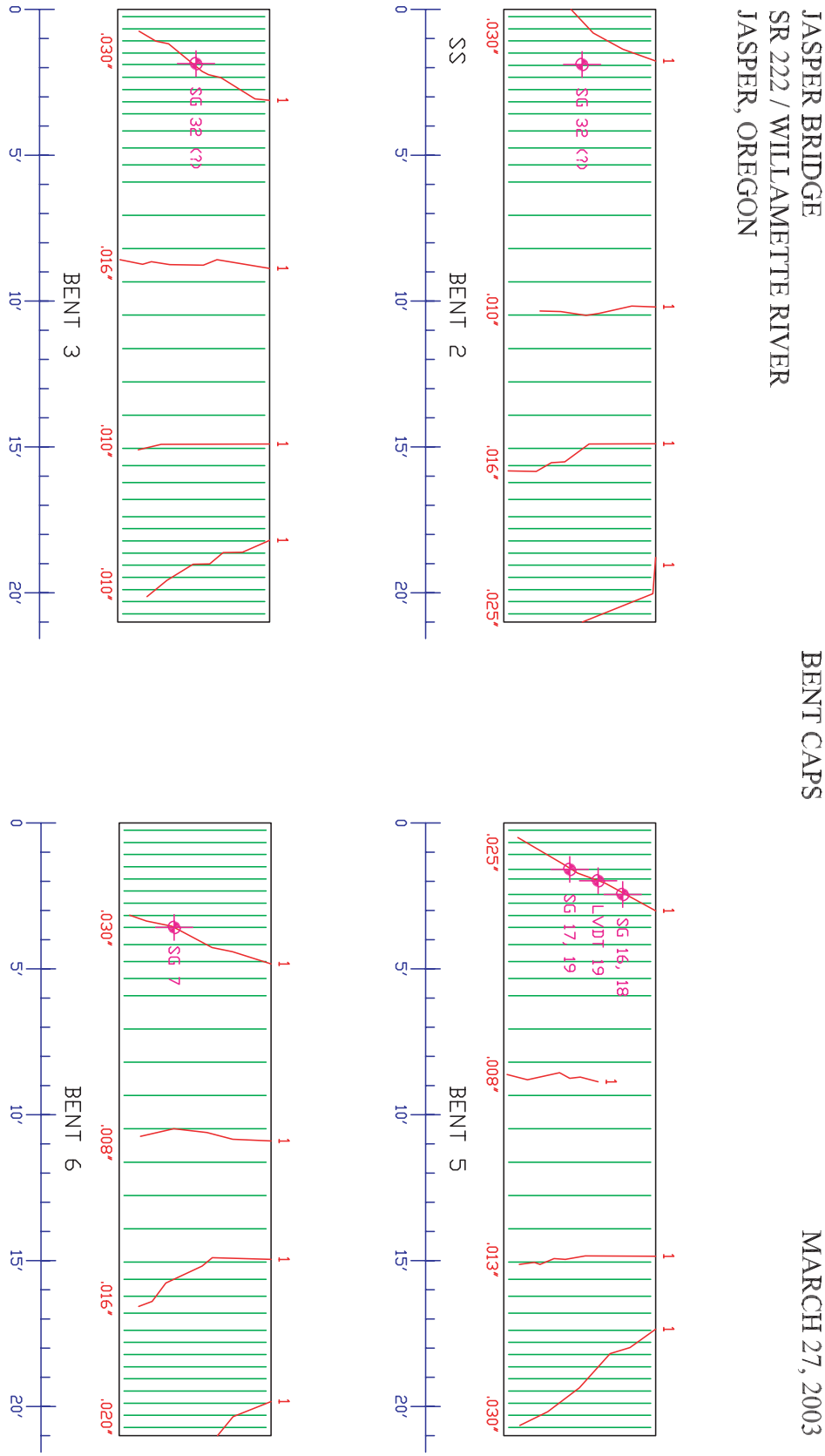

Figure 2.18g: Jasper Bridge crack and instrument locations on bent caps

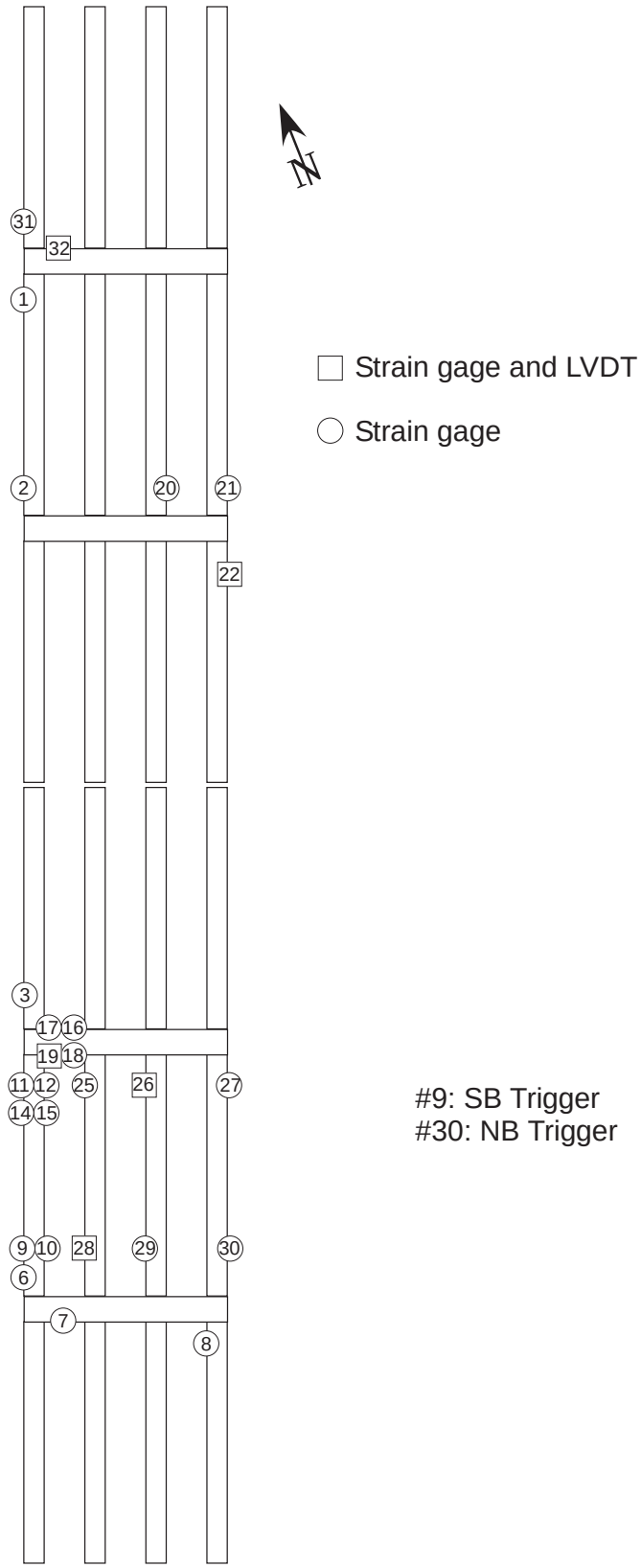

Figure 2.19: Schematic of sensor locations on Jasper Bridge

2.2.3 Testing Method

Three types of live load data were collected: response under ambient traffic loading, response under controlled truck loading, and response under commercial truck loads determined from a temporary vehicle weigh-station. The shear stirrup stresses and crack displacements generated by ambient traffic were recorded over a period of 11 days, in April 2003. The system also recorded individual event histories when stress thresholds exceeded 2.0 ksi at sensor location CH_9 (northbound) or 1.5 ksi at sensor location CH_30 (southbound).

For each northbound trigger event, data were recorded for eight seconds prior to and two seconds following the trigger. The pre and post trigger times were interchanged for the southbound trigger events. During these events, a video image of the corresponding vehicle was produced. Based on the video images taken during daylight hours, the observed vehicle configurations were categorized and are summarized in Figure 2.20. The type of cargo being transported by the observed vehicles is summarized in Figure 2.21. The most commonly observed axle configuration was 3-2 and the most frequently observed cargo type was forest products.

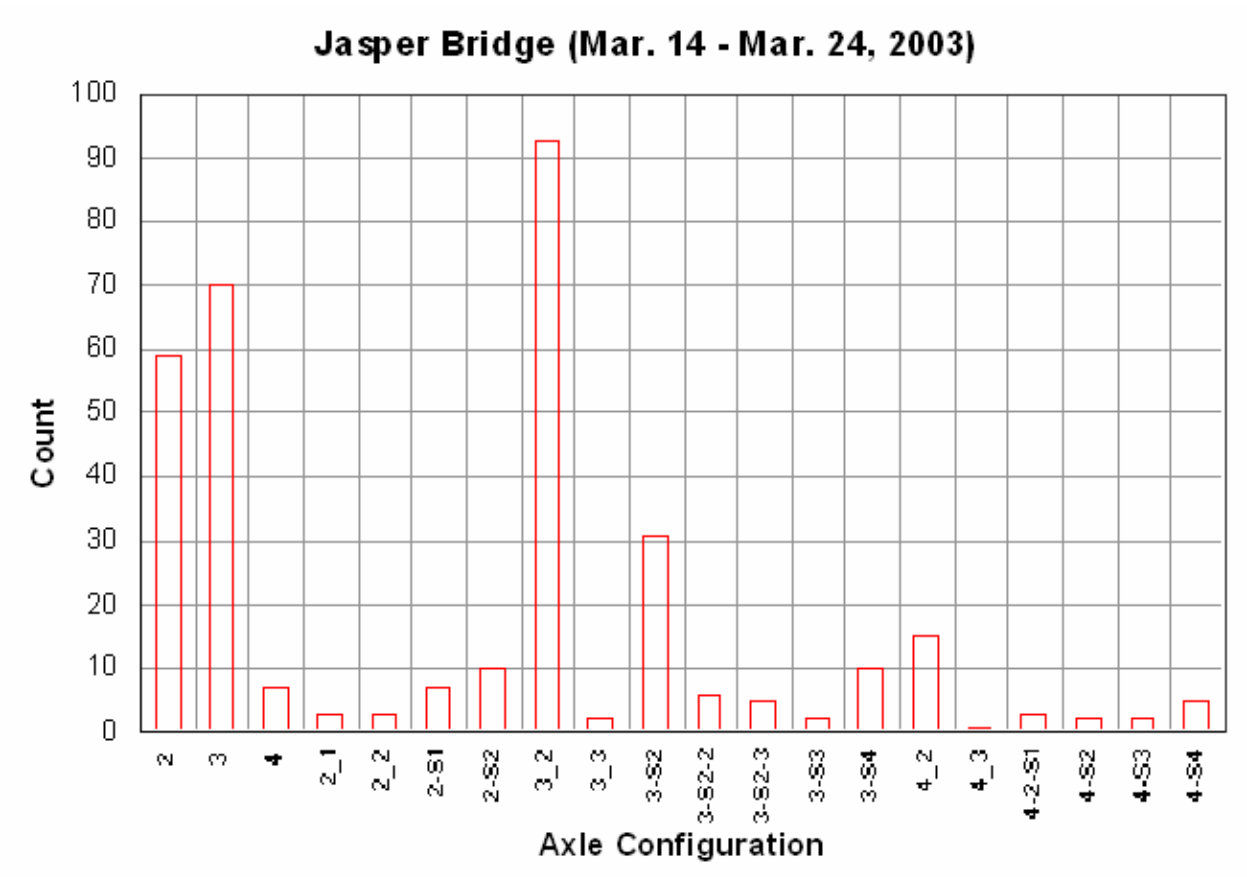

Figure 2.20: Classification of vehicle configuration based on video data from Jasper Bridge

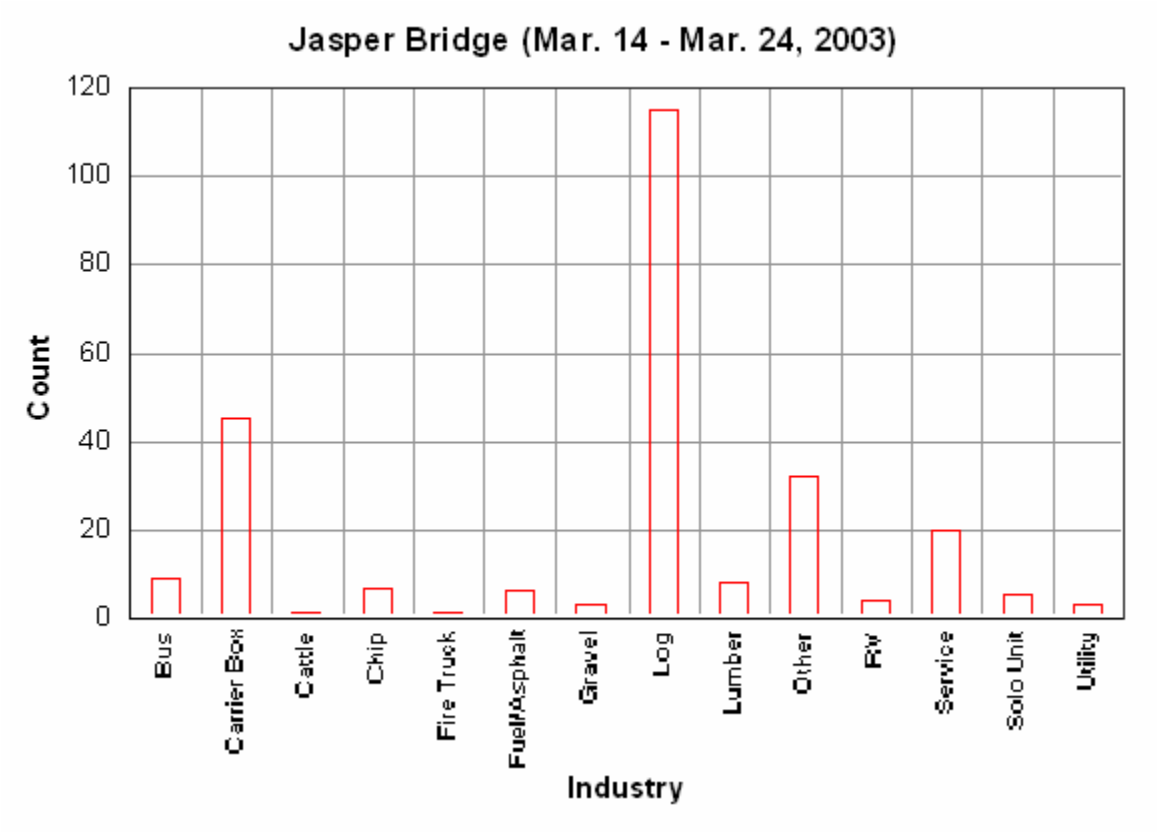

Figure 2.21: Classification of cargo type based on video data from Jasper Bridge

Controlled truck tests were conducted using a heavily loaded ODOT maintenance truck as shown in Figure 2.22a. The axle weights and spacing were determined before the test and are shown in Figure 2.22b. Traffic was temporarily stopped so that the control truck would be the only vehicle on the structure during data collection. The control truck passed over the bridge at several designated speeds and lane positions.

Figure 2.22a: Test truck used on Jasper Bridge

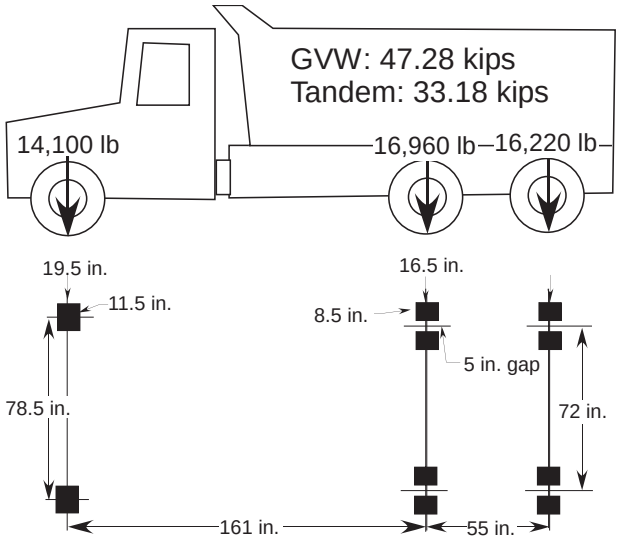

Figure 2.22b: Truck axle spacing and weights for tests on Jasper Bridge

Truck locations relative to girder positions are shown in Figure 2.23. Stirrup stresses for each of the test runs are shown in Figures 2.24a-j. and crack motions are shown in Figures 2.25 a-b. Test data are summarized in Tables 2.2a-b.

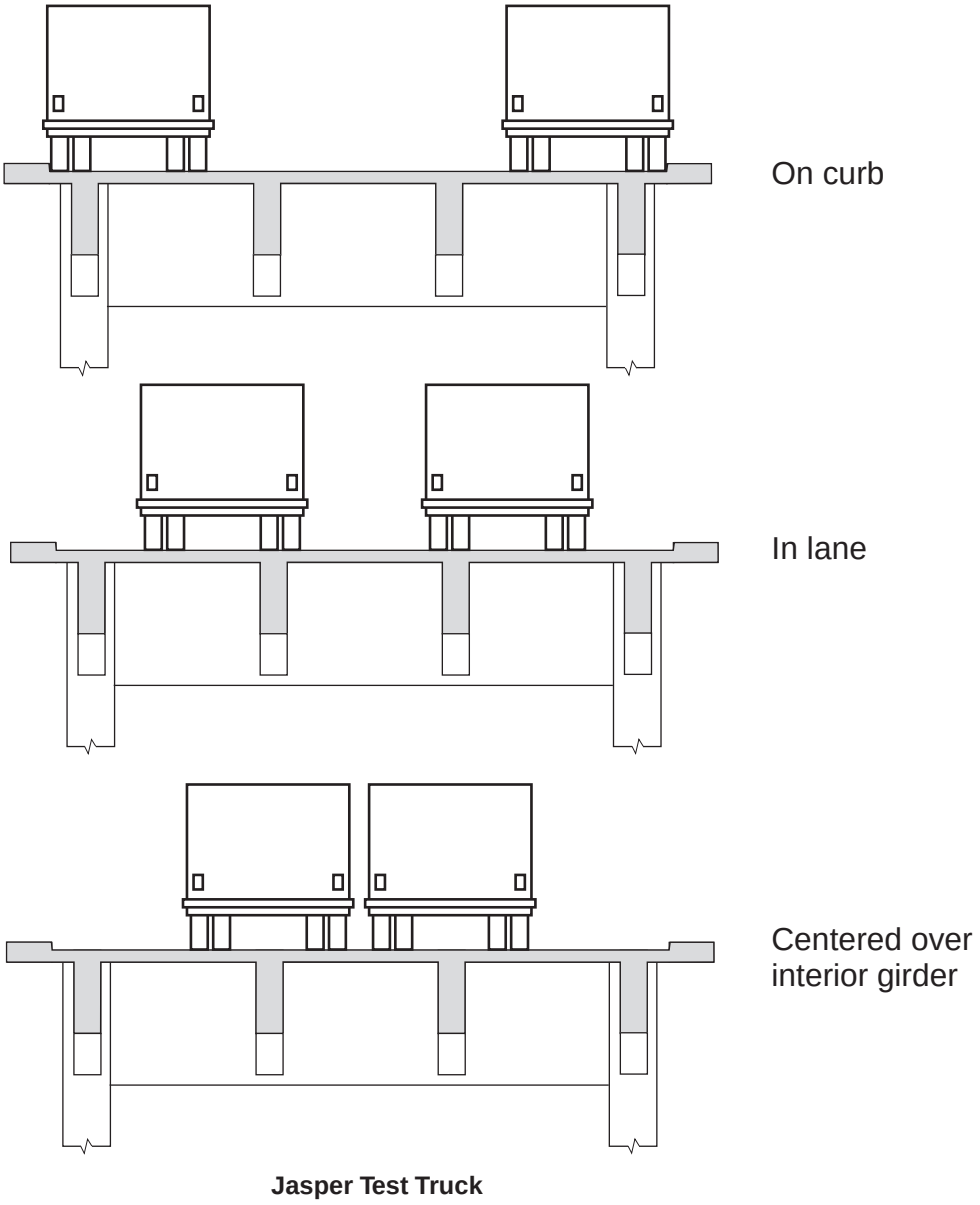

Figure 2.23: Truck position relative to girders for tests on Jasper Bridge

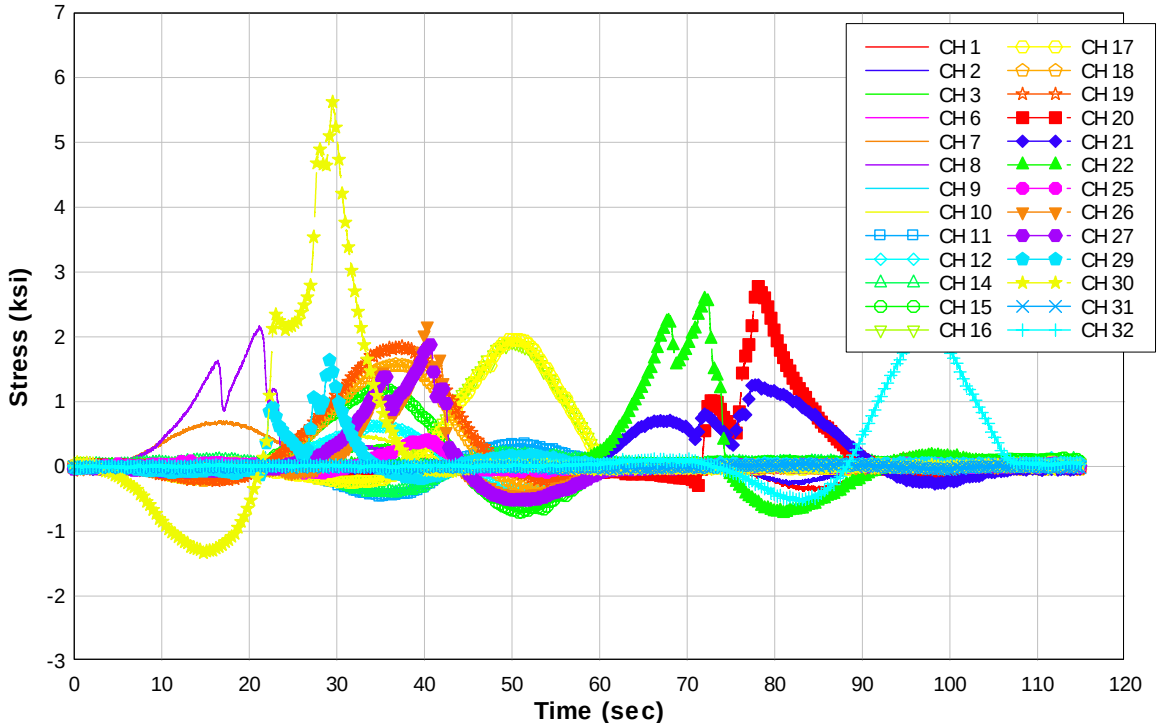

Figure 2.24a: Stirrup stress response for test truck heading northbound on curb at 3 mph

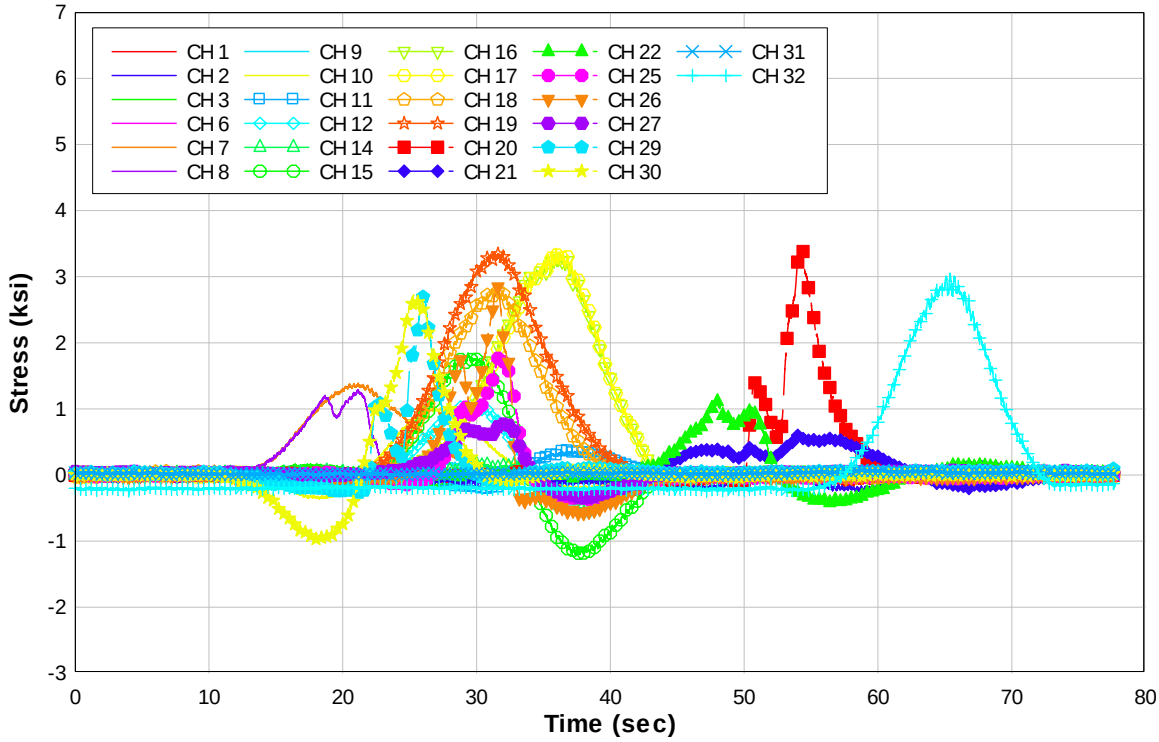

Figure 2.24b: Stirrup stress response for test truck heading northbound centered over first interior girder at 3 mph

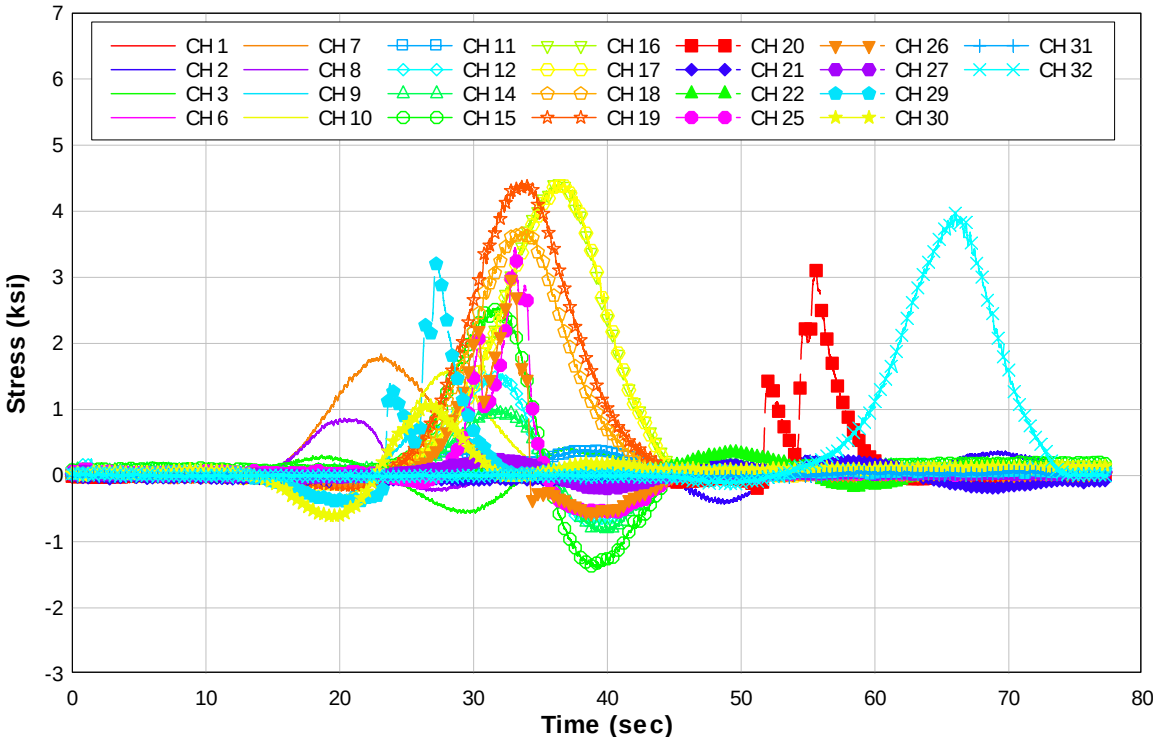

Figure 2.24c: Stirrup stress response for test truck heading northbound centered over second interior girder at 3 mph

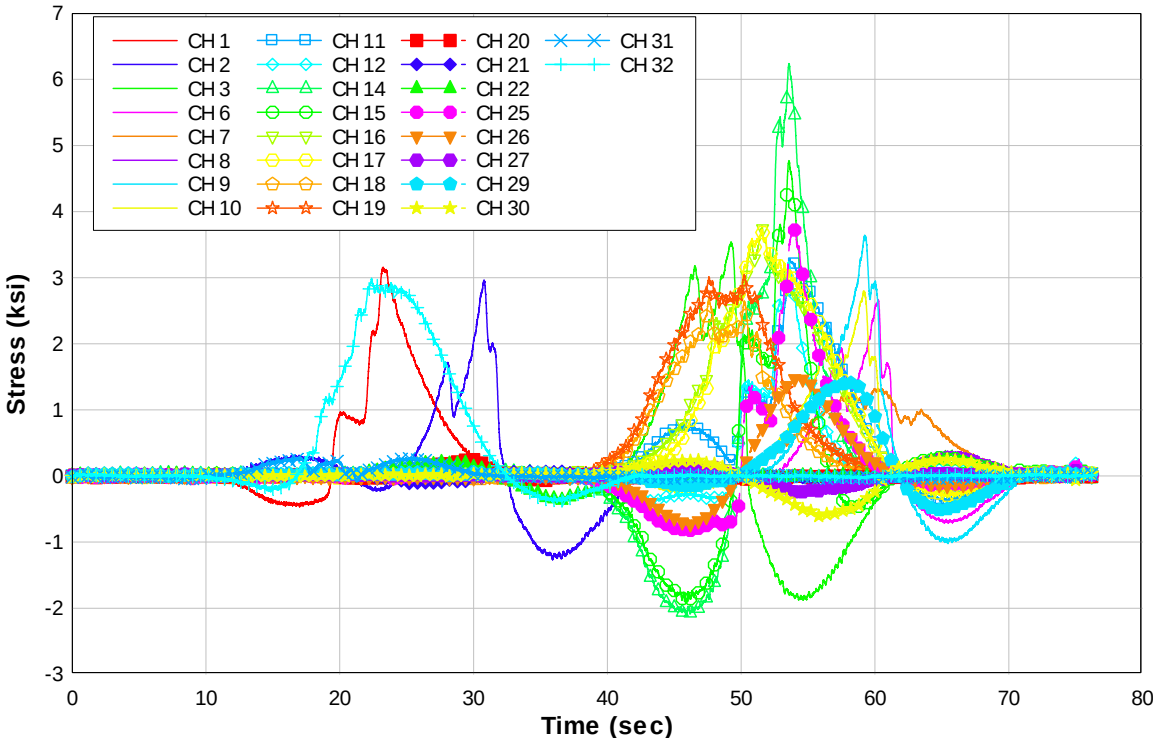

Figure 2.24d: Stirrup stress response for test truck heading southbound on curb at 3 mph

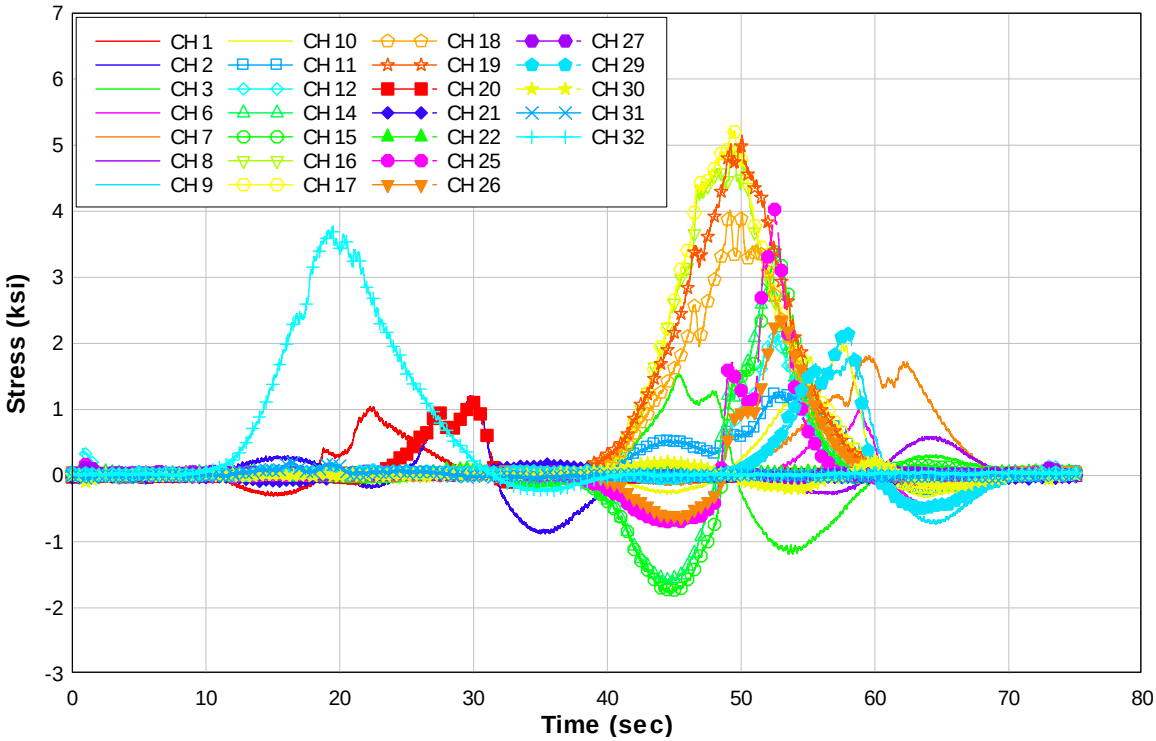

Figure 2.24e: Stirrup stress response for test truck heading southbound centered over first interior girder at 3 mph

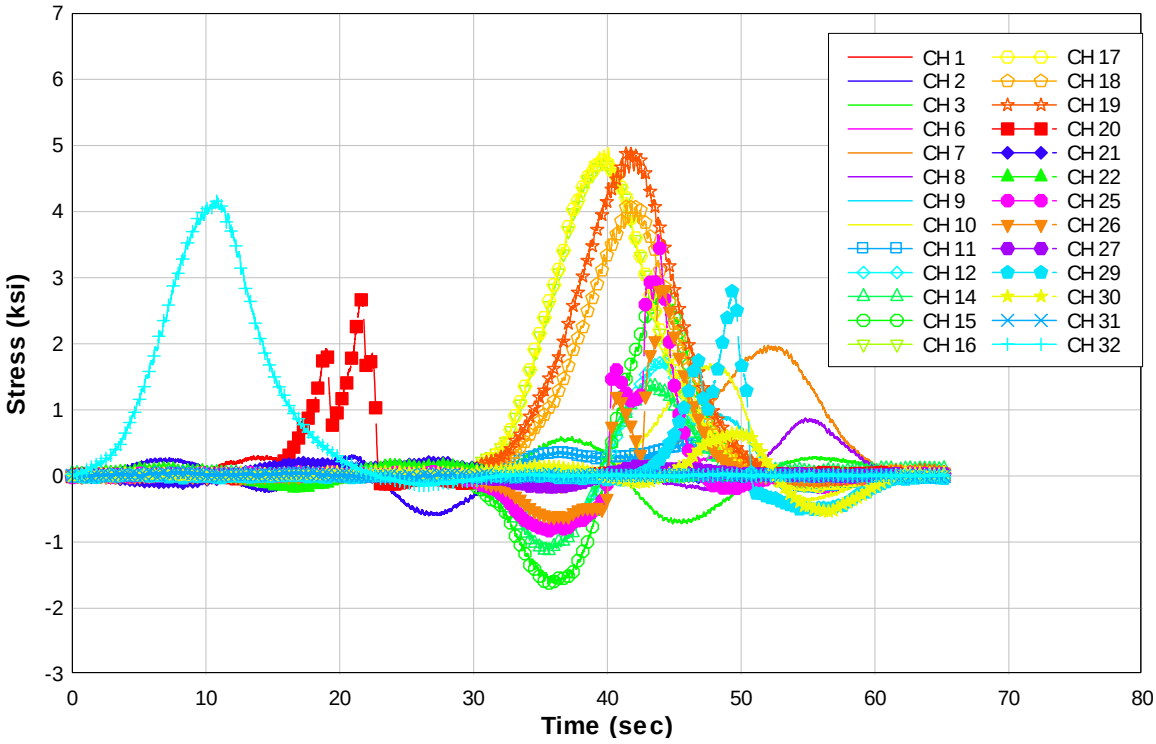

Figure 2.24f: Stirrup stress response for test truck heading southbound centered over second interior girder at 3 mph

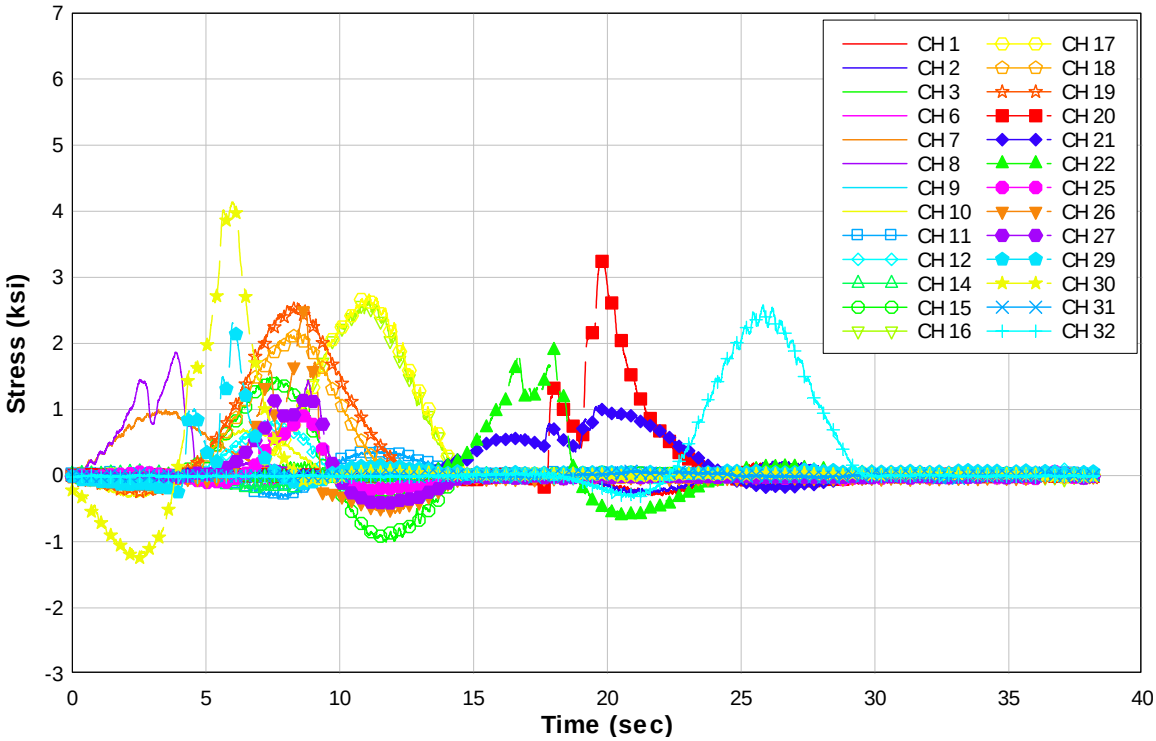

Figure 2.24g: Stirrup stress response for test truck in northbound lane at 5 mph

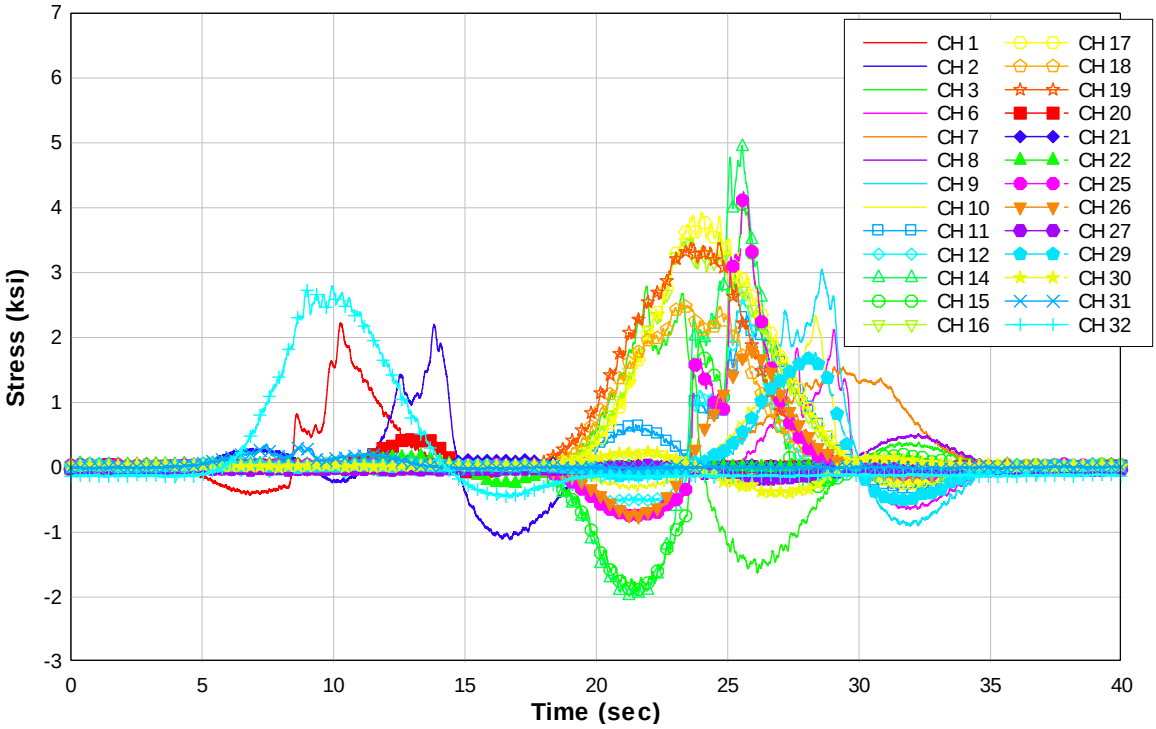

Figure 2.24h: Stirrup stress response for test truck in southbound lane at 5 mph

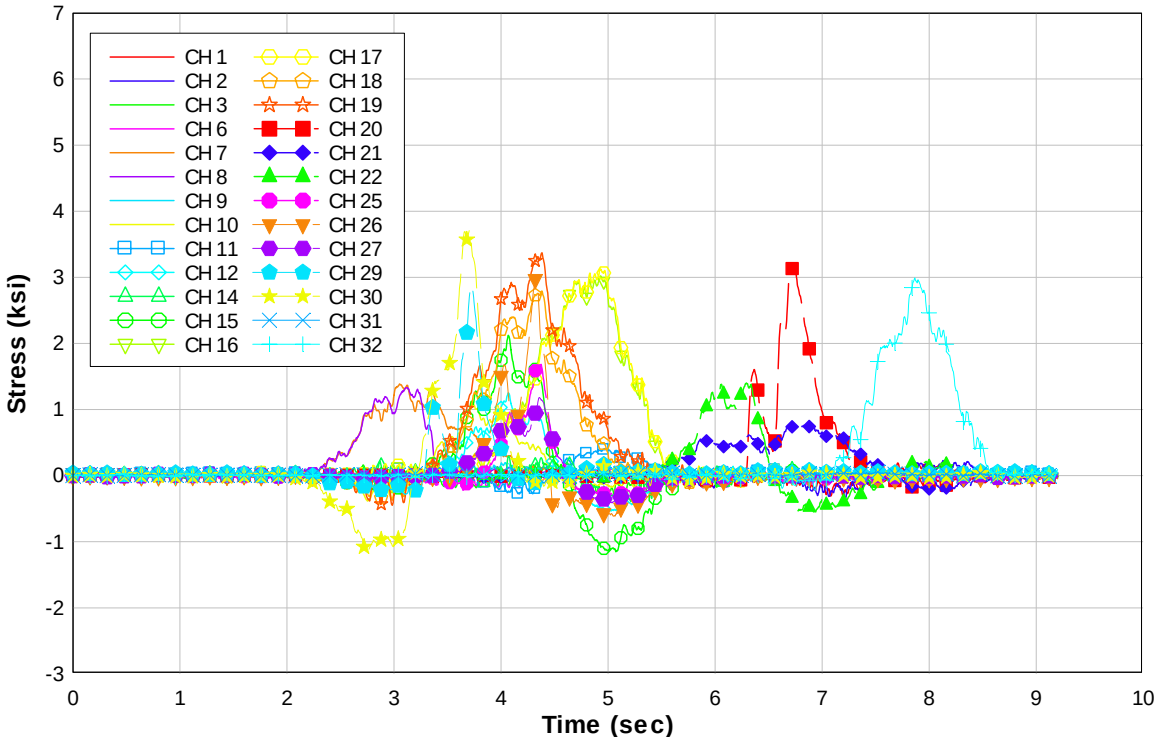

Figure 2.24i: Stirrup stress response for test truck in northbound lane at 34 mph

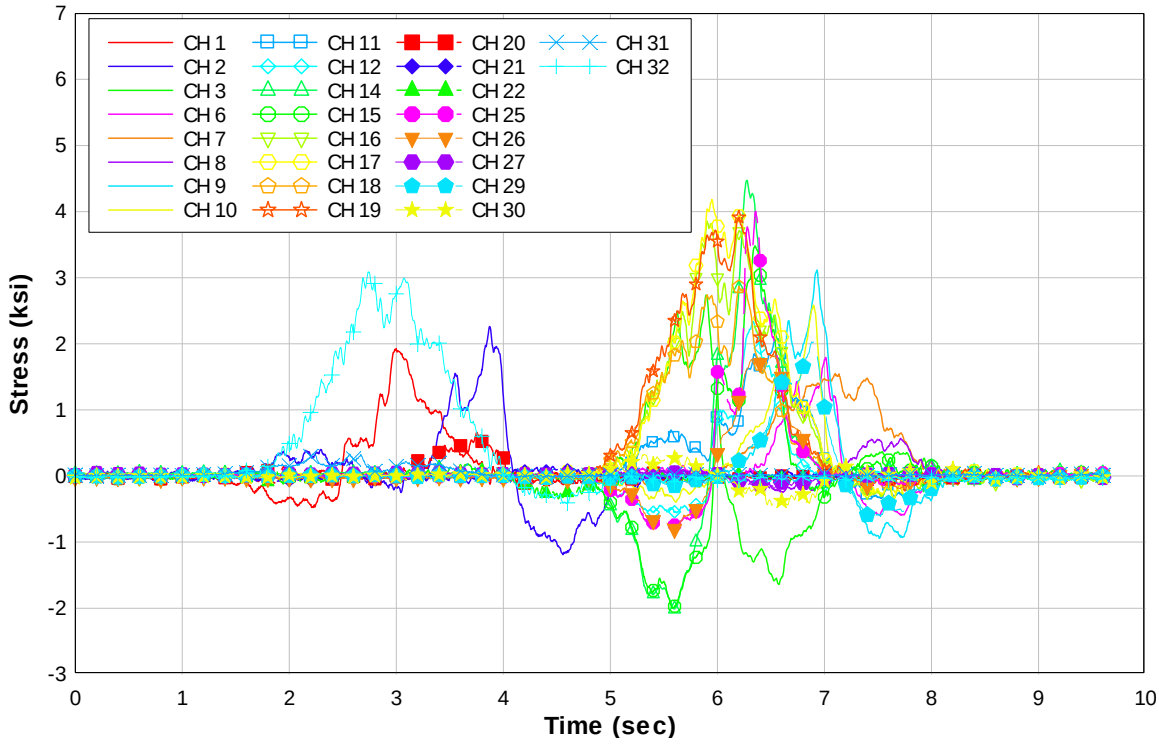

Figure 2.24j: Stirrup stress response for test truck in southbound lane at 32 mph

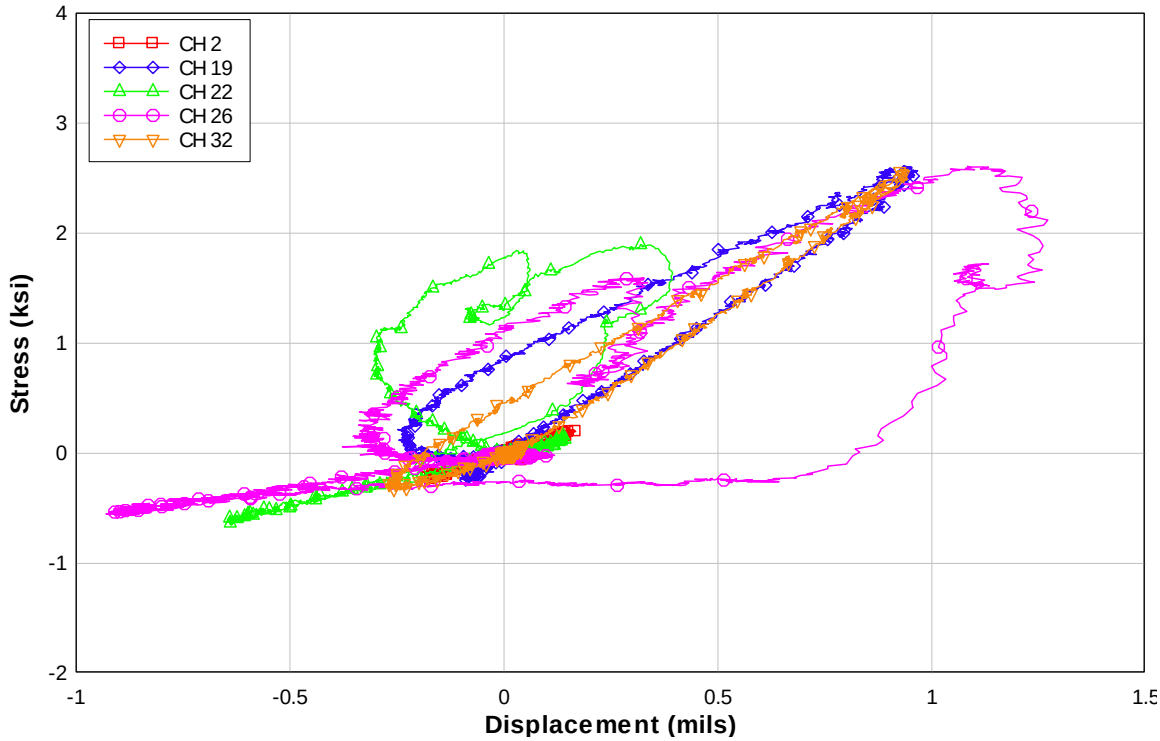

Figure 2.25a: Crack displacement-Stirrup stress response for test truck in northbound lane at 5 mph

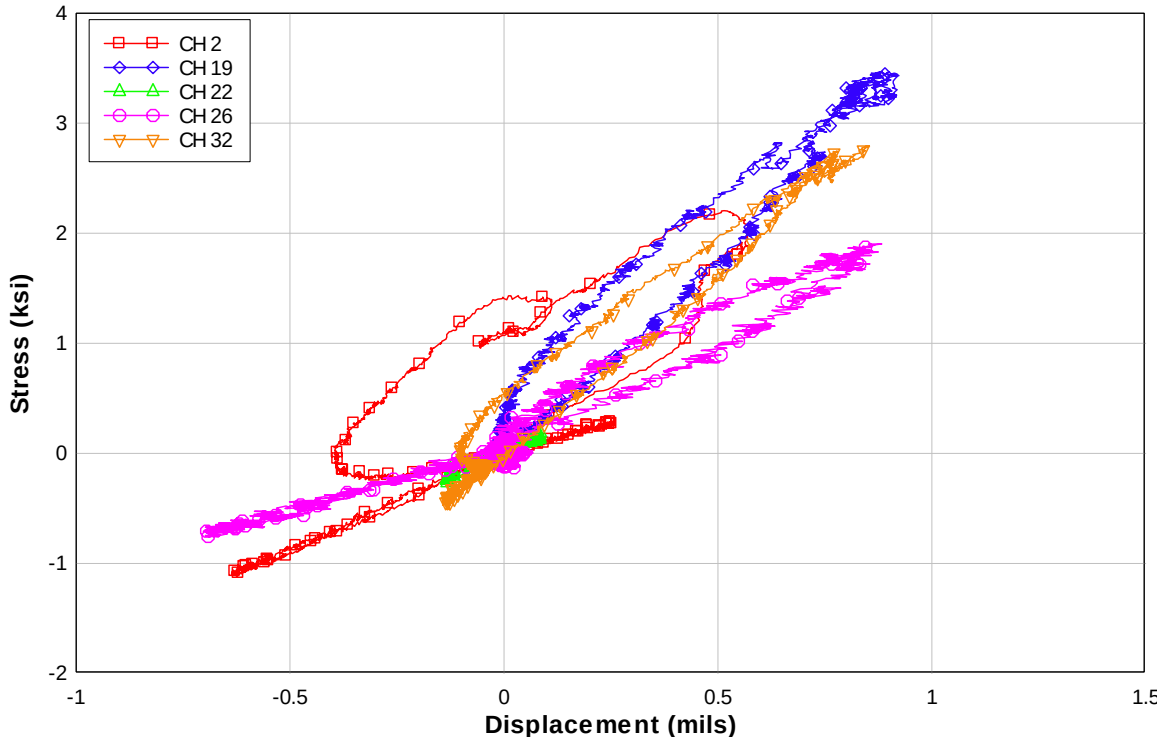

Figure 2.25b: Crack displacement-Stirrup stress response for test truck in northbound lane at 5 mph

Table 2.2a: Stresses at instrumented locations for slow speed tests of ODOT truck moving over Jasper Bridge

Maximum Stress

Truck Location	CH 1 (ksi)	CH 2 (ksi)	CH 3 (ksi)	CH 6 (ksi)	CH 7 (ksi)	CH 8 (ksi)	CH 9 (ksi)	CH 10 (ksi)	CH 11 (ksi)	CH 12 (ksi)	CH 14 (ksi)	CH 15 (ksi)	CH 16 (ksi)	CH 17 (ksi)	CH 18 (ksi)	CH 19 (ksi)	CH 20 (ksi)	CH 21 (ksi)	CH 22 (ksi)	CH 25 (ksi)	CH 26 (ksi)	CH 27 (ksi)	CH 29 (ksi)	CH 30 (ksi)	CH 31 (ksi)	CH 32 (ksi)
NB curb	0.24	0.22	0.35	0.11	0.71	2.17	0.17	0.50	0.36	0.65	0.22	1.22	1.94	1.99	1.59	1.87	2.80	1.28	2.63	0.44	2.17	1.90	1.66	5.65	0.06	2.16
NB Lane	0.20	0.22	0.23	0.15	1.00	1.87	0.10	0.71	0.38	0.83	0.13	1.49	2.64	2.75	2.20	2.61	3.24	1.06	1.90	0.98	2.61	1.45	2.32	4.14	0.08	2.58
NB Center Girder 2	0.13	0.21	0.17	0.14	1.39	1.29	0.27	1.03	0.36	1.11	0.18	1.84	3.36	3.43	2.80	3.37	3.43	0.62	1.12	1.80	2.84	0.81	2.76	2.73	0.09	3.05
NB Center Girder 3	0.18	0.38	0.43	0.26	1.84	0.87	0.76	1.59	0.40	1.54	1.02	2.55	4.46	4.45	3.70	4.43	3.12	0.24	0.39	3.45	3.02	0.26	3.24	1.08	0.08	3.98
SB Center Girder 2	0.31	0.31	0.59	0.34	1.98	0.88	0.94	1.70	0.51	1.75	1.38	2.81	4.92	4.97	4.11	4.92	2.70	0.23	0.18	3.65	2.89	0.16	2.85	0.66	0.08	4.22
SB Center Girder 3	1.05	1.21	1.54	1.00	1.81	0.59	1.80	2.01	1.25	2.14	2.83	3.44	4.93	5.26	4.01	5.15	1.14	0.17	0.11	4.08	2.42	0.16	2.26	0.23	0.22	3.76
SB Lane	2.23	2.20	2.79	2.12	1.55	0.52	3.05	2.34	2.33	2.63	4.96	4.05	3.62	3.93	2.53	3.47	0.51	0.14	0.19	4.25	1.90	0.05	1.76	0.29	0.36	2.79
SB Curb	3.16	2.96	3.54	2.66	1.33	0.38	3.64	2.80	3.29	3.24	6.24	4.77	3.78	3.72	2.70	3.04	0.29	0.10	0.23	3.75	1.49	0.15	1.48	0.28	0.28	2.99

Minimum Stresses

Truck Location	CH 1 (ksi)	CH 2 (ksi)	CH 3 (ksi)	CH 6 (ksi)	CH 7 (ksi)	CH 8 (ksi)	CH 9 (ksi)	CH 10 (ksi)	CH 11 (ksi)	CH 12 (ksi)	CH 14 (ksi)	CH 15 (ksi)	CH 16 (ksi)	CH 17 (ksi)	CH 18 (ksi)	CH 19 (ksi)	CH 20 (ksi)	CH 21 (ksi)	CH 22 (ksi)	CH 25 (ksi)	CH 26 (ksi)	CH 27 (ksi)	CH 29 (ksi)	CH 30 (ksi)	CH 31 (ksi)	CH 32 (ksi)
NB curb	-0.38	-0.29	-0.51	-0.26	-0.08	-0.09	-0.26	-0.29	-0.48	-0.39	-0.42	-0.72	-0.21	-0.26	-0.39	-0.25	-0.30	-0.28	-0.74	-0.12	-0.48	-0.55	-0.21	-1.33	-0.06	-0.56
NB Lane	-0.30	-0.29	-0.33	-0.18	-0.08	-0.16	-0.12	-0.33	-0.33	-0.51	-0.25	-1.01	-0.07	-0.08	-0.22	-0.26	-0.18	-0.22	-0.65	-0.23	-0.56	-0.47	-0.28	-1.26	-0.06	-0.34
NB Center Girder 2	-0.17	-0.25	-0.18	-0.11	-0.11	-0.05	-0.25	-0.36	-0.23	-0.59	-0.47	-1.21	-0.06	-0.12	-0.18	-0.22	-0.18	-0.21	-0.43	-0.41	-0.60	-0.35	-0.29	-0.98	-0.02	-0.25
NB Center Girder 3	-0.11	-0.43	-0.57	-0.20	-0.14	-0.24	-0.37	-0.36	-0.16	-0.72	-0.86	-1.40	-0.06	-0.16	-0.13	-0.18	-0.27	-0.21	-0.18	-0.58	-0.60	-0.22	-0.41	-0.64	-0.05	-0.13
SB Center Girder 2	-0.14	-0.60	-0.72	-0.26	-0.09	-0.23	-0.51	-0.37	-0.20	-0.83	-1.16	-1.64	-0.15	-0.17	-0.10	-0.10	-0.15	-0.13	-0.20	-0.83	-0.64	-0.19	-0.53	-0.56	-0.05	-0.16
SB Center Girder 3	-0.31	-0.88	-1.19	-0.49	-0.15	-0.29	-0.74	-0.33	-0.23	-0.71	-1.63	-1.79	-0.19	-0.21	-0.07	-0.10	-0.12	-0.10	-0.16	-0.72	-0.65	-0.06	-0.50	-0.23	-0.06	-0.24
SB Lane	-0.43	-1.12	-1.63	-0.65	-0.14	-0.24	-0.91	-0.37	-0.35	-0.54	-1.98	-1.91	-0.25	-0.27	-0.11	-0.10	-0.11	-0.06	-0.28	-0.76	-0.76	-0.24	-0.54	-0.45	-0.04	-0.47
SB Curb	-0.47	-1.27	-1.88	-0.71	-0.14	-0.28	-1.02	-0.27	-0.38	-0.40	-2.10	-1.90	-0.23	-0.32	-0.07	-0.07	-0.09	-0.13	-0.39	-0.82	-0.75	-0.25	-0.54	-0.62	-0.09	-0.41

Stress Range

Truck Location	CH 1 (ksi)	CH 2 (ksi)	CH 3 (ksi)	CH 6 (ksi)	CH 7 (ksi)	CH 8 (ksi)	CH 9 (ksi)	CH 10 (ksi)	CH 11 (ksi)	CH 12 (ksi)	CH 14 (ksi)	CH 15 (ksi)	CH 16 (ksi)	CH 17 (ksi)	CH 18 (ksi)	CH 19 (ksi)	CH 20 (ksi)	CH 21 (ksi)	CH 22 (ksi)	CH 25 (ksi)	CH 26 (ksi)	CH 27 (ksi)	CH 29 (ksi)	CH 30 (ksi)	CH 31 (ksi)	CH 32 (ksi)
NB curb	0.62	0.51	0.86	0.37	0.79	2.25	0.43	0.79	0.84	1.04	0.64	1.94	2.15	2.25	1.97	2.13	3.10	1.56	3.37	0.56	2.65	2.44	1.87	6.98	0.13	2.72
NB Lane	0.50	0.51	0.56	0.33	1.08	2.03	0.22	1.05	0.71	1.34	0.39	2.50	2.72	2.83	2.42	2.87	3.42	1.28	2.55	1.21	3.17	1.92	2.60	5.40	0.14	2.92
NB Center Girder 2	0.30	0.47	0.35	0.25	1.50	1.34	0.53	1.39	0.59	1.70	0.65	3.05	3.42	3.55	2.98	3.59	3.60	0.83	1.55	2.21	3.44	1.16	3.05	3.71	0.12	3.31
NB Center Girder 3	0.28	0.81	1.00	0.46	1.98	1.11	1.13	1.95	0.56	2.25	1.88	3.95	4.53	4.61	3.84	4.61	3.38	0.45	0.57	4.03	3.61	0.49	3.64	1.72	0.14	4.12
SB Center Girder 2	0.45	0.92	1.32	0.61	2.07	1.11	1.46	2.07	0.71	2.58	2.54	4.44	5.07	5.14	4.21	5.02	2.85	0.36	0.38	4.49	3.53	0.35	3.38	1.22	0.12	4.38
SB Center Girder 3	1.35	2.09	2.73	1.49	1.97	0.88	2.53	2.34	1.48	2.85	4.46	5.23	5.12	5.47	4.08	5.25	1.26	0.27	0.27	4.80	3.06	0.22	2.77	0.46	0.28	4.01
SB Lane	2.66	3.32	4.42	2.78	1.70	0.75	3.96	2.71	2.68	3.16	6.95	5.96	3.87	4.20	2.64	3.57	0.62	0.19	0.46	5.01	2.66	0.29	2.31	0.74	0.40	3.27
SB Curb	3.63	4.23	5.42	3.37	1.47	0.66	4.66	3.07	3.67	3.64	8.34	6.68	4.01	4.04	2.77	3.11	0.38	0.23	0.62	4.57	2.23	0.40	2.01	0.90	0.37	3.40

Table 2.2b: Maximum stress at instrumented locations for traveling speed tests of ODOT truck moving over Jasper Bridge

Truck Location	CH 1 (ksi)	CH 2 (ksi)	CH 3 (ksi)	CH 6 (ksi)	CH 7 (ksi)	CH 8 (ksi)	CH 9 (ksi)	CH 10 (ksi)	CH 11 (ksi)	CH 12 (ksi)	CH 14 (ksi)	CH 15 (ksi)	CH 16 (ksi)	CH 17 (ksi)	CH 18 (ksi)	CH 19 (ksi)	CH 20 (ksi)	CH 21 (ksi)	CH 22 (ksi)	CH 25 (ksi)	CH 26 (ksi)	CH 27 (ksi)	CH 29 (ksi)	CH 30 (ksi)	CH 31 (ksi)	CH 32 (ksi)
NB Lane 34mph	0.20	0.23	0.19	0.15	1.39	1.33	0.21	1.07	0.41	1.25	0.30	2.12	3.02	3.13	2.79	3.37	3.18	0.78	1.40	1.68	2.99	1.18	2.89	3.73	0.06	2.99
SB Lane 32mph	1.92	2.26	2.74	1.79	1.55	0.57	3.12	2.58	2.07	2.34	4.47	3.48	3.85	4.18	2.87	3.92	0.66	0.14	0.18	4.01	1.82	0.07	2.03	0.36	0.33	3.09

Additionally, the test truck was positioned at specific locations where the steering axle was located over a bent or end support and held at that location to determine static stirrup stress magnitudes as illustrated in Figure 2.26. The truck was positioned against the curb for each of these tests. Test positions are shown in Figure 2.27 and strain measurements for each of these positions are summarized in Tables 2.3a-d.

Figure 2.26: Static positioning of test truck along curb for Jasper Bridge

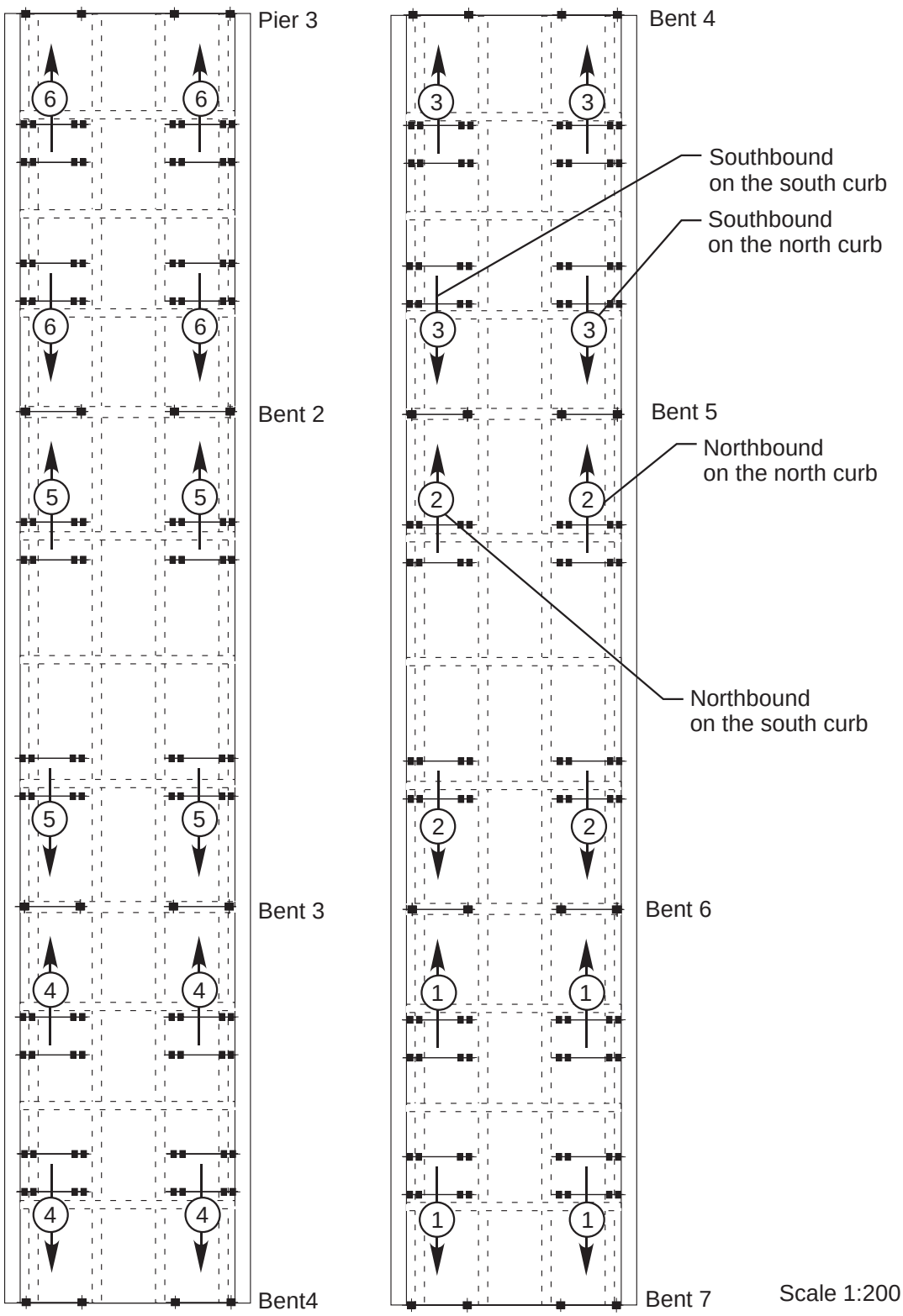

Figure 2.27: Static positioning locations for test truck on Jasper Bridge

Table 2.3a: Stresses at instrumented locations when ODOT truck oriented northbound against the north curb and stationary with steering axle over bents for Jasper Bridge

Truck Location	CH 1 (ksi)	CH 2 (ksi)	CH 3 (ksi)	CH 6 (ksi)	CH 7 (ksi)	CH 8 (ksi)	CH 9 (ksi)	CH 10 (ksi)	CH 11 (ksi)	CH 12 (ksi)	CH 14 (ksi)	CH 15 (ksi)	CH 16 (ksi)	CH 17 (ksi)	CH 18 (ksi)	CH 19 (ksi)	CH 20 (ksi)	CH 21 (ksi)	CH 22 (ksi)	CH 25 (ksi)	CH 26 (ksi)	CH 27 (ksi)	CH 29 (ksi)	CH 30 (ksi)	CH 31 (ksi)	CH 32 (ksi)
1	0.05	0.02	0.07	0.09	0.60	1.29	0.08	-0.22	0.02	-0.03	0.11	-0.06	0.05	0.02	-0.17	-0.16	-0.02	-0.02	0.02	0.08	-0.01	-0.07	-0.26	-1.24	0.02	0.08
2	0.08	0.04	0.30	-0.08	-0.07	0.06	-0.07	0.24	-0.35	0.49	-0.27	0.83	0.29	0.20	1.44	1.69	-0.02	-0.03	0.04	0.63	1.82	1.71	-0.31	-0.06	0.02	0.09
3	0.10	0.05	-0.24	0.13	-0.07	-0.07	0.09	-0.11	0.19	-0.22	0.19	-0.43	1.20	1.24	-0.29	-0.17	-0.01	-0.02	0.02	-0.26	-0.29	-0.42	0.12	0.08	0.01	0.09
4	0.17	0.11	0.10	0.07	-0.07	-0.05	0.07	0.00	0.02	0.08	0.13	0.13	0.10	0.02	-0.06	-0.02	-0.52	0.37	2.06	0.03	0.02	0.00	0.03	0.13	0.01	0.17
5	-0.15	-0.09	0.14	0.08	-0.07	-0.03	0.10	0.00	0.01	0.09	0.16	0.16	0.14	0.00	-0.06	-0.01	0.12	0.30	-0.27	0.04	0.02	0.02	0.04	0.16	0.03	0.06
6	0.26	0.21	0.17	0.09	-0.07	0.01	0.11	0.00	0.01	0.13	0.20	0.20	0.13	0.02	-0.06	-0.01	-0.01	-0.15	0.18	0.08	0.02	0.03	0.06	0.20	-0.02	1.30
start zero	0.04	0.02	0.02	0.05	-0.03	-0.02	0.00	0.01	0.00	0.03	0.04	0.04	0.03	0.01	0.01	0.02	-0.01	0.00	0.00	0.02	0.01	-0.03	-0.04	-0.01	0.00	0.05
end zero	0.14	0.11	0.18	0.07	-0.07	0.01	0.10	0.00	0.02	0.14	0.22	0.23	0.15	0.02	-0.07	0.01	-0.01	-0.05	0.07	0.10	0.02	0.01	0.07	0.21	0.00	0.13

Table 2.3b: Stresses at instrumented locations when ODOT truck oriented southbound against the north curb and stationary with steering axle over bents for Jasper Bridge

Truck Location	CH 1 (ksi)	CH 2 (ksi)	CH 3 (ksi)	CH 6 (ksi)	CH 7 (ksi)	CH 8 (ksi)	CH 9 (ksi)	CH 10 (ksi)	CH 11 (ksi)	CH 12 (ksi)	CH 14 (ksi)	CH 15 (ksi)	CH 16 (ksi)	CH 17 (ksi)	CH 18 (ksi)	CH 19 (ksi)	CH 20 (ksi)	CH 21 (ksi)	CH 22 (ksi)	CH 25 (ksi)	CH 26 (ksi)	CH 27 (ksi)	CH 29 (ksi)	CH 30 (ksi)	CH 31 (ksi)	CH 32 (ksi)
6	0.22	0.19	0.04	0.02	0.01	0.03	0.03	-0.02	0.02	0.03	0.06	0.04	0.02	0.03	0.00	0.02	-0.01	-0.09	0.16	0.02	0.03	0.02	0.04	0.01	-0.01	1.88
5	-0.11	-0.13	0.09	0.03	0.01	0.02	0.07	0.03	0.01	0.04	0.05	0.06	0.02	0.05	0.03	0.05	1.71	0.93	-0.56	0.05	0.01	0.03	0.05	0.06	0.00	-0.29
4	0.11	0.16	0.11	0.05	0.00	0.03	0.09	0.05	0.02	0.06	0.07	0.08	0.05	0.05	0.02	0.04	-0.41	0.32	0.75	0.06	0.01	0.01	0.04	0.06	0.01	0.07
3	0.08	0.11	-0.24	0.15	-0.02	-0.01	0.15	-0.09	0.31	-0.32	0.22	-0.52	1.92	1.97	0.10	0.35	0.03	0.02	0.04	-0.23	-0.36	-0.47	0.18	0.16	0.01	0.04
2	0.11	0.13	0.22	-0.12	0.21	0.26	-0.10	0.40	-0.14	0.34	-0.06	0.60	-0.06	-0.13	0.53	0.63	0.05	0.01	0.05	-0.09	0.05	0.22	1.37	5.64	-0.01	0.05
1	0.10	0.14	0.25	0.16	0.36	0.34	0.12	-0.17	0.06	0.06	0.19	0.06	0.10	0.06	-0.10	-0.06	0.06	0.01	0.04	0.16	0.07	0.09	-0.18	-0.95	0.00	0.05
start zero	0.03	0.04	0.01	0.02	0.01	0.01	0.03	-0.02	0.01	0.00	0.02	0.02	0.00	0.00	0.01	0.02	-0.01	0.01	-0.01	0.00	0.00	0.00	0.01	0.01	0.01	0.04
end zero	0.13	0.16	0.23	0.11	0.01	0.07	0.13	0.04	0.03	0.16	0.18	0.18	0.10	0.04	0.04	0.06	0.08	0.00	0.06	0.13	0.08	0.11	0.07	0.15	0.01	0.08

Table 2.3c: Stresses at instrumented locations when ODOT truck oriented northbound against the south curb and stationary with steering axle over bents for Jasper Bridge

Truck Location	CH 1 (ksi)	CH 2 (ksi)	CH 3 (ksi)	CH 6 (ksi)	CH 7 (ksi)	CH 8 (ksi)	CH 9 (ksi)	CH 10 (ksi)	CH 11 (ksi)	CH 12 (ksi)	CH 14 (ksi)	CH 15 (ksi)	CH 16 (ksi)	CH 17 (ksi)	CH 18 (ksi)	CH 19 (ksi)	CH 20 (ksi)	CH 21 (ksi)	CH 22 (ksi)	CH 25 (ksi)	CH 26 (ksi)	CH 27 (ksi)	CH 29 (ksi)	CH 30 (ksi)	CH 31 (ksi)	CH 32 (ksi)
1	0.04	0.01	0.31	-0.61	0.56	0.23	-0.74	-0.09	-0.24	0.15	-0.02	0.19	-0.15	-0.22	-0.02	-0.04	0.02	-0.01	0.00	-0.08	-0.12	0.02	-0.60	0.21	0.01	0.02
2	0.06	0.02	-1.48	-0.10	0.30	-0.13	0.34	0.50	2.80	3.11	5.56	4.52	3.24	3.38	1.65	2.01	0.01	-0.01	0.03	3.88	1.21	-0.17	0.34	-0.28	-0.01	0.04
3	0.06	0.05	0.65	0.08	-0.11	0.02	-0.05	-0.18	0.38	-0.90	-1.67	-1.48	0.26	0.11	1.11	1.28	0.03	0.00	0.03	-1.18	-0.41	0.06	-0.11	0.19	0.01	0.04
4	0.04	-1.27	0.00	0.04	-0.04	-0.03	0.05	0.00	0.04	0.03	0.11	0.06	0.03	-0.01	-0.01	0.03	-0.09	0.08	-0.24	0.01	0.02	-0.02	0.02	0.05	0.02	-0.22
5	1.96	-0.36	0.05	0.04	-0.04	-0.02	0.07	0.02	0.05	0.08	0.15	0.09	0.03	0.02	-0.01	0.05	-0.08	-0.08	0.10	0.05	0.03	0.00	0.04	0.07	0.08	3.05
6	-0.32	0.27	0.06	0.06	-0.03	-0.01	0.07	0.01	0.06	0.09	0.15	0.12	0.06	0.00	-0.03	0.05	0.08	-0.02	0.04	0.08	0.02	-0.02	0.02	0.08	0.12	-0.11
start zero	-0.01	0.03	0.02	0.01	-0.01	0.01	0.01	0.00	0.00	0.01	0.04	0.03	0.02	-0.01	-0.01	0.01	0.01	-0.01	0.01	0.03	0.01	0.03	0.03	0.06	-0.02	0.02
end zero	0.11	0.13	0.06	0.05	-0.03	-0.02	0.08	0.02	0.04	0.07	0.16	0.11	0.06	0.01	-0.02	0.05	0.05	0.00	0.05	0.06	0.02	-0.01	0.04	0.10	0.02	0.03

Table 2.3d: Stresses at instrumented locations when ODOT truck oriented southbound against the south curb and stationary with steering axle over bents for Jasper Bridge

Truck Location	CH 1 (ksi)	CH 2 (ksi)	CH 3 (ksi)	CH 6 (ksi)	CH 7 (ksi)	CH 8 (ksi)	CH 9 (ksi)	CH 10 (ksi)	CH 11 (ksi)	CH 12 (ksi)	CH 14 (ksi)	CH 15 (ksi)	CH 16 (ksi)	CH 17 (ksi)	CH 18 (ksi)	CH 19 (ksi)	CH 20 (ksi)	CH 21 (ksi)	CH 22 (ksi)	CH 25 (ksi)	CH 26 (ksi)	CH 27 (ksi)	CH 29 (ksi)	CH 30 (ksi)	CH 31 (ksi)	CH 32 (ksi)
6	-0.49	0.32	0.10	0.06	0.00	0.02	0.07	0.02	0.02	0.00	0.10	0.11	0.01	0.03	0.03	0.08	0.11	0.06	-0.03	0.08	0.02	0.05	0.03	0.09	0.14	0.99
5	0.25	2.26	0.13	0.08	-0.02	0.01	0.09	0.05	0.02	0.02	0.11	0.12	0.06	0.06	0.04	0.07	0.28	-0.06	0.19	0.09	0.03	0.03	0.02	0.12	-0.03	0.77
4	-0.01	-0.92	0.07	0.06	-0.04	0.01	0.09	0.05	0.02	-0.02	0.07	0.07	0.07	0.08	0.03	0.10	-0.06	0.06	-0.21	0.08	-0.01	0.03	0.03	0.14	-0.03	-0.23
3	0.06	0.10	2.62	0.15	-0.13	0.04	-0.02	-0.14	0.47	-0.91	-1.90	-1.62	2.02	1.83	2.67	3.04	0.03	0.00	0.03	-1.25	-0.54	0.12	-0.08	0.32	-0.04	-0.03
2	0.06	0.11	-0.66	1.91	0.92	-0.21	3.76	3.48	0.90	-0.26	0.19	-0.43	0.73	0.84	0.05	0.17	0.03	0.01	0.03	0.37	0.39	-0.05	1.44	-0.29	-0.04	-0.02
1	0.06	0.13	0.33	-0.37	0.19	0.23	-0.49	-0.03	-0.15	0.10	0.01	0.26	-0.08	-0.11	-0.04	0.01	0.02	0.01	0.04	0.08	-0.05	0.04	-0.35	0.32	-0.05	0.00
zero start	0.03	0.08	0.06	0.05	0.02	-0.02	0.06	0.02	-0.03	-0.02	0.05	0.08	0.01	0.05	0.04	0.07	0.04	0.01	0.01	0.03	0.03	0.04	0.01	0.07	-0.03	0.00
zero end	0.05	0.13	0.10	0.09	-0.01	-0.01	0.11	0.04	0.02	0.04	0.06	0.16	0.09	0.06	0.00	0.06	0.03	-0.02	0.03	0.15	0.02	0.03	0.04	0.21	-0.06	-0.02

A temporary vehicle weigh-station was used to obtain vehicle weight and axle spacing of commercial trucks crossing the bridge from the south. The data collection was performed on April 17, 2003 and April 23, 2003 from 9:00 a.m. to 1:00 p.m. The truck axle weights were determined from jump scales, and axle spacings were measured; these are shown in Figure 2.28 and summarized in Table 2.4.

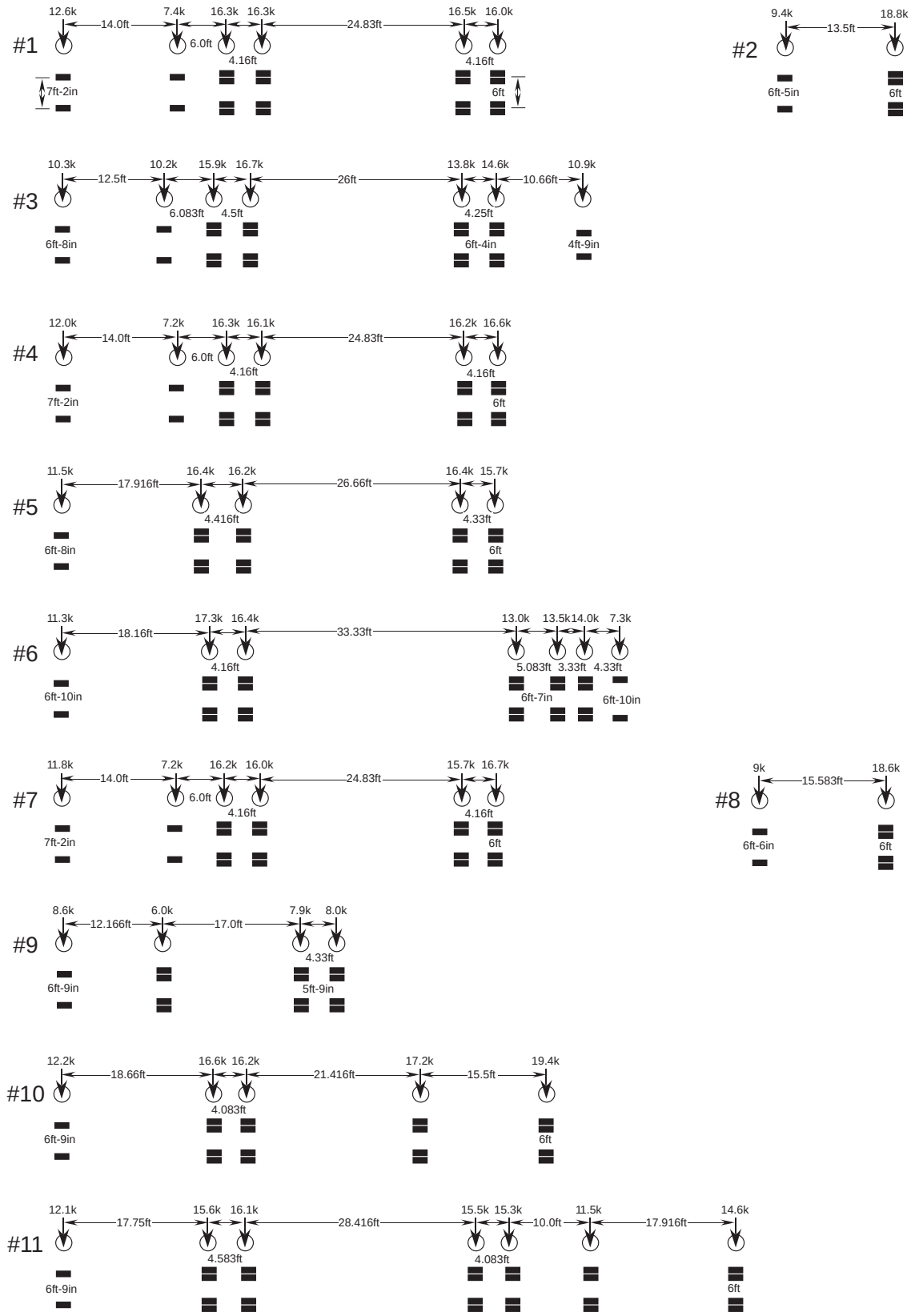

Figure 2.28: Axle weights and spacing for series of trucks crossing the Jasper Bridge

Table 2.4: Truck and axle weights from field measured trucks on Jasper Bridge

Truck ID	Gross Vehicle Weight (GVW) (kips)	Tandem Weight (kips)	Total Axle Weight within an 11 ft Length (kips)
1	84.8	32.5	40
2	28.2	18.8	28.2
3	92.4	32.6	42.8
4	84.4	32.8	39.6
5	76.2	32.6	32.6
6	92.8	33.7	47.8
7	83.6	32.4	39.4
8	27.6	18.6	27.6
9	30.5	15.9	15.9
10	81.6	32.8	32.8
11	100.7	31.7	42.3
ODOT Truck	47.28	33.2	33.2

After weighing and measuring axles, the trucks crossed the bridge and the induced stirrup stresses were measured and images were taken of each of these vehicles as shown in Figures 2.29a-k. The test data are summarized in Tables 2.5a-c. The influence of vehicle parameters (such as gross vehicle weight, tandem weight, and axle weights) on stirrup stress magnitude was evaluated within an 11 ft distance. For the trucks in the study, this corresponded to the most compact length of approximately evenly spaced axles as illustrated for Truck #6 in Figure 2.28.

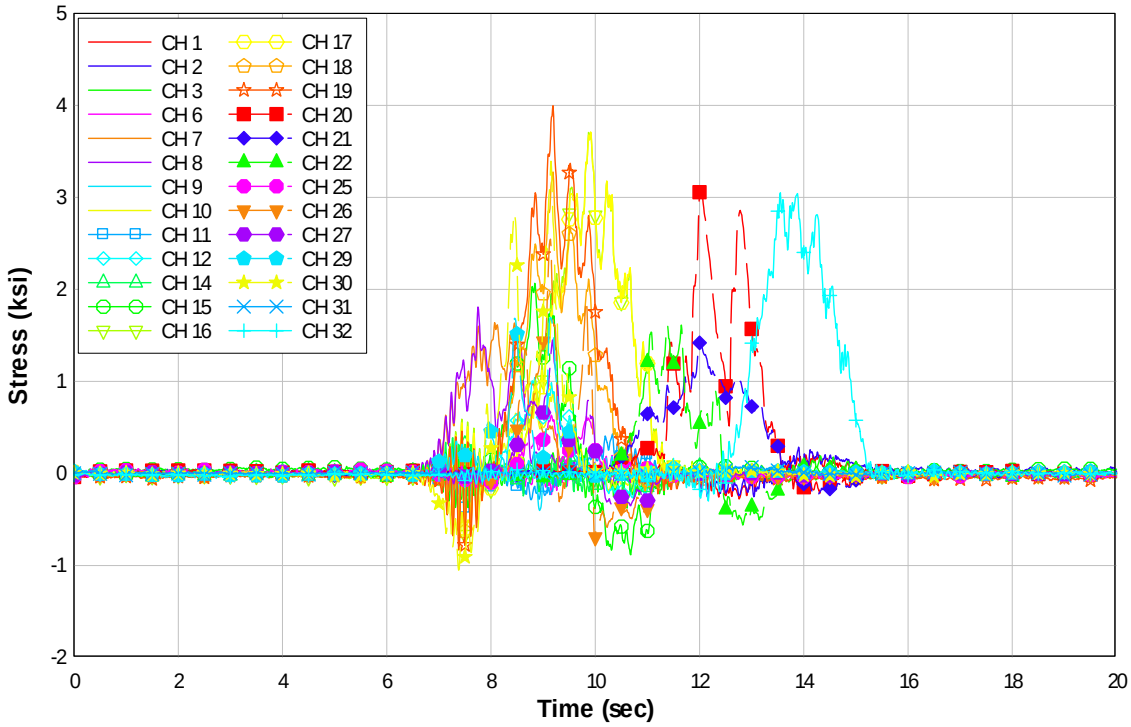

Figure 2.29a: Truck photograph and stress history produced for Truck #1 March 20, 2003

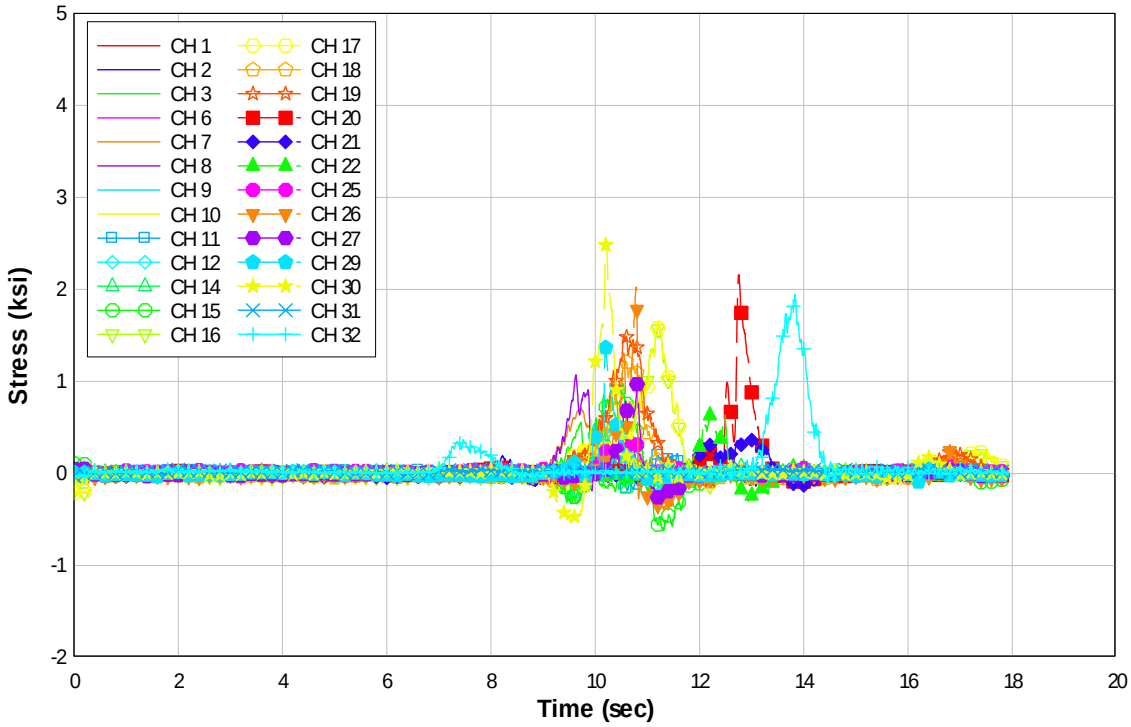

Figure 2.29b: Truck photograph and stress history produced for Truck #2 (note that first rear axle is not on roadway)

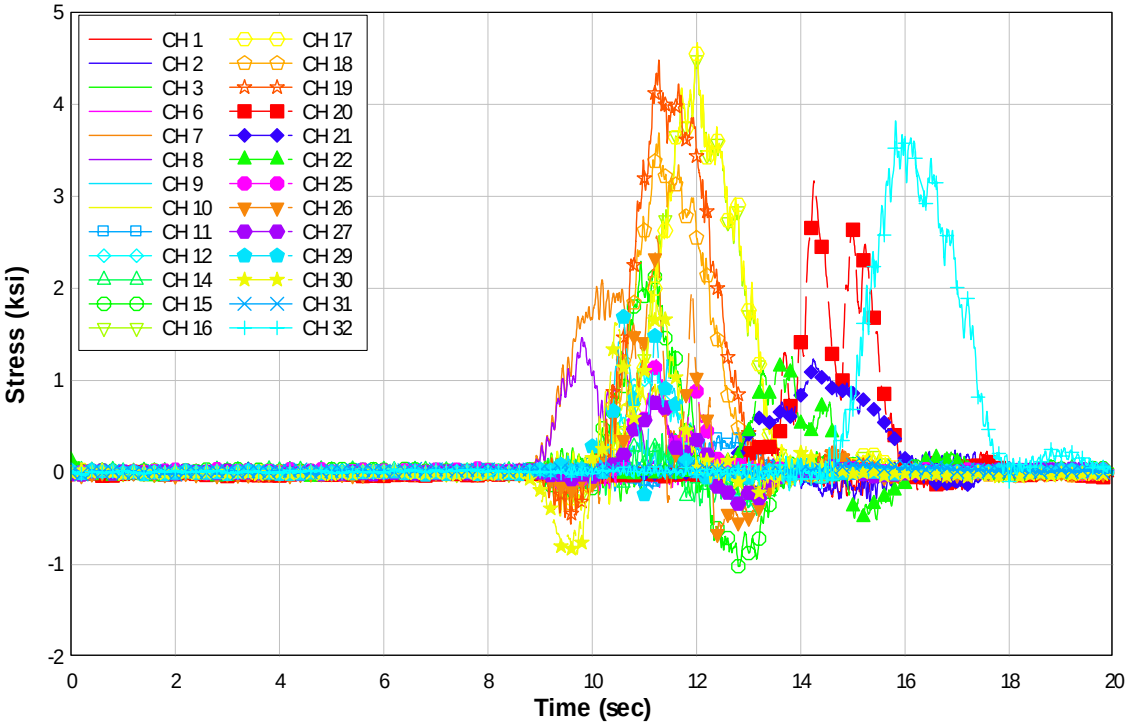

Figure 2.29c: Truck photograph and stress history produced for Truck #3

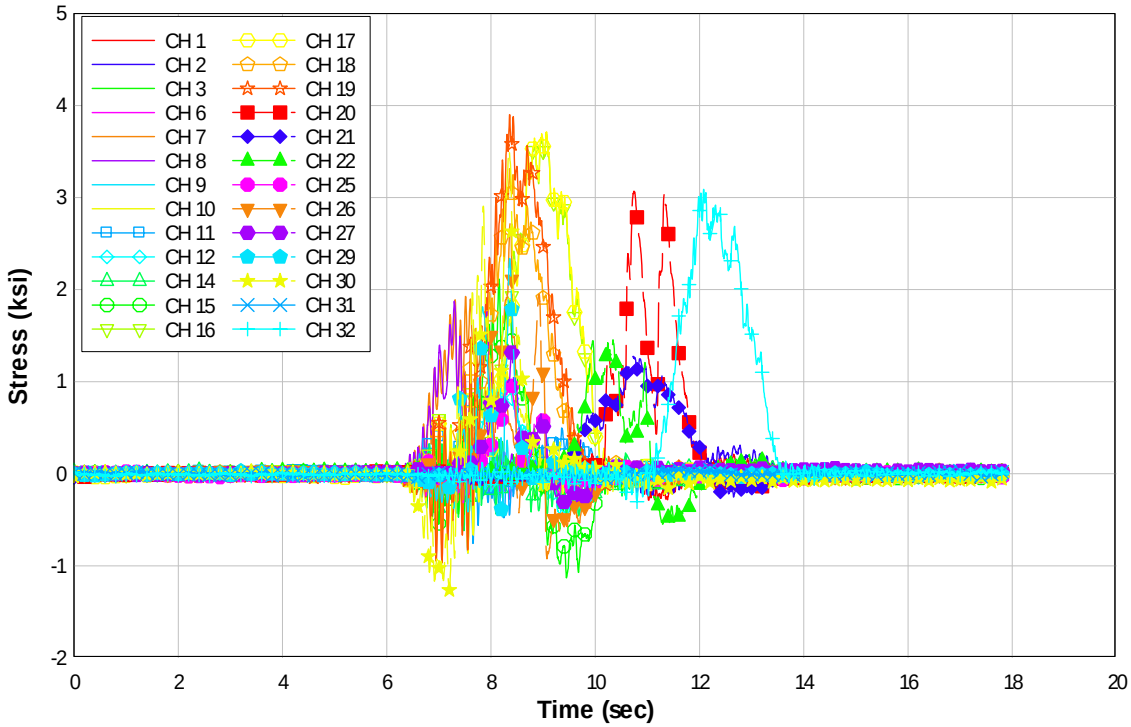

Figure 2.29d: Truck photograph and stress history produced for Truck #4

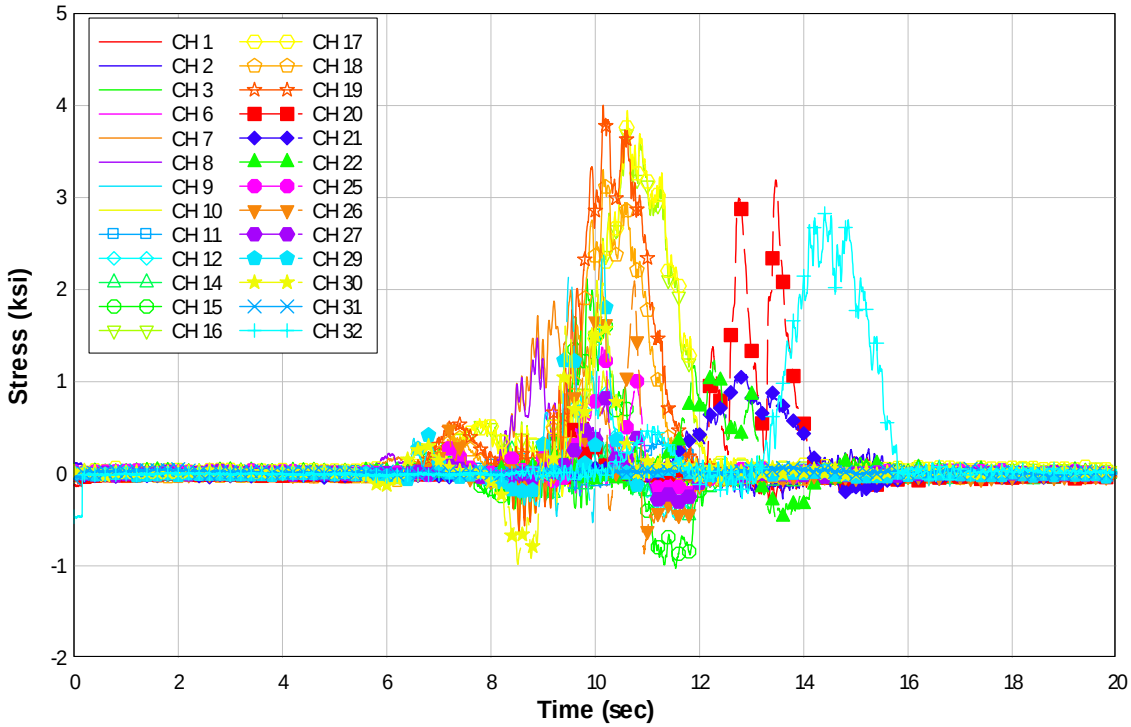

Figure 2.29e: Truck photograph and stress history produced for Truck #5

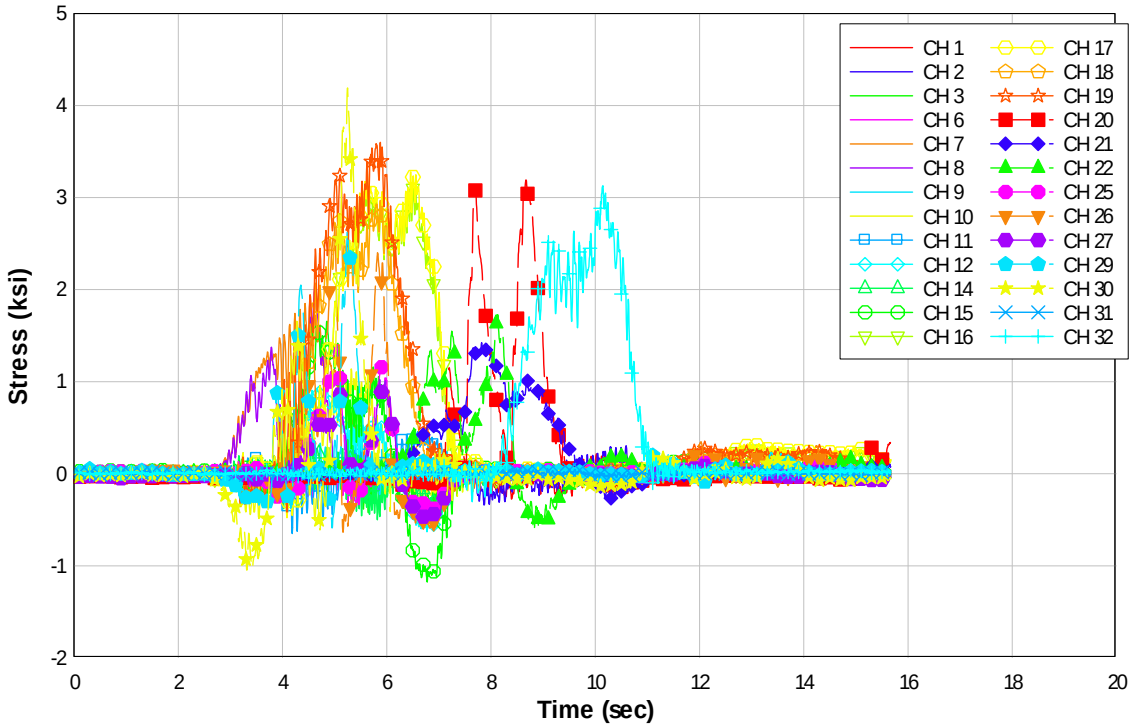

Figure 2.29f: Truck photograph and stress history produced for Truck #6

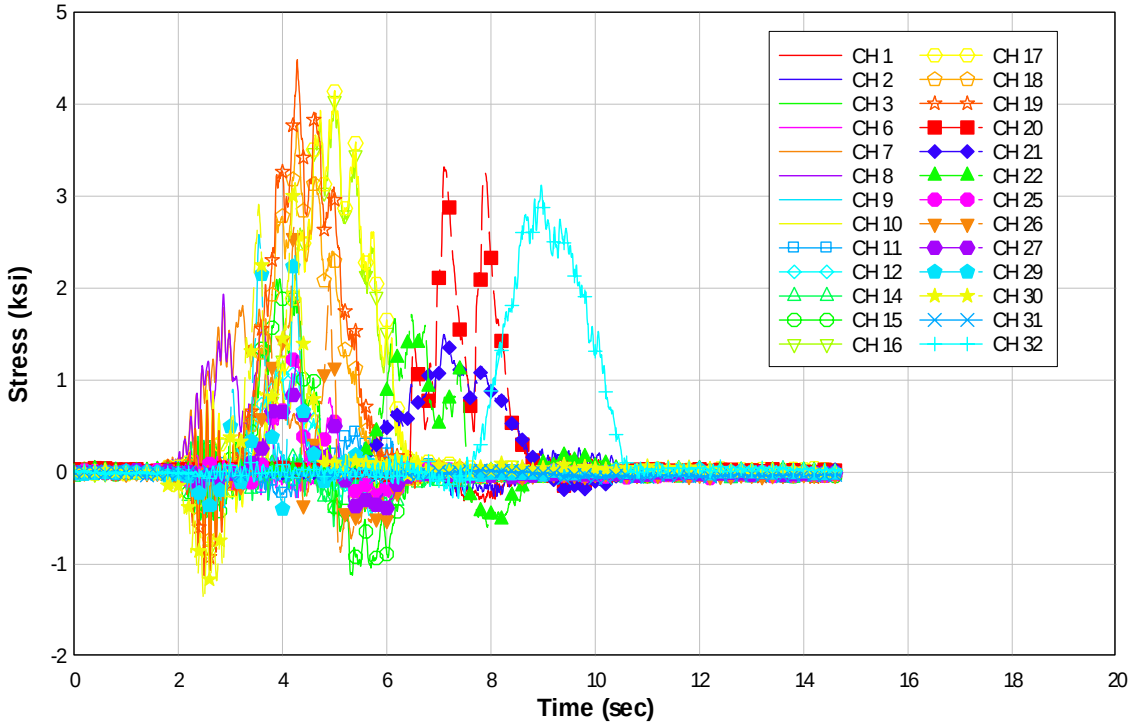

Figure 2.29g: Truck photograph and stress history produced for Truck #7

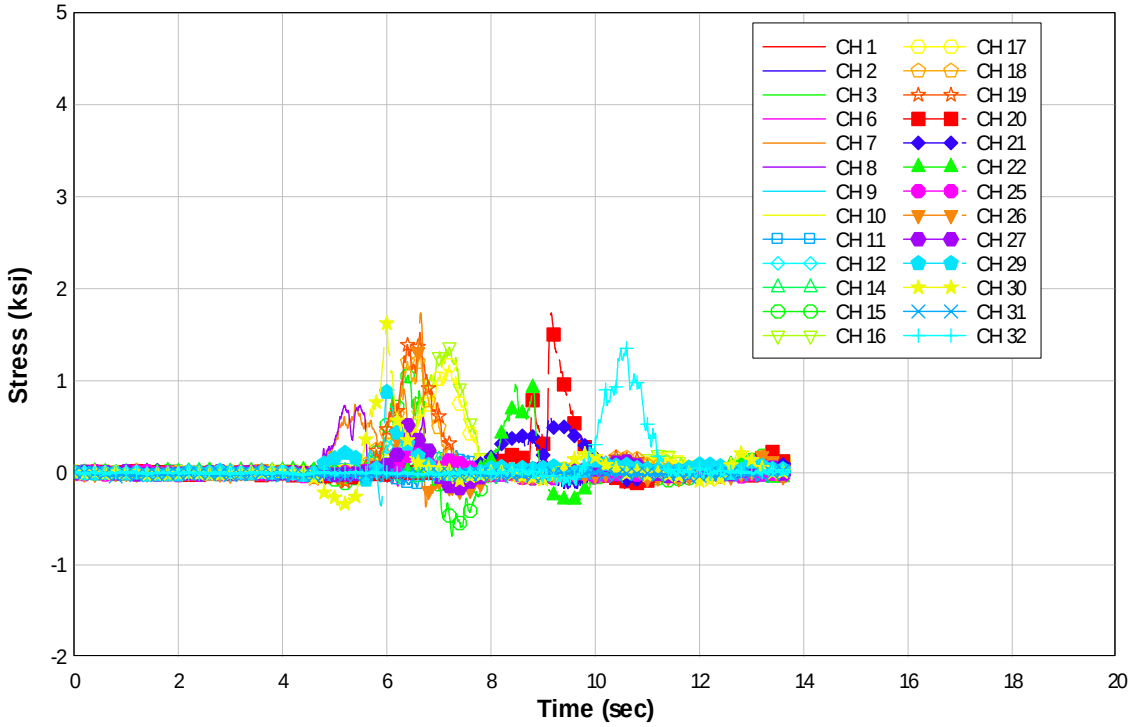

Figure 2.29h: Truck photograph and stress history produced for Truck #8 on April 1, 2003

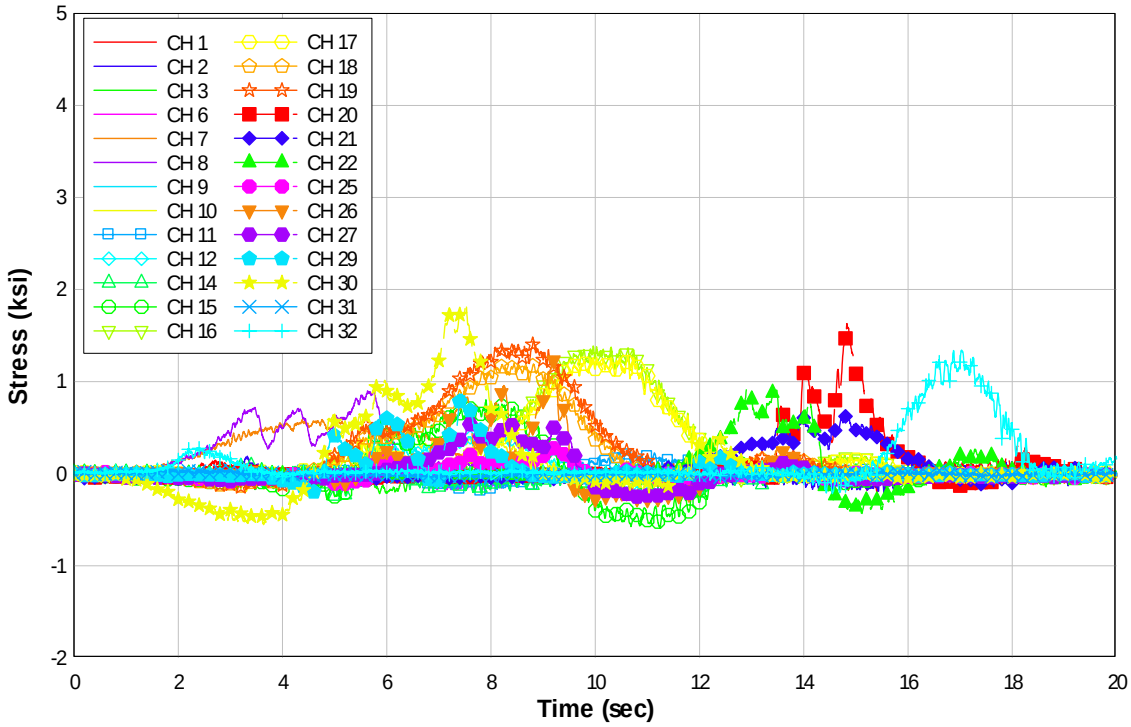

Figure 2.29i: Truck photograph and stress history produced for Truck #9

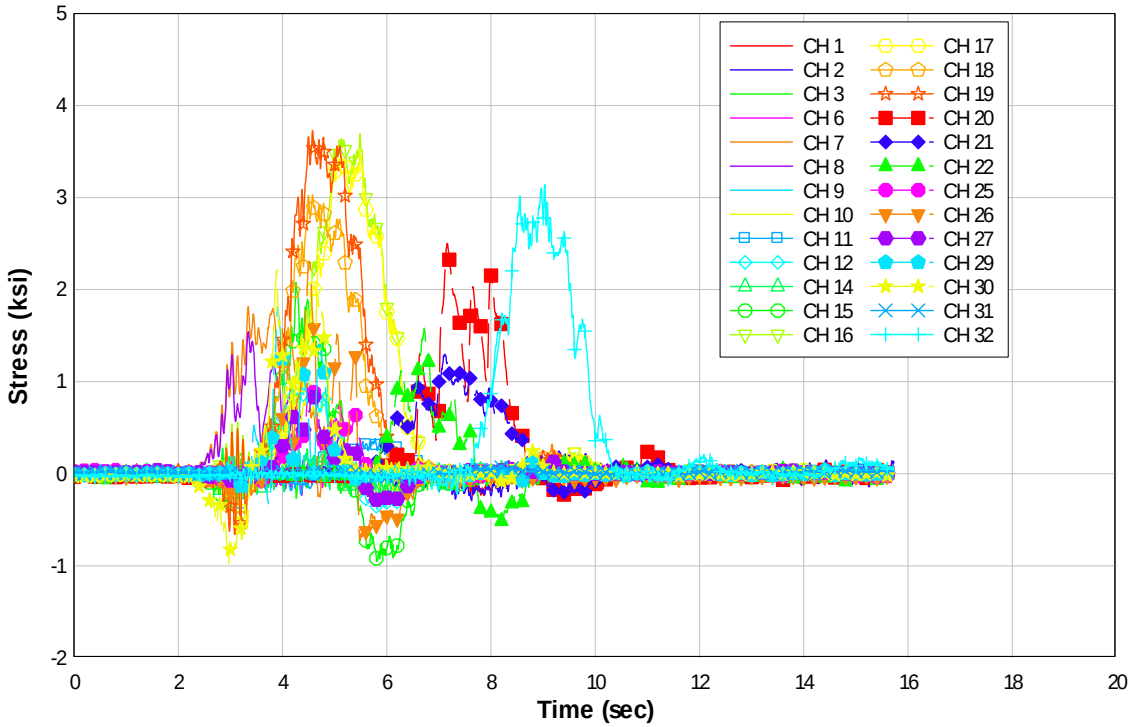

Figure 2.29j: Truck photograph and stress history produced for Truck #10

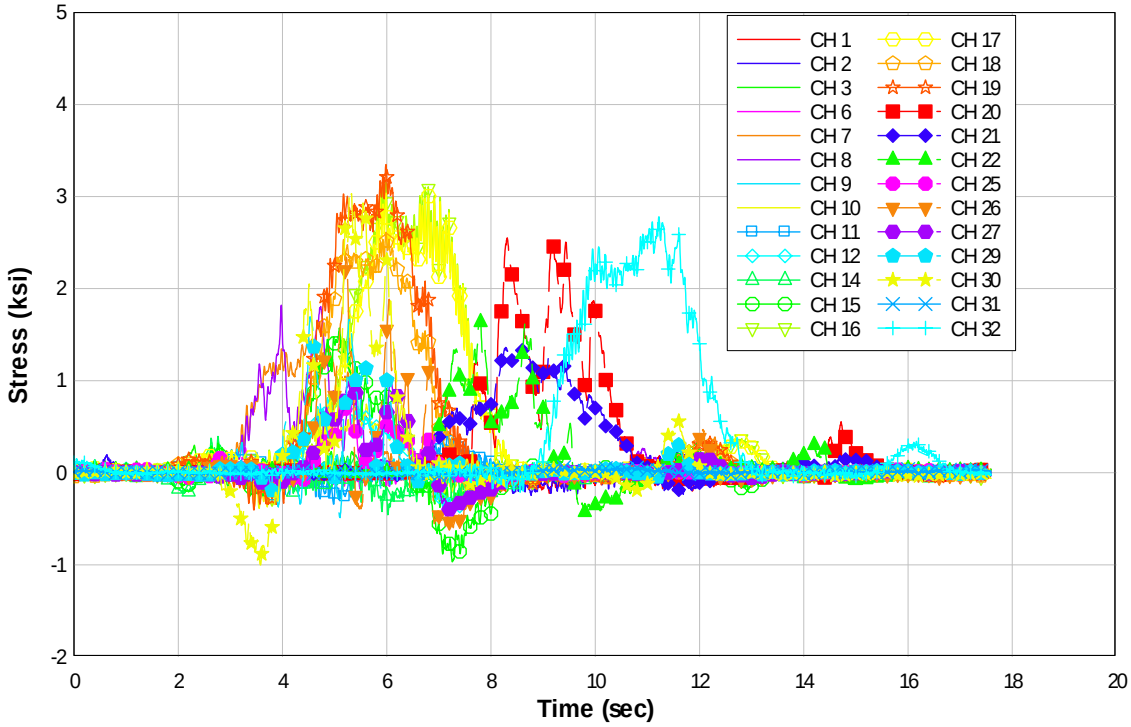

Figure 2.29k: Truck photograph and stress history produced for Truck #11

Table 2.5a: Maximum stresses for real trucks on Jasper Bridge

Truck ID	GVW (kips)	CH 1 (ksi)	CH 2 (ksi)	CH 3 (ksi)	CH 6 (ksi)	CH 7 (ksi)	CH 8 (ksi)	CH 9 (ksi)	CH 10 (ksi)	CH 11 (ksi)	CH 12 (ksi)	CH 14 (ksi)	CH 15 (ksi)	CH 16 (ksi)	CH 17 (ksi)	CH 18 (ksi)	CH 19 (ksi)	CH 20 (ksi)	CH 21 (ksi)	CH 22 (ksi)	CH 25 (ksi)	CH 26 (ksi)	CH 27 (ksi)	CH 29 (ksi)	CH 30 (ksi)	CH 31 (ksi)	CH 32 (ksi)
1	84.8	0.20	0.29	0.38	0.20	1.64	1.81	0.23	0.89	0.43	1.04	0.39	2.07	3.71	3.71	3.28	3.99	3.09	1.42	1.62	0.64	2.55	1.45	1.70	3.39	0.09	3.05
2	28.2	0.10	0.19	0.56	0.26	0.71	1.07	0.48	0.70	0.32	0.57	0.61	0.98	1.65	1.66	1.23	1.50	2.16	0.41	0.65	0.36	2.03	1.00	1.37	2.51	0.07	1.95
3	92.4	0.17	0.24	0.27	0.18	2.09	1.47	0.33	0.96	0.43	1.19	0.49	2.29	4.60	4.67	3.69	4.48	3.17	1.23	1.26	1.23	2.57	0.85	1.76	1.97	0.12	3.82
4	84.4	0.21	0.31	0.45	0.31	1.93	1.87	0.52	1.11	0.79	1.12	0.62	2.11	3.69	3.71	3.31	3.90	3.07	1.28	1.46	1.03	2.73	1.32	2.34	3.54	0.07	3.09
5	76.2	0.21	0.27	0.24	0.15	1.99	1.47	0.48	1.12	0.39	1.17	0.56	2.12	3.87	3.94	3.31	4.00	3.19	1.08	1.23	1.38	2.49	0.83	2.43	2.10	0.10	2.83
6	92.8	0.22	0.30	0.45	0.40	1.93	2.05	0.62	1.14	0.57	0.95	0.64	1.66	3.15	3.28	2.97	3.60	3.19	1.42	1.73	1.40	2.71	1.02	2.66	4.19	0.06	3.13
7	83.6	0.20	0.27	0.52	0.49	1.81	1.93	0.66	1.11	0.49	1.19	0.66	2.10	4.04	4.15	3.79	4.48	3.32	1.50	1.71	1.24	2.69	1.27	2.58	3.15	0.05	3.12
8	27.6	0.17	0.15	0.17	0.08	0.74	0.74	0.11	0.41	0.24	0.49	0.17	1.12	1.37	1.17	1.31	1.52	1.74	0.64	0.96	0.35	1.74	0.61	0.88	1.62	0.04	1.37
9	30.5	0.15	0.19	0.33	0.19	0.60	0.90	0.42	0.54	0.23	0.44	0.39	0.80	1.39	1.28	1.20	1.44	1.63	0.64	0.93	0.28	1.24	0.57	0.87	1.88	0.05	1.34
10	81.6	0.21	0.25	0.24	0.15	1.82	1.54	0.32	0.89	0.40	1.14	0.43	2.08	3.70	3.52	3.03	3.73	2.50	1.30	1.58	0.97	2.31	0.86	1.81	2.21	0.09	3.14
11	100.7	0.21	0.25	0.30	0.27	1.46	1.82	0.33	0.75	0.45	0.86	0.39	1.57	3.16	3.04	2.61	3.35	2.57	1.36	1.66	0.79	2.34	0.99	1.70	3.03	0.07	2.78
ODOT	47.28	0.20	0.23	0.19	0.15	1.39	1.33	0.21	1.07	0.41	1.25	0.30	2.12	3.02	3.13	2.79	3.37	3.18	0.78	1.40	1.68	2.99	1.18	2.89	3.73	0.06	2.99

Table 2.5b: Minimum stresses for real trucks on Jasper Bridge

Truck ID	GVW (kips)	CH 1 (ksi)	CH 2 (ksi)	CH 3 (ksi)	CH 6 (ksi)	CH 7 (ksi)	CH 8 (ksi)	CH 9 (ksi)	CH 10 (ksi)	CH 11 (ksi)	CH 12 (ksi)	CH 14 (ksi)	CH 15 (ksi)	CH 16 (ksi)	CH 17 (ksi)	CH 18 (ksi)	CH 19 (ksi)	CH 20 (ksi)	CH 21 (ksi)	CH 22 (ksi)	CH 25 (ksi)	CH 26 (ksi)	CH 27 (ksi)	CH 29 (ksi)	CH 30 (ksi)	CH 31 (ksi)	CH 32 (ksi)
1	84.8	-0.28	-0.25	-0.38	-0.23	-0.07	-0.11	-0.39	-0.49	-0.40	-0.26	-0.29	-0.88	-0.67	-0.60	-0.67	-0.83	-0.21	-0.23	-0.56	-0.15	-0.74	-0.35	-0.40	-1.05	-0.04	-0.30
2	28.2	-0.14	-0.17	-0.20	-0.10	-0.05	-0.19	-0.13	-0.23	-0.18	-0.22	-0.29	-0.62	-0.23	-0.22	-0.11	-0.12	-0.12	-0.16	-0.30	-0.08	-0.39	-0.26	-0.20	-0.55	-0.04	-0.10
3	92.4	-0.27	-0.32	-0.31	-0.19	-0.06	-0.05	-0.37	-0.47	-0.33	-0.37	-0.47	-1.02	-0.34	-0.36	-0.45	-0.56	-0.19	-0.17	-0.51	-0.19	-0.68	-0.35	-0.28	-0.89	-0.04	-0.20
4	84.4	-0.30	-0.23	-0.46	-0.39	-0.13	-0.10	-0.58	-0.64	-0.86	-0.47	-0.62	-1.13	-0.83	-0.86	-0.80	-0.97	-0.17	-0.25	-0.60	-0.31	-0.92	-0.31	-0.47	-1.27	-0.06	-0.30
5	76.2	-0.30	-0.27	-0.38	-0.21	-0.10	-0.07	-0.39	-0.57	-0.31	-0.50	-0.45	-1.03	-0.42	-0.44	-0.55	-0.63	-0.19	-0.24	-0.49	-0.24	-0.87	-0.33	-0.53	-0.99	-0.06	-0.49
6	92.8	-0.28	-0.34	-0.47	-0.32	-0.12	-0.34	-0.25	-0.49	-0.65	-0.63	-0.50	-1.17	-0.46	-0.48	-0.34	-0.42	-0.18	-0.26	-0.65	-0.42	-0.63	-0.49	-0.59	-1.05	-0.05	-0.30
7	83.6	-0.33	-0.26	-0.43	-0.30	-0.10	-0.06	-0.55	-0.74	-0.49	-0.49	-0.59	-1.12	-0.94	-0.96	-0.92	-1.13	-0.17	-0.21	-0.60	-0.35	-0.87	-0.43	-0.45	-1.41	-0.08	-0.28
8	27.6	-0.14	-0.17	-0.14	-0.14	-0.07	-0.13	-0.10	-0.16	-0.15	-0.16	-0.12	-0.69	-0.08	-0.06	-0.12	-0.16	-0.17	-0.13	-0.32	-0.09	-0.37	-0.21	-0.36	-0.41	-0.06	-0.15
9	30.5	-0.21	-0.21	-0.29	-0.19	-0.07	-0.09	-0.15	-0.19	-0.22	-0.27	-0.27	-0.59	-0.10	-0.09	-0.17	-0.17	-0.18	-0.14	-0.43	-0.14	-0.32	-0.26	-0.21	-0.55	-0.05	-0.22
10	81.6	-0.24	-0.29	-0.32	-0.23	-0.08	-0.08	-0.43	-0.58	-0.48	-0.38	-0.32	-0.95	-0.54	-0.48	-0.62	-0.66	-0.24	-0.21	-0.53	-0.15	-0.72	-0.32	-0.34	-1.02	-0.06	-0.22
11	100.7	-0.22	-0.25	-0.40	-0.18	-0.10	-0.11	-0.18	-0.39	-0.34	-0.42	-0.46	-0.97	-0.27	-0.20	-0.34	-0.40	-0.20	-0.23	-0.44	-0.15	-0.60	-0.40	-0.49	-1.00	-0.04	-0.21
ODOT	47.28	-0.31	-0.34	-0.32	-0.18	-0.05	-0.11	-0.22	-0.39	-0.28	-0.54	-0.43	-1.15	-0.26	-0.23	-0.37	-0.45	-0.17	-0.24	-0.55	-0.30	-0.61	-0.42	-0.29	-1.23	-0.03	-0.22

Table 2.5c: Stress ranges for real trucks on Jasper Bridge

Truck ID	GVW (kips)	CH 1 (ksi)	CH 2 (ksi)	CH 3 (ksi)	CH 6 (ksi)	CH 7 (ksi)	CH 8 (ksi)	CH 9 (ksi)	CH 10 (ksi)	CH 11 (ksi)	CH 12 (ksi)	CH 14 (ksi)	CH 15 (ksi)	CH 16 (ksi)	CH 17 (ksi)	CH 18 (ksi)	CH 19 (ksi)	CH 20 (ksi)	CH 21 (ksi)	CH 22 (ksi)	CH 25 (ksi)	CH 26 (ksi)	CH 27 (ksi)	CH 29 (ksi)	CH 30 (ksi)	CH 31 (ksi)	CH 32 (ksi)
1	84.8	0.48	0.54	0.75	0.43	1.71	1.92	0.63	1.39	0.83	1.31	0.68	2.95	4.37	4.32	3.95	4.83	3.31	1.65	2.18	0.79	3.29	1.80	2.10	4.44	0.13	3.35
2	28.2	0.23	0.36	0.75	0.37	0.76	1.26	0.60	0.93	0.50	0.79	0.90	1.60	1.87	1.89	1.35	1.62	2.28	0.57	0.95	0.45	2.42	1.26	1.57	3.06	0.12	2.05
3	92.4	0.44	0.56	0.58	0.37	2.15	1.51	0.70	1.43	0.75	1.57	0.95	3.32	4.93	5.03	4.14	5.04	3.36	1.40	1.77	1.42	3.25	1.21	2.05	2.86	0.16	4.02
4	84.4	0.51	0.54	0.92	0.70	2.05	1.97	1.10	1.75	1.66	1.59	1.24	3.25	4.52	4.58	4.11	4.87	3.24	1.53	2.05	1.34	3.65	1.63	2.81	4.81	0.14	3.39
5	76.2	0.51	0.55	0.62	0.36	2.10	1.55	0.87	1.69	0.70	1.67	1.01	3.14	4.29	4.39	3.85	4.63	3.38	1.32	1.73	1.61	3.36	1.16	2.96	3.08	0.15	3.31
6	92.8	0.49	0.64	0.91	0.72	2.04	2.39	0.87	1.62	1.22	1.58	1.14	2.83	3.62	3.76	3.31	4.02	3.37	1.69	2.38	1.83	3.35	1.52	3.25	5.24	0.11	3.43
7	83.6	0.53	0.53	0.95	0.79	1.91	2.00	1.21	1.84	0.98	1.68	1.25	3.22	4.98	5.10	4.71	5.61	3.48	1.70	2.31	1.59	3.56	1.69	3.03	4.56	0.13	3.40
8	27.6	0.31	0.32	0.31	0.23	0.82	0.86	0.21	0.58	0.40	0.65	0.29	1.81	1.45	1.23	1.43	1.68	1.91	0.77	1.28	0.44	2.11	0.81	1.24	2.03	0.10	1.52
9	30.5	0.36	0.40	0.61	0.38	0.67	0.99	0.57	0.73	0.45	0.71	0.67	1.39	1.49	1.37	1.37	1.61	1.81	0.78	1.36	0.41	1.56	0.82	1.08	2.44	0.11	1.56
10	81.6	0.44	0.54	0.56	0.38	1.89	1.62	0.74	1.47	0.88	1.53	0.74	3.03	4.24	4.01	3.65	4.39	2.73	1.51	2.11	1.12	3.03	1.18	2.16	3.23	0.15	3.36
11	100.7	0.43	0.50	0.70	0.45	1.56	1.93	0.51	1.13	0.79	1.29	0.85	2.54	3.43	3.23	2.95	3.75	2.77	1.59	2.09	0.95	2.94	1.39	2.18	4.03	0.12	2.99
ODOT	47.28	0.51	0.57	0.51	0.33	1.44	1.45	0.43	1.46	0.69	1.79	0.72	3.27	3.28	3.36	3.16	3.82	3.35	1.02	1.95	1.98	3.60	1.60	3.18	4.96	0.09	3.21

The relationships between stirrup stress and gross vehicle weight, tandem weight, and axle weights within a length of 11ft are shown in Figures 2.30 a, b, and c. As seen in these figures, gross vehicle weight did not correlate well with stirrup stress at instrumented locations. Stirrup stresses on main girders were more strongly influenced by the tandem weight, while the stirrup stresses on the bent caps were more strongly influenced by axle weights within the 11ft distance.

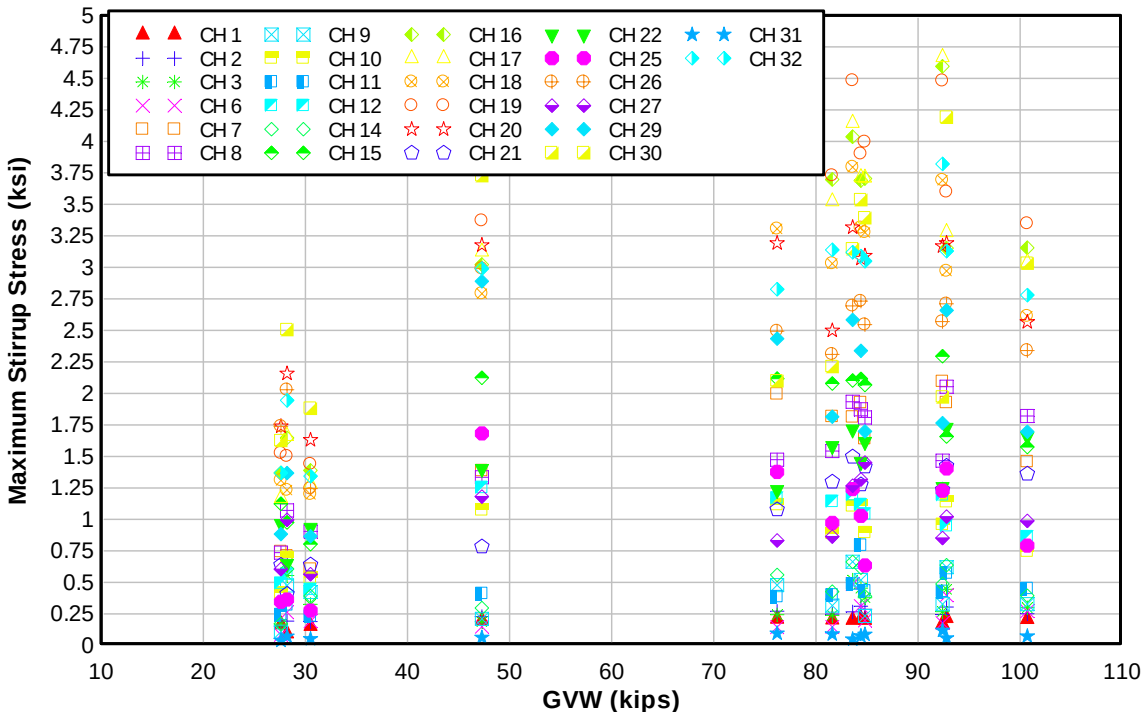

Figure 2.30a: Maximum stirrup stress produced for each known truck gross vehicle weight crossing Jasper Bridge

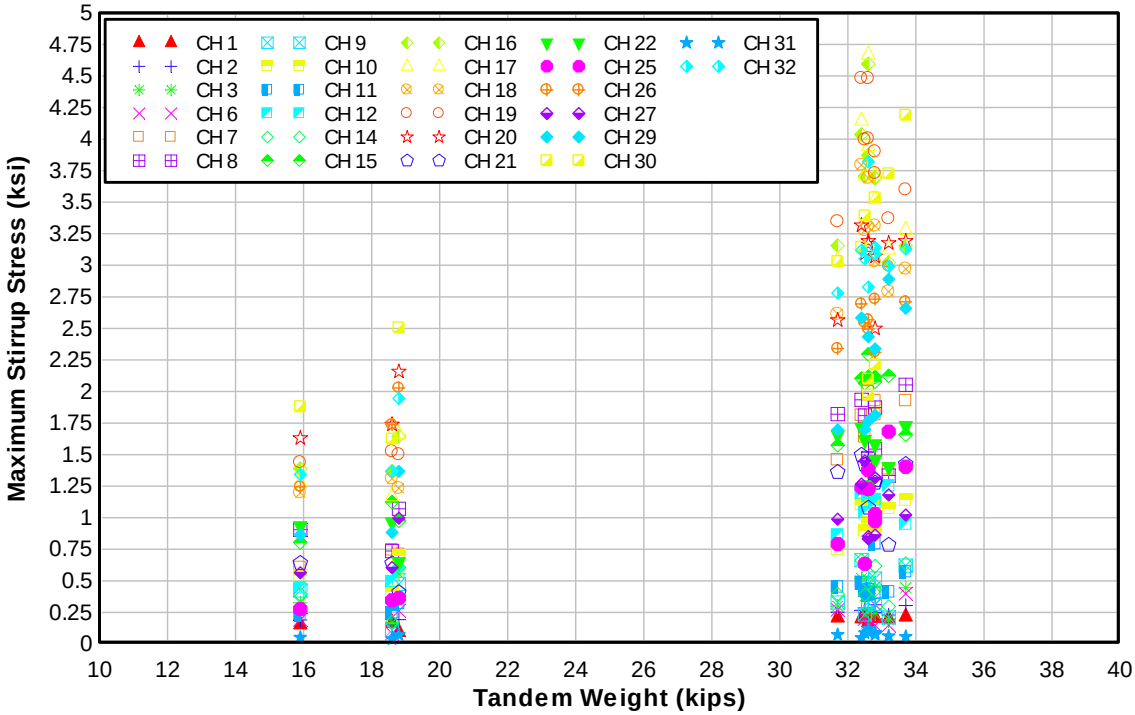

Figure 2.30b: Maximum stirrup stress produced for the maximum tandem weight on each known truck crossing Jasper Bridge

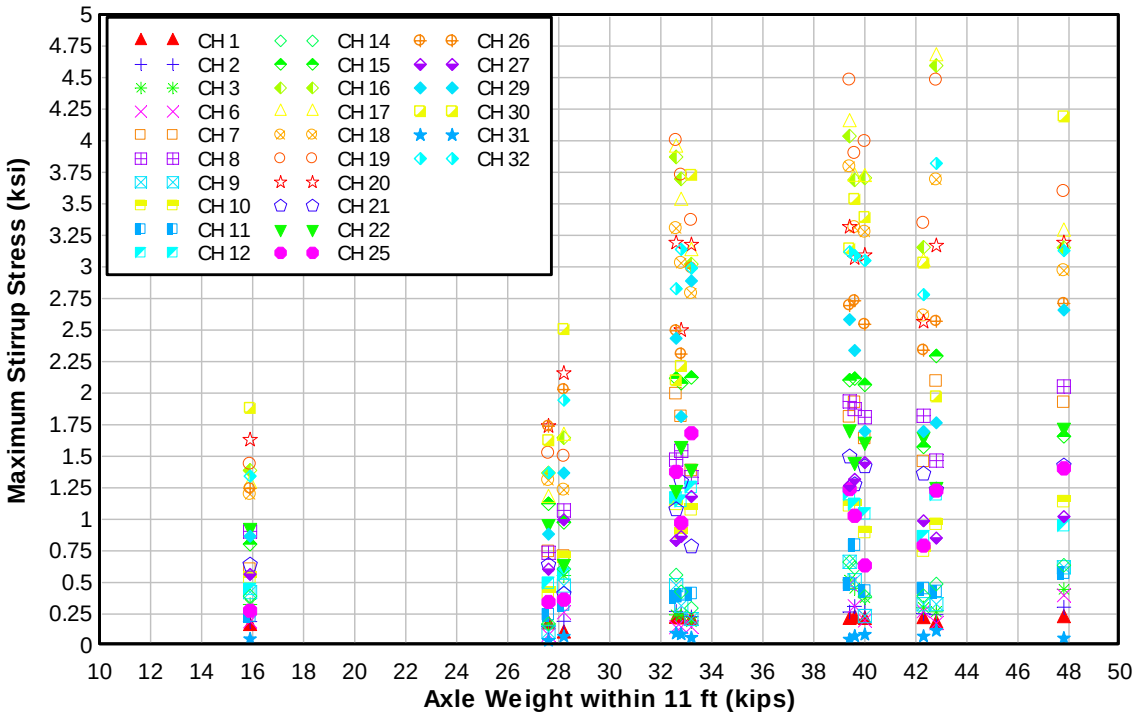

Figure 2.30c: Maximum stirrup stress produced for the axle weight within an 11 ft length on each known truck crossing Jasper Bridge

2.3 15 MILE CREEK BRIDGE, I84 EAST AND WESTBOUND, THE DALLES, OR (BRIDGE NUMBER 308A)

15 Mile Creek Bridge is located on I-84, just east of The Dalles, OR and spans 15 Mile Creek. The bridge consists of 5 spans, as shown in Figures 2.31a-c, with three box-girder main spans and two reinforced concrete deck girder spans at the northeast approach. The bridge carries two traffic lanes in the eastbound direction and two traffic lanes in the westbound direction. The bridge was designed in 1960.

2.3.1 Description of Tested Spans

The approach spans, shown in Figure 2.32, were selected for field study. The approach spans have equal span lengths of 52 ft that are continuous over Bent 5. Eastbound spans have a roadway width of 30 ft - 5.5 in. and westbound spans have a roadway width of 31 ft - 11.5 in. The eastbound and westbound deck overhangs share a longitudinal joint along their lengths that does not permit significant force transfer between spans. This was verified by field tests.

Four girders support two traffic lanes in each direction. The girders have an overall height of 48 in. with web widths that taper from 16.5 in. between quarter points to 24 in. at the support face. Diaphragms are 9 in. x 46 in. and located at the quarter points of each span. The concrete deck is 7 in. thick. Bent caps are supported by 15 in. diameter circular columns with the exterior girder framing into the bent cap outboard of the columns.

The bridge was designed in 1960. The specified concrete compression strength was 3300 psi and reinforcing steel consisted of ASTM A305 intermediate grade round bars with nominal yield stress of 40 ksi.

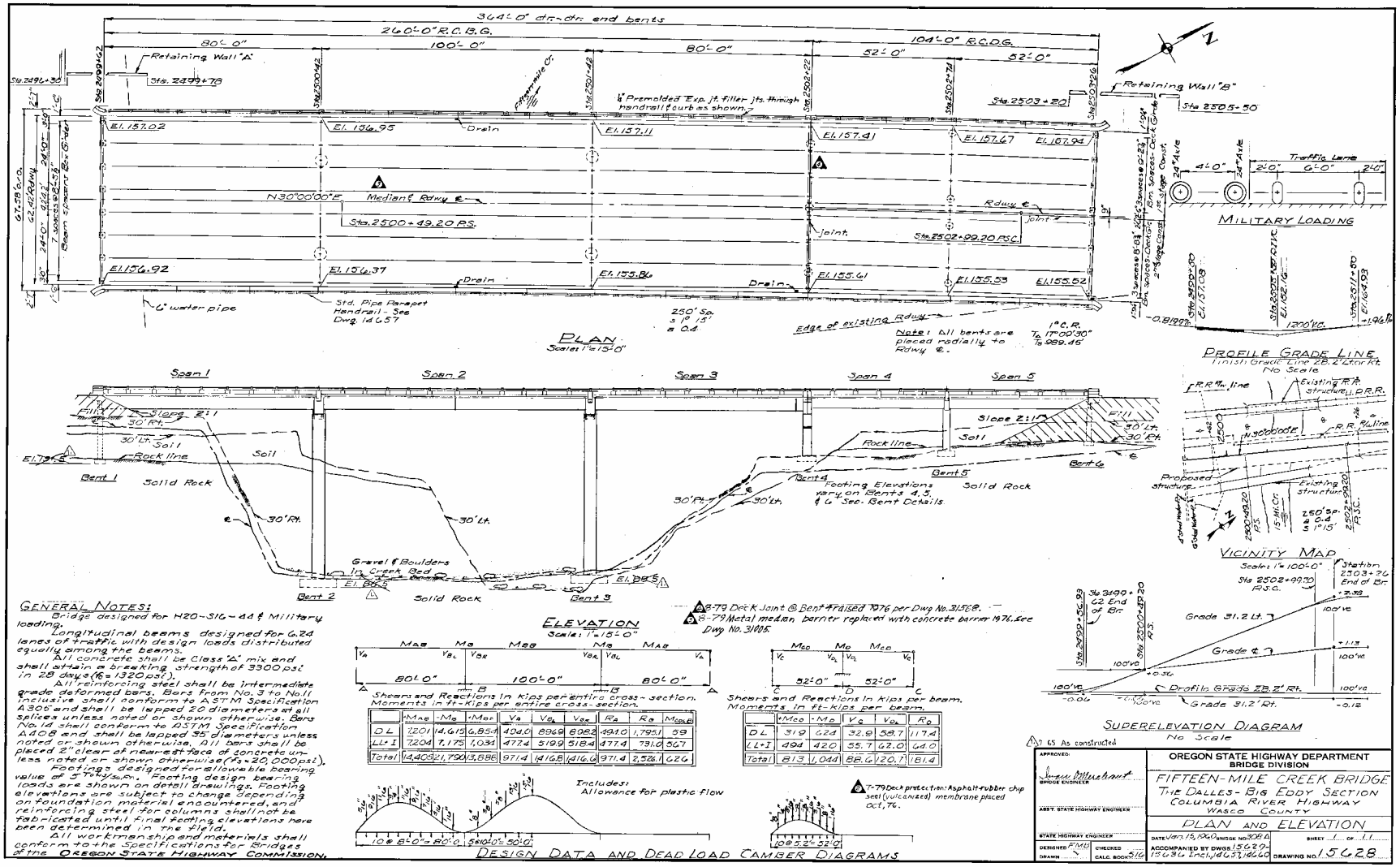

Figure 2.31a: Design drawings for 15 Mile Creek Bridge

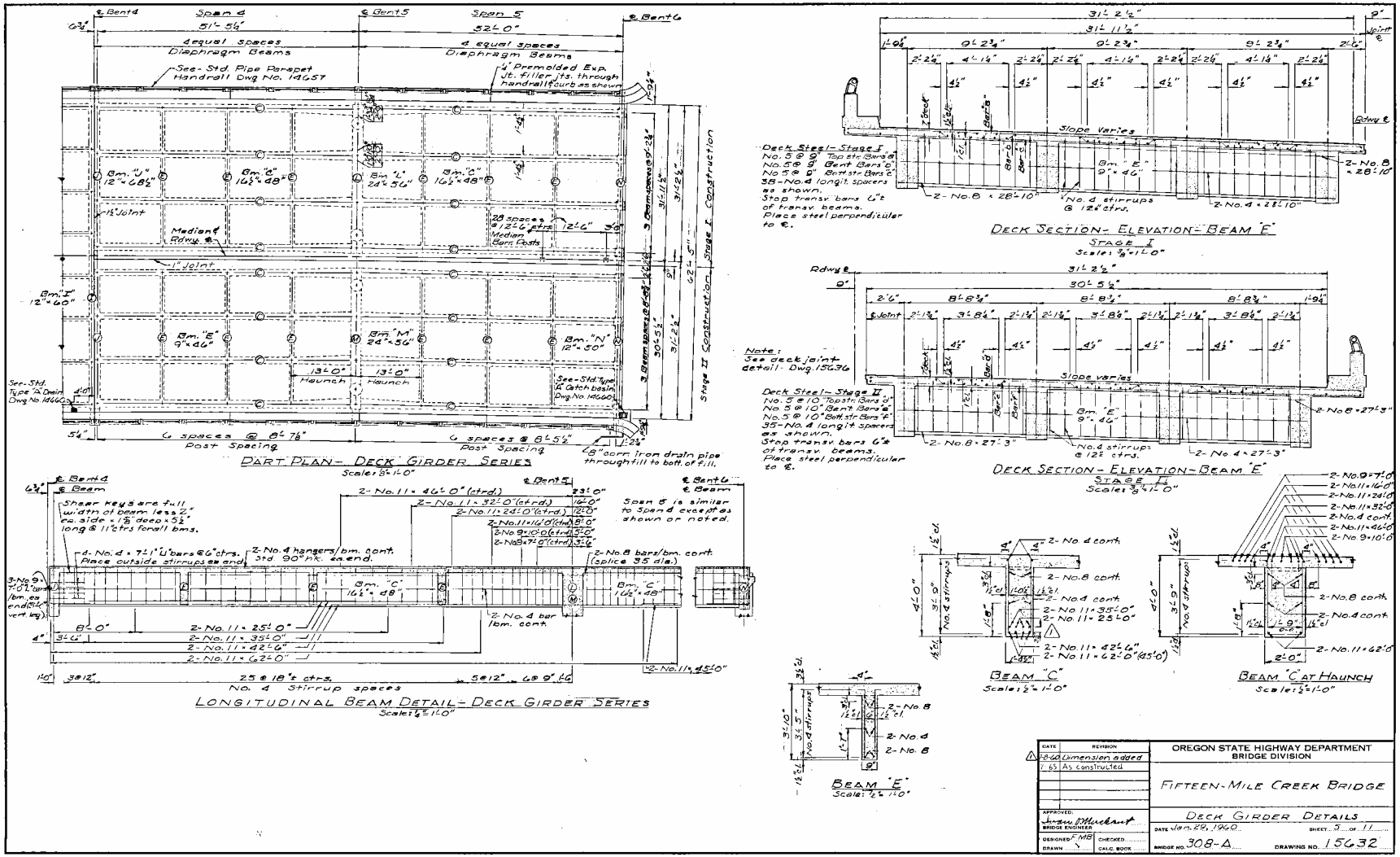

Figure 2.31b: Design drawings for 15 Mile Creek Bridge

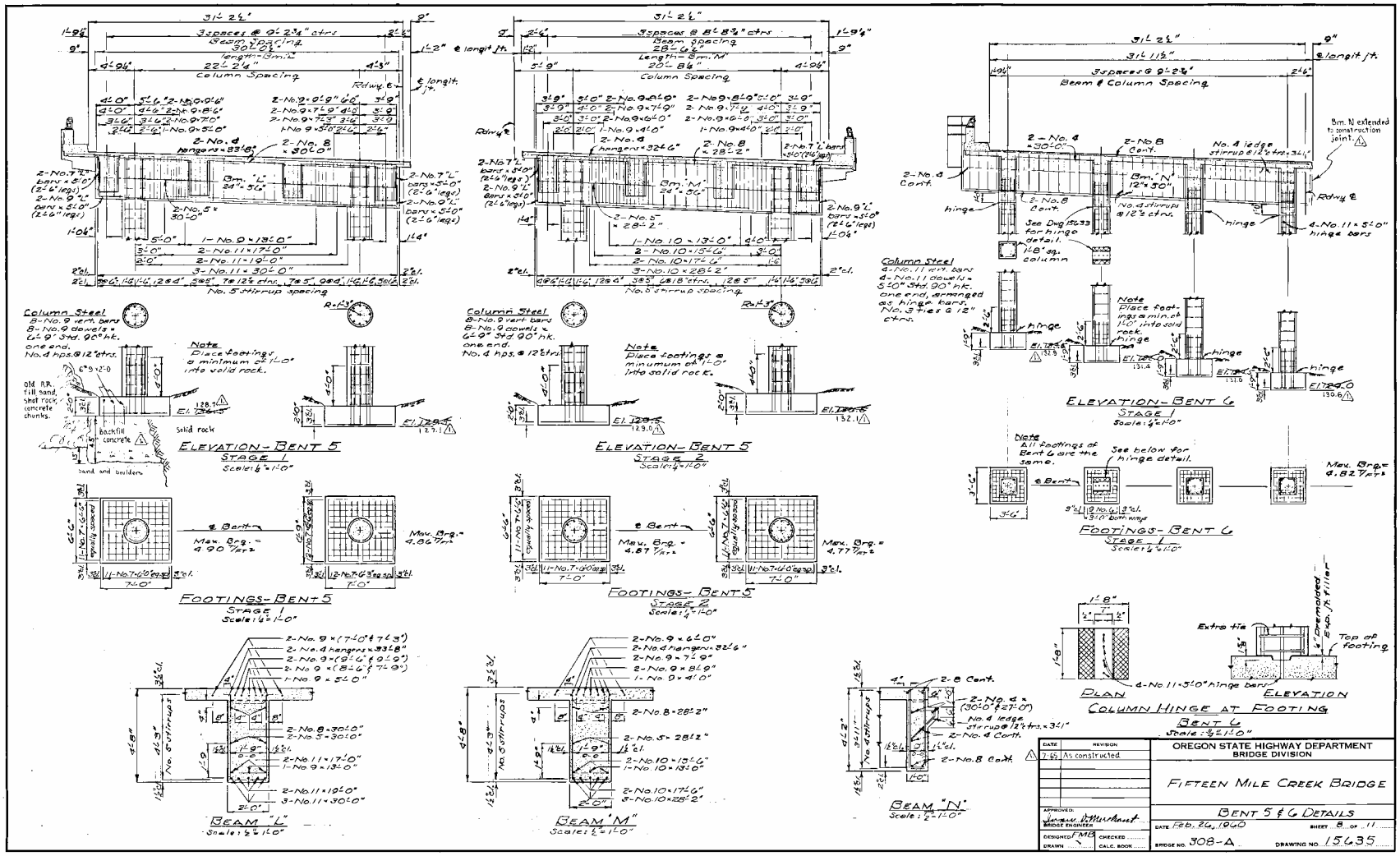

Figure 2.31c: Design drawings for 15 Mile Creek Bridge

Figure 2.32: Portion of 15 Mile Creek Bridge selected for field investigation

2.3.2 Crack Mapping and Instrumentation

The crack mapping and instrumentation techniques corresponded closely with those reported above. Diagonal-tension crack patterns for the girders and bent caps are shown in Figures 2.33a-e. Twenty-seven locations were selected for instrumentation. At two locations on the bent cap, strain gages were installed on multiple stirrup legs crossing a diagonal crack. At other locations, a single stirrup leg was instrumented. At two exterior girder locations, the flexural steel was instrumented, one on the eastbound and one on the westbound lanes near midspan of span 4 (T_east and T_west).

Position sensors were installed at six locations. Instrumentation locations and channel numbers are identified schematically in Figure 2.34. Data were again collected using a Campbell Scientific CR9000 data acquisition system. During the ambient monitoring period, data were sampled at 50 Hz. A digital high-pass filter was utilized with a cut-off frequency of 20 Hz. No digital camera was used for this field study due to communication problems with the camera. The data acquisition system converted sensor readings into corresponding stresses and displacements, and stored the data for later retrieval and analysis.

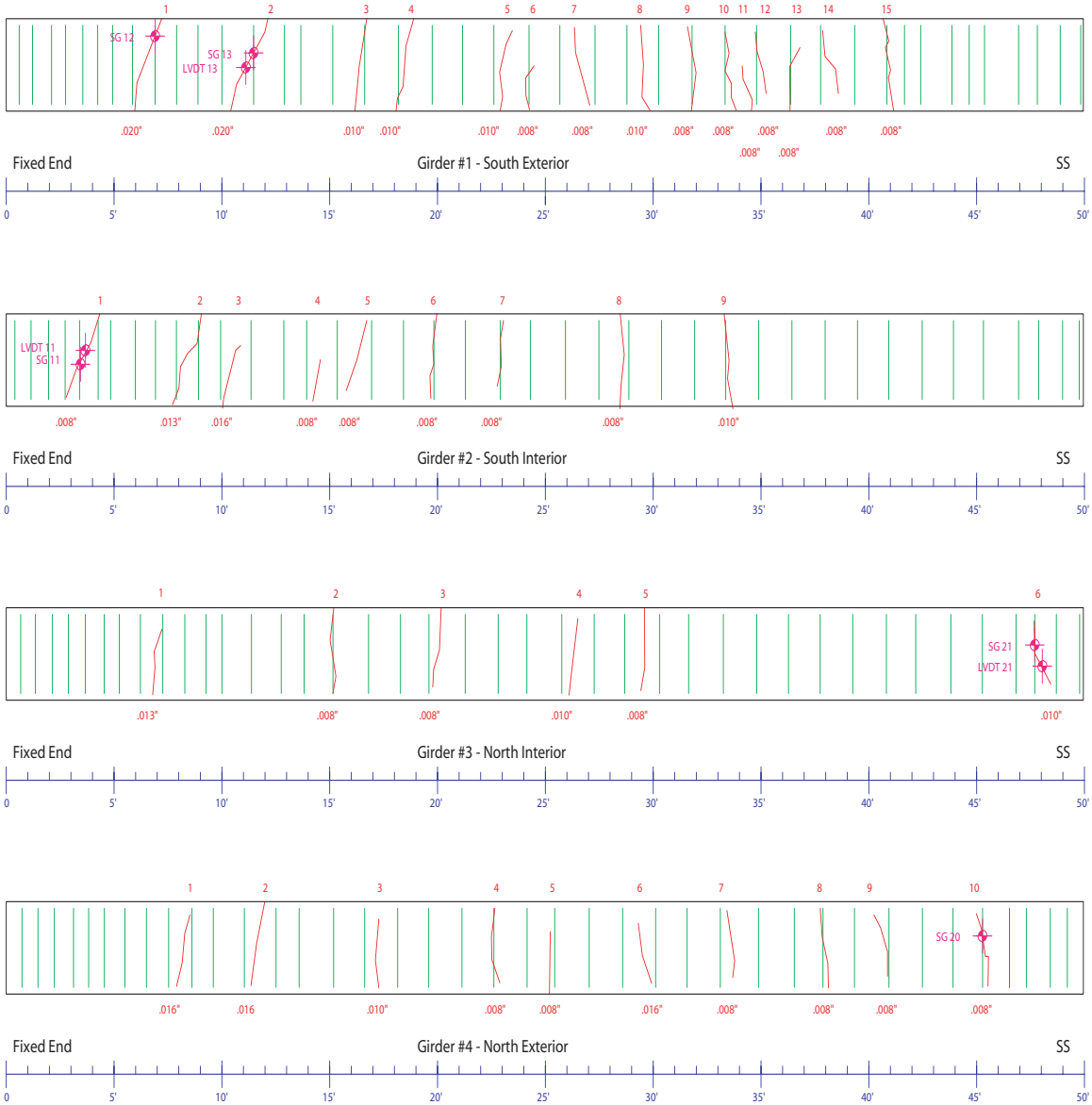

Figure 2.33a: 15 Mile Creek Bridge crack, stirrup, and instrumentation locations on span 5 eastbound

15 MILE CREEK BRIDGE
I-84 / 15 MILE CREEK
THE DALLES, OREGON

SPAN 4 - EAST-BOUND LANES

DECEMBER 15, 2003

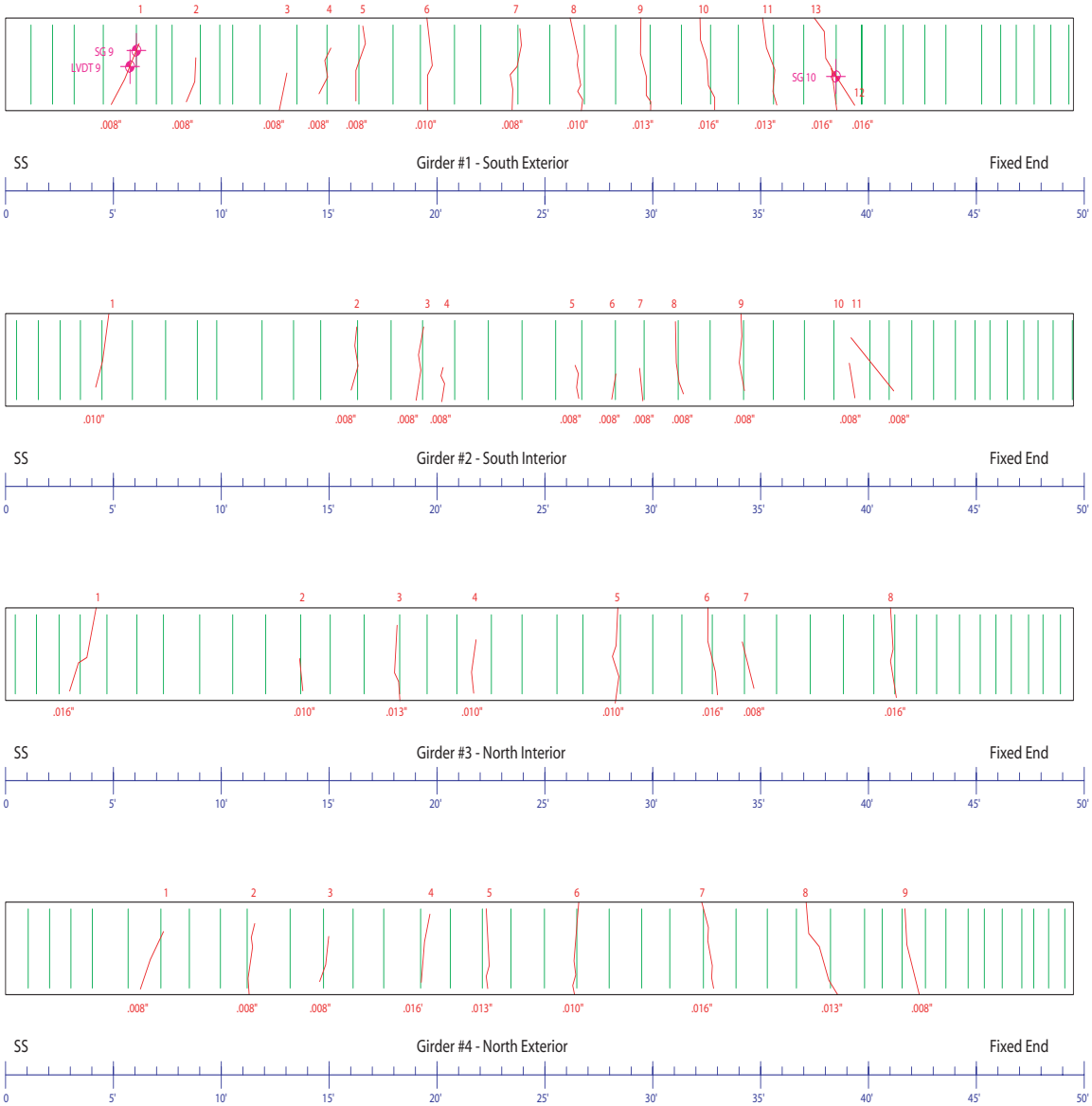

Figure 2.33b: 15 Mile Creek Bridge crack, stirrup, and instrumentation locations on span 4 eastbound

15 MILE CREEK BRIDGE SPAN 5 - WEST-BOUND LANES DECEMBER 15, 2003
I-84 / 15 MILE CREEK
THE DALLES, OREGON

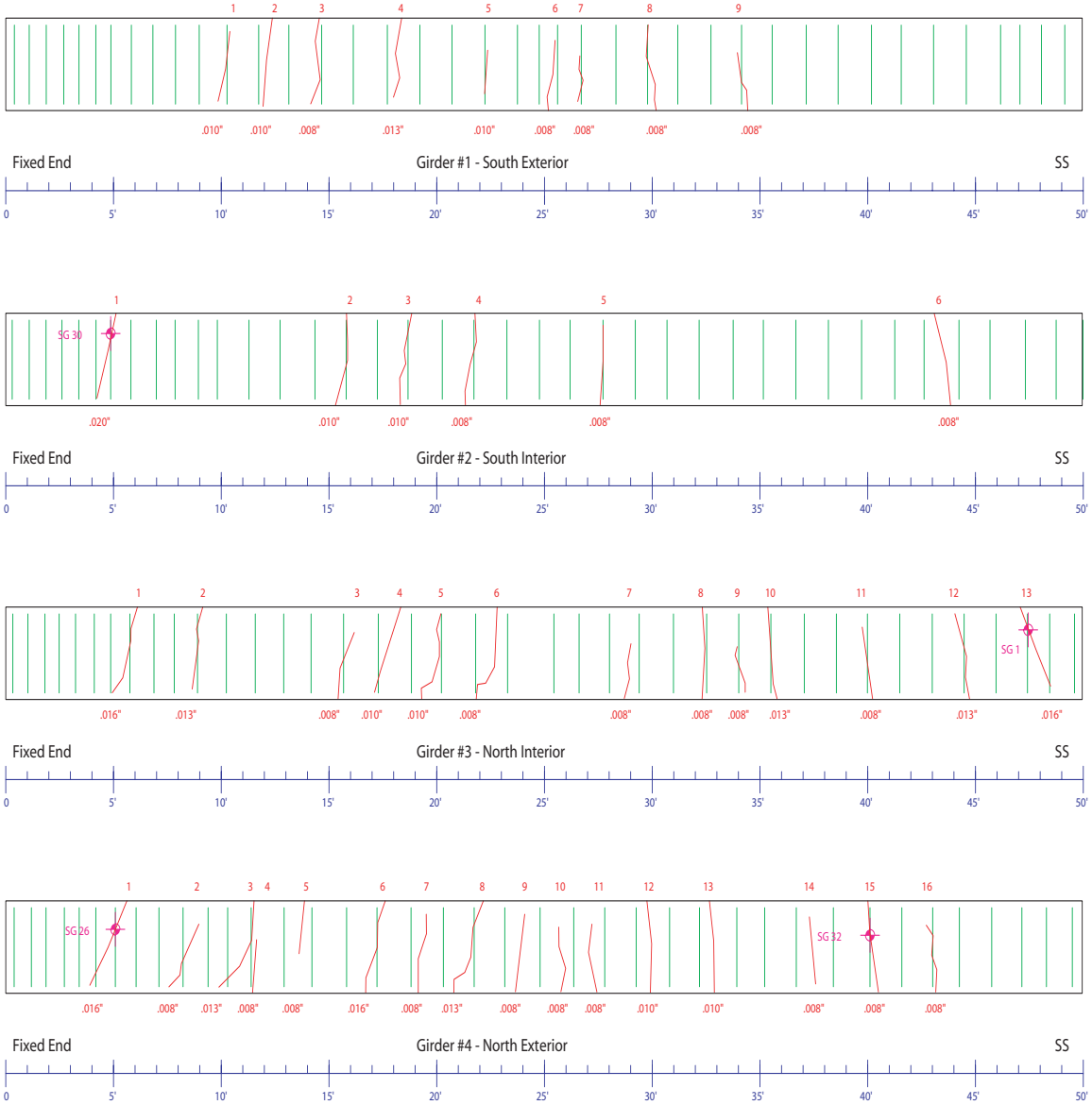

Figure 2.33c: 15 Mile Creek Bridge crack, stirrup, and instrumentation locations on span 5 westbound

15 MILE CREEK BRIDGE
I-84 / 15 MILE CREEK
THE DALLES, OREGON

SPAN 4 - WEST-BOUND LANES

DECEMBER 15, 2003

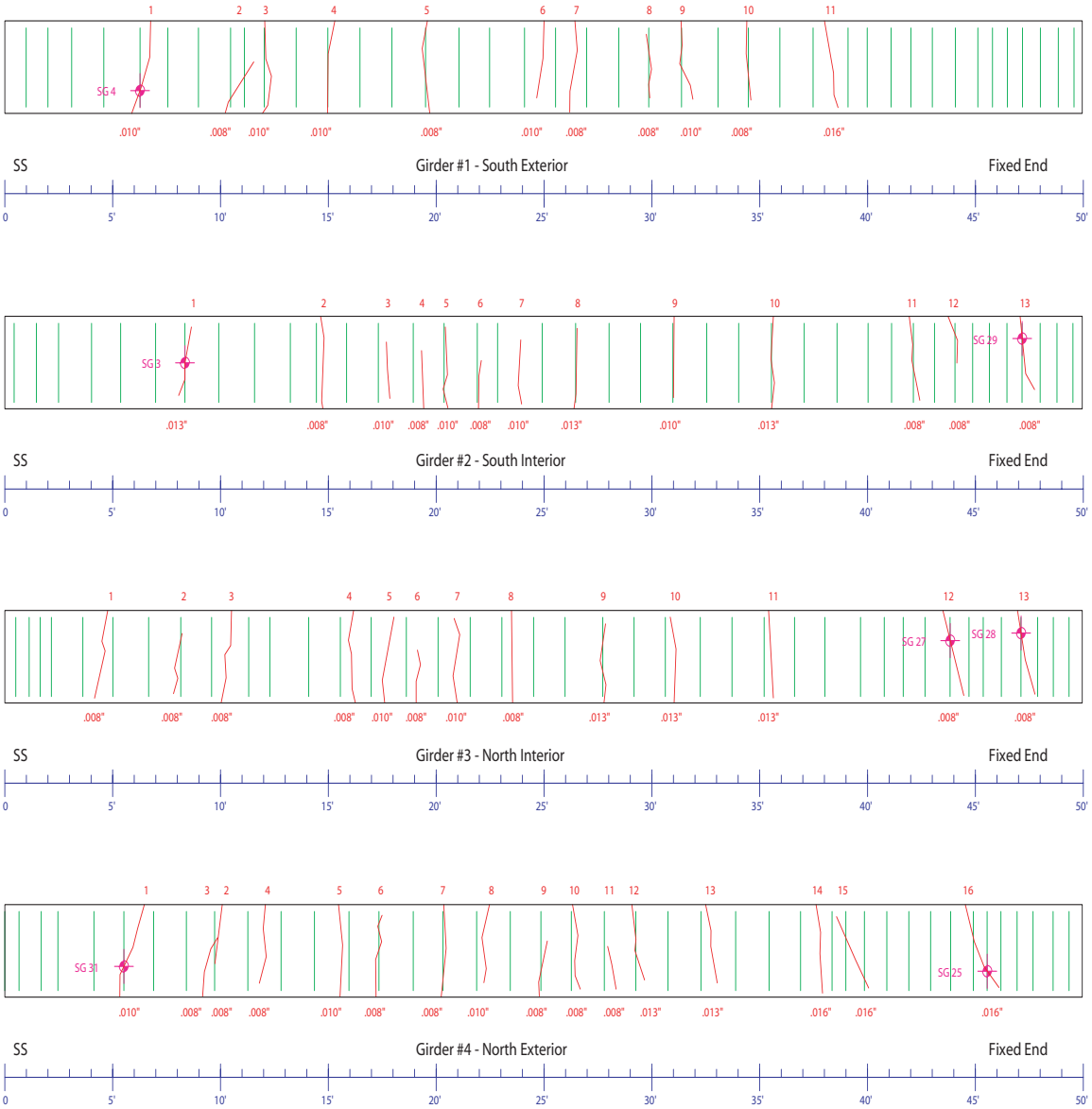

Figure 2.33d: 15 Mile Creek Bridge crack, stirrup, and instrumentation locations on span 4 westbound

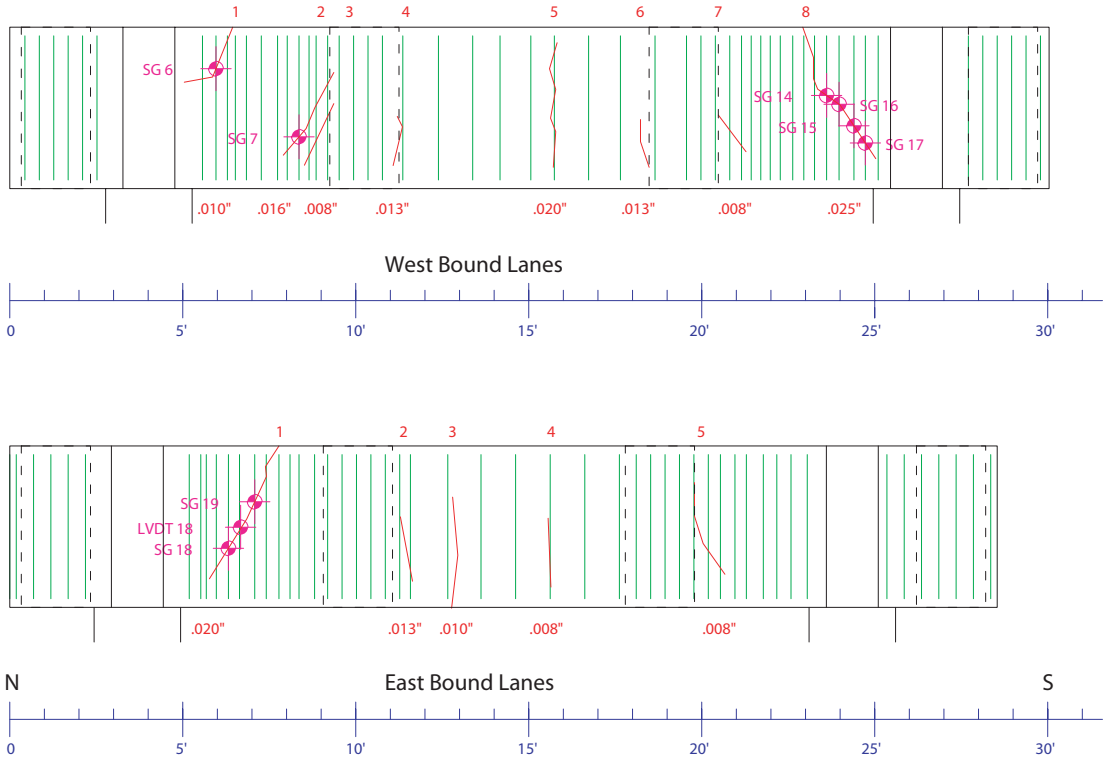

Figure 2.33e: 15 Mile Creek Bridge crack, stirrup, and instrumentation locations on bent caps

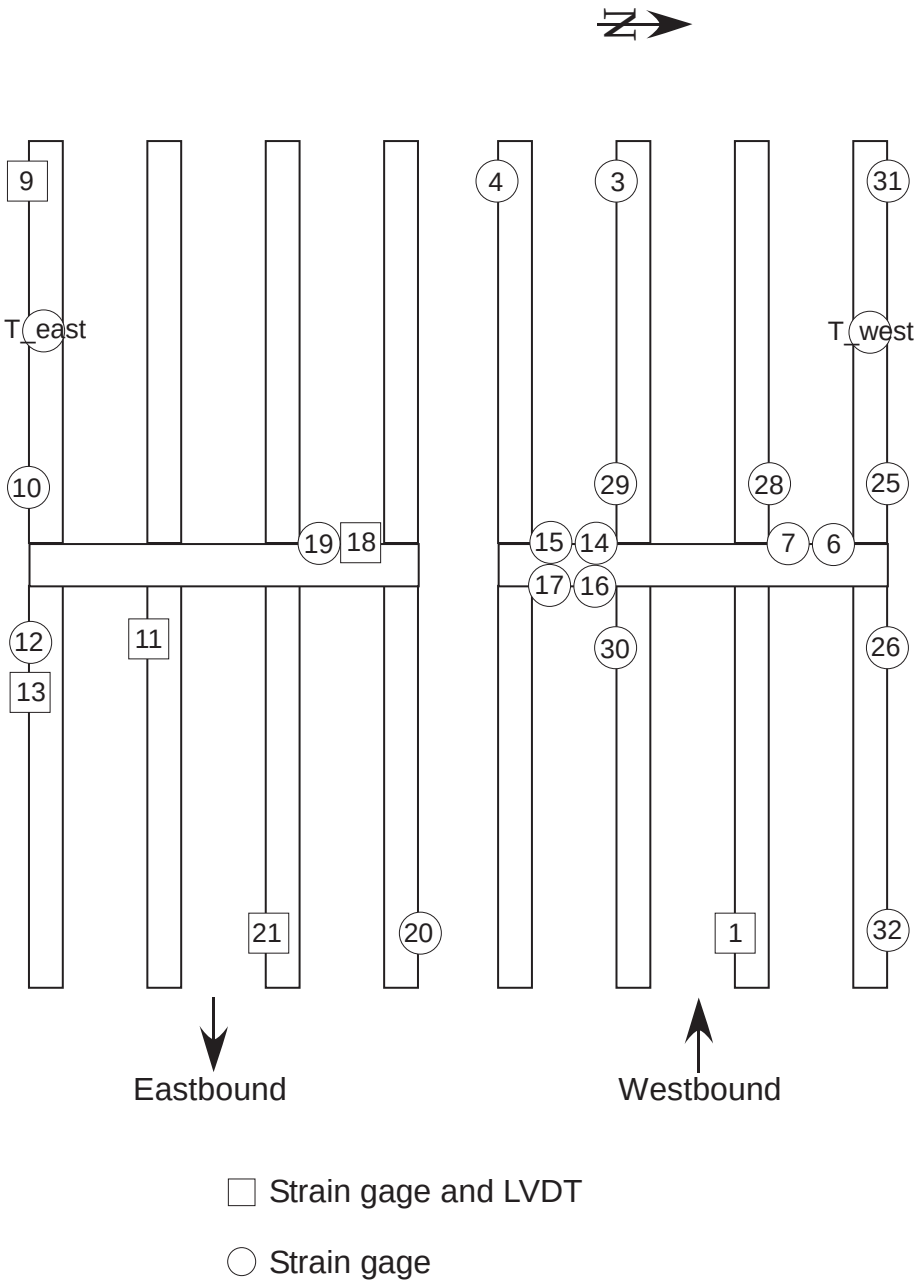

Figure 2.34: Schematic locations of instrumentation on 15 Mile Creek Bridge

2.3.3 Testing Method

Two series of live load data were collected: response under ambient traffic loading and response under controlled truck loading. The stirrup reinforcing stresses and crack displacements generated by normal traffic flow were recorded over a period of 8 calendar days from January 15 to 23, 2004. Individual event histories were recorded by the data logger when stress thresholds

exceeded 2.25 ksi at sensor location T_EAST or 2.75 ksi at sensor location T_WEST. For each trigger event, data were recorded for six seconds prior to and following the trigger. These event histories were used to confirm the presence of the larger magnitude stress ranges.

Controlled truck tests were conducted using a heavily loaded ODOT maintenance truck, as shown in Figure 2.35a. Axle weights and spacing were determined after the test and are shown in Figure 2.35b. Traffic was temporarily slowed using a rolling roadblock so that the control truck would be the only vehicle on the bridge during data collection. The control truck passed over the bridge at several designated speeds and lane positions. Test speeds varied from 5 mph to 66 mph.

Figure 2.35a: Test truck used on 15 Mile Creek Bridge

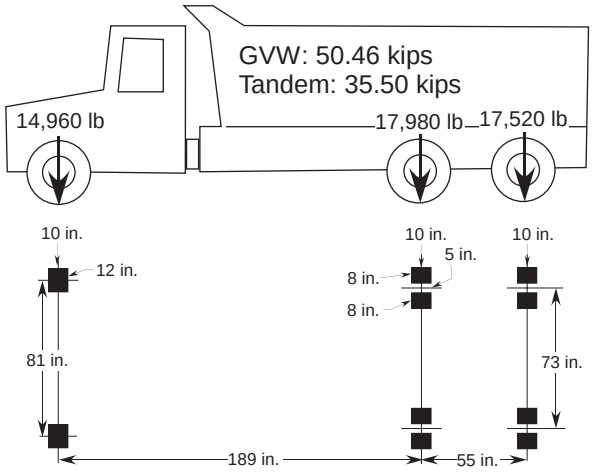

Figure 2.35b: Axle weights and spacing for test truck used on 15 Mile Creek Bridge

Lane locations included placing the truck in the truck lane and in the passing lane. Lane positions and the corresponding truck positions relative to the girder locations are illustrated in Figure 2.36. During each pass of the control truck, stirrup stresses and crack deflections were recorded for each instrumented location. Stirrup strain histories for each of the test runs are shown in Figures 2.37a-l and the crack motions are shown in Figures 2.38a-d. Peak values and stress ranges are summarized in Tables 2.6a and b.

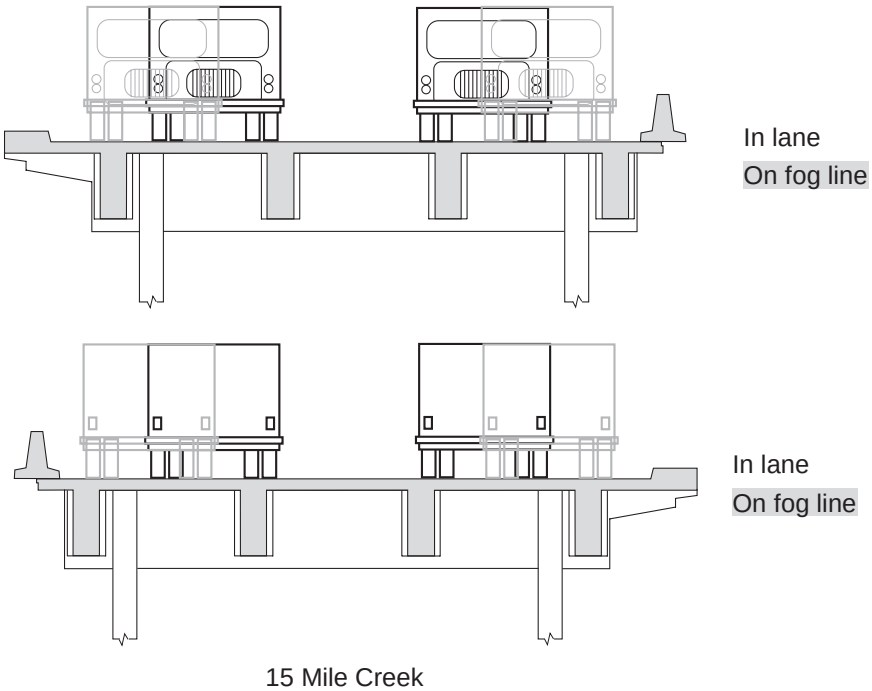

Figure 2.36: Test truck lane location relative to girder positions on 15 Mile Creek Bridge

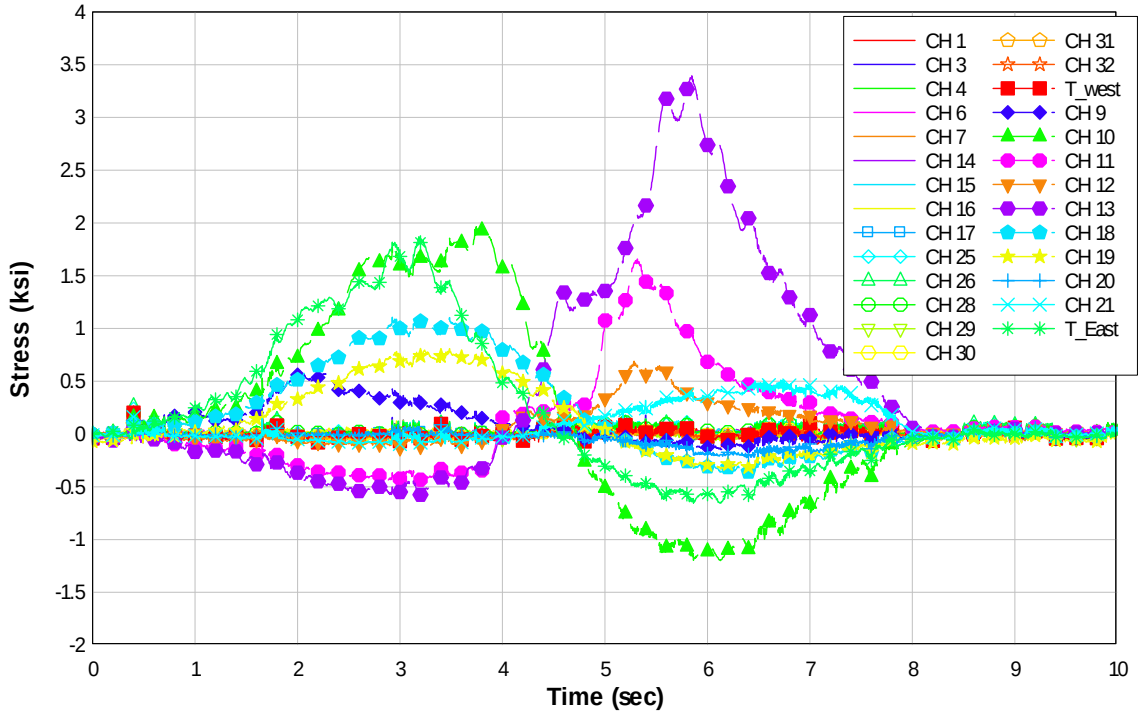

Figure 2.37a: Stirrup stress response for test truck in east-bound truck lane at 5 mph

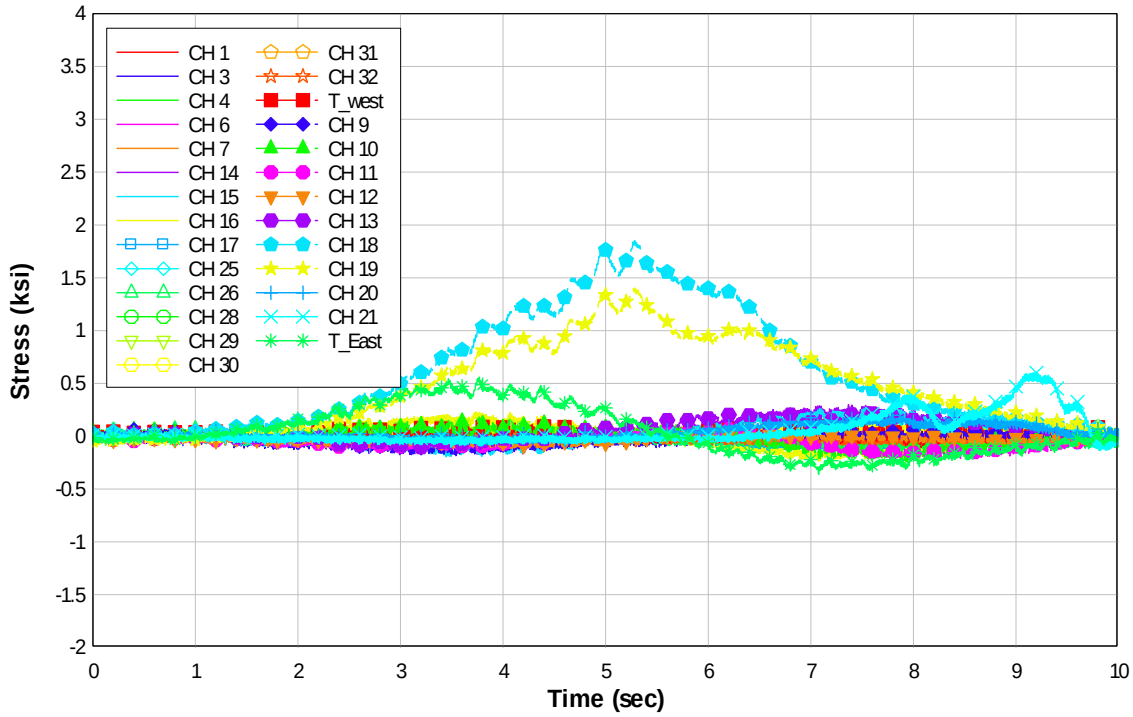

Figure 2.37b: Stirrup stress response for test truck in east-bound passing lane at 5 mph

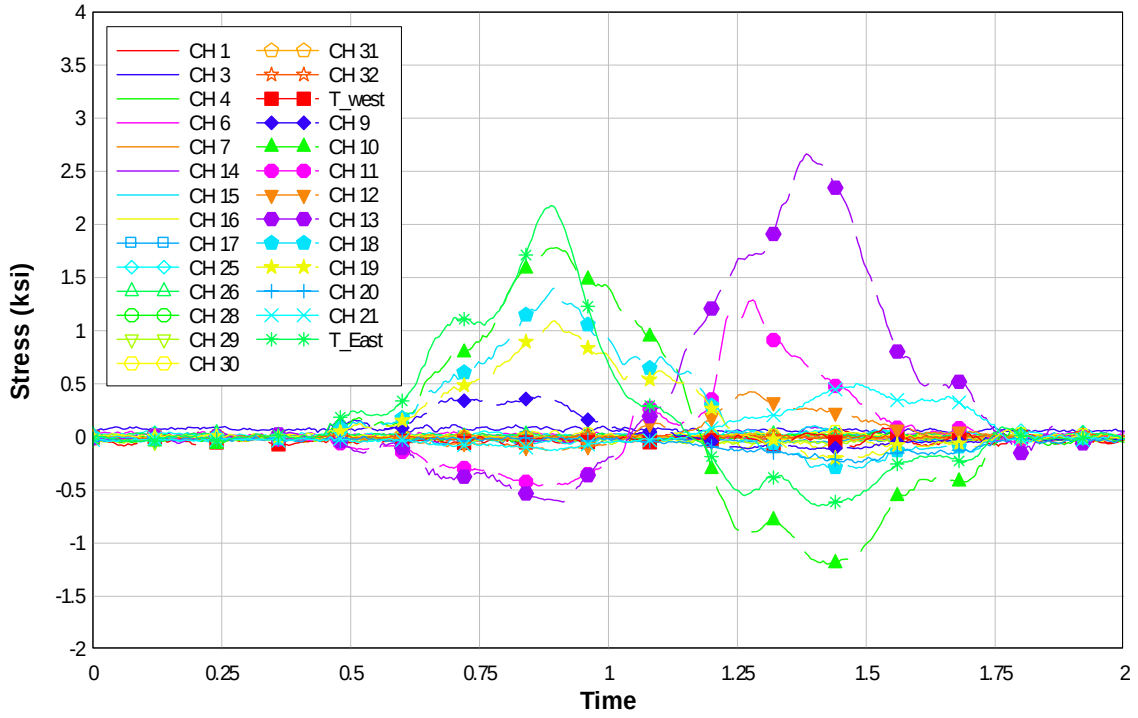

Figure 2.37c: Stirrup stress response for test truck in east-bound truck lane at 55 mph

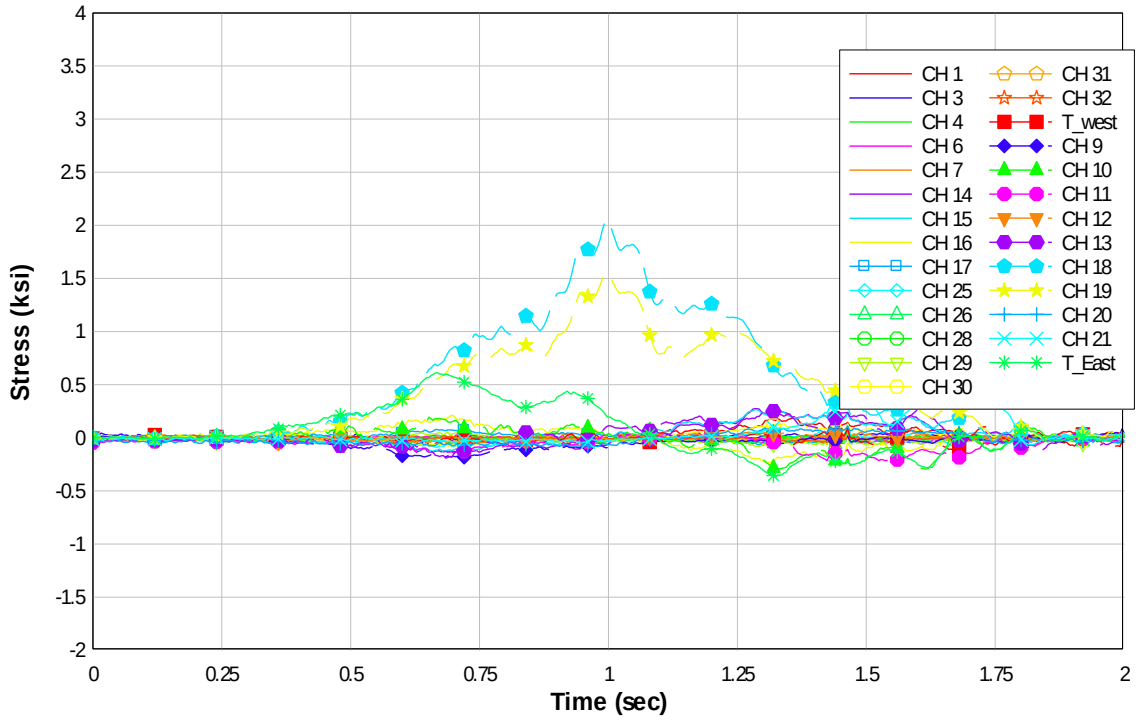

Figure 2.37d: Stirrup stress response for test truck in east-bound passing lane at 55 mph

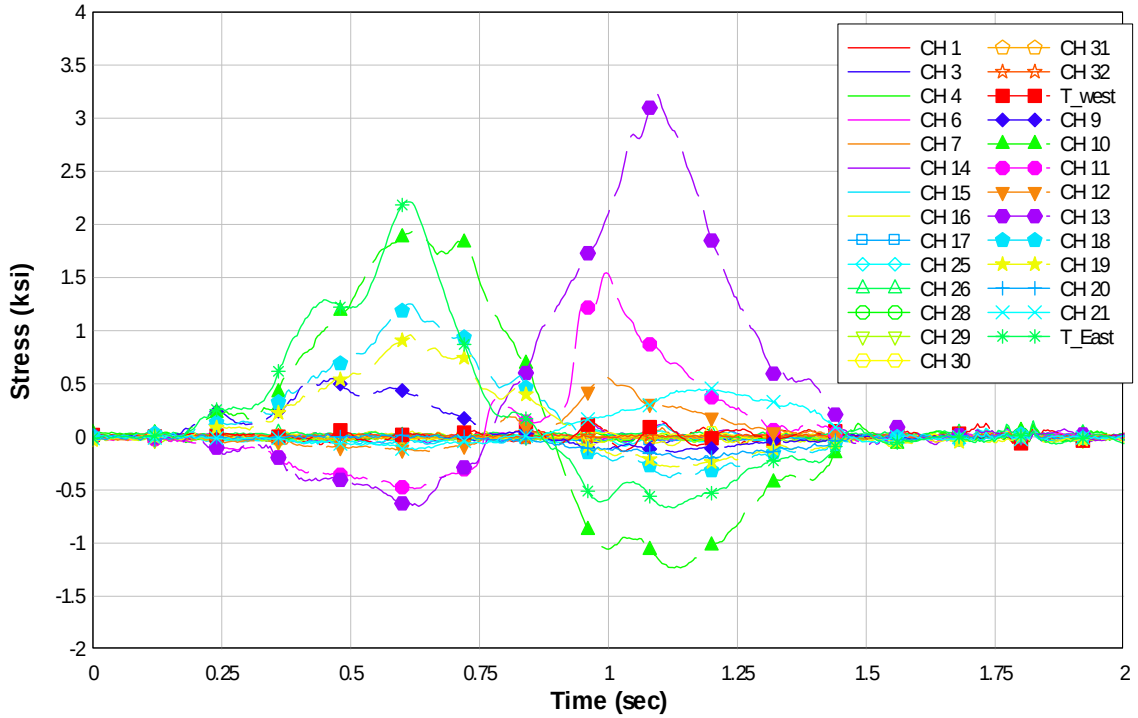

Figure 2.37e: Stirrup stress response for test truck in east-bound truck lane at 65 mph

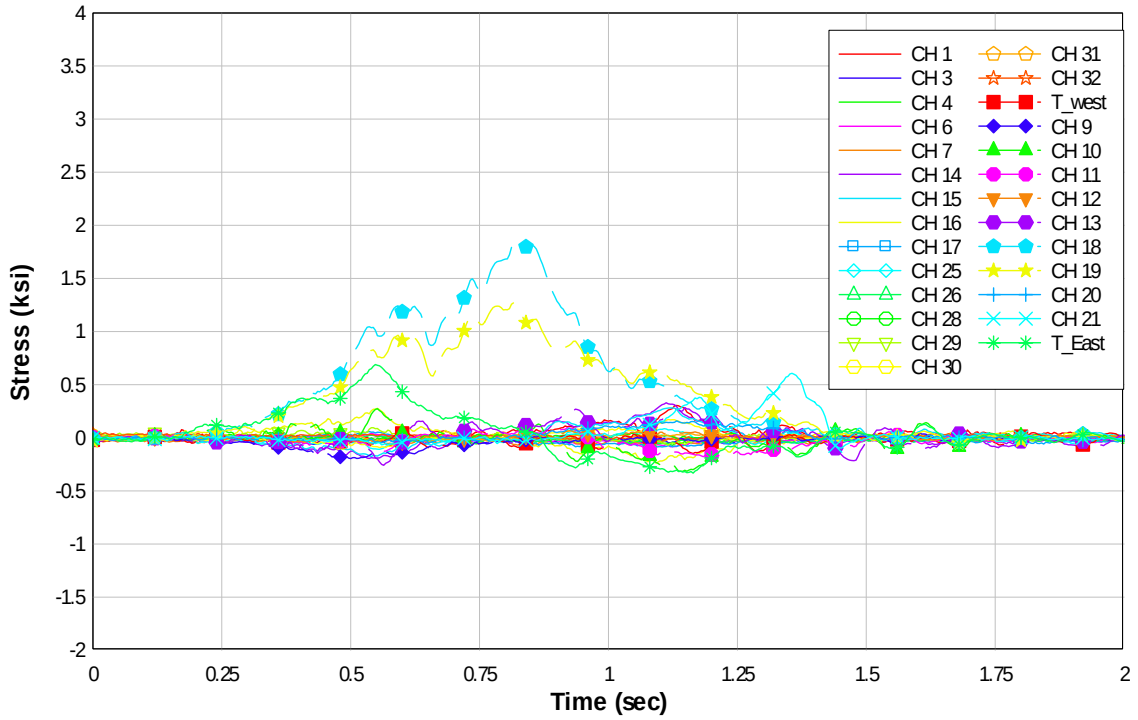

Figure 2.37f: Stirrup stress response for test truck in east-bound passing lane at 65 mph

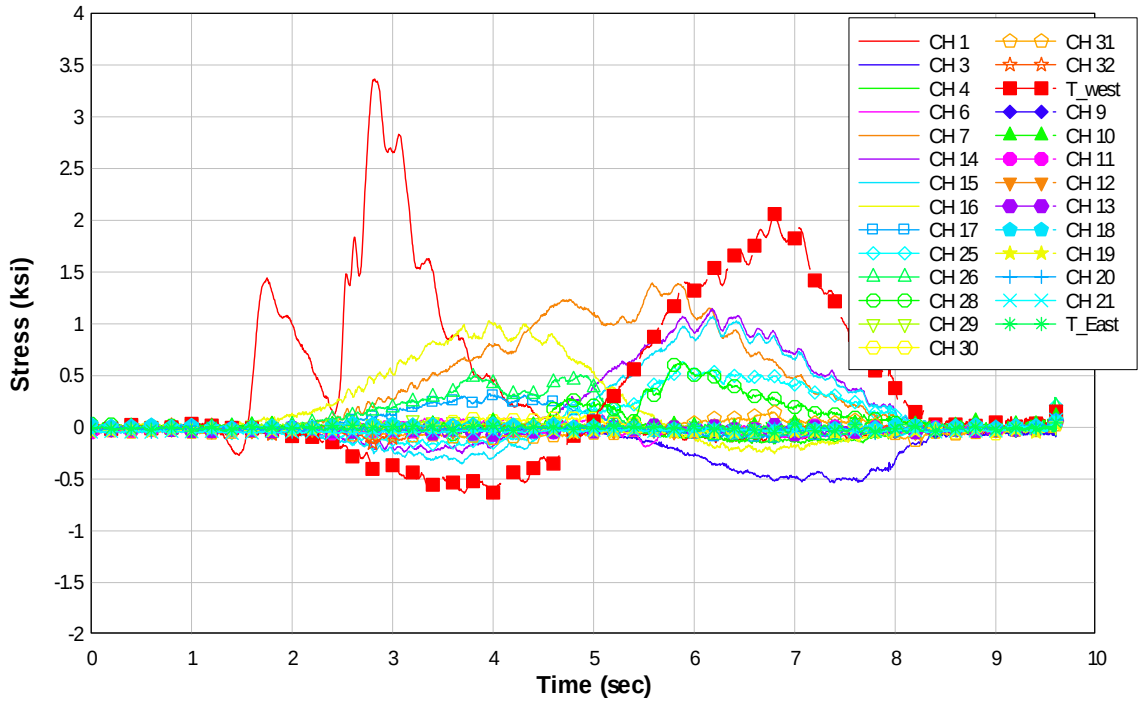

Figure 2.37g: Stirrup stress response for test truck in west-bound truck lane at 5 mph

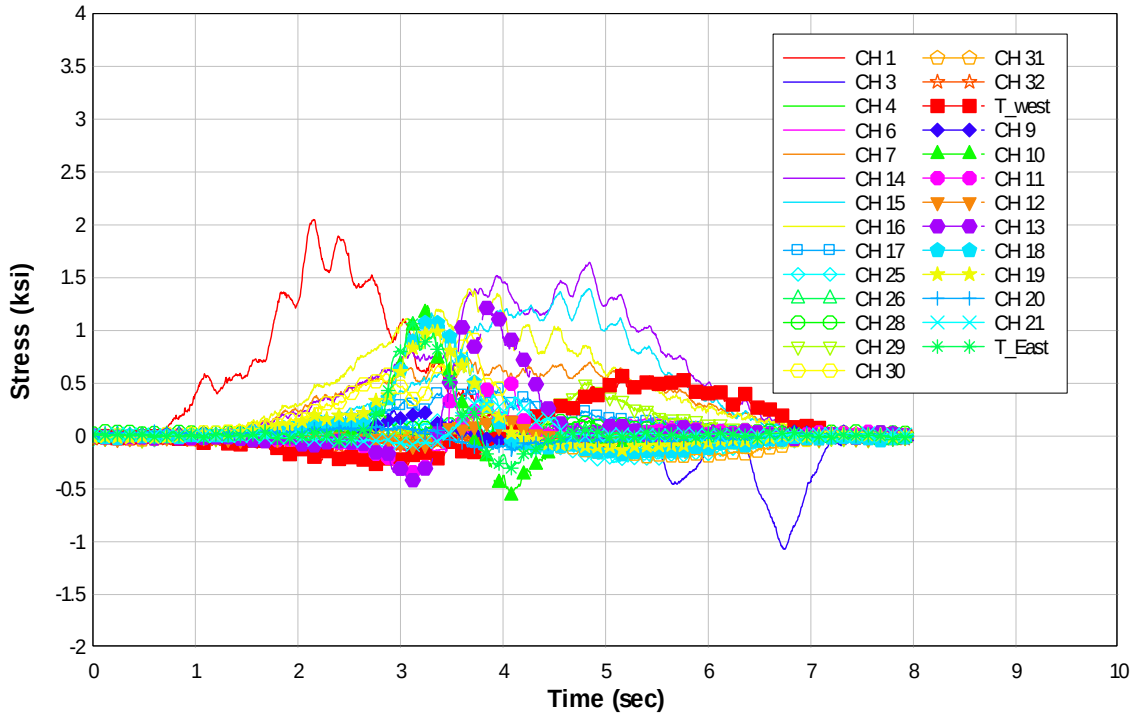

Figure 2.37h: Stirrup stress response for test truck in west-bound passing lane at 5 mph

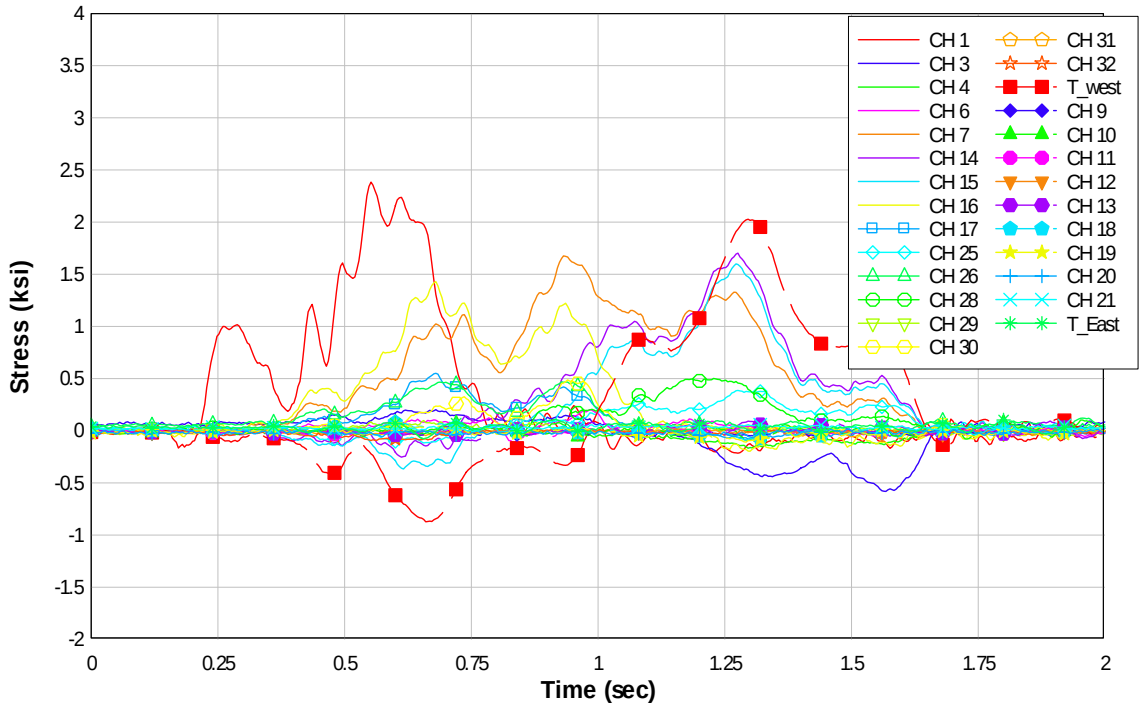

Figure 2.37i: Stirrup stress response for test truck in west-bound truck lane at 55 mph

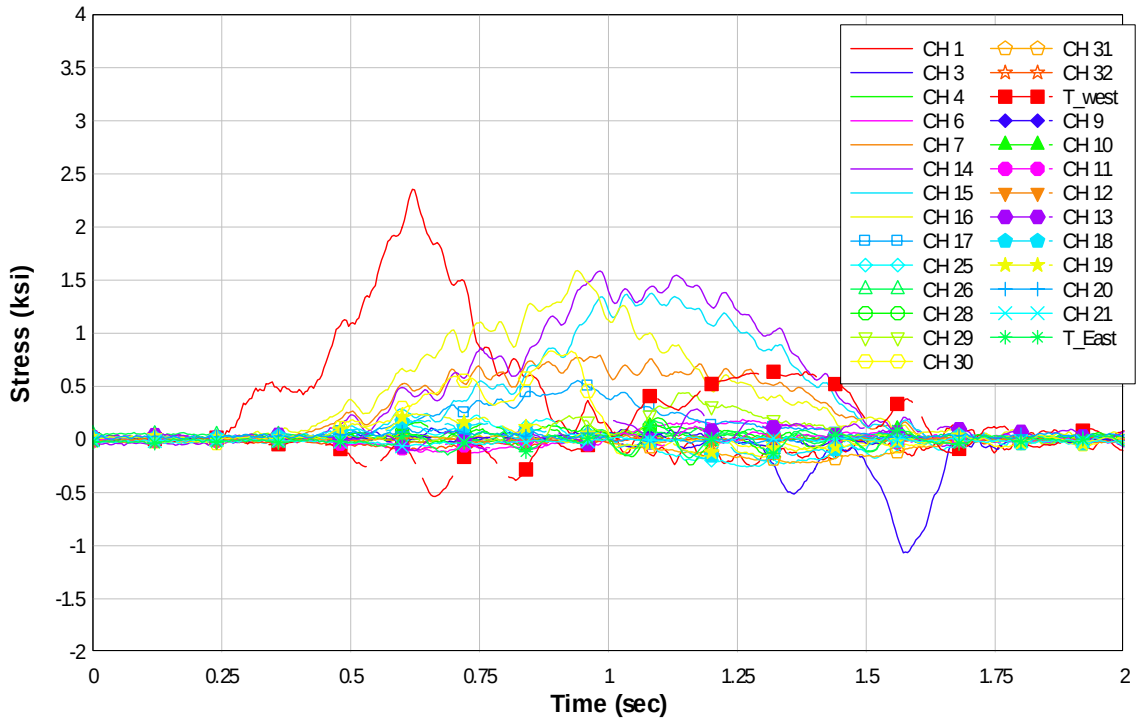

Figure 2.37j: Stirrup stress response for test truck in west-bound passing lane at 55 mph

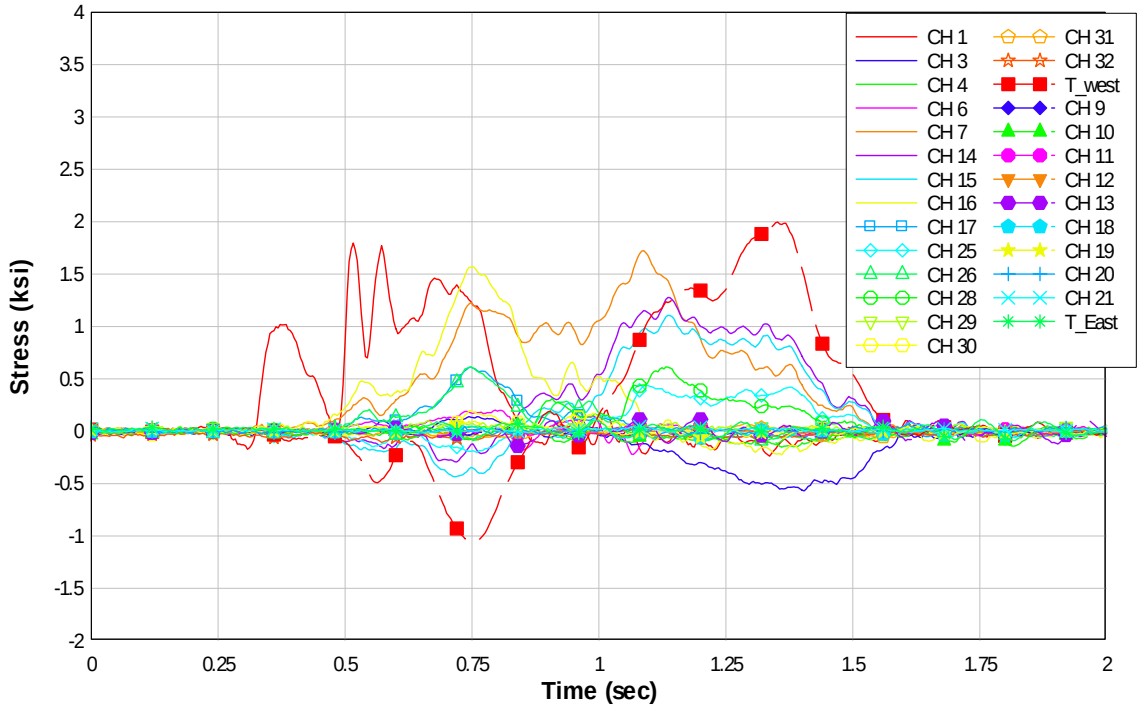

Figure 2.37k: Stirrup stress response for test truck in west-bound truck lane at 65 mph

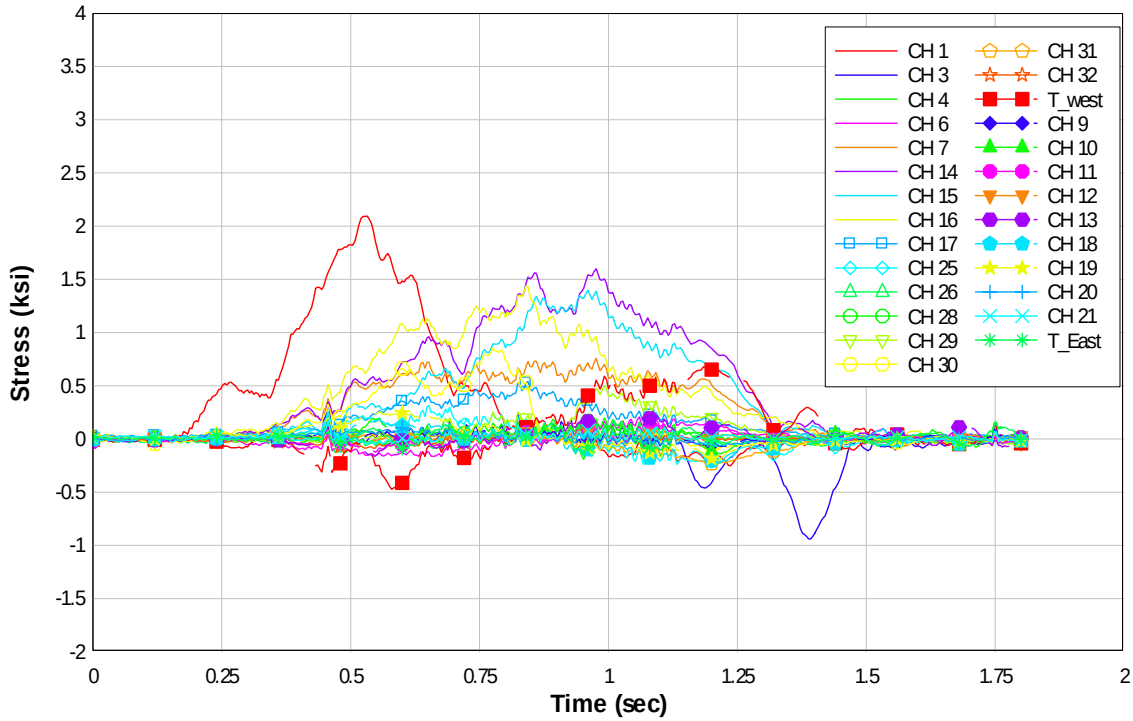

Figure 2.37l: Stirrup stress response for test truck in west-bound passing lane at 65 mph

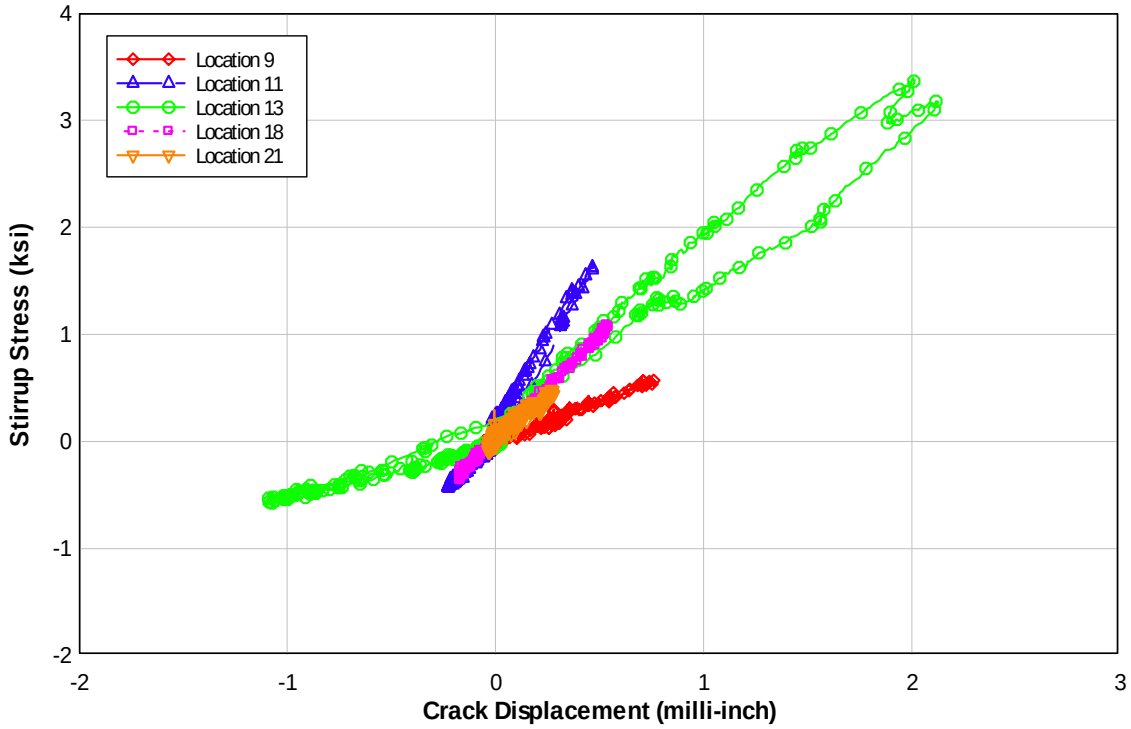

Figure 2.38a: Crack displacement-Stirrup stress response for test truck in east-bound truck lane at 5 mph

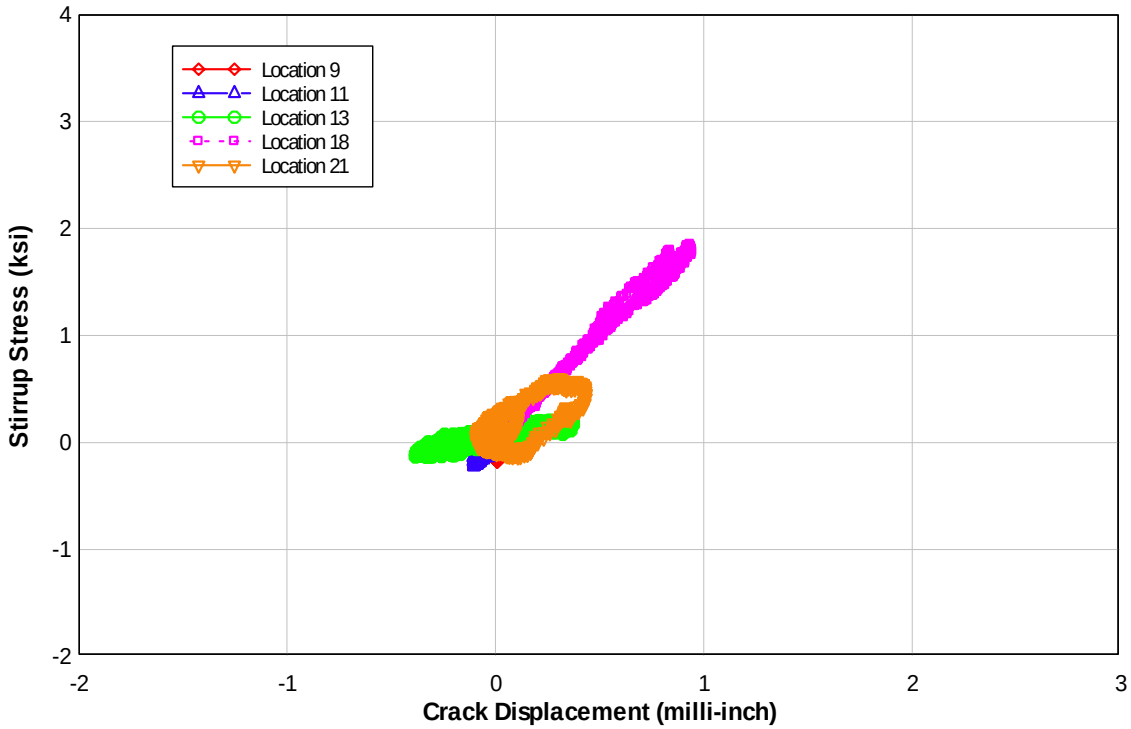

Figure 2.38b: Crack displacement-Stirrup stress response for test truck in east-bound passing lane at 5 mph

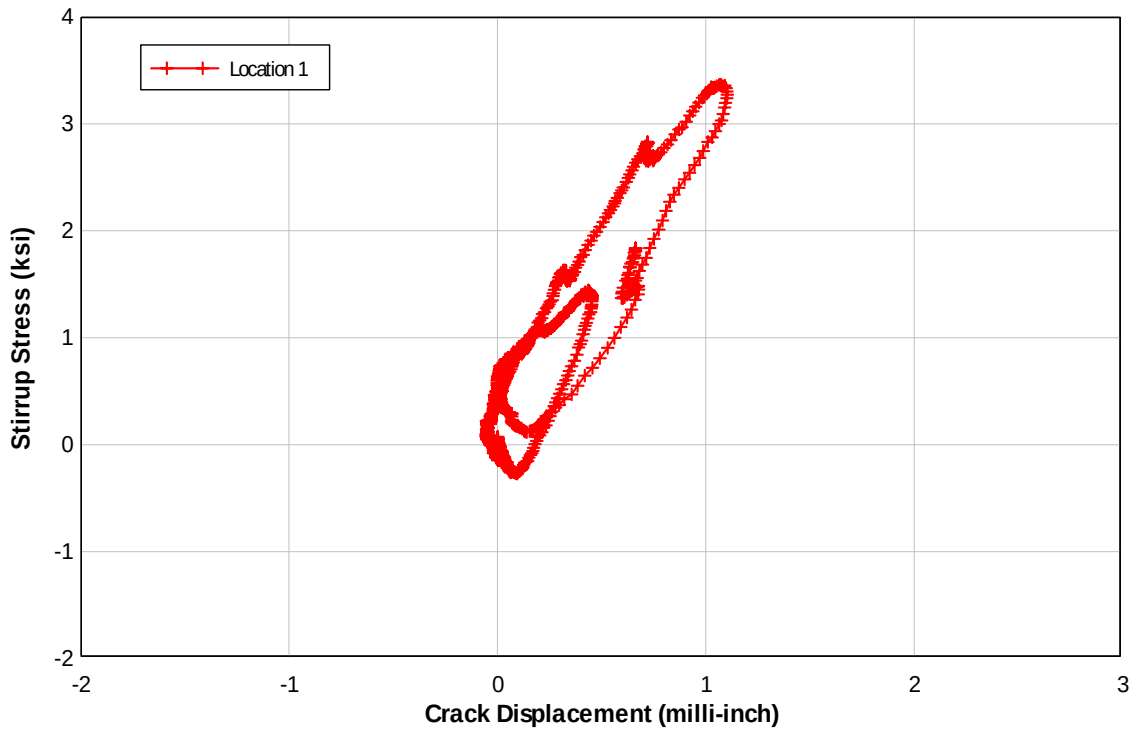

Figure 2.38c: Crack displacement-Stirrup stress response for test truck in west-bound truck lane at 5 mph

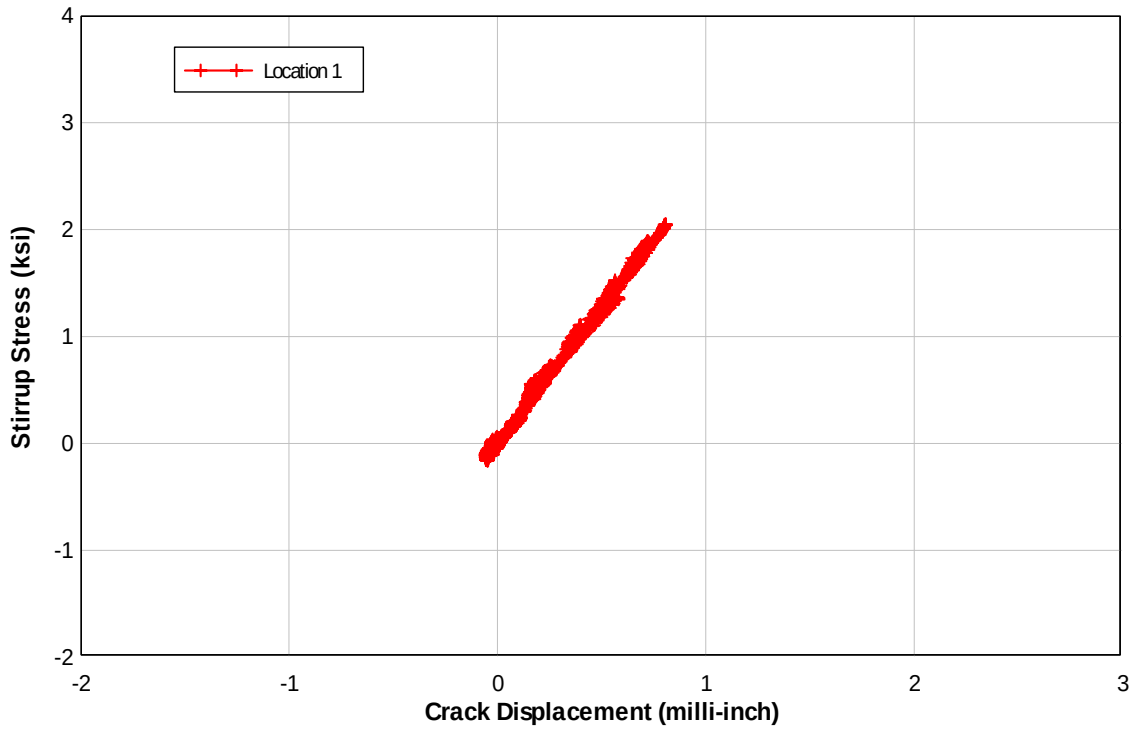

Figure 2.38d: Crack displacement-Stirrup stress response for test truck in west-bound passing lane at 5 mph

Table 2.6a: Maximum and minimum stresses and stress ranges at instrumented locations for test truck westbound on 15 Mile Creek Bridge

Maximum Stress

Truck Direction	Lane Position	Speed (mph)	CH_1 (ksi)	CH_3 (ksi)	CH_4 (ksi)	CH_6 (ksi)	CH_7 (ksi)	CH_14 (ksi)	CH_15 (ksi)	CH_16 (ksi)	CH_17 (ksi)	CH_25 (ksi)	CH_26 (ksi)	CH_28 (ksi)	CH_29 (ksi)	CH_30 (ksi)	CH_31 (ksi)	CH_32 (ksi)	T_West (ksi)
Westbound	Driving	5	3.37	0.15	0.16	0.12	1.40	1.15	1.07	1.03	0.33	0.63	0.51	0.63	0.15	0.12	0.15	0.08	2.07
Westbound	Passing	5	2.05	0.08	0.07	0.18	0.73	1.65	1.40	1.40	0.46	0.16	0.07	0.16	0.52	0.99	0.04	0.02	0.58
Westbound	Driving	55	2.38	0.20	0.04	0.20	1.68	1.70	1.60	1.43	0.55	0.39	0.47	0.50	0.10	0.49	0.04	0.02	2.03
Westbound	Driving	66	1.80	0.14	0.05	0.20	1.72	1.28	1.11	1.57	0.61	0.44	0.61	0.62	0.10	0.20	0.08	0.00	2.00
Westbound	Passing	55	2.36	0.11	0.07	0.19	0.79	1.59	1.38	1.59	0.56	0.23	0.12	0.14	0.44	0.83	0.04	0.03	0.64
Westbound	Passing	65	2.09	0.37	0.22	0.21	0.76	1.60	1.40	1.44	0.54	0.32	0.21	0.20	0.50	0.85	0.15	0.06	0.68

Minimum Stress

Truck Direction	Lane Position	Speed (mph)	CH_1 (ksi)	CH_3 (ksi)	CH_4 (ksi)	CH_6 (ksi)	CH_7 (ksi)	CH_14 (ksi)	CH_15 (ksi)	CH_16 (ksi)	CH_17 (ksi)	CH_25 (ksi)	CH_26 (ksi)	CH_28 (ksi)	CH_29 (ksi)	CH_30 (ksi)	CH_31 (ksi)	CH_32 (ksi)	T_West (ksi)
Westbound	Driving	5	-0.27	-0.53	-0.16	-0.19	-0.07	-0.25	-0.35	-0.25	-0.11	-0.18	-0.10	-0.08	-0.03	-0.08	-0.12	-0.16	-0.64
Westbound	Passing	5	-0.16	-1.07	-0.06	-0.15	-0.03	-0.03	-0.03	-0.03	-0.04	-0.25	-0.04	-0.02	-0.05	-0.09	-0.21	-0.10	-0.30
Westbound	Driving	55	-0.21	-0.58	-0.17	-0.11	-0.05	-0.25	-0.37	-0.20	-0.08	-0.12	-0.01	-0.05	-0.04	-0.04	-0.06	-0.09	-0.87
Westbound	Driving	66	-0.24	-0.57	-0.15	-0.22	-0.05	-0.29	-0.43	-0.22	-0.07	-0.20	-0.09	-0.04	-0.04	-0.06	-0.07	-0.11	-1.07
Westbound	Passing	55	-0.25	-1.07	-0.04	-0.13	-0.05	-0.09	-0.04	-0.01	-0.03	-0.26	-0.03	-0.04	-0.05	-0.14	-0.22	-0.10	-0.54
Westbound	Passing	65	-0.25	-0.94	-0.08	-0.16	-0.04	-0.05	-0.05	-0.03	0.00	-0.24	-0.11	-0.05	-0.05	-0.10	-0.23	-0.09	-0.47

Stress Range

Truck Direction	Lane Position	Speed (mph)	CH_1 (ksi)	CH_3 (ksi)	CH_4 (ksi)	CH_6 (ksi)	CH_7 (ksi)	CH_14 (ksi)	CH_15 (ksi)	CH_16 (ksi)	CH_17 (ksi)	CH_25 (ksi)	CH_26 (ksi)	CH_28 (ksi)	CH_29 (ksi)	CH_30 (ksi)	CH_31 (ksi)	CH_32 (ksi)	T_West (ksi)
Westbound	Driving	5	3.63	0.68	0.32	0.31	1.46	1.40	1.43	1.28	0.44	0.81	0.61	0.71	0.18	0.20	0.27	0.23	2.70
Westbound	Passing	5	2.21	1.15	0.13	0.33	0.76	1.68	1.43	1.43	0.50	0.41	0.11	0.18	0.56	1.09	0.25	0.12	0.88
Westbound	Driving	55	2.60	0.78	0.21	0.32	1.72	1.95	1.97	1.63	0.63	0.50	0.48	0.55	0.14	0.53	0.10	0.11	2.90
Westbound	Driving	66	2.03	0.71	0.21	0.42	1.77	1.57	1.54	1.80	0.69	0.64	0.70	0.66	0.14	0.25	0.15	0.11	3.06
Westbound	Passing	55	2.61	1.18	0.11	0.32	0.85	1.67	1.42	1.60	0.58	0.49	0.15	0.18	0.49	0.97	0.26	0.12	1.17
Westbound	Passing	65	2.35	1.31	0.30	0.37	0.80	1.65	1.45	1.47	0.54	0.56	0.32	0.25	0.55	0.95	0.38	0.15	1.15

Table 2.6b: Maximum and minimum stresses and stress ranges at instrumented locations for test truck eastbound on 15 Mile Creek Bridge

Maximum Stress

Truck Direction	Lane Position	Speed (mph)	CH_9 (ksi)	CH_10 (ksi)	CH_11 (ksi)	CH_12 (ksi)	CH_13 (ksi)	CH_18 (ksi)	CH_19 (ksi)	CH_20 (ksi)	CH_21 (ksi)	T_East (ksi)
Eastbound	Driving	5	0.58	1.97	1.66	0.69	3.40	1.11	0.81	0.13	0.51	1.87
Eastbound	Passing	5	0.13	0.18	0.08	0.05	0.22	1.85	1.40	0.20	0.60	0.56
Eastbound	Driving	55	0.38	1.78	1.29	0.43	2.67	1.40	1.09	0.01	0.50	2.18
Eastbound	Driving	64	0.55	1.94	1.55	0.58	3.24	1.25	0.96	0.06	0.46	2.21
Eastbound	Passing	55	0.06	0.20	0.06	0.07	0.28	2.06	1.56	0.11	0.60	0.61
Eastbound	Passing	65	0.05	0.27	0.10	0.07	0.28	1.86	1.27	0.16	0.61	0.69

Minumum Stress

Truck Direction	Lane Position	Speed (mph)	CH_9 (ksi)	CH_10 (ksi)	CH_11 (ksi)	CH_12 (ksi)	CH_13 (ksi)	CH_18 (ksi)	CH_19 (ksi)	CH_20 (ksi)	CH_21 (ksi)	T_East (ksi)
Eastbound	Driving	5	-0.15	-1.20	-0.44	-0.13	-0.57	-0.36	-0.33	-0.23	-0.10	-0.66
Eastbound	Passing	5	-0.18	-0.25	-0.23	-0.12	-0.14	-0.04	-0.10	-0.10	-0.14	-0.36
Eastbound	Driving	55	-0.12	-1.20	-0.47	-0.13	-0.61	-0.29	-0.21	-0.24	-0.13	-0.65
Eastbound	Driving	64	-0.14	-1.23	-0.49	-0.14	-0.65	-0.38	-0.28	-0.22	-0.12	-0.67
Eastbound	Passing	55	-0.18	-0.30	-0.22	-0.06	-0.19	-0.04	-0.02	-0.08	-0.07	-0.37
Eastbound	Passing	65	-0.20	-0.32	-0.18	-0.06	-0.26	-0.04	-0.06	-0.05	-0.10	-0.33

Stress Range

Truck Direction	Lane Position	Speed (mph)	CH_9 (ksi)	CH_10 (ksi)	CH_11 (ksi)	CH_12 (ksi)	CH_13 (ksi)	CH_18 (ksi)	CH_19 (ksi)	CH_20 (ksi)	CH_21 (ksi)	T_East (ksi)
Eastbound	Driving	5	0.73	3.16	2.10	0.82	3.97	1.48	1.14	0.36	0.61	2.53
Eastbound	Passing	5	0.32	0.43	0.30	0.17	0.35	1.89	1.51	0.29	0.74	0.92
Eastbound	Driving	55	0.50	2.98	1.76	0.55	3.28	1.70	1.30	0.25	0.63	2.83
Eastbound	Driving	64	0.69	3.17	2.03	0.72	3.89	1.64	1.24	0.27	0.57	2.88
Eastbound	Passing	55	0.24	0.49	0.28	0.13	0.47	2.10	1.58	0.20	0.66	0.98
Eastbound	Passing	65	0.24	0.59	0.27	0.13	0.54	1.90	1.33	0.21	0.70	1.02

2.4 AMBIENT TRAFFIC INDUCED STIRRUP STRESS

Ambient traffic induced stresses in stirrups at crack locations were monitored at each bridge for a period of at least 8 days. The stress-ranges and numbers of cycles recorded at the instrumented locations are shown in Figures 2.39a, b, and c for McKenzie River, Jasper, and 15 Mile Creek Bridges, respectively.

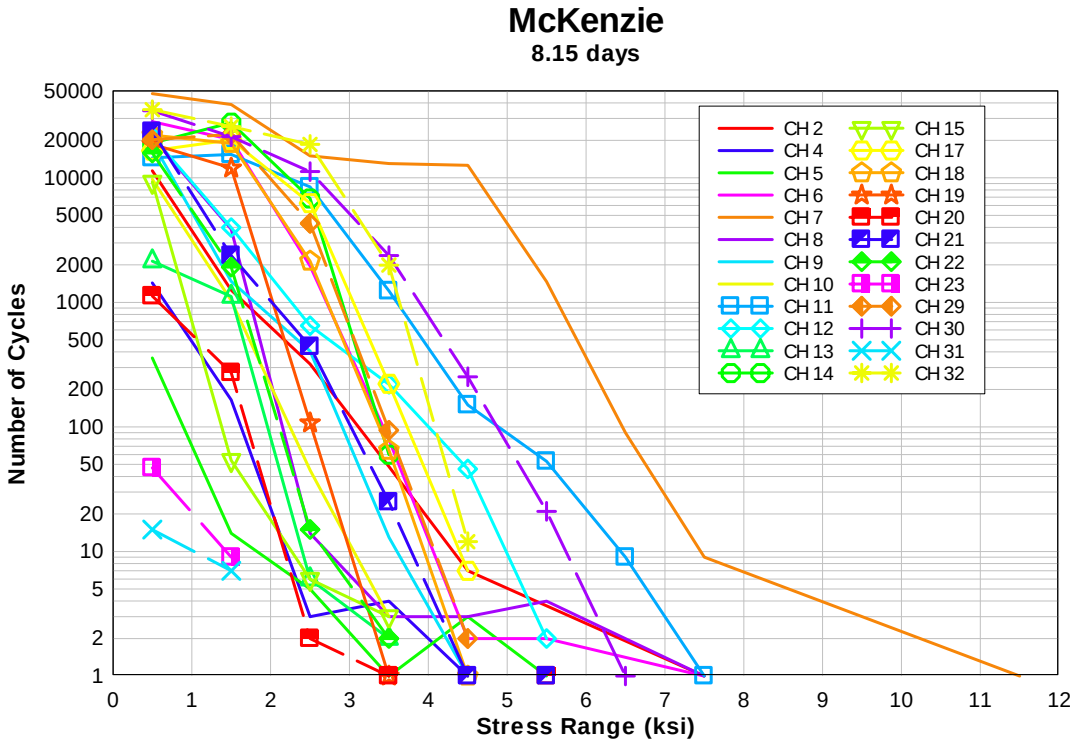

Figure 2.39a: S-N response for all instrumented locations on McKenzie River Bridge for period of 8.15 days

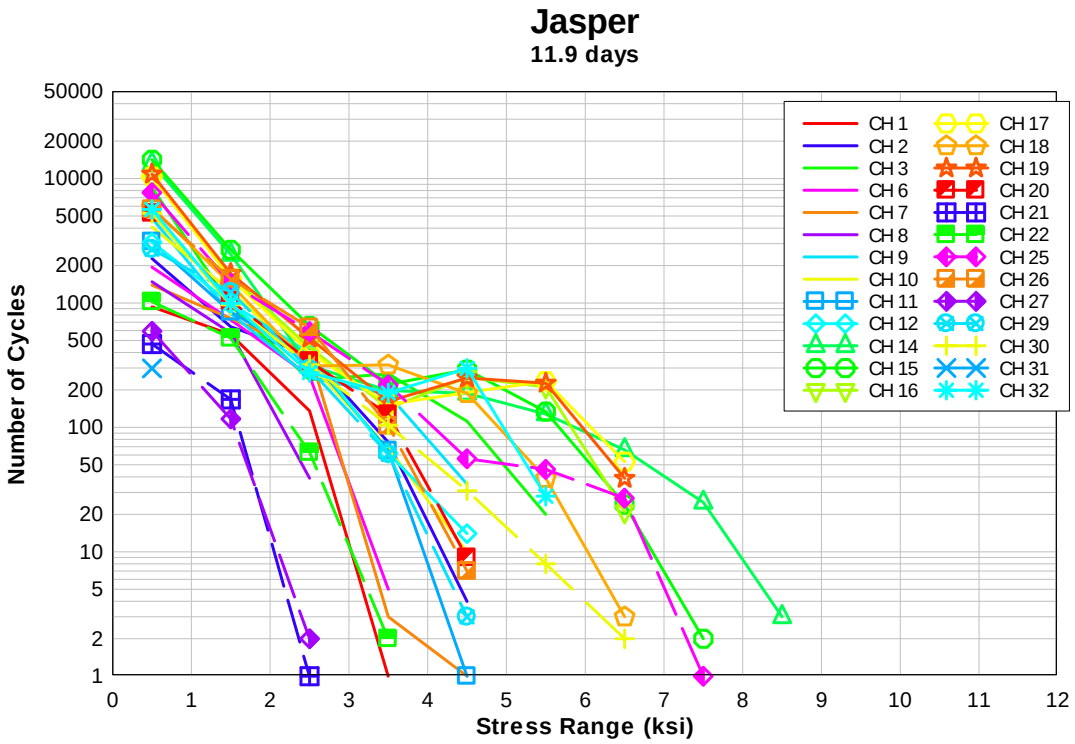

Figure 2.39b: S-N response for all instrumented locations on Jasper Bridge for period of 11.9 days

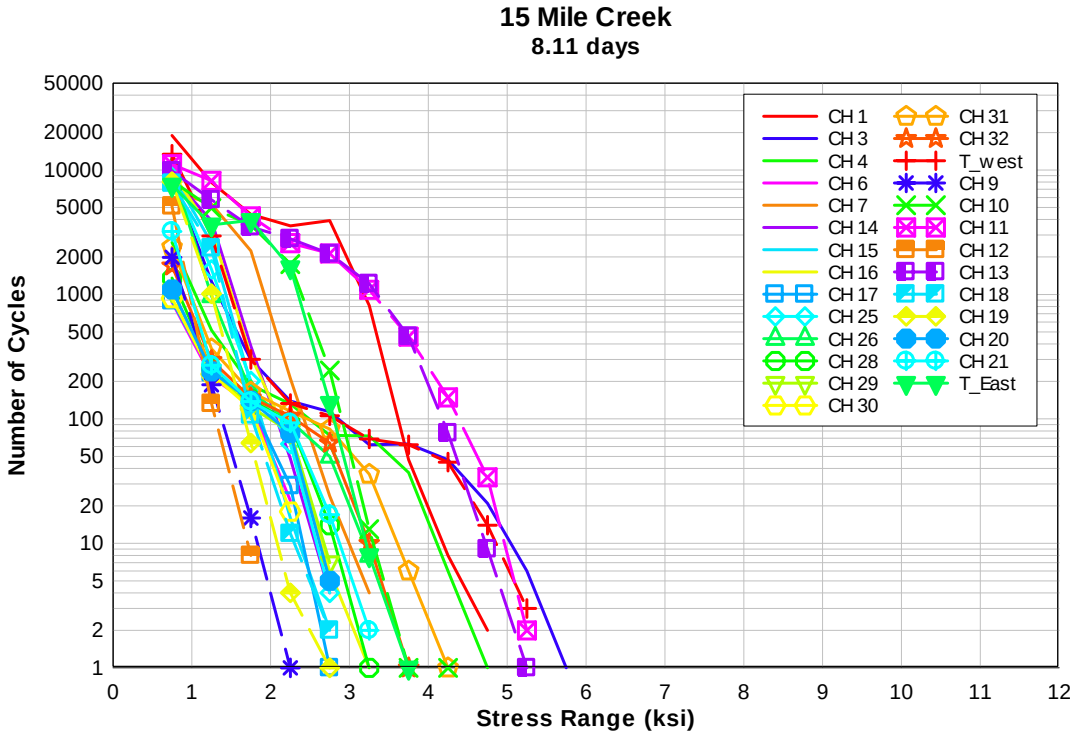

Figure 2.39c: S-N response for all instrumented locations on 15 Mile Creek Bridge for period of 8.1 days

The largest single stress-range measured at any location was approximately 12 ksi. Using Miner's Rule (*Miner 1945*), the variable amplitude stresses can be described as an equivalent constant amplitude stress-range for each of the instrumented locations:

$$SR_{eqv} = \sqrt[3]{\sum \frac{n_i}{N_{tot}} SR_i^3} \qquad \textbf{(2-1)}$$

where SR_i is the ith stress-range, n_i is the number of cycles observed for the ith stress-range, and N_{tot} is the total number of cycles at all stress ranges.

The equivalent constant amplitude stress-ranges were below 2 ksi at all locations (except for one on McKenzie River Bridge – 2.64 ksi at Location 7, an interior girder at the southern simple-support of the 3-span continuous portion) as seen in Table 2.7a, b, and c for McKenzie River, Jasper, and 15 Mile Creek Bridges, respectively.

Table 2.7a: Equivalent constant amplitude stress range for instrumented locations on McKenzie bridge

Instrument Location	Number of Cycles Measured in Field	Equivalent Constant Amplitude Stress Range (ksi)	Projected # of Cycles in 50 years	Laboratory Stress Range to Simulate 50 years of service
CH_2	13021	1.019	29171771	2.49
CH_4	1609	1.005	3604745	1.22
CH_5	383	1.580	858059	1.19
CH_6	50676	1.289	113532654	4.95
CH_7	128525	2.636	287942702	13.82
CH_8	25006	0.886	56022526	2.69
CH_9	21222	0.882	47544991	2.54
CH_10	10832	0.800	24267616	1.84
CH_11	39814	1.880	89197827	6.67
CH_12	26516	1.150	59405475	3.56
CH_13	3267	1.088	7319267	1.68
CH_14	53599	1.564	120081236	6.13
CH_15	9324	0.551	20889148	1.21
CH_17	43220	1.604	96828505	5.84
CH_18	43203	1.336	96790419	4.87
CH_19	30775	1.131	68947183	3.68
CH_20	1403	0.976	3143230	1.13
CH_21	26420	0.899	59190400	2.78
CH_22	17764	0.791	39797815	2.14
CH_23	56	0.865	125460	0.34
CH_29	46997	1.471	105290357	5.51
CH_30	69947	1.759	156706697	7.53
CH_31	22	1.050	49288	0.31
CH_32	81645	1.790	182914467	8.06

Table 2.7b: Equivalent constant amplitude stress range for instrumented locations on Jasper Bridge

Instrument Location	Number of Cycles Measured in Field	Equivalent Constant Amplitude Stress Range (ksi)	Projected # of Cycles in 50 years	Laboratory Stress Range to Simulate 50 years of service
CH_1	1627	1.37	2495189	1.47
CH_2	3386	1.53	5192815	2.10
CH_3	10091	1.49	15475693	2.94
CH_6	2938	1.33	4505756	1.75
CH_7	2544	1.53	3901513	1.91
CH_8	2097	1.09	3215987	1.28
CH_9	6104	1.44	9361176	2.42
CH_10	5734	1.34	8793739	2.19
CH_11	4393	1.39	6737164	2.09
CH_12	4534	1.45	6953403	2.20
CH_14	16590	1.77	25442647	4.14
CH_15	18191	1.68	27897962	4.05
CH_16	13076	1.86	20053529	4.01
CH_17	13007	1.91	19947710	4.11
CH_18	8142	1.81	12486681	3.34
CH_19	13811	1.89	21180735	4.16
CH_20	6776	1.32	10391765	2.29
CH_21	637	1.00	976912	0.79
CH_22	1611	1.22	2470651	1.31
CH_25	10090	1.65	15474160	3.26
CH_26	7978	1.38	12235168	2.52
CH_27	712	0.89	1091933	0.73
CH_29	4285	1.41	6571534	2.09
CH_30	6691	1.39	10261408	2.40
CH_31	298	0.50	457017	0.31
CH_32	7432	1.87	11397815	3.33

Table 2.7c: Equivalent constant amplitude stress range for instrumented locations on 15 Mile Creek Bridge

Instrument Location	Number of Cycles Measured in Field	Equivalent Constant Amplitude Stress Range (ksi)	Projected # of Cycles in 50 years	Laboratory Stress Range to Simulate 50 years of service
CH_1	39652	1.72	89229223	6.09
CH_3	10749	1.31	24188564	3.00
CH_4	3655	1.45	8224877	2.33
CH_6	1241	1.12	2792633	1.25
CH_7	14644	1.25	32953514	3.17
CH_14	13154	1.02	29600555	2.51
CH_15	12151	0.94	27343496	2.26
CH_16	13162	1.00	29618557	2.45
CH_17	1284	1.14	2889396	1.29
CH_25	10845	0.93	24404593	2.15
CH_26	11324	0.94	25482491	2.20
CH_28	1859	1.20	4183323	1.54
CH_29	1534	1.20	3451973	1.44
CH_30	1301	1.09	2927651	1.24
CH_31	3173	1.32	7140228	2.02
CH_32	2320	1.29	5220715	1.78
T_West	17095	1.18	38469020	3.15
CH_9	2191	0.84	4930425	1.14
CH_10	18794	1.46	42292293	4.03
CH_11	30032	1.86	67581258	6.02
CH_12	5268	0.78	11854624	1.41
CH_13	25764	1.92	57976942	5.91
CH_18	10279	0.94	23130919	2.13
CH_19	9129	0.86	20543064	1.87
CH_20	1559	1.20	3508231	1.44
CH_21	3734	1.03	8402651	1.67
T_East	16940	1.47	38120222	3.91

Fatigue tests of rebar indicate that long-life can be achieved if the stress-range is below 10 ksi at bend or tack welds (*McGregor 1997*). If no significant stress concentrations are found on the rebar, long-life can be achieved if the stress-range is below 20 ksi. Typical fatigue S-N curves for deformed reinforcing bars are shown in Figure 2.40. Given the relatively low equivalent constant amplitude stress-range identified at instrumented locations (52 diagonal crack locations on 3 different bridges), metal fatigue leading to fracture of the embedded stirrups is unlikely. However, there may be other sources of deterioration such as bond fatigue, repeated overloads, or corrosion that may adversely impact structural performance over time.

Field measured stress ranges and numbers of cycles for each instrumented stirrup location were used to determine an equivalent stress range for laboratory specimens subject to large numbers of service-level loads. For high-cycle laboratory specimens, 2,000,000 cycles of repeated loading was chosen to assess potential capacity deterioration under service conditions. The stress range required to produce equivalent damage in laboratory specimens at 2,000,000 cycles as that for bridge girders in the field over a period of 50 years, was estimated by computing an equivalent

stress range per Equation 2-1. It was conservatively assumed that the field recorded stress ranges and numbers of cycles remained constant over the life of the bridge.

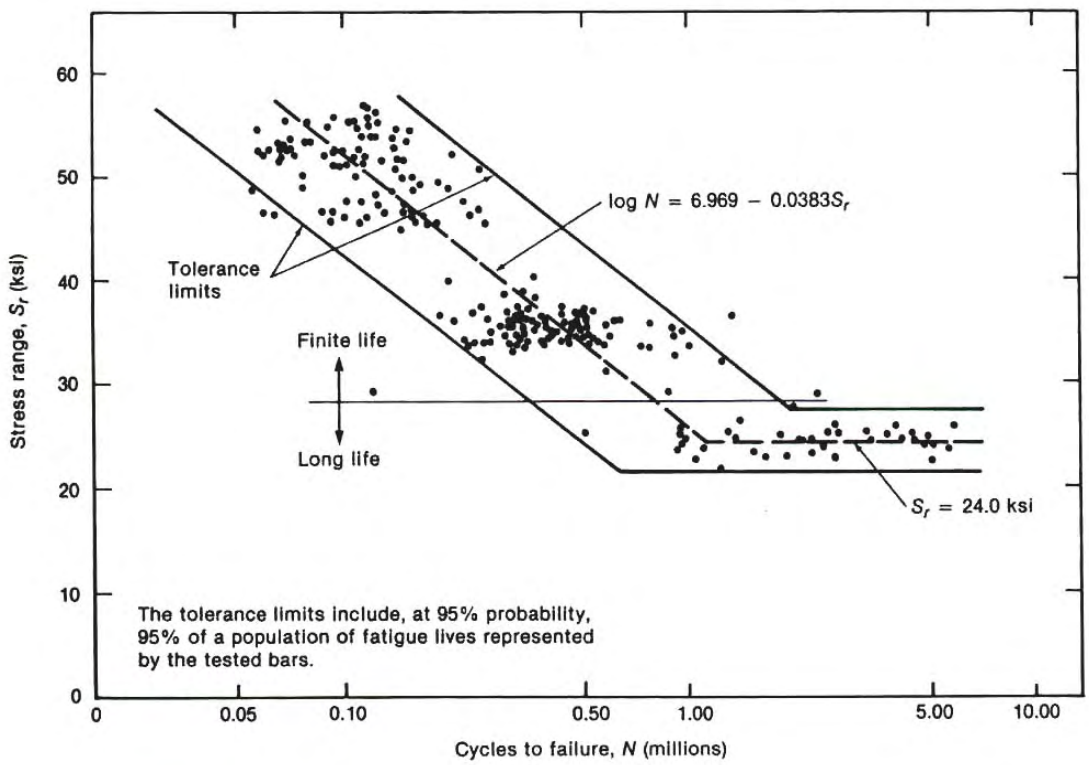

Figure 2.40: Fatigue behavior of reinforcing steel (*MacGregor 1997*)

The stress ranges required to impose stirrup damage equivalent to 50 years of service life for the laboratory specimens are shown in Tables 2.7a, b, and c. Later laboratory testing of full-size girder specimens was performed within and beyond this range of stresses to simulate high-cycle service-level loads occurring over the life of the bridge to assess their possible influence on structural behavior.

2.5 DYNAMIC INFLUENCE/IMPACT

As vehicles move across the bridge at speed, the static force effects may be amplified due to the dynamic response of the structure under the moving load and/or due to impact of the wheels on the deck surface, due to uneven approaches or deck surface imperfections. Using the control test truck data at each of the stirrup strain locations, an impact/dynamic coefficient was determined as the ratio of the peak strain produced by the truck as it moves in the marked lane at traveling speed, over the peak strain when the truck moves in the marked lane slowly (5 mph) across the bridge. For these comparisons, a minimum slow speed stirrup stress of 0.75 ksi was selected so that impact ratios using very small stress magnitudes would not skew results.

Additionally, impact coefficients were determined only for the truck lane position that produced the highest stress magnitude at the stirrup location for each of the different test speeds (for example: if the maximum stress is produced in a stirrup when the truck is in the passing lane, impact coefficients were determined for all test speeds, but only when the truck is located in the passing lane). This is consistent with the specification approach of applying impact effects to the maximum load effect.

For all test runs, the impact coefficients are shown in Figure 2.41. Solid symbols in this figure represent bent cap locations. As seen in this figure, there were cases when the dynamic effects reduce the strain amplitude (ratios less than 1.0). The single largest impact coefficient determined for any of the three bridges was 1.33. There is a trend of smaller impact coefficients as the creep stress magnitude increases.

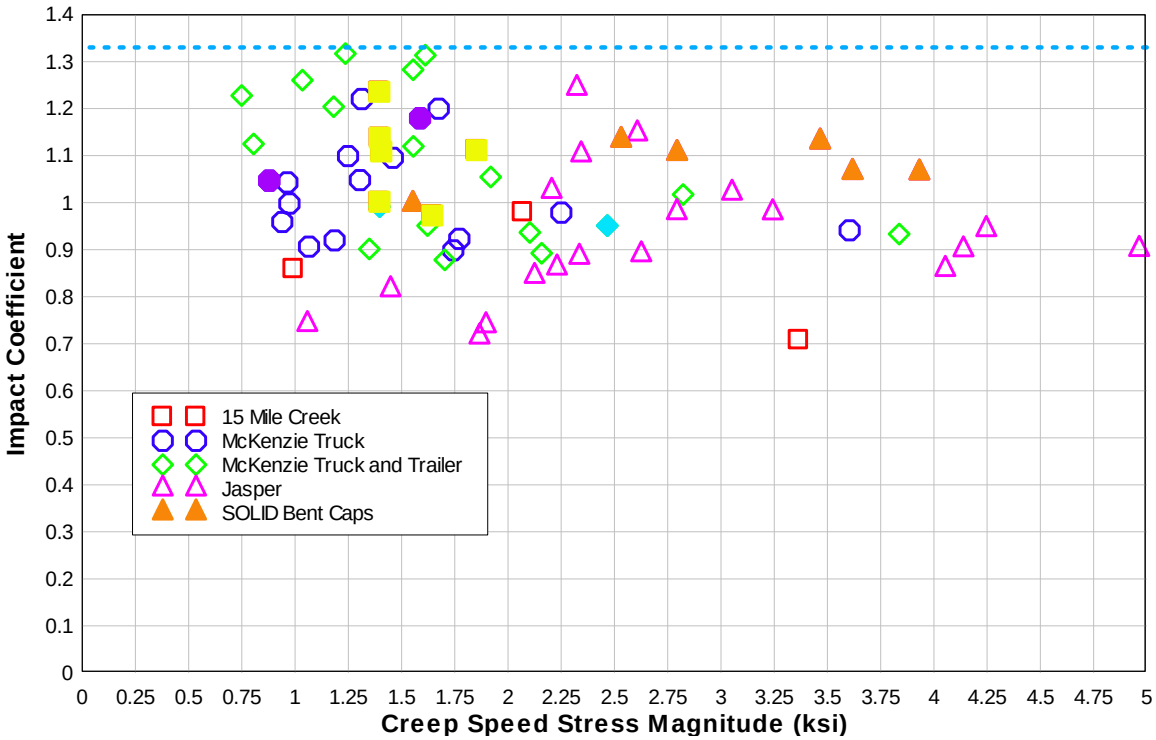

Figure 2.41: Impact coefficients for all three field study bridges

Previously completed field tests (*Higgins, et al. 2004*), identified an event with a larger impact coefficient of 1.46. Statistical analysis of the field data for the three field study bridges discussed here and the previously completed study described by Higgins, *et al*. (*2004*) was performed. Girders and bent caps were considered separately, and impact coefficients are shown in Table 2.8.

Table 2.8: - Statistical analysis of impact coefficients

	15 Mile Creek			McKenzie Bridge			Jasper Bridge			Willamette		
Girders	Average = 1.013			Average = 1.053			Average = 0.964			Average = 1.285		
	Maximum = 1.236			Maximum = 1.317			Maximum = 1.244			Maximum = 1.463		
	Normal	P_f	β	Normal	P_f	β	Normal	P_f	β	Normal	P_f	β
	μ = 1.013 σ = 0.189	0.0467	1.677	μ = 1.053 σ = 0.142	0.0255	1.951	μ = 0.964 σ = 0.154	0.0087	2.377	μ = 1.285 σ = 0.150	0.3821	0.300
Bent Caps	Average = 1.095			Average = 1.042			Average = 1.082					
	Maximum = 1.236			Maximum = 1.180			Maximum = 1.133					
	Normal	P_f	β	Normal	P_f	β	Normal	P_f	β			
	μ = 1.095 σ = 0.120	0.0251	1.958	μ = 1.042 σ = 0.133	0.0152	2.165	μ = 1.083 σ = 0.062	0.00003	3.984			

The AASHTO Standard Specification (*AASHTO 2002*) uses an impact factor of:

$$I = \frac{50}{L + 125} \qquad \text{AASHTO Eq. 3-1} \qquad \textbf{(2-2)}$$

where L is the length (ft) of the span loaded to produce the maximum load effect.

The maximum impact fraction is 30% (*AASHTO 2002*). This is the same impact factor that has been used in previous editions of the Specification. For a typical bridge (span length of 55 ft), the calculated impact fraction was 28%. The AASHTO LRFD Specification (*AASHTO LRFD 1998*) uses an impact factor of 15% for the fatigue load combination and 33% for factored load combinations.

On average, field measured impact fractions were less than those recommended by either AASHTO provision, and the maximum measured was close to 1.33. While a single instrumented location on a previous bridge produced an impact coefficient of 1.46, it seems unlikely that the shear force and moment acting on all components at a section (including several girders, the deck, multiple cracked/uncracked webs, and many stirrups) would all increase by this magnitude. Thus, based on statistical analysis of the impact coefficients of the field studied bridges and the trend of reduced impact magnitude with increasing stress levels, a 1.33 impact factor is recommended for amplification of the shear force effects. Selection of this value corresponds to a probability of exceedence of 0.026, 0.009, and 0.047 for the McKenzie River, Jasper, and 15 Mile Creek Bridges, respectively. This indicates that in the case of 15 Mile Creek Bridge, approximately 1 in every 213 trucks could produce a locally higher stirrup stress than that provided by the specification value of 1.33.

2.6 LOAD DISTRIBUTION

Distribution of shear across the multiple girders on each of the bridges was inferred from the relative magnitude of the peak measured stirrup strains in each girder across an instrumented section of the bridge. Distribution of shear was determined from maximum measured stirrup strains for truck passages at a creep speed (5 mph) in each of the lane positions.

Distribution factors were determined for a single truck in the lane and for two trucks in both lanes. Multiple lane load distributions were computed by superimposing the effects of the truck

in the passing lane with the truck located in the truck lane. The measured strain in each girder at a section of the bridge was divided by the sum of the strains on all girders at the section to determine the distribution factor.

Where possible, stirrup stresses from all girders at a given section were used to determine the distribution factors. Where adjacent girders were not instrumented, stresses in the uninstrumented girder were inferred based on symmetry of response from adjacent instrumented girders when the truck was positioned in the lane adjacent lane. At some instrumentation locations, stirrup strains on a girder that would have been more heavily loaded appeared to be lower than the adjacent girders. This was typically due to vertically oriented cracks which did not produce significant tension in the stirrup even when the load was positioned close to the instrumented location.

When available, measured data from each girder were used to determine the distribution factors. This resulted in conservative values. Distribution factors based on strain measurements for each of the field study bridges are shown in Tables 2.9a to 2.9e. As seen in these tables, worst case load distribution factors for shear (based on very low stress measured on one of the girders) were approximately 0.8 for one-lane loaded and 0.4 for two-lanes loaded. More typically, where consistent data were obtained across all girder lines, load distribution factors for shear were approximately 0.4 for one-lane loaded or 0.26 for two-lanes loaded. The distribution factors calculated here represent the proportion of the statical shear on the bridge assigned to an individual girder at the section under consideration.

Distribution factors for shear and moment were calculated using the previous AASHTO specifications, as well as the current AASHTO Standard Specification and AASHTO LRFD for comparison with field data results. The 1953 Standard Specification (*AASHO 1953*) load distribution factors were based on girder spacing. A wheel load fraction of S/5 was applied for interior girders with concrete floors on bridges supporting two or more traffic lanes, where S (ft) is the average spacing of girders. Exterior girders were designed assuming wheel loads were distributed by the deck acting as a simple beam between the girders. This technique is referred to as the “lever rule”. No distribution was permitted for the wheel/axle load located at the end of the girder.

The current AASHTO Standard Specification (*AASHTO 2002*) employs the same basic provisions for shear load distribution but now uses a wheel load fraction of S/6 for similar bridges with two or more traffic lanes. For the girder spacing and the AASHTO HS25 design truck, the shear forces and equivalent distribution factors were determined for the interior and exterior girders of the field study bridges. No distribution was used for the wheel/axle load located directly over the location where the shear force was computed and the other wheel loads were distributed as permitted by the code (S/5 for 1953 and S/6 for 2002). The code values are for two or more traffic lanes and thus multiple presence of load is implied in the distribution values.

Table 2.9a: Girder distribution for ODOT truck and truck and trailer traveling at crawl speed and located in different lane positions on McKenzie River Bridge (Note: TT is truck with trailer see Figure 2.12b)

ch 18,14,12,9

	Truck Fog	Truck Truck	Truck Passing	TT Fog	TT Truck	TT Passing	Two Trucks in Lane	TT Two Trucks in Lane
G1	72%	52%	16%	65%	50%	13%	34%	32%
G2	22%	35%	4%	28%	37%	6%	19%	21%
G3	1%	4%	14%	2%	4%	15%	9%	10%
G4	5%	9%	67%	5%	9%	65%	38%	37%

ch 10,13,15,19

	Truck Fog	Truck Truck	Truck Passing	TT Fog	TT Truck	TT Passing	Truck Two Trucks Lane	TT Two Trucks Lane
G1	83%	74%	16%	81%	70%	10%	45%	40%
G2	3%	6%	7%	4%	5%	4%	6%	5%
G3	3%	3%	25%	2%	3%	24%	14%	14%
G4	10%	17%	51%	13%	21%	61%	34%	41%

ch 29,23,20

	Truck Fog	Truck Truck	Truck Passing	TT Fog	TT Truck	TT Passing	Truck Two Trucks Lane	TT Two Trucks Lane
G1	64%	59%	14%	62%	61%	17%	36%	39%
G2	33%	31%	14%	33%	32%	15%	23%	23%
G3	2%	4%	15%	3%	2%	14%	9%	8%
G4	2%	6%	57%	2%	5%	54%	32%	30%

Table 2.9b: Girder distribution for real trucks traveling northbound on Jasper Bridge

CH 11,12,14,15,25,26,27

	Truck ID 1	2	3	4	5	6	7	8	9	10	11	34mph ODOT
G1	26%	25%	15%	21%	14%	17%	20%	19%	22%	17%	20%	17%
G2	45%	51%	45%	44%	43%	45%	43%	54%	49%	45%	47%	43%
G3	11%	9%	21%	16%	24%	23%	20%	11%	11%	19%	16%	24%
G4	18%	15%	19%	19%	18%	16%	18%	16%	18%	20%	17%	15%

CH 9,10,29,30

	Truck ID 1	2	3	4	5	6	7	8	9	10	11	34mph ODOT
G1	60%	56%	45%	53%	39%	54%	48%	59%	58%	48%	58%	51%
G2	20%	20%	27%	23%	30%	23%	26%	21%	18%	26%	21%	27%
G3*	13%	15%	18%	16%	20%	15%	17%	14%	14%	17%	14%	16%
G4	7%	9%	10%	8%	10%	8%	9%	6%	10%	9%	7%	6%

CH 2,20,21

	Truck ID 1	2	3	4	5	6	7	8	9	10	11	34mph ODOT
G1	22%	10%	19%	20%	17%	21%	22%	18%	19%	24%	24%	13%
G2	48%	55%	50%	48%	51%	48%	48%	50%	48%	46%	46%	54%
G3*	26%	30%	27%	27%	28%	26%	26%	27%	27%	25%	25%	29%
G4	4%	5%	4%	5%	4%	5%	4%	4%	6%	5%	5%	4%

Table 2.9c: Girder distribution for ODOT truck traveling at crawl speed and located in different lane positions on Jasper Bridge

CH 11,12,14,15,25,26,27

	NB N Curb	NB Lane	NB CL G2	NB CL G3	SB CL G2	SB CL G3	SB Lane	SB S Curb	Two Trucks in Lane
G1	37%	25%	13%	3%	2%	2%	1%	2%	13%
G2	42%	45%	45%	37%	35%	27%	20%	15%	33%
G3	9%	17%	28%	43%	44%	45%	44%	38%	30%
G4	12%	12%	14%	17%	19%	27%	36%	45%	24%

CH 9,10,29,30

	NB N Curb	NB Lane	NB CL G2	NB CL G3	SB CL G2	SB CL G3	SB Lane	SB S Curb	Two Trucks in Lane
G1	74%	60%	44%	20%	14%	5%	6%	6%	33%
G2	14%	23%	30%	39%	39%	34%	25%	20%	24%
G3*	9%	13%	19%	27%	29%	32%	31%	31%	22%
G4	3%	4%	7%	14%	18%	29%	38%	43%	21%

CH 2,20,21

	NB N Curb	NB Lane	NB CL G2	NB CL G3	SB CL G2	SB CL G3	SB Lane	SB S Curb	Two Trucks in Lane
G1	22%	17%	10%	4%	5%	5%	3%	2%	10%
G2	48%	52%	56%	57%	57%	31%	12%	6%	32%
G3*	26%	28%	30%	32%	32%	32%	32%	33%	30%
G4	4%	4%	3%	7%	7%	33%	52%	59%	28%

Table 2.9d: Girder distribution for static truck position #2 on Jasper Bridge

CH 11,12,14,15,25,26,27 Static Truck Position 2

	Stirrup Force (kips)	NB North Curb	Stirrup Force (kips)	NB South Curb	Two Trucks at curbs
G1	2.05	48%	-0.21	-3%	22.6%
G2	1.54	36%	1.03	14%	25.1%
G3	0.54	13%	3.29	45%	28.8%
G4	0.14	3%	3.20	44%	23.5%
Total	4.27		7.30		
	16.6%		28.4%		

CH 9,10,29,30 Static Truck Position 2

	Stirrup Force (kips)	SB North Curb	Stirrup Force (kips)	SB South Curb	Two Trucks at curbs
G1	7.01	79%	-0.36	-6%	36.5%
G2	1.09	12%	1.15	20%	16.1%
G3*	0.61	7%	2.05	35%	21.2%
G4	0.13	1%	2.95	51%	26.2%
Total	8.84	kips	5.80	kips	
	34.4%	of shear	22.6%		

CH 2,20,21 Static Truck Position 2

	Stirrup Force (kips)	SB North Curb	Stirrup Force (kips)	SB South Curb	Two Trucks at curbs
G1	0.75	28%	-0.04	-1%	13.2%
G2	1.42	52%	0.23	7%	29.7%
G3*	0.65	24%	1.12	34%	28.9%
G4	-0.11	-4%	2.01	61%	28.1%
Total	2.70		3.32		
	10.5%		12.9%		

Table 2.9e: Girder distribution for ODOT truck traveling at crawl speed and located in different lane positions on 15 Mile Creek Bridge

Eastbound

ch20, 21

	Truck	Passing	Two Trucks in Lane
G1	9%	14%	11%
G2	36%	42%	39%
G3*	42%	36%	39%
G4*	14%	9%	11%

ch11,12

	Truck	Passing	Two Trucks in Lane
G1*	4%	64%	34%
G2*	1%	31%	16%
G3	31%	1%	16%
G4	64%	4%	34%

Westbound

ch31,3,4

	Truck	Passing	Two Trucks in Lane
G1	24%	14%	19%
G2*	25%	24%	24%
G3	25%	34%	30%
G4	26%	28%	27%

ch25,28,29

	Truck	Passing	Two Trucks in Lane
G1	47%	10%	29%
G2	35%	9%	22%
G3	8%	30%	19%
G4*	10%	50%	30%

ch26,30

	Truck	Passing	Two Trucks in Lane
G1	31%	4%	17%
G2*	59%	7%	33%
G3	7%	59%	33%
G4*	4%	31%	17%

ch32,1

	Truck	Passing	Two Trucks in Lane
G1	1%	0%	0%
G2	62%	37%	50%
G3*	37%	62%	50%
G4*	0%	1%	0%

The 1953 AASHTO provisions did not require that exterior girders carry at least the amount of shear for the interior girders, but all girders were required to be able to carry the statical shear at any section. The current specification requires that exterior girders carry the same or greater magnitude of shear as interior girders. Load distribution factors were also determined by AASHTO LRFD per section 4.6.2.2. The LRFD provisions to determine the distribution factors for the interior girders consider the girder stiffness, girder spacing, span length, and thickness slab for moment and only the girder spacing for shear. Exterior girders use the lever rule for both moment and shear distribution, as well as the check per section 4.6.2.2.2d.

Load distribution factors for each of the methods is shown in Table 2.10 for the Standard specification, Table 2.11 for the LRFD specification, and Table 2.12 for the controlling cases. As seen in Table 2.12, the 1953 AASHTO load distribution method produces higher girder design forces than the current Standard Specification. As the Standard Specifications use wheel distribution factors, direct comparison between LRFD and Standard Specification factors will depend on the shape of the influence line for the load effect considered. For typical vintage RCDG bridge spans and indeterminacy, LRFD distribution factors would produce larger design moments and shears than if the Standard Specification factors were used. Comparison of the field estimated and code specified load distribution factors indicated that the specification conservatively assigns shear load effects on individual girders.

Table 2.10: Wheel load distribution factor by lever rule (AASHTO Standard Specification)

Bridge	Girder Spacing (ft)	Curb Dist. (ft)	Exterior Girder DF	Controlling # Lanes Loaded	Interior Girder DF	Controlling # Lanes Loaded	Exterior Girder DF Axle	Interior Girder DF Axle
McKenzie (3 span)	9.00	1.50	1.443	1	1.889	2	0.722	0.944
McKenzie (1 span)	9.00	1.50	1.443	1	1.889	2	0.721	0.944
Willamette Newberg (2 span)	8.67	2.00	1.538	1	1.846	2	0.769	0.923
Willamette Newberg (1 span)	6.50	2.06	1.403	1	1.291	2	0.701	0.645
Willamette Springfield	7.25	2.00	1.446	1	1.621	2	0.723	0.810
Jasper	7.67	1.50	1.346	1	1.696	2	0.673	0.848
15 Mile Creek EB	8.73	1.77	1.487	1	1.854	2	0.744	0.927
15 Mile Creek WB	9.23	1.77	1.517	1	1.916	2	0.759	0.958

Table 2.11: Lane load distribution by AASHTO LRFD Specification

Bridge	One Lane *Exterior* Girder Shear DF	Two Lane *Exterior* Girder Shear DF	2 LN Control *Exterior* Girder Shear DF	One Lane *Interior* Girder Shear DF	Two Lane *Interior* Girder Shear DF	One Lane *Exterior* Girder Moment DF	Two Lane *Exterior* Girder Moment DF	2 LN Control *Exterior* Girder Moment DF	One Lane *Interior* Girder Moment DF	Two Lane *Interior* Girder Moment DF	One Lane *Exterior* Girder Reaction	Two Lane *Exterior* Girder Reaction
McKenzie (3 span)	0.866	0.884	0.884	0.720	0.884	0.866	0.843	0.866	0.620	0.843	0.740	0.900
McKenzie (1 span)	0.866	0.884	0.884	0.720	0.884	0.866	0.851	0.866	0.626	0.851	0.740	0.900
Willamette Newberg (2 span)	0.923	0.861	0.923	0.707	0.861	0.923	0.822	0.923	0.602	0.822	0.757	0.915
Willamette Newberg (1 span)	0.842	0.707	0.842	0.620	0.707	0.842	0.675	0.842	0.508	0.675	0.648	0.773
Willamette Springfield	0.868	0.761	0.868	0.650	0.761	0.868	0.703	0.868	0.523	0.703	0.654	0.814
Jasper	0.808	0.791	0.808	0.667	0.791	0.808	0.693	0.808	0.515	0.693	0.723	0.891
15 Mile Creek EB	0.892	0.865	0.892	0.709	0.865	0.892	0.798	0.892	0.587	0.798	0.748	0.903
15 Mile Creek WB	0.910	0.900	0.910	0.729	0.900	0.910	0.831	0.910	0.608	0.831	0.753	0.930

Table 2.12: Load distribution factors for controlling cases by AASHTO LRFD Specification and Standard Specifications

Bridge	AASHTO LRFD Exterior Shear	AASHTO LRFD Interior Shear	AASHTO LRFD Exterior Moment	AASHTO LRFD Interior Moment	Lever Rule Exterior Girder DF Axle	Lever Rule Interior Girder DF Axle	S/6 Distribution Axle	S/5 Distribution Axle
McKenzie (3 span)	0.900	0.884	0.900	0.843	0.944	0.944	0.750	0.900
McKenzie (1 span)	0.900	0.884	0.900	0.851	0.944	0.944	0.750	0.900
Willamette Newberg (2 span)	0.923	0.861	0.923	0.822	0.923	0.923	0.722	0.867
Willamette Newberg (1 span)	0.842	0.707	0.842	0.675	0.645	0.645	0.542	0.650
Willamette Springfield	0.868	0.761	0.868	0.703	0.810	0.810	0.604	0.725
Jasper	0.891	0.791	0.891	0.693	0.848	0.848	0.639	0.767
15 Mile Creek EB	0.903	0.865	0.903	0.798	0.927	0.927	0.727	0.873
15 Mile Creek WB	0.930	0.900	0.930	0.831	0.958	0.958	0.769	0.923

2.7 COMBINED DEAD AND LIVE LOAD STRESS IN STIRRUPS

Stresses in stirrups, including that produced from weight of permanent components and the wearing surface, combined with superimposed live load stresses, were determined using data from the Jasper Bridge. Field stirrup stress data were used for the loading case of the test truck statically positioned on the bridge, at the curb, with the steering axle centered over the support. This enabled precise location of the loads for comparison with shear forces determined from elastic structural analysis.

The force carried by the stirrups was estimated by counting the numbers of stirrups crossing the diagonal crack, assuming uniform stress for all stirrups crossing the cracks, and multiplying by the nominal stirrup area. The vertical force in the stirrups was compared with the statical shear force at the section from analysis, and indicated that the stirrups carried between 10% and 35% of the applied shear as seen in Table F9d. It is anticipated that the dead load shear is carried at the girder section in the same proportion as the live load shear.

2.8 STIRRUPS STRESS DISTRIBUTIONS ACROSS A SINGLE CRACK

Comparisons of measured stirrup stress magnitudes on the same diagonal crack were performed from table values of maximum stirrup stress. Two different instrumentation configurations were investigated: 1) instrumented stirrups located on the same girder face or 2) instrumented stirrups located on opposite faces of the same girder. For the case where stirrups were instrumented on the same face of a girder, the stirrup located closer to the flexural tension region tended to have higher stress than the stirrup located near the compression face.

In cases where stirrups were located on opposite faces of the same crack, the stresses on the two stirrup legs were not necessarily equal, although they tended to be reasonably correlated when the load was located close to the instrumented section. Stirrups located across diagonal cracks in bent caps tended to have approximately equal stresses.

2.9 CONCLUSIONS

Field investigations of three cast-in-place reinforced concrete deck girder bridges were conducted. The bridges were designed between the period of 1950 to 1960 and incorporated single span, 2-span continuous and 3-span continuous approach spans. The bridges were inspected, and instrumented. Data from instrumented locations were collected under ambient traffic conditions as well as during controlled truck testing. Based on field data collection and subsequent analysis, the following conclusions are made:

- Exterior girders tended to exhibit more widespread diagonal cracking than interior girders.
- Diagonal cracks tended to be concentrated within the quarter span length adjacent to support locations. Vertical cracks associated with flexural tension were located in flexural tension

regions, and vertical cracks attributed to shrinkage tended to be distributed throughout the span length.

- Stirrups crossing the same diagonal crack, did not necessarily exhibit the same magnitude of stress. Stirrups located closer to the flexural tension region tended to have higher stress than those closer to the flexural compression region.

- Stirrups crossing the same diagonal crack on opposite faces of the girder tended to have similar stress magnitudes, particularly when the load was located close to the diagonal crack.

- Under ambient traffic loading, the single largest stress range measured on any of the stirrups in the bridges was 11.5 ksi.

- Based on the ambient traffic induced stress ranges, an equivalent stress range was determined for each of the instrumented locations. The equivalent constant amplitude stress range was below 2 ksi at all but one instrumented location (Location 7 on McKenzie River Bridge 2.67 ksi).

- Comparison of measured stress ranges with the fatigue behavior of deformed reinforcing bars, indicates that high-cycle fatigue leading to fracture of the stirrups is unlikely.

- Impact coefficients were determined for each of the instrumented locations. For the field study bridges; impact coefficients were below that recommended by the AASHTO LRFD provisions for strength determination.

- Load distribution factors for shear were determined based on the ratios of stirrup stress magnitudes across instrumented sections of the bridges. Using the most conservative data, the distribution factors for shear and hence the loading of girders were less than those recommended by the AASHTO provisions.

- Stress ranges required to produce the estimated equivalence of 50 years of service life damage in laboratory specimens were determined from field data for use in subsequent laboratory testing.

ASSESSMENT METHODOLOGY FOR DIAGONALLY CRACKED REINFORCED CONCRETE DECK GIRDERS

3.0 LABORATORY TESTING 121

3.1 SPECIMEN FABRICATION AND MATERIALS 121
3.2 CONTROL TESTS 127
3.2.1 Test Method 127
3.2.2 Support Condition Evaluation 129
3.2.3 Loading Protocol 133
3.2.4 Experimental Results 134
3.3 INCREASED LOADING RATE TEST 162
3.3.1 Test Method 162
3.3.2 Experimental Results 164
3.4 MOVING SUPPORT TESTS 164
3.4.1 Test Method 164
3.4.2 Experimental Observation 165
3.5 INFLUENCE OF FLEXURAL BAR DETAILS 165
3.5.1 Test Method 165
3.5.2 Experimental Results 165
3.6 SUMMARY OBSERVATIONS FROM CONTROL LABORATORY TESTS: 166
3.7 LOW-CYCLE FATIGUE TESTS 167
3.7.1 Test Method 168
3.7.2 Experimental Results 168
3.7.2.1 Low-Cycle Fatigue Specimen 5IT12L22 172
3.7.2.2 Low-Cycle Fatigue Specimen 6T6L22 172
3.7.2.3 Low-Cycle Fatigue Specimen 6IT6L22 174
3.7.2.4 Low-Cycle Fatigue Specimen 7IT6L22 175
3.7.2.5 Low-Cycle Fatigue Specimen 9IT12L22 176
3.7.2.6 Low-Cycle Fatigue Specimen 9T12L24 176
3.7.2.7 Low-Cycle Fatigue Specimen 10T24L24 178
3.7.3 Conclusions 179
3.8 HIGH-CYCLE FATIGUE TESTS 179
3.8.1 Test Method 180
3.8.2 Experimental Results 182
3.8.3 Results 191
3.8.4 Debonded Stirrup Specimens 199
3.8.4.1 Debonded Stirrup Test Results 199
3.8.5 Conclusions 203
3.9 MOVING LOAD TESTS 203

List of Figures

Figure 3.1: Typical specimen configuration 122
Figure 3.2a: Schematic of test frame with specimen for typical test 128
Figure 3.2b: Test frame with specimen for typical test 128
Figure 3.3: Typical instrumentation on test specimen 129
Figure 3.4: Setup for support condition evaluation 130
Figure 3.5: Roller conditions at opposite end of specimen for support condition evaluation 130
Figure 3.6: Displacement sensors to measure support component motions under lateral load applied to the base of the beam web 131
Figure 3.7: Horizontal displacements at supports for applied lateral force at base of beam web 131
Figure 3.8: Equivalent lateral stiffness of support for different amounts of vertical reaction 132
Figure 3.9: Estimated amount of free horizontal displacement required at supports for typical specimen with yielding flexural reinforcing steel 133
Figure 3.10: Control loading protocol (horizontal lines represent holding of load to mark and measure cracks) 134
Figure 3.11a: Load-displacement plot at midspan for Group 1 specimens 135
Figure 3.11b: Load-displacement plot at midspan for Group 2 specimens 136
Figure 3.11c: Load-displacement plot at midspan for Group 3 specimens 137
Figure 3.11d: Load-displacement plot at midspan for Group 4 specimens 138
Figure 3.11e: Load-displacement plot at midspan for Group 5 specimens 139
Figure 3.11f: Load-displacement plot at midspan for Group 6 specimens 140
Figure 3.11g: Load-displacement plot at midspan for Group 7 specimens 141
Figure 3.11h: Load-displacement plot at midspan for Group 8 specimens 142
Figure 3.11i: Load-displacement plot at midspan for Group 9 specimens 143
Figure 3.11j: Load-displacement plot at midspan for Group 10 specimens 144
Figure 3.11k: Load-displacement plot at midspan for Group 10 and 11 moving-load specimens 145
Figure 3.11l: Load-displacement plot at midspan for Group 11 moving-load specimens 146
Figure 3.12a: Digital photographs at failure for Group 1 specimens 147
Figure 3.12b: Digital photographs at failure for Group 2 specimens 148
Figure 3.12c: Digital photographs at failure for Group 3 specimens 149
Figure 3.12d: Digital photographs at failure for Group 4 specimens 150
Figure 3.12e: Digital photographs at failure for Group 5 specimens 151
Figure 3.12f: Digital photographs at failure for Group 6 specimens 152
Figure 3.12g: Digital photographs at failure for Group 7 specimens 153
Figure 3.12h: Digital photographs at failure for Group 8 specimens 154
Figure 3.12i: Digital photographs at failure for Group 9 specimens 155
Figure 3.12j: Digital photographs at failure for Group 10 specimens 156
Figure 3.12k: Digital photographs at failure for Group 11 specimens 157
Figure 3.13: Approach used to determine self-weight at the failure location for different specimens 160
Figure 3.14a: Crack motion for specimen C4T12 (unbonded stirrups) 161
Figure 3.14b: Crack motion for specimen IT18 161
Figure 3.15: Loading histories for specimen tested at higher loading rates 163
Figure 3.16: Typical applied force - stirrup strain response from low cycle fatigue specimen 9T12, part 4 171
Figure 3.17: Typical applied force - crack motion response from low cycle fatigue specimen 9T12, part 2 171
Figure 3.18: Instrumentation for damage sequencing of stirrups for specimen 6T6L22 173
Figure 3.19a: Schematic of high-cycle fatigue test setup 181
Figure 3.19b: Image of high-cycle fatigue test setup 181
Figure 3.20: Example strain ranges during HCF test (specimen 3IT12 south end) 185
Figure 3.21: Example strain gage means during HCF test (specimen 6IT10 North end) 185
Figure 3.22: Example load and crack motion sensor ranges during HCF test (specimen 3IT12) 186
Figure 3.23: Example load and crack motion sensor means during HCF test (specimen 5IT12-B1) 186
Figure 3.24: Increasing strain range in specimen 9T12-B4, having cut and straight bars during HCF test 191
Figure 3.25: Measured strain comparing two interval tests for specimen 6IT10 192

Figure 3.26: Example of debris associated with bond damage around stirrup legs: a) specimen 6T10; b) specimen 3IT12 193
Figure 3.27: Strain gage and associated crack motion sensor at the eventual failure crack in specimen 6IT10. Note that after many cycles, less strain is needed to achieve the same crack movement 193
Figure 3.28: Changes in strain range and crack range for specimen 3IT12 over a 2,000,000 cycle HCF test. 194
Figure 3.29: Ductile fracture of stirrup at ultimate strength: a) sensor GS8 on specimen 3IT18; b) another example from specimen 3IT12 195
Figure 3.30: Fracture surface on east leg of stirrup from high-cycle fatigue specimen 3IT18 at 9 in. below sensor GS2 195
Figure 3.31: Fracture surfaces on west leg of stirrup from high-cycle fatigue specimen 3IT18 at 2 in. above sensor GS7 196
Figure 3.32: Detail from specimen 3IT18 load and crack motion sensor means. Note the change after 1,750,000 cycles 197
Figure 3.33: Detail from specimen 3IT18 Load and crack motion sensor ranges. Note the change after 1,750,000 cycles 197
Figure 3.34: Detail from specimen 3IT18 South strain gage means. Note the change after 1,750,000 cycles. 198
Figure 3.35: Detail from specimen 3IT18 South strain gage ranges. Note the change after 1,750,000 cycles 198
Figure 3.36: Crack pattern and instrument locations for 5IT12-B4 and 7IT12 specimens 200
Figure 3.37: Load-midspan displacement plots for 5IT12-B4 and 7IT12 specimens 201
Figure 3.38b: Stirrup strains and crack displacements for 5IT12-B4 and 7IT12 specimens: a) stirrup strains in the north-end side; b) crack displacements 202

List of Tables

Table 3.1: Concrete Mix Design (5.5-bag Mix) 123
Table 3.2: Concrete Mix Design (5-bag Mix) 123
Table 3.3: Concrete properties at 28 days 124
Table 3.4: Concrete and steel properties for each specimen on the day of test 125
Table 3.4 (continued): Concrete and steel properties for each specimen on the day of test 126
Table 3.5: Salient test results for laboratory specimens 158
Table 3.5 (continued): Salient test results for laboratory specimens 159
Table 3.6a: Time to peak load at a bent cap for different span lengths and vehicle speeds 162
Table 3.6b: Loading rates for different test load increments 163
Table 3.7: Loading levels and number of cycles for low-cycle fatigue tests 169
Table 3.8: Average strain range for low-cycle fatigue tests (strain is microstrain) 170
Table 3.9: Precrack stage crack widths for HCF specimens 180
Table 3.10: Stirrup strain ranges at the beginning and completion of HCF testing 183
Table 3.11: Crack displacement ranges at the beginning and completion of HCF testing 184
Table 3.12a: Stirrup strain ranges during HCF interval tests 187
Table 3.12a (continued): Stirrup strain ranges during HCF interval tests 188
Table 3.12a (concluded): Stirrup strain ranges during HCF interval tests 189
Table 3.12b: Crack displacement ranges during fatigue interval tests 190

3.0 LABORATORY TESTING

Forty-four (44) laboratory tests were conducted to evaluate the behavior of large-sized lightly-reinforced RC girders with vintage proportions and properties. Member proportions were based on a database of cracked bridges within the ODOT inventory as described in Higgins, *et al*. (*2004*). Typical member cross-section was 48 in. overall height with a 14 in. wide stem and included a 6 in. thick deck portion that was 3 ft wide, as shown in Figure 3.1. Complete details for each of the specimens are described below and are contained in Appendix A1.

Two loading configurations were considered: T (deck in flexural compression) and inverted-T (IT) (deck in flexural tension). The T configuration reflects shear in the presence of positive moment, as at simply supported ends of a bridge. The IT configuration reflects shear in the presence of negative moment, as over continuous support locations such as bents and piers.

Several different loading protocols were investigated: incrementally increasing load amplitudes with unloading, high-cycle fatigue after initial diagonal cracking, and low-cycle fatigue. Different stirrup spacing, as well as anchorage and flexural bar cutoff details were included in the study.

Typical tests were performed under static conditions, although one test was performed to simulate loading rates associated with a heavy vehicle traveling over a bridge of typical span length. A series of tests was performed by changing the support conditions after significant cracking was imposed on the specimen in the initial support configuration. Finally, a series of tests was performed with a moving load on specimens representing a portion of a main girder from a typical vintage RCDG bridge. Each of these test series is described below.

3.1 SPECIMEN FABRICATION AND MATERIALS

Beam specimens used in the laboratory testing phase were produced by Morse Bros. Prestressed Concrete Group of Harrisburg, OR, a ready-mix/precast/prestressed concrete supplier. Formwork was constructed to allow four beam specimens to be cast at a time. To construct the 44 specimens used in the testing program, 11 groups of beams were produced. Specimens were designed by OSU and constructed according to OSU approved shop drawings that were prepared by Morse Bros. Shop drawings for the specimens are contained in Appendix A1.

Prior to concrete placement, the as-fabricated reinforcing cages were inspected and verified to correspond with shop drawings. Lifting locations required for specimen handling were carefully detailed to minimize supplemental force transfer at the interface between the deck and stem. This was accomplished by wrapping the lifting loops with foam or using PVC pipe to prevent concrete bearing on lifting inserts as detailed in the shop drawings.

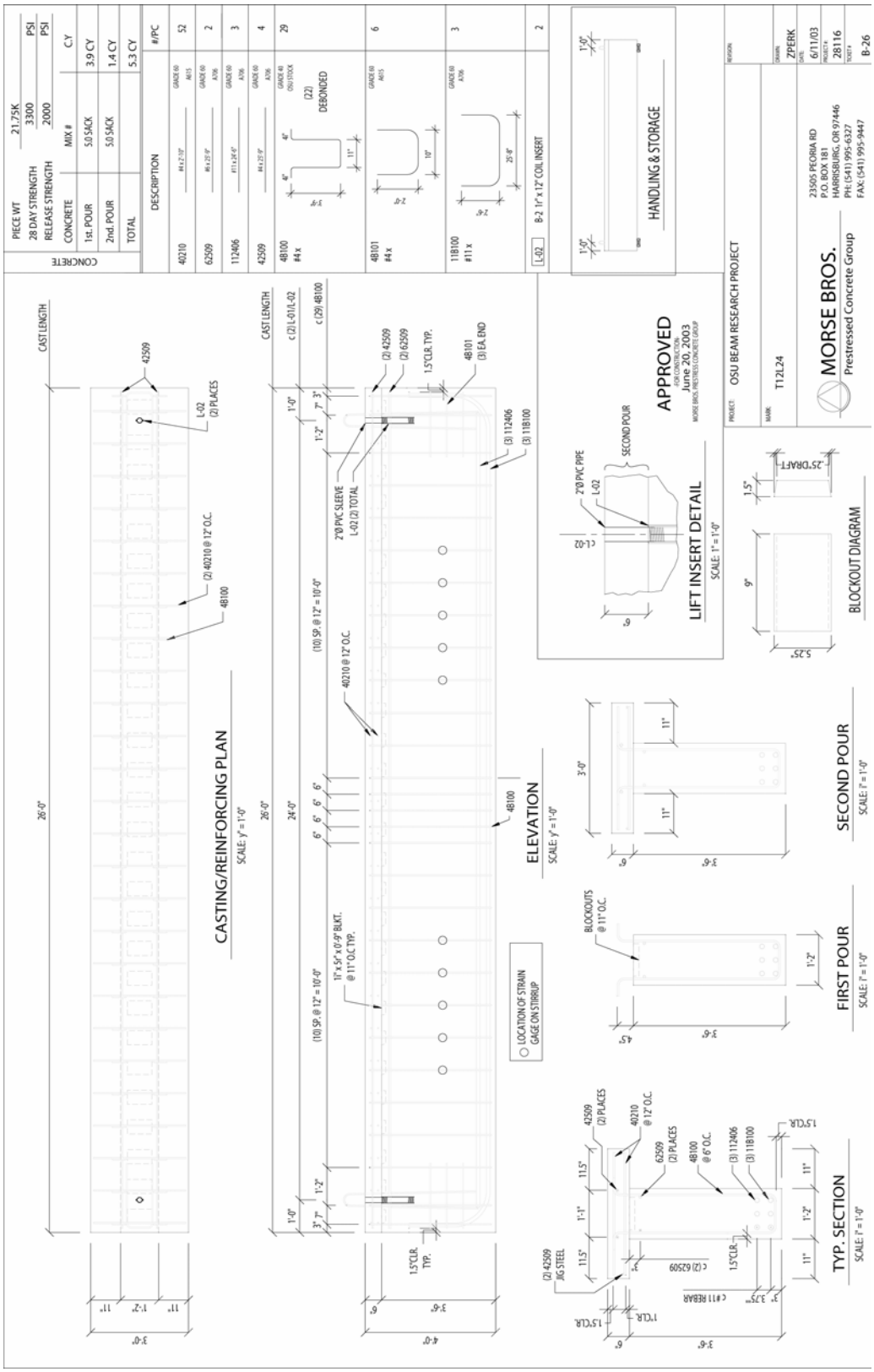

Figure 3.1: Typical specimen configuration

To reflect 1950's construction practice of cast in-place conventionally reinforced concrete deck-girder bridges, beam specimens were cast in two separate operations. In the first operation, the beam stems were cast and shear keys, spaced 11 in. on-center, were stamped into the web after concrete placement and consolidation as shown in Figure 3.1. Dimensions of the shear keys were 9 in. x 5.25 in. x 1.5 in. (length x width x depth) and were based on design details for bridges constructed in the mid-1950's. Beam stems were allowed to cure for 7 days prior to placing concrete for the deck. All beams were allowed to cure a minimum of 28 days before shipment to the laboratory for testing.

Beam specimens also reflected 1950's vintage AASHTO Class-A concrete consisting of cement, sand, aggregate, and water (*AASHTO 1953; AASHTO 1957*). A slight amount of air-entraining admixture was added to obtain desired workability and material properties. Concrete was batched on-site and transported to the formwork in a ready-mix truck. The amount of cement and the water-cement ratio were adjusted to provide a relatively low compressive strength typical of the specified 3300 psi concrete strength of the time. For the first set of beams (Cast 1) a 5.5-bag mix design was used with a mix ratio of 1:2.6:7.1:7 (Water: Cement: Coarse Aggregate: Fine Aggregate). This produced a 28-day strength of approximately 4500 psi. The remaining beams were cast using a 5 bag mix having a ratio of 1:3:11.4:10. Mix designs for both the 5.5 bag mix and 5 bag mix can be seen in Table 3.1 and 3.2.

Table 3.1: Concrete Mix Design (5.5-bag Mix)

Type I Cement	515	lb/yd^3
1/2" Coarse Aggregate	707	lb/yd^3
3/4" Coarse Aggragate	713	lb/yd^3
Fine Aggregate	1400	lb/yd^3
Water	200	lb/yd^3

Table 3.2: Concrete Mix Design (5-bag Mix)

Type I Cement	471	lb/yd^3
1/2" Coarse Aggregate	705	lb/yd^3
3/4" Coarse Aggregate	1052	lb/yd^3
Fine Aggregate	1539	lb/yd^3
Water	155	lb/yd^3

Compressive strengths of concrete for each specimen were determined by 6 x 12 in. cylinder breaks on the day-of-test using a 300 kip capacity concrete testing machine. Modulus of rupture and split cylinder tests were performed 28 days after casting for each group of specimens to determine tensile strength of the concrete. Testing procedures for concrete compression test, concrete split cylinder test, and modulus of rupture test were performed in accordance with ASTM C39, ASTM C496, and ASTM C78, respectively. Loading rates for the compression test, concrete split cylinder test, and modulus of rupture test were performed in the range of 1000 lbs/sec, 250 lbs/sec, and 30 lbs/sec, respectively. Compression tests on the day-of-test also included measurement of cylinder strains for stem concrete to obtain compressive stress-strain curves. The compressive stress-strain curves for each specimen is shown in Appendix A2.

Concrete properties at 28 days for each group of specimens are summarized in Table 3.3 and properties on the day-of-test are shown in Table 3.4. The average concrete strength for all groups was 4332 psi with a COV of 12.4% and average peak strain at the peak stress, ε'_c, from the concrete stress-strain curves was 0.0040 in/in with a COV of 14.7%. The average concrete strength for the specimens was higher than the design specified concrete strength of 3300 psi. The average peak strain was high compared to a typical strain of about 0.002 in/in for concrete having 4000 psi strength.

Table 3.3: Concrete properties at 28 days

Group	f'_c (psi)	f_{ct} (psi)	β_{ct}	f_r (psi)	β_r
1	4485	460	6.9	490	7.3
2	3160	364	6.5	455	8.1
3	3870	369	5.9	310	5.0
4	3600	344	5.7	388	6.5
5	3550	340	5.7	377	6.3
6	4225	411	6.3	430	6.6
7	4120	377	5.9	314	4.9
8	3870	391	6.3	367	5.9
9	3360	311	5.4	412	7.1
10	3835	357	5.8	518	8.4
11	3610	390	6.5	458	7.6
Avg.	3790	374	6.1	411	6.7
COV	10.2	10.6	7.3	16.4	17.1

Tensile strength of concrete was approximated as proportional to the square root of the compressive strength. Based on a large number of tests (*Mirza, et al. 1979*), the mean split cylinder strength over the square root of the compressive stress was 6.4 and the mean modulus of rupture over the square root of the compressive stress was 8.3. As shown in Table 3.4 for this research, the mean split cylinder strength over the square root of the compressive stress was 6.1, and the mean modulus of rupture over the square root of the compressive stress was 6.7. The relationship between the tensile strength and the compressive strength of the concrete obtained from the split cylinder tests was relatively similar to that described by Mirza *et al*. (*1979*) However, the relationship obtained from the modulus of rupture tests was lower.

All reinforcing steel was fabricated by a local rebar fabricator per OSU approved shop drawings. Selected stirrups were instrumented in the laboratory and then shipped to the precaster for construction of reinforcing cages. Reinforcing steel in the beams consisted of ASTM A615 Grade 40 and Grade 60 steel and flexural bars above size #6 were of ASTM A706 Grade 60. Stirrups used for all specimens were from a single heat of ASTM A615 Grade 40 reinforcing steel. The Grade 40 #4 reinforcing bars had a yield stress of 51 ksi. The bars were taken from the lowest yield-stress heat of steel produced by Cascade Steel Rolling Mills during a production run. Miscellaneous remaining #4 reinforcing steel used for the beams was ASTM A-615 Grade 60 and varied for each cast.

Table 3.4: Concrete and steel properties for each specimen on the day of test

Specimen	Concrete			Reinforcing Steel											
	Stem		Deck	#4 Grade 40			#11 Grade 60			#6 Grade 60			#4 Grade 60		
	f'_c (psi)	ε'_c	f'_c (psi)	σ_y (ksi)	σ_u (ksi)	σ_f (ksi)/ ε_f	σ_y (ksi)	σ_u (ksi)	σ_f (ksi)/ ε_f	σ_y (ksi)	σ_u (ksi)	σ_f (ksi)/ ε_f	σ_y (ksi)	σ_u (ksi)	σ_f (ksi)/ ε_f
1T6	4700	NA	4370	50.7	78.9	71.1/ 0.286	67.2	99.5	82.2/ 0.218	66.3	93.6	78.2/ 0.308	63.3	105.5	NA
1IT6	4775	NA	4515												
1T18	4925	0.0035	4360												
1IT18	4550	0.0035	4410												
2T10	3550	0.0039	3360				75.8	111.7	89.5/ 0.224	66.9	98.4	78.3/ 0.320	64.8	104.3	95.7/ 0.222
2IT10	3290	NA	3105												
2T12	3520	0.0038	3440												
2IT12	3575	0.0032	3005												
3T12	3990	0.0034	3660				69.7	103.7	82.0/ 0.220	60.7	88.1	70.8/ 0.325	67.3	107.1	NA
3IT12	4180	NA	3455												
3T18	3970	0.0044	3440												
3IT18	3915	0.0036	3220												
4IT6-10	3790	NA	3410				68.3	103.5	82.0/ 0.223	59.7	84.9	69.3/ 0.268	61.0	96.9	82.4/ 0.232
4IT8-12	3710	0.0030	3595												
4T10-12	3945	NA	2995												
4T12-18	4060	NA	3000												
5IT12-B1	3700	0.0037	4610				69.2	103.3	81.3/ 0.215	59.5	83.8	69.5/ 0.220	59.8	100.3	77.7/ 0.262
5IT12-B2	4160	0.0037	4640												
5IT12-B3	4310	0.0044	4530												
5IT12-B4	4130	NA	4130												
6T6	4590	0.0051	4260				71.6	106.4	83.0/ 0.221	62.9	89.1	70.4/ 0.223	NA	NA	NA
6IT6	5110	0.0042	3920												
6T10	4595	0.0048	4195												
6IT10	5495	0.0051	3875												

Table 3.4 (continued): Concrete and steel properties for each specimen on the day of test

Specimen	Concrete			Reinforcing Steel											
	Stem		Deck	#4 Grade 40			#11 Grade 60			#6 Grade 60			#4 Grade 60		
	f'_c (psi)	ε'_c	f'_c (psi)	σ_y (ksi)	σ_u (ksi)	σ_f (ksi)/ ε_f	σ_y (ksi)	σ_u (ksi)	σ_f (ksi)/ ε_f	σ_y (ksi)	σ_u (ksi)	σ_f (ksi)/ ε_f	σ_y (ksi)	σ_u (ksi)	σ_f (ksi)/ ε_f
7T6	4405	0.0044	4215	50.7	78.9	71.1/ 0.286	74.8	101.0	79.5/ 0.274	65.5	93.2	82.0/ 0.282	67.2	110.2	98.5/ 0.207
7IT6	4350	0.0043	3740												
7T12	4280	0.0044	4310												
7IT12	4165	0.0038	3995												
8IT10	4750	0.0041	4090				74.9	98.9	74.0/ 0.265	63.6	91.1	85.0/ 0.298	67.1	110.8	NA
8IT12	4840	0.0038	4045												
8T12-B3	5070	0.0043	4570												
8T12-B4	4995	0.0040	4725												
9IT12-B1	4285	0.0042	5405				70.8	96.1	68.5/ 0.271	62.6	90.0	89.0/ 0.287	NA	NA	NA
9IT12-B2	4605	0.0044	5465												
9T12-B3	4645	0.0045	4890												
9T12-B4	4705	0.0049	4910												
10T0	4610	0.0043	4445				69.3	107.3	88.7/ 0.217	69.4	98.9	76.3/ 0.273	64.5	94.1	78.0/ 0.263
10T12	4655	NA	4405												
10T24-B3	3450	0.0031	3995												
10T24-B4	3420	0.0027	3740												
11IT16	4635	0.0040	4430												
11T16.5	4970	0.0041	4170												
11T22-B3	4470	0.0032	3510												
11T22-B4	4750	0.0042	4010												
Avg.	4332	0.0040	4052				71.2	103.1	81.1/ 0.235	63.7	91.1	76.9/ 0.280	64.4	103.7	86.5/ 0.237
COV	12.4	14.7	15.6				4.3	4.4	7.7/ 10.4	5.2	5.6	9.0/ 12.9	4.5	5.9	11.5/ 10.4

Steel samples cut from the steel reinforcement in each specimen were tested to determine tensile properties. Yield stress (σ_y), ultimate stress (σ_u), fracture stress (σ_f), and fracture strain (ε_f) were obtained and are shown in Table 3.4. The #4 Grade-40, #4 Grade-60, and #6 Grade-60 steel were tested using the actual reinforcing bar cut to a length of 18 in. The #11 Grade-60 bar was machined in accordance with ASTM E8 for the 505 specimen size. The specimens were tested in a 110 kip capacity universal testing machine using a 2 in. gage length extensometer to measure strain. Tensile stress-strain curves for the steel are shown in Appendix A2.

Average yield stresses for #11 Grade-60, #6 Grade-60, #4 Grade-60, and #4 Grade-40 were 71.2, 63.7, 64.4, and 50.7 ksi, respectively. The average ultimate stresses for #11 Grade-60, #6 Grade-60, #4 Grade-60, and #4 Grade-40 were 103.1, 91.1, 103.7, and 78.9 ksi, respectively. The average fracture strains for #11 Grade-60, #6 Grade-60, #4 Grade-60, and #4 Grade-40 were 23.5%, 28.0%, 23.7%, and 28.6%, respectively.

After curing a minimum of 28 days at the precasting yard, specimens were shipped to the structural testing laboratory at OSU. Inverted-T beams were rolled into the inverted position before shipment. After arrival at the laboratory, specimens were placed in a reaction frame, instruments were installed, and the specimens were tested.

3.2 CONTROL TESTS

3.2.1 Test Method

The majority of tests were performed with a four-point loading configuration. Force was applied at midspan through a spreader beam to load points on the specimen spaced 24 in. apart. Applied load was measured with a 500 kip capacity load-cell mounted to the hydraulic actuator. The typical test setup is shown in Figures 3.2a and 3.2b. Instruments were applied to the specimen to capture both local and global behaviors; measurements were monitored during tests; and data were stored using a 16-bit PC-based data acquisition system.

For each test, data from approximately 42 sensors were collected. Sensors included load cells, strain gages, concrete clip gages, as well as displacement and tilt sensors. Sensors and their typical locations are illustrated in Figure 3.3. Specimen displacement at the load point was determined by subtracting support deformations from the load point deflection measurement taken relative to the strong floor. End rotations were measured using tilt sensors located on the specimen beyond the end supports. Strain gages were bonded to selected stirrups and installed prior to casting of concrete. For some tests, strain gages were installed on stirrups or flexural reinforcing bars at diagonal crack locations by chipping into the concrete to expose the embedded steel.

Crack widths were measured three ways: displacement transducers were placed on diagonals within the test span; individual displacement transducers were mounted across diagonal cracks; and at each load step a visual crack comparator was used to determine crack widths at selected locations on the specimen. Support locations were varied for different tests to permit testing of different shear-to-moment ratios. However, the typical center-to-center spacing of supports was 21.6 ft for the inverted-T and 24 ft for the T specimens.

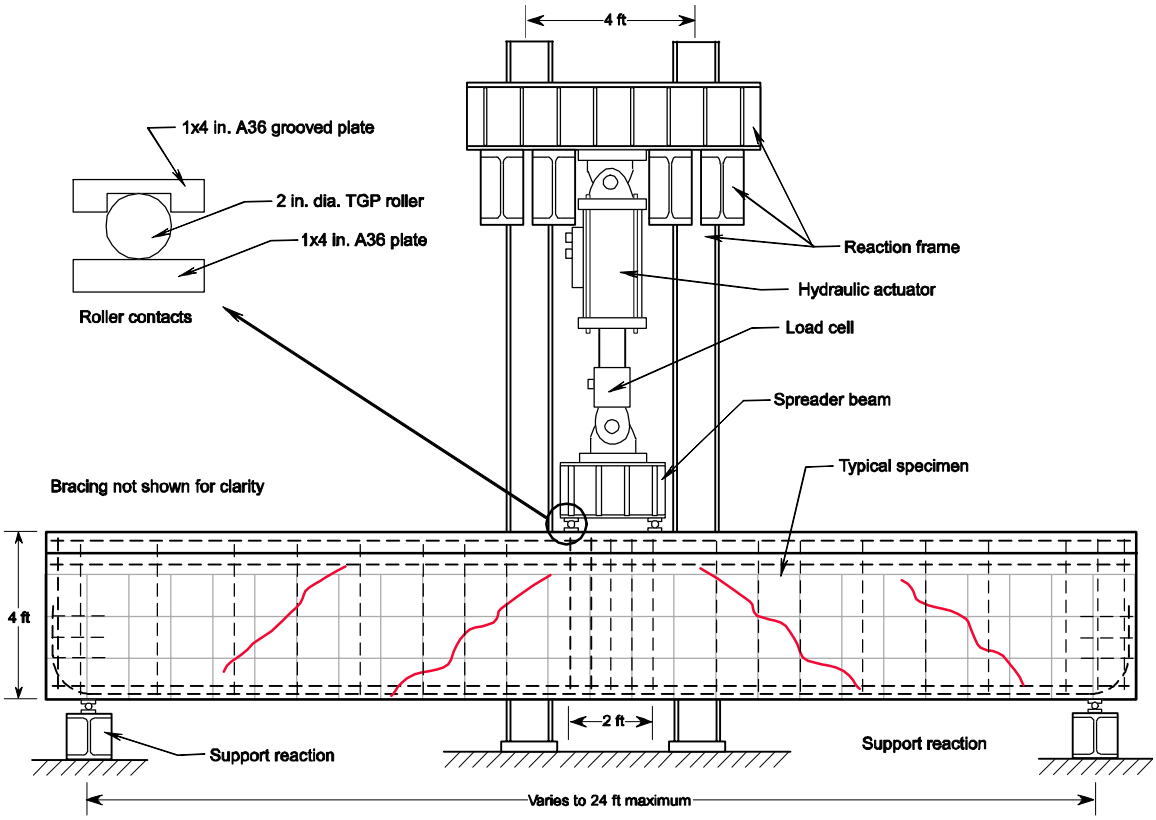

Figure 3.2a: Schematic of test frame with specimen for typical test

Figure 3.2b: Test frame with specimen for typical test

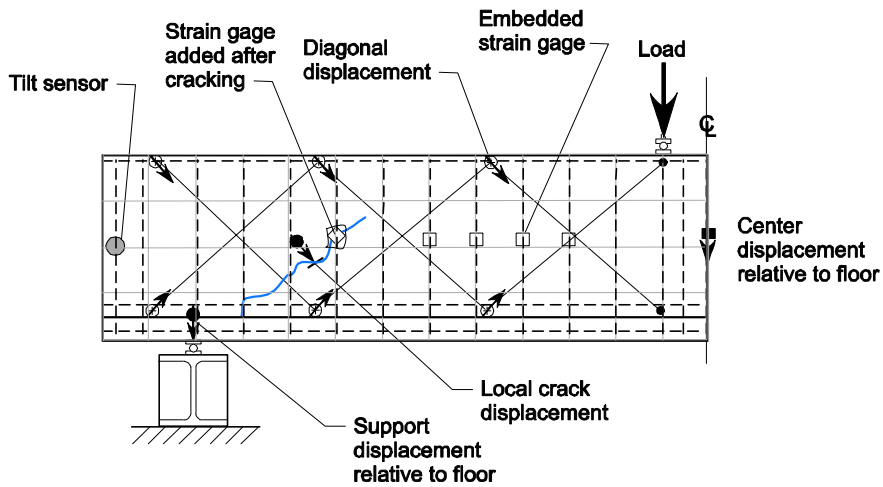

Figure 3.3: Typical instrumentation on test specimen

3.2.2 Support Condition Evaluation

Support conditions were idealized as roller supports permitting rotation with vertical force and minimal horizontal thrust. Actual support behavior was assessed in the lateral direction and the axial thrust generated was estimated. Support conditions used for testing all stationary loaded specimens consisted of a 2 in. diameter turned-ground-and-polished (TGP) roller captive in a grooved plate that was bolted to a W12x120 floor reaction beam. The specimens were supported on 1 in. thick x 4 in. x 16 in. mild steel plates that rested on the roller. The long dimension of the plate was oriented transverse to the span of the specimen.

To assess these boundary conditions, a specimen was placed on the support bearings and a horizontal force was applied at the base of the web by a hydraulic cylinder with load cell, as shown in Figure 3.4. The reaction at the opposite end of the beam consisted of a true roller, as shown in Figure 3.5. Horizontal force was increased and lateral displacement of the beam, bearing plate, and steel reaction beam (shown in Figure 3.6) were measured.

To assess the role of the vertical support reaction magnitude, different applied loads were considered. These were 1) self-weight of the beam and 2) 50 kips of applied vertical load at midspan of the beam. For these conditions, the vertical reaction at the support was 10.875 kips for the self-weight and 35.875 kips for the combined self-weight with 50 kips of applied load at midspan.

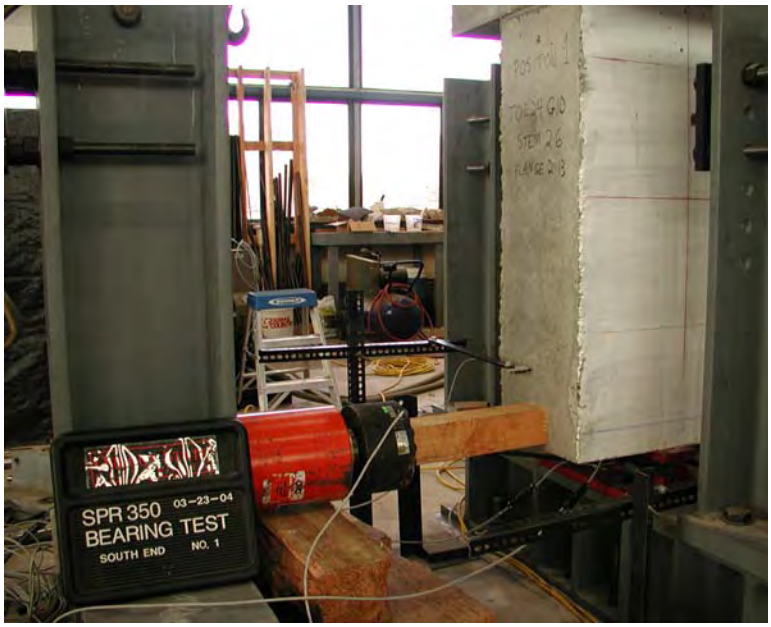

Figure 3.4: Setup for support condition evaluation

Figure 3.5: Roller conditions at opposite end of specimen for support condition evaluation

Figure 3.6: Displacement sensors to measure support component motions under lateral load applied to the base of the beam web

The support responses for these two cases are shown in Figure 3.7. As seen in this figure, when small vertical reactions are on the supports, the beam slips on the reaction plate at relatively low lateral load (static friction ~700 lbs). At the larger reaction, the beam slips on the bearing plate at 2900 lbs. The average friction coefficient corresponding to the slip force was 0.073 for the two cases.

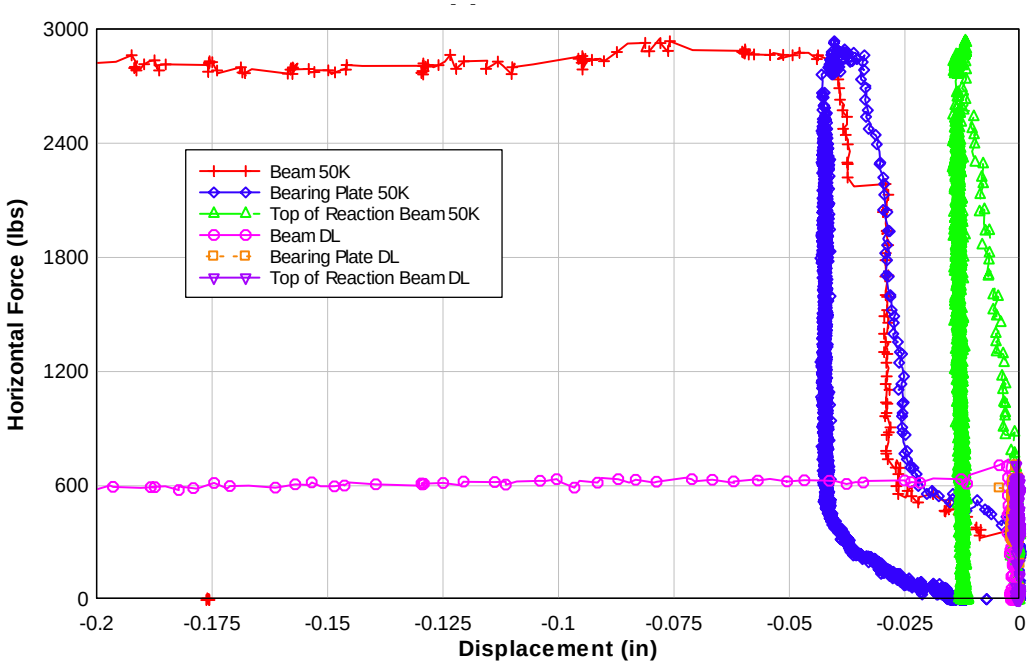

Figure 3.7: Horizontal displacements at supports for applied lateral force at base of beam web

For the case with larger vertical reaction, other support deformations occur before slip of the beam on the bearing plate. These included bearing plate movement relative to the reaction beam due to a gap between the roller and groove on the reaction beam (approximately 0.025 in.), as well as movement of the reaction beam relative to the laboratory floor. The friction force between the concrete beam and bearing plate develops approximately 7.3% of the shear at the support before slip occurs.

The secant stiffness of the support prior to slip was determined from the reaction beam displacement as 247 kips/in with an additional constant deformation component of 0.025 in. associated with the roller gap that occurs at low load. Combining the gap displacement and reaction beam stiffness components of the support conditions, an equivalent secant support stiffness was determined for the lateral force magnitude required to produce slip between the beam and bearing plate. Estimated equivalent support stiffness for different magnitudes of support reaction (shear force) is shown in Figure 3.8.

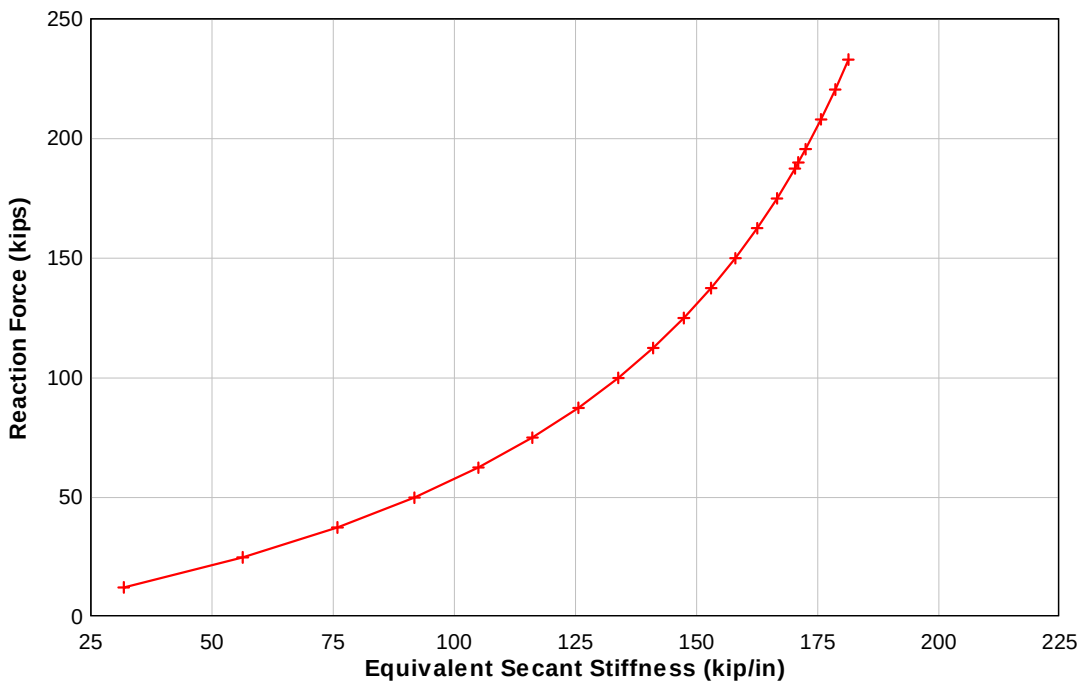

Figure 3.8: Equivalent lateral stiffness of support for different amounts of vertical reaction

Horizontal support displacement demands produced from flexure on a typical specimen were estimated by integrating longitudinal strains at the bottom of the beam over the length of the span. For this analysis, flexural tensile strains were taken at the level of the reinforcing steel. Strains were determined from moment-curvature analysis of the section with the Todeschini concrete constitutive rule for concrete f'_c=4000 psi and elasto-plastic material model for rebar with f_y=68 ksi (*Todeschini, et al. 1964*).

For a typical T-specimen with six #11 bars, the amount of longitudinal elongation of the beam at the level of the support was estimated at 0.015 in. just prior to yielding of the flexural rebar and 0.03 in. at ultimate (concrete crushing with the flexural steel yielding) as show in Figure 3.9.

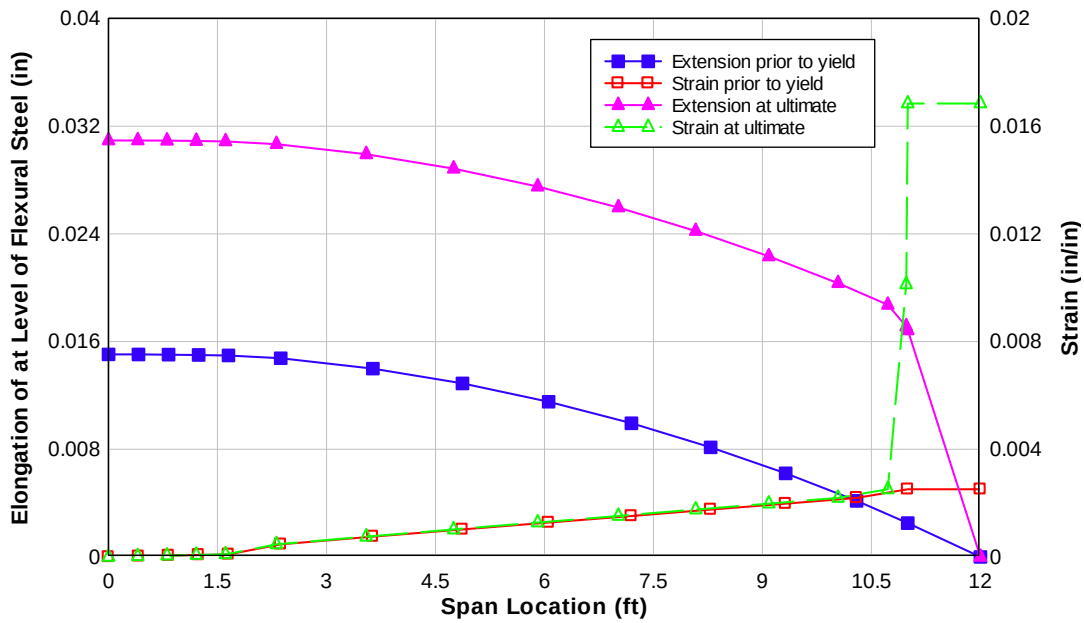

Figure 3.9: Estimated amount of free horizontal displacement required at supports for typical specimen with yielding flexural reinforcing steel

Substituting these lateral support displacements into the support stiffnesses determined previously (with V=190 kips for the flexural bars just prior to yielding and V=195.5 kips for the specimen at ultimate flexural capacity), the lateral force produced at the reactions was estimated at 2.6 kips just prior to flexural rebar yielding and 5.2 kips at ultimate. These values are below the slip force magnitude.

Slip between the plate and beam was not observed during control testing. Applying the support forces as external axial loads (approximated as applied to the centroid of the section), analysis of the section was performed using analysis program *Response 2000*™ (described further in the Analysis section) to determine the impact of these forces on the capacity prediction. Results indicated that for this relatively small magnitude of axial force, there was negligible impact on the resulting strength prediction for the typical beam specimen.

3.2.3 Loading Protocol

The imposed loading history consisted of loading and unloading cycles with each subsequent increment applied at a higher load magnitude. Typical tests were performed in displacement control using a closed-loop servo-hydraulic system. The loading protocol generally consisted of loading and unloading cycles with increasing load magnitudes in increments of 50 kips, as illustrated in Figure 3.10. When the peak force for each increment was achieved, the

displacement was held and crack widths were measured and crack extents were marked and recorded. The beam was subsequently unloaded and the crack widths were again measured and recorded when the load was near zero. This process was repeated until specimen failure.

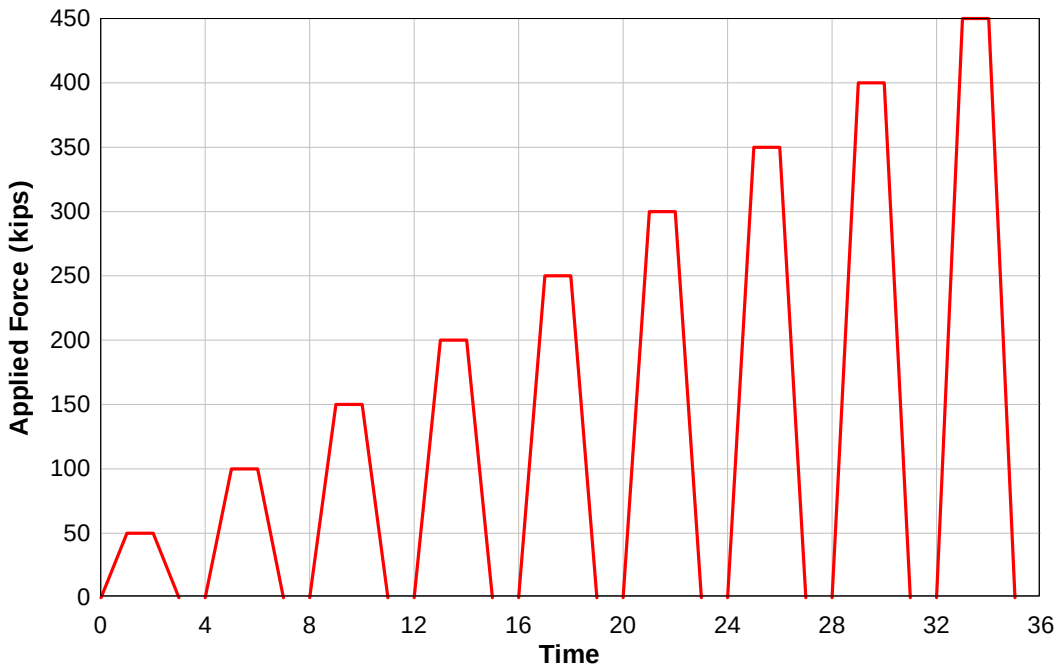

Figure 3.10: Control loading protocol (horizontal lines represent holding of load to mark and measure cracks)

3.2.4 Experimental Results

Overall load-deformation behavior of specimens is shown in Figures 3.11a-l. Digital photographs of specimens at failure are shown in Figures 3.12a-k. Instrument locations and crack patterns are contained in Appendix A3, and instrument data for specimens are contained in Appendix A4.

Key structural response quantities for each of the specimens are summarized in Table 3.5. Deflection reported in this table is taken from the specimen under the loading point and is corrected for support deformations. The largest diagonal crack width observed in the stem, w_{cr}, was measured with an ODOT crack comparator card or by a micrometer and occurred at the peak load in the cycle prior to failure.

Failure modes for most specimens were shear-compression failures (reported as Shear in Table 3.5), although flexural-tension and flexural-compression failures (reported as Flexural in Table 3.5) were observed for the specimens with 6 in. stirrup spacing. The IT specimen with 6 in. stirrup spacing failed in flexural compression while the T specimens with 6 in. stirrup spacing failed in flexural tension. Inverted-T beams with only 12 in. of flexural steel anchorage beyond the centerline of the support exhibited shear-tension failures (reported as Anchorage in Table 3.5) for widely spaced stirrups.

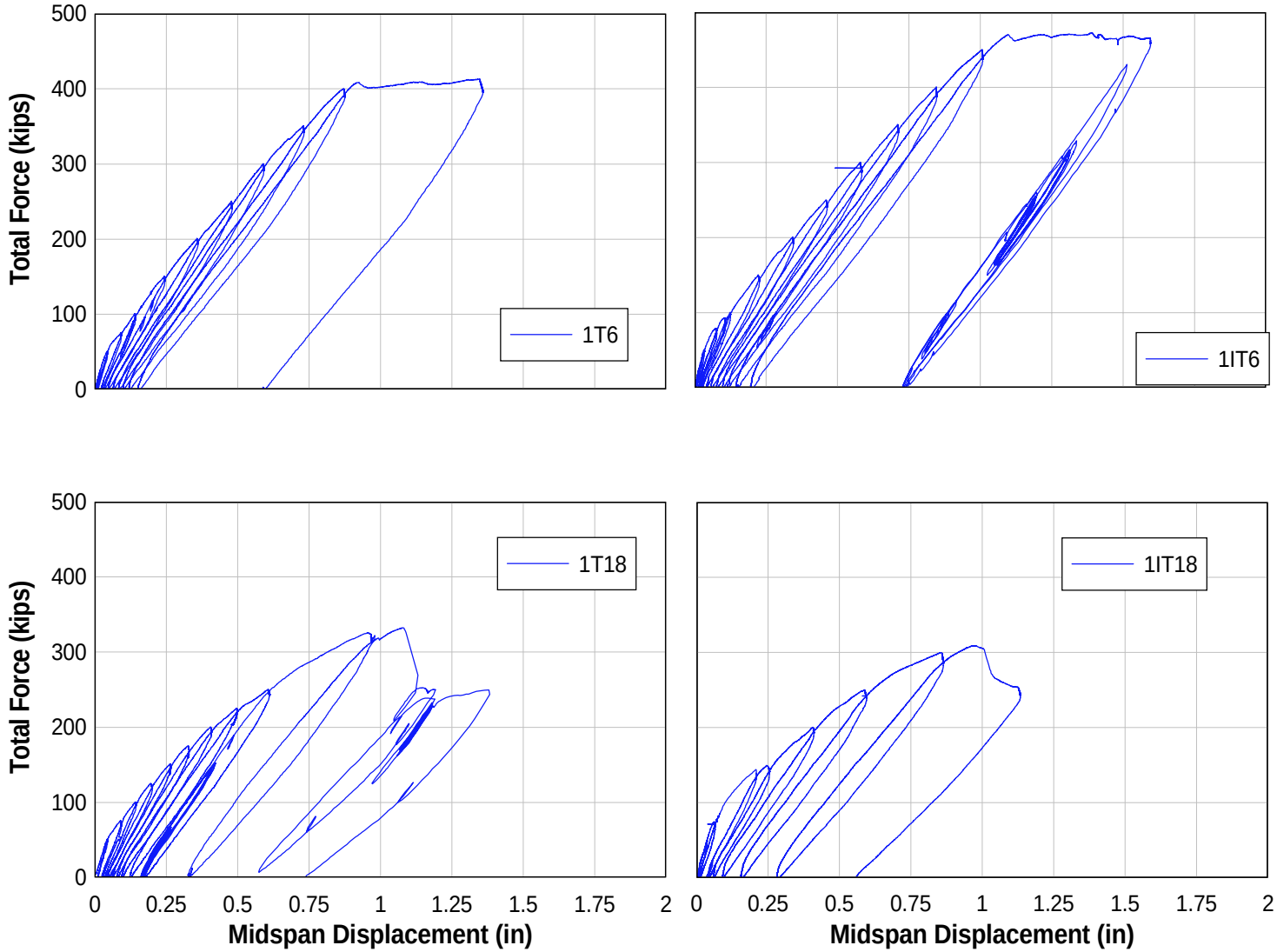

Figure 3.11a: Load-displacement plot at midspan for Group 1 specimens

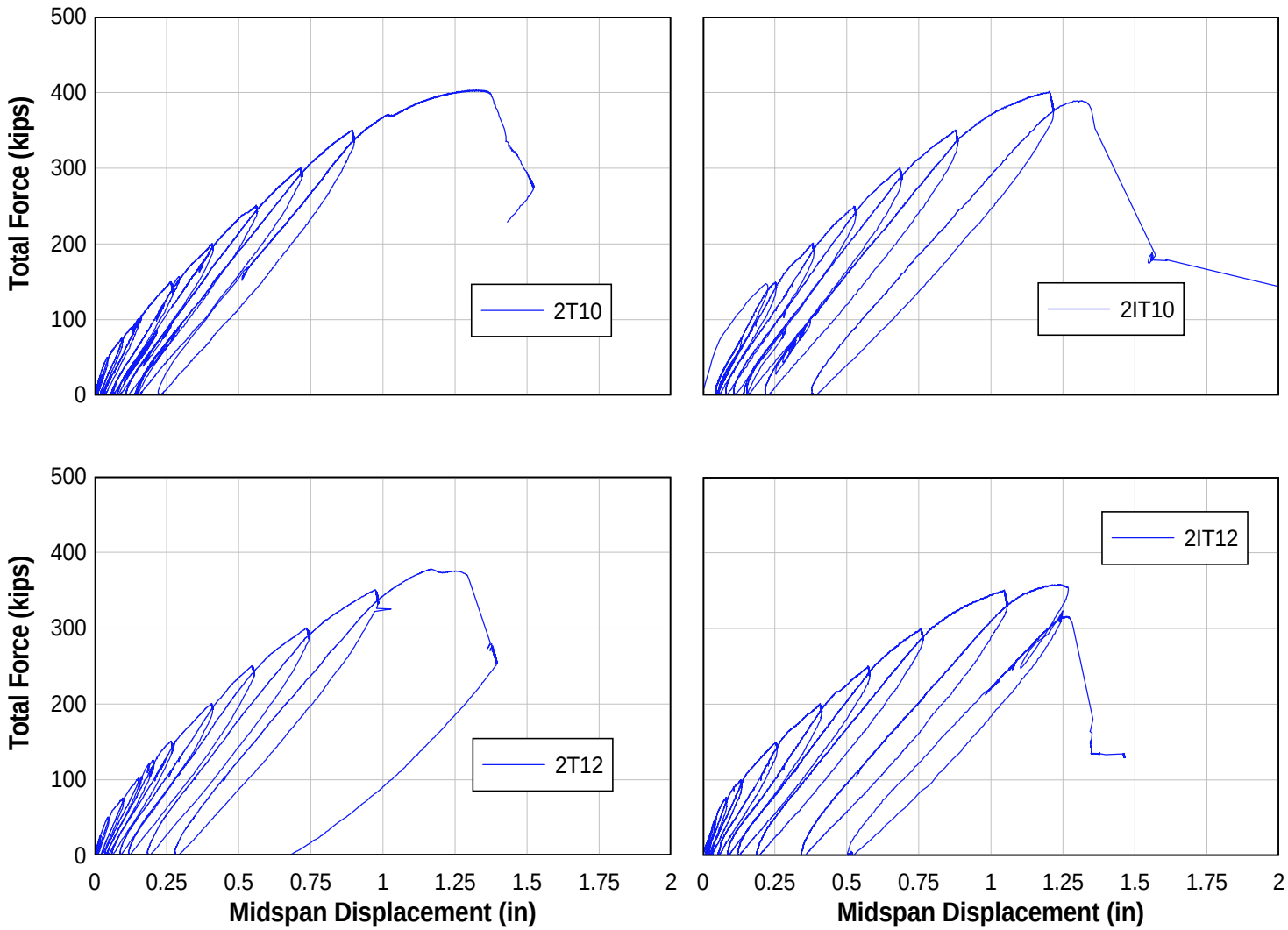

Figure 3.11b: Load-displacement plot at midspan for Group 2 specimens

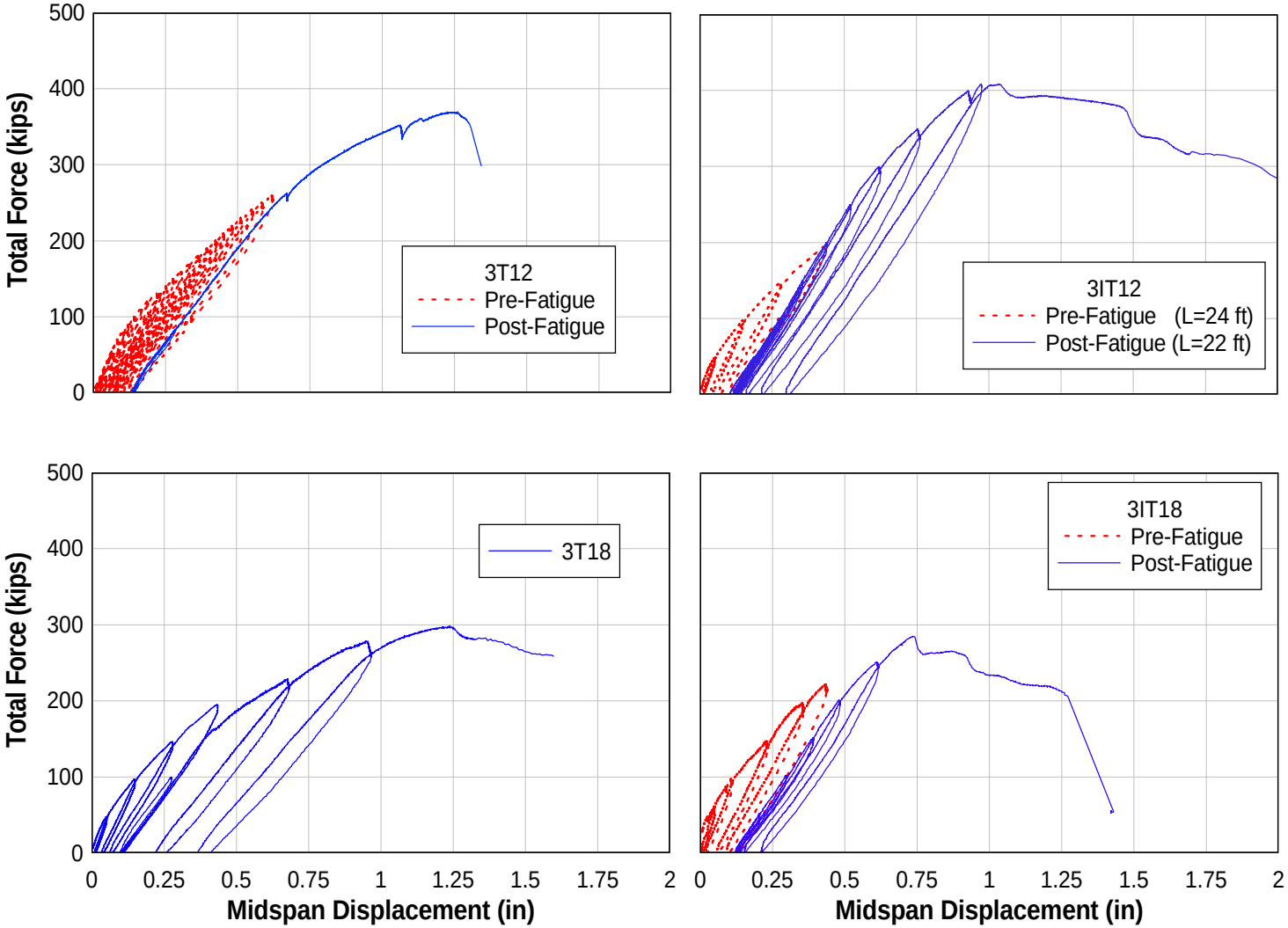

Figure 3.11c: Load-displacement plot at midspan for Group 3 specimens

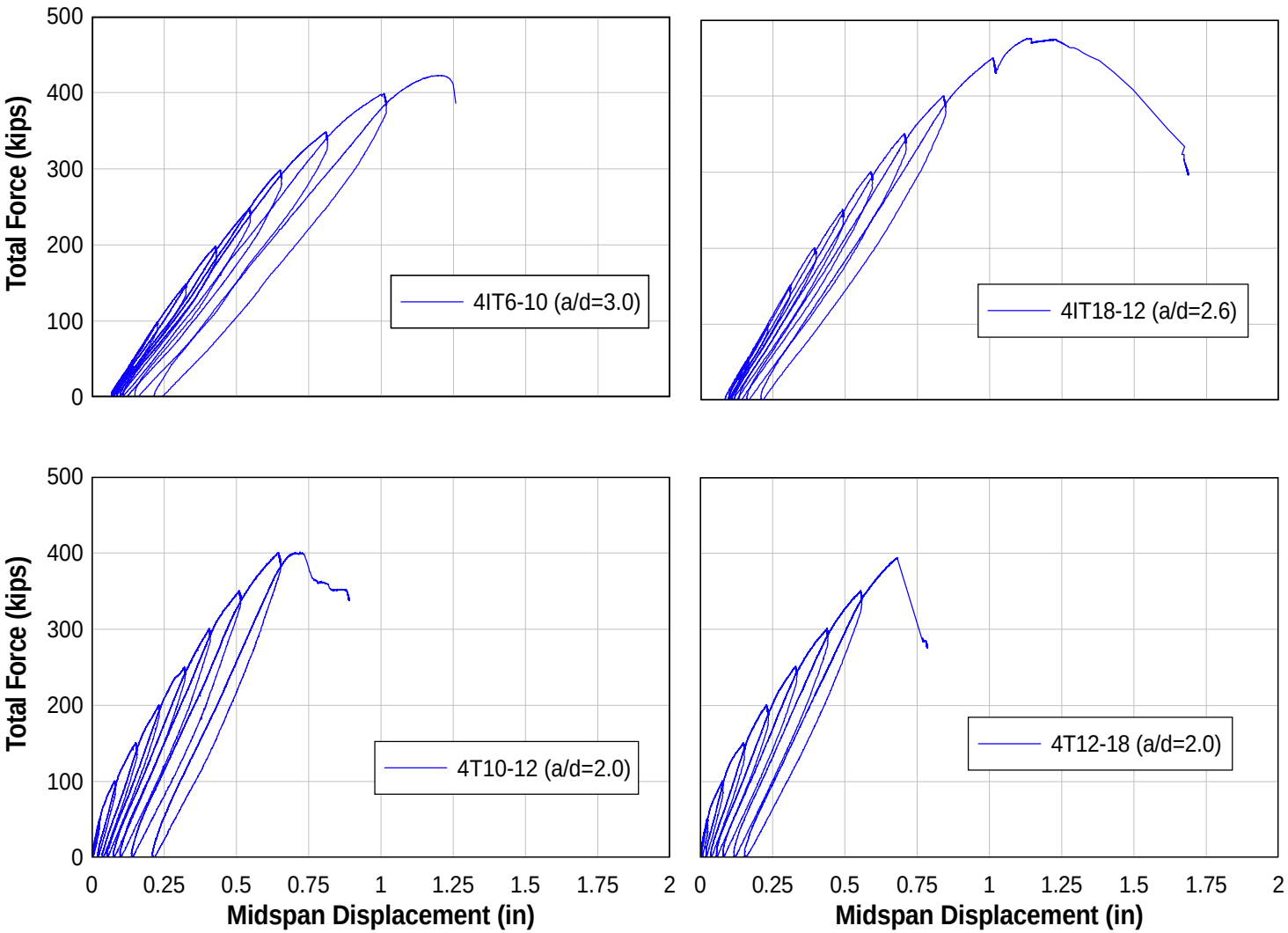

Figure 3.11d: Load-displacement plot at midspan for Group 4 specimens

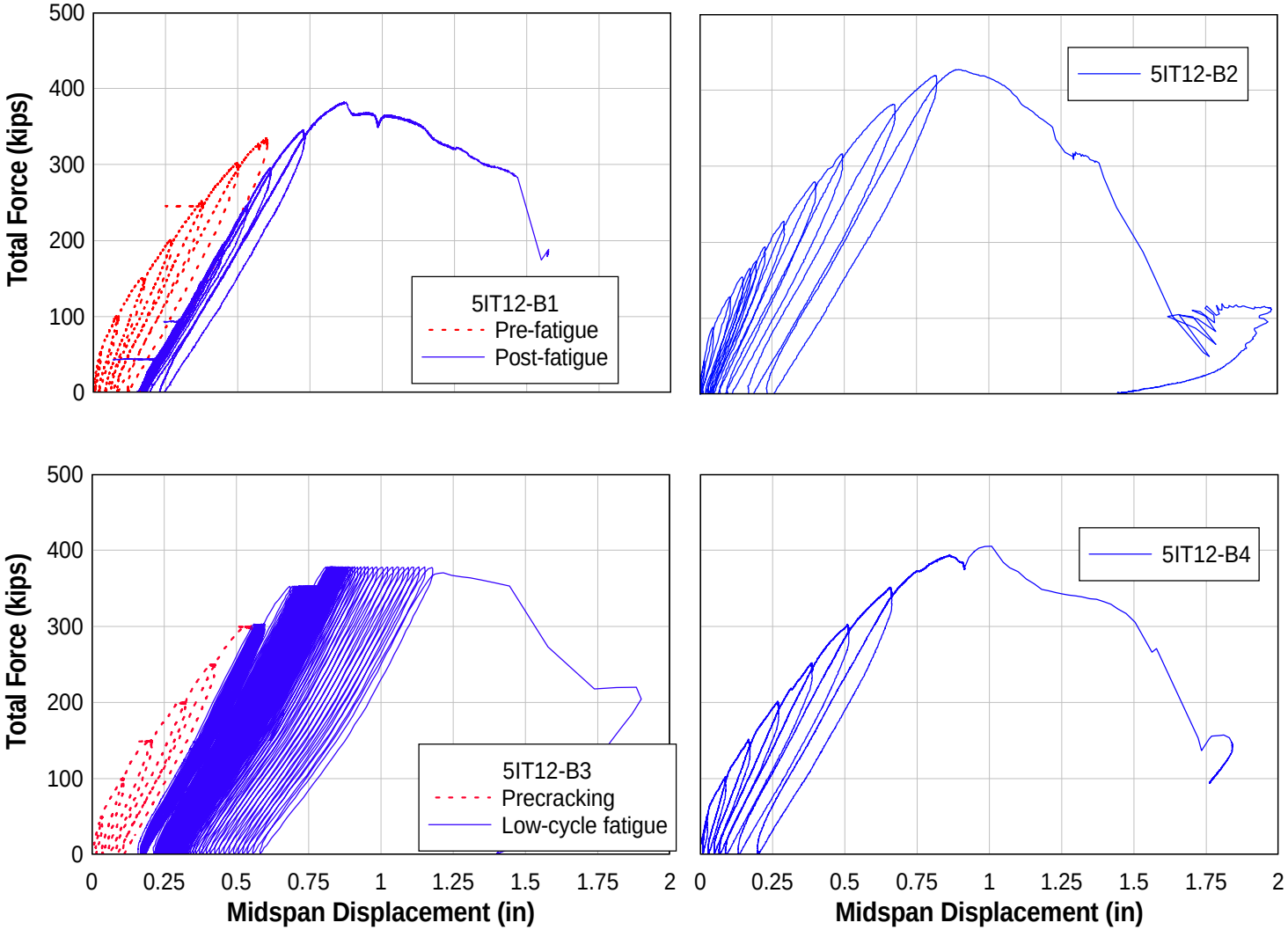

Figure 3.11e: Load-displacement plot at midspan for Group 5 specimens

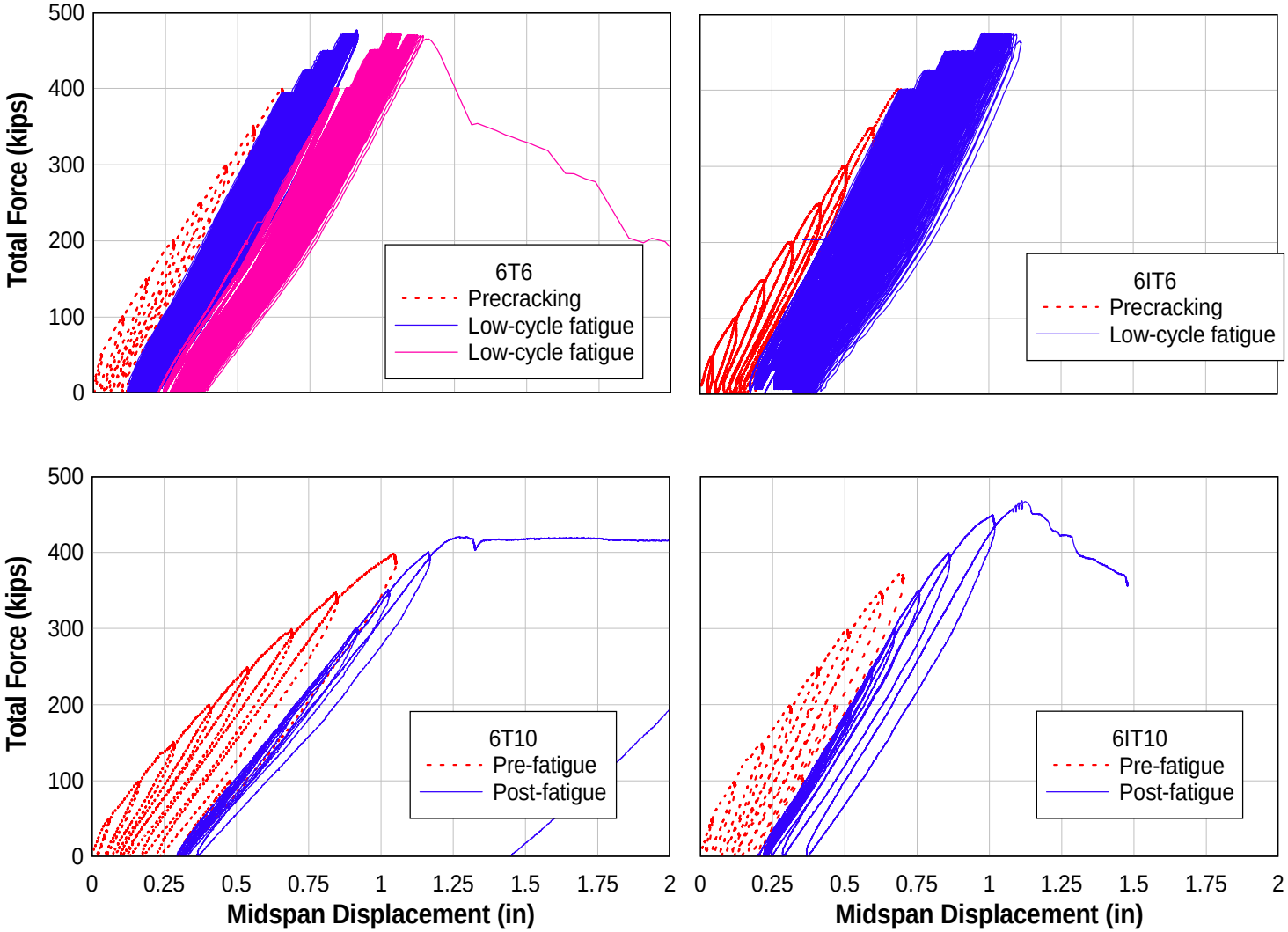

Figure 3.11f: Load-displacement plot at midspan for Group 6 specimens

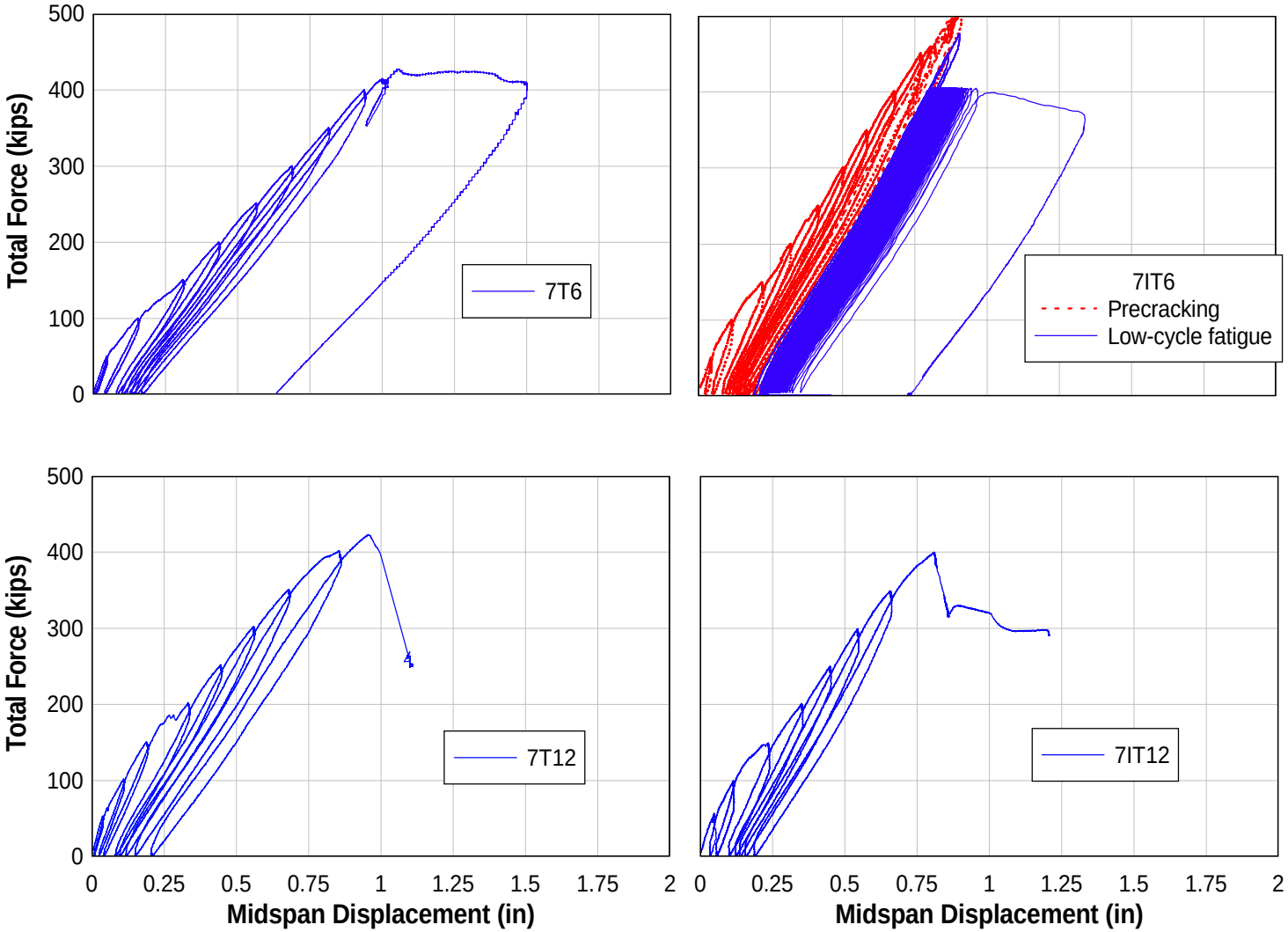

Figure 3.11g: Load-displacement plot at midspan for Group 7 specimens

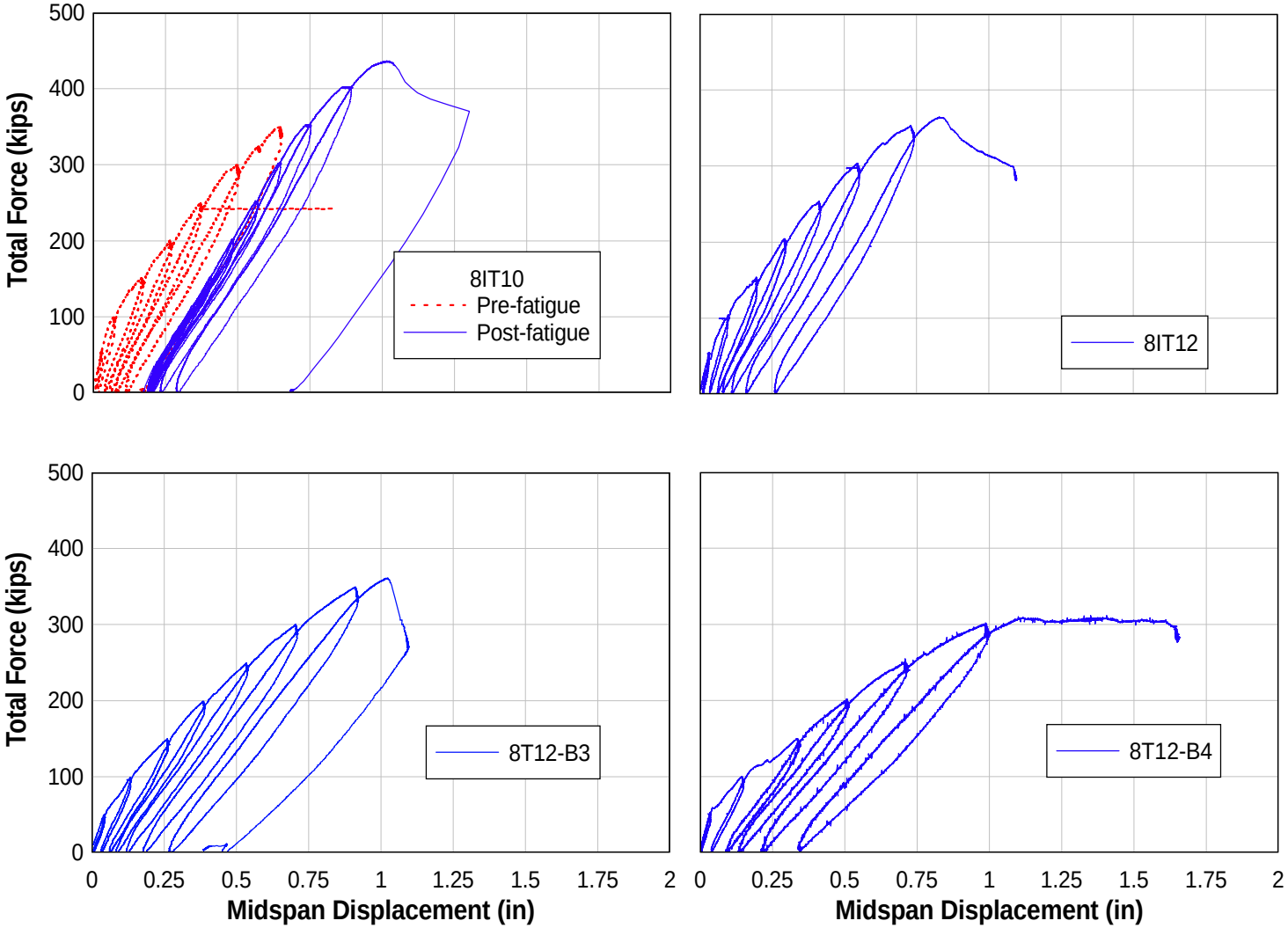

Figure 3.11h: Load-displacement plot at midspan for Group 8 specimens

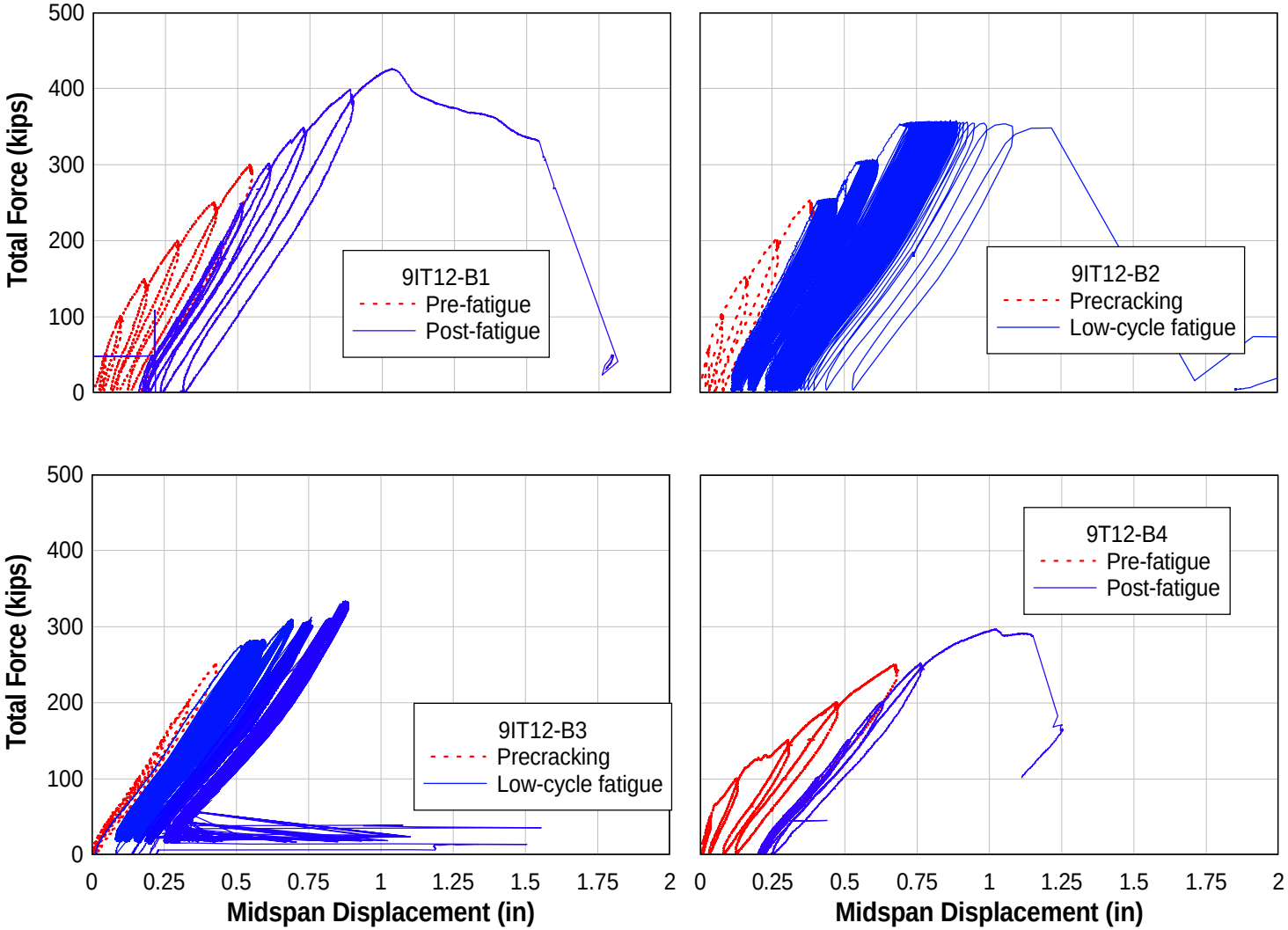

Figure 3.11i: Load-displacement plot at midspan for Group 9 specimens

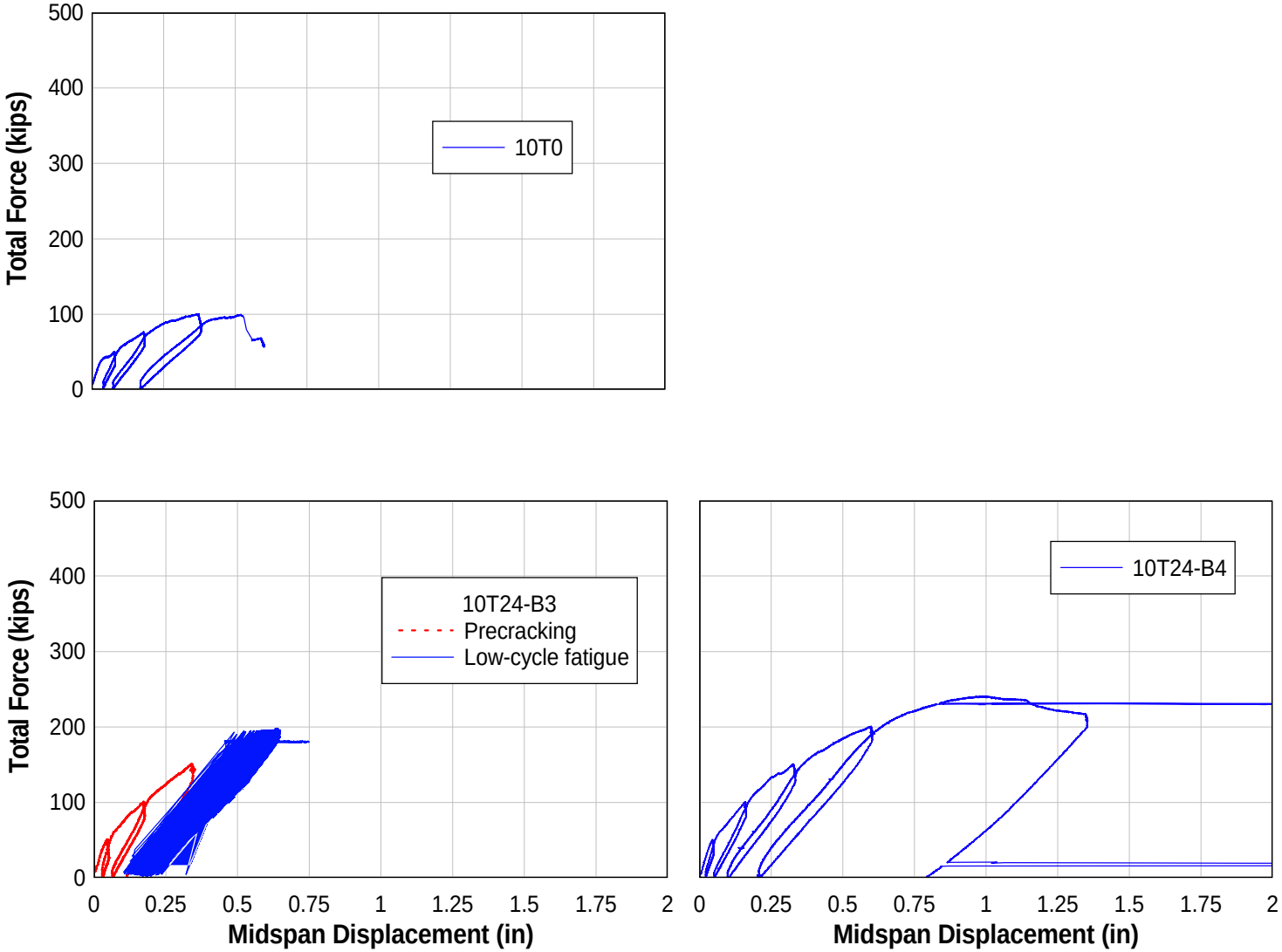

Figure 3.11j: Load-displacement plot at midspan for Group 10 specimens

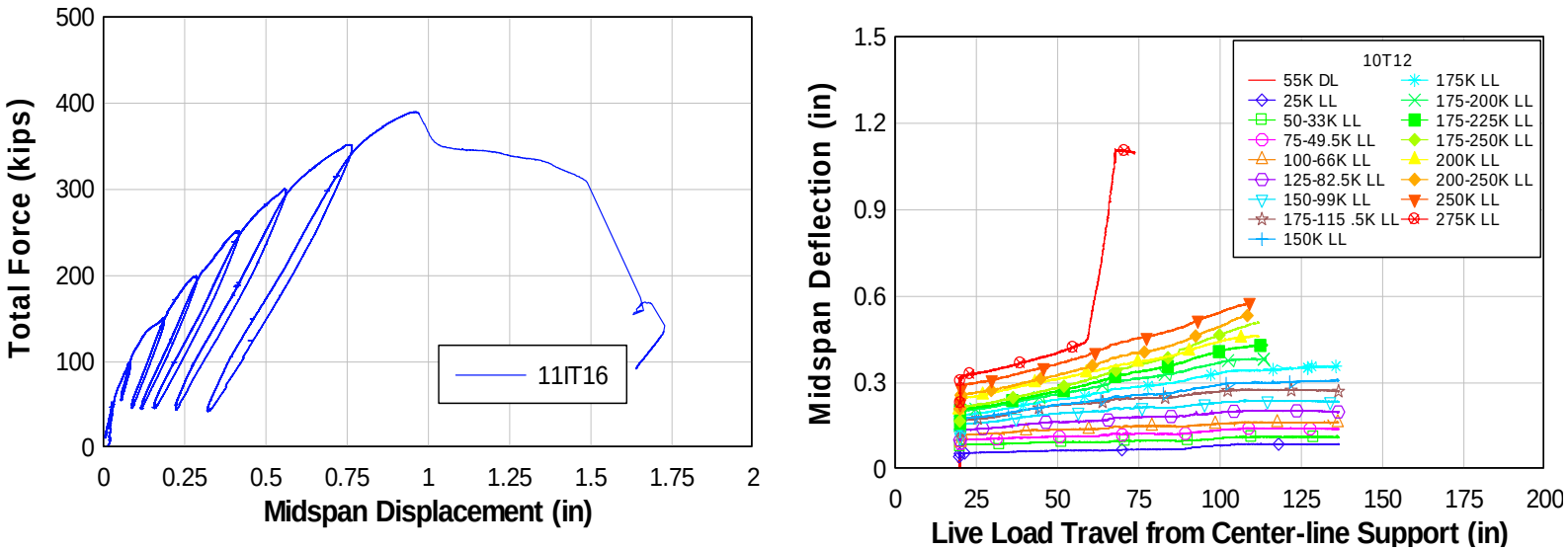

Figure 3.11k: Load-displacement plot at midspan for Group 10 and 11 moving-load specimens

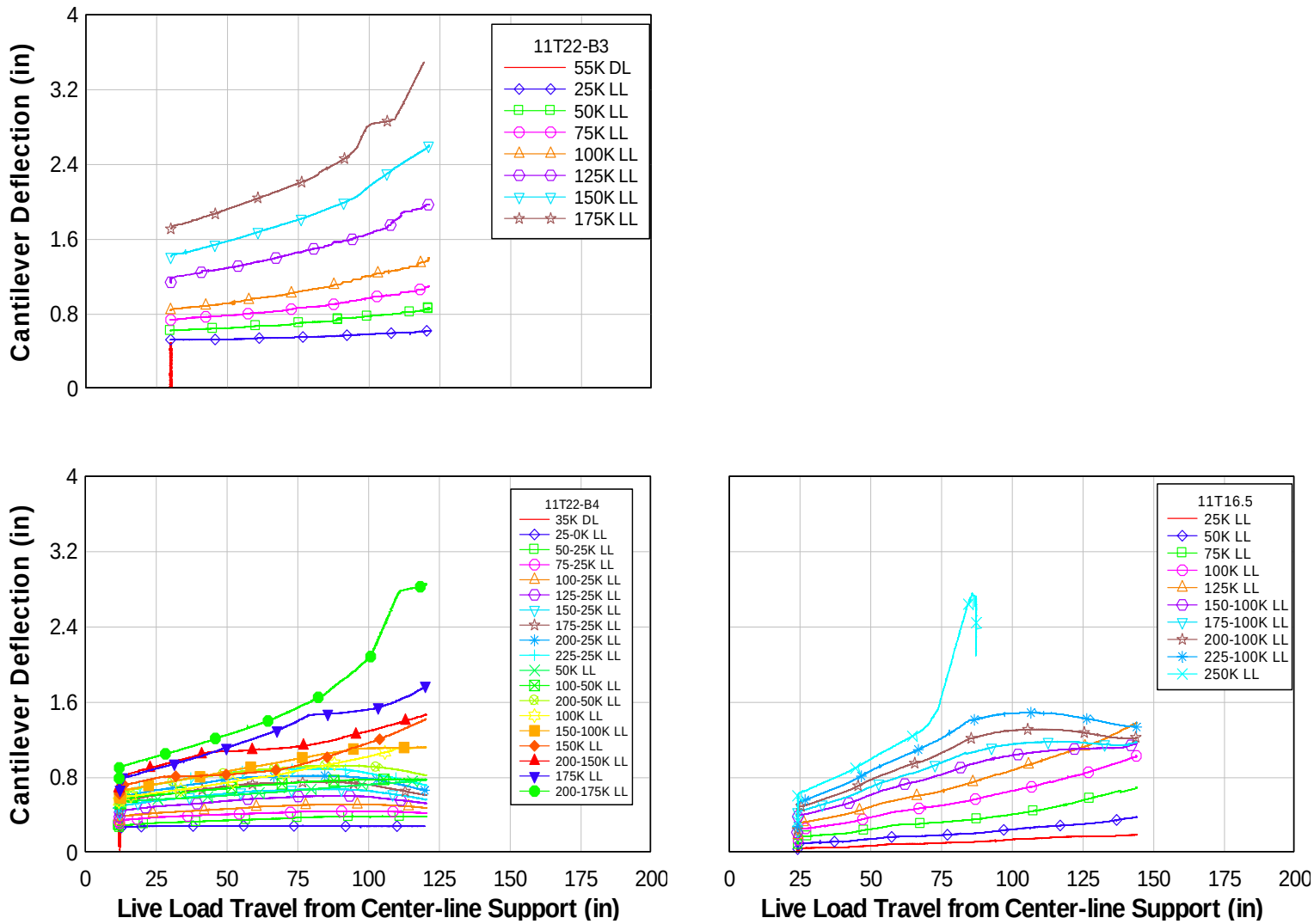

Figure 3.11l: Load-displacement plot at midspan for Group 11 moving-load specimens

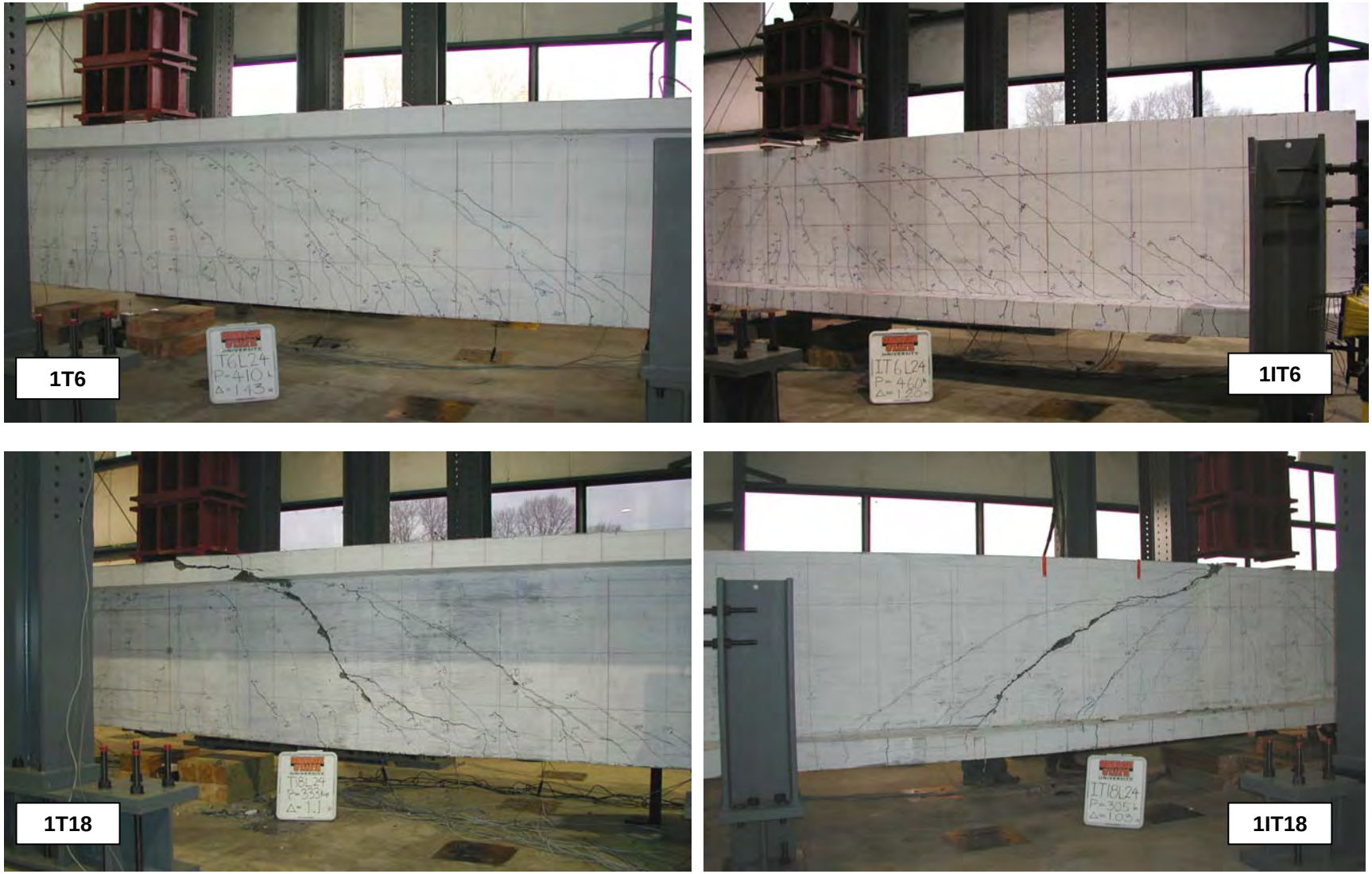

Figure 3.12a: Digital photographs at failure for Group 1 specimens

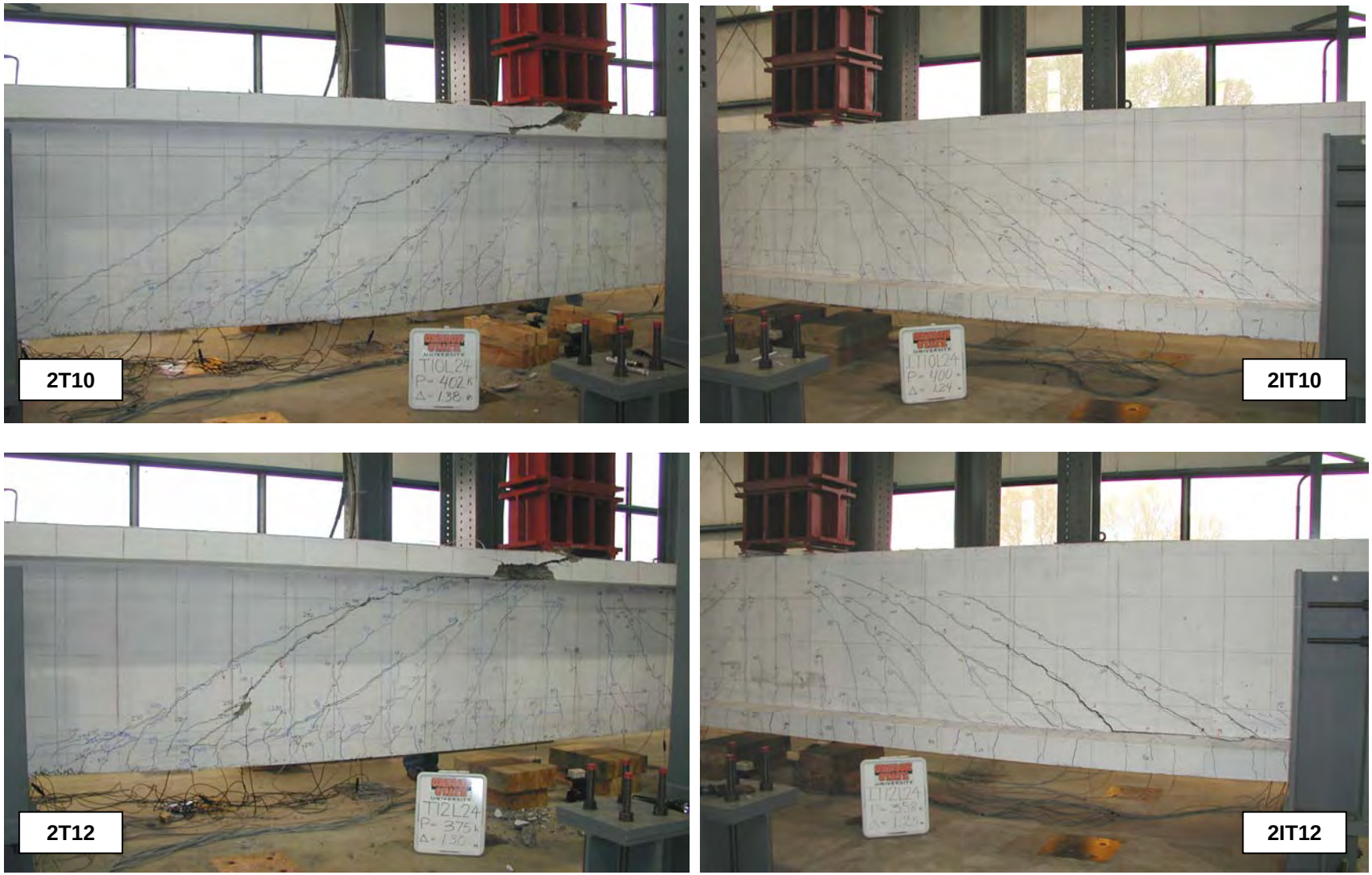

Figure 3.12b: Digital photographs at failure for Group 2 specimens

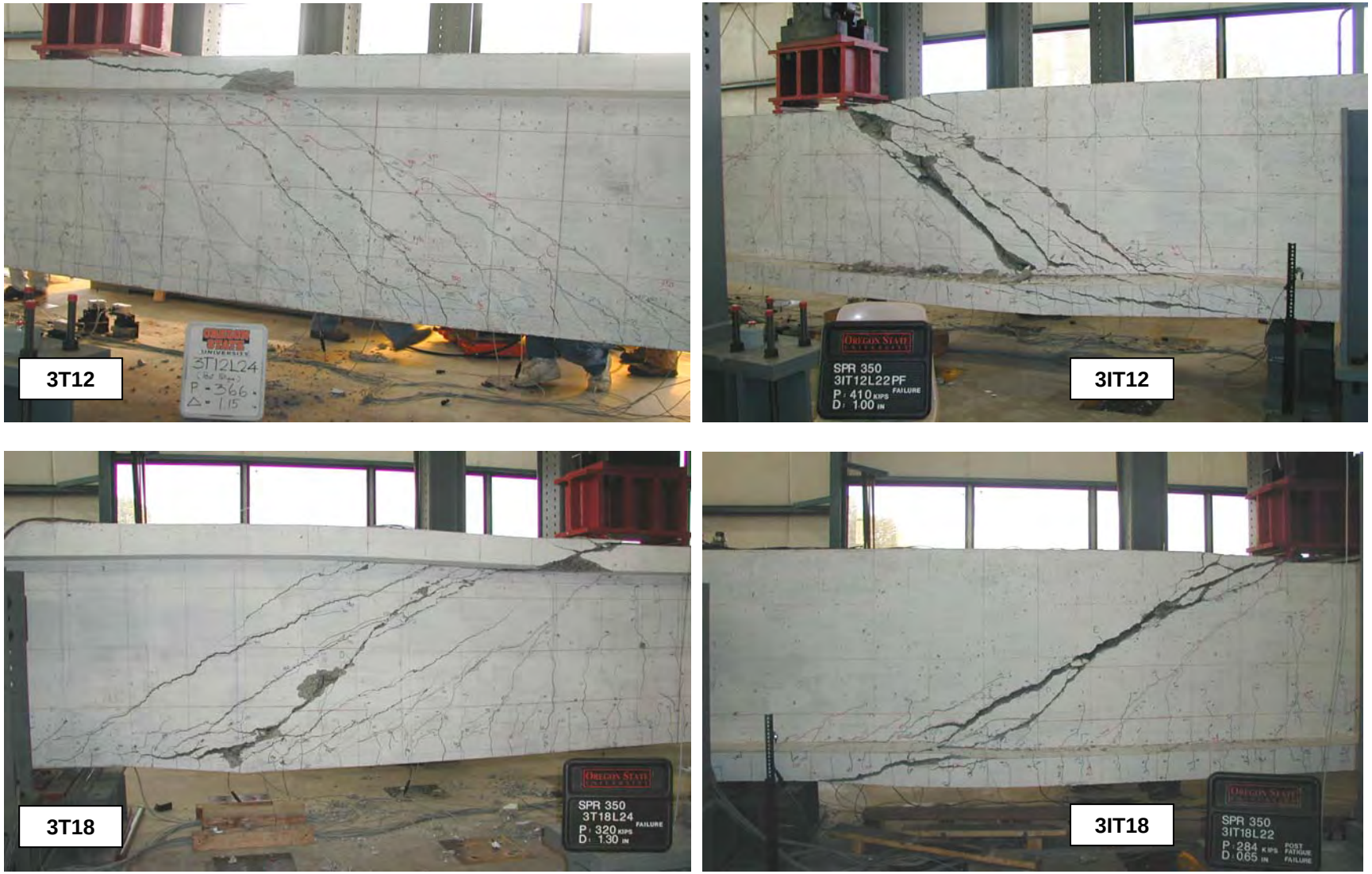

Figure 3.12c: Digital photographs at failure for Group 3 specimens

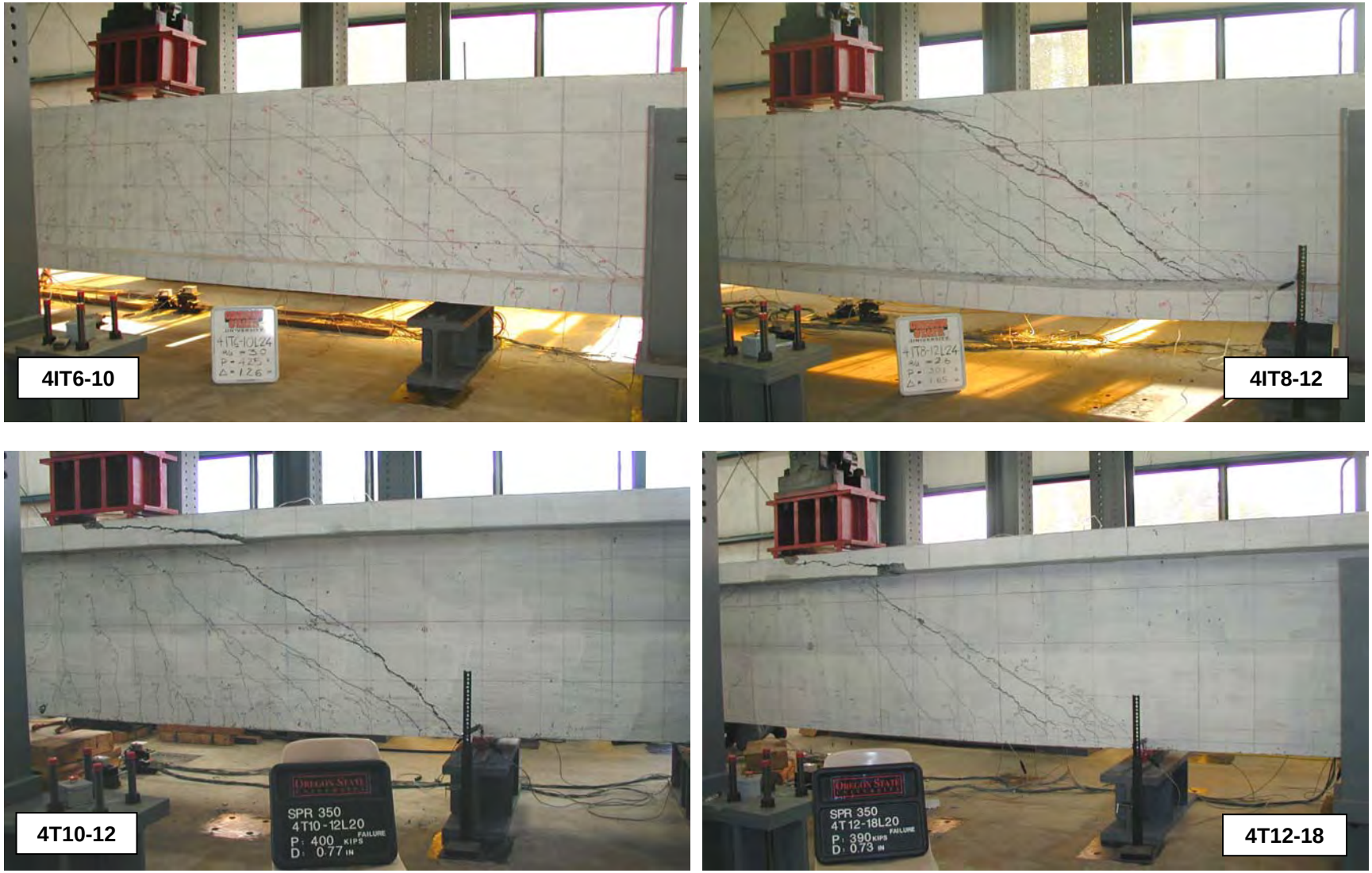

Figure 3.12d: Digital photographs at failure for Group 4 specimens

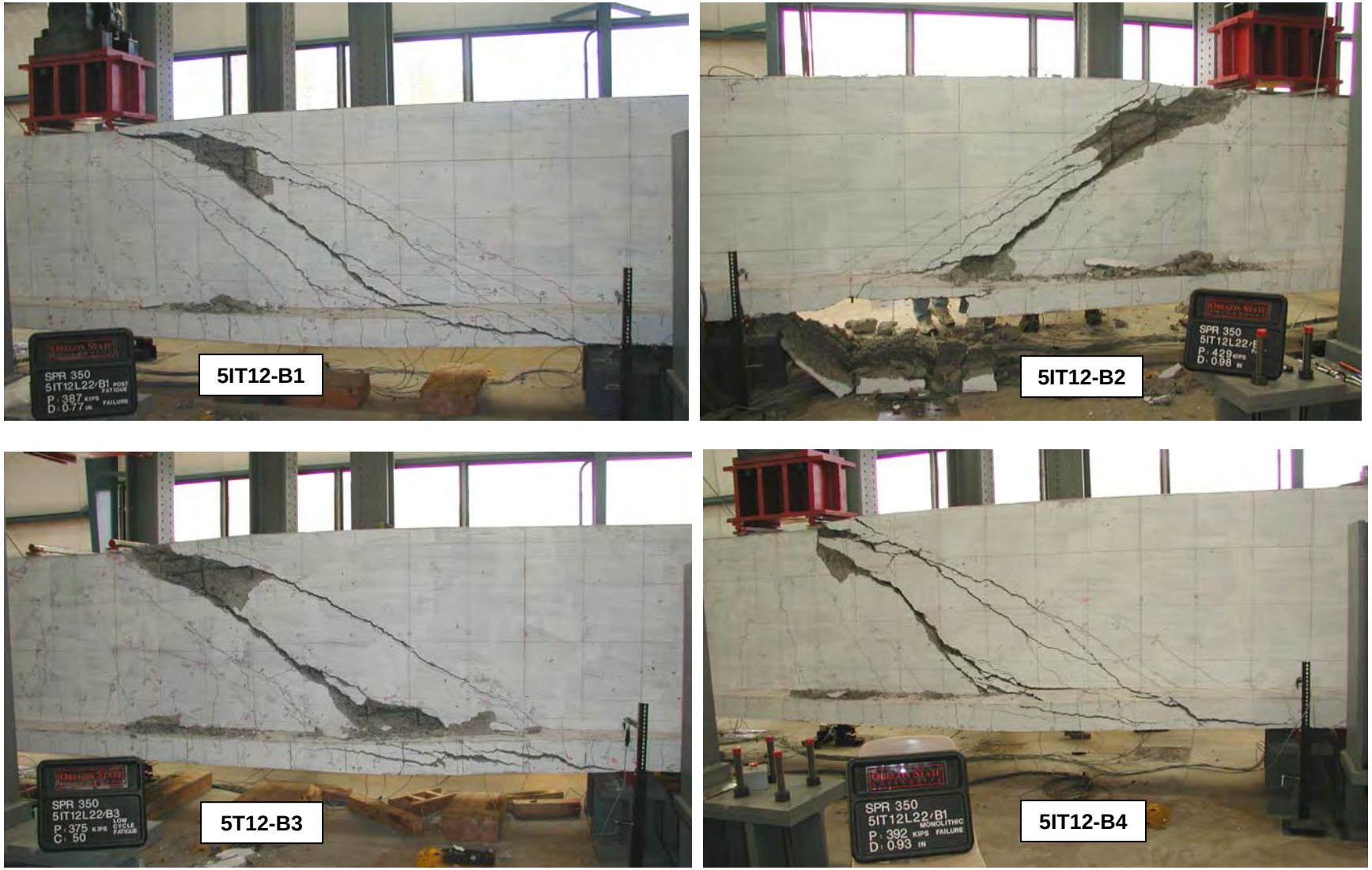

Figure 3.12e: Digital photographs at failure for Group 5 specimens

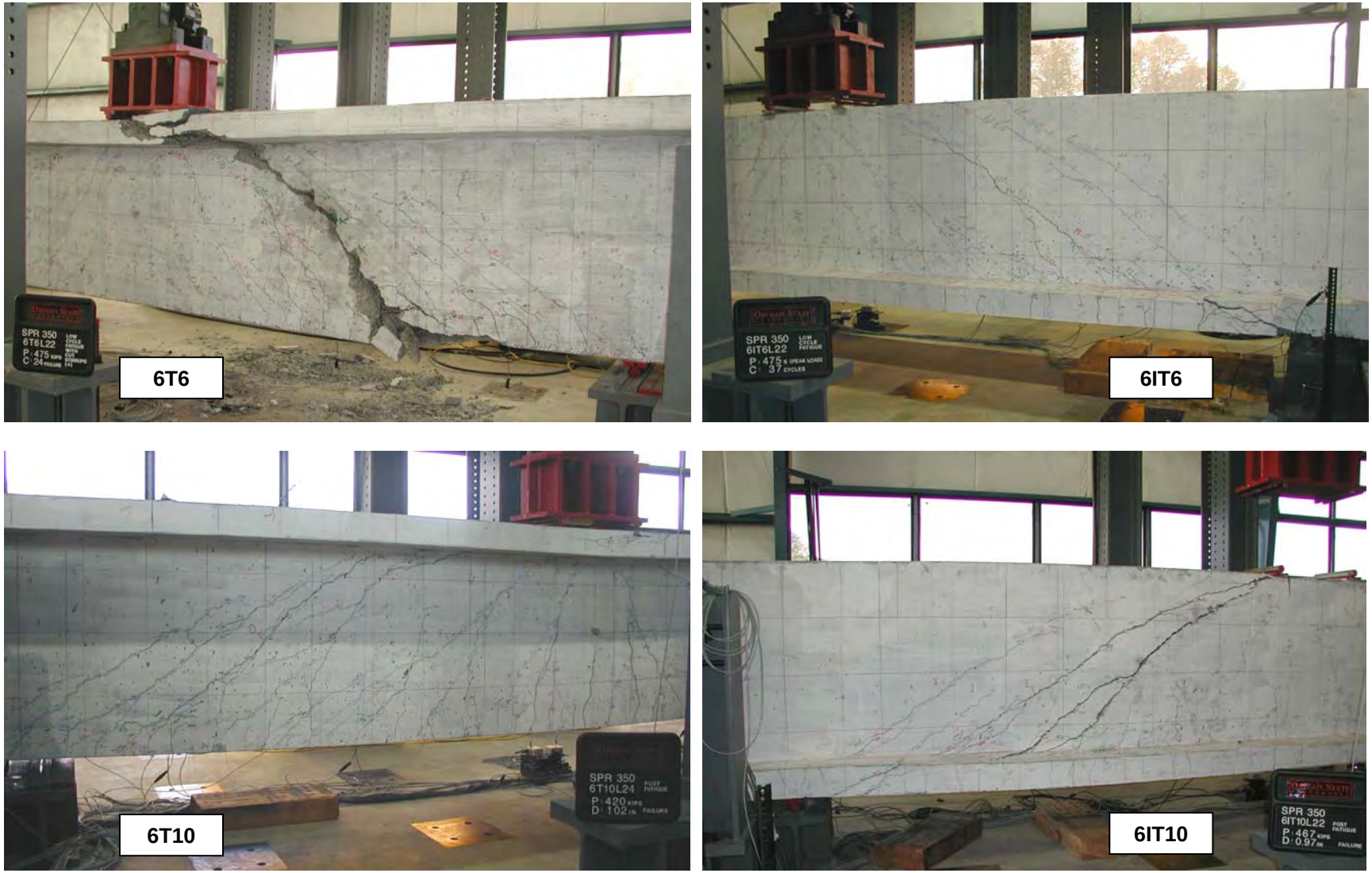

Figure 3.12f: Digital photographs at failure for Group 6 specimens

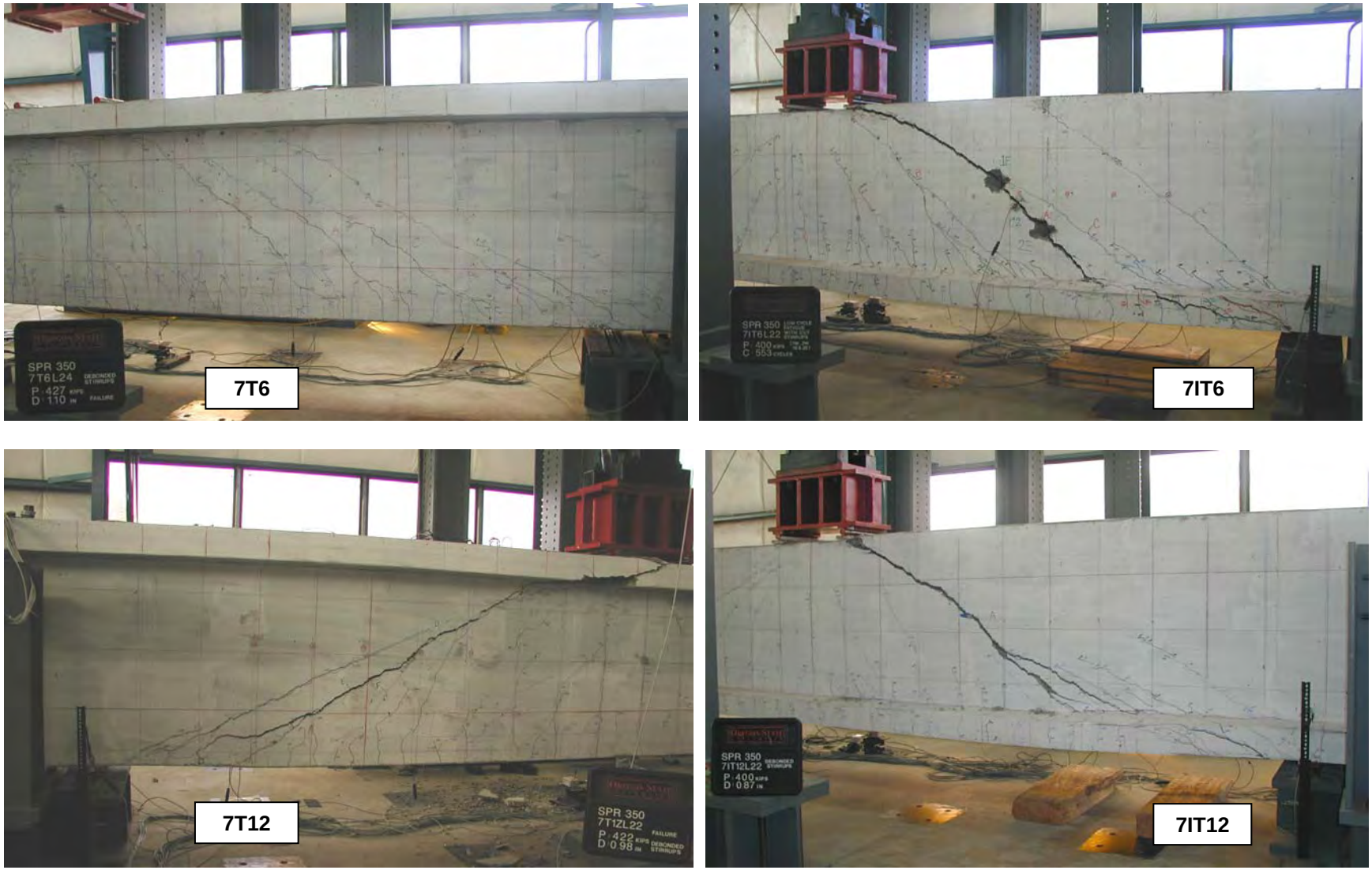

Figure 3.12g: Digital photographs at failure for Group 7 specimens

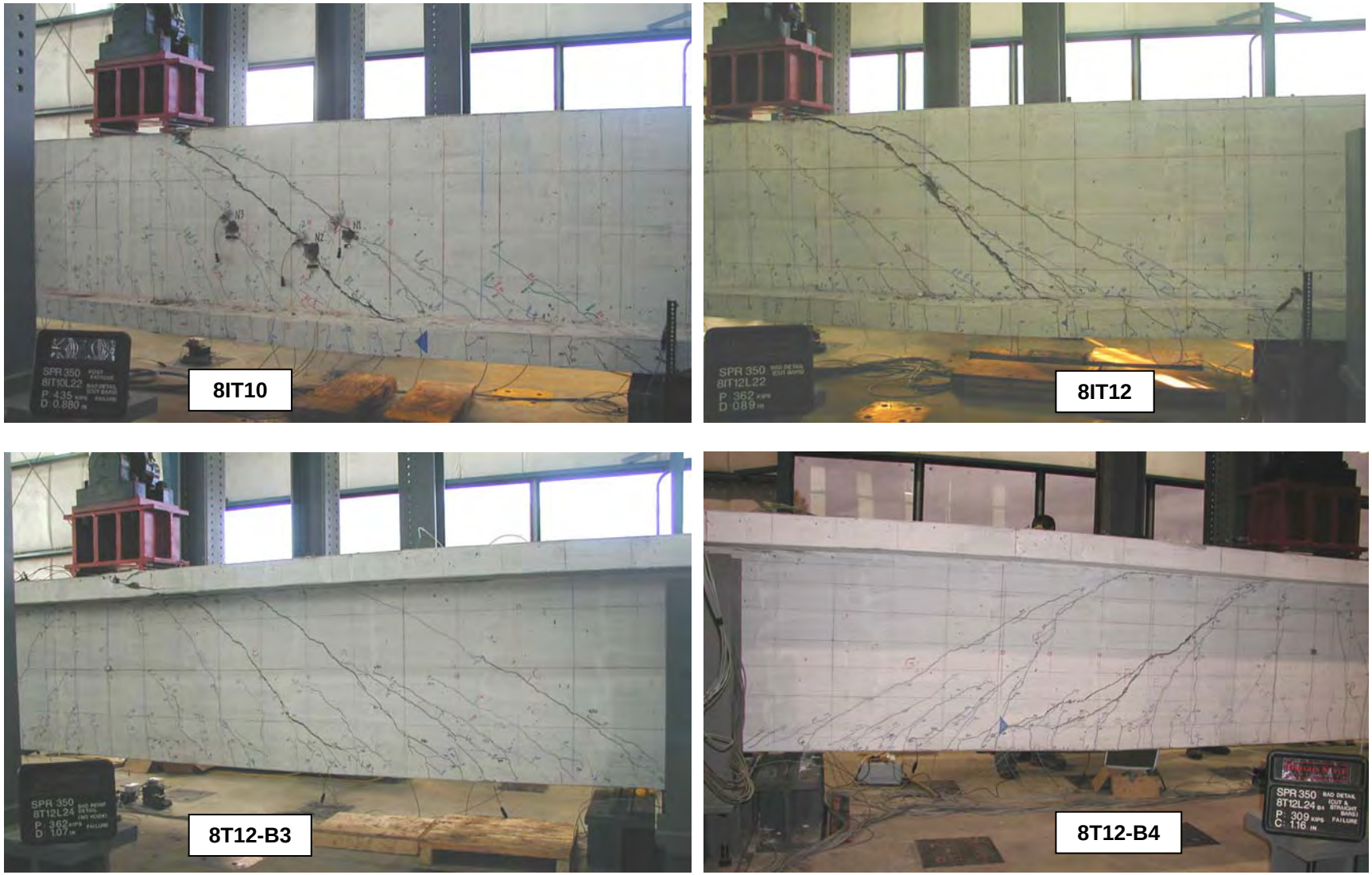

Figure 3.12h: Digital photographs at failure for Group 8 specimens

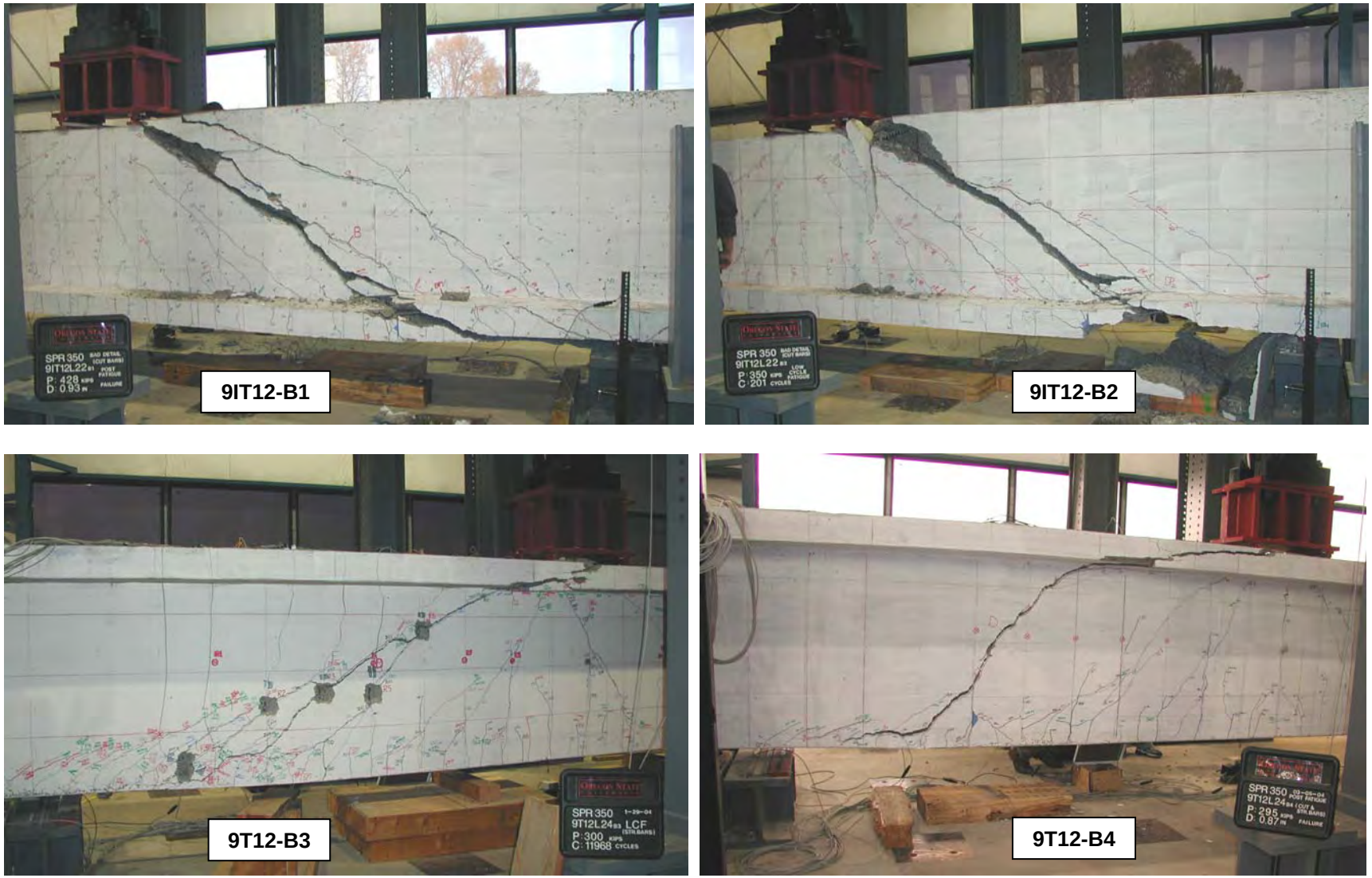

Figure 3.12i: Digital photographs at failure for Group 9 specimens

Figure 3.12j: Digital photographs at failure for Group 10 specimens

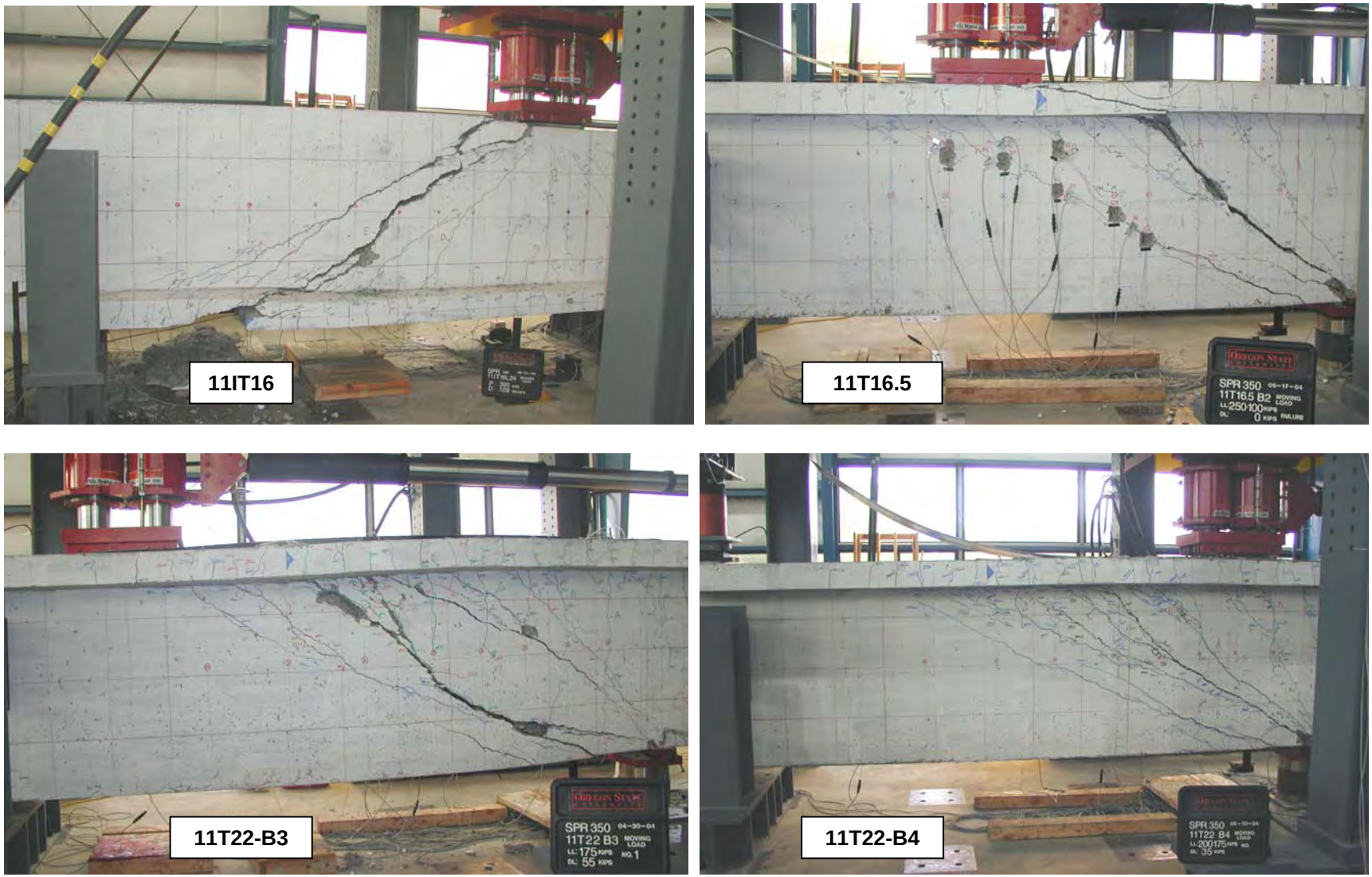

Figure 3.12k: Digital photographs at failure for Group 11 specimens

Table 3.5: Salient test results for laboratory specimens

No.	Specimen	Loading Protocol	Failure Mode	S (in)	f'_c (psi)		L (ft)	V_{EXP} (kips)	V_{DL} (kips)	V_{APP} (kips)	V_{cr} (kips)	Δ (in)	Δ_{Diag} (in)	w_{cr} (in)
					Stem	Deck								
1	1T6	Control	Flexural	6	4700	4370	24.0	206.5	0.0	206.5	37.0	1.35	0.32	0.030
2	1IT6	Control	Flexural	6	4775	4515	24.0	236.0	0.0	236.0	60.0	1.60	0.18	0.040
3	1T18	Control	Shear	18	4925	4360	24.0	166.1	3.7	169.8	34.0	1.08	0.34	0.165
4	1IT18	Control	Shear	18	4550	4410	24.0	154.5	4.3	158.8	36.5	0.97	0.38	0.188
5	2T10	Control	Shear	10	3550	3360	24.0	201.8	3.5	205.3	33.5	1.32	0.39	0.080
6	2IT10	Control	Anchorage	10	3290	3105	24.0	200.7	4.6	205.3	67.5	1.20	0.28	0.125
7	2T12	Control	Shear	12	3520	3440	24.0	188.9	4.0	192.9	11.0	1.17	0.28	0.109
8	2IT12	Control	Anchorage	12	3575	3005	24.0	179.2	4.6	183.8	45.0	1.24	0.34	0.104
9	3T12	HC Fatigue	Shear	12	3990	3660	24.0	184.8	3.9	188.7	40.0	1.22	0.41	0.109
10	3IT12	HC Fatigue	Shear	12	4180	3455	21.6	204.3	3.2	207.5	47.5	1.03	0.29	0.143
11	3T18	Control	Shear	18	3970	3440	24.0	149.5	3.8	153.3	27.0	1.24	0.50	0.210
12	3IT18	HC Fatigue	Shear	18	3915	3220	21.6	142.5	4.6	147.1	49.5	0.74	0.25	0.171
13	4IT6-10	Control	Anchorage	6 , 10	3790	3410	16, 24	211.4	5.1	216.5	88.5	1.13	0.24	0.080
14	4IT8-12	Control	Shear	8 , 12	3710	3595	16, 21.6	237.8	5.1	242.9	62.0	1.06	0.20	0.172
15	4T10-12	Control	Shear	10 , 12	3945	2995	20.0	240.9	3.5	244.4	49.0	0.72	0.20	0.081
16	4T12-18	Control	Shear	12 , 18	4060	3000	20.0	236.6	3.2	239.8	36.0	0.68	0.17	0.095
17	5IT12-B1	HC Fatigue	Shear	12	3700	4610	21.6	191.1	4.0	195.1	60.5	0.87	0.29	0.094
18	5IT12-B2	Control‡	Shear	12	4160	4640	21.6	213.5	4.0	217.5	76.5	0.89	0.28	0.101‡‡
19	5IT12-B3	LC Fatigue	Shear	12	4310	4530	21.6	189.3	4.0	193.3	69.5	1.18	0.65	0.240
20	5IT12-B4	Control	Shear	12	4130	4130	21.6	202.7	3.8	206.5	73.5	1.01	0.42	0.124
21	6T6	LC Fatigue	Shear	6*	4590	4260	21.6	236.6	3.4	240.0	NA	1.14	0.33	0.149
22	6IT6	LC Fatigue	Not Failed	6	5110	3920	21.6	237.6	0.0	237.6	NA	1.10	0.08	0.096
23	6T10	HC Fatigue	Flexural	10	4595	4195	24.0	210.4	0.0	210.4	NA	2.34	0.38	0.120
24	6IT10	HC Fatigue	Shear	10	5495	3875	21.6	234.0	3.8	237.8	NA	1.11	0.35	0.131
25	7T6	Control	Flexural	6	4405	4215	24.0	213.7	0.0	213.7	43.5	1.50	0.17	0.080
26	7IT6	LC Fatigue	Shear	6*	4350	3740	21.6	203.0	4.0	207.0	48.5	0.97	0.23	0.200
27	7T12	Control	Shear	12	4280	4310	21.6	211.5	4.1	215.6	65.0	0.96	0.27	0.216
28	7IT12	Control	Shear	12	4165	3995	21.6	200.1	4.3	204.4	55.5	0.81	0.20	0.132

Table 3.5 (continued): Salient test results for laboratory specimens

No.	Specimen	Loading Protocol	Failure Mode	S (in)	f'c (psi)		L (ft)	V_{EXP} (kips)	V_{DL} (kips)	V_{APP} (kips)	V_{cr} (kips)	Δ (in)	Δ_{Diag} (in)	w_{cr} (in)
					Stem	Deck								
29	8IT10	HC Fatigue	Shear	10	4750	4090	22	218.3	3.5	221.8	63.5	1.02	0.24	0.090
30	8IT12	Control	Shear	12	4840	4045	22	182.3	3.8	186.1	59.5	0.83	0.20	0.113
31	8T12-B3	Control	Shear	12	5070	4570	24	180.7	3.2	183.9	37.5	1.02	0.24	0.080
32	8T12-B4	Control	Shear	12	4995	4725	24	156.0	2.9	158.9	50.0	1.12	0.25	0.170
33	9IT12-B1	HC Fatigue	Shear	12	4285	5405	22	213.0	3.8	216.8	57.0	1.03	0.26	0.147
34	9IT12-B2	LC Fatigue	Shear	12	4605	5465	22	179.3	4.0	183.3	73.5	1.06	0.60	0.110
35	9T12-B3	LC Fatigue	Shear	12	4645	4890	24	166.8	3.5	170.3	34.5	0.98	0.33	0.138
36	9T12-B4	HC Fatigue	Shear	12	4705	4910	24	148.7	4.8	153.5	47.0	1.02	0.32	0.167
37	10T0	Control	Shear	0	4610	4445	24	50.4	4.4	54.8	NA	0.37	0.03	0.080
38	10T12	Moving Load	Shear	12	4655	4405	21	217.4	6.7	224.1	NA	0.45	NA	0.137
39	10T24-B3	LC Fatigue	Shear	24	3450	3995	24	103.7	4.2	107.9	41.0	0.93	0.55	0.284
40	10T24-B4	Control	Shear	24	3420	3740	24	120.7	4.6	125.3	49.5	1.00	0.48	0.097
41	11IT16	Moving Load	Shear	10.5	4635	4430	21	185	4.6	189.6	NA	0.95	NA	0.084
42	11T16.5	Moving Load	Shear	8	4970	4170	13.5†	244	8.9	252.9	NA	1.60	NA	0.04
43	11T22-B3	Moving Load	Shear	10.5-16	4470	3510	13.5†	208.2	7.6	215.8	NA	2.57	NA	0.229
44	11T22-B4	Moving Load	Shear	10.5	4750	4010	13.5†	194.4	8.4	202.8	NA	2.16	NA	0.07

* Cut-stirrup testing performed
‡ Using force control and faster loading rate
‡‡ Taken at 0 kip
† Length of cantilever

S is the stirrup spacing;
L is the span distance between supports;
V_{EXP} is the applied actuator shear force;
V_{DL} is the specimen self-weight shear force at the failure section;
V_{APP} is the total shear force from the actuator load and dead load shear at the failure section;
V_{cr} is the shear force at first diagonal cracking;
Δ is the midspan displacement at failure;
Δ_{Diag} is the maximum displacement measured on one of the web diagonal displacement sensors (crossing multiple cracks); and
w_{cr} is the maximum crack width measured at peak load prior to failure.

Shear forces reported in Table 3.5 include the applied shear on the specimen from the actuator, V_{EXP}, the shear force from the beam self-weight acting at the failure plane, V_{DL}, and the total shear force, V_{APP}. The shear force from specimen self-weight was estimated by computing the weight of concrete acting on the diagonally cracked failure plane as illustrated in Figure 3.13. A unit weight of reinforced concrete equal to 150 lb/ft^3 was used to estimate the additional specimen self-weight at the cracked section.

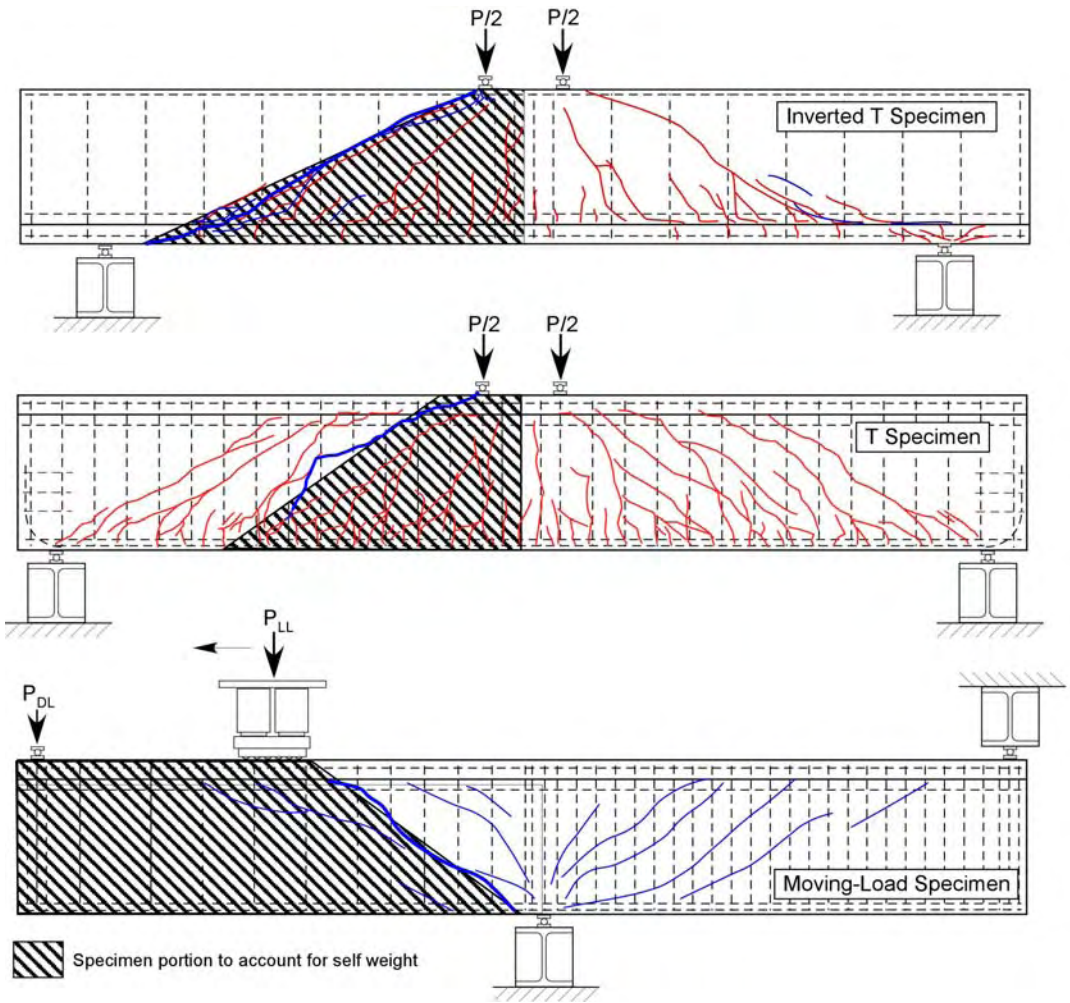

Figure 3.13: Approach used to determine self-weight at the failure location for different specimens

The average shear stress at the onset of diagonal cracking was estimated from the applied shear force based on observation of the first significant strain deviation for the instrumented stirrups. An estimated self-weight contribution (using the weight from a quarter span length) was added to the applied shear to estimate the total shear force at the onset of diagonal cracking. The combined shear force was divided by the web width and the effective depth to the flexural reinforcing steel (43.4 in. for T and 45 in. for IT specimens) to determine the diagonal cracking shear stress.

Maximum diagonal deformation was determined from one of the 12 displacement sensors mounted diagonally on the stem of the beam in one of the six segments along the span. Crack motions were monitored for selected specimens to determine the amount of deformation occurring in the parallel and transverse directions. This was performed by marking a grid of reference points on the specimen web across a diagonal crack. Digital photographs taken of the grid points prior to and during loading were superimposed to determine the crack motions. Two crack motion studies are shown in Figures 3.14a and 3.14b.

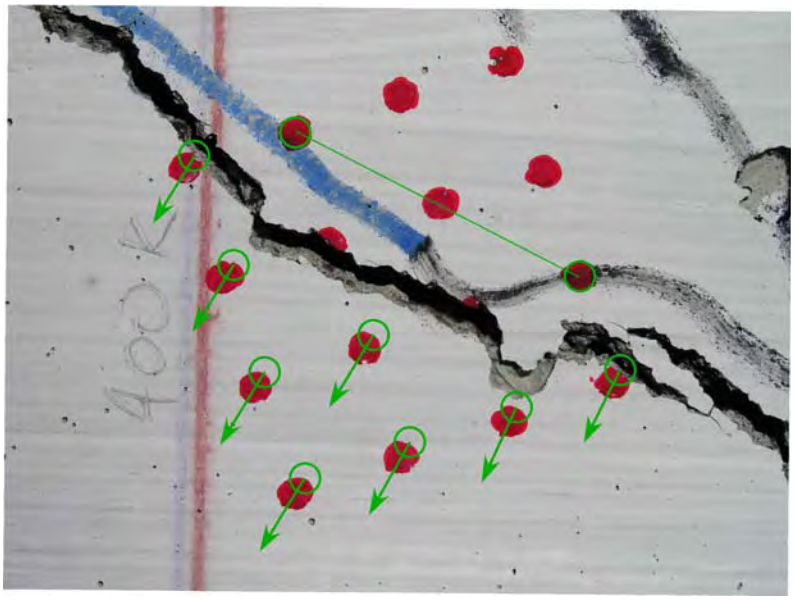

Figure 3.14a: Crack motion for specimen C4T12 (unbonded stirrups)

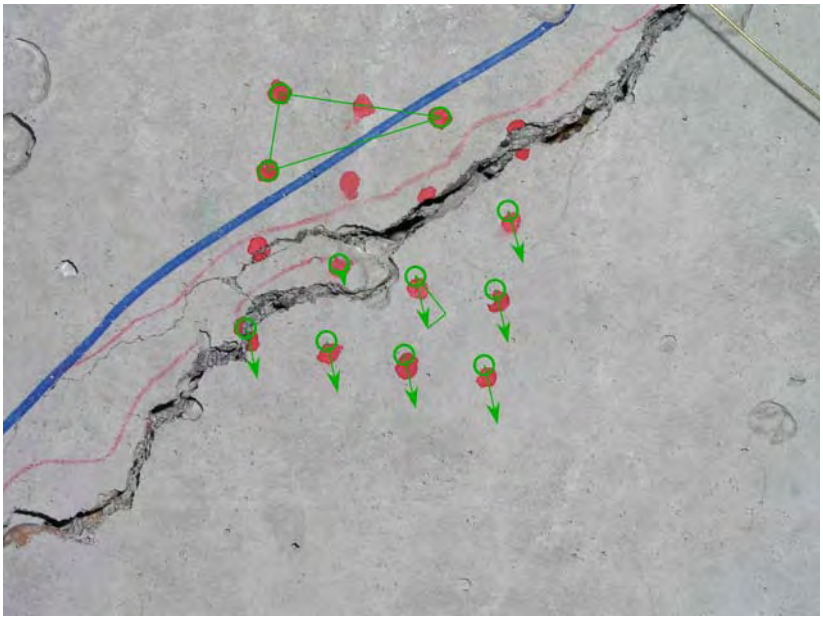

Figure 3.14b: Crack motion for specimen IT18

The specimen with debonded stirrups exhibited crack motions principally in the direction perpendicular to the crack (crack opening) (Figure 3.14a). Specimens with bonded stirrups typically exhibited crack motions with transverse deformations (crack opening) approximately three times that observed parallel to the crack (crack slipping) (Figure 3.14b). The observed crack motions and crack widths indicate that force transfer across the widest portions of the diagonal cracks near midheight is unlikely for the stationary loading considered.

3.3 INCREASED LOADING RATE TEST

3.3.1 Test Method

Typical capacity tests were performed near static conditions, with a slowly applied loading rate. To simulate the effect of a more realistic loading rate possible on a vintage RCDG bridge, a specimen (5IT12-B2) was tested under load control with variable load rates. A typical RCDG span length for a bridge identified as containing a high density of diagonal cracks was determined as 55 ft from a database of the ODOT bridge inventory (*Higgins, et al. 2004*). For a truck traveling over the bridge at the posted speed of 55 mph, a bent cap would reach peak load in approximately 0.7 sec and then unload in the same time period. Table 3.6a indicates typical time to reach peak load in a bent cap for various span lengths and vehicle speeds. Girders may be loaded much more rapidly, particularly at locations near supports where the load comes on suddenly. This was observed in the field test data presented in a previous section.

Table 3.6a: Time to peak load at a bent cap for different span lengths and vehicle speeds

Truck Speed (mph)	Span Length (ft)	Time to Peak (sec)
50	45	0.614
50	50	0.682
50	55	0.750
50	60	0.818
55	45	0.558
55	50	0.620
55	55	0.682
55	60	0.744
65	45	0.472
65	50	0.524
65	55	0.577
65	60	0.629

The test specimen was subjected to the conventional loading protocol of increasing loads followed by unloading, but instead of using displacement feedback for the servo-hydraulic control system, load control was used. Force was applied to the specimen using a ramp function to achieve the target load amplitude and was followed by unloading at the same rate. Loading rates were initially selected to be in the range of that observed in the field. However, once cracking occurred and the specimen stiffness reduced, the hydraulic flow available to the large

force actuator was not sufficient to permit achievement of the target loading rates. Thus the loading rate was reduced as higher load levels were imposed. The loading histories are shown in Figure 3.15 and are summarized in Table 3.6b. The highest loading rate achieved was 369 kips/sec. The specimen failed at a load of approximately 429 kips with a loading rate of 124 kips/sec.

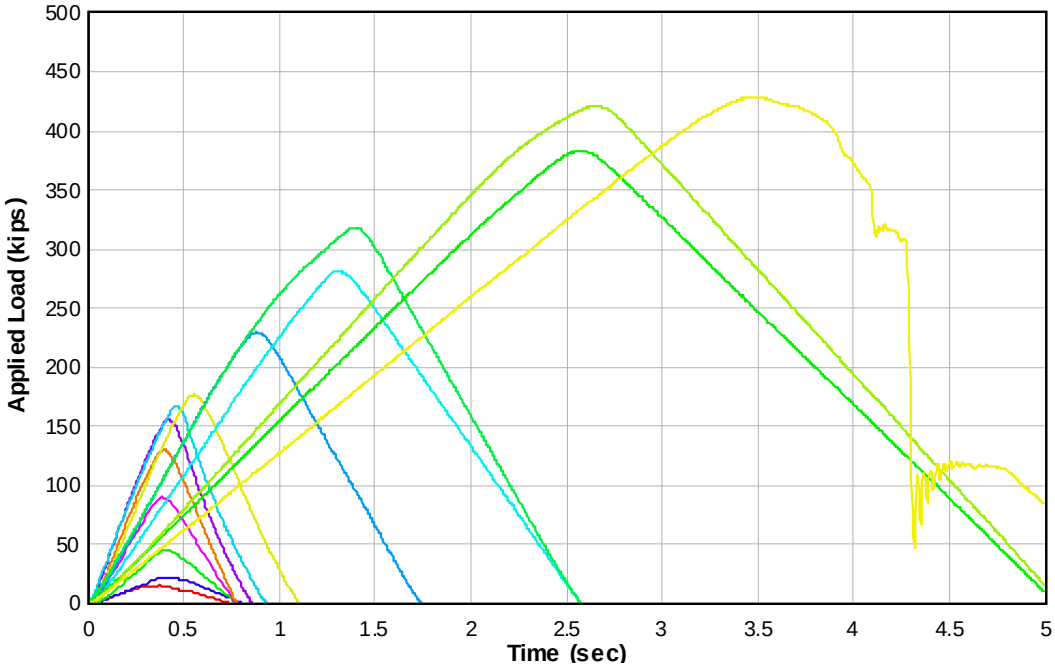

Figure 3.15: Loading histories for specimen tested at higher loading rates

Table 3.6b: Loading rates for different test load increments

Increment Number	Time to Peak (sec)	Peak Force (kips)	Loading Rate (kips/sec)
1	0.276	15.7	57
2	0.392	22.6	57
3	0.368	45.6	124
4	0.376	90.1	240
5	0.393	130.6	332
6	0.424	156.5	369
7	0.463	167.5	362
8	0.551	177.2	322
9	0.882	229.6	260
10	1.298	281.3	217
11	1.403	318.2	227
12	2.555	383.2	150
13	2.630	421.0	160
14	3.450	428.9	124

3.3.2 Experimental Results

During this test it was not possible to measure and mark cracks at the maximum load, as the specimen was fully unloaded after application of the loading ramp. The cracks were marked and measured with no force on the specimen. At this unloaded condition, flexural cracks were not easy to distinguish, but the diagonal cracks were quite evident. Diagonal cracks were visible after the peak force of 156 kips was achieved; however flexural cracks in the flange were not visible until the applied force increased to 178 kips. The specimen tested at the higher loading rate exhibited slightly higher capacity (5.3%) and lower overall displacement (11.9%) than a similar specimen cast within the same group (specimen 5IT12-B4) tested under the control loading protocol.

The reduced deflection observed with this specimen can be partially attributed to reduced creep deformations, as the load was never held at a large magnitude during crack mapping and inspection. The observed failure mode was similar to other specimens and the overall behavior was not markedly different. The slight increase in capacity at the higher loading rate may slightly offset some of the amplified force effects due to dynamic and impact response on actual bridge members due to vehicles traveling at highway speeds.

3.4 MOVING SUPPORT TESTS

3.4.1 Test Method

A series of two tests was performed by placing specimens on relatively closely spaced supports and loading using the conventional loading protocol until formation of significant diagonal cracks and achievement of a prescribed force level of 400 kips. After achieving the prescribed load magnitude, loading was halted and the supports were moved to new locations, thereby providing a longer test span.

The specimens had two different stirrup spacings, 6 in. near midspan and 10 in. near beam ends for 4IT6-10 specimen; and 8 in. near midspan and 12 in. near beam ends for 4IT8-12 specimen. Transverse reinforcement details of these specimens reflected reinforcement details near the mid-bent region of a girder in a continuous span bridge to the dead load points of inflection, where stirrup spacing becomes incrementally larger toward the midspan region.

The specimens were precracked using the control loading protocol with a span length equal to 16 ft. The precracking load was 400 kips for both specimens. Then the supports were pushed out to produce a span length of 24 ft for 4IT6-10 specimen and a span length of 21.6 ft for 4IT8-12 specimen before being loaded to failure. This testing procedure attempted to simulate load effects within a girder near the bent cap region. A vehicle could produce diagonal cracking within the region with tighter stirrup spacing and then produce a subsequent diagonal crack at a location further out on the span, where the stirrup spacing is larger.

3.4.2 Experimental Observation

Crack widths measured using a crack comparator card during the precracking stage were fairly narrow, 0.025 in. at 400 kips applied load for 4IT6-10 specimen and 0.04 in. at 400 kips applied load for 4IT8-12 specimen. During failure testing, new cracks formed outside the 16 ft span length and developed quickly. The largest crack widths measured at the loadstep prior to failure were 0.08 in. for specimen 4IT6-10 and 0.172 in. for specimen 4IT8-12.

The diagonal-tension crack widths previously formed in the precracking stage were fairly constant during the failure testing. Specimen 4IT6-10 failed due to an anchorage failure at the north-end support with a total applied load of 423 kips. Specimen 4IT8-12 exhibited a shear-compression failure in the north side with an applied load of 476 kips. The failure crack spanned from the support plate to the loading plate crossing both the 8 in. and 12 in. stirrup spacing regions.

3.5 INFLUENCE OF FLEXURAL BAR DETAILS

3.5.1 Test Method

Specimens from groups 8 and 9 were designed and fabricated with different anchorage and flexural bar cutoff details as shown in Appendix A1. Specimens 8IT10, 8IT12, 8T12-B4, 9IT12-B1, 9IT12-B2, and 9T12-B4 contained straight end bar anchorages and flexural bar cutoff details. Specimens 8T12-B3 and 9T12-B3 were reinforced with continuous reinforcing bars, except they used straight bar anchorages at the ends instead of 90° hooked anchorages.

For specimens with cutoff details, the flexural reinforcing steel (six #11 bars for Inverted-T specimens and five #11 bars for T specimens) provided adequate flexural capacity at the midspan region. The number of flexural bars was reduced toward the ends of the specimens. These cutoff locations, in the flexural tension region, combined with no additional stirrups, represent typical 1950s vintage construction details. For Inverted-T specimens, four #11 bars and for T specimens three #11 bars, were extended into the supports at the beam end regions.

The specimens were loaded with various loading protocols. Specimens 8IT12, 8T12-B3, and 8T12-B4 were tested with the control loading protocol. High-cycle fatigue loads were applied to specimens 8IT10, 9IT12-B1, and 9T12-B4; and specimens 9IT12-B2 and 9T12-B3 were subjected to low-cycle fatigue loading.

3.5.2 Experimental Results

Wide flexural cracks formed at the location of cut flexural bars, when the specimens were loaded with about 60% of the ultimate load. Flexural cracks at these locations propagated diagonally up toward the loading plate and eventually led to specimen failure. The specimens with straight end anchorages and cutoff details had smaller failure loads and displacements at the peak load than those of similar control specimens. For specimens in Groups 8 and 9, angles of the failure diagonal cracks were steeper than those of the control specimens. The failure load of specimen 8T12-B3 with straight end details was 361 kips and lower than that of 2T12 specimen (378 kips),

even though concrete strength of 8T12-B3 (5070 psi) was much higher than that of specimen 2T12 (3520 psi) and the same amount of flexural steel area was provided. This indicated that straight end flexural bar details caused the reduced specimen capacity.

3.6 SUMMARY OBSERVATIONS FROM CONTROL LABORATORY TESTS:

- Initial diagonal-tension cracking was observed at an average concrete shear stress approximately corresponding to $v_c = 1.4\sqrt{f'_c}$, with a coefficient of variation of 0.29.

- Anchorage of flexural steel was key to developing higher ultimate capacity, particularly for inverted-T specimens with straight bar development lengths.

- In regions of relatively high shear containing flexural reinforcing steel cutoffs, flexural cracks are likely to form into diagonal cracks near bar cutoffs due to the stress concentration at these locations. Diagonal cracks may not be as well constrained at the level of the flexural steel at these regions.

- Diagonal-tension crack widths measured above hairline were sufficiently wide to permit the stirrup to reach yield (at the crack location).

- Diagonal-tension cracks were quite wide at mid-depth of the beam, tapered to zero in the compression zone and were fine at the level of the flexural steel. This condition was also observed in the field.

- Offset of the concrete surface was observed locally at stirrup locations due to incipient spalling at diagonal crack locations and was attributed to localized stirrup debonding.

- Offset of the entire cross-section was observed for a test with widely spaced stirrups (18 in. spacing) and occurred near ultimate load.

- Stem cracking at the deck interface was observed in tests for both T and IT specimens. The stem/deck cracking at the interface exhibited lengths of approximately only 12 in. before intersecting another diagonal web crack.

- Initial cracking damage may not necessarily contribute to the final failure mode, as observed for specimens 4IT6-10 and 4IT8-12. Thus, if loading conditions change so as to create a new critical region in a beam, the beam may fail at a section that did not previously exhibit cracking.

- Crack width alone may not indicate the level of previous damage to the beam. Tightly spaced stirrups exhibited small crack widths at failure while widely spaced stirrups exhibited large and wider cracks at failure. Crack width for a given stirrup spacing may provide a better relative measure of damage.

- Observed crack motions indicated relatively little motion parallel to diagonal cracks, with more motion in the direction transverse to the crack. As a result, little or no aggregate interlock may be available. Further, little dowel action from the flexural steel may exist from these deformations. However, as seen in later analysis, methods to predict capacity of specimens that account for force transfer across cracks reasonably predicted capacity of the specimens, even with the wide cracks.

- Angle of diagonal crack was dependent on the interaction of moment and shear at the section. It was also influenced by the flexural reinforcing details.

- Diagonal-tension failure of the beam was generally attributed to failure at a particular section due to anchorage failure of flexural steel in tension zone or failure of compression zone, precipitated by the diagonal cracks. In all cases, diagonal cracks were sufficiently wide to permit yielding of stirrups.

- A specimen tested at a higher loading rate exhibited slightly higher capacity and lower overall displacement. The reduced displacement was likely due to reduced creep deformations.

3.7 LOW-CYCLE FATIGUE TESTS

Repeated loading effects can be divided into two phenomena: low-cycle fatigue and high-cycle fatigue. High-cycle fatigue (HCF) is generally characterized by millions of load cycles. Low-cycle fatigue (LCF), however, is less well defined. Low cycle fatigue generally consists of fewer than 10,000 cycles, but is defined as fatigue caused by repeated plastic deformations (*Bannantine, et al. 1990*). In reinforced concrete girders with diagonal cracks, LCF occurs when the girder is repeatedly subjected to load effects that produce stresses above yield in stirrups at diagonal crack locations.

The phenomenon of LCF has been studied previously, but earlier work has focused on flexural response during seismic events (*Manfredi and Pecce 1997*). During seismic loading, structures are exposed to a low number of cycles, but experience stress reversals that cause compression in the reinforcing steel. In bridges, stirrups are exposed primarily to tensile stresses without reversals causing compression. This is due to the self-weight of the structure acting at the diagonal crack location, so that even small live load induced unloading caused by continuous span effects may not produce compressive stress in the stirrups.

A series of tests was performed to evaluate the life of girders under repeated overloads that cause yielding of stirrups. The load ranges were selected to simulate different overload events. Specimen variables included: T and inverted-T configurations, stirrup spacing, and flexural reinforcing details. Test specimens were subjected to the conventional control loading protocol up to prescribed force levels between 72% and 85% of the nominal shear capacity. Nominal shear capacity was determined using AASHTO-MCFT (*AASHTO-LRFD 2003*). The specimen was then subjected to repeated applications of a prescribed force amplitude. Constant force amplitude loading was continued until the observed increment of deformation became linear or until a given number of cycles was achieved. Subsequently, load amplitudes were increased and

again a number of constant force amplitude cycles was applied until the eventual failure of the specimen.

3.7.1 Test Method

The loading frame for the low-cycle fatigue tests was the same as that used for the control tests, as described previously. The specimen was loaded until the desired force magnitude was reached and then additional strain gages and crack displacement sensors were added to the specimens at diagonal crack locations. After instruments were placed, testing was continued under load control, with force feedback to the servo-hydraulic control system provided by a load cell in series with the hydraulic actuator.

Two 15 GPM servovalves were used to facilitate application of the repeated load at frequencies between 0.1 and 0.25 Hz. This relatively low loading rate required several days to complete testing for some specimens. The fluctuating fatigue load was applied to the specimens at midspan through a spreader beam with reaction points on the specimen spaced 24 in. on-center.

During testing, the fatigue loading was suspended and the crack widths and extents were measured and recorded. These inspection intervals varied for the different specimens but were performed before a higher load range was applied or after a certain number of cycles was achieved. Crack widths were measured using an ODOT crack comparator with the actuator load magnitude held constant at applied forces between 150 and 200 kips. The observed crack extensions during low-cycle fatigue testing are shown in Appendix A5 for each of specimens.

3.7.2 Experimental Results

Seven specimens were subjected to low-cycle fatigue testing. These included specimens 5IT12-B3, 6T6, 6IT6, 7IT6, 9IT12, 9T12, and 10T24. The specimens tested were both T and inverted-T configurations, and contained stirrups spaced between 6 and 24 in. as well as different flexural reinforcing bar details. Specimen details are shown in Appendix A1. Initial force amplitudes were varied for the different specimens and are summarized in Table 3.7 with the number of cycles for each force amplitude.

Measured stirrup stress ranges varied between specimens due to the different specimen configurations and loading levels imposed during fatigue testing. However, strain gages on stirrup legs crossing diagonal crack locations indicated strains at or above the yield strain for the load amplitudes investigated. The measured stirrup strain ranges for the instrumented stirrups applied after diagonal cracking, are summarized in Table 3.8. These data were taken from the response histories near the end of the particular cycle load range.

Table 3.7: Loading levels and number of cycles for low-cycle fatigue tests

Specimen	Load Level (kips)	Vn (kips)	V/Vn	Vs/Vn	Vs/Vc	N
5IT12	303	186	0.836	0.436	1.091	50
	353	186	0.970	0.436	0.816	10
	303	186	0.836	0.436	1.091	10
	353	186	0.970	0.436	0.816	190
	378	186	1.038	0.436	0.725	49
					Total Cycles	309
Specimen	Load Level (kips)	Vn (kips)	V/Vn	Vs/Vn	Vs/Vc	N
6T6	394	235	0.853			200
	425	235	0.919			200
	450	235	0.972			200
	472	235	1.019			100
	400	235	0.866			600
	450	235	0.972			200
	472	235	1.019			200
	400	235	0.866			150
	450	235	0.972			150
	472	235	1.019			24
					Total Cycles	2024
Specimen	Load Level (kips)	Vn (kips)	V/Vn	Vs/Vn	Vs/Vc	N
6IT6	401	256	0.783	0.634	4.240	150
	426	256	0.832	0.634	3.196	200
	451	256	0.881	0.634	2.565	200
	474	256	0.926	0.634	2.170	37
					Total Cycles	587
Specimen	Load Level (kips)	Vn (kips)	V/Vn	Vs/V	Vs/Vc	N
7IT6	404	253	0.814			553
					Total Cycles	553
Specimen	Load Level (kips)	Vn (kips)	V/Vn	Vs/Vn	Vs/Vc	N
9T12	282	173	0.835	0.586	2.353	1000
	301	173	0.890	0.586	1.928	365
	309	173	0.913	0.586	1.792	10500
	332	173	0.980	0.586	1.489	1468
					Total Cycles	13333
Specimen	Load Level (kips)	Vn (kips)	V/Vn	Vs/V	Vs/Vc	N
9IT12	255	182	0.723	0.446	1.610	200
	305	182	0.860	0.446	1.076	100
	357	182	1.003	0.446	0.800	201
					Total Cycles	501
Specimen	Load Level (kips)	Vn (kips)	V/Vn	Vs/V	Vs/Vc	N
10T24	195	123	0.827	0.330	0.663	10000
	207	123	0.876	0.330	0.604	4057
					Total Cycles	14057

Table 3.8: Average strain range for low-cycle fatigue tests (strain is microstrain)

10T24

	V/Vn=.823	ε range	Yield?
Internal	Green 1	1294	No
	Green 4	753	No
External	Green 5	3254	Yes
	Green 6	2089	Yes
	Green 7	832	Yes
Internal	Grey 2	3935	Yes
	Grey 3	-480	Yes
External	Grey 4	244	No
	Grey 5	3467	Yes
	Grey 7	2170	Yes

	V/Vn=.875	ε range	Yield?
Internal	Green 1	1443	No
External	Green 4	852	No
	Green 5	3447	Yes
	Green 6	2316	Yes
	Green 7	820	Yes
Internal	Grey 3	-3	Yes
External	Grey 4	434	No
	Grey 5	3878	Yes
	Grey 7	2249	Yes

9T12

	V/Vn=.835	ε range	Yield?
External	Yellow 2	1815	Yes
Internal	Yellow 5	1248	No
External	Red 6	2336	Yes

	V/Vn=.890	ε range	Yield?
Internal	Yellow 5	1464	No

	V/Vn=.913	ε range	Yield?
External	Yellow 1	2877	Yes
	Yellow 2	2284	Yes
	Yellow 3	2306	Yes
	Yellow 4	2488	Yes
Internal	Yellow 5	1428	No
External	Yellow 6	1906	Yes
External	Red 2	2129	Yes
	Red 3	3190	Yes
External	Red 5	3099	Yes
	Red 6	2619	Yes

	V/Vn=.980	ε range	Yield?
External	Yellow 1	3465	Yes
	Yellow 3	2654	Yes
External	Yellow 4	2701	Yes
	Yellow 6	2139	Yes
External	Red 2	2851	Yes
	Red 3	3414	Yes
	Red 5	3575	Yes
	Red 6	3808	Yes

9IT12

	V/Vn=.723	ε range	Yield?
Internal	Yellow 1	1348	No
	Yellow 3	1312	No
	Yellow 4	903	No
	Yellow 5	1528	No
Internal	Red 1	552	No
	Red 2	4346	Yes
	Red 3	863	Yes
	Red 4	1670	Yes
	Red 5	32	No

	V/Vn=.860	ε range	Yield?
Internal	Yellow 1	1746	No
	Yellow 3	1875	Yes
	Yellow 4	1253	No
	Yellow 5	1558	Yes
Internal	Red 1	890	No
	Red 2	481	Yes
	Red 3	3144	Yes
	Red 4	1728	Yes
	Red 5	17	No

	V/Vn=1	ε range	Yield?
Internal	Yellow 1	2012	Yes
	Yellow 3	2664	Yes
	Yellow 4	1386	Yes
	Yellow 5	1622	Yes
Internal	Red 2	826	Yes
	Red 4	1730	Yes
	Red 5	14	No

6T6

	V/Vn=.866	ε range	Yield?
External	Green 1	2176	Yes
	Green 2	2014	Yes
	Green 3	1788	Yes
	Green 4	1896	Yes

	V/Vn=.972	ε range	Yield?
External	Green 1	Cut	Yes
	Green 2	Cut	Yes
	Green 3	3352	Yes
	Green 4	Cut	Yes

6IT6

No Strain Gages Used

5IT12

	V/Vn=.836	ε range	Yield?
Internal	Red 1	-57	No
	Red 2	30	No
	Red 3	244	No
	Red 4	979	No
	Red 5	1145	Yes
Internal	Yellow 1	-7	No
	Yellow 2	52	No
	Yellow 3	-3151	Yes Comp
	Yellow 4	2145	Yes
	Yellow 5	581	No
	Yellow 6	1547	Yes

	V/Vn=.970	ε range	Yield?
Internal	Red 1	-63	No
	Red 2	57	No
	Red 3	421	No
	Red 4	1516	Yes
	Red 5	1639	Yes
Internal	Yellow 1	-8	No
	Yellow 2	66	No
	Yellow 3	-428.3	Yes Comp
	Yellow 4	2144	Yes
	Yellow 5	869	No
	Yellow 6	1816	Yes

	V/Vn=1.04	ε range	Yield?
Internal	Red 1	-61	No
	Red 2	68	No
	Red 3	500	No
	Red 5	1701	Yes
Internal	Yellow 1	-5	No
	Yellow 2	69	No
	Yellow 3	-399	Yes Comp
	Yellow 4	869	Yes
	Yellow 5	1583	No

7IT6

	V/Vn=.836	ε range	Yield?
Internal	Grey 2	1324	Yes
	Grey 4	1191	Yes
	Grey 5	1343	Yes
	Grey 6	1208	Yes
External	Grey 8	1689	Yes
Internal	Green 1	587	No
	Green 2	1199	No
	Green 3	173	No
	Green 4	2168	Yes
Internal	Green 6	1796	Yes
External	Green 7	1595	Yes

Example stirrup strain response during a typical low-cycle fatigue test is shown in Figures 3.16. The strain range remains consistent even as the mean value tends to increase. The mean strain increase occurred rapidly after the initial load cycle was applied and then diminished to a steady increment during subsequent cycles.

Example crack displacement response during a typical low-cycle fatigue test is shown in Figure 3.17. This exhibits similar behavior to that observed for the stirrup strains. Complete histories of

stirrup strain and diagonal crack motions during fatigue tests as well as other sensor data are contained in Appendix A5 and individual test descriptions are summarized below.

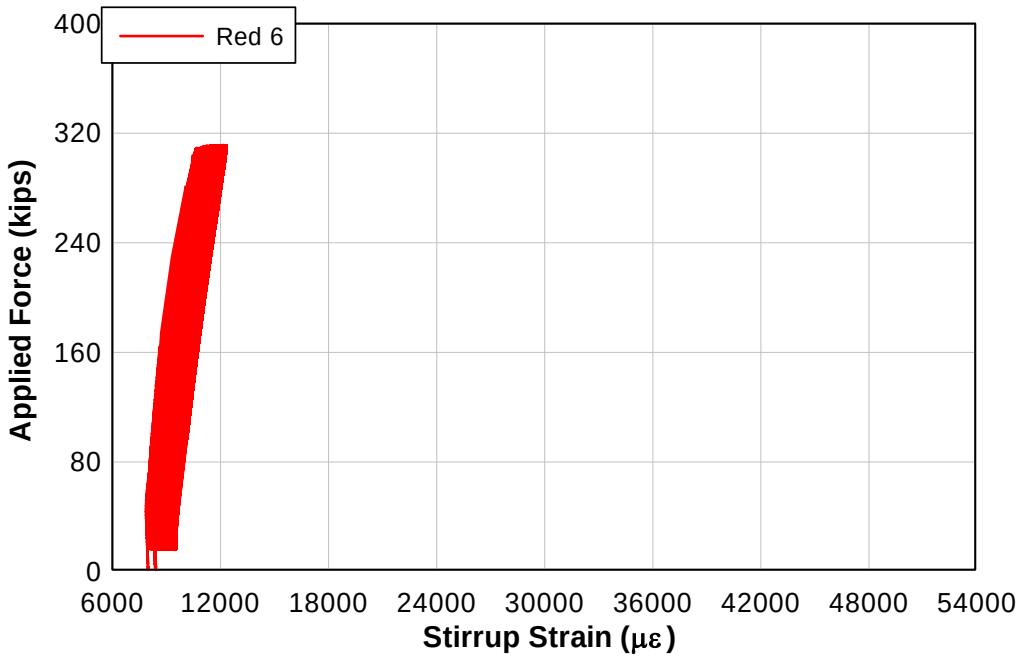

Figure 3.16: Typical applied force - stirrup strain response from low cycle fatigue specimen 9T12, part 4

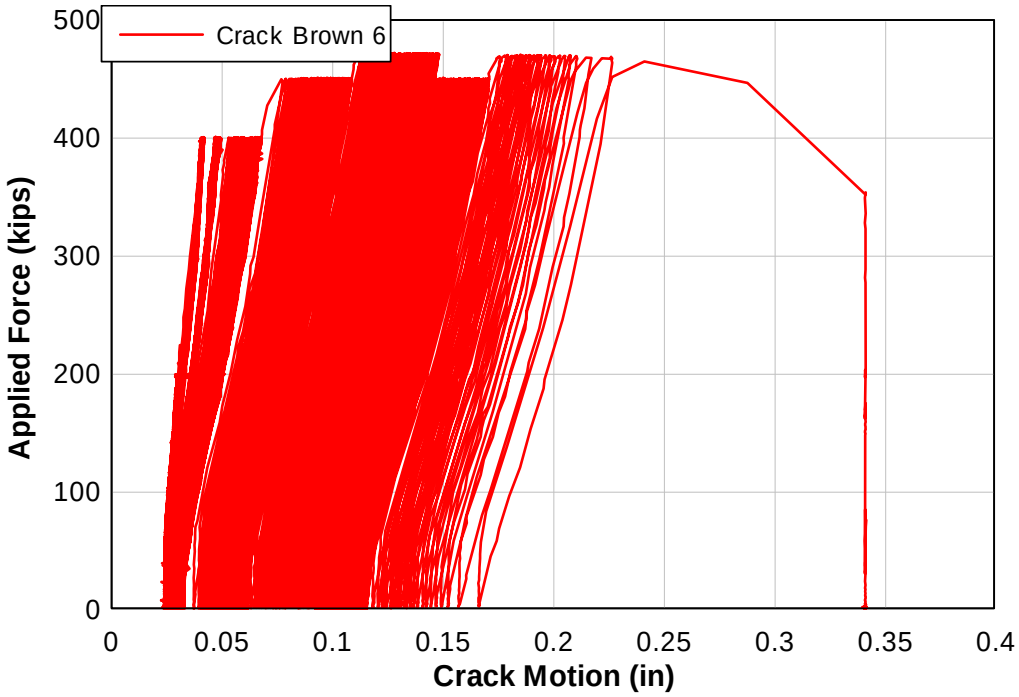

Figure 3.17: Typical applied force - crack motion response from low cycle fatigue specimen 9T12, part 2

3.7.2.1 Low-Cycle Fatigue Specimen 5IT12L22

The specimen was initially loaded using the control testing protocol up to a load level of 303 kips, which corresponds to a V/V_n ratio of 0.84. Four additional strain gages and five additional crack displacement sensors were added to the specimen and a low-cycle fatigue loading protocol was applied to the specimen. The loading sequence for the low-cycle fatigue test consisted of 50 cycles with force amplitudes ranging from 4 to 303 kips (V/V_n=0.84), 10 cycles from 4 to 353 kips (V/V_n=0.97), 10 cycles from 4 to 303 kips (V/V_n=0.84), 190 cycles from 4 to 353 kips (V/V_n=0.97), and 49 cycles from 4 to 378 kips (V/V_n=1.04). Low-cycle fatigue loads were applied at a frequency of 0.10 Hz. Before moving to a higher load range, crack measurements were made while holding the actuator force at 150 kips, except after achieving the first 60 cycles, where measurements were made at a force of 179 kips.

Centerline beam deflections for the initial 303 and 353 kip loadings increased in a nonlinear fashion in the cycles that immediately followed application of the new load range. After initial cycles, the rate of change of the deflections decreased and eventually became steady with linearly increasing displacements with each cycle. There was a small increase in crack width during the initial 303 kip loading cycles with all measured cracks along the length of the beam increasing during the first 50 cycles. Some cracks also coalesced after the first 10 cycles at the 303 kip peak force.

The peak force was increased to 353 kips and applied to the specimen. After 10 cycles at 353 kips were completed, the beam was then subjected to 10 cycles at the original force level of 303 kips. During these 10 cycles at the reduced load level, the centerline displacement and crack widths did not measurably increase. The loading was then increased back to the 353 kip level for an additional 190 cycles. A crack sensor indicated continued growth at the higher load level, however crack measurements taken at a stationary load of 179 kips were not measurably different from those previously recorded at 150 kips. The peak load was then increased to 378 kips. At this load level several crack sensors and visual observation indicated significant crack width increase. Eventually, the specimen failed in shear-compression after 49 cycles at the peak force level of 378 kips.

3.7.2.2 Low-Cycle Fatigue Specimen 6T6L22

The specimen was initially loaded using the control testing protocol up to a load level of 400 kips, which corresponded to a V/V_n ratio of 0.87. Four additional strain gages and five additional crack displacement sensors were added to the specimen and a low-cycle fatigue loading protocol was applied to the specimen. The loading sequence for the low-cycle fatigue test consisted of 200 cycles with force amplitudes ranging from 4 to 400 kips (V/V_n=0.87), 200 cycles from 4 to 425 kips (V/V_n=0.92), 200 cycles from 4 to 450 kips (V/V_n=0.97), and 100 cycles from 4 to 472 kips (V/V_n=1.02). Low-cycle fatigue loads were applied at a frequency of 0.10 Hz. Before moving to a higher load range, crack measurements were made while holding the actuator force at 200 kips.

During the first several cycles of each new load increment, increasing beam deflections were observed. However, deflections did not change after approximately 100 cycles. The

test was eventually halted after 100 cycles with a peak load range of 472 kips, because there was no sign of damage (crack widths and deformations did not change). It was not possible to increase the load above this level due to the force capacity of the hydraulic actuator.

Because failure of the specimen was not possible, it was used to study the effects of sequential stirrup fracture occurring along a diagonal crack. A diagonal crack on the north end of the specimen was selected as a critical location based on the observed crack width of 0.04 in. and location (approximately the effective depth away from the loading point). At the crack location, strain gages were bonded on the stirrups crossing the crack. The four gages were identified as Gr1, Gr2, and Gr3 on the east face and Gr4 on the west face. Two crack gages, identified as Br3 and Br6, were attached on the east face of the specimen across the crack near the instrumented stirrup locations. The specimen and instrumentation are shown in Figure 3.18.

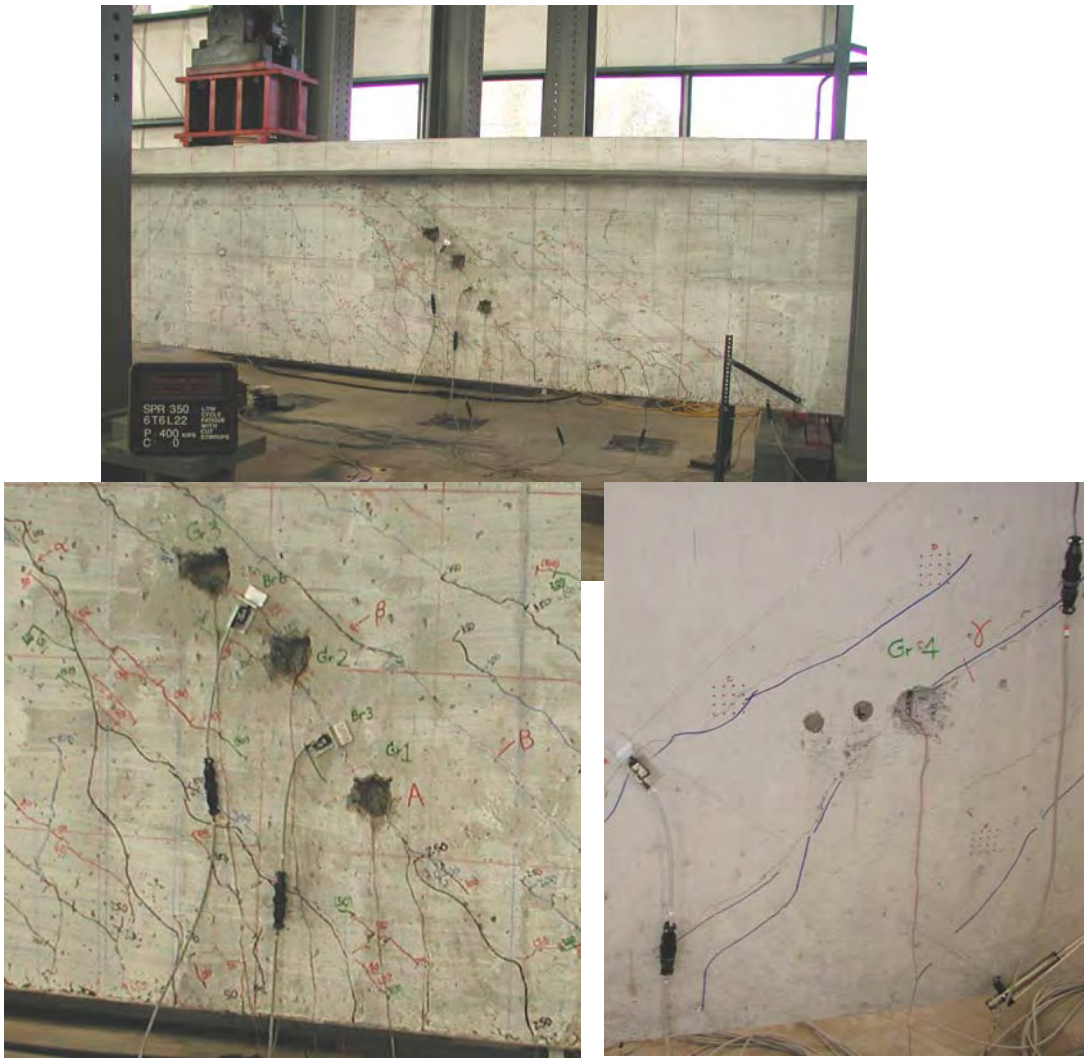

Figure 3.18: Instrumentation for damage sequencing of stirrups for specimen 6T6L22

The specimen was loaded to 200 kips and crack measurements were taken for reference. Subsequently, 150 cycles at a peak load of 400 kips were applied. Strains of approximately 1200 με (at maximum) were observed at Gr1, Gr2, and Gr4, while 900 με was seen at location Gr3. The specimen deflection and crack widths did not exhibit significant changes.

The load was reduced to zero and the stirrup instrumented with strain gage Gr2 was cut with an angle grinder. An additional 150 cycles at a peak load of 400 kips were applied to the specimen. The maximum strain was 2000 με at Gr1 and about 1200 με at Gr3 and Gr4. No significant change in specimen deflection or crack widths was observed.

Next, the load was again reduced to zero and the stirrup instrumented with strain gage Gr1 was cut with an angle grinder. The specimen was subjected to 150 cycles with a 400 kip peak load. Instrumented stirrups Gr3 and Gr4 indicated 1200 με at maximum load. At this stage, crack widths began to increase with a maximum crack width measured at 0.07 in. compared to 0.05 in. at the beginning of this test.

Next, the stirrup instrumented with strain gage Gr4 was cut with an angle grinder. A sequence of low-cycle fatigue loads was applied as follows: 150 cycles with a 400 kip peak load; 200 cycles with a 450 kip peak load; and 200 cycles with a 472 kip peak load. The maximum strain in the remaining instrumented stirrup (Gr3) exceeded 2800 με. The maximum crack width increased to 0.177 in. However, the increasing deflection of the specimen exhibited the same trend as previously observed; relatively large increases in deflections during the first several cycles gradually decreasing rates of change and then becoming steady.

Finally, a stirrup leg was cut on the opposite face of that for the instrumented stirrup Gr1 (final cut stirrup located on the west face). A sequence of low-cycle fatigue loads was applied as follows: 150 cycles with a 400 kip peak load; 150 cycles with a 450 kip peak load; and 24 cycles with a 472 kip peak load which eventually produced a shear-compression failure of the specimen. A maximum crack width of 0.222 in. was measured after the final 200 cycles at the 450 kip peak load amplitude.

3.7.2.3 Low-Cycle Fatigue Specimen 6IT6L22

The specimen was initially loaded using the control testing protocol up to a load level of 401 kips, which corresponded to a V/V_n ratio of 0.78. Subsequently, low-cycle fatigue loading was applied to the specimen. The sequence of the low-cycle fatigue was: 150 cycles with a peak load of 401 kips (V/V_n=0.78), 200 cycles with a peak load of 425 kips (V/V_n=0.83), 200 cycles with a peak load of 450 kips (V/V_n=0.88), and 37 cycles at a peak load of 475 kips (V/V_n=0.93), at which point the test was terminated for safety reasons. Diagonal crack measurements were made at intervals when the applied load was held constant at 200 kips.

Five displacement sensors were attached to the beam after monotonic loading to monitor crack motions. Instruments designated Br1 and Br2 were attached on the east face of the

north side of the specimen. Instruments designated Br4, Br5, and Br6 were attached on the east face of the south side of the specimen. Diagonal crack measurements were made after each set of cycles was completed and with the applied load held constant at 200 kips.

Upon achieving peak force amplitude for the first time, beam displacements incrementally increased with successive cycles. The rate of change in the beam deflection slowed on subsequent cycles and tended to fit a limiting exponential curve. After 150 cycles at the peak load of 400 kips, no significant changes in either crack width or centerline displacement were observed.

The cyclic load amplitude was then increased to a peak load of 425 kips. Noise appearing to be associated with the flexural rebar anchorage was noted in the vicinity of the supports. Crack Br6 closed rapidly after 25 cycles from 0.023 in. to only 0.011 in. After 50 cycles, the support plate at the south end had almost slipped off the roller and testing was suspended while the plate was repositioned. This required that support deformation sensors be removed while the support plates were repositioned. Data acquisition was restarted and the specimen was loaded to 205 kips to measure crack widths. Crack widths and centerline displacements increased slightly during the 425 kip loading cycles.

The load was increased to 450 kips. Crack sensors Br6 and Br5 indicated the instrumented diagonal cracks were closing. Crack sensors Br1, Br2, and Br4 indicated diagonal crack opening as the number of cycles increased. Centerline displacement continued to increase. The load was further increased to 475 kips. After 37 cycles, the specimen began to tilt toward the east. Testing was halted and specimen was loaded to 205 kips to permit measurement of the diagonal cracks. Cracks at sensor locations Br1 and Br4 opened sharply during this portion of the testing, while crack location Br5 closed sharply due to twisting of the cross-section. Testing was stopped due to safety concerns.

3.7.2.4 Low-Cycle Fatigue Specimen 7IT6L22

Specimen 7IT6L22 was initially loaded using the control testing protocol up to a load level of 2193kN (493 kips), which corresponded to a V/V_n ratio of 0.97, without specimen failure. This was the maximum load that could be applied with the testing system. However, to develop additional data on specimen response under stirrup damage progression, the specimen was further tested after instrumentation and subsequent cutting of stirrup legs at diagonal crack locations. The tests were performed under a low-cycle fatigue tested protocol.

A crack (identified as Crack A) located on the north side of the specimen was selected to be a critical crack based on the observed crack width and location (0.070 in. at 493 kips prior to low-cycle loading). Additional strain gages (identified as 1E, 2E, 1W, 2W) were applied to both the east and west legs of the two stirrups that crossed diagonal crack A. The 2E strain gage failed after initial installation. Two crack gages (identified as C1 and C2) were also added near the middle of the crack, one on the west face (C1) and one on the east face (C2). Crack displacement sensors Br2 and Br6 were removed to permit the additional sensor channels.

The specimen was loaded statically to 475 kips and then unloaded. After unloading, stirrup 1W was cut with an angle grinder and low-cycle fatigue loading was applied to the specimen with 50 cycles ranging from 5 kips to a peak load of 404 kips (V/V_n=0.81). After the cycles were complete, stirrup 2E was cut with an angle grinder and an additional 100 cycles from 5 kips to a peak load of 404 kips was applied to the specimen. After this sequence, stirrup 1E was cut with an angle grinder and 200 cycles from 5 kips to a peak load of 400 kips was applied. Finally, stirrup 2W was cut with an angle grinder and 203 additional cycles from 5 kips to 400 kips was applied until the specimen failed in shear-compression. All low-cycle loadings were applied at a frequency of 0.10 Hz and diagonal crack measurements were made at an applied 200 kips.

After stirrup cutting 1W, the stirrup strain in 2W increased at a higher rate than 1E, which was the other leg of the cut stirrup. After stirrup 2E was cut and the fatigue load applied, the width of crack A, and the measured stirrup strains across crack A increased sharply upon initial reloading; and then crack widths and strains continued to increase but at a slower rate. Similar behavior was observed after stirrup 1E was cut, where crack widths and strains in crack A increased sharply immediately after the stirrup was cut. The strain in stirrup 2W increased rapidly to a maximum recorded strain of 6252με after 33 cycles and then went out of range. Both diagonal crack measurements continued to increase with location C2 increasing more quickly than location C1. At this point, Stirrup 2W was cut. Crack widths and strains in crack A increased sharply after the stirrup was cut and crack widths at crack A increased rapidly immediately prior to failure.

3.7.2.5 Low-Cycle Fatigue Specimen 9IT12L22

Specimen 9IT12L22 was initially loaded using the control testing protocol up to a load level of 255 kips, which corresponded to a V/V_n ratio of 0.72. Low-cycle fatigue loading (load control) was then applied to the specimen. The sequence of the low-cycle fatigue is described as follows: 200 cycles from 4 kips to a 255 kip peak load (V/V_n=0.72); 100 cycles from 4 kips to a 305 kip peak load (V/V_n=0.86), and 201 cycles from 4 kips to a 357 kip peak load (V/V_n=1.00). The beam exhibited a shear-compression failure. Low-cycle fatigue load was applied at a frequency of 0.1 Hz and diagonal crack measurements were made at a constant applied load of 250 kips.

Centerline displacement response for this specimen closely followed that observed for previous tests, whereby after the peak load was achieved on the first cycle, displacement continued to increase quickly on subsequent cycles, but the rate of change slowly decreased until linear displacement increments were achieved. This was also observed for diagonal crack displacements. Prior to failure, the displacements began to increase rapidly for each subsequent cycle and continued to increase until the specimen failed.

3.7.2.6 Low-Cycle Fatigue Specimen 9T12L24

Specimen 9T12L24 was initially loaded using the control testing protocol up to a load level of 250 kips, which corresponded to a V/V_n ratio of 0.72. Low-cycle fatigue loading (load control) was then applied to the specimen. The sequence of the low-cycle fatigue is described as follows: 1000 cycles from 4 kips to a 282 kip peak load (V/V_n=0.84); 365

cycles from 4 kips to a 301 kip peak load (V/V_n=0.89), 10500 cycles from 4 kips to a 309 kip peak load (V/V_n=0.91), and 1468 cycles from 4 kips to a 332 kip peak load (V/V_n=0.98). The beam exhibited a shear-compression failure. Low-cycle fatigue load was applied at a frequency of 0.25 Hz and diagonal crack measurements were made at a constant applied load of 150 kips.

After 100 cycles at the 275 kip peak load magnitude, strain gages were rebalanced because several of the readings had exceeded the range capability of the data acquisition system. After 1000 cycles at the 275 kip peak load, testing was suspended because the specimen had shifted on the end supports. The beam was adjusted back to its original position and diagonal crack sensor identified as Br1 was moved to an adjacent crack location because the crack that was being monitored closed. The peak load was increased to 301 kips for 365 cycles and was then increased to 309 kips for another 135 cycles before the test was stopped for the day.

Before restarting the test, high-elongation strain gages were bonded to the stirrups crossing selected cracks. These included sensors identified as Rd2, Rd3, Rd5, and Rd6 on the south side and sensors identified as Ye1, Ye2, Ye3, and Ye6 on the north side of the specimen. Residual strains from the data taken the previous day were taken as the initial strains for the new gages. Residual strains for several stirrups were not known precisely because the strain gages on those stirrups had gone out of range. In these cases, the maximum previously recorded strain was used as the residual strain. Strain gages were also added on the flexural reinforcement on both the north and south sides of the beam and two clip gages were bonded to the deck surface, centered over the web, and located 12 in. from the spreader beam contact points on both the north and south sides.

The second day of low-cycle fatigue testing consisted of 2,500 cycles at a peak load of 309 kips. The beam again shifted in the supports after only 22 cycles. Testing was suspended and the beam was readjusted onto the supports. After 1,825 total cycles, there was a sharp pop emitted from the north end of the beam. After 2,140 total cycles another pop was heard in the south end of the beam near the Rd5 gage. Four more pops were heard from the south side of the beam after 2,220 cycles, 2,295 cycles, 2,326 cycles, and 2,436 cycles. After testing, concrete was removed around stirrup locations and revealed three fractured stirrup locations. The other popping sounds were attributed to stirrup slip.

The third day of low-cycle fatigue testing consisted of 5,000 cycles at a peak load of 1374kN (309 kips). After 4,234 total cycles, the beam position was again readjusted. A crack in the deck was observed after 6,900 total cycles. The crack extended from a diagonal crack identified as D in the instrumentation plan.

Before starting tests for the fourth day, the beam was again repositioned on the supports and then 2,762 cycles at a peak load of 309 kips were applied to the specimen. After the first cycle, a loud noise sounding like steel on steel was heard from the south end support, but no evidence of damage was observed. The south end support required adjustment after 9,280 total cycles. After 11,762 total cycles, the peak load was increased to 320 kips. Eventually, failure occurred after 13,333 total cycles with the specimen exhibiting a shear compression failure.

3.7.2.7 Low-Cycle Fatigue Specimen 10T24L24

Specimen 10T24L24 was initially loaded using the control testing protocol up to a load level of 190 kips, which corresponded to a V/V_n ratio of 0.80. Low-cycle fatigue loading (load control) was then applied to the specimen. The sequence of the low-cycle fatigue is described as follows: 10,000 cycles from 4 kips to a 195 kip peak load (V/V_n=0.83) and 4057 cycles from 4 kips to a 207 kip peak load (V/V_n=0.88). The beam exhibited a shear-compression failure. Low-cycle fatigue load was applied at a frequency of 0.22 Hz and diagonal crack measurements were made at a constant applied load of 100 kips.

Before application of the low-cycle loading, five high-elongation strain gages were bonded to stirrups crossing diagonal cracks on the west face of the specimen. Two were applied to the north end and three were applied to the south end. Low-cycle fatigue loading was then applied to the specimen. During loading, raveling of the concrete along the diagonal cracks and crack extension along the deck-stem interface were observed. After 1507 cycles, the loading increased slightly to 198 kips for 495 cycles and then reduced back to 195 kips.

Over the course of the day, the sun angle changed and reflected off the specimen, thereby heating the strain gages and other instruments located on the exposed face. Shading was provided to reduce temperature effects on the sensor measurements. Centerline displacement increased nonlinearly over the first 1000 cycles and then increased in a linear fashion thereafter. Diagonal crack sensor identified as Br1 indicated increased crack movement over the first 1000 cycles and changed linearly after during subsequent cycles. Diagonal crack sensor identified as Br2 indicated increasing crack growth during the first 400 cycles and then became linear after that point. Diagonal crack sensors identified as Br4 and Br5 indicated decreasing crack motions. The test was halted at the end of the day and restarted the following day.

Prior to beginning testing on the second day, the beam was repositioned on the supports and the centerline displacement and support displacement sensors were reset. Strain gages Gy3 and Gy4 jumped slightly from the previous days testing. This was most likely caused by a temperature differential from the end of the previous day. After 3089 cycles, an external strain gage went out of range. The gage was replaced and rebalanced while there was a 100 kip load on the specimen at 4002 cycles. Strains continued to increase slowly during the second day of testing.

At the end of the day, the testing was suspended and restarted on the third day after again repositioning the specimen on the supports. The centerline displacement sensor was also reset. After 10,000 total cycles, the load was increased to 207 kips. At this load level, strain gages identified as Gn5 and Gn6 began to increase more quickly than during the previous load step. The other strain measurements increased at about the same rate as at the previous lower load amplitude. Prior to failure, the centerline displacement began to increase rapidly as did cracks locations identified as Br1 and Br2. The beam eventually failed in a shear-compression failure mode.

3.7.3 Conclusions

Full-size tests of conventionally-reinforced concrete (CRC) girders, designed and constructed to reflect 1950's vintage details and materials, were performed under low-cycle fatigue. Low-cycle fatigue loading was applied after specimens were initially loaded to between 72% and 85% of the nominal shear capacity. Constant force amplitude loading was applied until the observed increment of deformation became linear or until a given number of cycles was achieved. Load amplitudes were increased and loading cycles were applied until the eventual failure of the specimen. Based on these tests, the following conclusions are presented:

- LCF damage occurs at loads sufficient to cause yielding in stirrups across diagonal cracks.
- Damage from LCF was observed from bond deterioration and cumulative plasticity of the stirrups.
- Failure was controlled by progressive fracture of stirrups.
- Damage from LCF was observed to occur in three distinct phases: an initial nonlinear phase, a middle linear phase, and a final nonlinear phase leading to eventual specimen failure.
- Rates at which incremental deformations occurred during LCF in each of the three damage phases increased with higher loading ratios (V/V_n).
- Diagonal deformations across the web increased under LCF and at failure were larger than similar specimens subjected to the control loading protocol. Diagonal deformations based on conventional monotonic loading may be used as an estimate of the cumulative diagonal deformations under LCF.
- Specimens were able to sustain relatively large numbers of cycles of repeated loads at large loading ratios.
- For sequenced loads of varying magnitudes, low magnitude load cycles occurring after a higher amplitude load exhibited incremental deformations associated with the lower magnitude in the middle linear phase accumulation range.

3.8 HIGH-CYCLE FATIGUE TESTS

Diagonal cracks have been identified on reinforced concrete deck-girder (RCDG) bridges, which are exposed to millions of load cycles during service life. The anticipated life of these bridges in the cracked condition under repeated service loads is uncertain. A series of tests was performed to evaluate possible deterioration in load-carrying capacity or reduction in service life. Specimen variables included: T and inverted-T configurations, stirrup spacing, and flexural reinforcing details. Stirrup strain data previously collected during field investigations of four in-service RCDG bridges were used as a reference for the laboratory high-cycle fatigue (HCF) tests.

Test specimens were initially cracked to impose diagonal cracks of the desired width prior to initiation of fatigue testing. Precracking of the specimens was performed in the setup described previously for the tests conducted to failure. The specimens were then moved to a separate test frame to apply the high-cycle fatigue loading protocol. After application of fatigue loads, the specimens were moved back to the original load frame and tested to failure to observe differences in capacity from similar non-fatigued specimens.

3.8.1 Test Method

Test specimens were precracked to produce a desired diagonal crack width as measured by an ODOT crack comparator both with and without applied load. Diagonal crack width conditions at peak load and at zero load for the high-cycle fatigue specimens are shown in Table 3.9. Initial specimens were loaded so as to produce crack widths corresponding to field observations. The diagonal cracks were at least 0.025 in. when the specimens were unloaded. Some cracks were larger because precracking was performed with discrete load increments. Sensor data recorded during precracking is contained in Appendix A4. After pre-cracking, the specimens were moved to a separate load frame for HCF testing.

Table 3.9: Precrack stage crack widths for HCF specimens

Specimen	Precrack Load [kips]	Maximum w_{cr} [in]		
		At precrack load	At 0 kip	At 100 kip Total Load
3T12	260	0.050	0.025	0.030
3IT12	260	0.040	0.025	NA
3IT18	225	0.105	0.070	NA
5IT12-B1	330	0.060	0.050	NA
6T10	400	0.110	0.070	0.080
6IT10	375	0.070	0.040	0.050
8IT10	350	0.060	0.030	0.040
9IT12-B1	300	0.060	0.025	0.040
9T12-B4	250	0.095	0.06+	0.080

The loading frame for high-cycle fatigue tests consisted of a 110 kip capacity fatigue-rated actuator mounted to a large steel reaction frame as shown in Figures 3.19a and b. Fatigue tests were performed in load control, with force feedback to the servo-hydraulic control system provided by a load cell in series with the hydraulic actuator. A 30 GPM servovalve was used to allow application of the repeated load at a frequency of 2.4Hz. This permitted application of approximately 200,000 cycles of repeated loading per day. The alternating fatigue load was applied at midspan through a spreader beam with reaction points spaced 24 in. on-center.

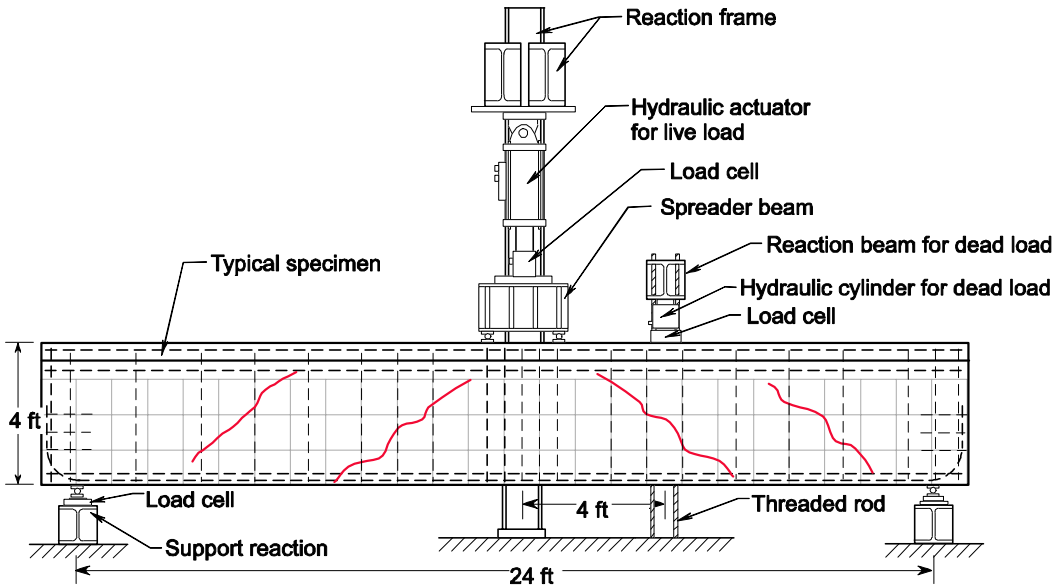

Figure 3.19a: Schematic of high-cycle fatigue test setup

Figure 3.19b: Image of high-cycle fatigue test setup

A simulated dead load of between 80-100 kips was also applied to the specimen, using a complementary loading system. This dead load represents the associated weight of portions of a bridge attributed to a girder, but not reflected in the self-weight of the specimen. The dead load force was applied with a hydraulic cylinder attached to a hydraulic accumulator. The hydraulic pressure in the cylinder and the nitrogen pressure in the hydraulic accumulator were adjusted to provide as consistent a level of dead load force as possible. The accumulator compensated for the pressure drop in the dead load hydraulic cylinder due to deformation of the specimen from the applied fatigue force. Adjustments of the dead load cylinder were required periodically due to hydraulic oil temperature changes and seal leakage.

Applied dead load was measured directly using a load cell in-series with the hydraulic cylinder. The dead load cylinder was located 4 ft from the beam centerline. From static analysis of the simply supported beam specimens, 33% of the dead load is attributed to the support farthest from the applied dead load force, and 66% is attributed to the support closest to the applied dead load. These force distributions were verified by three different load cells located on the fatigue loading actuator, south support reaction, and dead load cylinder.

The magnitude of the fatigue load ranged from 4 to 84 kips to ensure the actuator remained in contact with the specimen. This produced a load range of 80,000 lbs, which corresponds roughly to the gross vehicle weight of a typical 18-wheel container truck. The load range was applied to each of the high-cycle fatigue specimens 2 million times to simulate damage produced during the service life of a bridge girder. Stress ranges and numbers of cycles to represent 50 years of service life were previously determined from instrumentation of field study bridges. These are compared with the laboratory stress ranges imposed on test specimens as described below.

Fatigue loading was suspended at regular intervals and a series of performance tests were conducted for specimens in the latter phases of testing. These tests were performed at intervals of approximately every 100,000 cycles up to 500,000 cumulative cycles and then every 250,000 cycles until 2 million cumulative cycles were achieved. Crack widths were measured with the fatigue load magnitude at approximately 2 kips using the ODOT crack comparator and crack extents were monitored and recorded. The crack extensions during fatigue testing are shown in Appendix A3 for each of specimens.

Displacement sensors were reattached and a sequence of loading tests were performed: 10 cycles ranging from 4 to 84 kips at 0.5 Hz; 5 cycles ranging from 4 to 104 kips at 0.1 Hz; and finally another 10 cycles ranging from 4 to 84 kips at 0.5 Hz. The first 15 cycles of the sequence were used to ensure seating of the reapplied sensors, and data were taken from the final 10 cycles of this sequence to assess changes in response. No specimen failure was observed during fatigue loading and after completion of 2 million load cycles. Specimens were moved back to the original test setup and loaded to failure.

3.8.2 Experimental Results

Nine specimens were subjected to the fatigue testing protocol as listed in Table 3.9. Specimen details are shown in Appendix A1. Measured stirrup stress ranges varied between specimens, even as the applied fatigue load range and peak value were held constant for all tests. This was due to the different specimen configurations and initial cracking levels imposed at the start of

fatigue testing, as well as the applied dead load effects. The average measured stirrup strain ranges and crack displacement ranges, at the beginning of fatigue testing and after completion of 2 million cycles, are summarized in Tables 3.10 and 3.11, respectively.

Table 3.10: Stirrup strain ranges at the beginning and completion of HCF testing

Specimen	Strain Gage	ε Range (με)	
		After precrack	After 2million cycles
3IT12	GS1	10	5
	GS2	170	150
	GS3	250	255
	GS4	230	240
	GS5	430	450
	GS6	130	120
	GS7	390	390
	GS8	420	460
	GN1	10	10
	GN2	15	10
	GN3	*	*
	GN4	280	290
	GN5	860	830
	GN6	*	*
	GN7	610	610
	GN8	*	*
3T12	GS1	360	350
	GS2	50	40
	GS3	320	310
	GS4	230	190
	GS5	5	5
	GS6	*	*
	GS7	500	460
	GS8	460	420
	GN1	*	*
	GN2	280	280
	GN3	330	320
	GN4	640	630
	GN5	270	260
	GN6	*	*
	GN7	400	380
	GN8	750	720
3IT18	GS1	15	20
	GS2	30	15
	GS3	800	0
	GS4	230	360
	GS5	20	30
	GS6	850	1350
	GS7	990	30
	GS8	550	980
	GN1	15	20
	GN2	15	30
	GN3	870	870
	GN4	50	80
	GN5	20	20
	GN6	810	840
	GN7	1520	1480
	GN8	800	600

Specimen	Strain Gage	ε Range (με)	
		After precrack	After 2million cycles
5IT12-B1	GS1	5	10
	GS2	5	10
	GS3	30	20
	GS4	120	110
	GS5	420	400
	GS6	570	630
	GS7	600	650
	GS8	230	740
	GN1	10	10
	GN2	15	20
	GN3	300	240
	GN4	340	300
	GN5	190	90
	GN6	690	650
	GN7	1010	900
	GN8	660	560
6IT10	GS1	720	750
	GS2	600	620
	GS3	*	*
	GS4	290	330
	GS5	410	440
	GS6	460	480
	GN1	490	530
	GN2	560	610
	GN3	540	570
	GN4	590	550
	GN5	630	620
	GN6	180	230
6T10	GS1	650	650
	GS2	650	650
	GS3	350	10
	GS4	440	520
	GS5	410	470
	GS6	470	530
	GS7	360	410
	GS8	110	170
	GN1	440	520
	GN2	460	540
	GN3	360	460
	GN4	320	410
	GN5	420	410
	GN6	640	610
	GN7	920	840
	GN8	720	640

*indicates a broken gage, provided value taken before gage broke if possible

Specimen	Strain Gage	ε Range (με)	
		After precrack	After 2million cycles
8IT10	GS1	440	420
	GS2	350	300
	GS3	10	170
	GS4	410	470
	GS5	30	20
	GS6	570	480
	GS7	590	500
	GS8	550	440
	GN1	400	420
	GN2	510	560
	GN3	420	560
	GN4	260	430
	GN5	*	*
	GN6	820	800
	GN7	1070	1110
	GN8	490	590
9IT12-B1	GS1	400	400
	GS2	440	430
	GS3	*	*
	GS4	50	50
	GS5	2150	220
	GS6	570	550
	GS7	800	760
	GS8	700	690
	GS9	500	480
	GN1	*	*
	GN2	460	490
	GN3	290	250
	GN4	240	250
	GN5	270	250
	GN6	630	570
	GN7	760	720
9T12-B4	GS1	460	600
	GS2	40	30
	GS3	5	2
	GS4	180	190
	GS5	5	4
	GS6	840	890
	GS7	960	980
	GS8	530	460
	GN1	*	*
	GN2	5	5
	GN3	400	410
	GN4	60	20
	GN5	280	310
	GN6	870	630
	GN7	1260	1030
	GN8	790	880

Table 3.11: Crack displacement ranges at the beginning and completion of HCF testing

Specimen	Crack Gage	Crack Range (in.)	
		After precrack	After 2million cycles
3IT12	#1	0.0042	0.0052
	#2	0.0160	0.0193
	#4	0.0068	0.0091
	#5	0.0060	0.0072
3T12	#1	0.0082	0.0084
	#2	0.0030	0.0034
	#4	0.0066	0.0056
	#6	0.0066	0.0059
5IT12-B1	#1	0.0002	0.0069
	#2	0.0050	0.0057
	#5	0.0090	0.0093
3IT18	#2	0.0112	0.0123
	#3	0.0102	0.0120
	#4	0.0085	0.0130
	#5	0.0068	0.0094
	#6	0.0050	0.0078
6IT10	#2	0.0060	0.0148
	#3	0.0063	0.0086
	#4	0.0075	0.0095
	#5	0.0046	0.0062
	#6	0.0033	0.0063
6T10	#1	0.0061	0.0098
	#2	0.0107	0.0134
	#3	0.0091	0.0121
	#4	0.0062	0.0098
	#5	0.0038	0.0070
	#6	0.0076	0.0134
9IT12-B1	#1	0.0082	0.0096
	#4	0.0132	0.0143
	#5	0.0082	0.0088
8IT10	#1	0.0091	0.0096
	#2	0.0068	0.0085
	#3	0.0073	0.0101
	#4	0.0063	0.0072
	#5	0.0044	0.0062
	#6	0.0074	0.0075
9T12-B4	#1	0.0084	0.0054
	#2	0.0115	0.0060
	#3	0.0084	0.0146
	#4	0.0132	0.0124
	#5	0.0081	0.0080

An example of measured stirrup strain ranges and mean strain response during a fatigue test are shown in Figures 3.20 and 3.21, respectively. Example crack displacement range and mean crack width changes during a typical fatigue test are shown in Figures 3.22 and 3.23. Complete histories of stirrup strain and diagonal crack motions during fatigue tests are contained in Appendix A6. Stirrup stress and deformation ranges determined during each of the interval tests are summarized in Table 3.12a and b.

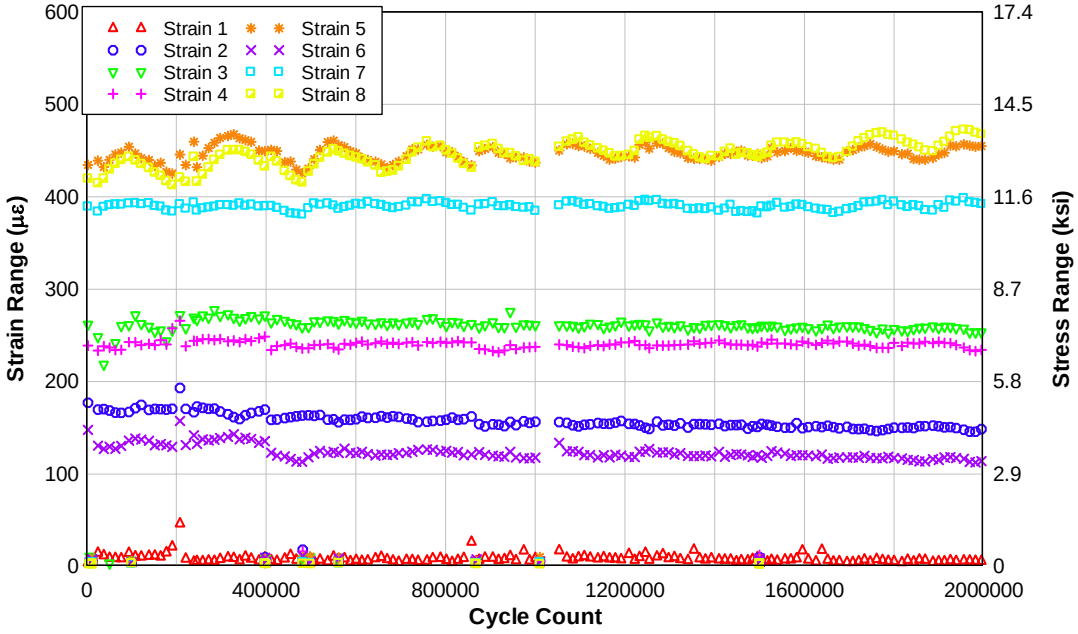

Figure 3.20: Example strain ranges during HCF test (specimen 3IT12 south end)

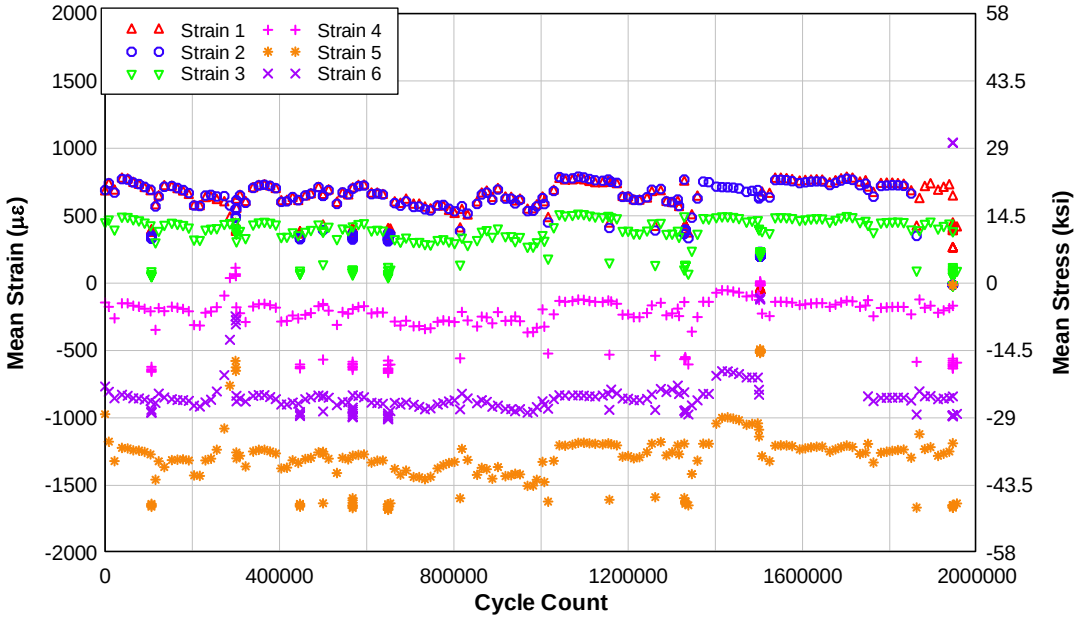

Figure 3.21: Example strain gage means during HCF test (specimen 6IT10 North end)

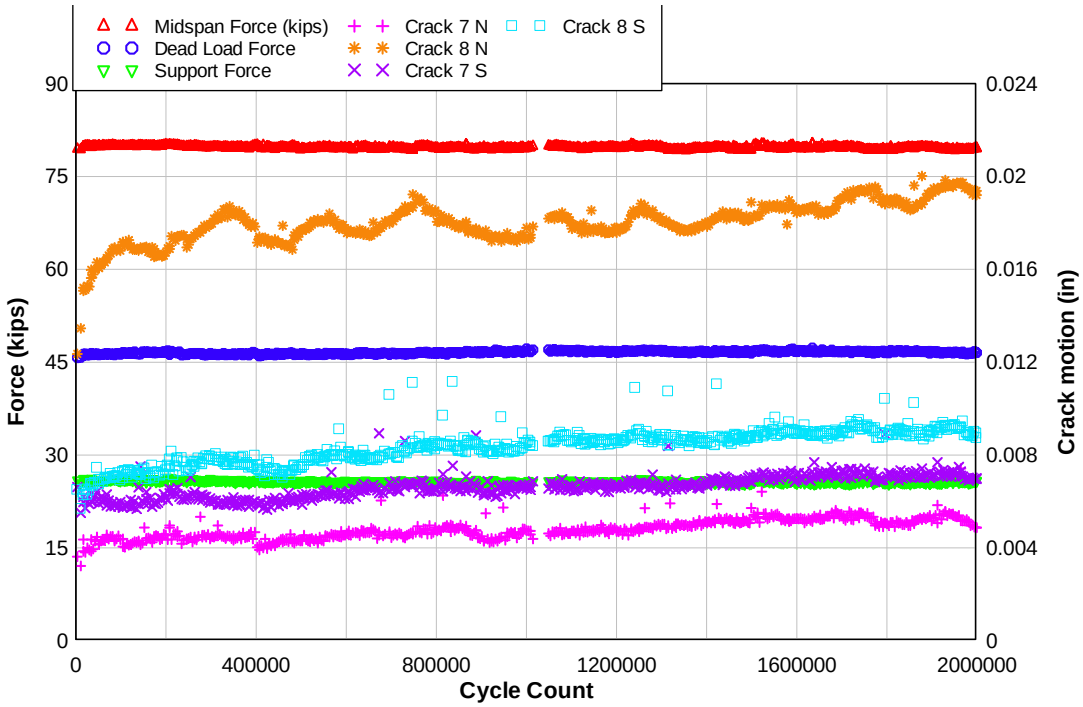

Figure 3.22: Example load and crack motion sensor ranges during HCF test (specimen 3IT12)

Figure 3.23: Example load and crack motion sensor means during HCF test (specimen 5IT12-B1)

Table 3.12a: Stirrup strain ranges during HCF interval tests

Specimen	Strain Gage	Check test											
		0k	100k	200k	300k	400k	500k	750k	1M	1.25M	1.5M	1.75M	2M
3IT12	GS1	22						16	16	20	13	18	
	GS2	178						165	162	157	160	153	
	GS3	270						269	271	265	272	263	
	GS4	252						252	248	247	257	244	
	GS5	451						456	447	463	444	457	
	GS6	148						138	126	139	130	122	
	GS7	392						390	385	391	386	389	
	GS8	438						451	436	455	440	462	
	GN1	19						17	15	19	22	15	
	GN2	22						17	22	36	26	20	
	GN3	0						0	0	0	0	0	
	GN4	285						297	286	287	286	292	
	GN5	871						851	0	0	0	0	
	GN6	0						0	0	0	0	0	
	GN7	602						611	600	604	610	608	
	GN8	0						0	0	0	0	0	
3T12	GS1	375								369	405		435
	GS2	63								77	103		108
	GS3	9								330	385		0
	GS4	220								212	234		260
	GS5	60								64	74		70
	GS6	0								0	0		0
	GS7	448								462	400		450
	GS8	476								494	432		469
	GN1	0								0	0		0
	GN2	284								287	323		327
	GN3	357								331	369		397
	GN4	657								633	640		696
	GN5	281								281	306		312
	GN6	3418								0	0		0
	GN7	414								383	374		408
	GN8	773								740	708		720
3IT18	GS1	19	22	30	20	24	19	18	19	29	24	33	31
	GS2	33	31	31	35	34	34	37	40	43	42	49	19
	GS3	766	697	14	192	729	336	37	15	903	921	929	0
	GS4	279	223	227	223	236	218	250	257	304	281	283	395
	GS5	27	22	22	22	27	24	31	32	41	34	32	40
	GS6	537	513	520	505	511	494	622	666	661	659	681	968
	GS7	969	890	920	897	917	876	1079	1123	1113	1103	1077	34
	GS8	864	773	795	774	791	760	910	944	955	952	977	1325
	GN1	23	15	22	21	21	14	21	25	25	35	33	25
	GN2	20	18	27	26	21	24	26	30	29	30	45	36
	GN3	832	938	934	946	915	940	895	894	869	901	924	910
	GN4	58	78	93	116	101	139	70	79	67	73	83	93
	GN5	25	24	30	24	39	21	24	30	31	26	29	36
	GN6	742	782	789	792	787	785	833	820	807	816	825	829
	GN7	1331	1493	1497	1510	1472	1490	1464	1410	1412	1433	1465	1459
	GN8	767	834	808	843	789	829	687	660	659	622	615	628
5IT12-B1	GS1		16		12		11	10	15			15	11
	GS2		20		16		14	9	17			15	13
	GS3		33		29		31	30	27			27	25
	GS4		123		125		121	117	111			106	116
	GS5		416		411		419	415	407			403	403
	GS6		539		545		570	573	587			628	596
	GS7		561		586		602	595	596			636	593
	GS8		702		713		723	709	713			725	691
	GN1		15		18		14	16	23			15	17
	GN2		17		21		24	18	19			21	28
	GN3		324		318		318	301	279			238	271
	GN4		360		354		357	341	331			307	317
	GN5		197		153		115	111	108			79	108
	GN6		627		632		640	635	605			618	621
	GN7		942		918		916	913	898			886	852
	GN8		630		605		593	589	590			558	546

Table 3.12a (continued): Stirrup strain ranges during HCF interval tests

Specimen	Strain Gage	Check test											
		0k	100k	200k	300k	400k	500k	750k	1M	1.25M	1.5M	1.75M	2M
6IT10	GS1	711	720	720	758	765	755	679	785	775	671	736	
	GS2	590	599	601	626	628	621	557	643	638	555	613	
	GS3	8	10	230	422	431	435	346	11	438	389	10	
	GS4	268	291	300	333	334	336	299	345	337	289	319	
	GS5	407	402	401	441	444	440	385	454	434	371	432	
	GS6	431	451	456	489	490	490	432	503	483	419	474	
	GN1	492	473	478	492	485	487	414	491	620	0	536	
	GN2	557	552	549	545	551	549	496	547	718	633	644	
	GN3	549	536	520	504	505	500	466	481	685	620	607	
	GN4	550	596	587	571	567	563	612	560	665	628	589	
	GN5	544	622	608	565	607	616	689	582	726	713	686	
	GN6	145	190	198	189	196	202	250	169	315	365	252	
6T10	GS1	677	643	624	629	625		689	699	697	674	628	674
	GS2	689	638	618	611	616		685	691	690	670	622	669
	GS3	321	23	242	361	10		12	12	10	12	10	11
	GS4	410	440	451	435	452		543	532	539	535	477	532
	GS5	415	402	406	394	403		487	479	486	480	429	479
	GS6	505	449	434	426	438		540	544	546	540	476	534
	GS7	407	334	315	308	316		427	431	433	426	365	414
	GS8	123	88	84	85	88		157	181	184	176	141	164
	GN1	481	419	382	381	387		530	546	546	533	437	525
	GN2	504	433	395	395	400		554	569	568	550	465	544
	GN3	386	339	314	317	319		461	474	478	468	395	462
	GN4	342	319	306	310	309		418	441	442	425	382	420
	GN5	445	422	423	420	424		439	437	441	434	426	427
	GN6	690	649	643	640	635		637	633	636	637	633	638
	GN7	1055	919	912	911	906		866	872	878	877	908	877
	GN8	732	740	746	738	734		694	679	680	681	693	668
8IT10	GS1			473	469	465	463	470	461			456	449
	GS2			313	318	300	303	301	288			283	271
	GS3			6	5	6	8	24	141			157	162
	GS4			326	346	358	459	547	539			571	573
	GS5			29	28	31	27	27	31			29	29
	GS6			573	567	555	553	552	555			547	540
	GS7			566	571	560	549	549	567			557	572
	GS8			501	506	492	479	476	498			487	499
	GN1			440	434	434	436	438	433			440	436
	GN2			557	548	544	545	554	545			560	539
	GN3			482	479	483	483	488	494			507	494
	GN4			294	282	285	284	290	296			339	322
	GN5			0	0	0	0	0	0			0	0
	GN6			824	795	786	790	781	784			799	768
	GN7			1078	1070	1054	1047	1036	1053			1062	1033
	GN8			518	510	518	522	522	540			547	542
9IT12-B1	GS1		398	391	406	388	392	413	391	368	427	404	411
	GS2		451	441	446	434	438	447	468	459	455	461	450
	GS3		0	0	0	0	0	0	0	0	0	0	0
	GS4		61	59	78	59	70	61	68	64	59	58	58
	GS5		2119	1946	1993	1983	1994	1768	428	188	164	156	170
	GS6		567	565	570	564	568	560	590	584	557	553	554
	GS7		804	796	799	795	795	771	814	806	767	752	766
	GS8		690	688	698	696	699	676	748	734	684	668	689
	GS9		493	496	499	501	503	483	573	561	483	480	487
	GN1		0	0	0	0	0	0	0	0	0	0	0
	GN2		484	482	495	487	492	510	499	504	531	524	514
	GN3		266	266	269	270	265	259	235	239	239	219	212
	GN4		256	256	276	258	265	256	265	271	269	272	265
	GN5		280	272	274	261	269	255	266	271	271	269	263
	GN6		647	640	635	628	629	609	695	691	600	596	591
	GN7		794	789	790	787	789	769	903	893	761	765	753

Table 3.12a (concluded): Stirrup strain ranges during HCF interval tests

Specimen	Strain Gage	Check test											
		0k	100k	200k	300k	400k	500k	750k	1M	1.25M	1.5M	1.75M	2M
9T12-B4	GS1	526	483	0	0	0	0	0		0	0	0	0
	GS2	183	49	137	36	30	139	37		38	39	51	43
	GS3	241	85	157	17	21	132	17		4	9	5	4
	GS4	234	181	223	186	193	295	207		253	252	248	267
	GS5	221	28	112	24	18	135	22		9	21	20	8
	GS6	720	841	810	804	818	815	883		992	1004	840	1148
	GS7	798	963	924	912	931	921	1019		1110	1113	948	1251
	GS8	551	526	513	503	504	498	523		585	580	464	612
	GN1	0	0	0	0	0	0	0		0	0	0	0
	GN2	24	8	7	9	11	10	0		0	0	0	0
	GN3	554	0	0	0	0	0	0		0	0	0	0
	GN4	178	124	221	31	33	192	27		29	27	30	30
	GN5	352	273	287	286	294	307	307		327	325	332	329
	GN6	907	849	791	799	800	803	819		989	984	667	1027
	GN7	1266	1266	1194	1201	1200	1205	1231		1480	1473	1073	1533
	GN8	813	789	770	766	766	785	809		874	841	698	897

After completion of the fatigue loading protocol, specimens were tested to failure using the previously described conventional loading history consisting of incrementally higher loads followed by unloading until failure. The applied shear and specimen displacement at the loading point of the specimens during precracking were combined with that measured during failure testing. This was performed by using the last displacement measurement recorded during precracking as the initial displacement for the failure test. Any offset produced by fatigue loading was ignored. The combined responses are shown in Figure 3.11 and do not indicate an abrupt change between the precracking and initial reloading responses during final testing. Photographs of the specimens after failure are shown in Figure 3.12. Other data from the failure tests are contained in Appendix A4.

Table 3.12b: Crack displacement ranges during fatigue interval tests

Specimen	Crack Gage	Check test											
		0k	100k	200k	300k	400k	500k	750k	1M	1.25M	1.5M	1.75M	2M
3IT12	#1	0.0047						0.0048	0.0055	0.0051	0.0057	0.0056	
	#2	0.0175						0.0188	0.0176	0.0186	0.0180	0.0194	
	#4	0.0074						0.0087	0.0086	0.0089	0.0091	0.0106	
	#5	0.0072						0.0069	0.0076	0.0071	0.0077	0.0083	
3T12	#1	0.0086								0.0087	0.0035		0.0090
	#2	0.0036								0.0034	0.0032		0.0038
	#4												0.0082
	#6												0.0077
3IT18	#2	0.0091	0.0122	0.0126	0.0137	0.0131	0.0141	0.0142	0.0134	0.0131	0.0134	0.0140	0.0137
	#3	0.0089	0.0095	0.0098	0.0098	0.0096	0.0094	0.0111	0.0110	0.0109	0.0116	0.0118	0.0118
	#4	0.0071	0.0082	0.0086	0.0084	0.0085	0.0081	0.0097	0.0100	0.0099	0.0104	0.0111	0.0132
	#5	0.0059	0.0064	0.0071	0.0067	0.0070	0.0072	0.0076	0.0078	0.0084	0.0086	0.0091	0.0096
	#6	0.0041	0.0051	0.0054	0.0054	0.0053	0.0054	0.0063	0.0066	0.0070	0.0073	0.0076	0.0078
5IT12-B1	#1		0.0044		0.0049		0.0051	0.0054	0.0052	0.0051	0.0054	0.0054	0.0053
	#2		0.0005		0.0065		0.0066	0.0070	0.0068	0.0065	0.0066	0.0066	0.0069
	#5		0.0087		0.0091		0.0096	0.0093	0.0097	0.0095	0.0092	0.0093	0.0089
6IT10	#2	0.0049	0.0066	0.0069	0.0069	0.0086	0.0091	0.0113	0.0113	0.0151	0.0157	0.0156	
	#3	0.0061	0.0067	0.0070	0.0065	0.0075	0.0071	0.0059	0.0075	0.0093	0.0078	0.0083	
	#4	0.0068	0.0085	0.0084	0.0083	0.0088	0.0086	0.0081	0.0087	0.0090	0.0085	0.0092	
	#5	0.0044	0.0050	0.0053	0.0049	0.0053	0.0058	0.0049	0.0057	0.0059	0.0054	0.0061	
	#6	0.0031	0.0041	0.0054	0.0045	0.0048	0.0050	0.0048	0.0056	0.0057	0.0055	0.0065	
6T10	#1	0.0055	0.0061	0.0064	0.0062	0.0063		0.0093	0.0098	0.0099	0.0100	0.0083	0.0101
	#2	0.0097	0.0110	0.0113	0.0118	0.0118		0.0133	0.0137	0.0141	0.0140	0.0133	0.0142
	#3	0.0081	0.0106	0.0108	0.0114	0.0114		0.0114	0.0129	0.0124	0.0111	0.0128	0.0127
	#4	0.0060	0.0066	0.0070	0.0074	0.0078		0.0090	0.0098	0.0099	0.0117	0.0097	0.0104
	#5	0.0027	0.0042	0.0045	0.0045	0.0052		0.0063	0.0065	0.0069	0.0069	0.0071	0.0074
	#6	0.0000	0.0000	0.0000	0.0000	0.0000		0.0000	0.0000	0.0000	0.0000	0.0000	0.0000
8IT10	#1			0.0093	0.0091	0.0098	0.0095	0.0091	0.0098			0.0103	0.0102
	#2			0.0072	0.0075	0.0080	0.0076	0.0077	0.0081			0.0085	0.0082
	#3			0.0087	0.0098	0.0086	0.0088	0.0088	0.0093			0.0096	0.0095
	#4			0.0069	0.0075	0.0072	0.0073	0.0072	0.0076			0.0088	0.0074
	#5			0.0050	0.0057	0.0057	0.0052	0.0055	0.0058			0.0069	0.0071
	#6			0.0076	0.0085	0.0077	0.0076	0.0078	0.0083			0.0083	0.0084
9IT12-B1	#1		0.0090	0.0094	0.0096	0.0097	0.0098	0.0099	0.0120	0.0122	0.0102	0.0103	0.0104
	#4		0.0141	0.0145	0.0147	0.0147	0.0147	0.0148	0.0164	0.0166	0.0146	0.0149	0.0159
	#5		0.0085	0.0086	0.0089	0.0088	0.0105	0.0089	0.0102	0.0103	0.0090	0.0090	0.0108
9T12-B4	#1	0.0086	0.0089	0.0086	0.0086	0.0086	0.0089	0.0097		0.0112	0.0137	0.0102	0.0111
	#2	0.0095	0.0117	0.0115	0.0123	0.0127	0.0130	0.0141		0.0113	0.0115	0.0083	0.0124
	#3	0.0077	0.0087	0.0164	0.0084	0.0086	0.0086	0.0086		0.0157	0.0167	0.0138	0.0179
	#4	0.0116	0.0134	0.0128	0.0129	0.0133	0.0132	0.0134		0.0162	0.0155	0.0140	0.0156
	#5	0.0089	0.0084	0.0079	0.0078	0.0082	0.0095	0.0077		0.0101	0.0101	0.0088	0.0107

3.8.3 Results

The specimens included both T and inverted-T configurations, stirrup spacings ranging from 10 to 18 in., as well as different flexural reinforcing bar details. Comparing specimen performance during high-cycle fatigue tests, specimens with flexural cutoffs and hooked bars (specimens 8IT10 and 9IT12-B1) did not exhibit significant differences from other specimens. However, the specimen with flexural bar cutoffs and straight-bar anchorage (9T12-B4) appeared to have higher rates of diagonal crack width growth as well as strain range and mean increases. Considering test durations when the dead load remained fairly constant (steady pressure in the applied dead load cylinder), the stirrup strain range increased along the eventual failure crack as shown in Figure 3.24. This diagonal crack intersected the flexural steel just past the cutoff location.

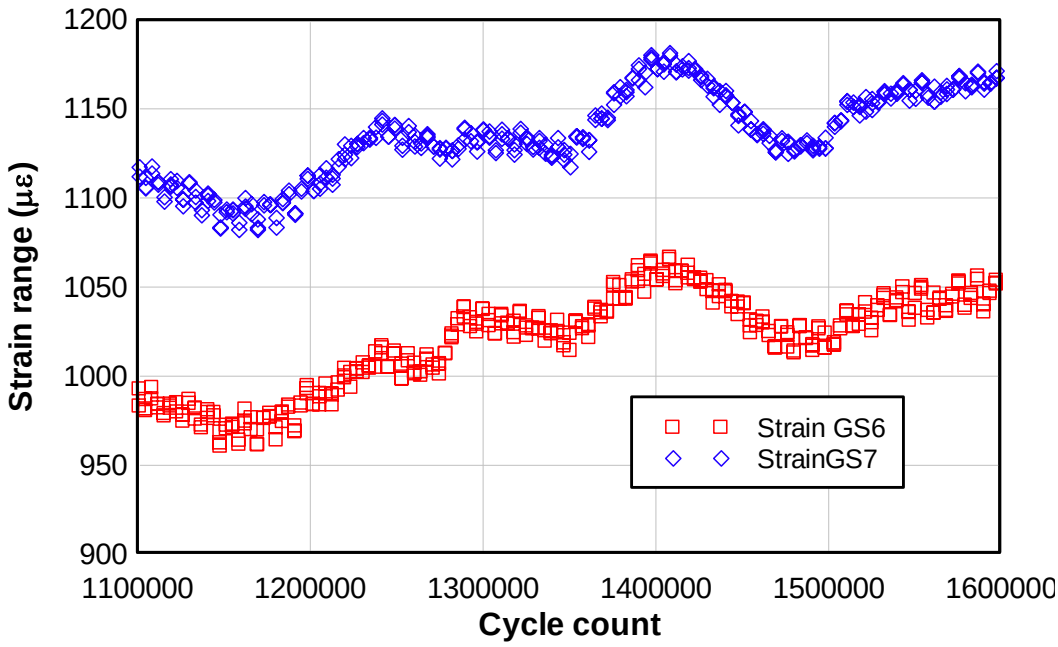

Figure 3.24: Increasing strain range in specimen 9T12-B4, having cut and straight bars during HCF test

On each specimen, at least one strain gage sensor measured a stress range of approximately 13.8 ksi at diagonal crack locations on the south half of the beam. The 13.8 ksi stress range is above the single highest stress range observed in the field testing portion of this research program. Further, based on field testing of three typical 1950's RCDG bridges, the 13.8 ksi stress range applied for 2,000,000 cycles corresponds to approximately 50 years of service life, using a linear damage model (Minor's Rule) and an equivalent constant amplitude fatigue stress derived from the variable amplitude strain field measurements at the highest strain location (Location #7 on McKenzie River Bridge).

On the north side, stress ranges were even higher, although the stress field was more complex due to the positioning of the dead load cylinder. During the warmer months, stress ranges in the stirrups at locations where concrete cover was removed show oscillation at approximately a 24-hour interval due to heating and cooling at the exposed surface. Adjustments to the dead load

cylinder also had a noticeable effect on stirrup stress ranges. As an example, Figures A6.13 and A6.15 in Appendix A6 show the effects of applied dead load increase at about 700,000 cycles, and Figures A6.25 and A6.27 show the effects of dead load decrease at about 500,000 cycles. Measured stress ranges remained fairly consistent during high-cycle fatigue as illustrated in Figure 3.25, where strains changed slightly over a long period of cyclic loading. There were also several instances of instruments going out of range due to the demanding test protocol.

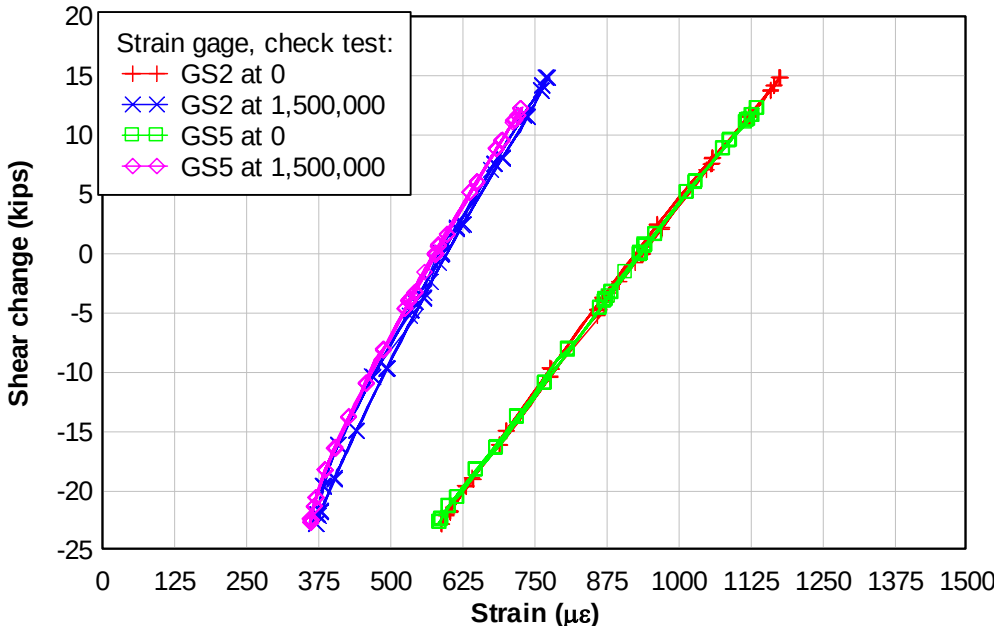

Figure 3.25: Measured strain comparing two interval tests for specimen 6IT10

Only small visible growths in crack width or extensions were observed over the 2,000,000 cycles for each specimen. Crack displacement tended to increase slightly, though typically not of a sufficient magnitude to be perceived using the visual ODOT crack comparator. Accounting for sensors and load fluctuations during the long-duration tests, the crack motion ranges typically increased, as shown in Table 3.10. These increases were attributed to bond slip of the stirrup relative to the concrete at the diagonal cracks. Concrete debris, shown in Figure 3.26a and b, and relative slip between the stirrup and concrete were visually observed at locations where concrete cover was removed to install strain gages on the stirrup leg.

Figure 3.26: Example of debris associated with bond damage around stirrup legs: a) specimen 6T10; b) specimen 3IT12

Corresponding rebar strains did not change at the same rate as the crack displacements. Similar magnitudes of stirrup strain were produced even as diagonal crack displacements became larger, as shown in Figure 3.27. Comparison of the strain gage and associated crack motion sensor ranges in Figure 3.28, over the course of the fatigue test further illustrate this behavior.

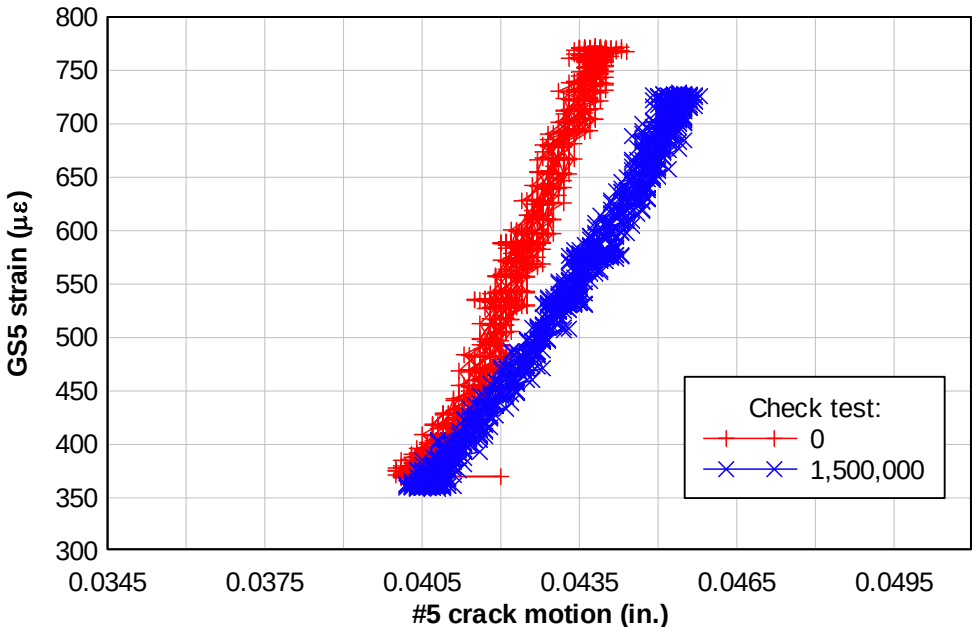

Figure 3.27: Strain gage and associated crack motion sensor at the eventual failure crack in specimen 6IT10. Note that after many cycles, less strain is needed to achieve the same crack movement

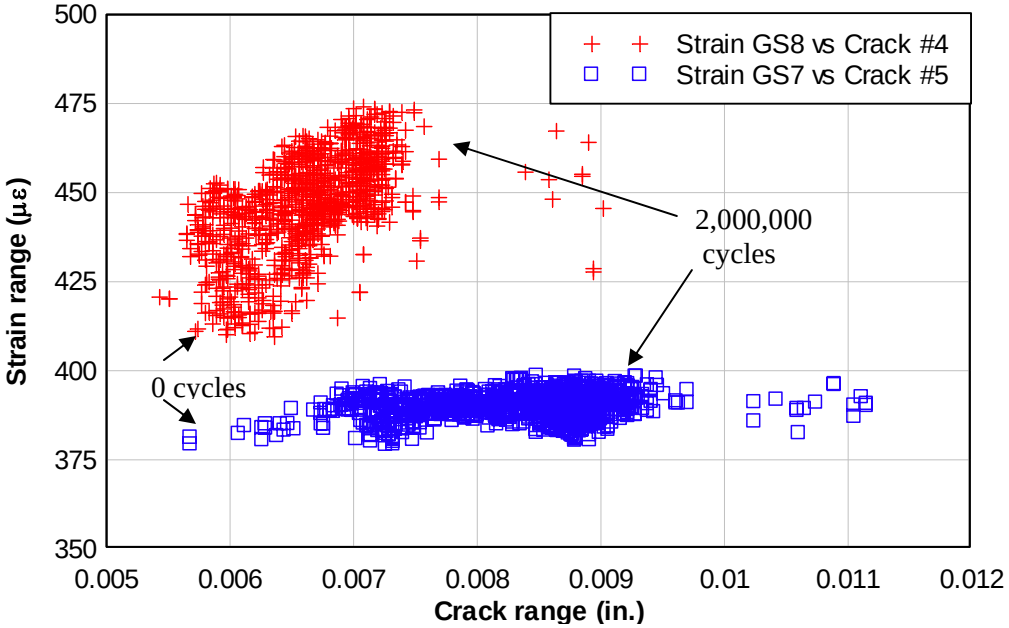

Figure 3.28: Changes in strain range and crack range for specimen 3IT12 over a 2,000,000 cycle HCF test

One sensor location shows the strain range increasing along with the crack range, while the other shows increasing crack motion with almost constant strain range. Thus, if the diagonal crack displacement increases without a corresponding increase in stirrup stress, the effective gage length of the rebar is likely increasing, indicating a reduction in bond. This degradation process was observed to be gradual. To evaluate the impact of stirrup debonding on the capacity and behavior of the girders, a series of tests was performed as described in the next section.

Metal fatigue of the stirrups occurred in only one specimen that contained the widest stirrup spacing considered in the HCF test series (3IT18). Testing at failure exposed two stirrups exhibiting cleavage failure surfaces instead of the ductile fracture surface commonly associated with previous ultimate strength tests as shown in Figure 3.29.

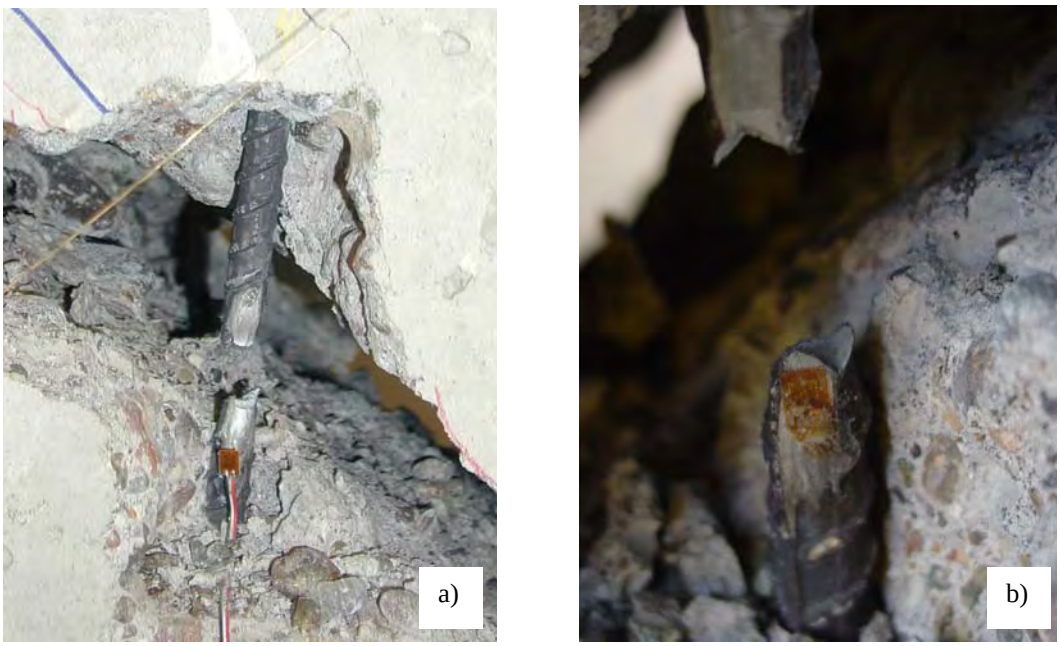

Figure 3.29: Ductile fracture of stirrup at ultimate strength: a) sensor GS8 on specimen 3IT18; b) another example from specimen 3IT12

One high-cycle fatigue fracture was located approximately 9 in. below strain gage GS2 on the east face stirrup leg and the other was located about 2 in. above GS7 on the west face stirrup leg; both are pictured in Figures 3.30 and 3.31.

Figure 3.30: Fracture surface on east leg of stirrup from high-cycle fatigue specimen 3IT18 at 9 in. below sensor GS2

Figure 3.31: Fracture surfaces on west leg of stirrup from high-cycle fatigue specimen 3IT18 at 2 in. above sensor GS7

The west face stirrup leg fracture occurred just after 1,750,000 cycles during fatigue testing as observed by the abrupt strain decrease in the stirrup and resulting increases in the neighboring stirrup strains and crack displacement sensor readings, as shown in Figures 3.32 and 3.33 for the crack motions and Figures 3.34 and 3.35 for the strain readings.

The measured stress range in stirrup GS7 was approximately 29 ksi as measured by the strain gage applied 2 in. above the eventual fracture location. The east stirrup leg fatigue fracture was not detected from the sensor measurements, but may have occurred at about the same time, so that the combined effect was blended into the measurements. The higher stress ranges carried by the adjacent stirrups would have caused these to fatigue at a higher rate and likely lead to their eventual fracture.

Subsequent strength testing of fatigued specimens did not indicate significant change in capacity as compared to the unfatigued specimens. However, to approximate the impact of very substantial stirrup debonding on the capacity and behavior of the girders, a series of tests was performed as described below.

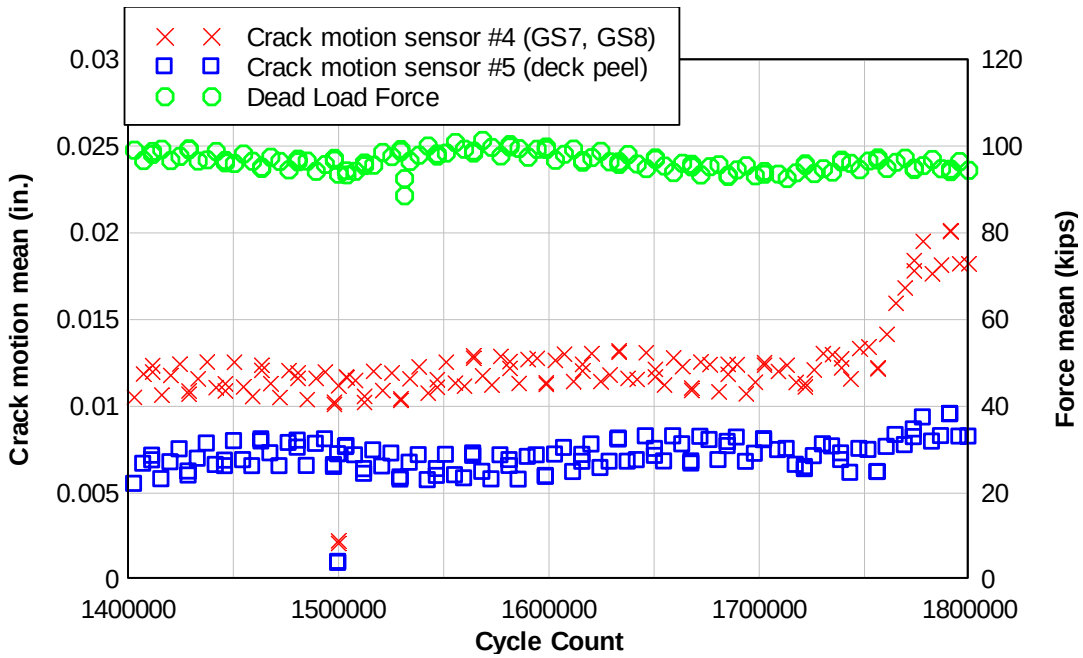

Figure 3.32: Detail from specimen 3IT18 load and crack motion sensor means. Note the change after 1,750,000 cycles

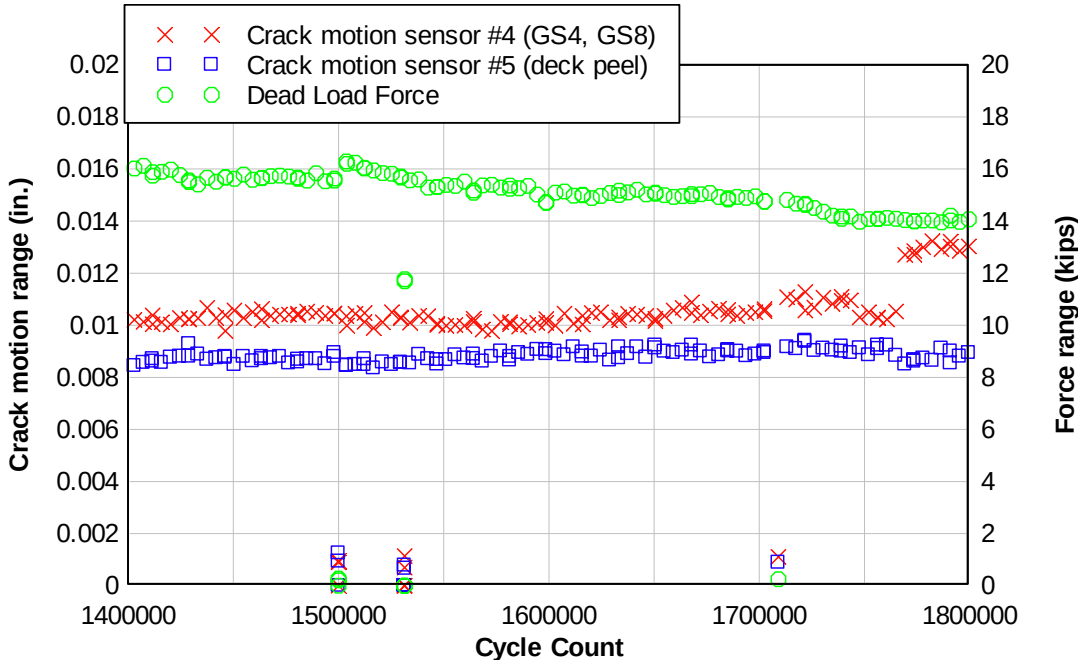

Figure 3.33: Detail from specimen 3IT18 Load and crack motion sensor ranges. Note the change after 1,750,000 cycles

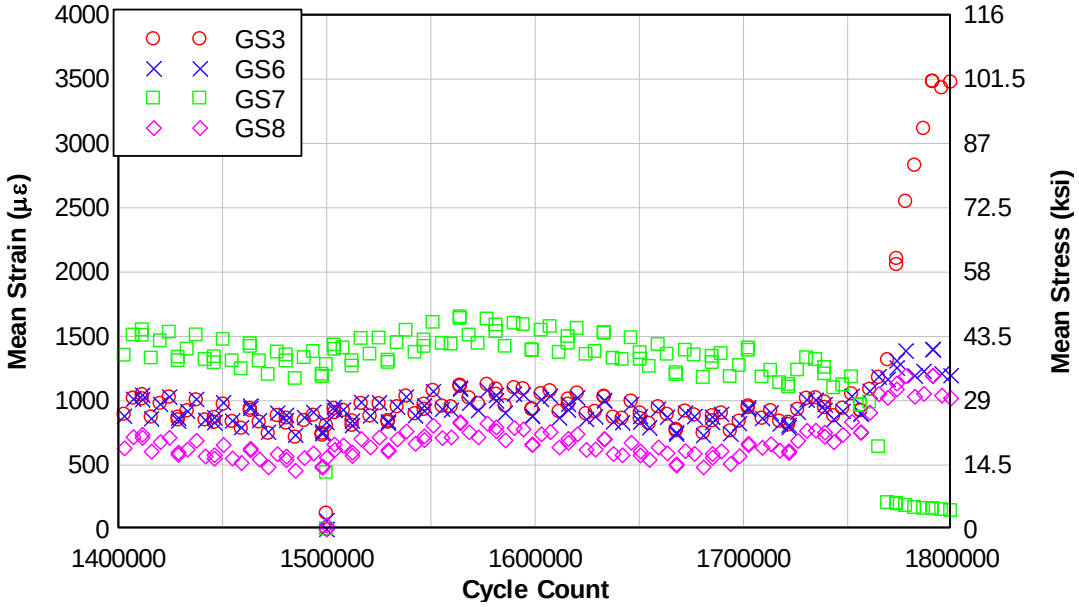

Figure 3.34: Detail from specimen 3IT18 South strain gage means. Note the change after 1,750,000 cycles

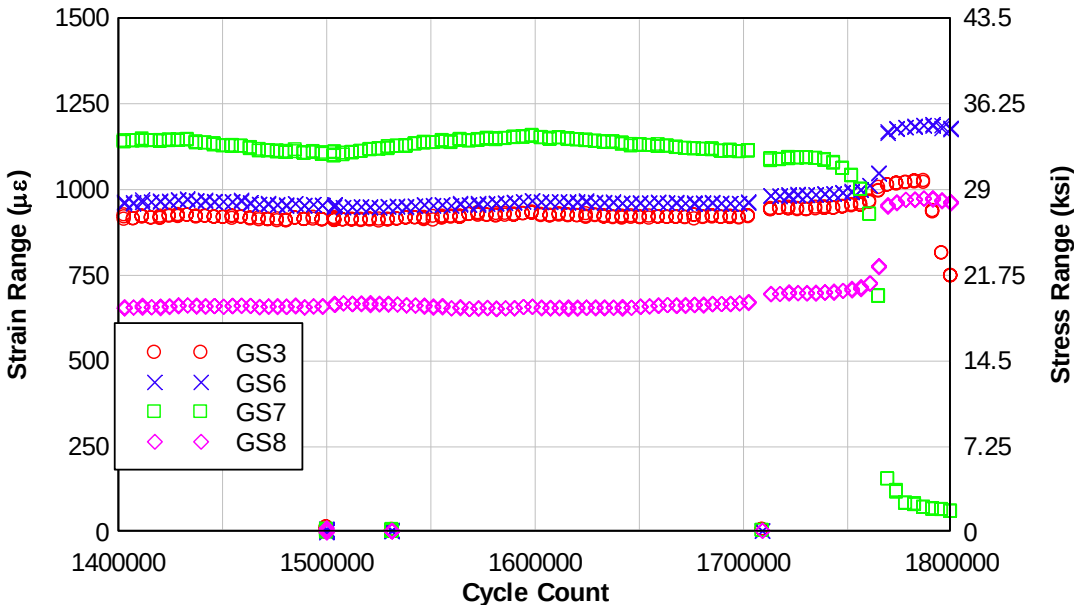

Figure 3.35: Detail from specimen 3IT18 South strain gage ranges. Note the change after 1,750,000 cycles

3.8.4 Debonded Stirrup Specimens

Based on the observed deterioration of the stirrup-concrete bond under high-cycle fatigue, a series of experiments was performed to assess the impact of stirrup debonding on the capacity and behavior of test specimens. During 2 million cycles of fatigue loading, the stirrups did not become fully debonded from the concrete along the entire leg length. However, if the high-cycle fatigue tests were permitted to be run continuously and at a sufficiently low threshold so as not to induce metal fatigue (stress range below 20 ksi) it could be possible to produce the condition of fully debonded stirrups. Due to the space, time, and equipment demands to achieve this condition, it was not possible to conduct these tests in the laboratory.

To simulate this effect, four specimens were constructed (7T6, 7T12, 7IT6, and 7IT12) with all the stirrup legs within the test span debonded from the concrete. The vertical straight leg portions of the stirrups were wrapped with plastic strand sheathing to prevent bond between the stirrup leg and surrounding concrete. The horizontal portion at the hooked end and the horizontal length between bends at the beam soffit were not wrapped. These specimens were tested using the control loading protocol described previously.

3.8.4.1 Debonded Stirrup Test Results

Experimental results from 5IT12-B4 specimen were used for comparisons of behavior between specimens with and without debonded stirrups, since these specimens had similar beam details and were subjected to the same test protocols. The stem concrete strengths of 5IT12-B4 and 7IT12 specimens were also similar, 4130 psi and 4165 psi, respectively.

Both specimens exhibited shear-compression failures with applied load of 405.4 kips for 5IT12-B4 specimen and 400.2 kips for specimen 7IT12. Failures occurred on the north end of both specimens. Specimen displacement under the load point at the failure load was 1.01 in. for the 5IT12-B4 specimen and 0.81 in. for the 7IT12 specimen. Fewer but wider diagonal-tension cracks were observed in 7IT12 specimen as shown in Figure 3.36.

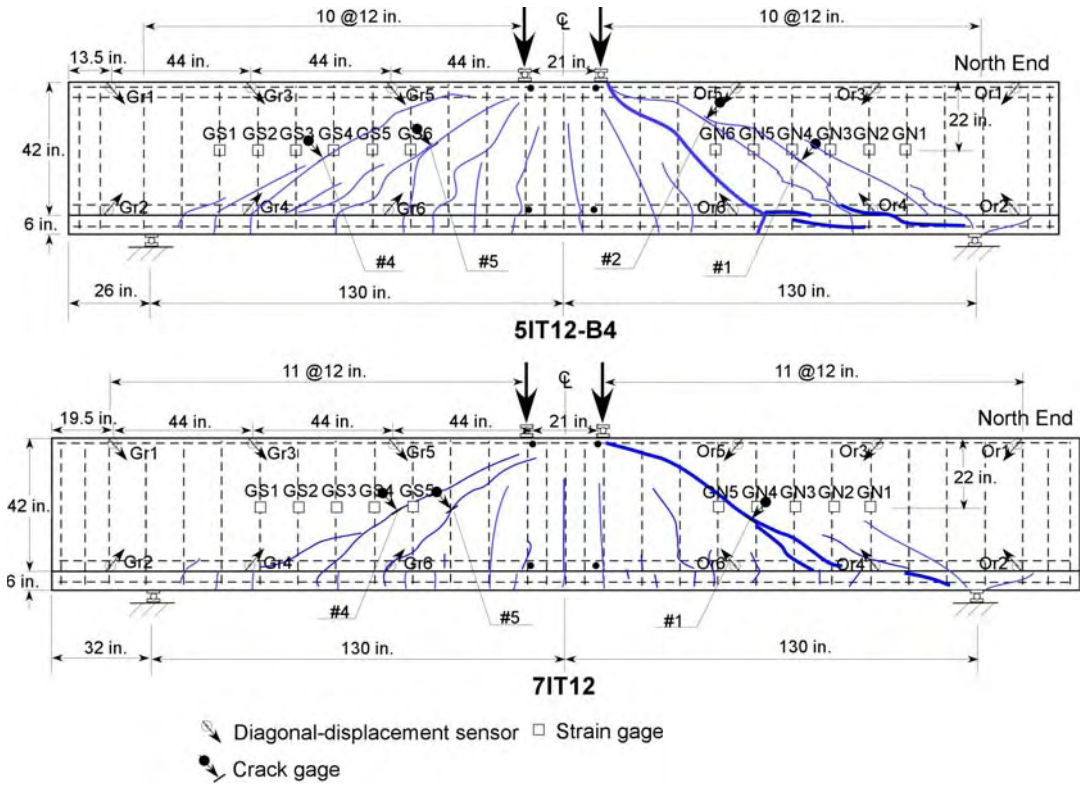

Figure 3.36: Crack pattern and instrument locations for 5IT12-B4 and 7IT12 specimens

The largest crack width measured with the visual crack comparator at the load step prior to failure was 0.124 in. for specimen 5IT12-B4 and 0.132 in. for specimen 7IT12. Specimen 5IT12-B4 was stiffer than 7IT12 specimen as shown in Figure 3.37. Although failure loads of both specimens were relatively similar, specimen 7IT12 was less ductile.

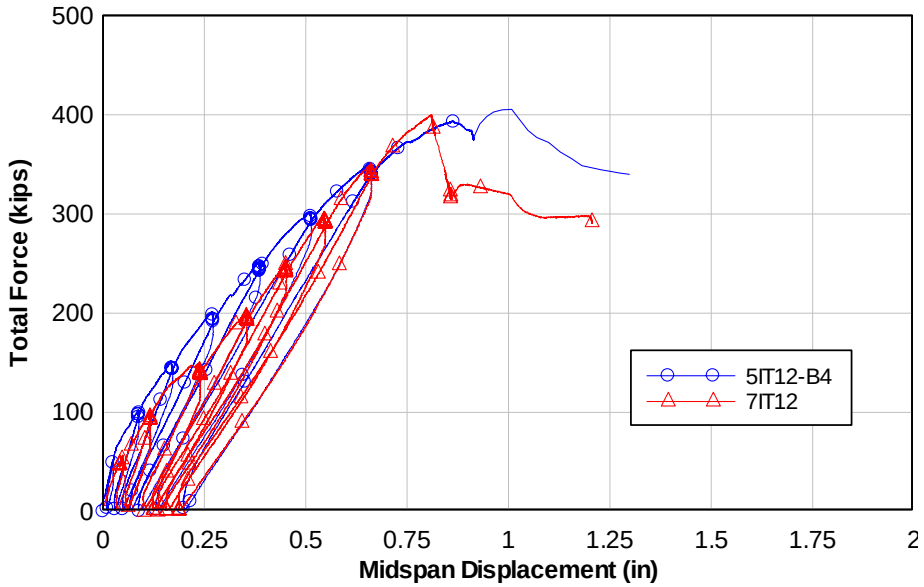

Figure 3.37: Load-midspan displacement plots for 5IT12-B4 and 7IT12 specimens

Diagonal-tension cracks in specimen 7IT12 formed earlier than those in 5IT12-B4 specimen, as indicated by the first abrupt change in stirrup strains shown in Figure 3.38a. Smaller crack widths at unloading were observed for the 7IT12 specimen due to the debonded stirrups as shown in Figure 3.38b. This was a result of reduced local stirrup yielding at crack locations due to the longer effective gage length of the stirrup leg.

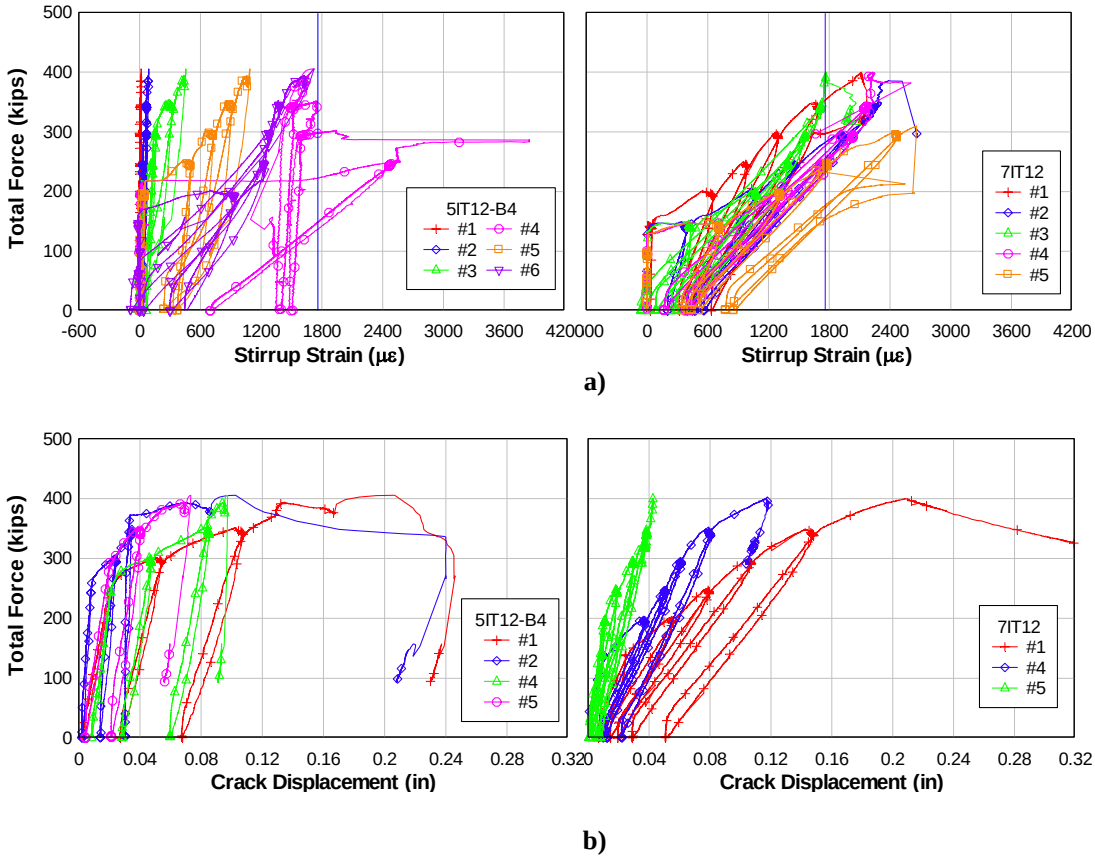

Figure 3.38b: Stirrup strains and crack displacements for 5IT12-B4 and 7IT12 specimens: a) stirrup strains in the north-end side; b) crack displacements

Typically, strain gages located near midheight of specimens with bonded reinforcing bars measured large strains in stirrups when diagonal-tension cracks form across or near the instrumentation locations on the stirrups, as occurred in specimen 5IT12-B4. Strain sensors GN1 and GN2 in specimen 5IT12-B4 indicated small strains throughout the test, as shown in Figure 3.38a, because they were not located near a diagonal crack. For specimen 7IT12, large stirrup strains were observed from sensors GN1-GN3 although no diagonal cracks formed near the strain gages.

Strains in all instrumented stirrups of specimen 7IT12 exhibited similar response for both loading and unloading and exceeded the yield strain indicated by a vertical line in Figure 3.38a. When strains in all stirrups across a diagonal-tension crack reach the yield stress for the debonded condition, the section is likely near failure. For specimen 5IT12-B4, failure occurred before the strain in sensor GN6 was close to the yield strain. Specimen 7IT12 failed after sensor GN3 reached the yield stress.

3.8.5 Conclusions

Full-size tests of conventionally-reinforced concrete (CRC) girders, designed and constructed to reflect 1950's vintage details and materials, were performed under high-cycle fatigue. Prior to fatigue loading, specimens were precracked to achieve desired crack widths corresponding to observed field conditions. High-cycle fatigue loading was applied to the precracked specimens with a constant amplitude load range of 80 kips for 2,000,000 cycles. The specimens were then tested to ultimate. A series of tests with fully debonded stirrups was also performed to simulate a condition of serious bond deterioration. Based on these tests, the following conclusions are presented:

- Repeated loading in the service range can lead to metal fatigue of embedded stirrups. Stress ranges needed to meet this condition exceeded 20 ksi and appear to be represented by fatigue data for reinforcing steel as discussed in the field testing section.

- Diagonal crack widths tended to increase under repeated loading.

- Stirrup strain range changes varied for different specimens, although in general these remained fairly similar from the start to the end of high-cycle fatigue testing.

- Flexural bar cutoffs combined with straight-bar anchorage appeared to have more rapid changes for both crack displacement as well as strain ranges and means than otherwise similar specimens with well-anchored flexural reinforcement.

- The mechanism for damage from high-cycle fatigue (if fracture is precluded) is bond fatigue at the stirrup/concrete interface.

- Bond fatigue may eventually lead to longer gage lengths for stirrups and reduced constraint at diagonal crack locations, thereby leading to wider diagonal cracks.

- Wider cracks resulting from bond deterioration under HCF may reduce capacity based on modified compression-field theory (MCFT). Analysis methods to account for bond deterioration are discussed in a subsequent section.

- The specimen with fully debonded stirrups exhibited only slightly reduced capacity than an otherwise similar specimen with bonded stirrups. Stirrup debonding resulted in fewer but wider diagonal cracks, although the overall specimen displacement was reduced at failure.

- For the specimens and loading conditions considered, HCF loading did not significantly diminish the capacity of the specimens, when metal fatigue of the stirrups was precluded.

3.9 MOVING LOAD TESTS

Moving load tests are described in a separate appendix to this report.

ASSESSMENT METHODOLOGY FOR DIAGONALLY CRACKED REINFORCED CONCRETE DECK GIRDERS

4.0 ANALYSIS OF SHEAR CAPACITY FOR VINTAGE RC GIRDERS AND BENT CAPS 205

4.1 ACI METHOD 205
4.2 RESPONSE 2000™ 208
4.3 MODIFIED COMPRESSION FIELD THEORY 223
4.4 ANALYSIS OF MOVING SUPPORTS 226
4.4.1 Analysis Description 226
4.4.1.1 Specimen 4IT6-10 226
4.4.1.2 Specimen 4IT8-12 229
4.5 ANALYSIS FOR SPECIMENS WITH CUTOFF AND ANCHORAGE 231
4.5.1 Anchorage of Flexural Reinforcing 231
4.5.2 Flexural Reinforcing Cutoff Locations 233
4.6 COMPARISON ANALYSES FOR COMMON MATERIAL PROPERTIES 235
4.7 STRUT-AND-TIE METHOD 238
4.7.1 STM Model for Test Specimens 239
4.7.2 STM for Bent Caps 241
4.8 FINITE ELEMENT ANALYSIS 244
4.9 PREDICTION OF SERVICE LEVEL STIRRUP STRESS FOR FATIGUE ASSESSMENT 249
4.9.1 Service Level Prediction Methodology 250
4.9.2 Amplification Factor for Yielding of the Stirrups at Diagonal Cracks 252
4.9.3 Reloading of Previously Cracked Sections 253
4.9.4 Stirrup Strain Prediction 254
4.9.5 Shear-Moment Interaction Curves for Stirrup Yielding 257
4.10 LIFE PREDICTION FOR LOW-CYCLE FATIGUE 259
4.11 CONCLUSIONS 269

List of Figures

Figure 4.1a: Comparison of experimental and predicted shear using simplified ACI method 207
Figure 4.1b: Comparison of experimental and predicted shear using detailed ACI method 207
Figure 4.2a: Experimental and *Response2000*™ predicted behavior for Group 1 specimens 209
Figure 4.2b: Experimental and *Response2000*™ predicted behavior for Group 2 specimens 210
Figure 4.2c: Experimental and *Response2000*™ predicted behavior for Group 3 specimens 211
Figure 4.2d: Experimental and *Response2000*™ predicted behavior for Group 4 specimens 212
Figure 4.2e: Experimental and *Response2000*™ predicted behavior for Group 5 specimens 213
Figure 4.2f: Experimental and *Response2000*™ predicted behavior for Group 6 specimens 214
Figure 4.2g: Experimental and *Response2000*™ predicted behavior for Group 7 specimens 215
Figure 4.2h: Experimental and *Response2000*™ predicted behavior for Group 8 specimens 216
Figure 4.2i: Experimental and *Response2000*™ predicted behavior for Group 9 specimens 217
Figure 4.2j: Experimental and *Response2000*™ predicted behavior for Group 10 specimens 218
Figure 4.3: Location of critical section with respect to failure crack location 219

Figure 4.4: Comparison of experimental and predicted shear using *Response 2000*™ 222
Figure 4.5: MCFT strains and forces on cracked section (*AASHTO LRFD 2003*) 224
Figure 4.6: Comparison of experimental and predicted shear using AASHTO MCFT 225
Figure 4.7: Moment and shear diagrams for 4IT6-10 specimen 227
Figure 4.8: M-V envelope of capacity for 4IT6-10 specimen; a) using *Response2000*™ program; b) using AASHTO MCFT method 228
Figure 4.9: Moment and shear diagrams for 4IT8-12 specimen 229
Figure 4.10: M-V envelope of capacity for 4IT8-12 specimen: a) using *Response 2000*™ program; and b) using AASHTO MCFT method 230
Figure 4.11: Forces at end region of inverted-T specimens 231
Figure 4.12: Effective cross-sectional area of flexural bars for T specimens with cutoff details 234
Figure 4.13: Effective cross-sectional area of flexural bars for Inverted-T specimens with cutoff details 235
Figure 4.14: Sections, loading and material properties for analyses using common material properties 236
Figure 4.15: Predicted shear capacity using same material properties: a) Inverted-T specimens; b) T specimens 237
Figure 4.16: Simple strut-and-tie models for shear capacity prediction of control specimen group 239
Figure 4.17: Predicted and measured shear capacity for control group of specimens using STM 241
Figure 4.18: Single strut STM models for shear capacity prediction of field study bridge bent caps 242
Figure 4.19a: Capacity predictions and demand on bent caps for McKenzie River Bridge 243
Figure 4.19b: Capacity predictions and demand on bent caps for 15 Mile Creek Bridge 244
Figure 4.19c: Capacity predictions and demand on bent caps Jasper Bridge 244
Figure 4.20: Finite element model of specimen 10T24 and strain gage location 246
Figure 4.21: Deformed shape and principal tensile strain pattern of 10T24 FE model close to failure 246
Figure 4.22: FE analysis and experimental results of specimen 10T24: a) load-displacement at midspan plot; b) load-stirrup strain plot 247
Figure 4.23: Finite element model of moving-load specimen 11T22 248
Figure 4.24: Deformed shape and principal tensile strain pattern of specimen 11T22 model: a) at loadstep prior to failure; b) at failure load 249
Figure 4.25: Approximate sectional MCFT analysis (*Collins and Mitchell 1991*) 250
Figure 4.26a: Shear-moment interactions for capacity prediction of specimen 2T12 251
Figure 4.26b: Shear-moment interactions for capacity prediction of specimen 2IT12 251
Figure 4.26c: Shear-moment interactions for capacity prediction of specimen 10T24 252
Figure 4.27: Cracking strain, ε_{cr}, determination for specimen 2T12 254
Figure 4.28: V-ε_t at south side M/V=4 ft for a) specimen 3T12; and b) specimen 2T12 255
Figure 4.29: V-ε_t at north side M/V=4ft for a) specimen 2T12; and b) M/V=6 for specimen 2T12 255
Figure 4.30: V-ε_t at south side M/V=6 ft for a) specimen 2T12; and b) specimen 2IT12 256
Figure 4.31: V-ε_t at south side M/V=6 ft for a) specimen 2IT12; and b) specimen 10T24 256
Figure 4.32: Shear-moment interaction for stirrup yielding for specimen 2T12 258
Figure 4.33: Shear-moment interaction for stirrup yielding for specimen 2IT12 258
Figure 4.34: Shear-moment interaction for stirrup yielding for specimen 10T24 259
Figure 4.35: The three damage phases for low cycle fatigue specimen as illustrated by, force-diagonal deflection response from specimen 10T24 260
Figure 4.36: Incremental diagonal displacement during initial damage phase for inverted-T specimens with 12in. stirrup spacing 260
Figure 4.37: Incremental diagonal displacement during initial damage phase for specimens with similar load ranges 261
Figure 4.38: Incremental diagonal displacement during secondary damage phase for specimens with various load ranges 261
Figure 4.39: Incremental diagonal displacement during tertiary damage phase for specimens with various load ranges 262
Figure 4.40: Example of graphical analysis used to estimate the number of cycles to achieve equivalent diagonal displacement at failure 263
Figure 4.41: Midspan displacement Δ_0 with increasing loading ratio for specimens with 12in. stirrup spacing 264
Figure 4.42: Midspan displacement Δ_0 with increasing loading ratio for specimens with 24in. stirrup spacing 264
Figure 4.43: Coefficient for initial phase of low cycle fatigue for specimens with 12in. stirrup spacing for increasing V/V_n ratios 265

Figure 4.44: Coefficient for initial phase of low cycle fatigue for specimens with 24in. stirrup spacing for increasing V/V_n ratios 266
Figure 4.45: Coefficient for secondary phase of low cycle fatigue for specimens with 12in. stirrup spacing for increasing V/V_n ratios 267
Figure 4.46: Coefficient for secondary phase of low cycle fatigue for specimens with 24in. stirrup spacing for increasing V/V_n ratios 267
Figure 4.47: Number of cycles to failure for different V/V_n ratios for girders with 12in. stirrup spacing 268
Figure 4.48: Number of cycles to failure for different V/V_n ratios for girders with 24in. stirrup spacing 269

List of Tables

Table 4.1: ACI predicted shear capacities for laboratory specimens 206
Table 4.2: Length of crack extension beyond critical section 219
Table 4.3: Predicted shear capacities for laboratory specimens (COV in %) 220
Table 4.4: Least tensile strength used for capacity prediction of specimens subjected to cyclic loading and specimens with fully debonded stirrups 223
Table 4.5: Bond strength comparisons 226
Table 4.6: Shear capacity predictions for specimens with flexural bar cutoff details (COV in %) 235

4.0 ANALYSIS OF SHEAR CAPACITY FOR VINTAGE RC GIRDERS AND BENT CAPS

Five different analysis methods were used to the predict shear capacity of the RC girders and bent caps with vintage reinforcing details. These included: traditional ACI approach (*AASHTO Standard Specification 2002*), *Response 2000*™ (*Bentz 2000*), Modified Compression Field Theory (MCFT) (*AASHTO-LRFD 2003*), Strut-and-Tie Method (STM) (*AASHTO-LRFD 2003*), and the finite element method. Each of these methods is described below, and comparisons of predicted shear capacity were made with experimental results. Based on experimental results of low-cycle fatigue tests, deterioration effects can be incorporated into the analysis.

4.1 ACI METHOD

The most common method for computing the shear strength of CRC elements consists of the superposition of the concrete and stirrup contributions to shear resistance (*AASHTO 2002*):

$$V_n = V_c + V_s \tag{4-1}$$

$$V_c = 2\sqrt{f'_c}\, b_w d \tag{4-2}$$

$$V_s = \frac{A_v f_y d}{s} \tag{4-3}$$

where V_n is the nominal shear resistance, V_c is the shear resistance of the concrete (lbs), V_s is the shear resistance of the transverse steel (lbs), f'_c is the compressive strength of the concrete (psi), b_w is the width of the beam stem (in), A_v is the area of the transverse steel (in^2), f_y is the yield strength of the transverse steel (psi), d is the effective depth (in), and s is the spacing of the transverse steel (in).

A more detailed equation for the concrete contribution to shear based on empirical fit for shear test results for beams without shear reinforcement (*AASHTO 2002*) is:

$$V_c = (1.9\sqrt{f'_c} + 2500\rho \frac{V_u d}{M_u}) b_w d \le (3.5\sqrt{f'_c}) b_w d \tag{4-4}$$

where ρ is the reinforcement ratio, V_u is the factored shear at the design section, and M_u is the factored moment at the design section.

Shear capacity for the experimental beams was determined using actual concrete strengths and rebar yield stresses. Results are summarized in Table 4.1 and shown in Figs. 4.1a and 4.1b. As seen in these figures, the ACI approaches provided a reasonably simple method to estimate shear capacity of the large CRC beams with at least minimum stirrups (as defined by the specification).

Table 4.1: ACI predicted shear capacities for laboratory specimens

No.	Specimen	V_{APP} (kips)	Stem f'_c (psi)	d (in)	a/d ratio	S (in)	V_s (kip)	ACI 1		ACI 2				V_{APP}/V_{ACI}	
								V_c (kip)	V_{total} (kip)	ρ_ω	$V_u d/M_u$	V_c (kip)	V_{total} (kip)	1	2
1	1T6	206.5	4700	43.4	3.0	6	147.6	83.3	230.9	0.0154	0.477	90.3	237.9	NA	NA
2	1IT6	236.0	4775	45.3	2.9	6	154.0	87.6	241.7	0.0148	0.508	95.1	249.2	NA	NA
3	1T18	169.8	4925	43.4	3.0	18	49.2	85.3	134.5	0.0154	0.477	92.2	141.4	1.26	1.20
4	1IT18	158.8	4550	45.3	2.9	18	51.3	85.6	136.9	0.0148	0.508	93.2	144.5	1.16	1.10
5	2T10	205.3	3550	43.4	3.0	10	88.5	72.4	160.9	0.0154	0.477	79.9	168.5	1.28	1.22
6	2IT10	205.3	3290	45.3	2.9	10	92.4	72.8	165.2	0.0148	0.508	81.0	173.4	NA	NA
7	2T12	192.9	3520	43.4	3.0	12	73.8	72.1	145.9	0.0154	0.477	79.7	153.4	1.32	1.26
8	2IT12	183.8	3575	45.3	2.9	12	77.0	75.8	152.8	0.0148	0.508	83.9	160.9	NA	NA
9	3T12	188.7	3990	43.4	3.0	12	73.8	76.8	150.5	0.0154	0.477	84.1	157.9	1.25	1.20
10	3IT12	207.5	4180	45.3	2.6	12	77.0	82.0	159.0	0.0148	0.604	92.0	169.1	1.30	1.23
11	3T18	153.3	3970	43.4	3.0	18	49.2	76.6	125.8	0.0154	0.477	83.9	133.1	1.22	1.15
12	3IT18	147.1	3915	45.3	2.6	18	51.3	79.4	130.7	0.0148	0.604	89.5	140.9	1.13	1.04
13	4IT6-10	216.5	3790	45.3	2.9	10	92.4	78.1	170.5	0.0148	0.508	86.1	178.5	NA	NA
14	4IT8-12	242.9	3710	45.3	2.6	10	92.4	77.3	169.7	0.0148	0.604	87.5	179.9	1.43	1.35
15	4T10-12	244.4	3945	43.4	1.9	10	88.5	76.3	164.9	0.0154	1.000	95.9	184.4	1.48	1.33
16	4T12-18	239.8	4060	43.4	1.9	12	73.8	77.4	151.2	0.0154	1.000	96.9	170.7	1.59	1.40
17	5IT12-B1	195.1	3700	45.3	2.6	12	77.0	77.2	154.2	0.0148	0.604	87.4	164.4	1.27	1.19
18	5IT12-B2	217.5	4160	45.3	2.6	12	77.0	81.8	158.8	0.0148	0.604	91.9	168.9	1.37	1.29
19	5IT12-B3	193.3	4310	45.3	2.6	12	77.0	83.3	160.3	0.0148	0.604	93.2	170.3	1.21	1.14
20	5IT12-B4	206.5	4130	45.3	2.6	12	77.0	81.5	158.5	0.0148	0.604	91.6	168.6	1.30	1.22
21	6T6	240.0	4590	43.4	2.7	18	49.2	82.3	131.5	0.0154	0.566	91.4	140.6	1.82	1.71
22	6IT6	237.6	5110	45.3	2.6	6	154.0	90.7	244.7	0.0148	0.604	100.3	254.3	NA	NA
23	6T10	210.4	4595	43.4	3.0	10	88.5	82.4	170.9	0.0154	0.477	89.4	178.0	NA	NA
24	6IT10	237.8	5495	45.3	2.6	10	92.4	94.0	186.4	0.0148	0.604	103.5	195.9	1.28	1.21
25	7T6	213.7	4405	43.4	3.0	6	147.6	80.7	228.2	0.0154	0.477	87.8	235.3	NA	NA
26	7IT6	207.0	4350	45.3	2.6	12	77.0	83.7	160.7	0.0148	0.604	93.6	170.6	1.29	1.21
27	7T12	215.6	4280	43.4	2.7	12	73.8	79.5	153.3	0.0154	0.566	88.8	162.5	1.41	1.33
28	7IT12	204.4	4165	45.3	2.6	12	77.0	81.9	158.9	0.0148	0.604	91.9	168.9	1.29	1.21
29	8IT10	221.8	4750	45.3	2.6	10	92.4	87.4	179.8	0.0098	0.604	92.5	184.9	1.23	1.20
30	8IT12	186.1	4840	45.3	2.6	12	77.0	88.2	165.3	0.0098	0.604	93.3	170.3	1.13	1.09
31	8T12-B3	183.9	5070	43.4	3.0	12	73.8	86.5	160.3	0.0154	0.477	93.4	167.1	1.15	1.10
32	8T12-B4	158.9	4995	43.8	3.0	12	74.5	86.7	161.1	0.0127	0.483	91.8	166.2	0.99	0.96
33	9IT12-B1	216.8	4285	45.3	2.6	12	77.0	83.0	160.0	0.0098	0.604	88.3	165.3	1.35	1.31
34	9IT12-B2	183.3	4605	45.3	2.6	12	77.0	86.1	163.1	0.0098	0.604	91.2	168.2	1.12	1.09
35	9T12-B3	170.3	4645	43.4	3.0	12	73.8	82.8	156.6	0.0154	0.477	89.8	163.6	1.09	1.04
36	9T12-B4	153.5	4705	43.8	3.0	12	74.5	84.1	158.6	0.0127	0.483	89.3	163.8	0.97	0.94
37	10T0	54.8	4610	45.0	2.9	0	0	85.6	85.6	0.0074	0.503	87.2	87.2	0.64	0.63
39	10T24-B3	107.9	3450	43.8	3.0	24	37.2	72.0	109.3	0.0127	0.483	77.9	115.1	0.99	0.94
40	10T24-B4	125.3	3420	43.8	3.0	24	37.2	71.7	108.9	0.0127	0.483	77.6	114.8	1.15	1.09
													Avg.	1.24	1.17
													COV (%)	16.7	15.5

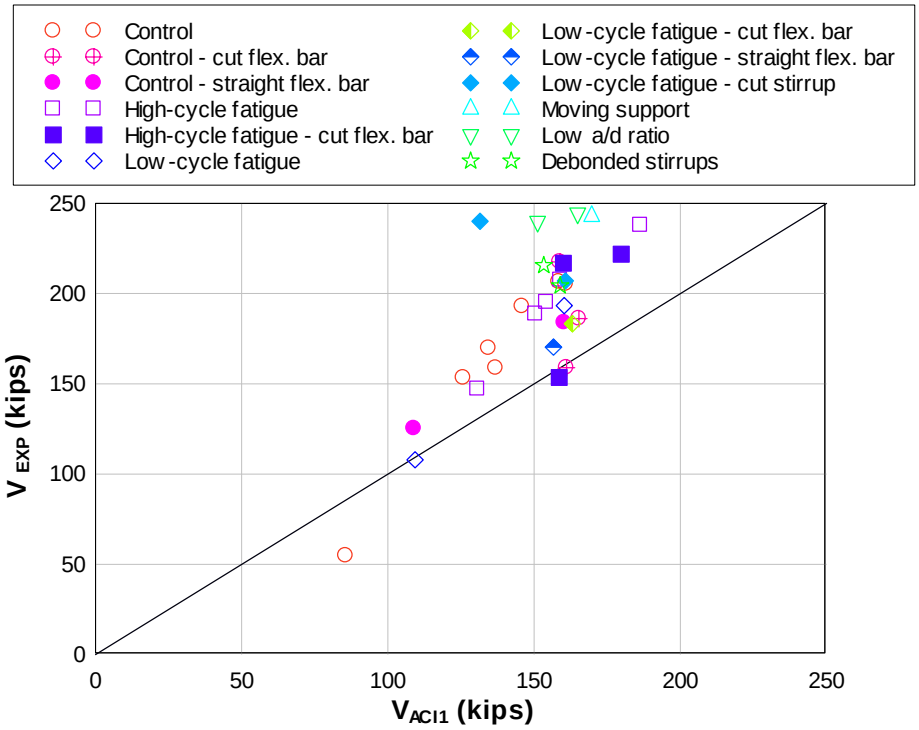

Figure 4.1a: Comparison of experimental and predicted shear using simplified ACI method

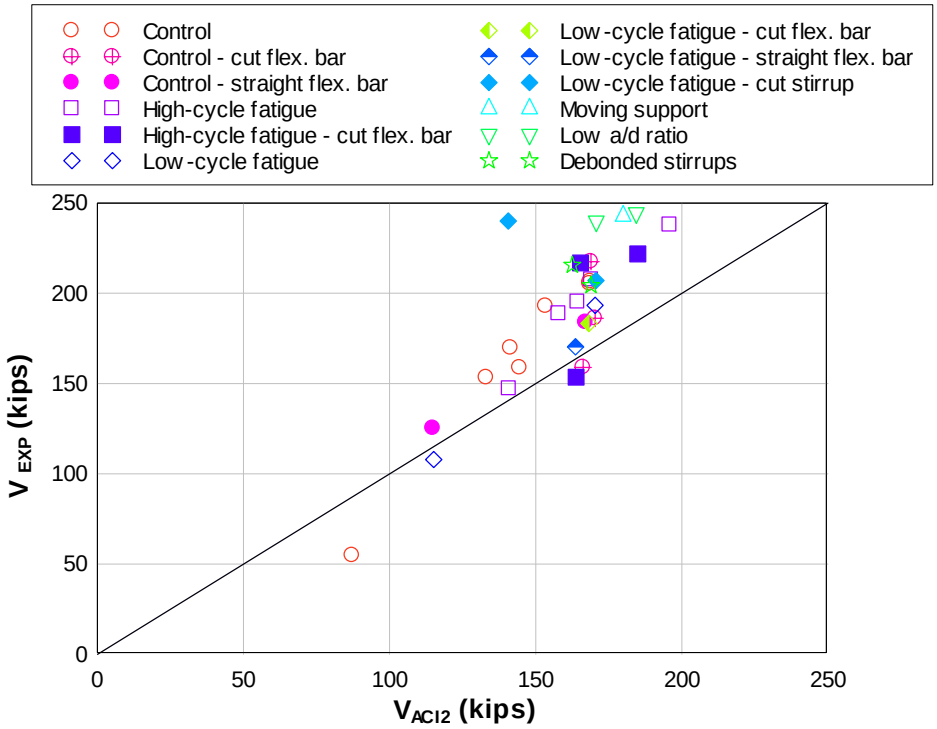

Figure 4.1b: Comparison of experimental and predicted shear using detailed ACI method

However, for the large and unreinforced specimen (without stirrups), the ACI methods significantly overestimated shear capacity. For all tests, the mean value for the ratio of experimental to predicted shear strength was 1.24 with a coefficient of variation of 0.17 for the simple approach (Equation 4-2), and the ratio of experimental to predicted shear strength was 1.17 with a coefficient of variation of 0.16 for the complex equation (Equation 4-4).

There is no rational method to incorporate damage from stirrup debonding from high-cycle fatigue or cumulative damage from low-cycle fatigue into these capacity equations, except to apply empirical coefficients based on the measured strength reductions for the different amounts of laboratory imposed fatigue damage. However, given the inherent scatter of results over the spectrum of test variables that are not incorporated into the ACI equations, the results from this approach would be questionable. This is particularly so, as other methods provide better correlation with experiments and can be modified to include damage effects, as seen subsequently.

4.2 RESPONSE 2000™

The beam specimens were analyzed with a specialty computer program called *Response 2000*™. The program was developed by E. Bentz at the University of Toronto (*Bentz 2000*). The program uses a sectional analysis approach to assess the load-deformation response of cross-sections subject to bending moments, shear forces, and axial loads. Constitutive relationships between stresses and strains at a section are based on Modified Compression Field Theory (MCFT). The program accommodates many different cross-sectional shapes, is easy to use, and is available free on the Internet (see http://www.ecf.utoronto.ca/~bentz/r2k.htm). The program predicts the shear-moment capacity curve for a specified cross-section, although the V-M response for high shear to moment ratios is not well predicted. Additionally, the program computes the AASHTO nominal V-M capacity curve based on MCFT for a specified cross-section (this is referred to here as AASHTO-MCFT).

There are two analysis options for member assessment: a) sectional analysis, and b) member analysis. Member analysis is performed for specified beam span and loading conditions. This may be used to directly compare with discrete laboratory specimens. The overall member response is predicted and local concrete and reinforcing stresses are determined. This method was used for comparison with the laboratory specimen load-centerline deformation responses of all specimens as shown in Figs. 4.2a-j. Actual materials properties for each specimen were used as input for the analyses. As seen in these figures, the member analysis provided reasonably good prediction of the backbone or envelope force-displacement response for test specimens, considering the range of stirrup spacings and material properties. However, specimens with unsymmetrical support conditions, variable stirrup spacing, and flexural bar cutoffs within the test span were not as well predicted, as the program does not currently provide direct analysis of these conditions.

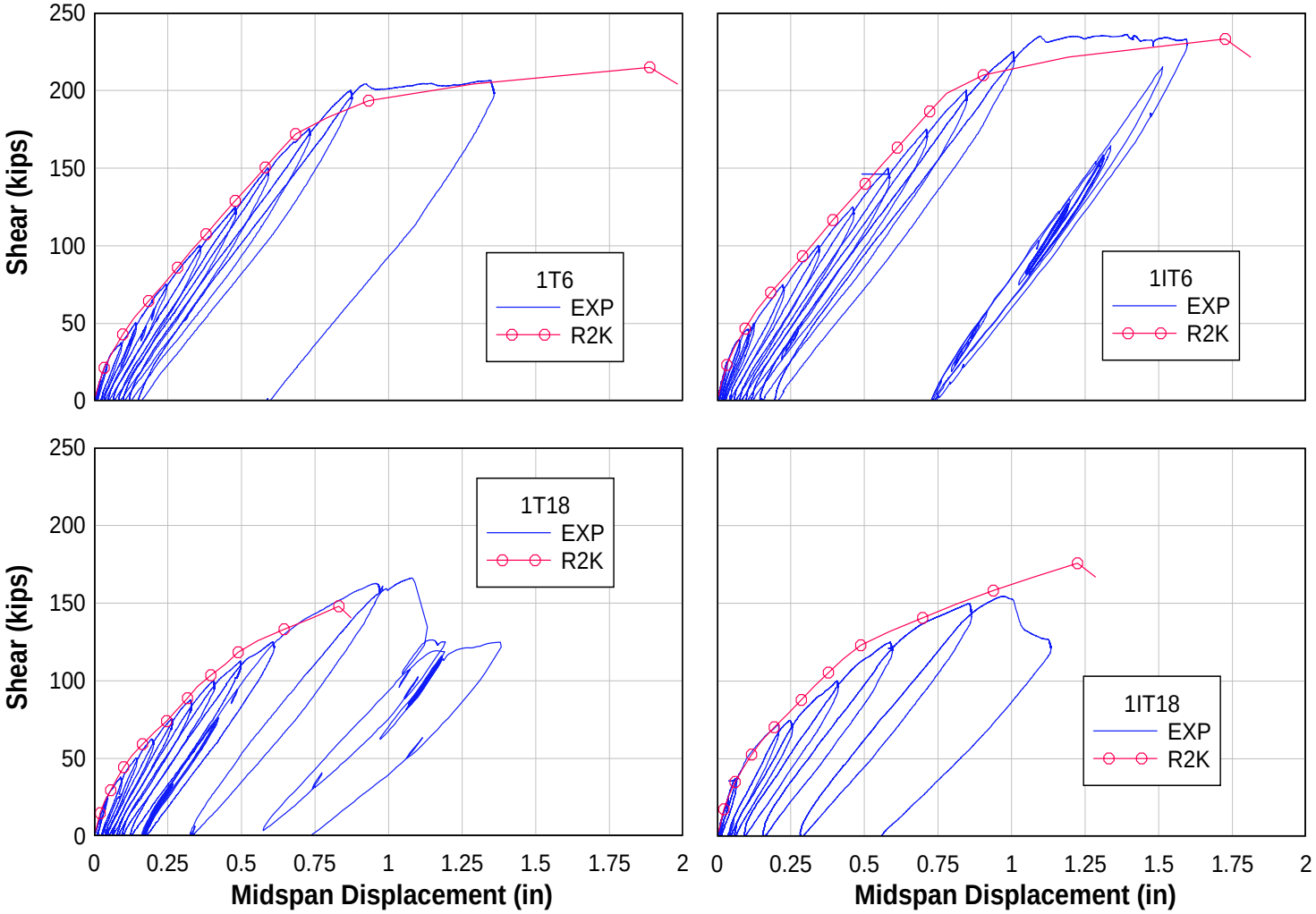

Figure 4.2a: Experimental and *Response2000*™ predicted behavior for Group 1 specimens

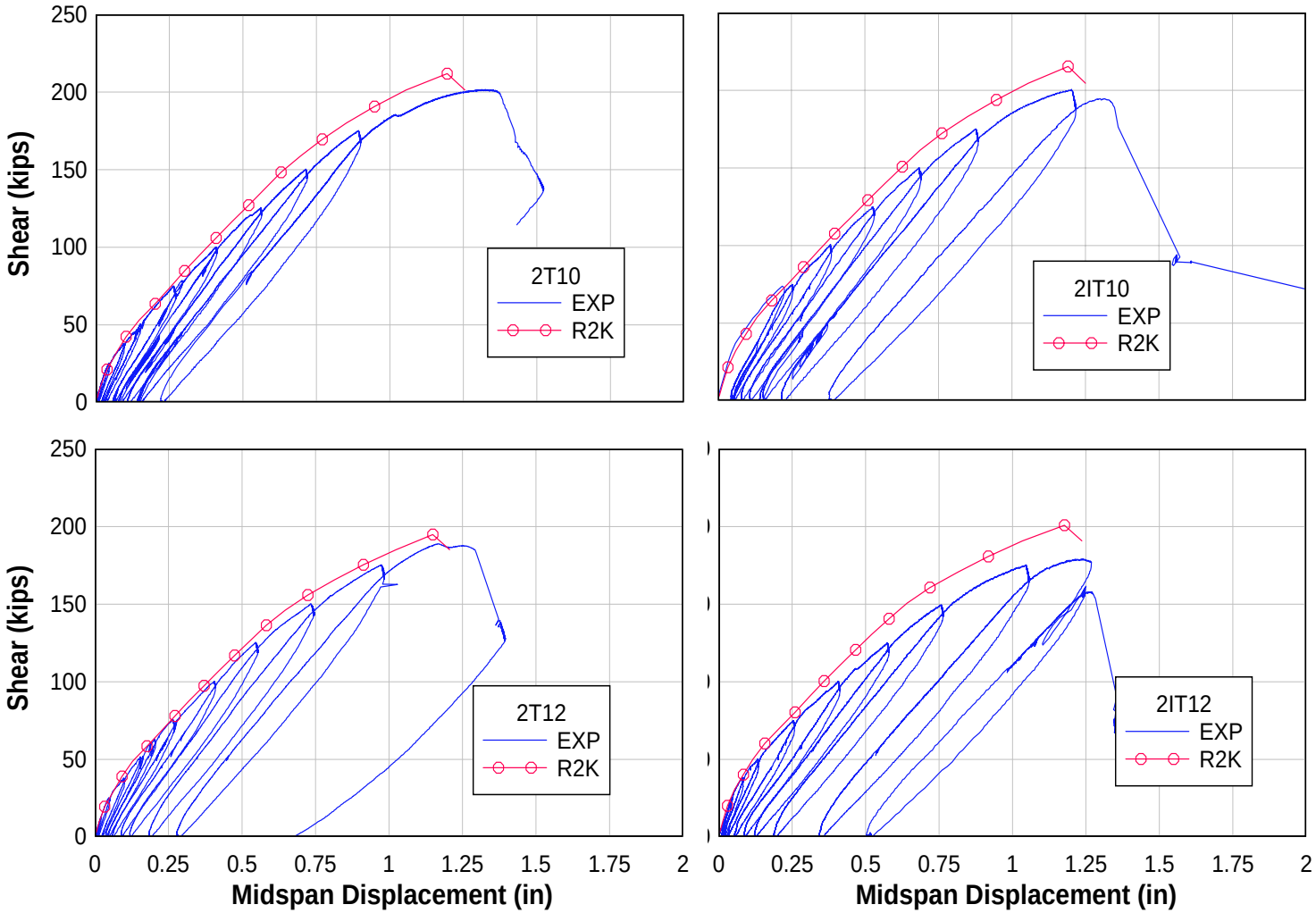

Figure 4.2b: Experimental and *Response2000*™ predicted behavior for Group 2 specimens

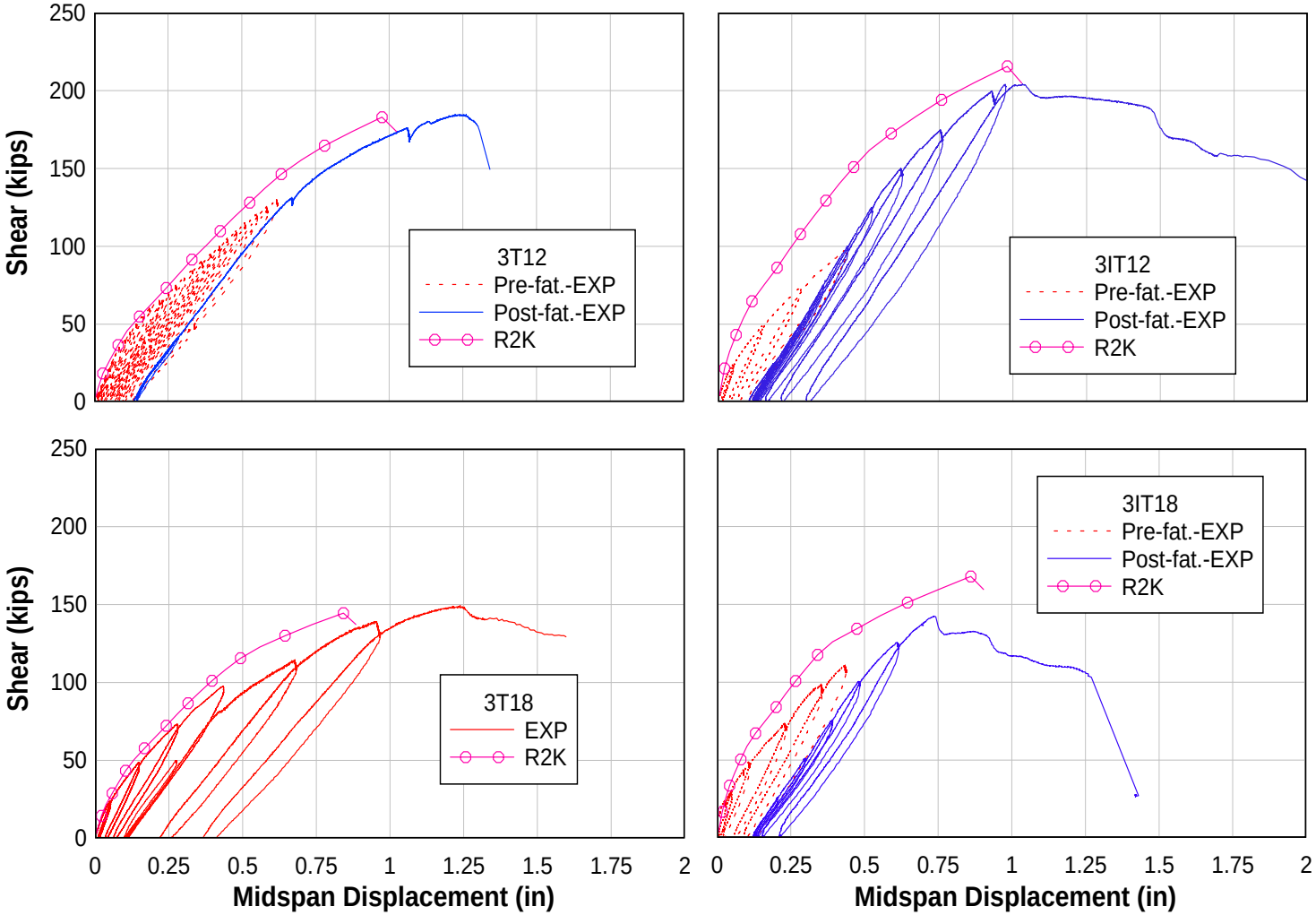

Figure 4.2c: Experimental and *Response2000*™ predicted behavior for Group 3 specimens

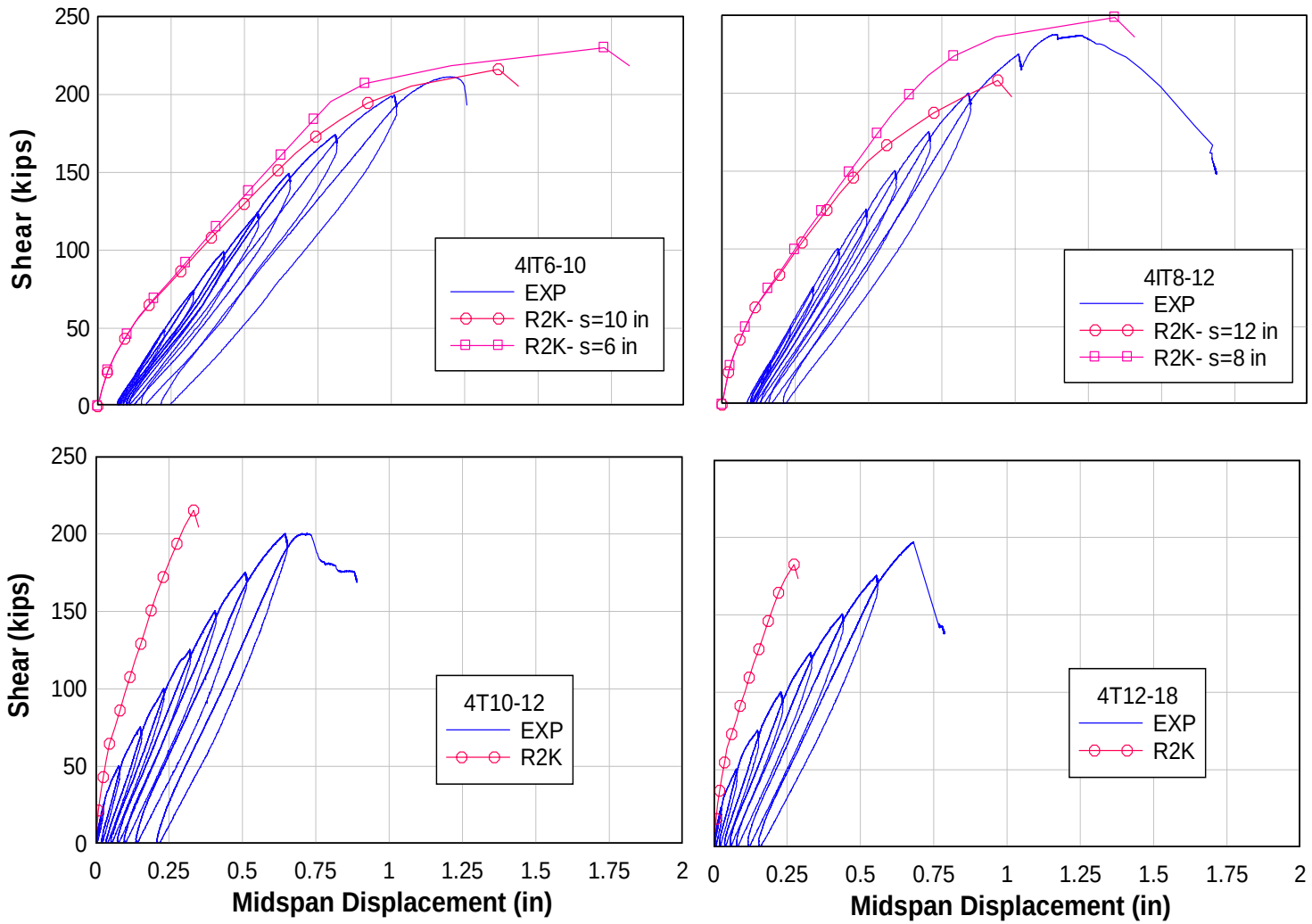

Figure 4.2d: Experimental and *Response2000*™ predicted behavior for Group 4 specimens

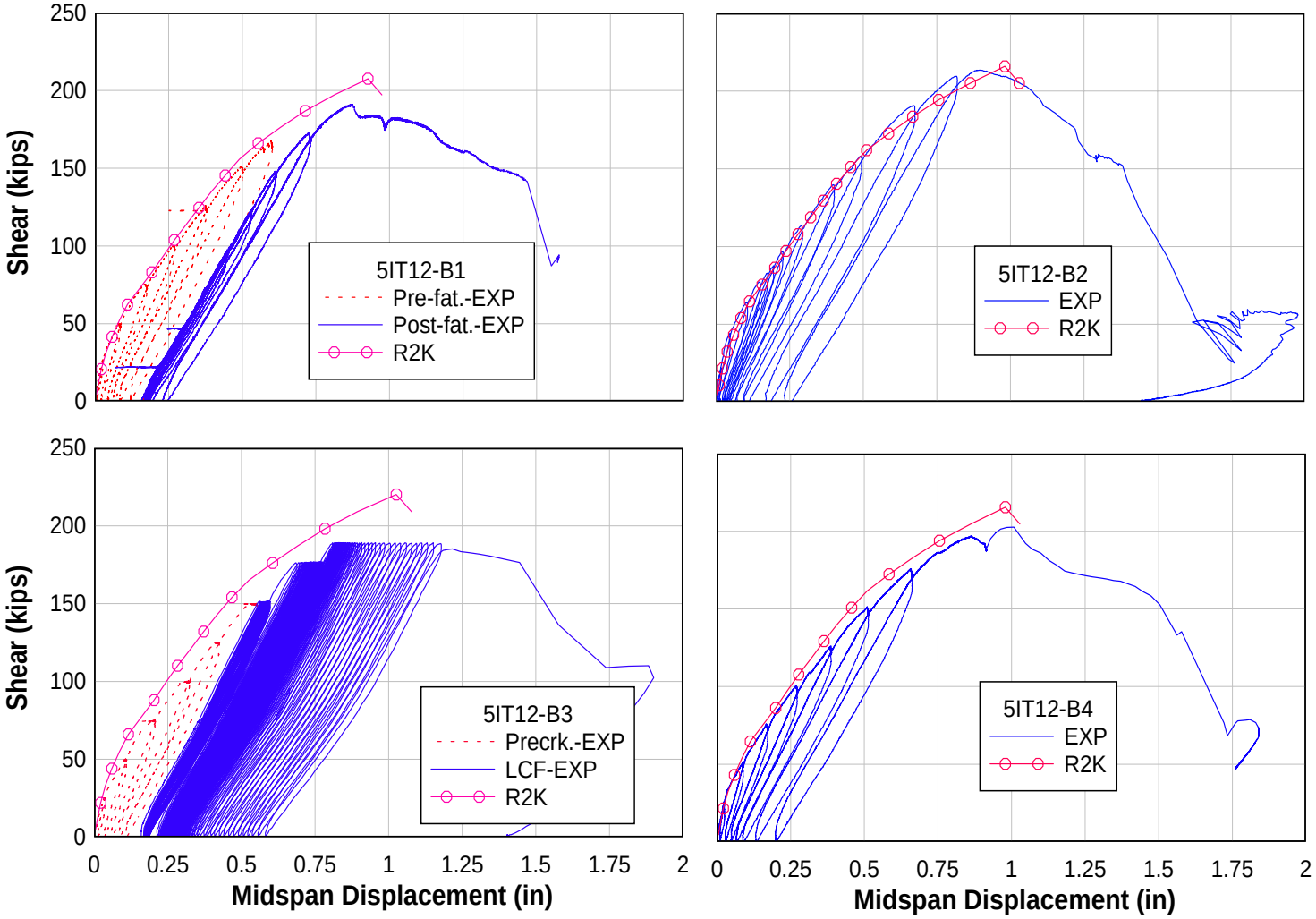

Figure 4.2e: Experimental and *Response2000*™ predicted behavior for Group 5 specimens

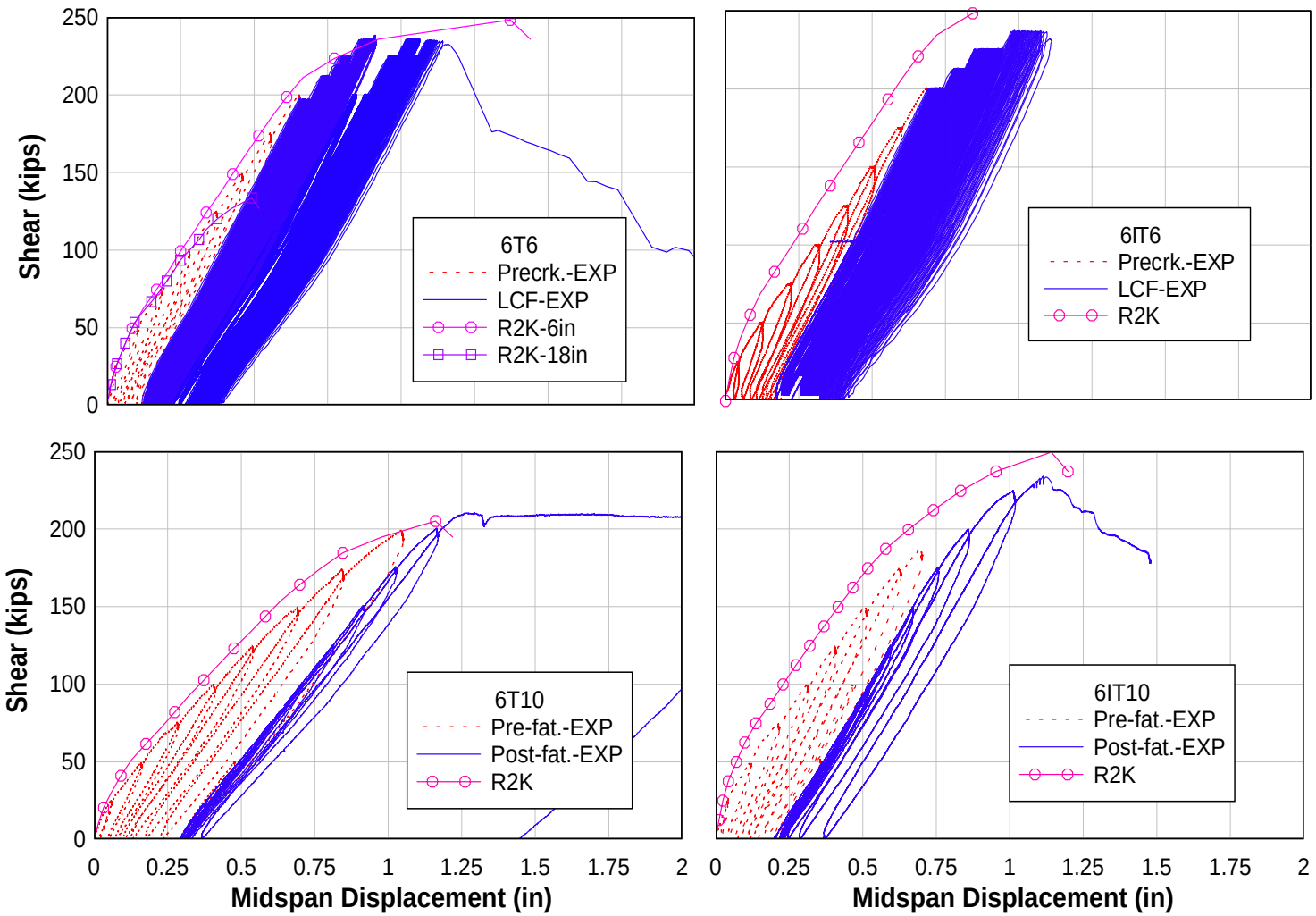

Figure 4.2f: Experimental and *Response2000*™ predicted behavior for Group 6 specimens

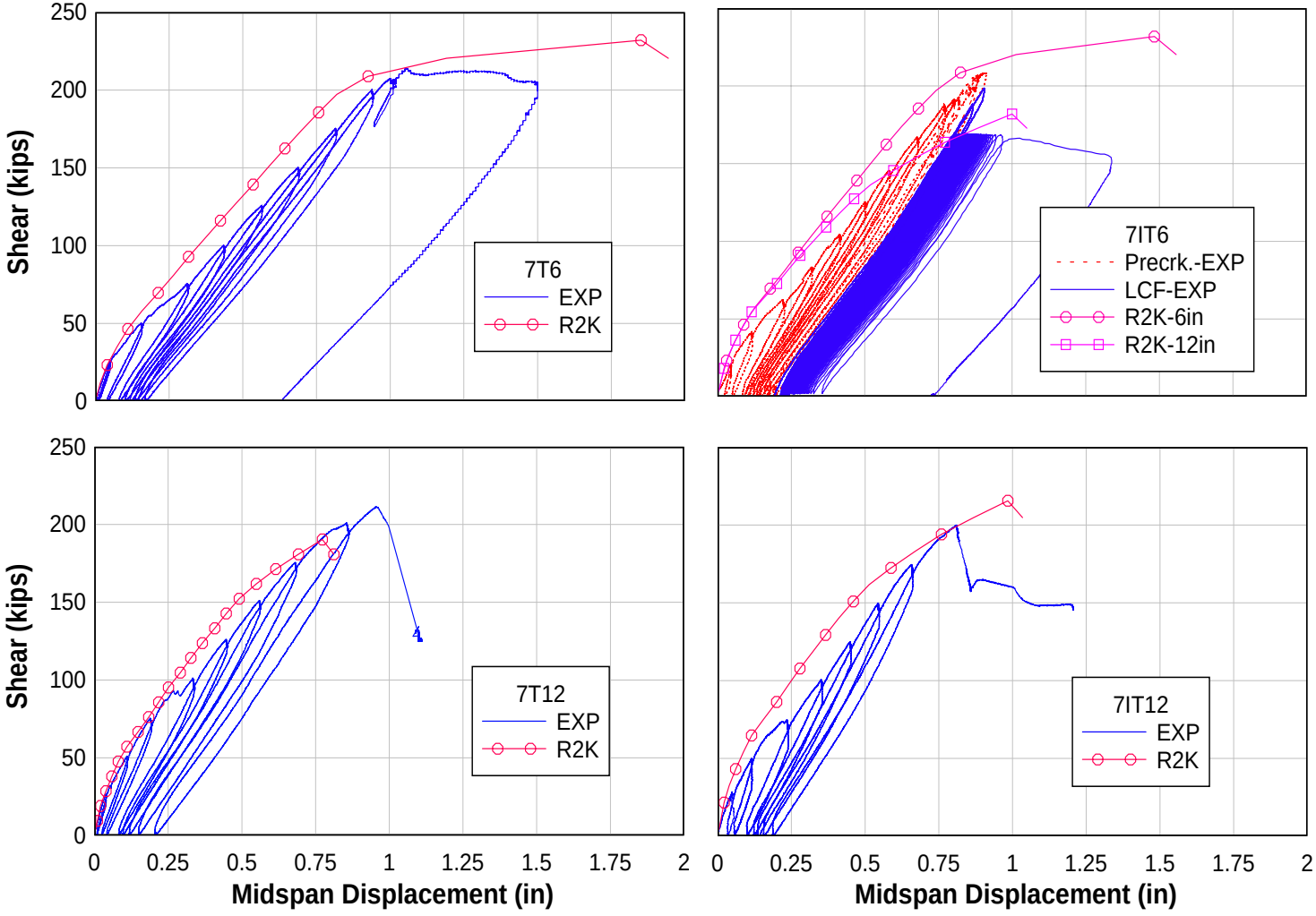

Figure 4.2g: Experimental and *Response2000*™ predicted behavior for Group 7 specimens

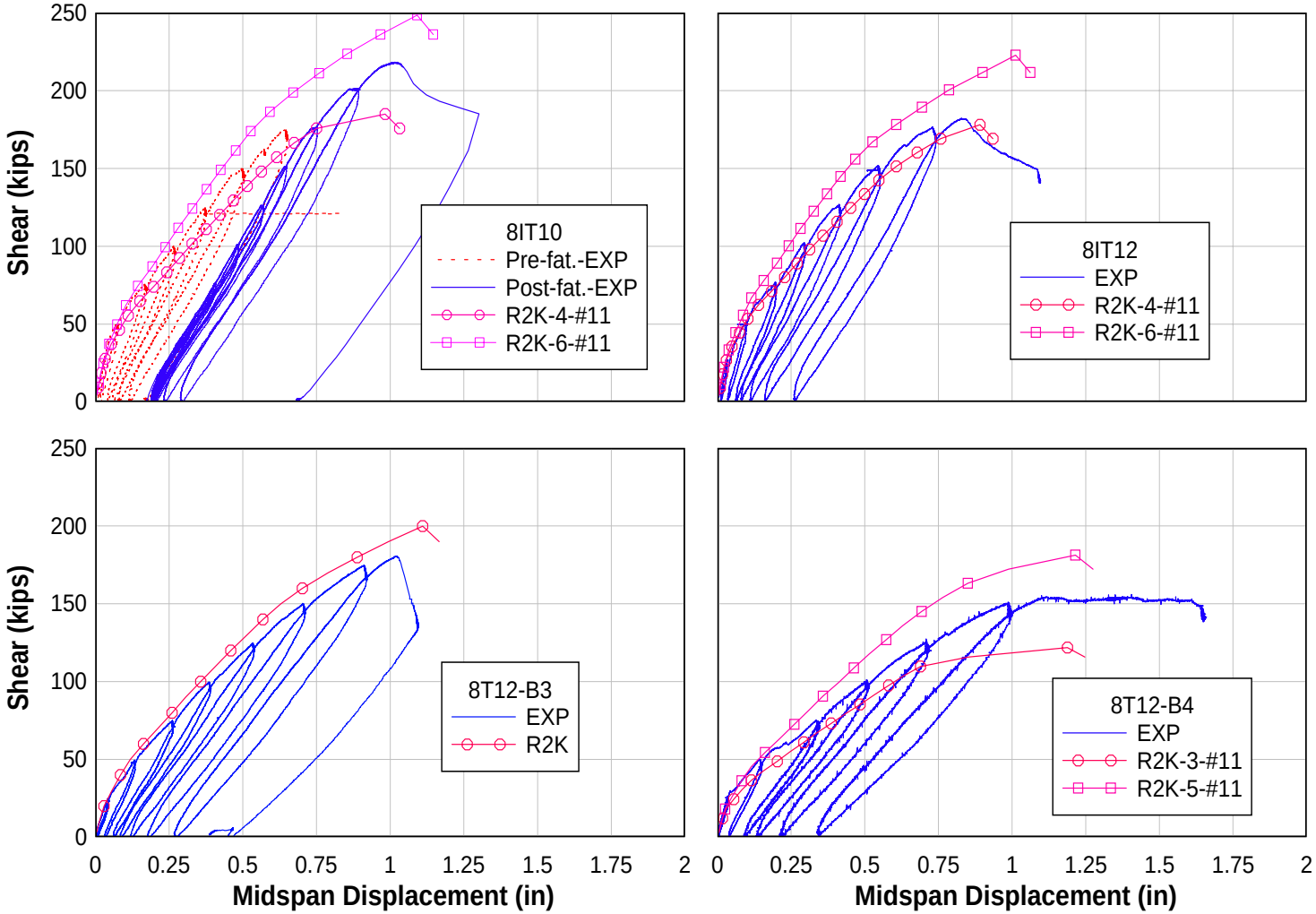

Figure 4.2h: Experimental and *Response2000*™ predicted behavior for Group 8 specimens

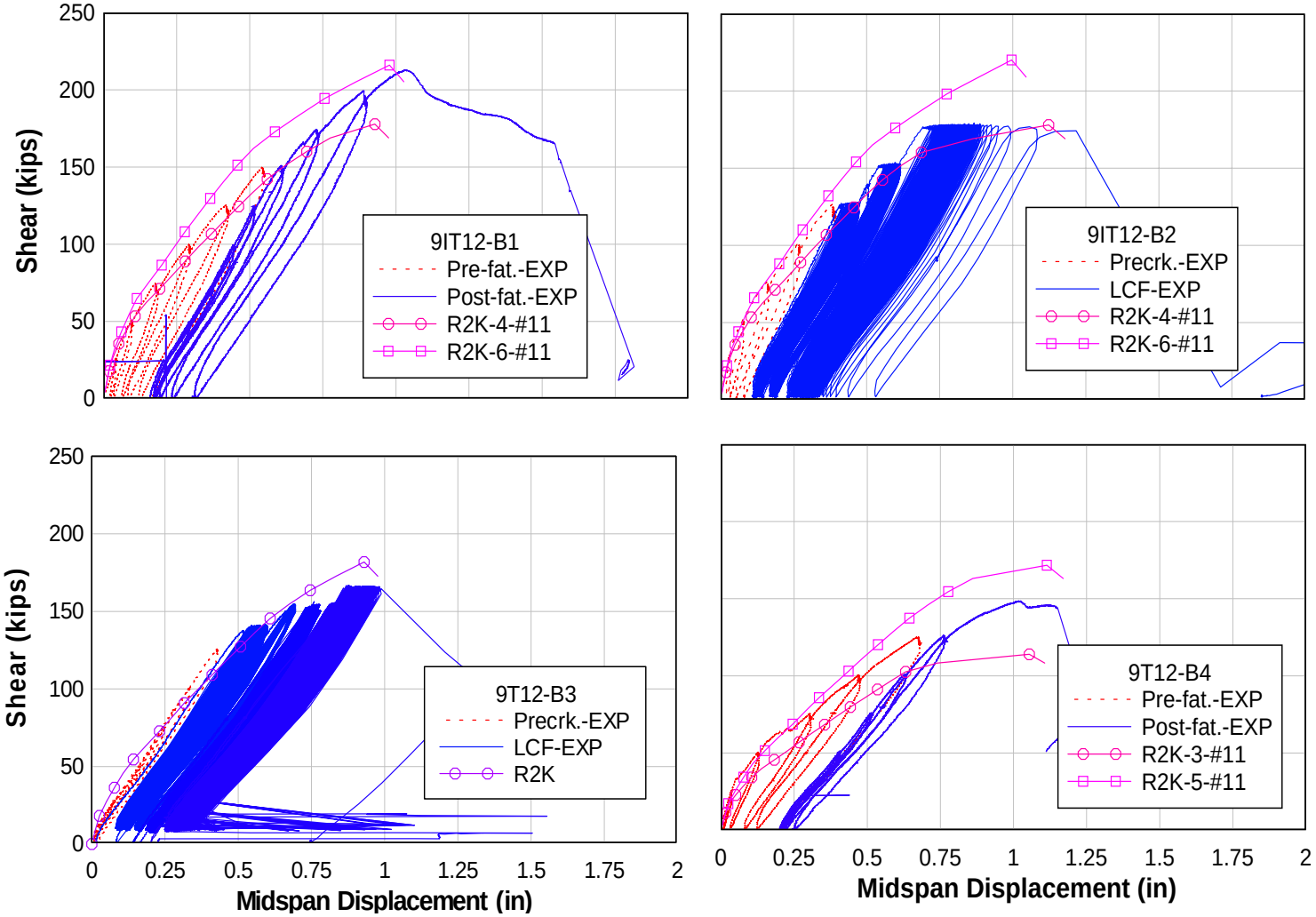

Figure 4.2i: Experimental and *Response2000*™ predicted behavior for Group 9 specimens

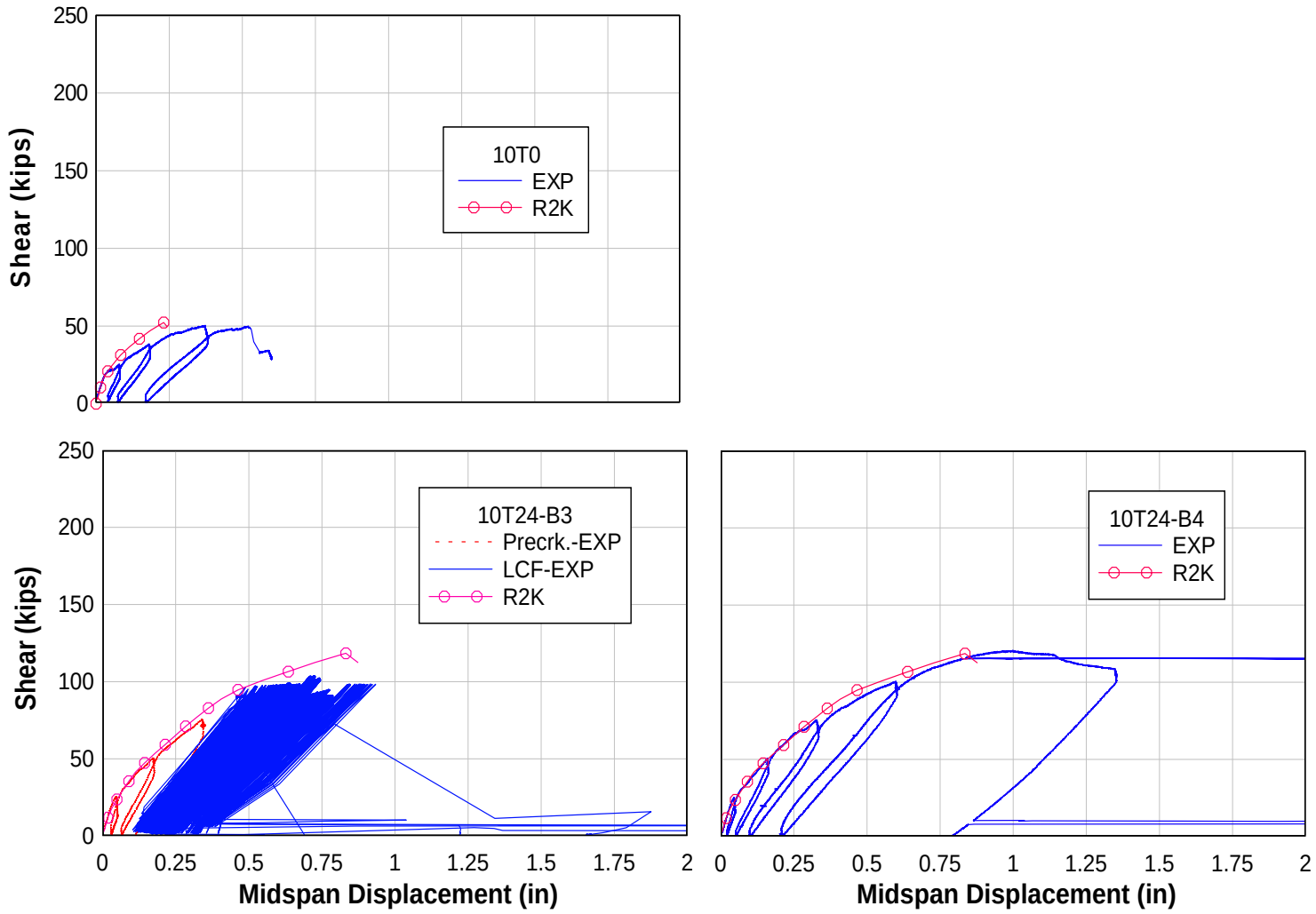

Figure 4.2j: Experimental and *Response2000*™ predicted behavior for Group 10 specimens

The sectional analysis option in *Response 2000*™ permits a cross-section to be directly assessed independent of the support and loading conditions. Program output provides the shear-moment interaction for the section. Local sectional stresses as well as other response details such as predicted crack widths and patterns are also computed and displayed. The sectional analysis option is the approach that would be used to determine the capacity of bridge girders for comparison with load effects. Using the sectional analysis option, the shear-moment interactions were determined for each of the specimens. Capacity calculation for the specimens that exhibited a shear-compression failure was performed at a critical section located at 0.9 times the effective depth (dv) away from the edge of the loading plate as shown in Figure 4.3.

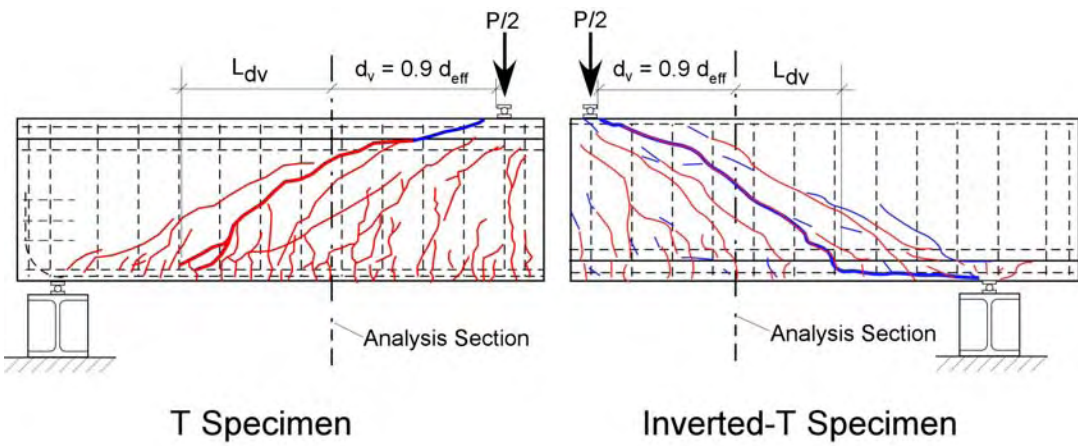

Figure 4.3: Location of critical section with respect to failure crack location

To illustrate the location of the critical section with respect to the failure crack location, the distance that the failure crack extended past the critical section (Ldv) was measured, as a percentage of dv. The lengths of crack extension beyond the critical section for each specimen are summarized in Table 4.2. Analysis results are summarized in Table 4.3 and Figure 4.4.

Table 4.2: Length of crack extension beyond critical section

Specimen	M/V (ft)	dv (in.)	L_{dv}(%)	Specimen	M/V (ft)	dv (in.)	L_{dv} (%)
1T18	7.58	39.1	72.7	7IT6	6.25	40.8	71.4
1IT18	7.44	40.8	96.2	7T12	6.39	39.1	150.9
2T10	7.58	39.1	68.7	7IT12	6.25	40.8	98.6
2T12	7.58	39.1	132.8	8IT10	6.25	40.8	27.2
3T12	7.58	39.1	90.8	8IT12	6.25	40.8	42.5
3IT12	6.25	40.8	43.0	8T12-B3	7.58	39.1	36.9
3T18	7.58	39.1	131.8	8T12-B4	7.55	40.8	50.2
3IT18	6.25	40.8	93.7	9IT12-B1	6.25	40.8	44.7
4IT8-12	6.25	40.8	136.2	9IT12-B2	6.25	40.8	77.0
4T10-12	3.58	39.1	101.9	9T12-B3	7.58	39.1	107.0
4T12-18	3.58	39.1	78.0	9T12-B4	7.55	40.8	101.5
5IT12-B1	6.25	40.8	71.0	10T0	7.46	40.5	175.5
5IT12-B2	6.25	40.8	64.4	10T24-B3	7.55	39.4	175.2
5IT12-B3	6.25	40.8	97.7	10T24-B4	7.55	39.4	142.3
5IT12-B4	6.25	40.8	50.2				
6T6	6.39	39.1	70.5	**Average L_{dv} for T specimens**			105.4
6IT10	6.25	40.8	68.0	**Average L_{dv} for IT specimens**			72.1

Table 4.3: Predicted shear capacities for laboratory specimens (COV in %)

No.	Specimen	f'_c (psi)	V_{APP} (kips)	S (in)	M/V (ft)	V_{ACI1} (kips)	V_{ACI2} (kips)	V_{R2K} (kips)	$V_{R2K\ f_t \to 0}$ (kips)	V_{AASHTO} (kips)	V_{APP}/V_{ACI1}	V_{APP}/V_{ACI2}	V_{APP}/V_{R2K}	$V_{APP}/V_{R2K\ ft \to 0}$	V_{APP}/V_{AASHTO}
Control															
1	1T6	4700	206.5	6	7.58	230.9	237.9	213.7	211.0	208		Flexural Failure			
2	1IT6	4775	236.0	6	7.44	241.7	249.2	247.1	225.1	235		Flexural Failure			
3	1T18	4925	169.8	18	7.58	134.5	141.4	167.1	161.3	151	1.26	1.20	1.02	1.05	1.12
4	1IT18	4550	158.8	18	7.44	136.9	144.5	177.5	162.2	157	1.16	1.10	0.89	0.98	1.01
5	2T10	3550	205.3	10	7.58	160.9	168.5	212.8	198.4	178	1.28	1.22	0.96	1.03	1.15
6	2IT10	3290	205.3	10	0.39	165.2	173.4	193.0	170.4	186		Anchorage Failure			
7	2T12	3520	192.9	12	7.58	145.9	153.4	199.5	183.2	164	1.32	1.26	0.97	1.05	1.18
8	2IT12	3575	183.8	12	0.39	152.8	160.9	181.0	158.4	174		Anchorage Failure			
11	3T18	3970	153.3	18	7.58	125.8	133.1	166.5	152.6	144	1.22	1.15	0.92	1.00	1.06
										Avg.	1.25	1.19	0.95	1.02	1.11
										COV	4.9	5.2	4.9	3.2	6.1
Control specimens with additional detail															
18	5IT12-B2	4160	217.5	12	6.25	158.8	168.9	217.4	198.8	185	1.37	1.29	1.00	1.09	1.18
20	5IT12-B4	4130	206.5	12	6.25	158.5	168.6	217.6	198.2	184	1.30	1.22	0.95	1.04	1.12
30	8IT12	4840	186.1	12	6.25	165.3	170.3	212.7	207.6	184	1.13	1.09	0.87	0.90	1.01
31	8T12-B3	5070	183.9	12	7.58	160.3	167.1	207.3	200.5	176	1.15	1.10	0.89	0.92	1.04
32	8T12-B4	4995	158.9	12	7.55	161.1	166.2	157.1	153.0	154	0.99	0.96	1.01	1.04	1.03
37	10T0	4610	54.8	0	7.46	85.6	87.2	53.0	0.0	57	0.64	0.63	1.03	NA	0.96
40	10T24-B4	3420	125.3	24	7.55	108.9	114.8	134.3	122.6	123	1.15	1.09	0.93	1.02	1.02
										Avg.	1.10	1.05	0.96	1.00	1.05
										COV	21.7	20.5	6.5	7.8	6.9
Moving supports and Two stirrup spacings															
13	4IT6-10	3790	216.5	10	0.39	170.5	178.5	202.1	171.7	191		Anchorage Failure			
14	4IT8-12	3710	242.9	10	6.25	169.7	179.9	229.6	212.4	195	1.43	1.35	1.06	1.14	1.25
a/d ratio=2.0															
15	4T10-12	3945	244.4	10	3.58	164.9	184.4	238.8	NA	201	1.48	1.33	1.02	NA	1.22
16	4T12-18	4060	239.8	12	3.58	151.2	170.7	202.0	NA	187	1.59	1.40	1.19	NA	1.28
										Avg.	1.53	1.36	1.11	NA	1.25
										COV	4.8	4.1	10.5	NA	3.8

Table 4.3 (continued): Predicted shear capacities for laboratory specimens (COV in %)

No.	Specimen	f'_c (psi)	V_{APP} (kips)	S (in)	M/V (ft)	V_{ACI1} (kips)	V_{ACI2} (kips)	V_{R2K} (kips)	$V_{R2K\ f_t \to 0}$ (kips)	V_{AASHTO} (kips)	V_{APP}/V_{ACI1}	V_{APP}/V_{ACI2}	V_{APP}/V_{R2K}	$V_{APP}/V_{R2K\ ft \to 0}$	V_{APP}/V_{AASHTO}
High-cycle fatigue															
9	3T12	3990	188.7	12	7.58	150.5	157.9	194.6	185.7	168	1.25	1.20	0.97	1.02	1.12
10	3IT12	4180	207.5	12	6.25	159.0	169.1	218.8	200.7	185	1.30	1.23	0.95	1.03	1.12
12	3IT18	3915	147.1	18	6.25	130.7	140.9	169.8	156.1	156	1.13	1.04	0.87	0.94	0.94
17	5IT12-B1	3700	195.1	12	6.25	154.2	164.4	207.5	190.8	180	1.27	1.19	0.94	1.02	1.08
23	6T10	4595	210.4	10	7.58	170.9	178.0	205.5	200.8	185		Flexural Failure			
24	6IT10	5495	237.8	10	6.25	186.4	195.9	243.1	236.5	210	1.28	1.21	0.98	1.01	1.13
29	8IT10	4750	221.8	10	6.25	179.8	184.9	222.7	217.1	198	1.23	1.20	1.00	1.02	1.12
33	9IT12-B1	4285	216.8	12	6.25	160.0	165.3	214.5	199.7	180	1.35	1.31	1.01	1.09	1.20
36	9T12-B4	4705	153.5	12	7.55	158.6	163.8	150.3	146.8	147	0.97	0.94	1.02	1.05	1.04
										Avg.	1.22	1.16	0.97	1.02	1.10
										COV	10.0	10.1	5.1	3.9	7.0
Low-cycle fatigue															
19	5IT12-B3	4310	193.3	12	6.25	160.3	170.3	219.9	201.3	186	1.21	1.14	0.88	0.96	1.04
21	6T6	4590	240.0	18	6.39	131.5	140.6	177.1	162.6	152	1.82	1.71	1.36	1.48	1.58
22	6IT6	5110	237.6	6	6.25	244.7	254.3	269.0	263.8	256		Not Failed			
26	7IT6	4350	207.0	12	6.25	160.7	170.6	221.7	203.5	186	1.29	1.21	0.93	1.02	1.11
34	9IT12-B2	4605	183.3	12	6.25	163.1	168.2	204.1	199.4	182	1.12	1.09	0.90	0.92	1.01
35	9T12-B3	4645	170.3	12	7.58	156.6	163.6	197.2	192.7	173	1.09	1.04	0.86	0.88	0.98
39	10T24-B3	3450	107.9	24	7.55	109.3	115.1	134.7	123.3	123	0.99	0.94	0.80	0.88	0.88
										Avg.	1.25	1.19	0.96	1.02	1.10
										COV	23.8	22.8	21.0	22.4	22.4
Debonded stirrups															
25	7T6	4405	213.7	6	7.58	228.2	235.3	233.2	229.6	225		Flexural Failure			
27	7T12	4280	215.6	12	6.39	153.3	162.5	215.8	198.5	176	1.41	1.33	1.00	1.09	1.23
28	7IT12	4165	204.4	12	6.25	158.9	168.9	218.6	200.2	185	1.29	1.21	0.94	1.02	1.10
										Avg.	1.35	1.27	0.97	1.05	1.16
										COV	6.3	6.5	4.7	4.4	7.3
						For all specimens except low-cycle fatigue specimens and specimen 3IT18				**Avg.**	1.24	1.17	0.98	1.03	1.12
										COV	15.3	13.8	6.7	5.3	7.5

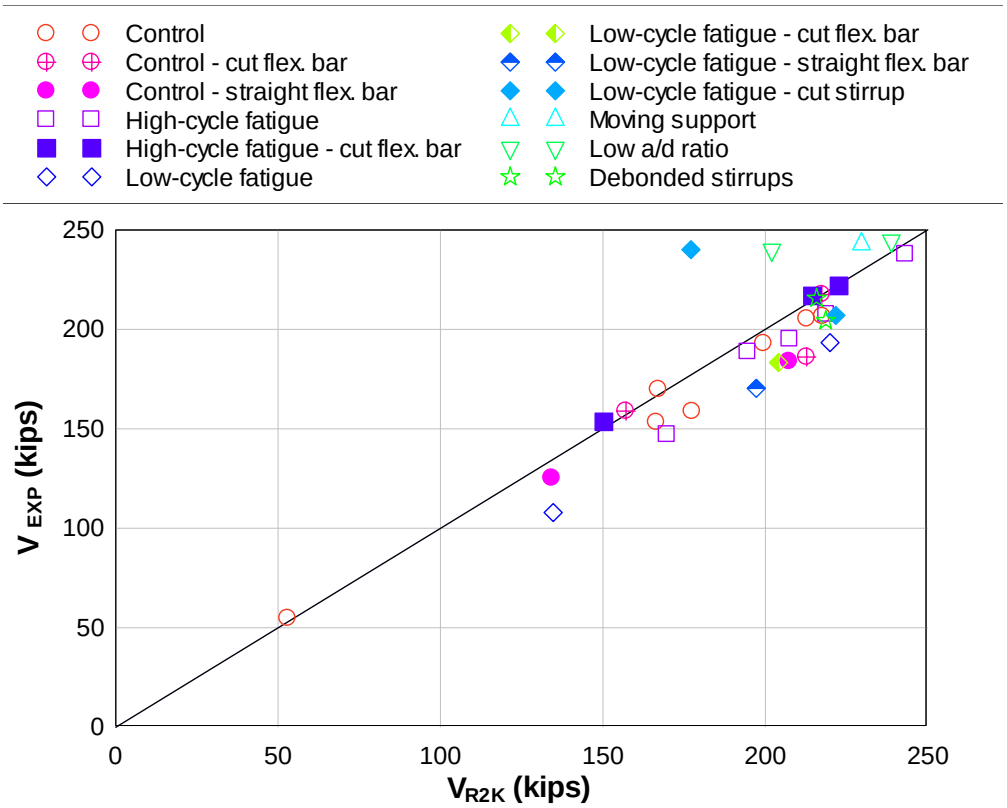

Figure 4.4: Comparison of experimental and predicted shear using *Response 2000*™

As seen in the table and figure, *Response 2000*™ provided excellent capacity prediction over the full range of test variables considered. Specimens with common details were sorted independently for statistical comparisons. These groups included: control specimens, control specimens with different flexural details, high-cycle fatigue, low-cycle fatigue, moving supports, low span-to-depth ratio, and debonded. The mean values and coefficients of variation for each of these groups are shown in Table 4.3, but considering all specimens (except low-cycle fatigue specimens and the high-cycle fatigue specimen with fractured stirrups 3IT18) the mean experimental to predicted shear capacity was 0.98 with a 0.07 coefficient of variation. This is remarkably good for the range of parameters investigated.

Response 2000™ was also employed to predict the capacity of specimens subjected to cyclic loading and the specimens with fully debonded stirrups. To account for debonding effects and reduced stirrup constraint at cracks under repeated loads, the tensile strength of the concrete was set near zero to significantly reduce the contribution of the tensile stresses in the concrete between cracks. The tensile stresses in the concrete could be reduced due to million cycles of fatigue loading. For each specimen analysis, the smallest tensile strength (close to zero) was obtained through iteration until convergence of solution was achieved. Analysis results and the tensile strengths used for all specimens are summarized in Tables 4.3 and 4.4, respectively.

Table 4.4: Least tensile strength used for capacity prediction of specimens subjected to cyclic loading and specimens with fully debonded stirrups

No.	Specimen	f'_c (psi)	V_{APP} (kips)	S (in)	f_t (psi)	V_{R2K} $f_t \rightarrow 0$ (kips)
Control						
1	1T6	4700	206.5	6	3	211.0
2	1IT6	4775	236.0	6	3	225.1
3	1T18	4925	169.8	18	6	161.3
4	1IT18	4550	158.8	18	7	162.2
5	2T10	3550	205.3	10	2	198.4
6	2IT10	3290	205.3	10	1	170.4
7	2T12	3520	192.9	12	3	183.2
8	2IT12	3575	183.8	12	1	158.4
11	3T18	3970	153.3	18	3	152.6
Control specimens with distinctive detail						
18	5IT12-B2	4160	217.5	12	8	198.8
20	5IT12-B4	4130	206.5	12	8	198.2
30	8IT12	4840	186.1	12	12	207.6
31	8T12-B3	5070	183.9	12	5	200.5
32	8T12-B4	4995	158.9	12	5	153.0
37	10T0	4610	54.8	0	NA	0.0
40	10T24-B4	3420	125.3	24	4	122.6
High-cycle fatigue						
9	3T12	3990	188.7	12	5	185.7
10	3IT12	4180	207.5	12	10	200.7
12	3IT18	3915	147.1	18	14	156.1
17	5IT12-B1	3700	195.1	12	7	190.8
23	6T10	4595	210.4	10	4	200.8
24	6IT10	5495	237.8	10	12	236.5
29	8IT10	4750	221.8	10	10	217.1
33	9IT12-B1	4285	216.8	12	10	199.7
36	9T12-B4	4705	153.5	12	4	146.8

No.	Specimen	f'_c (psi)	V_{APP} (kips)	S (in)	f_t (psi)	V_{R2K} $f_t \rightarrow 0$ (kips)
Low-cycle fatigue						
19	5IT12-B3	4310	193.3	12	9	201.3
21	6T6	4590	240.0	18	11	162.6
22	6IT6	5110	237.6	6	7	263.8
26	7IT6	4350	207.0	12	11	203.5
34	9IT12-B2	4605	183.3	12	11	199.4
35	9T12-B3	4645	170.3	12	5	192.7
39	10T24-B3	3450	107.9	24	4	123.3
Moving supports and Two stirrup spacings						
13	4IT6-10	3790	216.5	10	1	171.7
14	4IT8-12	3710	242.9	10	8	212.4
a/d ratio=2.0						
15	4T10-12	3945	244.4	10	NA	NA
16	4T12-18	4060	239.8	12	NA	NA
Debonded stirrups						
25	7T6	4405	213.7	6	3	229.6
27	7T12	4280	215.6	12	7	198.5
28	7IT12	4165	204.4	12	10	200.2

Specific treatment of anchorages and effective flexural reinforcing areas are detailed in subsequent sections.

4.3 MODIFIED COMPRESSION FIELD THEORY

Modified Compression Field Theory (MCFT) (*Vecchio and Collins 1986*) is the shear design methodology prescribed by the AASHTO-LRFD Bridge Design Specification (*2003*). MCFT takes into account residual concrete stresses in cracked concrete that permit the concrete section to resist higher shear forces. The model simplifies the complex shear behavior of a beam into a series of parallel diagonal cracks at an angle θ from the horizontal, and assumes equivalent forces exist on the cross-section as shown in Figure 4.5.

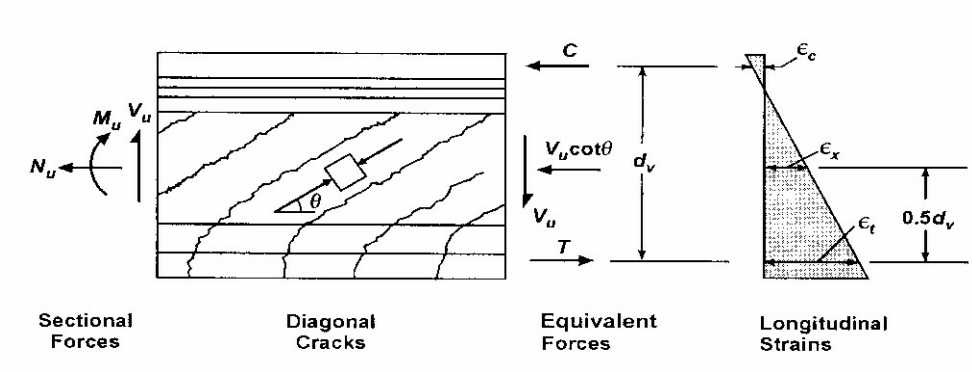

Figure 4.5: MCFT strains and forces on cracked section (*AASHTO LRFD 2003*)

The shear capacity for a non-prestressed concrete beam is computed as in Equation 4-1. The stirrup and concrete strength contributions depend on the crack angle and average strain on the section as:

$$V_s = \frac{A_v f_y d_v \cot(\theta)}{s} \quad \textbf{for straight leg stirrups} \qquad \textbf{(4-5)}$$

$$V_c = 0.0316\beta\sqrt{f'_c}\, b_v d_v \qquad \textbf{(4-6)}$$

where A_v is the area of stirrups (in^2), f_y is the yield stress of the stirrups (ksi), s is the stirrup spacing (in), b_v is the effective width of the beam (in), d_v is the distance between compression and tension resultants from moment equilibrium (in), f'_c is the concrete compressive strength (ksi), β is a factor related to θ (degrees) the crack angle, and ε_x is the average longitudinal strain in the section.

When the cross-section has at least minimum stirrups, the average longitudinal strain can be determined as:

$$\varepsilon_x = \frac{\frac{M_u}{d_v} + 0.5(V_u \cot(\theta))}{2E_s A_s} \leq 0.002 \qquad \textbf{(4-7)}$$

where M_u (kip-in) is the factored applied moment, V_u (kips) is the factored applied shear, A_s (in^2) is the area of flexural steel that is adequately developed at the section, and E_s (ksi) is the modulus of elasticity for the flexural steel.

If the section has less than minimum area of stirrups, Equation 4-7 is multiplied by 2. Minimum stirrup area is defined as:

$$A_v \geq 0.0316\sqrt{f'_c}\,\frac{b_v s}{f_y} \quad \textbf{(units for } \mathbf{f_y} \textbf{ and } \mathbf{f'_c} \textbf{ are ksi)} \qquad \textbf{(4-8)}$$

Values of β and θ are chosen from tables within the AASHTO specification and the capacity of the section is computed. Alternatively, *Response 2000*™ may be used to compute the shear-moment interaction curve. AASHTO-MCFT analysis results determined using *Response 2000*™ are summarized in Table 4.3 and Figure 4.6. AASHTO-MCFT results had a mean value of experimental to predicted shear capacity of 1.12 with a coefficient of variation of 0.08 for all specimens except low-cycle fatigue specimens and the high-cycle fatigue specimen 3IT18.

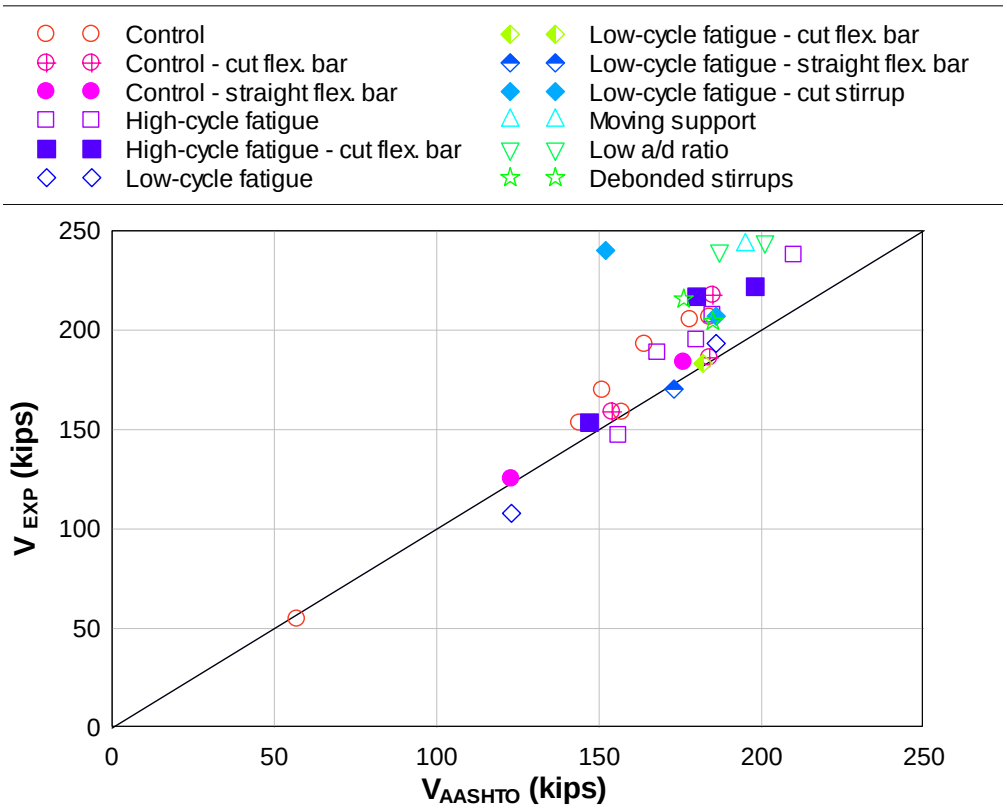

Figure 4.6: Comparison of experimental and predicted shear using AASHTO MCFT

The AASHTO-MCFT method is recommended for prediction of the capacity of vintage RCDG girders. It provided good agreement with experimental results, incorporates interaction between shear and moment, is the current standard for determining shear strength of concrete members in the AASHTO-LRFD provisions, and provides a relatively simple way to account for the complex stress state in concrete members under the combined actions of shear and moment. The method can be applied for individual cross-sections at locations with diagonal-tension cracks. Further, the method should also be familiar to designers and consultants.

Sectional methods such as *Response 2000*™ and AASHTO-MCFT tended to reasonably predict capacity of sections with span to depth ratios (a/d ratios) above approximately 2.5, which are not strongly influenced by the disturbed regions associated support locations. However, the sectional analyses underpredicted shear capacities for sections with low a/d ratios. This is observed for Group4 T specimens and moving load specimens, which include specimens 4T10-

12, 4T12-18, 10T12, 11T16.5, 11T22-B3, and 11T22-B4. Portions of a beam very close to the support reactions are considered disturbed regions due to nonuniform stress flow through the section at these locations. Within the disturbed region, the beam carries load in a very different manner than that assumed by sectional analysis techniques, and failure may be controlled by concrete bearing or crushing as well as anchorage pullout. The strut-and-tie method may better approximate the internal stress actions in disturbed regions and is a more suitable analysis technique for beams with short span to depth ratios.

4.4 ANALYSIS OF MOVING SUPPORTS

4.4.1 Analysis Description

4.4.1.1 Specimen 4IT6-10

The bond strength of specimen 4IT6-10 was computed and is shown in Table 4.5. The tension force developed in the bottom flexural bars at failure was higher than the tension provided by the bond strength. Capacity of three sections, with 6 in., 8 in., and 10 in. stirrup spacings, were computed using the *Response 2000*™ program and AASHTO-MCFT method.

Table 4.5: Bond strength comparisons

Specimen	V_{APP} (kips)	f'_c (psi)	f_y (ksi)	d_v (in)	V_s (kips)	θ (deg)	l_d (in) ACI	l_d (in) AASHTO	μ_{avg} (psi)	l_{em} (in)	μ_{mod} (psi)	T_μ (kips)	T (kips)
2IT10	205.3	3290	75.8	38.7	60.8	32.0	79.6	81.5	328	16.8	383	163	280
2IT12	183.8	3575	75.8	36.8	40.6	29.0	77.5	78.2	342	17.4	397	175	295
4IT6-10	216.5	3790	68.3	41.3	81.1	32.5	66.8	68.4	352	16.7	411	174	276
5IT12-B4	206.5	4130	69.2	39.3	60.8	34.3	64.9	66.4	367	30.9	401	329	258

For the precracking stage, a critical section with an M/V ratio of 3.44 ft was considered as shown in Figure 4.7. For the failure-testing stage, two M/V ratios were considered: M/V ratio of 3.6 ft was located at a section from the edge of the reaction support plate; M/V ratio equal to 7.44 ft was located at a section from the edge of the applied loading plate.

M-V envelopes of each section were developed and shown in Fig 4.8. Prediction for the 6 in. spacing section with a span length of 16 ft was anticipated to be lower than the existing section capacity, due to the low a/d ratio (1.85). *Response 2000*™ and AASHTO-MCFT did not take into account this deep beam condition. The capacity prediction was expected to be reasonable for the span length of 24 ft, since the a/d ratio was 2.9.

Capacity predictions using the AASHTO-MCFT method were more conservative than those using *Response 2000*™. Further comparisons between experimental results were made using *Response 2000*™, as this method provided better correlation as shown in Table 4.3.

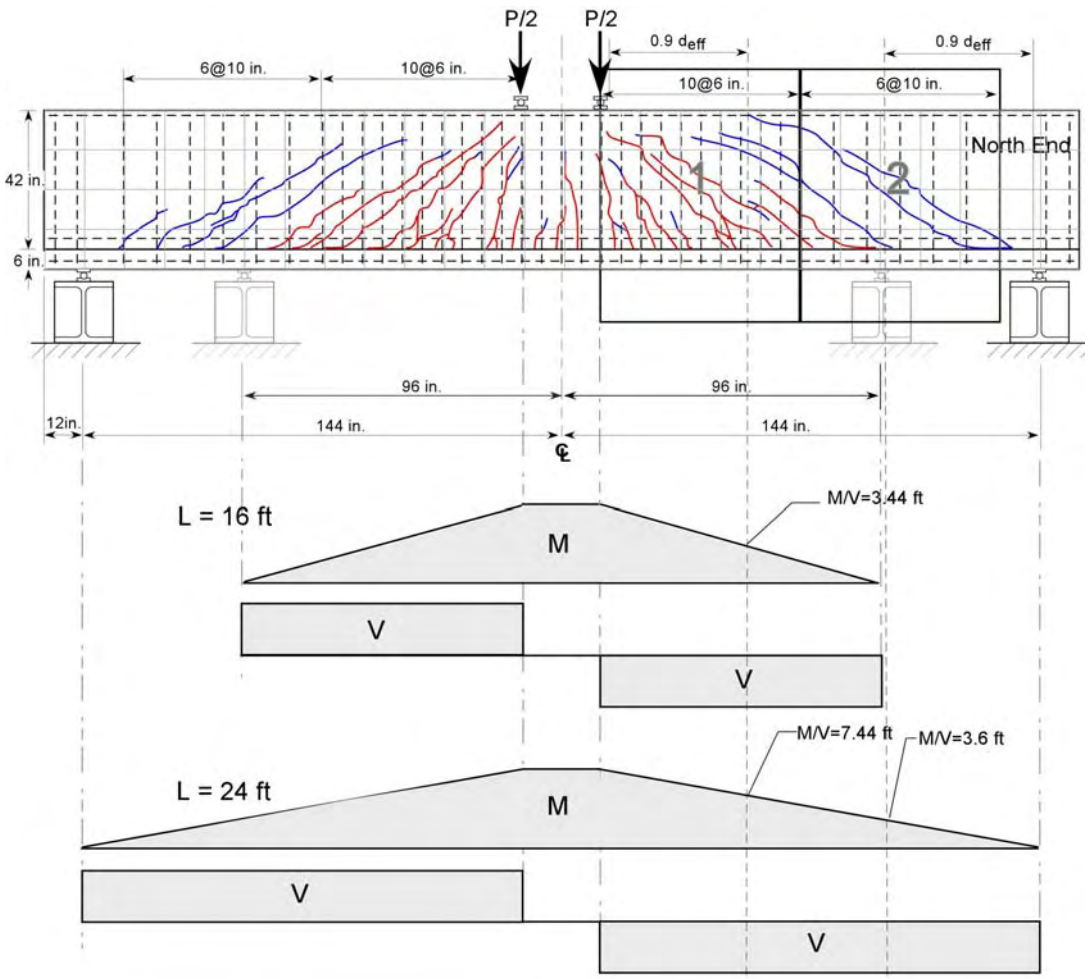

Figure 4.7: Moment and shear diagrams for 4IT6-10 specimen

The applied shears and moments were within the predicted shear and moment envelope as shown in Figure 4.8a. At the 3.44 ft M/V ratio section of the specimen with the 16 ft span length, the precracking (in initial support locations) shear and moment were 200 kips and 688 ft-kips, respectively. The predicted ultimate shear and moment were 313 kips and 1081 ft-kips. These made $V_{Precrack}/V_{R2K}$ and $M_{Precrack}/M_{R2K}$ ratios equal to 0.64 and 0.64, respectively. The capacity predictions of 3.6 ft and 7.44 ft M/V ratio sections for the failure testing stage were also higher than the experimental shear and moment at failure. V_{EXP}/V_{R2K} and M_{EXP}/M_{R2K} ratios for the M/V ratio of 3.6 ft were 0.88 and 0.89, respectively. V_{EXP}/V_{R2K} and M_{EXP}/M_{R2K} ratios for the M/V ratio of 7.44 ft were 0.86 and 0.86, respectively.

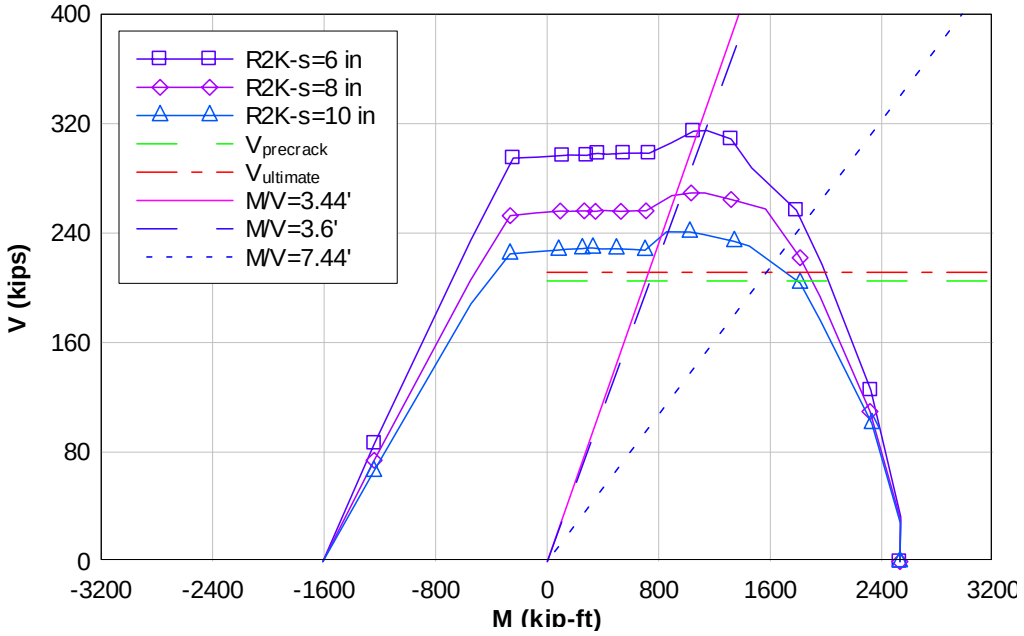

a)

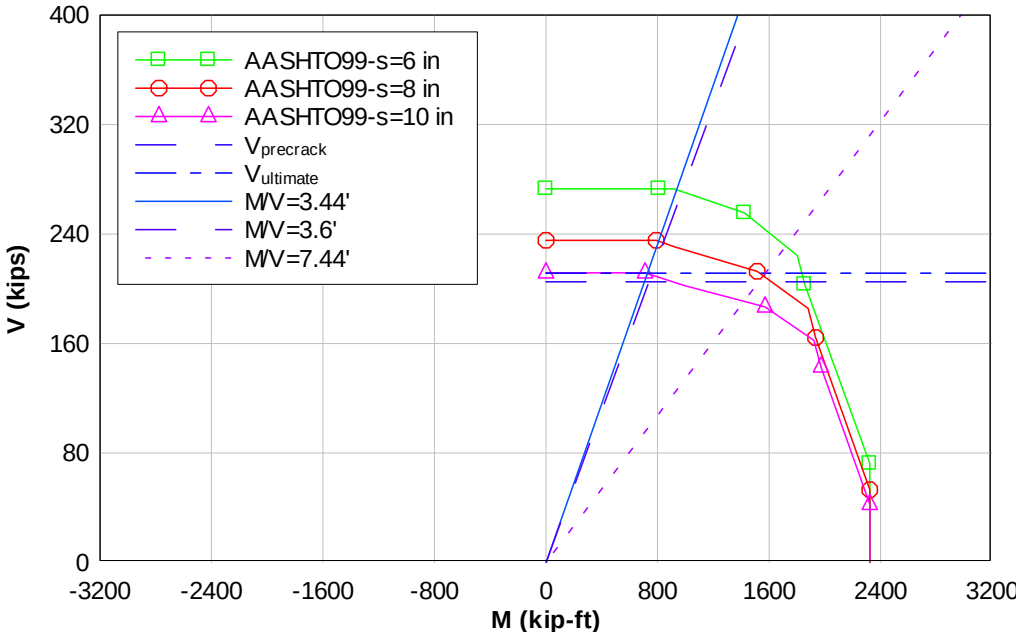

b)

Figure 4.8: M-V envelope of capacity for 4IT6-10 specimen; a) using *Response2000*™ program; b) using AASHTO MCFT method

4.4.1.2 Specimen 4IT8-12

For the precracking stage, a critical section with an M/V ratio of 3.44 ft was considered as shown in Figure 4.9. For the failure-testing stage, an M/V ratio of 3.6 ft was taken at a section located from the edge of the reaction support plate, and an M/V ratio equal to 6.25 ft was taken at a section from the edge of the applied loading plate. M-V envelopes for 8 in., 10 in., and 12 in. spacing sections were developed and shown in Fig 4.10.

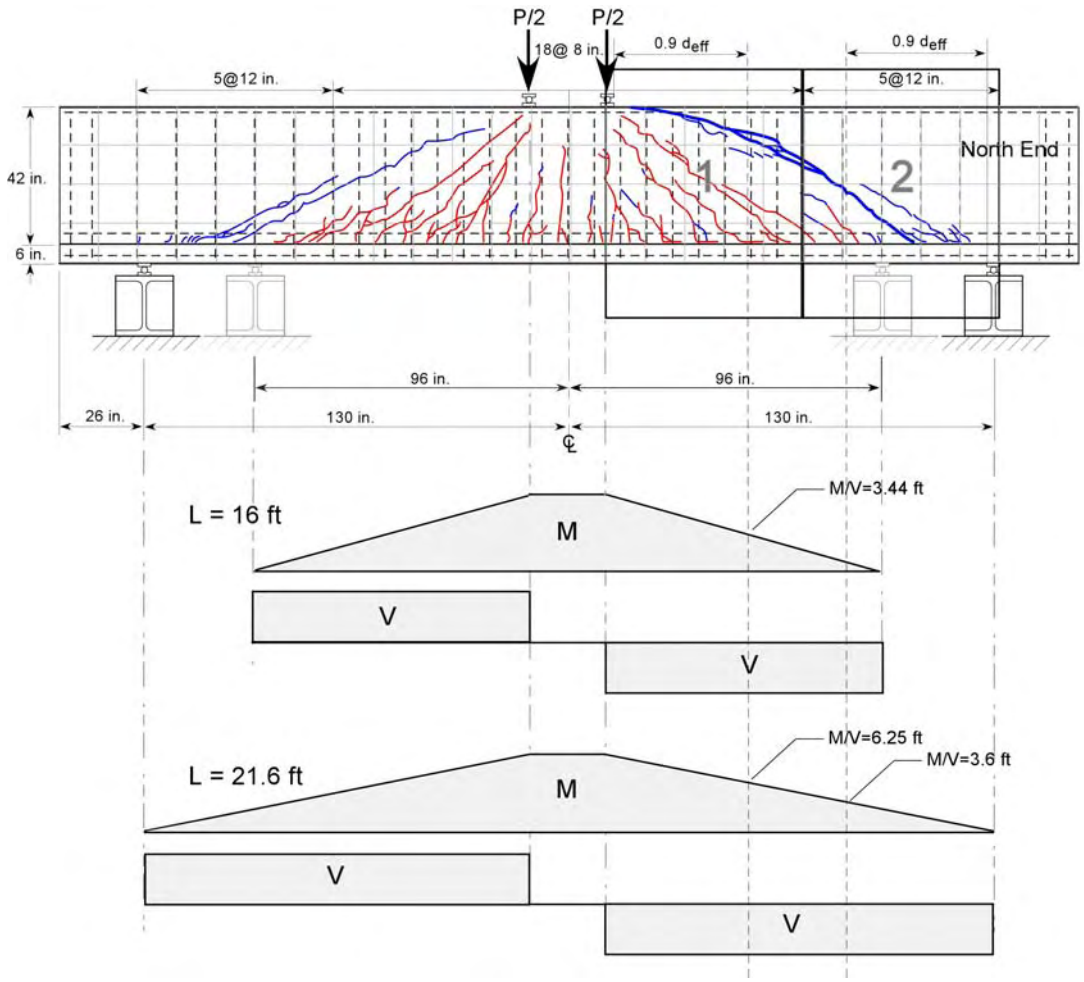

Figure 4.9: Moment and shear diagrams for 4IT8-12 specimen

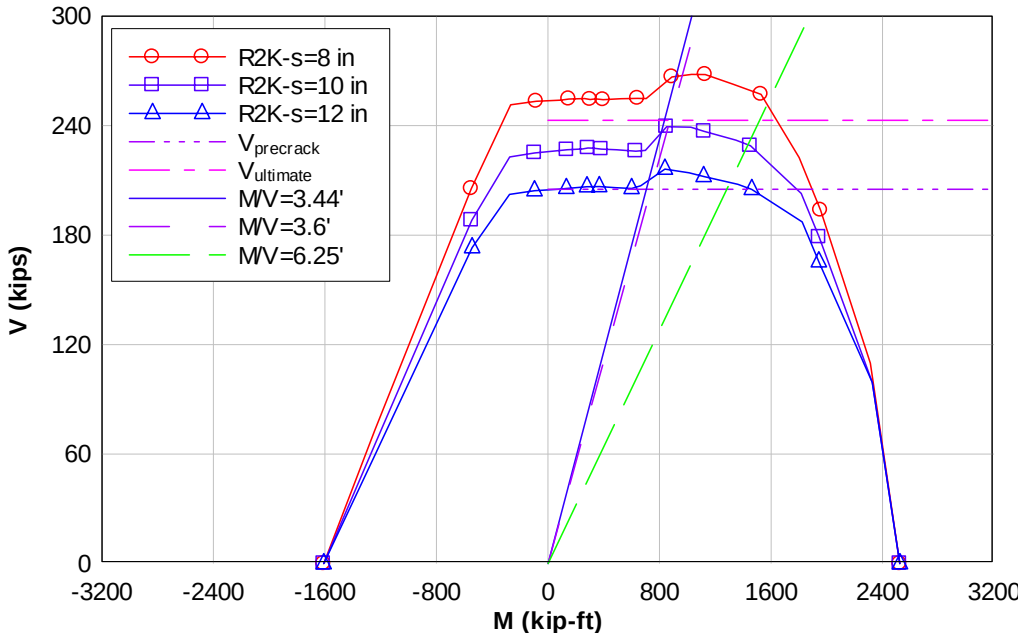

a)

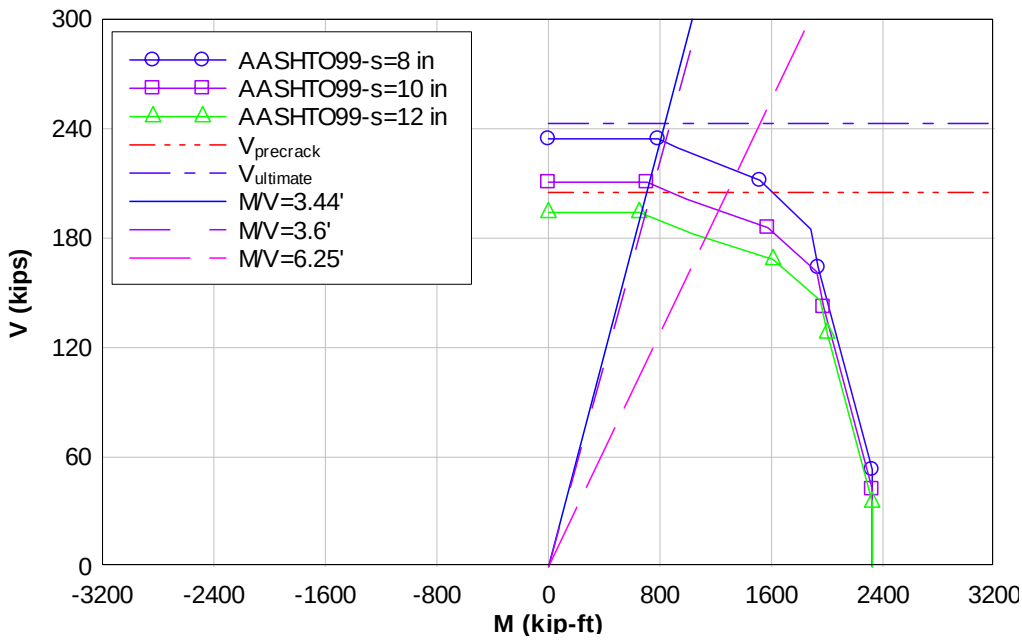

b)

Figure 4.10: M-V envelope of capacity for 4IT8-12 specimen: a) using *Response 2000*™ program; and b) using AASHTO MCFT method

At the 3.44 ft M/V ratio section, the precracking shear and moment were 200 kips and 688 ft-kips, respectively for the initial support locations. The predicted ultimate shear and

moment at the 8 in. spacing were 266 kips and 933 ft-kips. $V_{Precrack}/V_{R2K}$ and $M_{Precrack}/M_{R2K}$ ratios were 0.75 and 0.74, respectively. The precracking shear and moment were well below the predicted capacities. Diagonal-tension failure could occur at two sections with M/V ratios of 3.6 ft and 6.25 ft, shown in Figure 4.10a. The two sections were in the space between the 8 in. and 10 in. spacing envelopes. An average stirrup spacing equal to 10.9 in. was computed using a horizontal projection of the failure crack equal to 76 in. divided by seven stirrups crossing the failure crack. The analysis tended to underestimate the capacity of the specimens tested with moving support locations.

4.5 ANALYSIS FOR SPECIMENS WITH CUTOFF AND ANCHORAGE

4.5.1 Anchorage of Flexural Reinforcing

Bond stress from the flexural-tension rebar at the end region was considered for analysis of specimens 2IT10, 2IT12, and 4IT6-10. These specimens exhibited anchorage failures. A free body diagram of the end region of the specimens is shown in Figure 4.11.

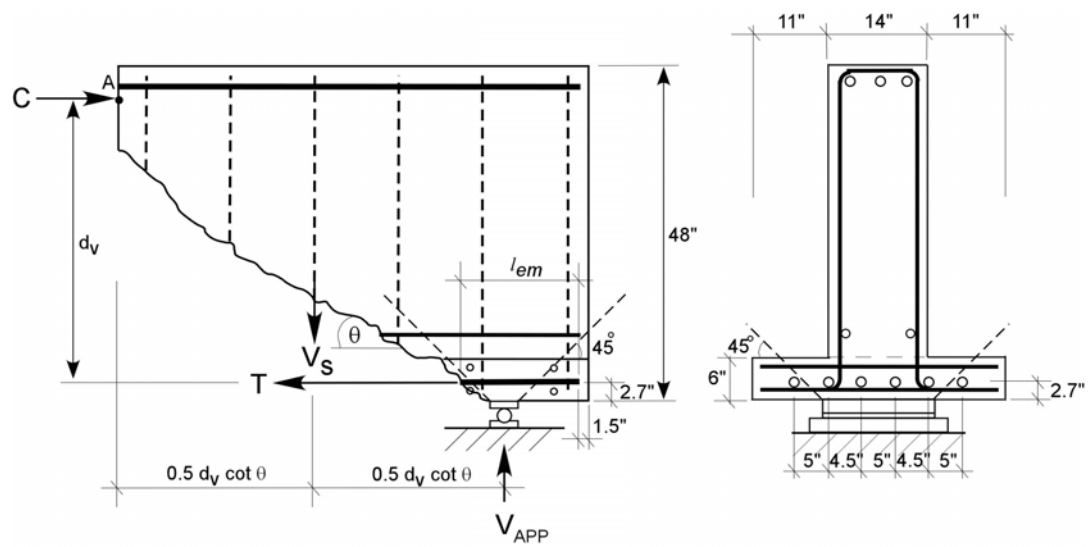

Figure 4.11: Forces at end region of inverted-T specimens

Applied moment and resistance force along the crack interface were neglected due to the anchorage failure at the support location. Applied tensile force, *T*, in the bottom flexural tensile rebar was obtained by taking moments at Point A, which are

$$T = \left(V_{APP} - 0.5V_s\right)\cot\theta \qquad \textbf{(4-9)}$$

where *T* is the applied tensile force in flexural rebars (kips), *C* is the compressive force in the compression zone (kips), V_{APP} is the applied shear including specimen self-weight (kips), V_s is the

total force in the yielded stirrups across the diagonal tension crack (kips), and θ is the angle of inclination of the diagonal-tension crack (degrees).

Angle of inclination of the diagonal-tension crack (θ), the effective shear depth (dv) at the end region, and number of stirrups across the diagonal-tension crack were obtained from crack pattern photographs (see Figure 3.12 in the previous chapter).

Stress in stirrups across the failure crack was assumed to reach a yield stress of 50,700 psi. Development length was calculated using ACI 318 (Equation 4-10) and AASHTO-LRFD (Equation 4-11) procedures as:

$$l_d = d_b \frac{3}{40} \frac{f_y}{\sqrt{f'_c}} \frac{\alpha\beta\gamma\lambda}{\left(\frac{c+K_{tr}}{d_b}\right)} \quad \textbf{ACI 318-02} \qquad \textbf{(4-10)}$$

$$l_d = \frac{1.25 A_b f_y}{\sqrt{f'_c}} \quad \textbf{AASHTO-LRFD} \qquad \textbf{(4-11)}$$

where l_d is the development length (in), f_y is the yielding stress of rebars (psi), f'_c is the compressive strength of concrete (psi), α is the bar location factor equal to 1.0, β is the coating factor equal to 1.0, γ is the bar size factor equal to 1.0, λ is the lightweight aggregate factor equal to 1.0, c is the spacing or cover dimension (in) equal to 2.25 in. for inverted-T specimens and 2.15 in. for T specimens, K_{tr} is the transverse reinforcement index defined as $A_{tr}f_y$/1500 sn, A_{tr} is the total cross-sectional area of all transverse reinforcement equal to 0.4 in2, f_{yt} is the yield stress of transverse reinforcement (psi) taken as 50,700 psi, s is the maximum spacing of transverse reinforcement within l_d (in), n is the number of bars being developed along the plane of splitting, d_b is the diameter of #11 flexural bar (in) equal to 1.41 in., A_b is the cross-sectional area of #11 flexural bar (in^2) equal to 1.56 in^2 $\left(\frac{c+K_{tr}}{d_b}\right)$ should not exceed a value of 2.5, but not be less than 1.5, and $\sqrt{f'_c}$ shall not exceed 100 psi.

The development lengths and variables for each specimen are summarized in Table 4.5. The average of the development lengths computed using AASHTO-LRFD equation are about 2 % longer than obtained from ACI 318 equations. Using the development length based on AASHTO-LRFD specification, average bond strength was computed as:

$$\mu_{avg} = \frac{f_y d_b}{4 l_d} \qquad \textbf{(4-12)}$$

where μ_{avg} is the average bond strength (psi).

Embedded length (l_{em}) of the flexural rebar from the end to the intersection point between the flexural-rebar centroid and diagonal-tension crack was a combination of the horizontal length from the edge of support plate to the crack plane (2.7 in. cot θ), the width of the support plate (4

in), and the overhang toward the end of the bar (8.5 in.). Of this embedded length, a length of 9.4 in., obtained from a 45° projection from the edges of the support plate, was influenced by bearing stresses that increase confinement and reduce the potential for horizontal splitting at the anchorage. According to ACI 318-02, an increase of 30 percent in the value of Mn/Vu is permitted when the ends of reinforcement are confined by a compressive reaction. Likewise, bond strength over the 45° projection length could be multiplied by a factor of 1.3.

The modified bond strength for each specimen was summarized in Table 4.5. A total tensile force generated by the bond strength over the embedded length was computed using Equation 4-13. The modified bond strength was used for only the four flexural bars within the confinement zone shown in Figure 4.11, whereas the average bond strength was used for the two outer bars. The tensile force due to bond strength was compared to the applied tensile force obtained from Equation 4-9.

$$T_{\mu} = \mu \pi d_b l_{em} \qquad \textbf{(4-13)}$$

where T_{μ} is the tensile force developed due to the bond strength per bar (kips), μ is the bond strength (ksi), l_{em} is the embedded length (in).

The applied tensile forces for specimens 2IT10, 2IT12, and 4IT6-10 were 72%, 69%, and 59%, respectively, higher than the tensile forces developed due to the bond strength over the embedded length of flexural bars. These calculations validated the anchorage failure of the specimens. Anchorage failure was not desirable, as this results in reduced capacity. To prevent anchorage failure, support conditions were modified using 1 in. x 4 in. x 36 in. steel support plates for inverted-T specimens in Groups 3 - 11 and the testing span length was shortened from 24 ft to 21.6 ft. Bond strength calculation was made for specimen 5IT12-B4, as shown in Table 4.5, to show that anchorage failure prevention was predicted. The applied tensile force was 21% lower than the capacity from the available bond strength.

4.5.2 Flexural Reinforcing Cutoff Locations

Reduced amounts of flexural bar area were obtained as shown in Figure 4.12 for T specimens and Figure 4.13 for inverted-T specimens, by multiplying the full cross-sectional area of flexural bars by a ratio of actual embedded length (from the end to a critical section) to development length of the flexural bars. Development lengths were computed using ACI procedure (Equation 4-10).

The Response2000TM program was employed to compute shear capacity of specimens with cutoff details using the reduced section of the flexural bar area. Variables and results are summarized in Table 4.6. The analysis results correlated well with the experimental results with an average Vapp/VR2K ratio of 0.97 and a coefficient of variation of 6.7 percent. This indicated that capacity predictions for specimens with partially developed flexural steel were reasonable.

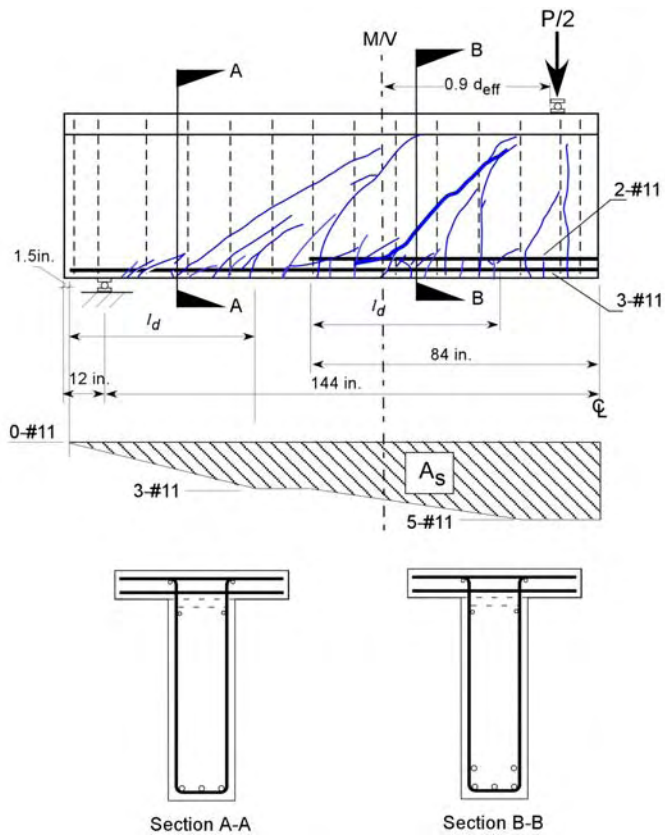

Figure 4.12: Effective cross-sectional area of flexural bars for T specimens with cutoff details

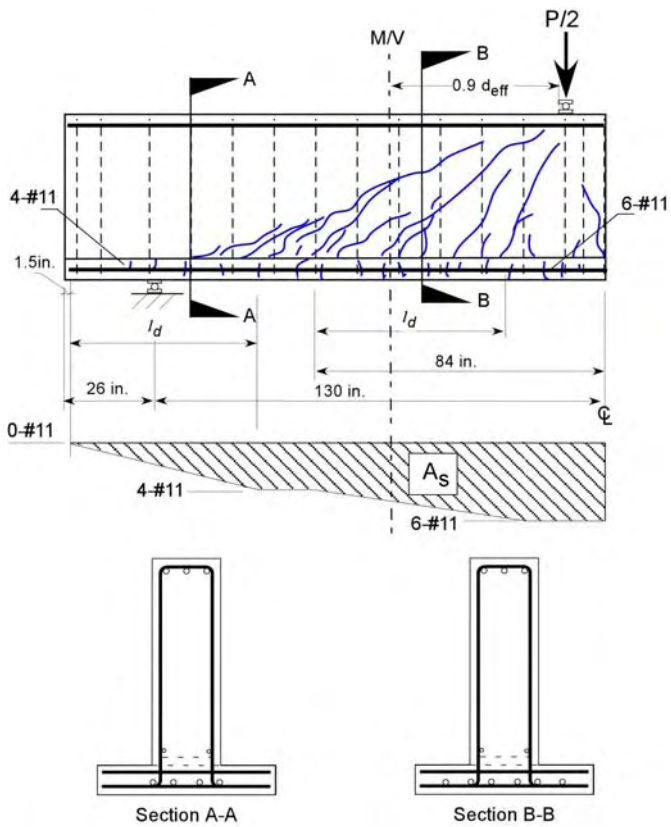

Figure 4.13: Effective cross-sectional area of flexural bars for Inverted-T specimens with cutoff details

Table 4.6: Shear capacity predictions for specimens with flexural bar cutoff details (COV in %)

Specimen	V_{APP} (kips)	f'_c (psi)	f_y (ksi)	l_d (in) ACI	M/V (ft)	l_{em} (in)	Eff A_s (in^2)	Total A_s (in^2)	V_{R2K} (kips)	V_{APP} / V_{R2K}
8T12-B4	158.9	4995	74.9	58.2	7.55	30.6	0.819	6.32	157.1	1.01
9T12-B4	153.5	4705	70.8	56.7	7.55	30.6	0.841	6.36	150.3	1.02
8IT10	221.8	4750	74.9	55.4	6.25	29.7	0.837	7.91	222.7	1.00
8IT12	186.1	4840	74.9	57.1	6.25	29.7	0.812	7.86	212.7	0.87
9IT12-B1	216.8	4285	70.8	57.3	6.25	29.7	0.808	7.86	214.5	1.01
9IT12-B2	183.3	4605	70.8	55.3	6.25	29.7	0.838	7.92	204.1	0.90
									Avg.	0.97
									COV	6.7

4.6 COMPARISON ANALYSES FOR COMMON MATERIAL PROPERTIES

Concrete strengths of the specimens were variable, even with the same mix design, making direct capacity comparisons among specimens sometimes difficult. Using different analysis methods, capacity predictions were made for a set of common materials and parameters. Predictions of

shear capacity were performed, by *Response2000*™ (R2K), AASHTO-MCFT, and ACI methods, using the same M/V ratio, material, and section properties. *Response2000*™ was also used to predict capacity for cut-flexural bar details (cut-bar R2K), and to reflect stirrup debonding effects, the tensile strength of concrete was reduced (low-f_t R2K). Sections with six different stirrup spacings (6 in., 10 in., 12 in., 18 in., 24 in., and no stirrups) were used for the analyses, as shown in Figure 4.14.

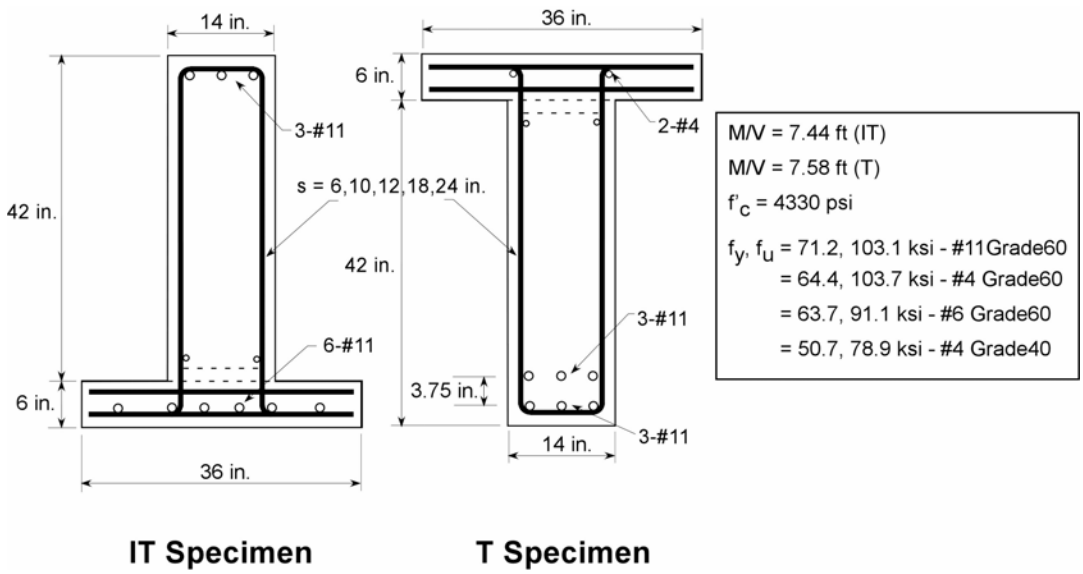

Figure 4.14: Sections, loading and material properties for analyses using common material properties

For the sections with cut-flexural bar detail, two of six flexural bars were placed starting at 5 ft from the end supports. Reduced flexural steel cross-sectional areas at the sections were computed based on ACI development lengths. Material properties were average concrete strengths, steel yielding stress, and ultimate stress for all specimens. M/V ratios for T and inverted-T specimen were 7.58 ft and 7.44 ft, respectively. Predicted results are shown in Figure 4.15.

Similar trends were observed for both inverted-T and T specimens. Strength prediction of sections with no stirrups was very low using low-f_t R2K. When the stirrup spacing decreased, the differences in strength predictions were smaller compared to R2K predictions. Similar predictions by R2K and cut-bar R2K were observed for sections with large stirrup spacings, while the correlation deviated when the stirrup spacings were smaller than 18 in. ACI predicted higher strength than the other methods for the section with no stirrups, but a lower prediction was found when stirrups were present in the sections. For 24 in. stirrup spacing sections, AASHTO-MCFT predicted lower shear capacities compared to the other methods due to the stirrup spacing being lower than the minimum stirrup requirement. Overall predictions by AASHTO-MCFT were fairly conservative compared to other methods used for sections with stirrups.

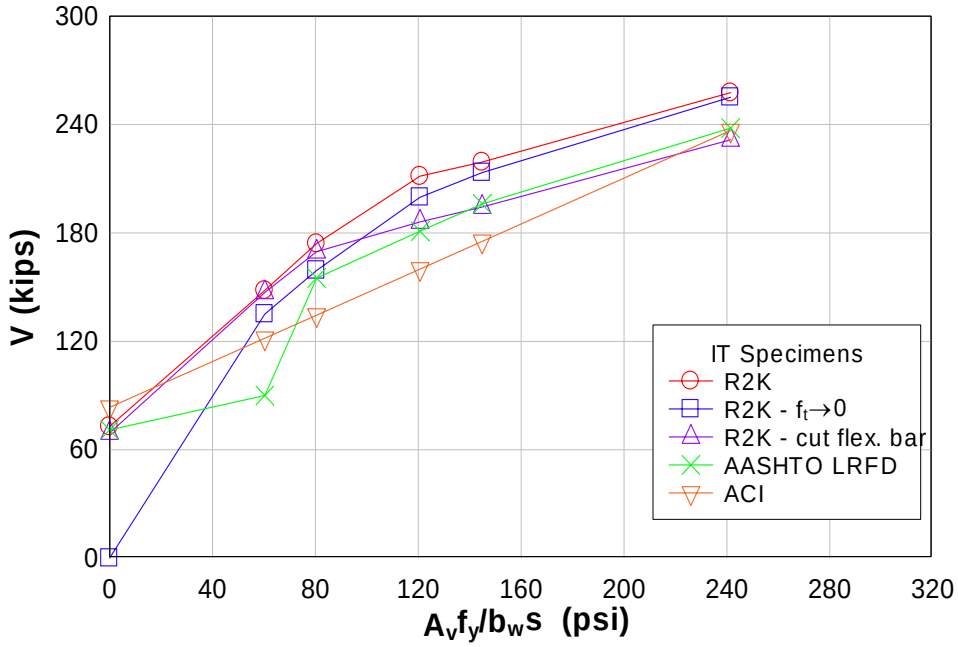

a)

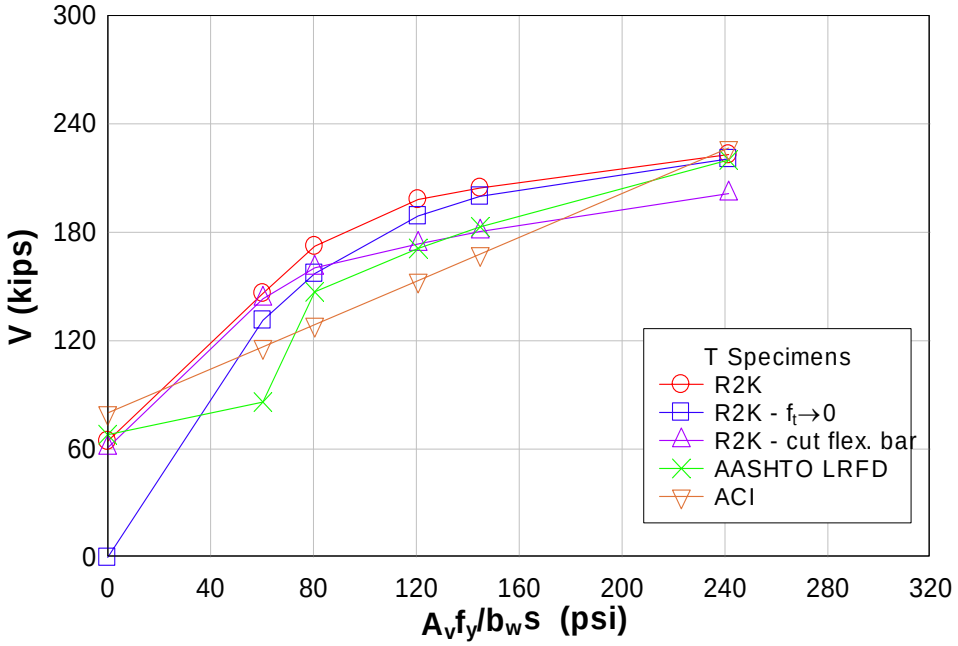

b)

Figure 4.15: Predicted shear capacity using same material properties: a) Inverted-T specimens; b) T specimens

4.7 STRUT-AND-TIE METHOD

The Strut-and-Tie Method (STM) was recently adopted for use in ACI 318-02 (*2002*) and is also incorporated in the AASHTO-LRFD specification (*2003*). This method is recommended by AASHTO for locations where concentrated loads are applied and where the applied load and the supporting reactions are less than twice the member height (*AASHTO 2003*). The STM attempts to model the distribution of forces in the concrete section by idealizing the member as an equivalent truss consisting of compression force struts and tension ties. The struts and ties are connected by nodal regions, which transfer forces between the internal elements as well as at external boundaries. An excellent overview of the analysis method with examples is given by Collins and Mitchell (*1991*) and Reineck (*2002*).

The AASHTO application of STM is slightly different from that in ACI 318-02 for the values and factors used to determine capacity of model elements, although the overall approach is similar. The factored resistance of a strut or tie component, P_r (kips), is taken as:

$$P_r = \phi P_n \quad \textbf{AASHTO 5.6.3.2-1} \qquad \textbf{(4-14)}$$

where P_n (kips) is the nominal strength of the strut or tie, and ϕ is 0.7 for struts or nodal zones and 1.0 for tension ties.

The nominal strength of a strut without reinforcement parallel to the strut depends on the compressive stress, f_{cu} (ksi) that can be carried in the element and the area of the strut, A_{cs} (in^2), and is determined as:

$$P_{ns} = f_{cu} A_{cs} \qquad \textbf{(4-15)}$$

$$f_{cu} = \frac{f'_c}{0.8 + 170\varepsilon_1} \le 0.85 f'_c \quad \textbf{AASHTO 5.6.3.3.3-1} \qquad \textbf{(4-16)}$$

where f'_c (ksi) is the compressive strength of the concrete, and ε_1 (in/in) is the principal tensile strain across the strut. The principal tensile strain is computed as:

$$\varepsilon_1 = \varepsilon_s + (\varepsilon_s + 0.002)\cot^2 \alpha_s \quad \textbf{AASHTO 5.6.3.3.3-2} \qquad \textbf{(4-17)}$$

where ε_s is the tensile strain in the tension tie (stirrup) and α_s (degrees) is the smallest angle between the compressive strut and the tension tie.

The tensile strain in the tension tie may be taken as 0.002 in/in, if the stirrups are expected to be at yield under factored loads.

The nominal strength of tension ties in sections without prestressing is determined as:

$$P_{nt} = A_{st} f_y \quad \textbf{AASHTO 5.6.3.4.1-1} \qquad \textbf{(4-18)}$$

where A_{st} is the area of the reinforcing steel attributed to the tie (in^2) and f_y is the yield strength of the steel (ksi).

The concrete compressive stress in nodal regions varies depending on the conditions at the node as:

$$f_{cnode} = 0.85\phi f_c' \quad \textbf{CCC nodal regions} \qquad \textbf{(4-19a)}$$

$$f_{cnode} = 0.75\phi f_c' \quad \textbf{CCT nodal regions} \qquad \textbf{(4-19b)}$$

$$f_{cnode} = 0.65\phi f_c' \quad \textbf{CTT nodal regions} \qquad \textbf{(4-19c)}$$

where ϕ is the resistance factor of 0.7 for bearing on concrete, and CCC is a nodal region subjected to compression forces only, CCT is a nodal region subjected to compression forces and a single tension tie force, and CTT is a nodal region subjected to compression force and two tension tie forces.

4.7.1 STM Model for Test Specimens

Relatively simple and regular two-dimensional STM models were developed for the specimen beams to facilitate their use by ODOT personnel for possible practical analysis of RCDGs. The half symmetry model consisted of two inclined struts, two horizontal struts, three tension ties, and four nodes as shown in Figure 4.16. Two of the tension ties (T1 and T2) consist of the flexural steel and the second tension tie (T3) represents the shear reinforcement. The amount of shear reinforcement included in T3 is the area of stirrups crossing both inclined struts. The four nodes in the model consisted of two CCT nodes (B and D in Figure 4.16), a CTT node (C in Figure 4.16), and a CCC node (A in Figure 4.16).

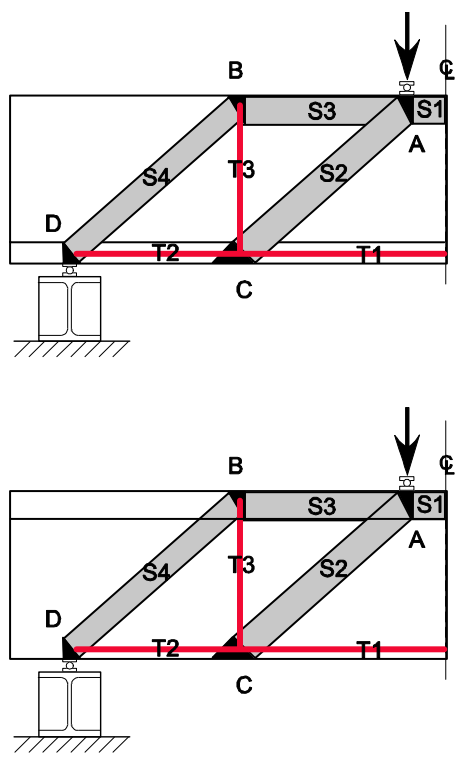

Figure 4.16: Simple strut-and-tie models for shear capacity prediction of control specimen group

The width of the struts, w_s, was determined as:

$$w_s = w_t \cos\theta + l_b \sin\theta \qquad \textbf{(4-20)}$$

where θ (degrees) is the angle of the strut, l_b is the length of the bearing plate (4 in. for all specimens), and w_t is the height of the tie region.

The height of the tie region (Node D) for T specimens was taken as 9.1 in., for two layers of flexural steel and 5.4 in. when a single layer of steel was present. The strut angle for the T beams varied for different specimens, but was in the range of 32°. This resulted in a corresponding strut width of 9.8 in. at the bottom. For the IT series, the width of the tie region was taken as 6 in. (thickness of the deck) because the flexural steel was located in a single layer. The resulting strut angle was approximately 30° to 32° and the corresponding strut width was 7.2 in. Nodes A and B were sized by setting the force couple from the flexural design equations to a maximum, producing a 11 to 18 in. nodal height for the IT specimens, depending on the particular concrete strength and flexural steel yield stress. Nodes A and B varied from 4 to 6 in. for the different T specimens.

The strut widths were determined based on the nodal geometry. For IT specimens, the struts were all assumed to be prismatic, having widths of 7.2 in. for Struts 2 and 4. For the T specimens, Strut 4 was assumed nonprismatic, having a width of 9.8 in. controlled by the nodal geometry at location D, and Strut 2 was also assumed nonprismatic, having a width of approximately 8 in. controlled by the nodal geometry at location A. The compressive stress in the struts was determined assuming strains in the stirrups at failure were equal to the yield strain (0.0017in/in).

The area of Tie 1 was 9.36 in^2 for most T and all IT specimens. The tie capacity for T2 was determined from the available anchorage at the edge of nodal zone D. An increased bond stress of 1.3 times that prescribed by the AASHTO-LRFD specification was used to account for the beneficial confining effects within a projected 45° influence zone at the support location. Tie 3 represented the shear stirrups and the area varied depending on stirrup spacing. Tie 2 ranged from 9 in^2 (6 in. spacing) to 3 in^2 (18 in. spacing).

Predicted and empirical shear capacity for the STM models are shown in Figure 4.17. As seen in this figure, the chosen STM model with code prescribed factors tended to underestimate the shear strength for all cases. Failure was found based on the maximum nominal capacity of the different truss components. The controlling elements varied between specimens and including bearing failure at Node D, compression failure of Strut 4, and yielding of Tie 3. The STM models produced a mean ratio of experimental to predicted shear capacity of 1.42 with a coefficient of variation of 0.27.

The STM approach may be difficult to apply to actual girders in bridge structures, as the loads on the girders are not necessarily from directly applied point loads from truck tires on the deck. This makes selection of nodal regions and strut angles uncertain and an equivalent truss-model difficult to define. However, STM models may be appropriate for bent caps which are primarily loaded at locations where the main girders frame into the cap and at column intersections.

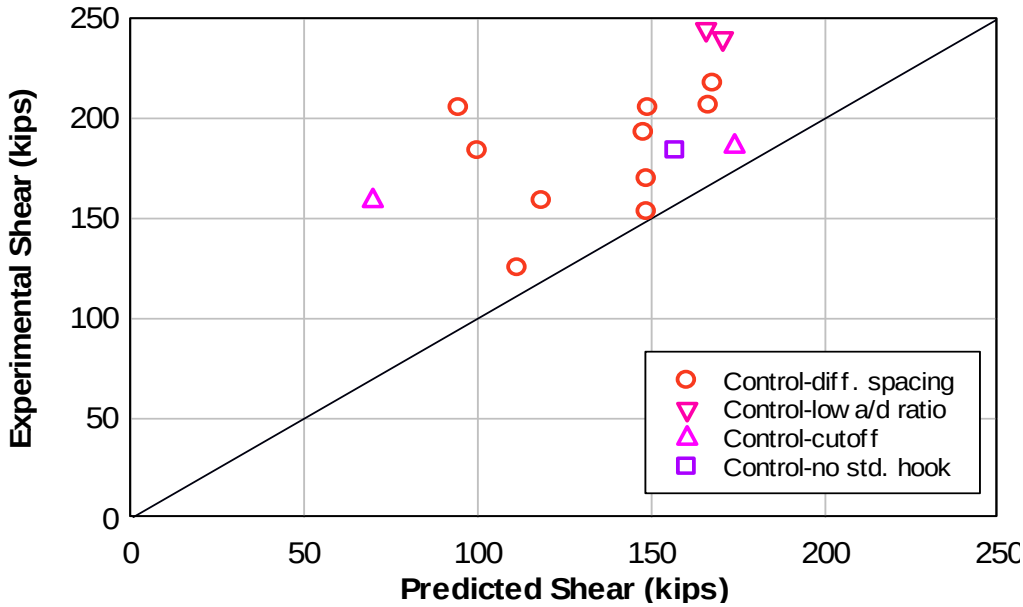

Figure 4.17: Predicted and measured shear capacity for control group of specimens using STM

4.7.2 STM for Bent Caps

Simple single-strut STMs were developed for the bent caps of the field study bridges considered previously. These models are shown in Figure 4.18. For these single diagonal strut models, the critical detail controlling capacity is the anchorage of the flexural steel at the column face. Bent caps from the 1950's vintage RCDG bridges typically contain relatively low flexural steel reinforcement ratios and the flexural steel is generally inadequately anchored.

Development lengths for flexural bars were computed according to AASHTO-LRFD specification section 5.11.2. For flexural reinforcing steel being developed within the highly compressed zone of the column reaction, bond strengths were increased by a factor of 1.3 to permit a shorter development length. For the available development lengths, an effective flexural steel tie area (at yield stress) was computed at the face of the nodal zone. A required diagonal strut force was calculated to balance the tension tie force based on the angle of the strut from the top of the interior girder to the column reaction.

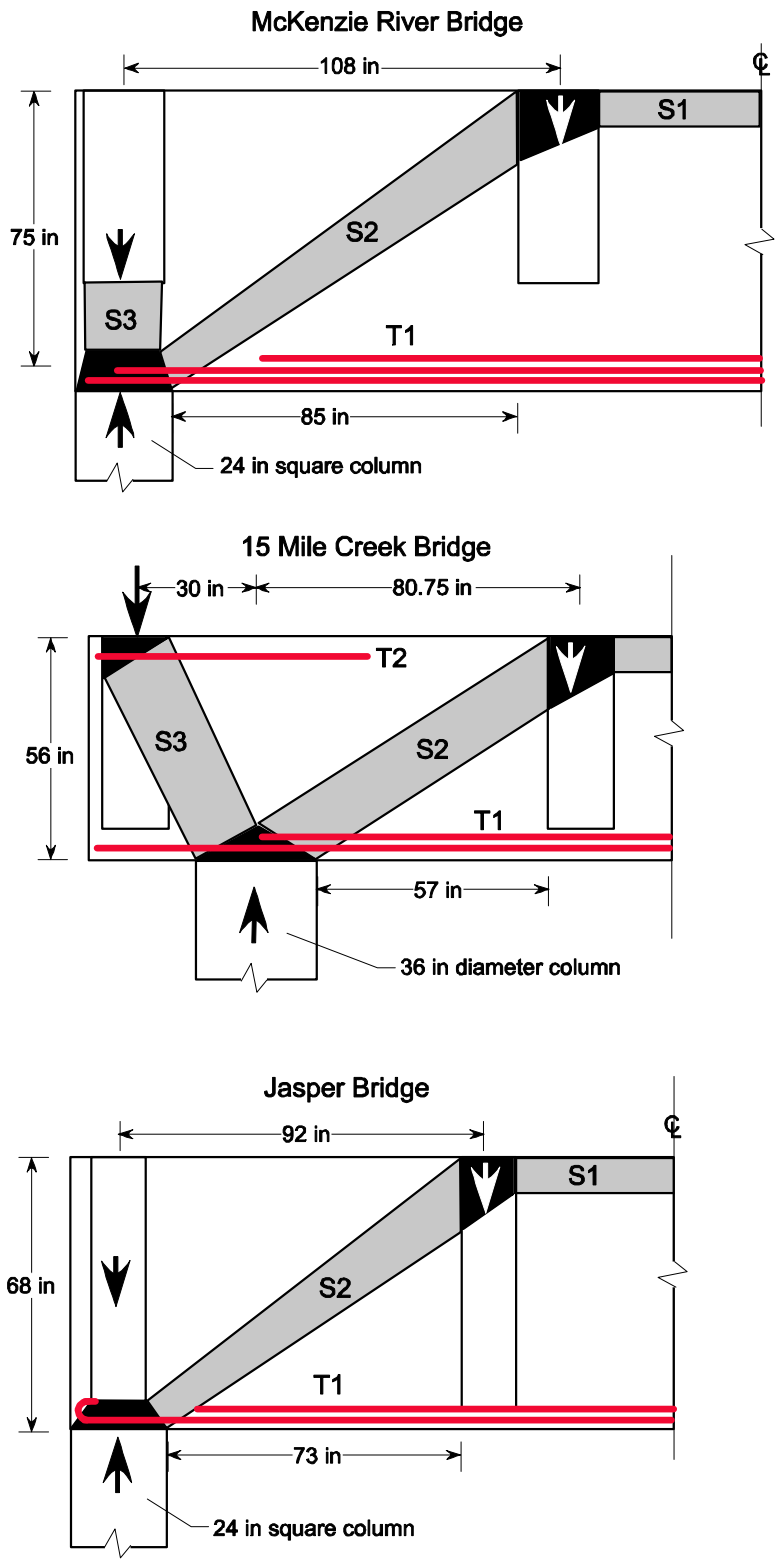

Figure 4.18: Single strut STM models for shear capacity prediction of field study bridge bent caps

The vertical component of the strut force represents the amount of shear that can be carried by the bent cap without exceeding the anchorage capacity. The capacities of the bent caps were also calculated using AASHTO-MCFT and *Response 2000*™. Nominal capacities computed by these three methods are shown in Figures 4.19a-c. Bent cap shear forces from applied loads were determined using the ODOT rating vehicles as well as the AASHTO-LRFD recommended load cases for continuous support locations (a: 90% of two trucks each with 14 ft axle spacings, spaced 50 ft apart combined with 90% of design lane load; and b: two design tandems spaced 26 feet apart combined with design lane load). The multiple presence factor of 1.2, impact factor of 1.33, and load factor of 1.35 (for rating) were used in the analysis to compare with predicted capacities. Dead weight of components and dead weight of the wearing surface were also incorporated with a load factor of 1.25 used for both.

The factored bent cap load effects for each of the three bridges are shown in relation to the predicted capacities in Figures 4.19a-c. As seen in this figure, the predicted nominal capacities are well below the factor load effects. In fact, the STM method indicates that there is only minimal capacity for live load, as the self-weight of the structure alone approaches the capacity of the flexural anchorage at the column face. None of the three methods appears to reasonably predict the capacity of the bent caps. It is possible that a more refined strut and tie model, considering multiple arching struts with associated vertical ties could better predict capacity of the bent caps. However, the anchorage of the flexural reinforcing steel at the column face remains of questionable capacity. Additional research is scheduled to address issues related to capacity prediction of bent caps for RCDG bridges.

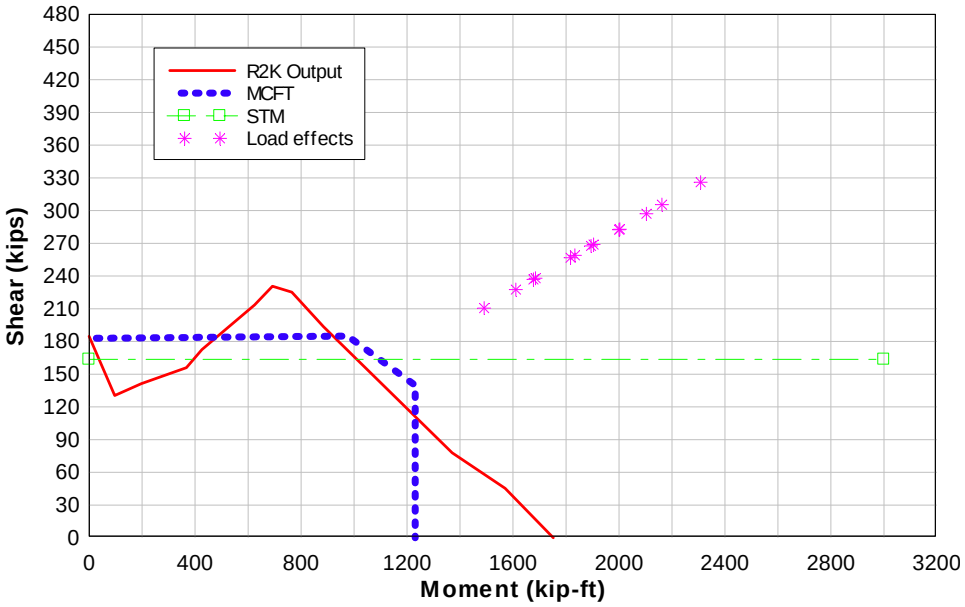

Figure 4.19a: Capacity predictions and demand on bent caps for McKenzie River Bridge

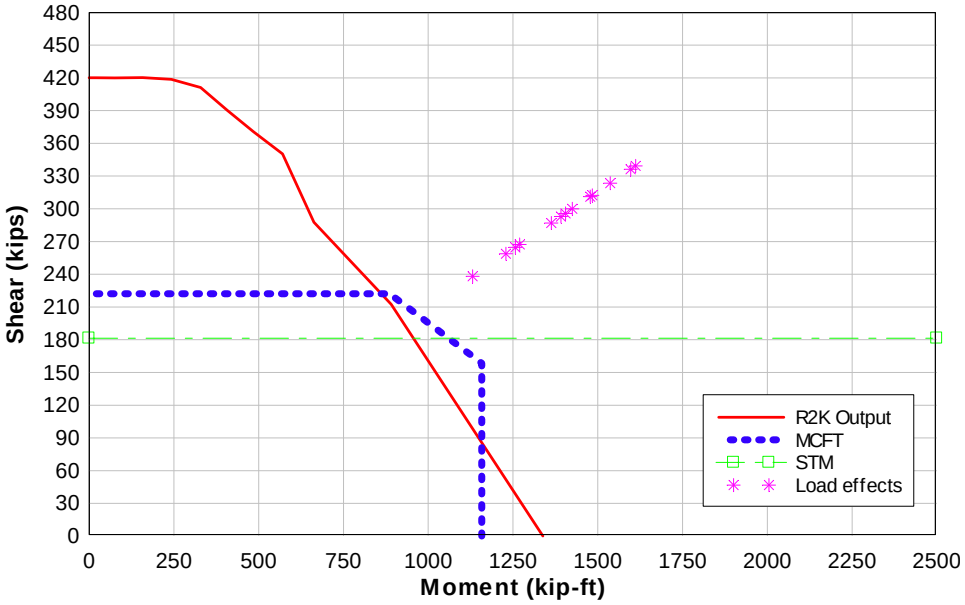

Figure 4.19b: Capacity predictions and demand on bent caps for 15 Mile Creek Bridge

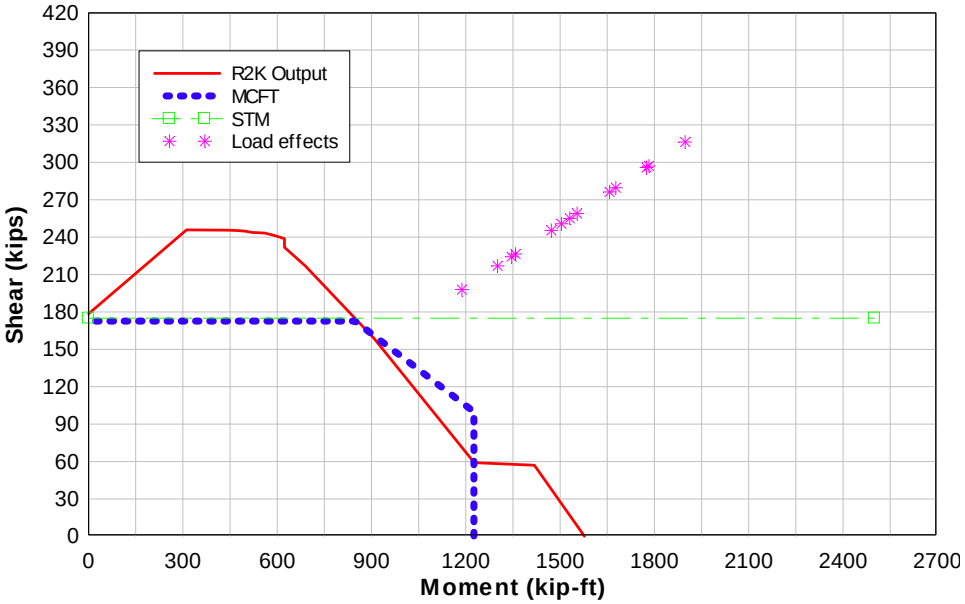

Figure 4.19c: Capacity predictions and demand on bent caps Jasper Bridge

4.8 FINITE ELEMENT ANALYSIS

Nonlinear finite element analyses (FEA) were employed for test specimens. While they provide a method to predict the strength and behavior of lightly-reinforced CRC girders, they are not a

practical way for engineers to routinely assess bridge members. A major drawback for their use in actual bridges is the difficulty in being able to model the section of interest efficiently and prescribe loading and reaction locations that can produce the desired shear and moment at the section. Assessment of individual girders or bent caps under well-defined loading conditions can be performed with relative ease.

FEA of beam specimens was performed using ANSYS version 7.0. Specimens 10T24 and 11T22 were modeled for demonstration of FEA. Only a quarter of the test beam was modeled by taking advantage of symmetry for specimen 10T24, as shown in Figure 4.20. For specimen 11T22, half of the test beam was modeled due to unsymmetrical stirrup spacing along the beam length and the support condition (a cantilever) as shown in Figure 4.23.

Embedded reinforcing steel was modeled using nonlinear truss elements rigidly connected to the surrounding concrete elements. Rebar material properties were determined from tensile tests. Concrete was modeled using 8-node solid elements. Constitutive modeling of the concrete was performed using the modified Hognestad compressive stress-strain relationship (*Hognestad 1951*) with concrete strength obtained from the day-of-test cylinders. To account for confining effects at the load application points, concrete elements were modified to permit reduced post-peak decay in compressive stress near the support and loading locations.

Locations of supports and load applications for FEA of specimens 10T24 and 11T22 are shown in Figure 4.20 and Figure 4.23, respectively. For the FE model of specimen 11T22, loading was statically applied at 41.5 in. from the end to predict section capacity in this region, since the flexural bar cutoff point was located at 72 in. from the cantilever end. Diagonal-tension failure was anticipated to occur in the region due to the cutoff detail.

Analyses were performed using a quasi-displacement control technique whereby high-stiffness springs are used to control the midspan displacement of the model and the resulting forces are computed based on support reactions. The spring stiffness is adjusted through trial and error such that numerical stability of the solution is achieved, as the model becomes highly nonlinear at concrete cracking/crushing and rebar yielding, without loss of precision. Without this technique, solution times become exceedingly large and peak and post-peak response cannot be well captured using current concrete models in ANSYS.

Predicted deformed shape and principal tensile strain pattern for specimens 10T24 and 11T22 are shown in Figure 4.21 and Figure 4.24, respectively. Load-deformation and load-stirrup strain plots from FEA for specimen 10T24 are shown in Figures 4.22a,b along with member response using *Response2000*™. FEA predicted a higher capacity with a smaller deformation at the peak load compared to the test data as shown in Figure 4.22a. As seen in this figure, R2K provided similar results compared to FEA for applied loads up to about 50% peak load, however R2K provided better prediction of load-deformation response near the failure. For load-stirrup strain behavior of specimen 10T24, abrupt change of strains occurred earlier in the test beam as shown in Figure 4.22b. Large strains exceeding the yield strain were measured at strain gages no. 1-3 in the test beam. Conversely, only one strain in the FE model was close to the yield strain.

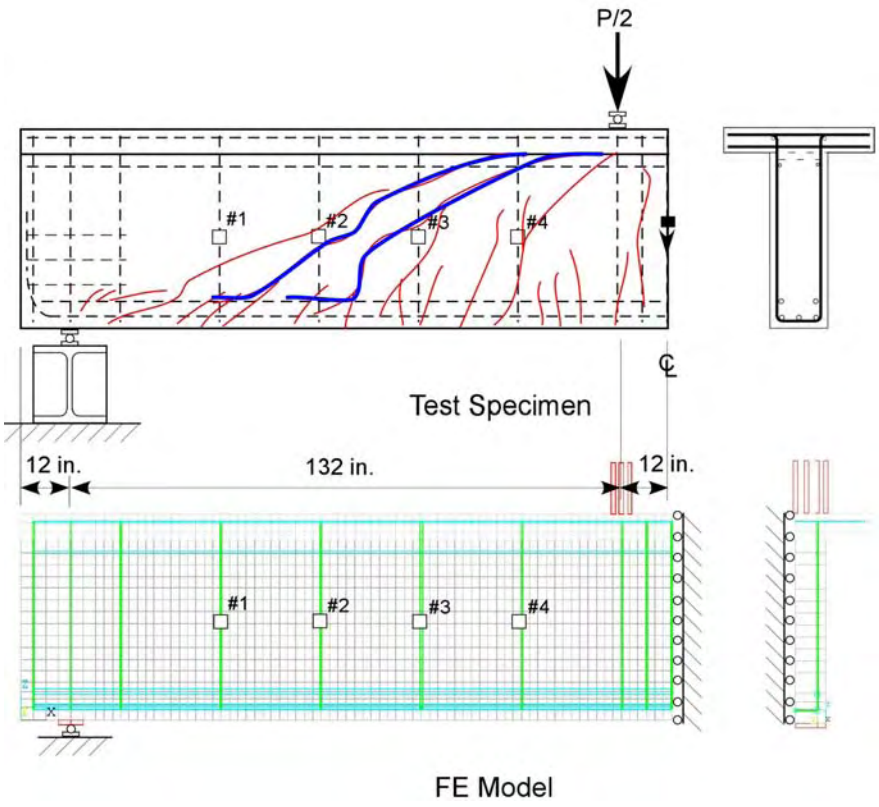

Figure 4.20: Finite element model of specimen 10T24 and strain gage location

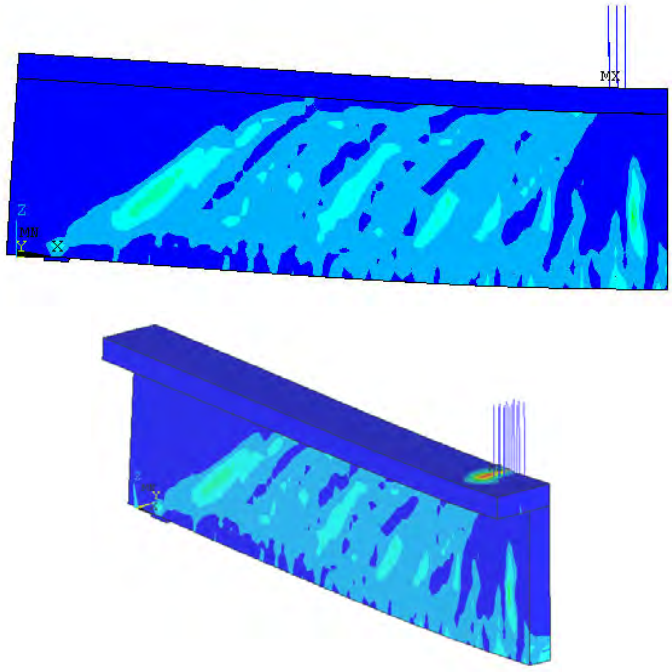

Figure 4.21: Deformed shape and principal tensile strain pattern of 10T24 FE model close to failure

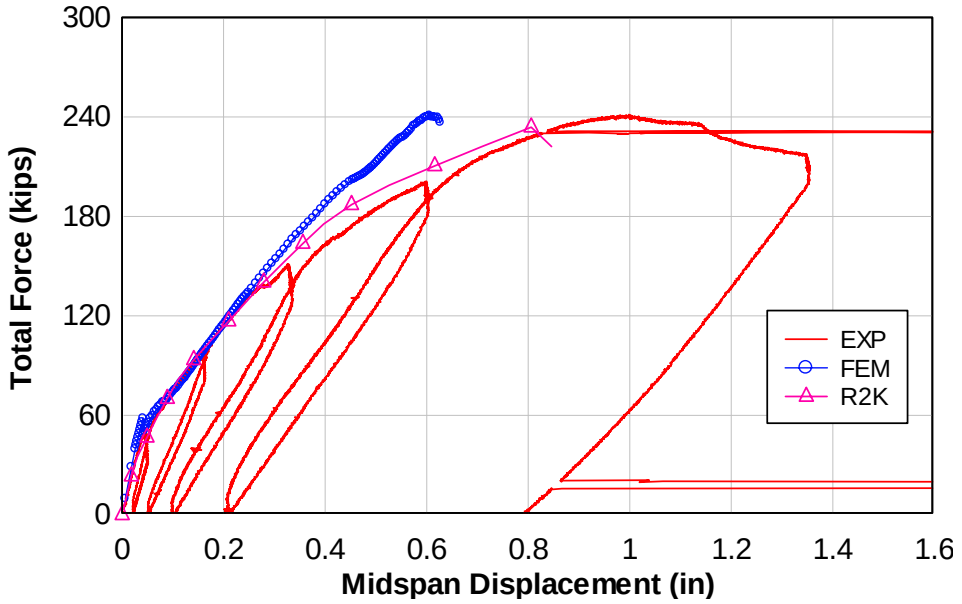

a)

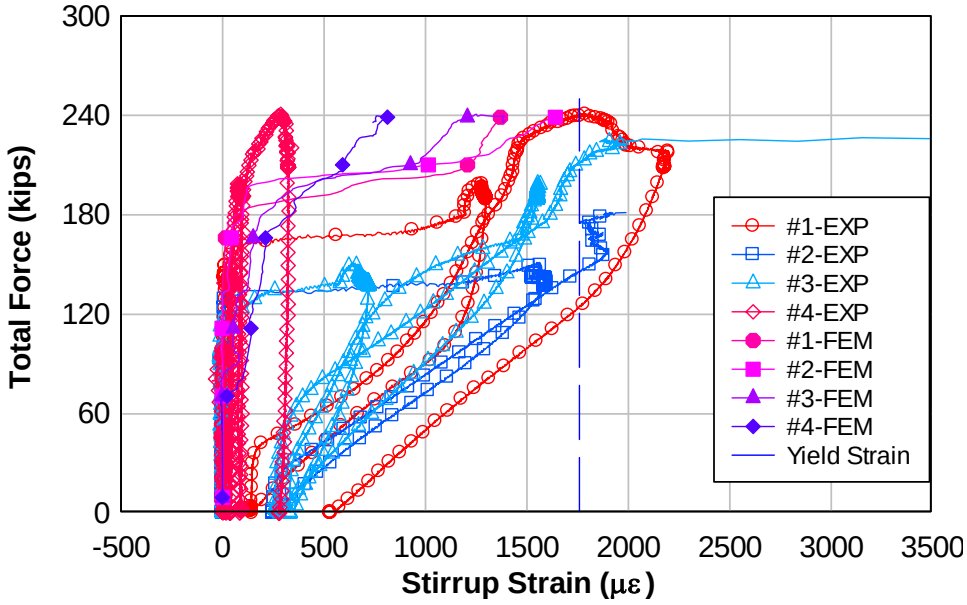

b)

Figure 4.22: FE analysis and experimental results of specimen 10T24: a) load-displacement at midspan plot; b) load-stirrup strain plot

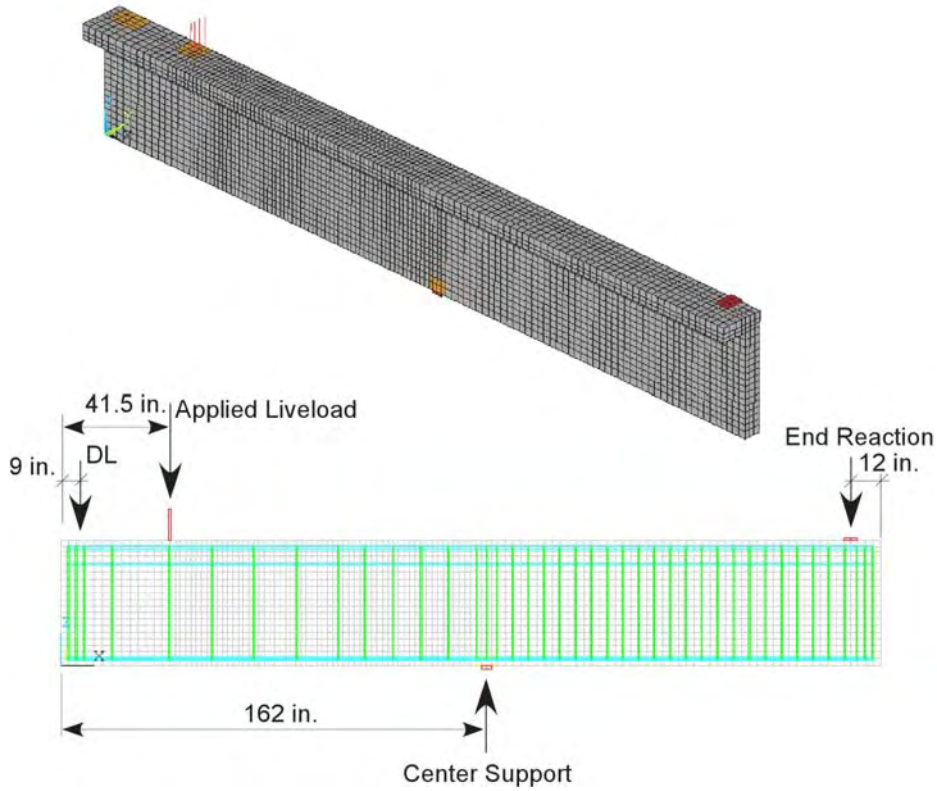

Figure 4.23: Finite element model of moving-load specimen 11T22

For specimen 11T22, the diagonal-tension failure predicted by FEA was located at approximately 72 in. from the end with an applied load of 226.5 kips and 2.3 in. end deflection. Experimentally, specimen 11T22 failed at a load of 215.8 kips with a diagonal crack located at 52 in. from the cantilever end and a 2.6 in. end deflection. In general, FEA tended to overpredict section capacity and underpredict deformation of test specimens.

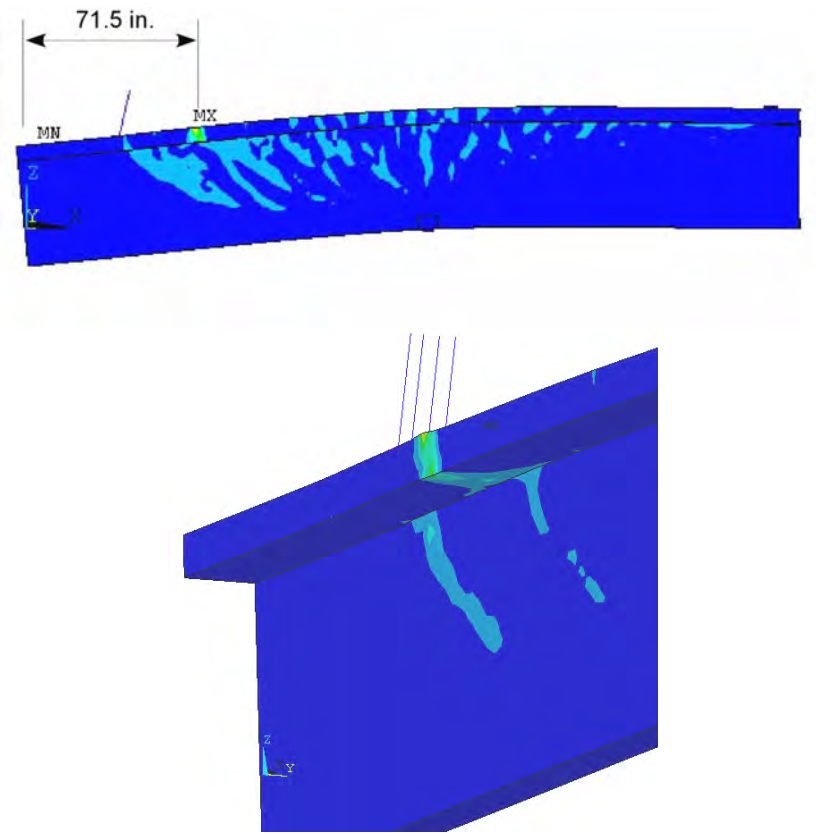

Figure 4.24: Deformed shape and principal tensile strain pattern of specimen 11T22 model: a) at loadstep prior to failure; b) at failure load

4.9 PREDICTION OF SERVICE LEVEL STIRRUP STRESS FOR FATIGUE ASSESSMENT

As shown previously, both AASHTO-MCFT and *Response 2000*^{TM} provided rapid analysis techniques that reasonably predicted the capacity of the girder specimens over the wide range of test variables. MCFT as implemented in AASHTO and *Response 2000*^{TM} does not depend on the loading path to predict capacity, and the initial conditions are typically assumed to be uncracked. However, assessment for fatigue requires prediction of the stirrup strain range, and service level stirrup stress ranges are path dependent. To predict service level response for stirrup strains, modifications were made for MCFT to account for the concrete material reloading in the initially uncracked condition as well as strain amplification at diagonal crack locations. Comparisons were made between the analytically predicted stirrup strain responses and laboratory specimens during reloading portions of the test histories. The method developed permits prediction of shear forces and the corresponding moments that produce yield stress in the stirrups. This yield threshold can be compared with load effects at a particular section, for low-cycle fatigue life predictions.

4.9.1 Service Level Prediction Methodology

The analysis methodology developed for service level stress range prediction employs MCFT, using the approximate sectional analysis approach described by Vecchio and Collins (*1988*). The approximate method of sectional analysis using MCFT sets the angle of principal strain to be constant throughout the height of the cross-section. Thus, every sublayer utilizes the same principal strain angle, as illustrated in Figure 4.25.

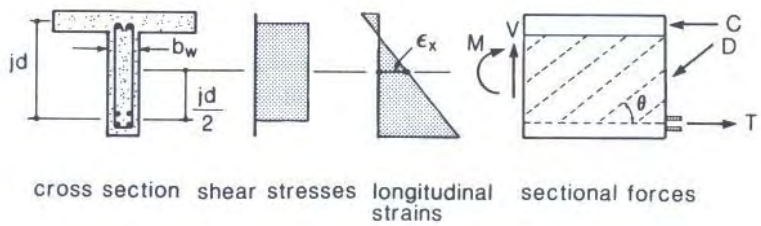

Figure 4.25: Approximate sectional MCFT analysis (*Collins and Mitchell 1991*)

Collins and Vecchio demonstrated that the approximate method using a constant angle of principal strain provided reasonable results compared with the detailed sectional analysis. This approximate analysis method was implemented in a computer program called *Response* (*Collins and Mitchell 1991*), and the procedure used to solve the moment-shear interaction by the approximate analysis is outlined by Collins and Mitchell (*1991*). The approximate sectional analysis method employed in *Response* was implemented in a spreadsheet to permit modifications to the constitutive relationships in MCFT for predicting stirrup strain response in the cracked condition. The spreadsheet output was verified with that from *Response* for an example problem (*Vecchio and Collins 1988*).

The spreadsheet implementation was compared with instrumented behaviors from three of the laboratory specimens: 2T12, 2IT12 and 10T24. The spreadsheet predictions for moment-shear capacity curves (identified as MR in figures) are compared with *Response 2000*™, AASHTO-MCFT, and *Response* capacity curves as shown in Figures 4.26a-c. The spreadsheet implementation of the approximate MCFT sectional analysis typically provided results above *Response* and below *Response 2000*™. This was likely due to improved convergence control available with the spreadsheet implementation.

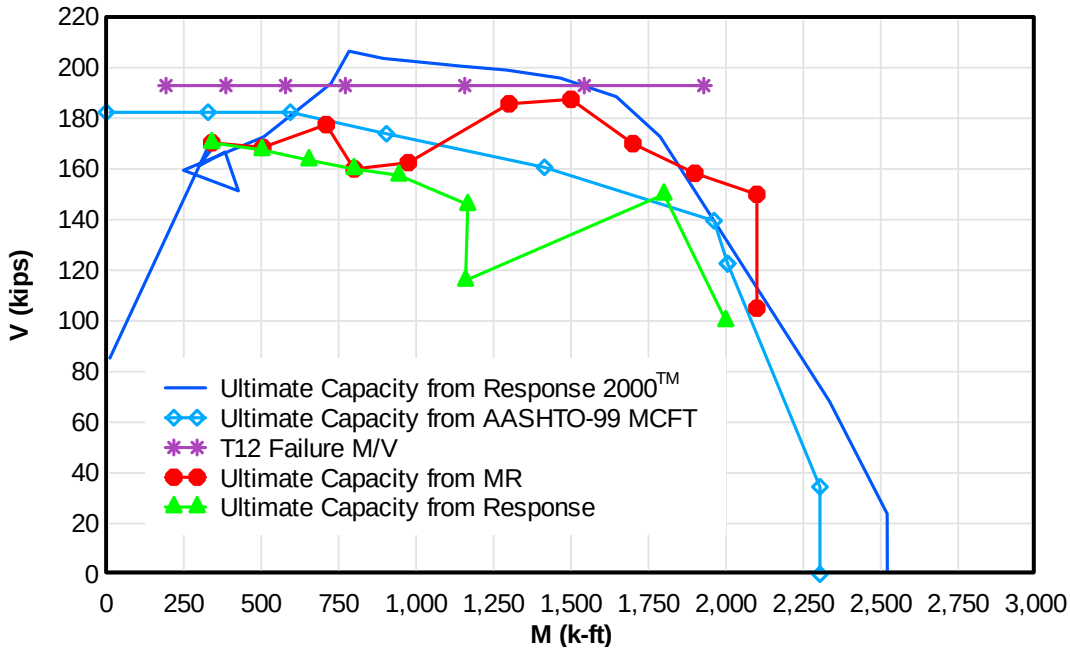

Figure 4.26a: Shear-moment interactions for capacity prediction of specimen 2T12

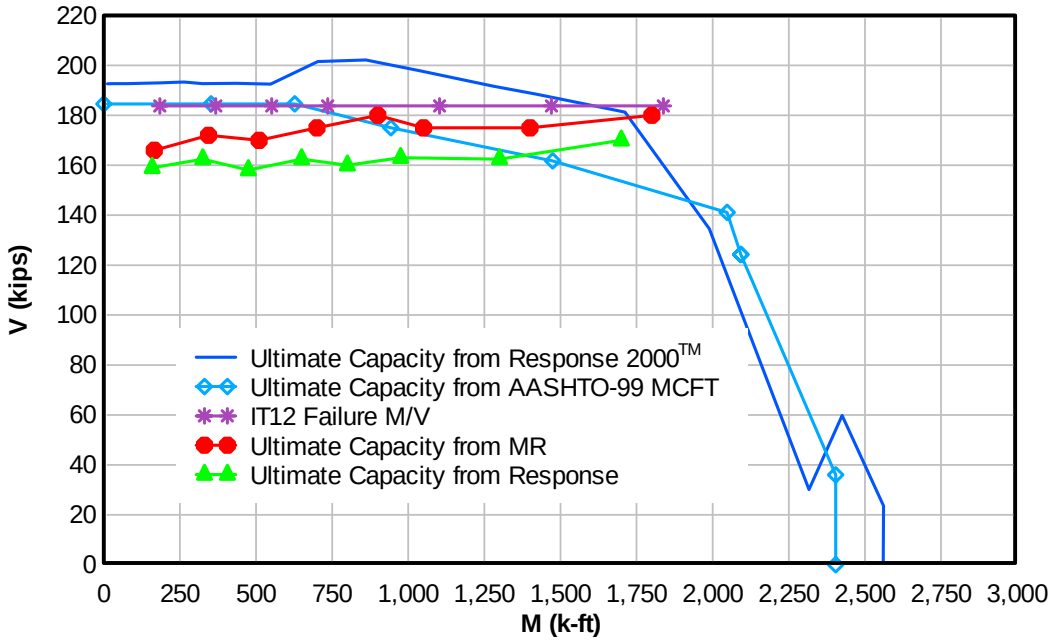

Figure 4.26b: Shear-moment interactions for capacity prediction of specimen 2IT12

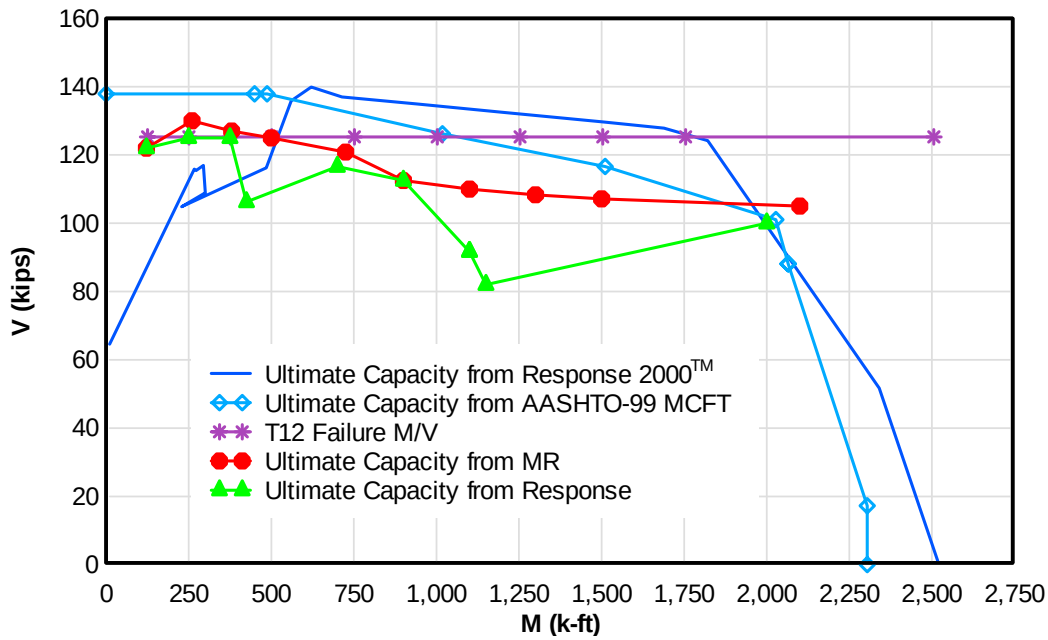

Figure 4.26c: Shear-moment interactions for capacity prediction of specimen 10T24

4.9.2 Amplification Factor for Yielding of the Stirrups at Diagonal Cracks

Based on experimental observations, stirrups adequately bonded to the concrete yielded at diagonal crack locations. Stirrup strain gages located away from diagonal cracks were at a lower strain. Thus, there are variations of transverse strain through the height of the section, with some sections having locally higher strains. For the purpose of estimating the onset of yielding in the transverse reinforcement, an amplification factor was utilized to relate the average strains over the section to the maximum stirrup strain at a diagonal crack location.

Average strains were taken over the section height between the compression and flexural reinforcement, referred to here as *DV*. Transverse strain distribution may be better represented by a parabolic shape over the actual shear depth, *h*, which corresponds with visual observations of crack widths distributed within the specimen height. An amplification factor is derived from simple geometry and calculus to relate the average strain over the whole section to a corresponding maximum strain in a parabolic distribution. The relationship is described by:

$$\varepsilon_{parabola_\max} = \frac{3}{2}\frac{(DV)}{h}\varepsilon_{tave} \qquad \textbf{(4-21)}$$

where *h* is the distance from the flexural tension reinforcement to the edge of the deck/stem interface for a T-section and the distance from the flexural tension reinforcement to the bottom of compression zone computed based on an equivalent rectangular stress block at ultimate. For equal values of DV and h, the strain is locally amplified at mid-depth by 1.5.

A potential limitation of using this strain amplification approach arises in high moment to shear (M/V) ratios. At high M/V ratios, the strain in the flexural steel at the bottom of the section may increase, permitting larger transverse strains at the level of the reinforcement. This may distort the transverse strain distribution. The new shape exhibits transverse strains greater than zero at the level of flexural steel due to the reduced constraint. This causes the transverse strain distribution to trend toward an average transverse strain condition. Therefore, for high M/V ratios, the amplification factor would be smaller.

Additionally, where repeated stresses may reduce the bond between stirrups and concrete, the transverse strains through the section would become more like the average strain. Thus, all stirrups crossing a diagonal crack would tend to exhibit similar strain ranges.

4.9.3 Reloading of Previously Cracked Sections

MCFT is typically applied for reinforced concrete sections that are initially uncracked. As a result, the stirrups experience little strain until after cracks form in the concrete. By contrast, in diagonally cracked sections, the stirrups strain almost from the onset of loading (after crack faces decompress). For the initial analysis assuming uncracked concrete, the stress at first cracking was taken as:

$$f_{cr} = 4\sqrt{f'_c} \qquad \textbf{(f}'_{\textbf{c}}\textbf{ in psi)} \qquad \textbf{(4-22)}$$

Beyond this stress magnitude, cracks begin to form, the concrete begins to soften, and the stirrups begin to strain more substantially. However, this magnitude of cracking stress no longer applies for the onset of tension stiffening in a beam already containing diagonal cracks. Reloading of a cracked specimen induces tension stiffening behavior sooner, once the crack surfaces have decompressed. To model the cracked condition, a reduced value of f_{cr} is required.

Laboratory stirrup strain data from test specimens were analyzed to determine a cracking stress representative of the force required to compress the crack face. The cracking stress for use in MCFT was derived from applied shear and stirrup strain relationships in test specimens (where stress and strain are taken as proportional to one another in the elastic range). The stress magnitude was selected based upon the shear force level at which significant stirrup strain deviation was observed. These values were in the range of between 33% and 50% of the initial cracking stress, with 33% being more typical for strain gages near diagonal cracks, as shown in Figure 4.27. Therefore, a cracking stress equal to 33% of the initial value was used to analyze the sections with diagonal cracks to predict reloading stirrup strain response.

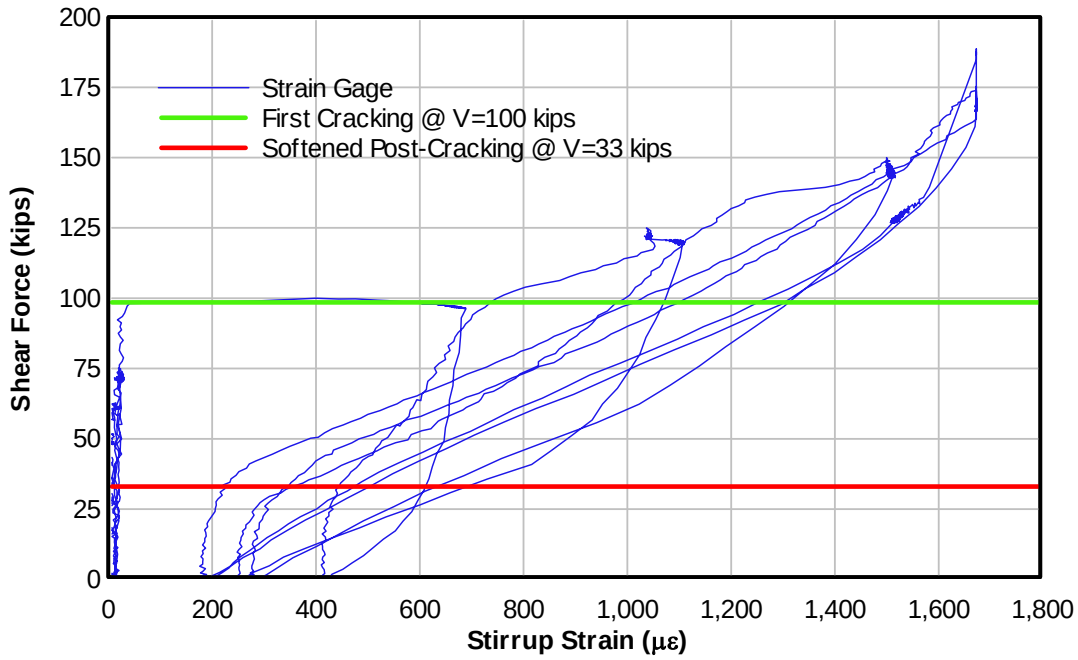

Figure 4.27: Cracking strain, ε_{cr}, determination for specimen 2T12

4.9.4 Stirrup Strain Prediction

Laboratory data were employed to verify the use of a reduced cracking strain for analyzing the effects of reloading on a diagonally cracked section. The three previously mentioned laboratory specimens were used for this evaluation. The cracking stress was taken as 33% of the initial cracking stress, as discussed previously, and the analysis was carried out using the spreadsheet implementation of the approximate method of sectional analysis using MCFT. Results of this analysis corresponded well with the reloading branches of the laboratory specimens, demonstrating that the reduced cracking strain provided suitable modification to MCFT relationships to reasonably predict stirrup strain reloading behavior for the diagonally cracked specimens (Figures 4.28 - 4.31). The model for reloading based on MCFT, adjusted with a reduced cracking strain, can be seen as the dashed curves on each plot. The curve has been shown both at the origin and offset to the strain where softening behavior is more readily evident.

In addition, the amplification factors from Equation 4-21 were applied to the model using the spreadsheet implementation of the approximate sectional analysis by MCFT and compared with the laboratory data. In general, the results showed that the amplified strains corresponded more reasonably to the initial loading branch, while the unamplified (average transverse) strains provided a better correlation with the softened reloading branches after cracking. It is likely that stirrups on initial loading are well bonded to the surrounding concrete and, therefore, the strains vary more locally throughout the height of the section, reaching maximum magnitude at the diagonal crack locations. This is better predicted using the transverse strain amplification factor. However, upon repeated reloading after cracking, stirrup bond may diminish, permitting more

uniform yielding over the stirrup leg, thereby approaching the average transverse strain condition.

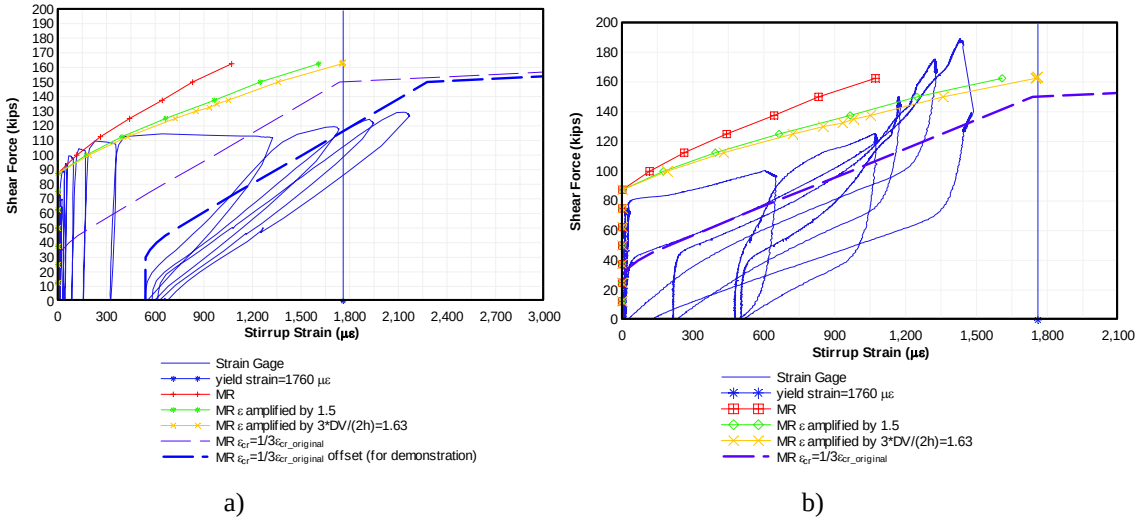

a) b)

Figure 4.28: V-ε_t at south side M/V=4 ft for a) specimen 3T12; and b) specimen 2T12

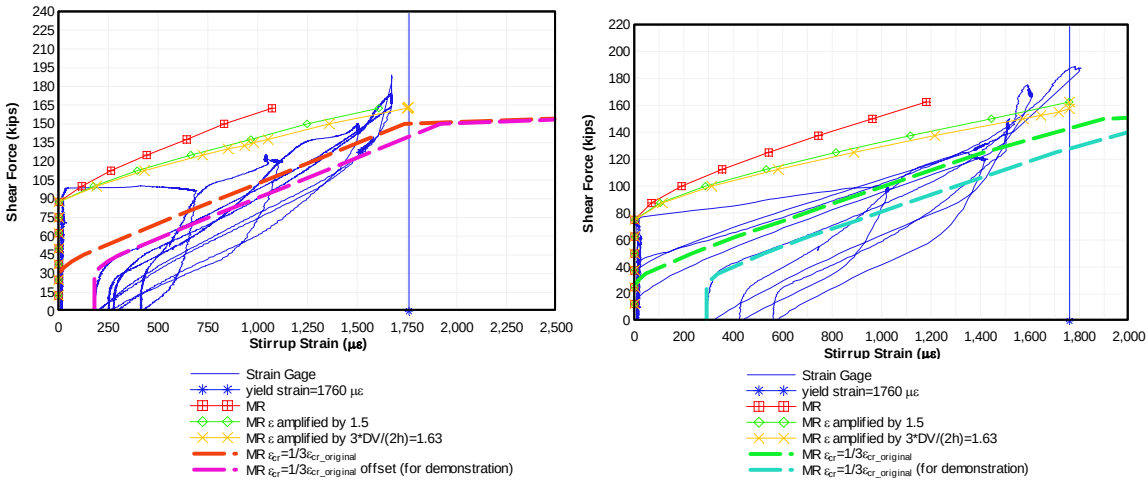

a) b)

Figure 4.29: V-ε_t at north side M/V=4ft for a) specimen 2T12; and b) M/V=6 for specimen 2T12

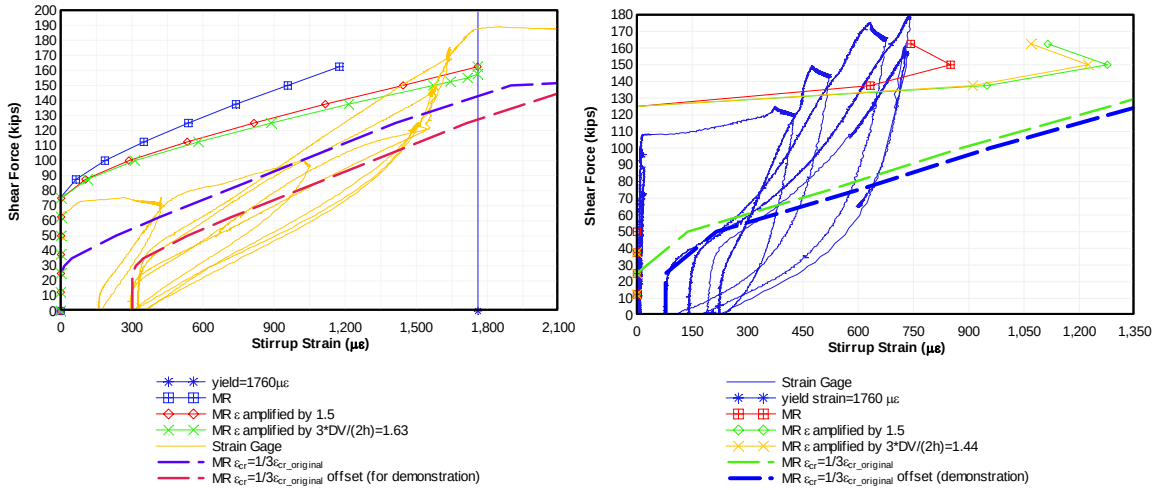

a) b)

Figure 4.30: V-ε_t at south side M/V=6 ft for a) specimen 2T12; and b) specimen 2IT12

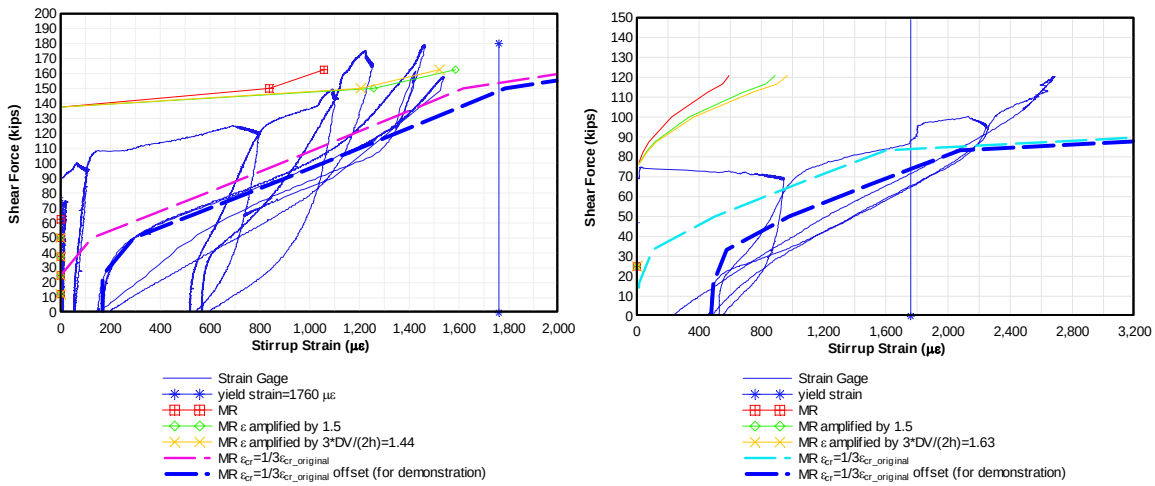

a) b)

Figure 4.31: V-ε_t at south side M/V=6 ft for a) specimen 2IT12; and b) specimen 10T24

Experiments on specimens with fully unbonded stirrups indicated that stirrup strains were uniform (average) across the diagonal crack (specimen 7IT12 and 7T12 in Appendix L3b). Consequently, stirrup strain for the reloading branch may be better predicted using average strains over the section height (the unamplified model) due to reduced bond between the stirrups and concrete. For an in-service diagonally cracked reinforced concrete bridge girder subject to millions of repeated cycles, average transverse strains may better predict reloading strain behavior. However, use of amplified transverse strain values results in yield strains at lower load levels, and is conservative.

An additional factor that affected the correlation of the predicted strain response and the experimental results was the location of the strain gage relative to the diagonal crack(s). The model predicted strains and the empirical strains corresponded reasonably well when a sensor was located near a diagonal crack location. However, analytically predicted stirrup strains were not as well correlated with the strain sensor measurements when the diagonal crack was located away from the strain gage location (Figure 4.30b).

4.9.5 Shear-Moment Interaction Curves for Stirrup Yielding

The reduced cracking stress for the concrete constitutive model permits stirrups to begin to strain earlier in the loading history. This was used to predict the shear and moment combination that cause yielding in the stirrups. Two cases were considered: 1) use the average transverse strain to estimate stirrup strains through the section; or 2) use amplification of the average transverse strains to predict local stirrup strains at diagonal cracks. The second case results in a lower estimate of the shear and moment combination required to produce yielding of the stirrups. The first case may better represent the stirrup stress range for in-service bridge girders having local bond slip at the stirrups.

The three laboratory specimens were analyzed to predict the shear and corresponding moment that produced stirrup strains equal to the yield strain at diagonal cracks. Average transverse strains were used for this analysis, as these better captured the reloading behavior of the specimens. Analytical results from the approximate sectional analysis indicated that shear and corresponding moment to produce stirrup yield for specimen 2T12 were approximately 67% of the ultimate capacity as predicted by the AASHTO-MCFT for M/V ratios from 3 to 20 ft (Figure 4.32); approximately 69% for specimen 2IT12 for M/V ratios from 3 to 10 ft (Figure 4.33); and 63% for specimen 10T24 with M/V ratios from 3 through 20 ft (Figure 4.34).

Considering the shear and corresponding moment curves that predict yield in the stirrups, it was found that at higher M/V ratios, there is a point at which the stirrups no longer yield before the capacity of the section is reached. As a result, beam sections with large M/V ratios do not appear to be prone to low-cycle fatigue damage to the transverse steel.

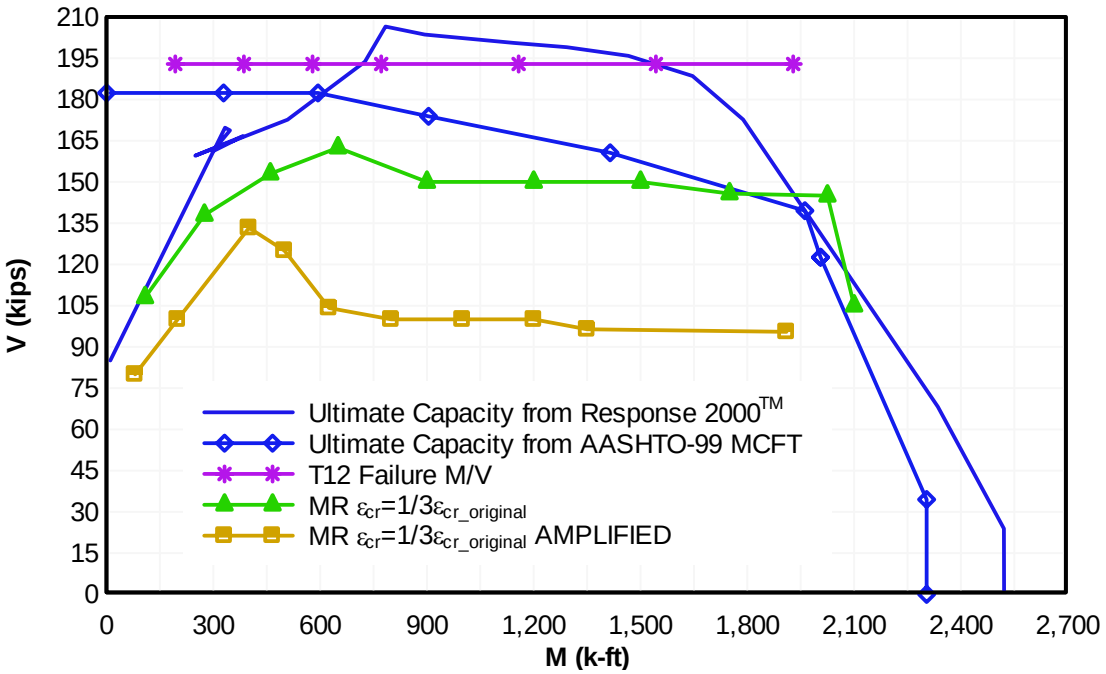

Figure 4.32: Shear-moment interaction for stirrup yielding for specimen 2T12

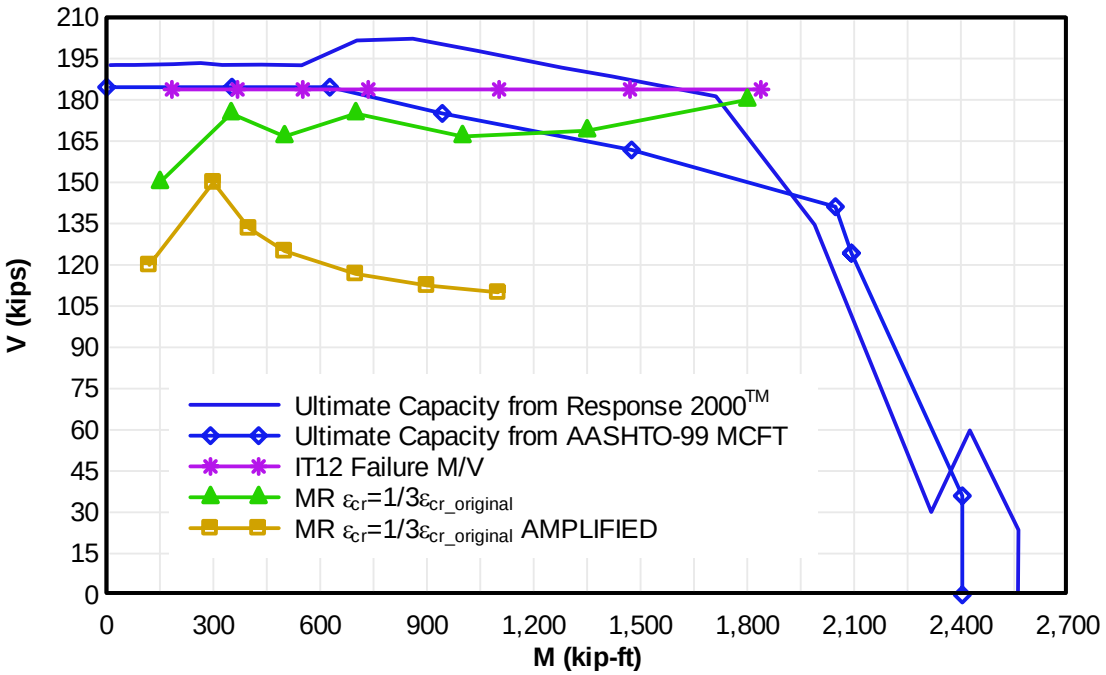

Figure 4.33: Shear-moment interaction for stirrup yielding for specimen 2IT12

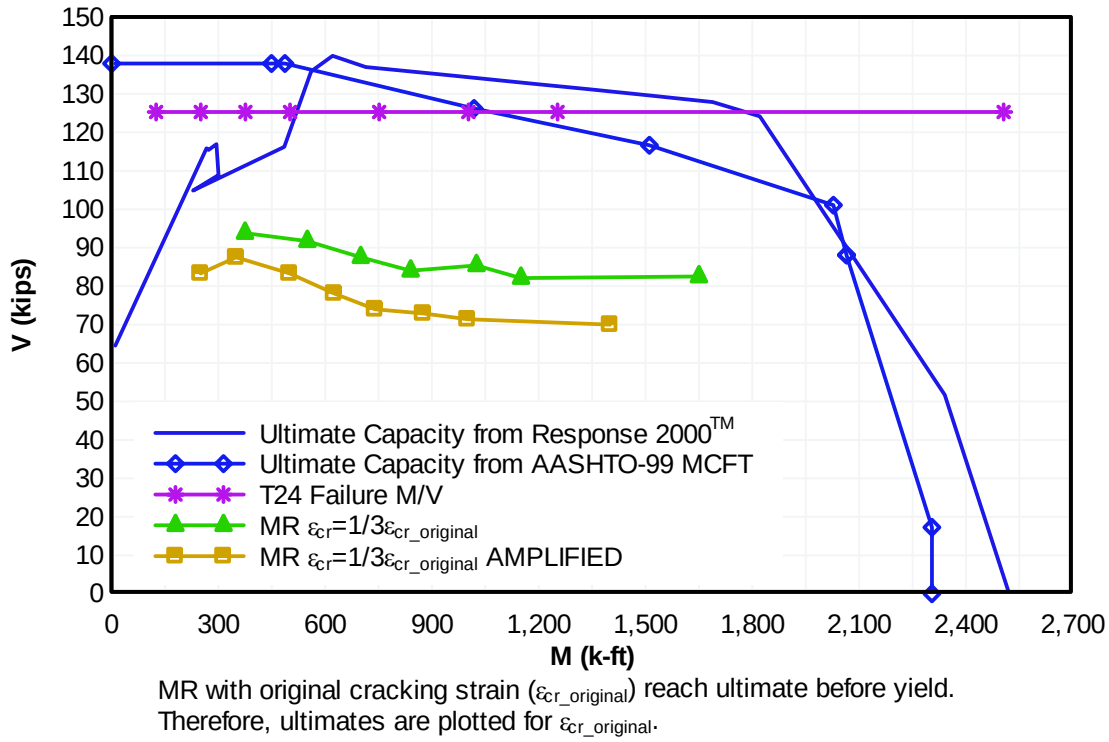

Figure 4.34: Shear-moment interaction for stirrup yielding for specimen 10T24

4.10 LIFE PREDICTION FOR LOW-CYCLE FATIGUE

Low-cycle fatigue (LCF) damage to conventionally reinforced concrete beams with diagonal cracks consists principally of accumulation of plastic strains in the transverse steel and bond deterioration between the stirrups and concrete. Ultimate failure of laboratory specimens was primarily dependent on fracture of the stirrups. In order to produce low-cycle fatigue damage to the stirrups, the peak live load stress combined with the dead load stress must be sufficient to cause yielding of the stirrups. Laboratory test data of large-scale specimens indicated that most bonded strain gages applied to stirrups at diagonal cracks indicated strain above the yield range during load events sufficient to cause incremental increases in the specimen deformation. Strain ranges remained approximately constant during a given load step, but the mean value of the strains increased. This accumulation of plastic damage led to stirrup fracture, resulting in the eventual failure of the specimen.

The observed response of specimens during LCF was characterized by three distinct phases as illustrated in Figure 4.35. LCF specimen behavior was similar to that reported for bond fatigue experiments (*Balazs 1998*). The initial phase was characterized by exponential limiting non-linearly increasing deformations, as shown in Figures 4.36 and 4.37. The secondary phase consisted of approximately linearly increasing deformations as shown in Figure 4.38. The tertiary phase consisted of exponentially increasing deformations that eventually resulted in beam failure as shown in Figure 4.39.

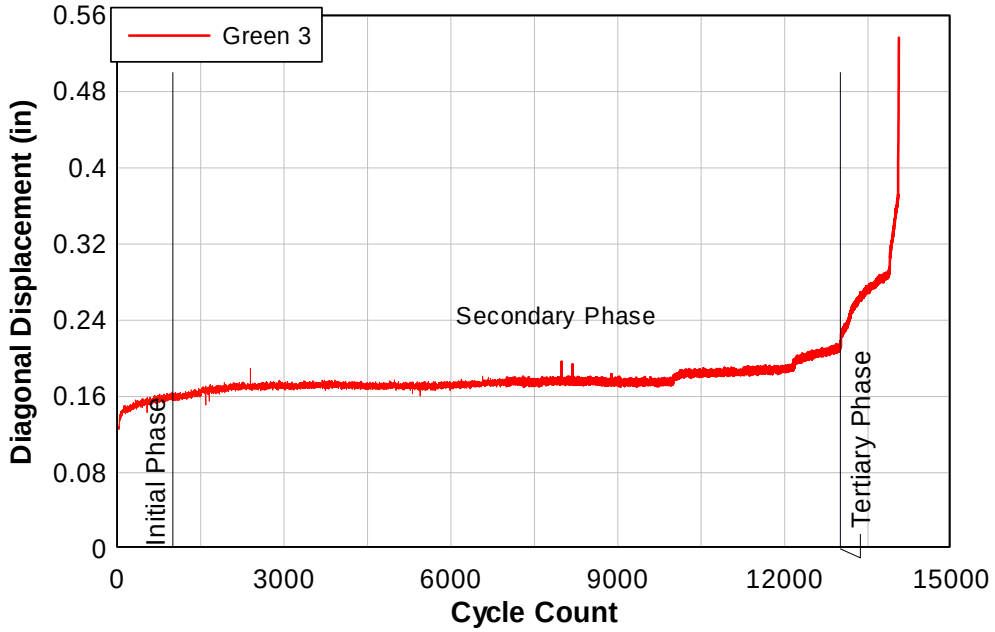

Figure 4.35: The three damage phases for low cycle fatigue specimen as illustrated by, force-diagonal deflection response from specimen 10T24

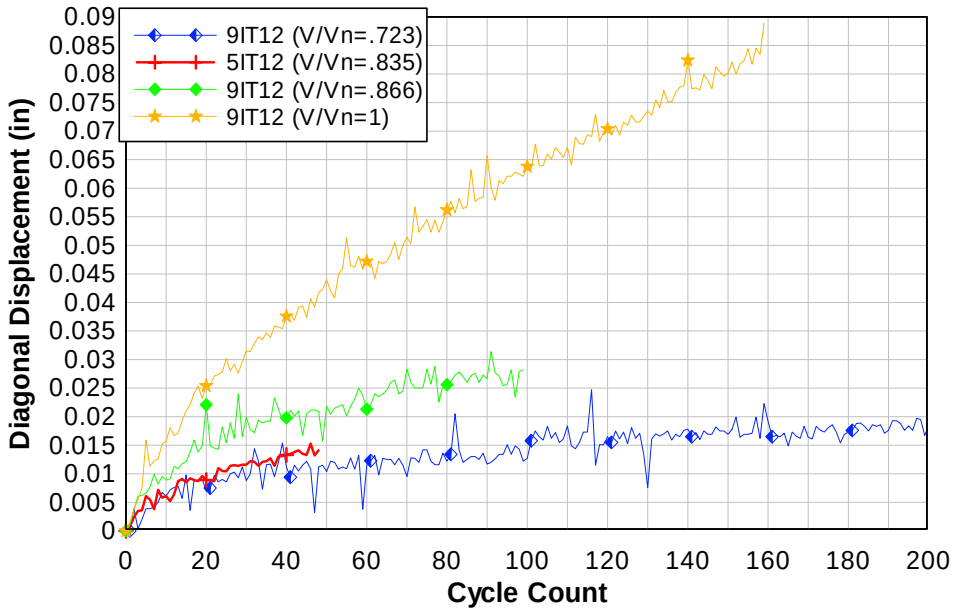

Figure 4.36: Incremental diagonal displacement during initial damage phase for inverted-T specimens with 12in. stirrup spacing

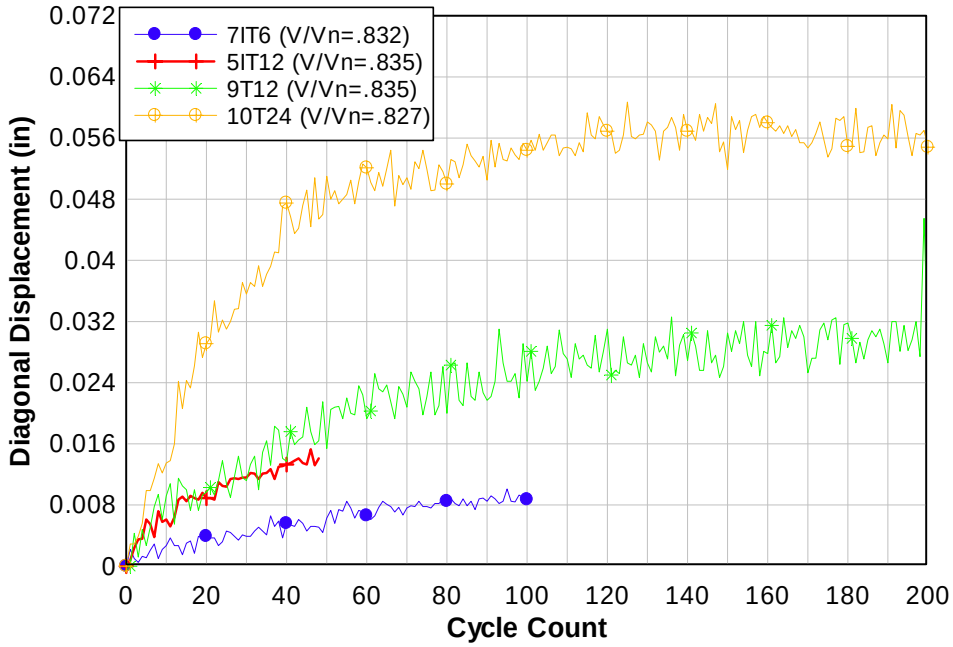

Figure 4.37: Incremental diagonal displacement during initial damage phase for specimens with similar load ranges

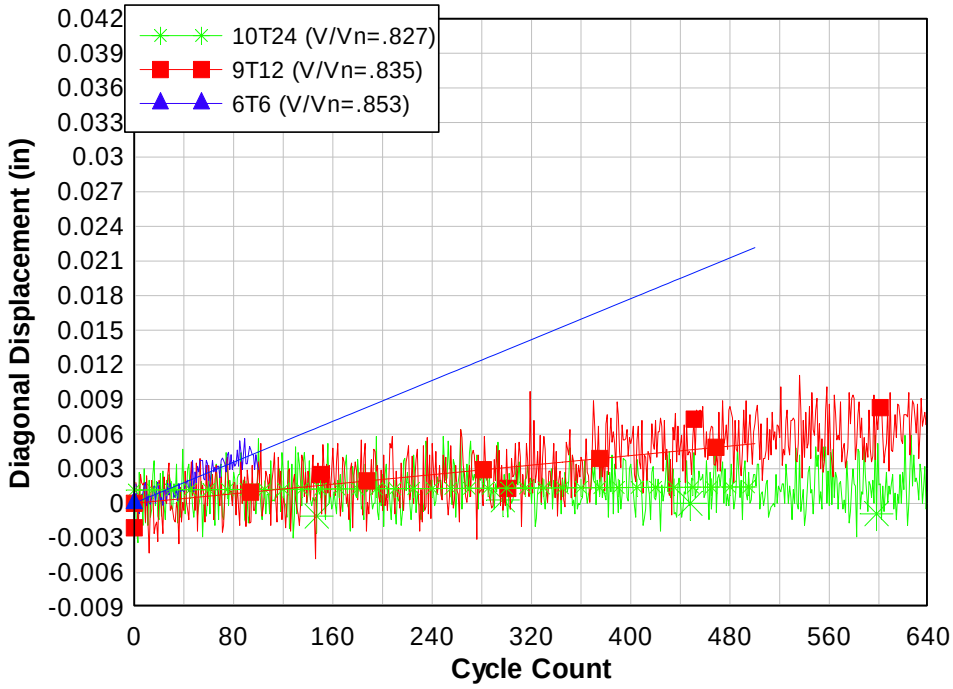

Figure 4.38: Incremental diagonal displacement during secondary damage phase for specimens with various load ranges

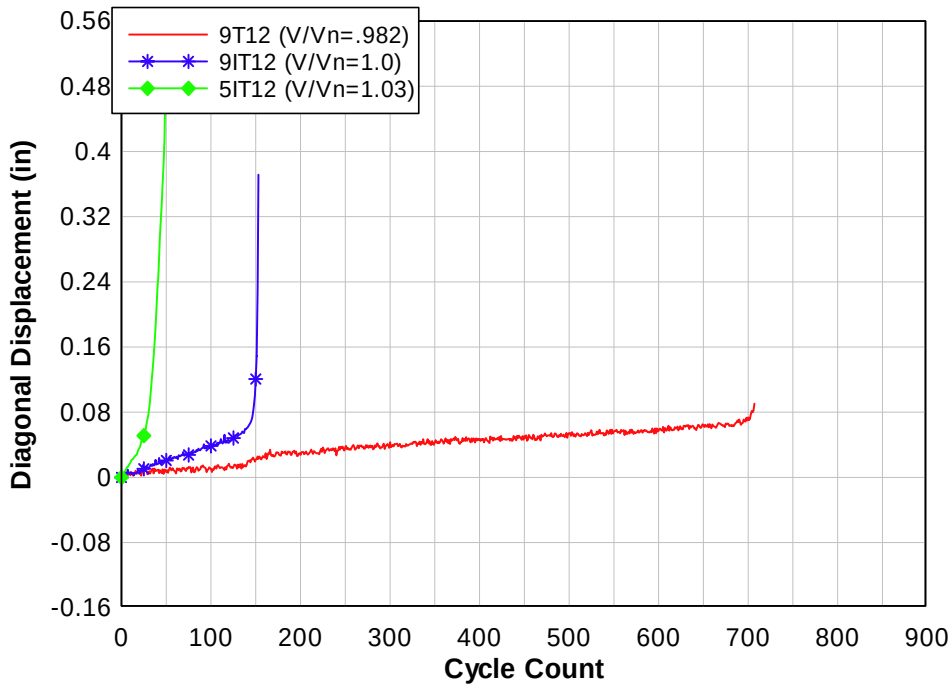

Figure 4.39: Incremental diagonal displacement during tertiary damage phase for specimens with various load ranges

Although two of the three phases consist of nonlinear damage components, the damage is cumulative and may combine in accordance with Miner's rule (*Bannantine, et al. 1990*). Comparison of the total deformations observed for the LCF specimens with otherwise similar specimens tested under monotonic conditions, indicated that LCF loading produced increased deflections, in terms of overall specimen deformation and local diagonal deformation. This observation was used to establish the deformation capacity of specimens under LCF loading.

Cumulative damage to LCF specimens was ascertained from several different sources. Centerline deflection provided a more integrated value of cumulative deformation reflecting the whole specimen, while diagonal displacement provided more localized deformation characterization, particularly in the failure region. Diagonal deformations provided a better indicator of beam health, as deformations tended to concentrate in regions rather than be distributed across the member. Once the limiting diagonal deformation capacity (based on monotonic specimens) was reached under repeated loads (that produced yield in the stirrups), it was conservatively assumed that the LCF specimen would fail. All of the LCF specimens exhibited larger diagonal displacements than corresponding control specimens.

Displacement rates observed in LCF test specimens indicated faster damage accumulation as the magnitude of the applied load, relative to the capacity, increased. This was also observed during the secondary phase of damage. For a sequence of loads, whereby a load was applied that was less than a previous load magnitude, deformation rates in the secondary phase returned approximately to the rate previously observed at the lower load.

Specimen life at a constant load range was derived both graphically and by curve fitting the different phases of damage. Graphical analysis consisted of matching the slope of the secondary phase and continuing that rate of damage until a stirrup fractured, as illustrated in Figure 4.40. At that point, a new rate of damage must be used until another stirrup fractured or the tertiary phase began. A secant line was used to match the rate of the tertiary phase. Graphical analysis of the second or later load steps was performed in the same manner, but the higher level of the initial phase was estimated by curve fitting specimens loaded at higher load ratios. The beam was considered to reach failure once the cumulative deformation from LCF reached the failure deformation level of the monotonic specimen.

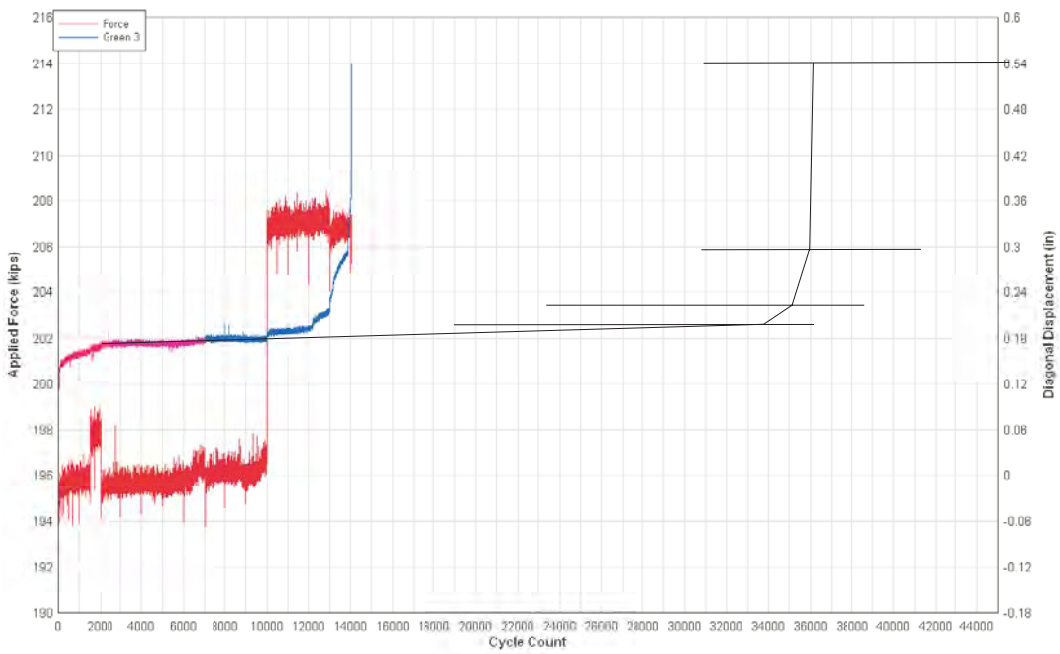

Figure 4.40: Example of graphical analysis used to estimate the number of cycles to achieve equivalent diagonal displacement at failure

A second method of analysis was performed by establishing relationships between the rate of deformation increase with the load ratio for different specimens within the three damage phases. The initial deformation produced on the first cycle for a specimen must be established as Δ_0. This can be estimated from analysis of the section with *Response 2000*™ (*Bentz 2000*). Initial experimental diagonal displacements for specimens with 12in. stirrup spacing and 24in. stirrup spacing are shown in Figure 4.41 and Figure 4.42, respectively. The initial displacement is followed an exponential limiting function that can be approximated with the form:

$$y(x) = \frac{aN + c}{N + b} \qquad \textbf{(4-23)}$$

where the coefficient *a* is the asymptote achieved after approximately 100 to 200 cycles, N is the number of cycles, and c and b are empirical coefficients.

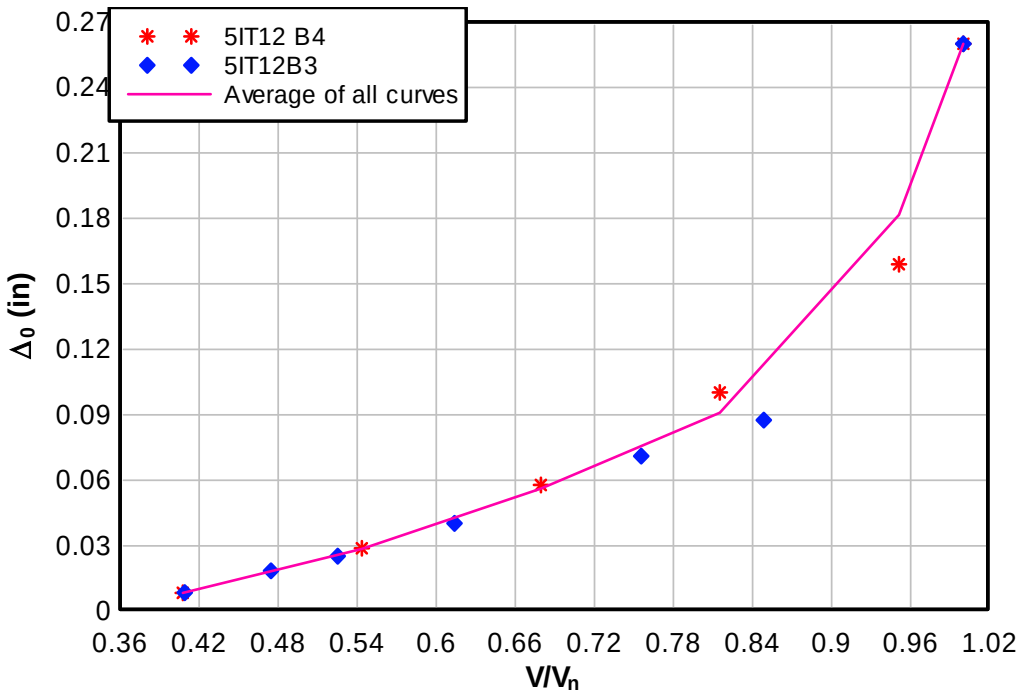

Figure 4.41: Midspan displacement Δ_0 with increasing loading ratio for specimens with 12in. stirrup spacing

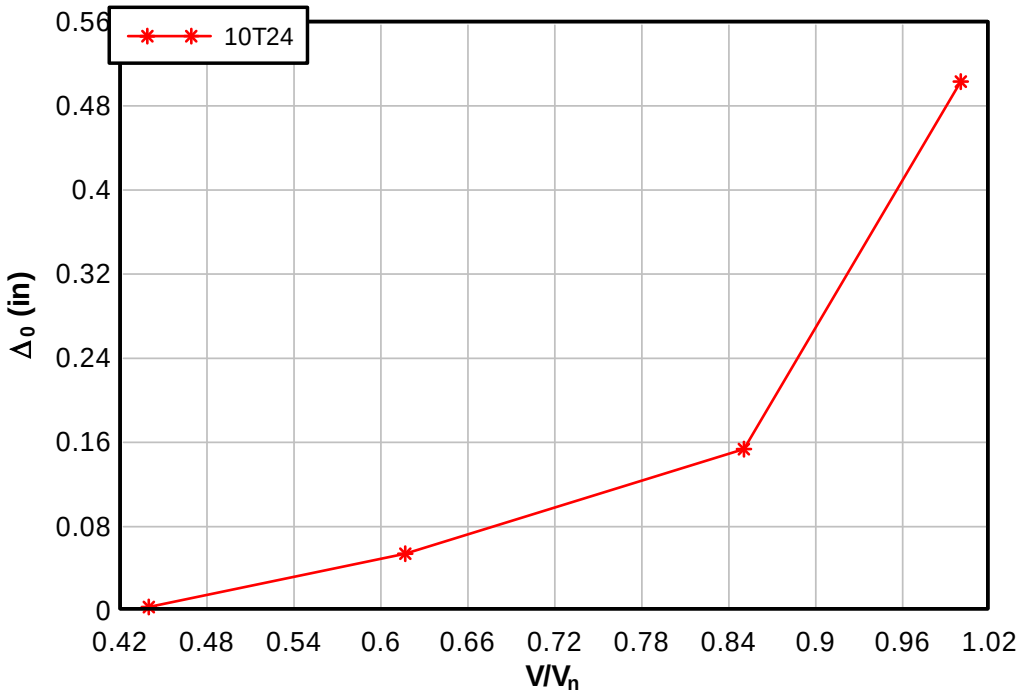

Figure 4.42: Midspan displacement Δ_0 with increasing loading ratio for specimens with 24in. stirrup spacing

More damage occurred in the initial phase as the V/V_n ratio was increased as shown in Figure 4.36. More damage also occurred as the stirrup spacing increased as shown in Figure 4.37, for similar load ratios. Using available initial phase data, coefficient *a* was derived for the specimens with 12in. stirrup spacing, as shown in Figure 4.43, and for specimens with 24in. stirrup spacing, as shown in Figure 4.44.

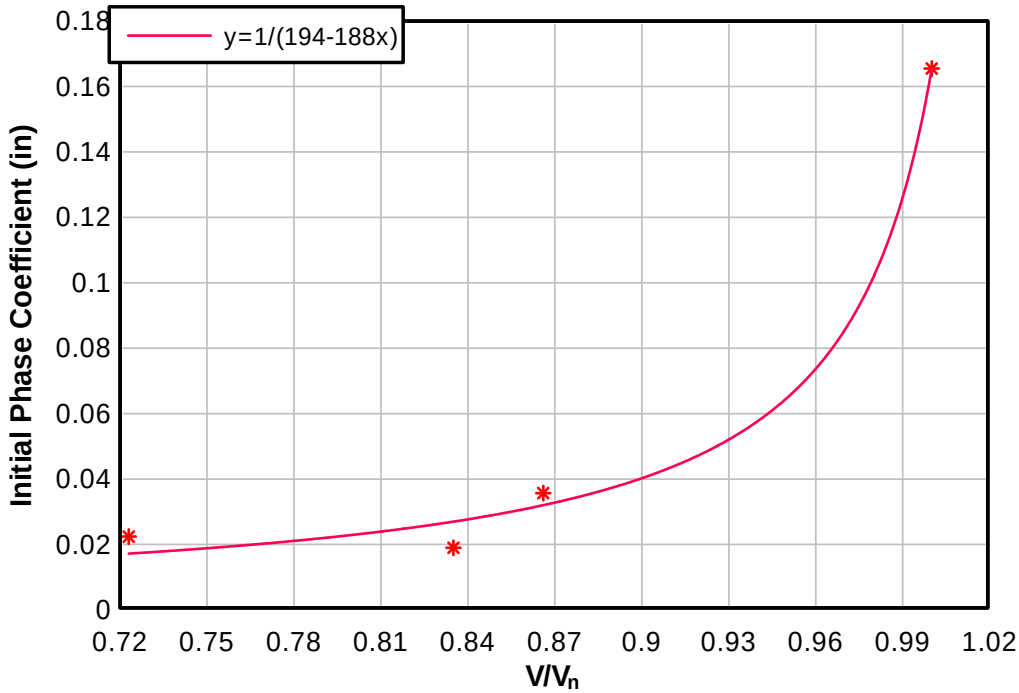

Figure 4.43: Coefficient for initial phase of low cycle fatigue for specimens with 12in. stirrup spacing for increasing V/V_n ratios

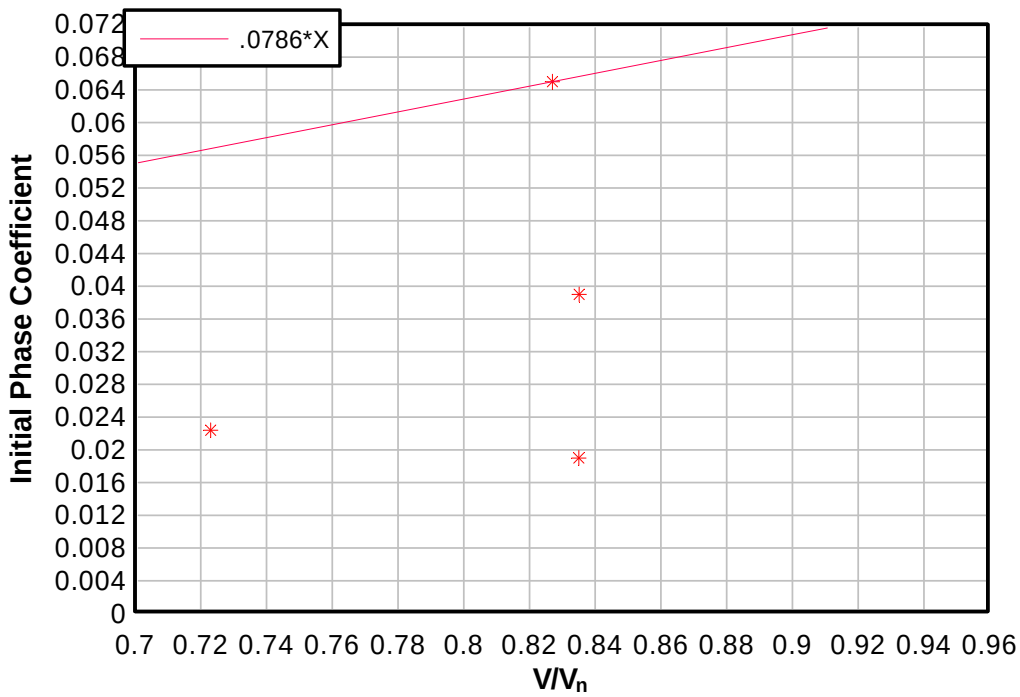

Figure 4.44: Coefficient for initial phase of low cycle fatigue for specimens with 24in. stirrup spacing for increasing V/V_n ratios

The damage became approximately linear after 200 cycles, as the specimen entered the secondary phase. Responses from available specimens were used to estimate the slope of the secondary phase. Several specimens with 12in. stirrup spacing had fewer than 100 cycles at a given load level, which originally resulted in an overestimation of the secondary slope. This was overcome by considering only those data after 200 cycles to develop the slope of the secondary phase.

The slopes of the secondary phase for specimens with 24 and 12in. stirrup spacings are shown in Figure 4.45 and Figure 4.46, respectively. Damage rates increased as the level of loading increased or after a stirrup fractured. Strain ranges also increased as the level of loading increased and after a stirrup fractured. It was decided that the tertiary phase should be neglected when estimating life, because for the specimens with lower loading ratios the secondary phase continued until the monotonic deformation limit was reached, and it is conservative to ignore the relatively small number of additional cycles available in the tertiary phase.

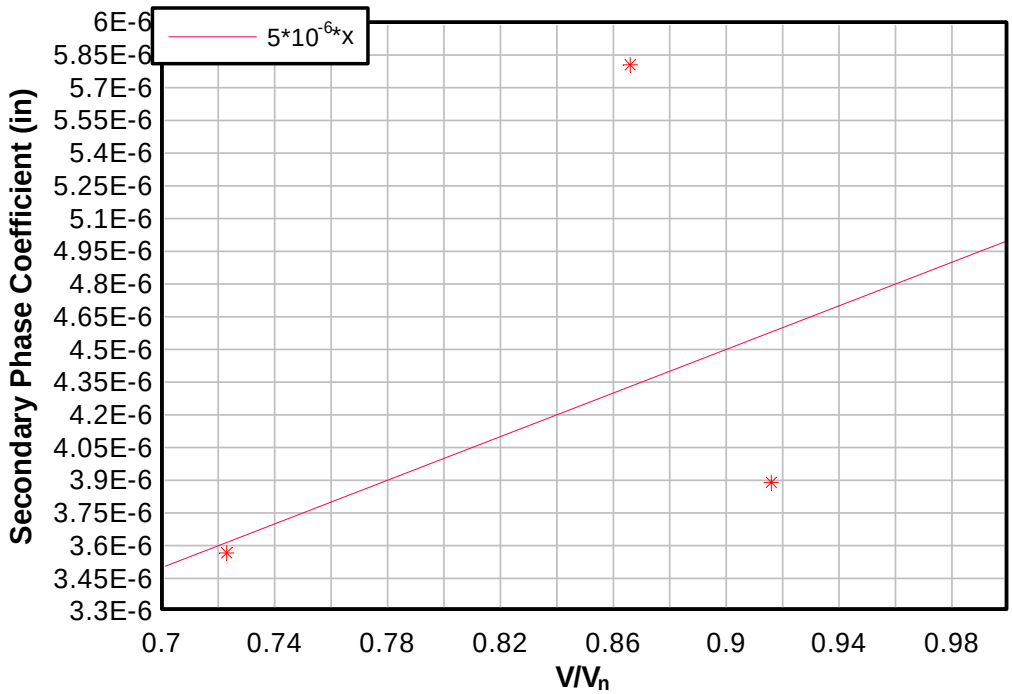

Figure 4.45: Coefficient for secondary phase of low cycle fatigue for specimens with 12in. stirrup spacing for increasing V/V_n ratios

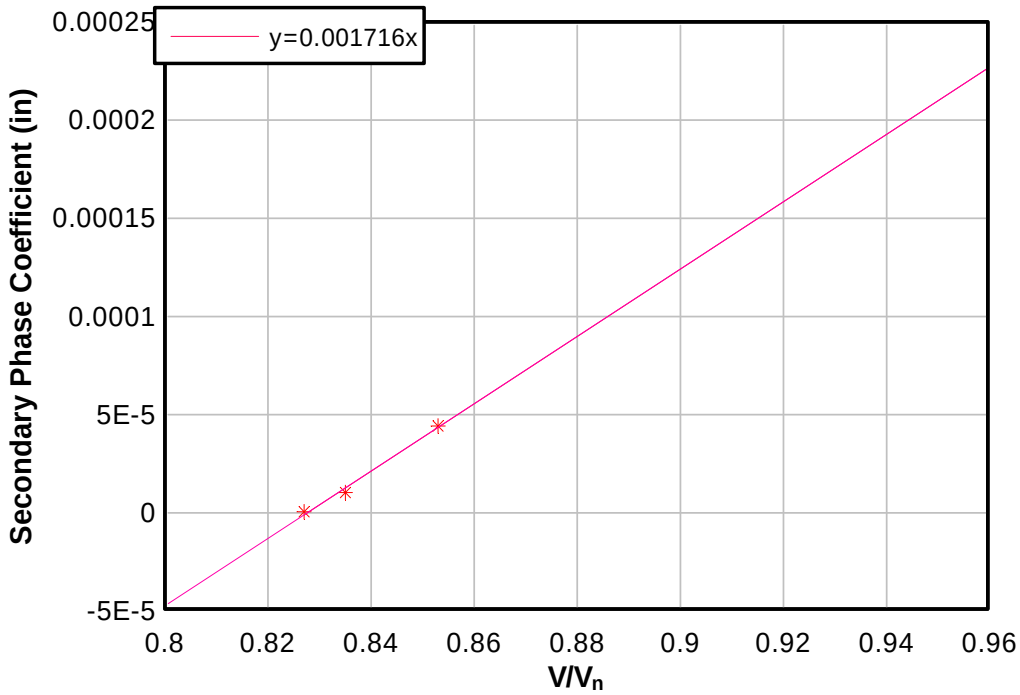

Figure 4.46: Coefficient for secondary phase of low cycle fatigue for specimens with 24in. stirrup spacing for increasing V/V_n ratios

Fatigue life based on the initial damage and curve fitting of cumulative damage in the first two phases can be seen in Figures 4.47 and 4.48 for specimens with 12in. and 24in. stirrup spacings, respectively. Results from the graphical method of analysis are plotted on the same figures. Both methods achieve similar results.

A method to compare damage rates for different load levels is needed. The load ratio, V/V_n, was selected as the simplest method to compare different load levels. However, this is valid only for specimens of the same stirrup spacing. Doubling the amount of stirrup force that can be carried across a diagonal crack does not double the nominal capacity of the section. An alternative to the V/V_n ratio for specimens of different stirrup spacing may be the applied strain range compared to the monotonic strain at ultimate, as determined from sectional analysis of members with existing diagonal cracks.

The number of cycles to failure was generally large even for the load ranges applied to the specimens. Given the relatively small number of load events that may produce yielding of the stirrups, the time to reach the anticipated life is expected to be long. However, low-cycle fatigue failure is possible if loads increase substantially in the future or long-term degradation from corrosion occurs. Corrosion of stirrups may greatly reduce the stirrup cross-sectional area, thereby permitting yielding and accumulation of damage from relatively light vehicles.

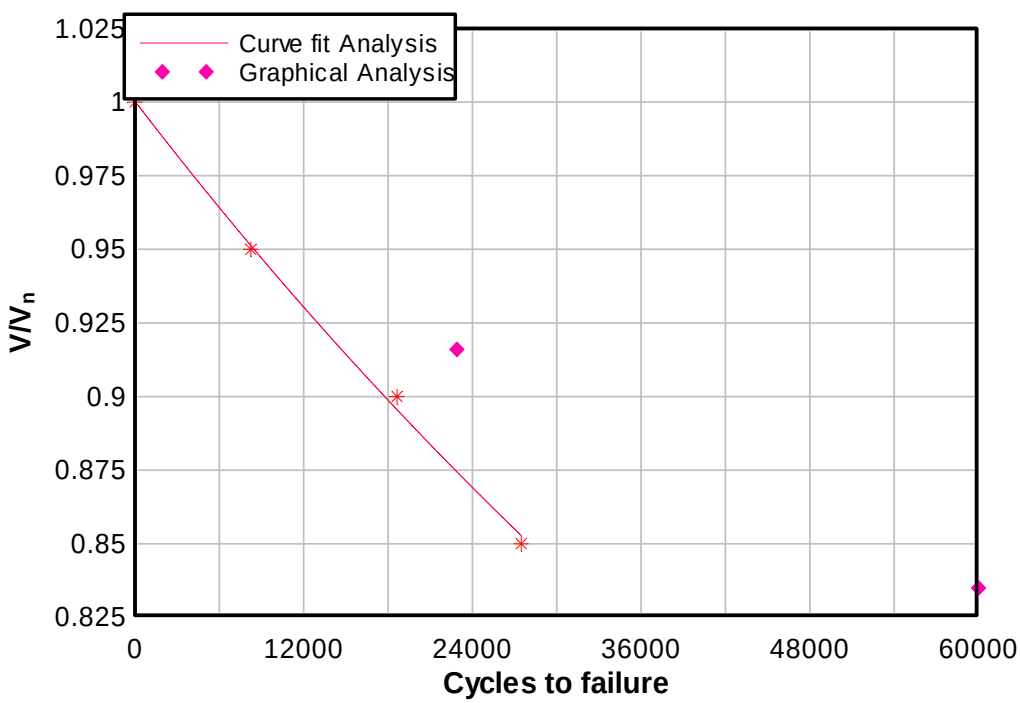

Figure 4.47: Number of cycles to failure for different V/V_n ratios for girders with 12in. stirrup spacing

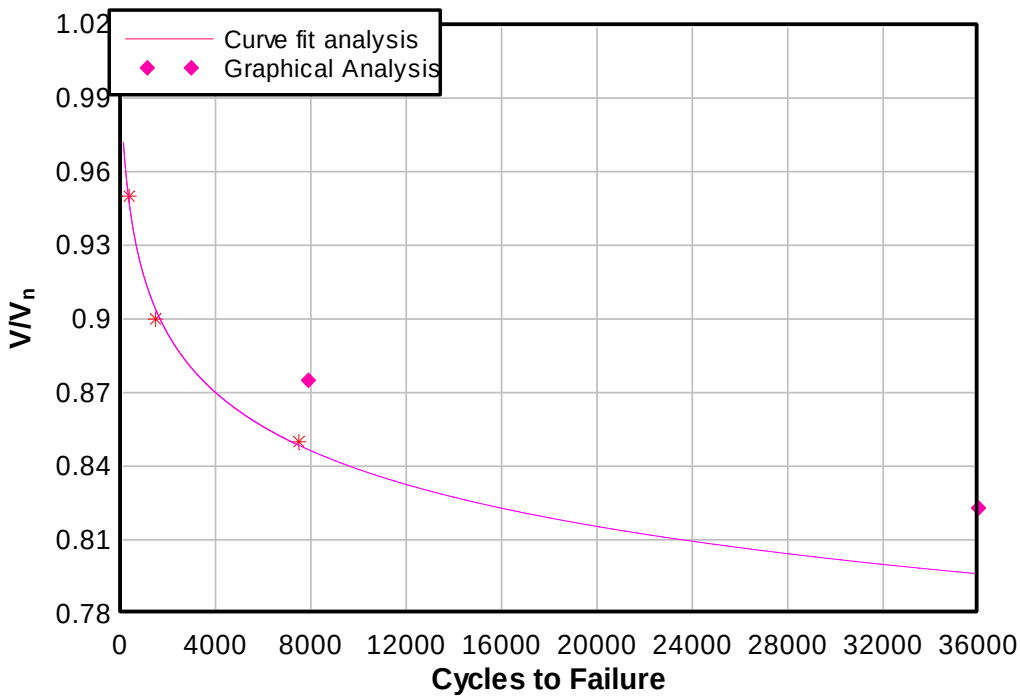

Figure 4.48: Number of cycles to failure for different V/V_n ratios for girders with 24in. stirrup spacing

4.11 CONCLUSIONS

Five different analysis methods were used to the predict shear capacity of the RC girders and bent caps with vintage reinforcing details including: ACI method, specialty analysis program *Response 2000*™, AASHTO-MCFT, Strut-and-Tie Method (STM), and the finite element method. A method to predict service level strains for previously cracked elements was developed for fatigue analysis. Life estimation for low-cycle fatigue loading was derived from empirically observed cumulative deformations. Based on these analyses and comparisons with experimental results, the following conclusions are presented:

- The ACI method tended to conservatively predict capacity of specimens. However, it provided unconservative results for the specimen without stirrups.
- AASHTO-MCFT reasonably predicted capacity of the specimens over the range of variables considered and tended to be slightly conservative compared to *Response 2000*™.
- *Response 2000*™ reasonably predicted capacity of the specimens over the range of variables considered, and further provided the best correlation with experimental results.
- Accurate modeling of flexural reinforcing details was required to predict specimen capacity using MCFT analysis methods. Equivalent flexural reinforcing steel areas were used to account for partially developed bars based on available development lengths.

- The analysis methods reasonably predicted capacity even for specimens with very wide diagonal cracks and substantial previous damage.

- The capacity of specimens with debonded stirrups, which could occur over the life of an in-service bridge girder subjected to repeated loading, was best predicted using *Response 2000*™ and reducing the concrete tensile strength to near zero.

- The STM method tended to conservatively predict specimen capacity, using simple truss models.

- For bridge elements with small a/d ratios, such as bent caps, the simple single strut models and the AASHTO-MCFT based methods predicted low capacity compared with factored load effects. Shear capacity was limited by anchorage of the flexural steel at the bent column locations. More refined methods and models may be required to better predict capacity of these elements.

- Nonlinear finite element analyses results for a limited number specimens indicated that the capacity was over estimated and the deformation was underestimated. *Response 2000*™ provided better member response prediction and was much easier to implement.

- Reloading stirrup strain behavior of previously cracked girders was reasonably predicted by MCFT by incorporating an adjustment factor for the concrete cracking stress.

- To provide a better correlation with experimental results during the initial loading phase, transverse strains in the cross-section were amplified to account for higher stresses in the stirrups at diagonal cracks, attributed to good bond between the stirrups and surrounding concrete.

- Average transverse strains provided better correlation with experimental results for reloading conditions, attributed to bond slip from repeated loading.

- For in-service bridge girders subject to millions of cycles, average transverse strains may better predict reloading strain behavior. However, use of amplified transverse strain values provides a lower yield curve, and is conservative.

- For high M/V ratios, there is a limit at which the stirrups may not yield when the section reaches capacity. This region is unlikely to be susceptible to low-cycle fatigue damage.

- The approximate sectional analysis method using MCFT with modified cracking stress, permitted estimation of a shear and corresponding moment interaction curve that estimated yielding in stirrups for service level loading.

- The shear force and corresponding moment interaction curve can be compared with load effects to determine the number of cycles that cause yielding in the stirrups for low-cycle fatigue evaluation.

- Life estimation using low-cycle fatigue was based on three distinct regions of damage accumulation. Rates of cumulative deformation under LCF were predicted based on loading ratio and varied for specimen details.

- An empirical approach was used to predict cumulative deformations based on projection of incremental damage in the first two regions. Failure under LCF was chosen to coincide with the diagonal displacement observed for specimens subjected to the control loading protocol.

- Additional refinement of the low-cycle fatigue life prediction is required to provide a generalized approach. However, under LCF with the high loading ratios investigated, specimens were able to achieve substantial numbers of cycles before failure.

ASSESSMENT METHODOLOGY FOR DIAGONALLY CRACKED REINFORCED CONCRETE DECK GIRDERS

5.0 RELIABILITY BASED ASSESSMENT METHODOLOGY 273

5.1 BACKGROUND 273
5.2 REQUIREMENTS FOR RELIABILITY ASSESSMENT 275
5.3 VEHICLE LOAD DATA 276
5.3.1 Permit Data 278
5.3.2 REALTIME Data 280
5.3.3 Raw WIM Data 281
5.4 VEHICLE DATA ANALYSIS 281
5.4.1 Truck Spectrum Characteristics 281
5.4.2 Vehicle Load Effects 291
5.4.3 Representative Rating Vehicle Load Effects 293
5.5 ASSESSMENT METHODOLOGY WITH APPLICATION 296
5.5.1 Bridge Description 298
5.5.2 Identify Potential Critical Sections 299
5.5.3 Calculate Load Effects 299
5.5.3.1 Dead Load 300
5.5.3.2 Vehicle Load 300
5.5.4 Prediction of the Load Induced Diagonal Cracking 303
5.5.5 Predict Capacity 305
5.5.6 Safety Assessment: One-Time Overloads 308
5.5.7 Calculation of Reliability Index 310
5.5.8 Comparison of Reliability Indexes 313
5.5.9 Evaluate Longitudinal Reinforcement 313
5.6 EVALUATION OF LOW-CYCLE FATIGUE 314
5.7 CONCLUSIONS 316
5.8 METHODOLOGY SUMMARY 318
5.9 LIMITATIONS 318
5.9.1 Skew bridges 318
5.9.2 Bent caps 318
5.9.3 Temperature and shrinkage 319
5.9.4 Low-Cycle Fatigue 320
5.9.5 Girder geometry 321
5.9.6 Stem-flange interface cracks 321
5.10 RECOMMENDATIONS FOR IMPLEMENTATION 321

List of Figures

Figure 5.1: Flowchart for extracting truck and bridge response statistics 277
Figure 5.2: Permits issued by Oregon Motor Carrier in 2002 (105,781 Total) 278
Figure 5.3: Single Trip Permits issued by Oregon Motor Carrier in 2002 (28,091 Total) 279
Figure 5.4: Woodburn POE GVW distribution December 18, 2002 (1,868 Trucks) 280
Figure 5.5: GVW histograms for all trucks captured by Wilbur WIM 282
Figure 5.6: Accumulated WIM collection in 2003 283
Figure 5.7: Comparison of WIM stations on Interstate 5 284
Figure 5.8: Axle weight histograms for all trucks captured by Wilbur WIM 285
Figure 5.9: Steer axle weight histograms for all trucks captured by Wilbur WIM 286
Figure 5.10: Histograms of vehicle type for all trucks captured by Wilbur WIM 287
Figure 5.11: Histograms of axle number per vehicle for all trucks captured by Wilbur WIM 288
Figure 5.12: Histograms of steer to rear axle length for all trucks captured by Wilbur WIM 289
Figure 5.13: Histogram of Permit Table classification for all trucks captured by Wilbur WIM 290
Figure 5.14: Comparison of WIM vehicle permit classifications 291
Figure 5.15: Load effect history of Rating Vehicle 8 on three (50 ft) - span continuous bridge 292
Figure 5.16: Maximum load effects for 1 year of Wilbur WIM permit vehicles (14,510) on a four (50ft) – span continuous bridge 294
Figure 5.17: Maximum load effects for 1 year of Wilbur WIM permit vehicles (14,510) on a three (120 ft) – span continuous bridge 294
Figure 5.18: Maximum load effects for 1 year of Wilbur WIM vehicles (14,510) on a two (25 ft) – span continuous bridge 295
Figure 5.19: Flowchart for safety assessment and low cycle fatigue evaluation 297
Figure 5.20: McKenzie River bridge deck cross-section 298
Figure 5.21: Profile view of McKenzie River bridge with cross-section locations (feet) 298
Figure 5.22: Existing cracks on the McKenzie River bridge exterior girder in span 1 near support B. The first diaphragm framing is 12.5 ft from support B centerline 299
Figure 5.23: Modal shear produced at 42 ft in span 1 of three (50 ft) - span continuous bridge 302
Figure 5.24: Service level performance histogram for diagonal cracking for the McKenzie River bridge at 42 ft. in span 1 (AASHTO-LRFD). 303
Figure 5.25: Service level performance histogram for diagonal cracking for the McKenzie River bridge at 42 ft. in span 1 (Field data). 304
Figure 5.26: Histogram of experimental to AASHTO-MCFT predicted shear capacity from results of 31 full-scale RCDG specimens 305
Figure 5.27: Cross-section for McKenzie River Bridge at 42 ft in span 1 (*Response2000*™) 307
Figure 5.28: Disconnect of AASHTO-MCFT compared to R2K at points of inflection 307
Figure 5.29: Illustration of how the reliability index is calculated. 309
Figure 5.30: Safety assessment for exterior girder of McKenzie River bridge (08175N) using ODOT Rating Vehicles 311
Figure 5.31: Safety assessment for the exterior girder for the cross-section at 42 ft. in span 1. Live load distribution and impact factors from AASHTO-LRFD are applied. 312
Figure 5.32: Safety assessment for the exterior girder for the cross-section at 42 ft. in span 1. Live load distribution and impact factors from field data are applied. 312
Figure 5.33: Low cycle fatigue evaluation for exterior girder of McKenzie R. bridge at 42 ft. in span 1 (AASHTO-LRFD). One year (14,510) Wilbur WIM permit vehicles 315
Figure 5.34: Low cycle fatigue evaluation for exterior girder of McKenzie R. bridge at 42 ft. in span 1 (field data). One year (14,510) Wilbur WIM permit vehicles. 315
Figure 5.35: Annual cycles with load effects greater than the amplified yield points. Results from low cycle fatigue evaluation at 42 ft. in span 1 for exterior girder of the McKenzie R. Bridge (AASHTO-LRFD). 316
Figure 5.36: Digital photograph of bridge near Mitchell Oregon, with 14-year record of diagonal crack width measurements 320

List of Tables

Table 5.1: Correlation between load effects from rating vehicles and WIM permit vehicle classifications 295
Table 5.2: Distribution and impact factors for McKenzie River Bridge exterior girder 301
Table 5.3: Shear prediction statistics of analysis methods to laboratory results 306

5.0 RELIABILITY BASED ASSESSMENT METHODOLOGY

Assessment of an existing bridge is needed when the structure exhibits signs of distress, the structure usage changes, or as part of a routine bridge management program. Assessment practices require refinement in the calculation of loading and resistance, while maintaining an acceptable level of safety, to minimize costs associated with repair, replacements, and weight restrictions. The following section details an investigation of the vehicle loading found in Oregon, using available collected data for truck traffic within the State.

Load effects produced by these vehicles were calculated for a suite of bridges with different indeterminacies and span lengths. The service level loading was evaluated to explain diagonal cracking exhibited by many of Oregon's 1950's vintage RCDG bridges. A methodology was developed for safety assessment of an RCDG bridge girder relative to the load demand. An example is illustrated using the methodology and incorporates laboratory testing and field data. The methodology provides a rational basis for determining weight restrictions and prioritizations for replacement or repair.

5.1 BACKGROUND

The bridges considered in this study were built in the period between 1947 and 1962, prior to the introduction of load and resistance factor design. In the 1970's and 1980's, the application of probability theory to quantify the risk (relative safety) associated with design practices in structural engineering was introduced. This new approach recognized that absolute reliability is unattainable in the presence of uncertainty and variability in the loading and resistance. Reliability-based design insures that the probability of unfavorable performance is economically acceptably small (*Ellingwood, et al. 1980*). Earlier safety factors used as part of a working-stress design philosophy were phased out, as they could not provide a consistent safety margin throughout a design or system.

Capacity (R) and load (S) are characterized as random variables by probability distributions. Variables comprising the capacity include material properties, section geometry, and specified strengths, to name a few. Statistics for the random variables in the capacity of conventionally reinforced concrete, for both shear and moment, and considering various members and components, were developed by Ellingwood, et al. (*1980*). Statistical parameters for a bridge live load model were developed by Nowak and Hong (*1991*) from truck surveys and by simulation. Assuming both the capacity and loading distributions are Normal, then the reliability problem reduces to the simple R-S form:

$$p_f = P[R < S] = P[R - S < 0] = P[M < 0] \qquad \textbf{(5-1)}$$

$$p_f = \Phi\left(\frac{\mu_S - \mu_R}{\sqrt{\sigma_S^{\ 2} + \sigma_R^{\ 2}}}\right) = \Phi\left(\frac{0 - \mu_M}{\sigma_M}\right) \qquad \textbf{(5-2)}$$

where, M=R-S is the safety margin (or limit state function), μ and σ are the mean and standard deviation (first and second statistical moment) of the respective random variables, and $\Phi(\cdot)$ = the standard normal cumulative distribution function.

The term p_f represents the probability that a limit state will be met or exceeded during the design life. The reliability index, β, is simply the number of standard deviations from the mean of the safety margin to the failure criteria (M=0) and is related to the probability of failure, p_f, through the following equation:

$$p_f = \Phi(-\beta) \qquad \textbf{(5-3)}$$

A value of β = 3.5 corresponds to a probability of exceedence of 2 in 10,000, while β =2.5 corresponds to 62 in 10,000. However, since probability laws cannot be determined exactly, p_f is referred to as a "notional" probability, indicating that it should be interpreted in a comparative sense rather than in a relative frequency sense (*Ellingwood, et al. 1980*). Even so, β is a useful comparative measure of reliability and can be used to evaluate relative safety of various designs as long as the first and second statistical moments are handled consistently (*Ellingwood, et al. 1980*).

Provisions in the current AASHTO-LRFD Bridge Design Specification (*2003*) are calibrated for a target reliability index of 3.5. This index was derived for a severe traffic-loading case (including the presence of 5,000 Annual Daily Truck Traffic) in the LRFD design criteria. Following this approach, it is natural that the current state-of-the-art method for load rating bridges also uses load and resistance factors. The AASHTO Manual for Condition Evaluation and Load and Resistance Factor Rating (LRFR) of Highway Bridges (*2003*) adopts a reduced target reliability index of 2.5. This index was calibrated to past AASHTO operating level load ratings and reflects the reduced exposure period, consideration of site realities, and the economic considerations of rating vs. design.

Examples of risk-based approaches to bridge safety assessment are shown in work by Stewart, *et al.* (*2002*) and Akgul and Frangopol (*2003*). The example bridges used by Stewart, *et al.* (*2002*) were simply supported and the limit state examined was for the situation when flexure at mid-span exceeded the structural resistance. The AASHTO live load model was used. Akgul and Frangopol (*2003*) showed how initial operational bridge rating factors compared to initial system reliability indices. For the comparison, the capacity was calculated using the AASHTO Standard Specification 16th Edition (*1996*), and the loading distribution also used the AASHTO live load model.

A reliability-based safety assessment follows, but with two distinctions from previous work. In earlier work – as in the AASHTO Standard Specification 16th Edition for capacity – moment and shear were each treated separately so each could be resolved into a simple *R*-*S* problem.

However, the method to calculate capacity has changed to Modified Compression Field Theory (MCFT) both in AASHTO-LRFD (*2003*) and AASHTO-LRFR (*2003*). This research creates an *R-S* problem while accounting for the simultaneous moment-shear interaction in strength (capacity) prediction. In addition, an Oregon-specific load spectrum will be developed and applied.

The State of Oregon has collected weigh-in-motion data and permit data for vehicles on the state highway system. Over 14,000 vehicles that exceeded legal limits were captured by one WIM station in one year alone. The current specification is based on surveys performed in the Detroit area by Agarwal and Wolkowicz (*1976*) and covered about 10,000 heavy vehicles (only trucks that appeared to be heavily loaded were measured and included in the database). In addition, the load effects were calculated for simple spans ranging from 30-200 ft in length (*Nowak and Hong 1991*). In this study they are calculated for multiple bridge indeterminacies and span lengths representative of bridges contained in a database of Oregon bridges (*Higgins, et al. 2004*).

Therefore, in the following reliability assessment of 1950's vintage conventionally reinforced concrete deck girder bridges, MCFT is used to predict capacity, and the load demand used in the analysis will be Oregon-specific. Note that instead of treating load as a random quantity using a statistical distribution (which is the goal for future work) it is treated as a discrete value in this reliability analysis using MCFT. The key to the study is that random quantities will be characterized consistently using statistical measures of central tendency (mean) and dispersion (standard deviation) between all examined bridge sections and β will be treated in a truly relative sense.

The information collected for the load and resistance has potential use for risk ranking as a bridge management tool. Risk ranking allows the comparison of bridges by evaluating bridges with a conditional probability (developed by Stewart and Val (*1999*)) that reflects relative frequency of overloads, years in service, inspection information, and consequence of failure (where the consequence of failure is similar for all bridges considered so risk-ranking is appropriate) (Stewart, et al., 2002). Thus, risk ranking is an area for possible application of the load spectrum developed herein.

5.2 REQUIREMENTS FOR RELIABILITY ASSESSMENT

Development and implementation of a reliability based assessment methodology required several elements:

- characterization of an Oregon-specific load spectrum;
- transformation of load spectrum into load effects (shear and moment);
- determination of load effects produced by the rating vehicles used by the ODOT Bridge Section to assess their ability to reasonably represent load effects produced by collected vehicle data for a suite of bridge spans and indeterminacies;

- evaluation of the likelihood that operating loads exceed the cracking shear in high moment regions;

- development of a safety assessment method to evaluate one-time overloads at various sections along a bridge girder; and

- evaluation of low-cycle fatigue on cracked RCDG bridge girders.

The flow chart in Figure 5.1 illustrates the process used to create the load spectrum, service level performance histogram, and the approach required to compare load effects with the resistance/strength of the bridges. The bold boxes indicate the requirements for assessment. The chart is organized to illustrate calculations of load effects on the left and resistance on the right. The method integrates load data, bridge data, field data and laboratory data. Dotted lines encircle items that are input and output. An item with a dashed line indicates an area for possible future development. Items with a shadow box indicate that additional data may continually be added as they are collected for further refinement.

5.3 VEHICLE LOAD DATA

There are two sources of truck data regularly collected by ODOT: permit data and weigh-in-motion data. Permit data are the collection of permits issued for vehicles that exceed legal limits, whether due to height, length, or weight. These permits are individual forms filled out for each truck. The data are kept for 39 months.

Weigh-in-motion (WIM) is the process of collecting vehicle information such as length, speed, axle weights, and gross vehicle weight (GVW) while the vehicle is moving. There is a +/- 2-3% error rate as a result of the fluctuation of weight distribution due to the truck being in motion (*Fifer 2002*). This is most evident for trucks hauling liquids, livestock, and for log trucks without middle supports. In Oregon, the current WIM system is set up near weigh stations, but could be located anywhere additional information on trucks may be desired. WIM data are further divided into two types, REALTIME and raw.

REALTIME data combine both the raw data and static data recorded at the weigh station. REALTIME is the result of the Green Light Program that allows trucks with transponders and within their registered limit to bypass weigh stations instead of having to stop. When a truck goes into a weigh station and is weighed, the static readings over-write the WIM data for that vehicle. The data lines for all trucks receiving either a green light or a static reading are then kept in a Microsoft Excel friendly format as a record of enforcement. REALTIME data are only collected during operating hours of the weigh station.

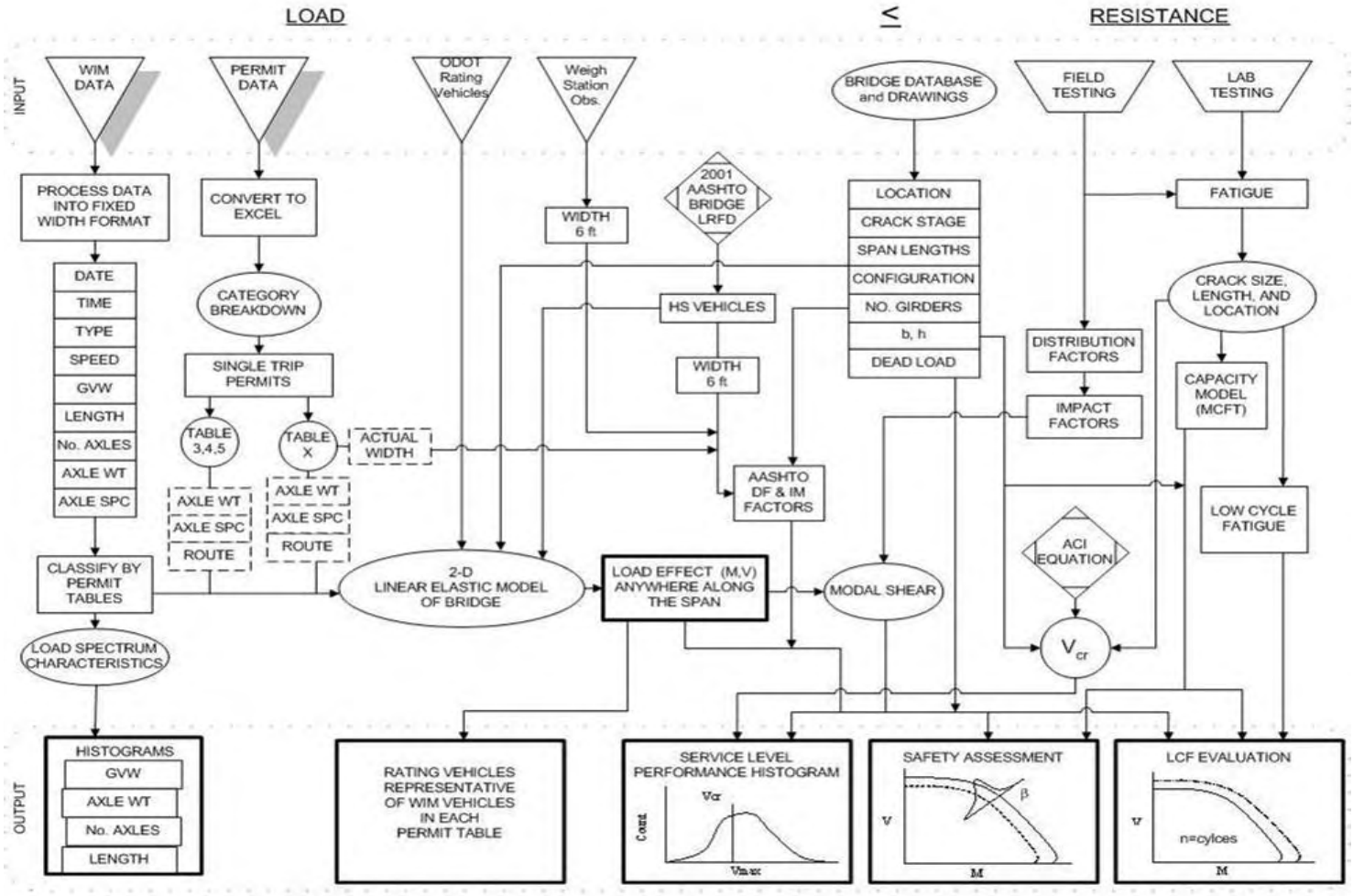

Figure 5.1: Flowchart for extracting truck and bridge response statistics

Raw data, on the other hand, are purely WIM measurements. The record is collected for the entire day, every day and contains all vehicles (including cars, RVs, motorcycles, etc.), but it can be filtered to show only vehicles classified, for example, as Type 5 or above. In other words, the record can be narrowed to contain only truck data, as it has for this study. It is stored in a text file and saved for 100 days.

5.3.1 Permit Data

Figure 5.2 shows the category breakdown of all the permits issued in 2002. Permits are either Continuous Trip (CTP) or Single Trip (STP). The first three segments are Continuous Trip permits. These permits are issued on a yearly basis. The truck driver receives a map showing roads not to be used and is expected to comply. Table 1 permits allow vehicles that have legal weights, but exceed the height or length limits or fall into Exception 1 or 2. Table 2 permits are trucks that have legal axles, but are longer, so the GVW is allowed to exceed the 80,000 lb legal limit but must be less than 105,500 lbs. The first part of Permit Table 3 – up to 98,000 lbs – is continuous-trip heavy-hauls. These vehicles are allowed more weight on a shorter wheelbase. Permit Table 3 trucks are allowed 43,000 lb tandem axles whereas Permit Tables 1 and 2 only allow 34,000 lb tandems.

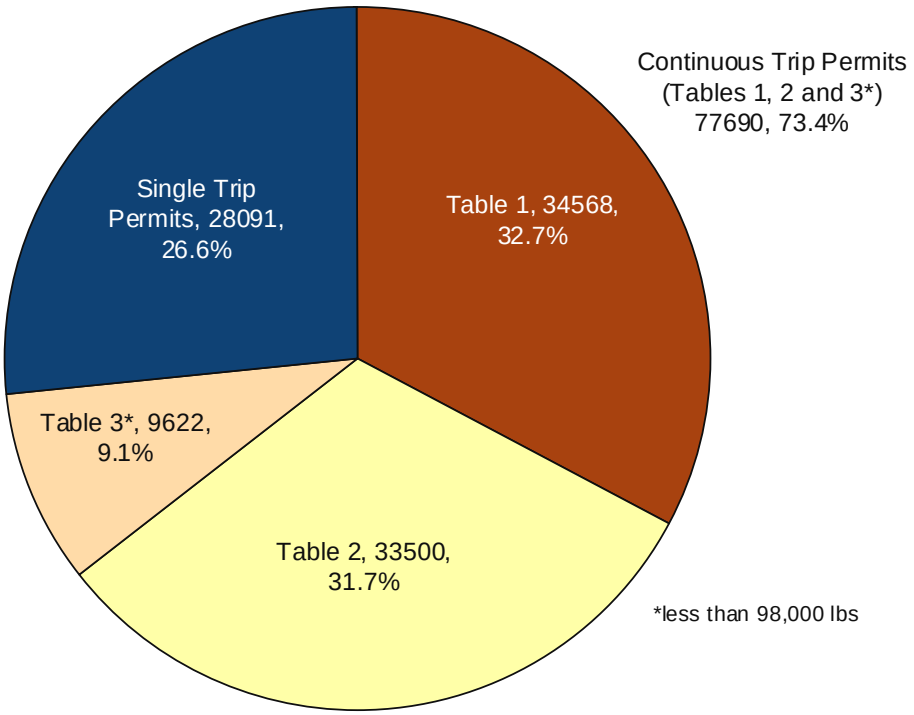

Figure 5.2: Permits issued by Oregon Motor Carrier in 2002 (105,781 Total)

Single Trip permits, on the other hand, are issued on a per trip basis. The truck has between 3 and 7 days to make the trip before the permit expires, and the route to be used is stated explicitly

on the permit. The Single Trip permit category can be broken down again, as shown in Figure 5.3. Since these vehicles can make only one trip with the permit, one-way or round-trip, these numbers are better indicators of how many trucks of this type are on the road. These permits tend to be related to the construction, logging and power industries to name a few.

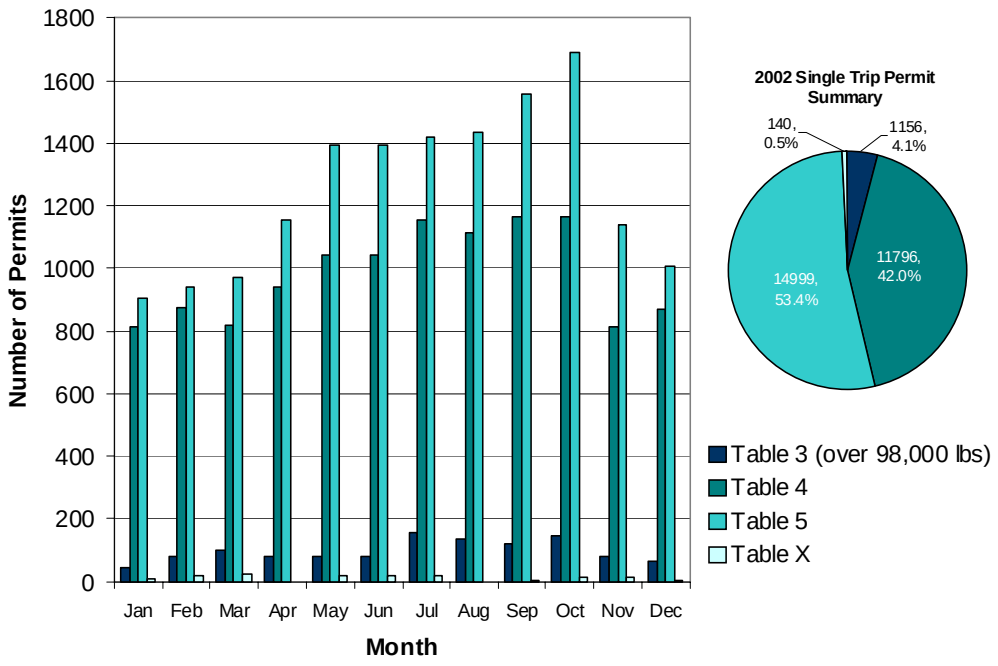

Figure 5.3: Single Trip Permits issued by Oregon Motor Carrier in 2002 (28,091 Total)

From the monthly breakdown it is evident that more of these permits are issued during Oregon's drier months, which coincides with the construction season and thus the increased need to transport large construction equipment. Over half of the single trip permits are for Permit Table 5 which allows vehicles to have the most weight on the shortest wheel base. It also allows triple axles of 65,000 lbs.

Permits are also issued for trucks that fall outside of Permit Table 5. These trucks will be referred to as Permit Table X. For a truck like this, the axle weights and spacings must be known at the time of application, and the configuration approved by the ODOT Bridge Section. The route is explicitly stated. Many times specific directions are also given for speed and time of travel as well as for flaggers and escort vehicles.

The permit data as currently collected do not provide enough information (excluding Table X) to accurately depict a vehicle for use in the load model. The information about axle grouping is given by the permit table, the load length, and the number of axles. It will be shown subsequently

that there is no clear boundary between the load effects produced by vehicles that are classified in the various permit tables.

A program was written to convert the limited information provided in the permit data into individual axle weights and spacings. A group of WIM vehicles that appeared fully loaded was selected to evaluate the program. The load effects produced by the program had poor correlation to the load effects produced by the actual WIM data. Therefore, the permit data could not be used to reliably estimate load effects for these trucks. The permit data, however, are important because trucks with STPs take shorter trips, and therefore are not as likely to be captured at WIM stations. Since WIM stations are not located in close proximity to most bridges in the system, there is reason to believe that permit vehicles could cross bridges and not be included in the WIM data. The importance of these infrequent large loads will become apparent when considering low-cycle fatigue.

5.3.2 REALTIME Data

REALTIME data are easier to use since they are already in an Excel friendly format. The Woodburn weigh stations on Interstate 5 will be used in an example, since these stations have the most activity of any in the State. The distribution of GVW for trucks at the Woodburn Port-of Entry (POE) (southbound) is shown in Figure 5.4 graphed on normal probability paper.

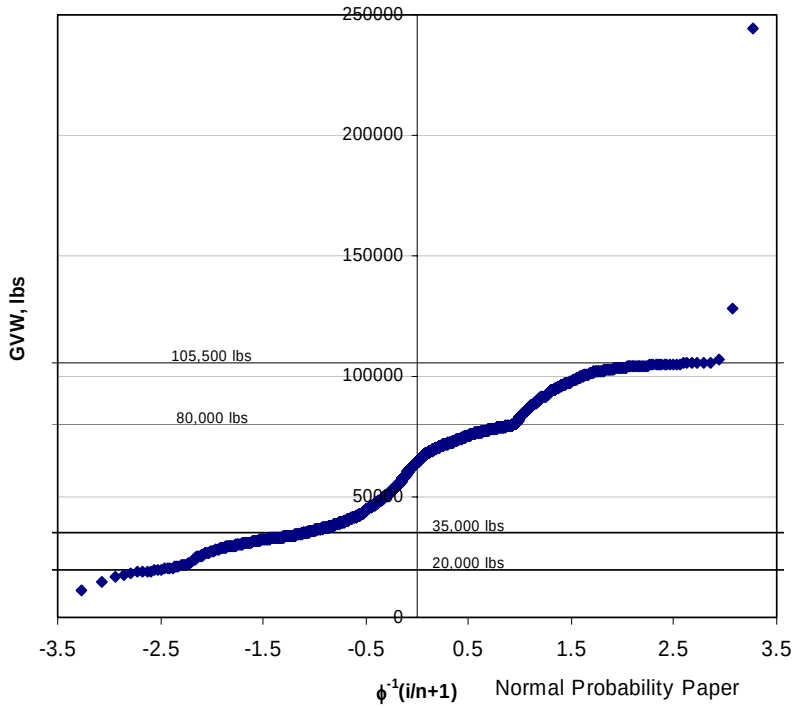

Figure 5.4: Woodburn POE GVW distribution December 18, 2002 (1,868 Trucks)

If the GVWs were distributed normally, then the points would line up in a straight diagonal line. Since the points do not line up, it is quite clear that either the distribution is not normal and/or the

GVW distribution is multimodal. When the plot becomes more horizontal it indicates that a large number of trucks is near that GVW. This occurs at 20,000 lbs, 35,000 lbs, 80,000 lbs, and again near 105,500 lbs. These last two are the GVW limits of Permit Table 1 and Table 2, indicating, as expected, that many trucks operate near the table limits.

Bridge response is a function of load effect, and the load effect from each truck will be dependent on many factors. These factors are GVW, length, width, number of axles, individual axle weight, and axle spacings of the truck, as well as the geometry of each particular bridge (*Moses and Ghosn 1985*). Since REALTIME data contain GVW, number of axles and axle group weights, but they do not include length, and they are collected only during the hours of operation of the weigh station, they do not provide all the required information needed for creating the load spectrum.

5.3.3 Raw WIM Data

The text format of raw WIM data requires considerable post-processing to be useful in this study. The data must undergo a format transformation, but this can be done only after all spurious data have been removed (currently a labor intensive process). From this data all the information needed about each truck, except for the width, can be extracted either directly or indirectly. The items extracted directly are the truck type, GVW, speed, time, front to rear axle length, and the individual axle weights. Indirectly, from the pictogram included in the data, the number of axles can be counted, and the relative spacing of each axle can be proportioned to the front-to-rear axle length to obtain estimates of individual axle spacings.

The format transformation was performed using a FORTRAN program written specifically for this purpose. The resulting file lists the time, type, speed, GVW, length, number of axles, axle weights, and axle spacings for each truck, and can be used in Microsoft Excel for data regression and analysis. The data were then classified into the various permit tables with the aide of another FORTRAN program written for this purpose. The classification program does not take into account any of the exceptions allowed for each permit table. For example, a vehicle that is normally classified as Permit Table 1 using Exception 1 will be classified as Permit Table 3 by the program. (Exception 1 allows two consecutive tandems up to 34,000 lbs each if the axle spacing is at least 30 ft Permit Table 1 without the exceptions would require 39 ft) The WIM data are classified by the program for use in the Representative Rating Vehicle section.

5.4 VEHICLE DATA ANALYSIS

5.4.1 Truck Spectrum Characteristics

Currently, one year of data (January 2003 – January 2004) from the Wilbur WIM collector 7 miles north of Roseburg on I-5 have been analyzed. Figures 5.5 to 5.10 show the characteristics of the truck traffic.

The GVW for all WIM trucks captured at Wilbur during the first collection period of 97 days (238,463 trucks) is shown in Figure 5.5 in both arithmetic and logarithmic scale. GVW is plotted in 1 ton increments. The number of trucks is plotted logarithmically to make it easier to see the

large but infrequent GVW values. The GVW peaks are near 10,000 lbs, 32,000 lbs, 70,000 lbs, and 98,000 lbs. These last three peaks correspond to the category limits represented by the horizontal portions of the normal linearized cumulative distribution function (CDF) of GVW using REALTIME data (Figure 5.4).

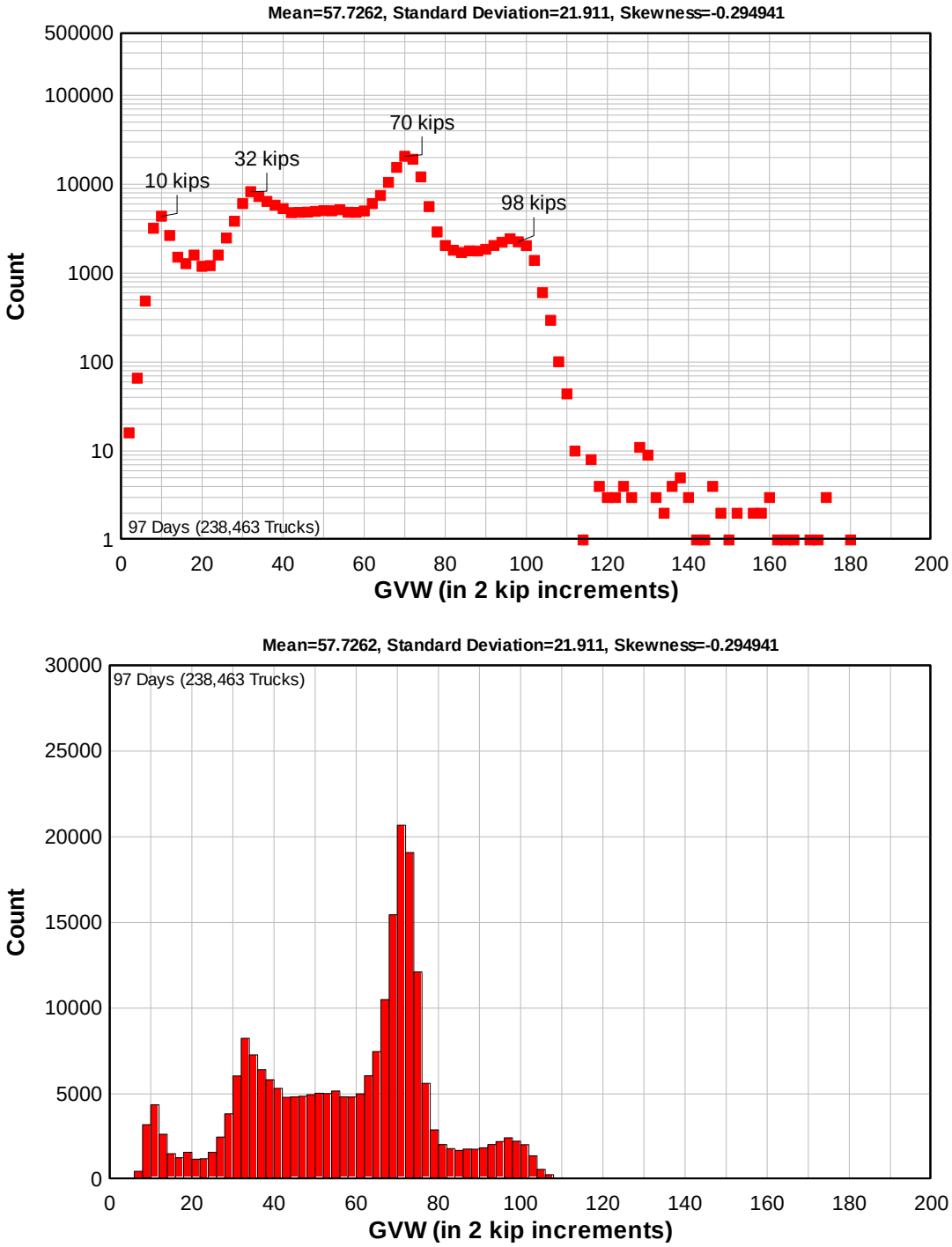

Figure 5.5: GVW histograms for all trucks captured by Wilbur WIM

The accumulation of WIM data for extended periods of time refines the tail distribution for large GVWs as illustrated by Figure 5.6. The vehicle counts are normalized to the number of vehicles in each respective collection period. It is evident that in a short time period the general shape and modes are defined. It also shows that as more data are added to the load spectrum, the upper tail becomes more clearly defined.

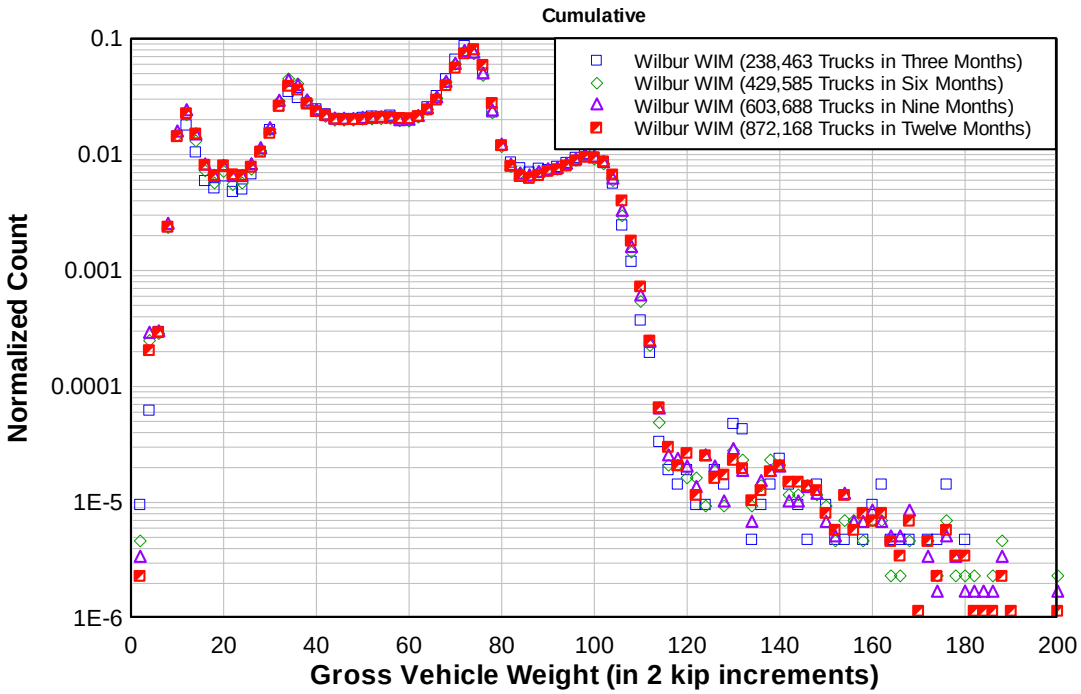

Figure 5.6: Accumulated WIM collection in 2003

A comparison of GVW is made between three WIM collection sites on Interstate 5 in Figure 5.7. Woodburn POE is southbound, while Wilbur and Booth Ranch are southbound and northbound, respectively, at the same location. The normalized GVW histograms indicate that the vehicle pattern is consistent for the three stations. Note that the largest amount of data is shown for Wilbur, while Woodburn POE only contains one month and Booth Ranch has just two weeks. The normalized data indicate the proportion of GVWs captured at each site. The histogram for Woodburn POE in Figure 5.7 indicates that a larger proportion of vehicles with large GVWs is observed at the Woodburn POE site compared to Wilbur or Booth Ranch.

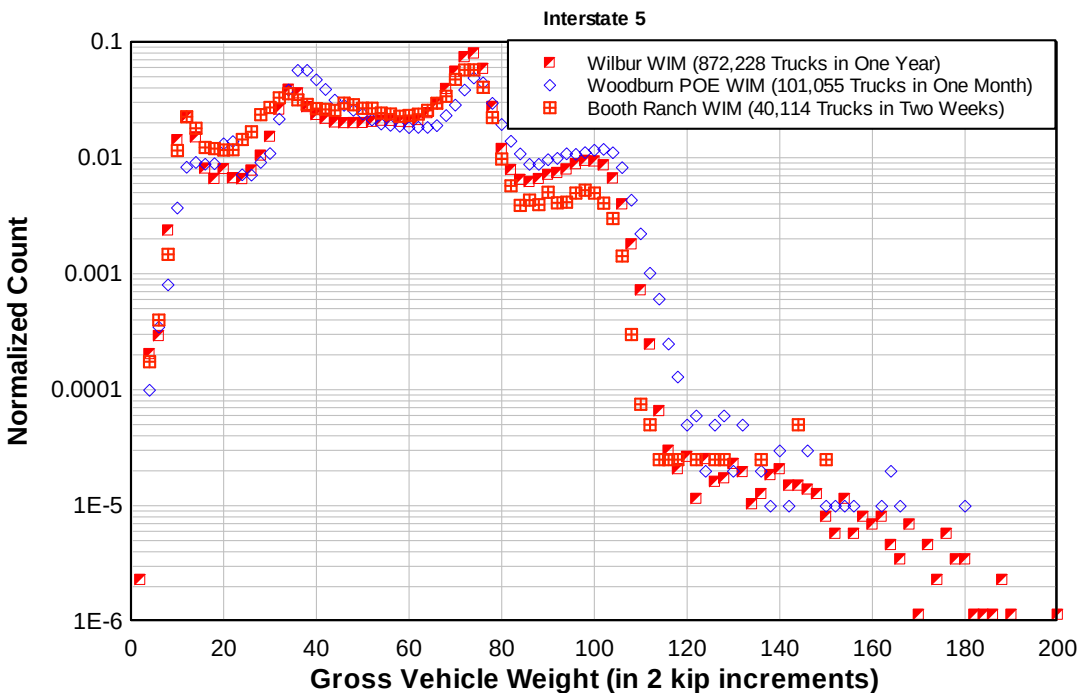

Figure 5.7: Comparison of WIM stations on Interstate 5

For the first collection time period at Wilbur (97 days), the histogram for axle weights in 1 ton increments for 1,268,978 axles is shown in Figure 5.8 in both arithmetic and logarithmic scale. The two peaks are at 10,000 and 14,000 lbs. A legal tandem axle is 34,000 lbs, and this may explain why the second individual axle weight peak is about half that value. When only the weight of the steer (front) axle is plotted, it shows that the most common weight is 10,000 lbs as shown in Figure 5.9, and presumably drives the first peak in Figure 5.8.

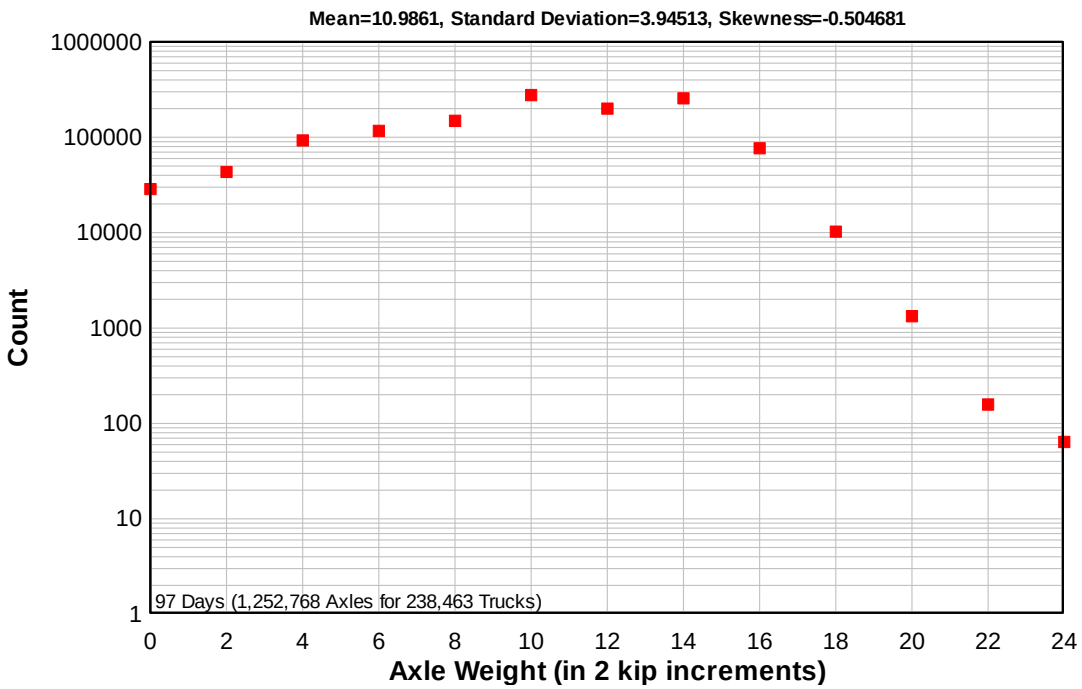

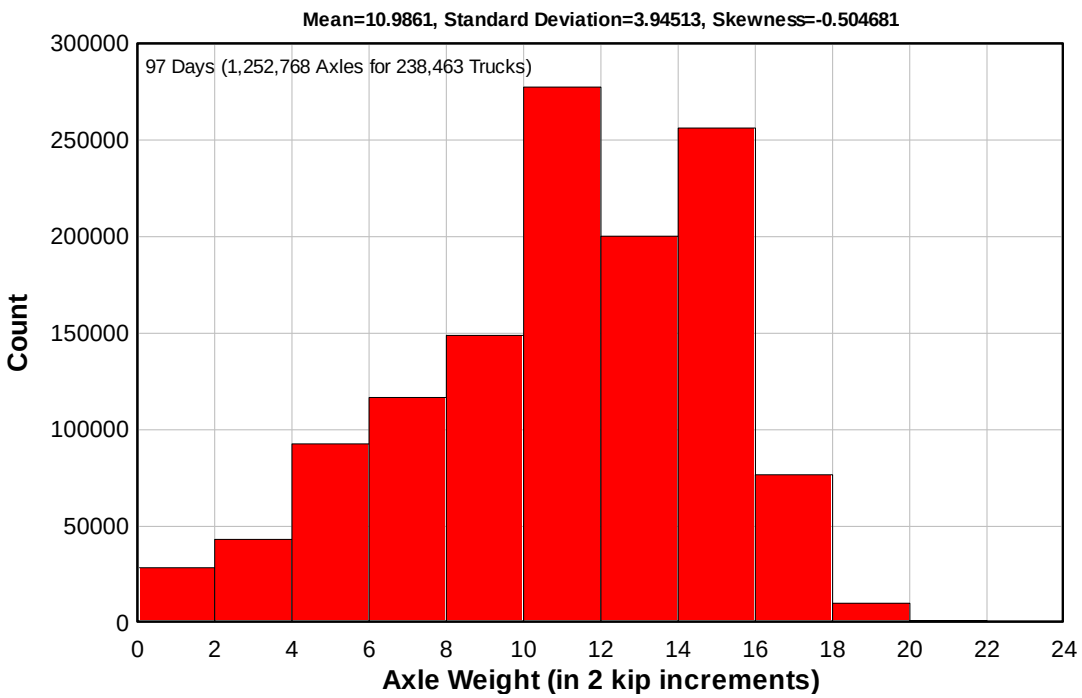

Figure 5.8: Axle weight histograms for all trucks captured by Wilbur WIM

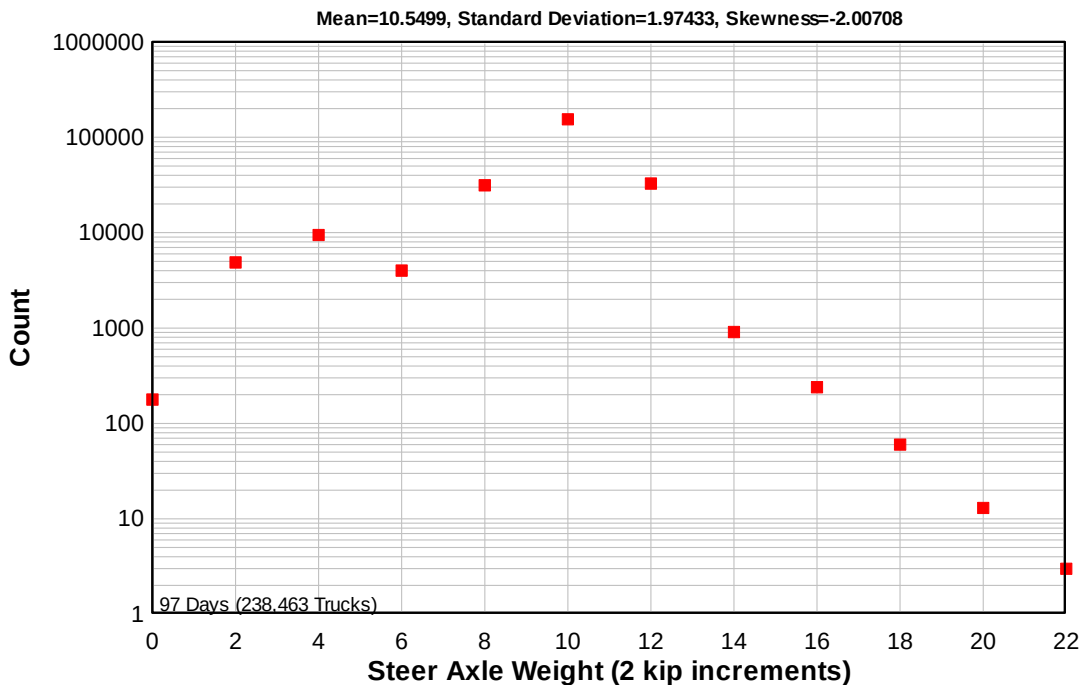

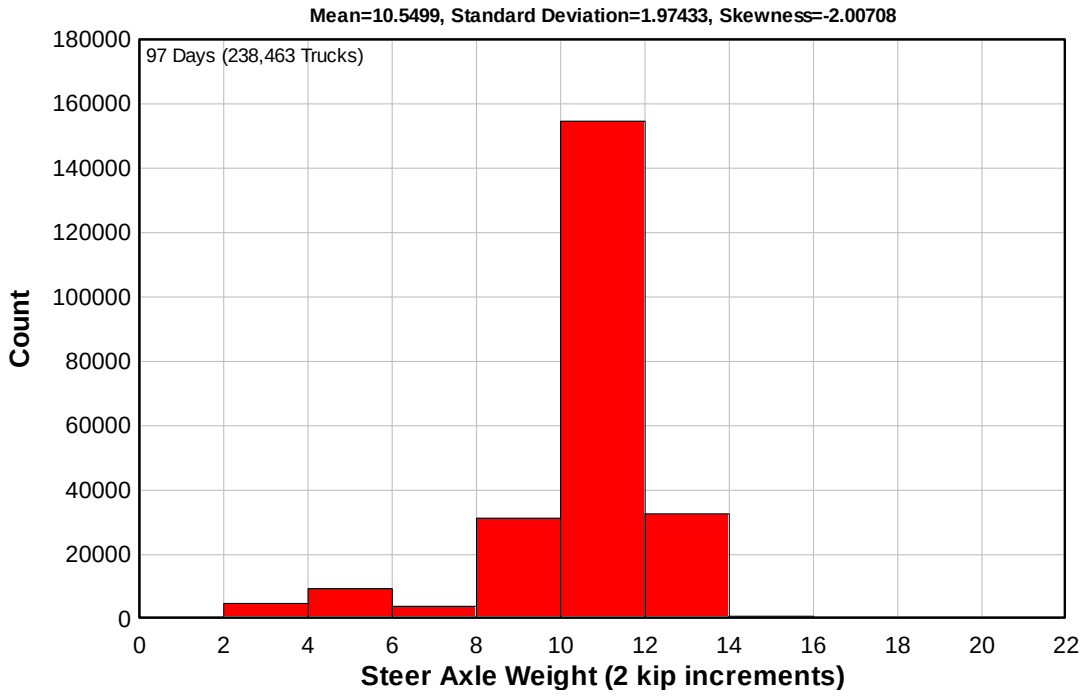

Figure 5.9: Steer axle weight histograms for all trucks captured by Wilbur WIM

Vehicle type and number of axles are also collected in WIM data. Type 11 is a 5-axle semi-truck. The histograms for vehicle type and number of axles clearly show that the dominant vehicle is a

5-axle semi-truck as illustrated in Figures 5.10 and 5.11. It is also observed that in the 97-day collection period at Wilbur, as well as for the entire year, there were no vehicles with more than eleven axles.

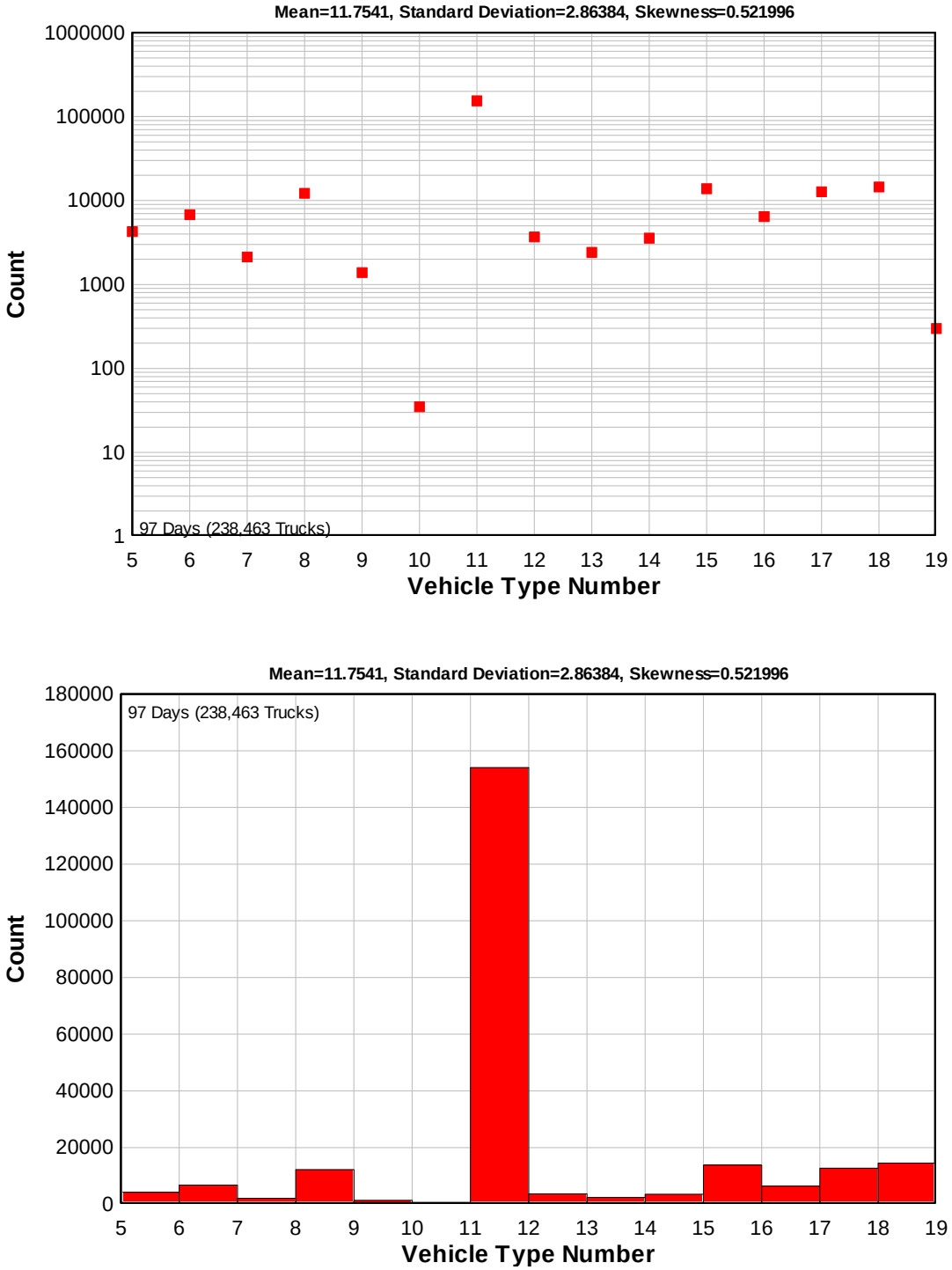

Figure 5.10: Histograms of vehicle type for all trucks captured by Wilbur WIM

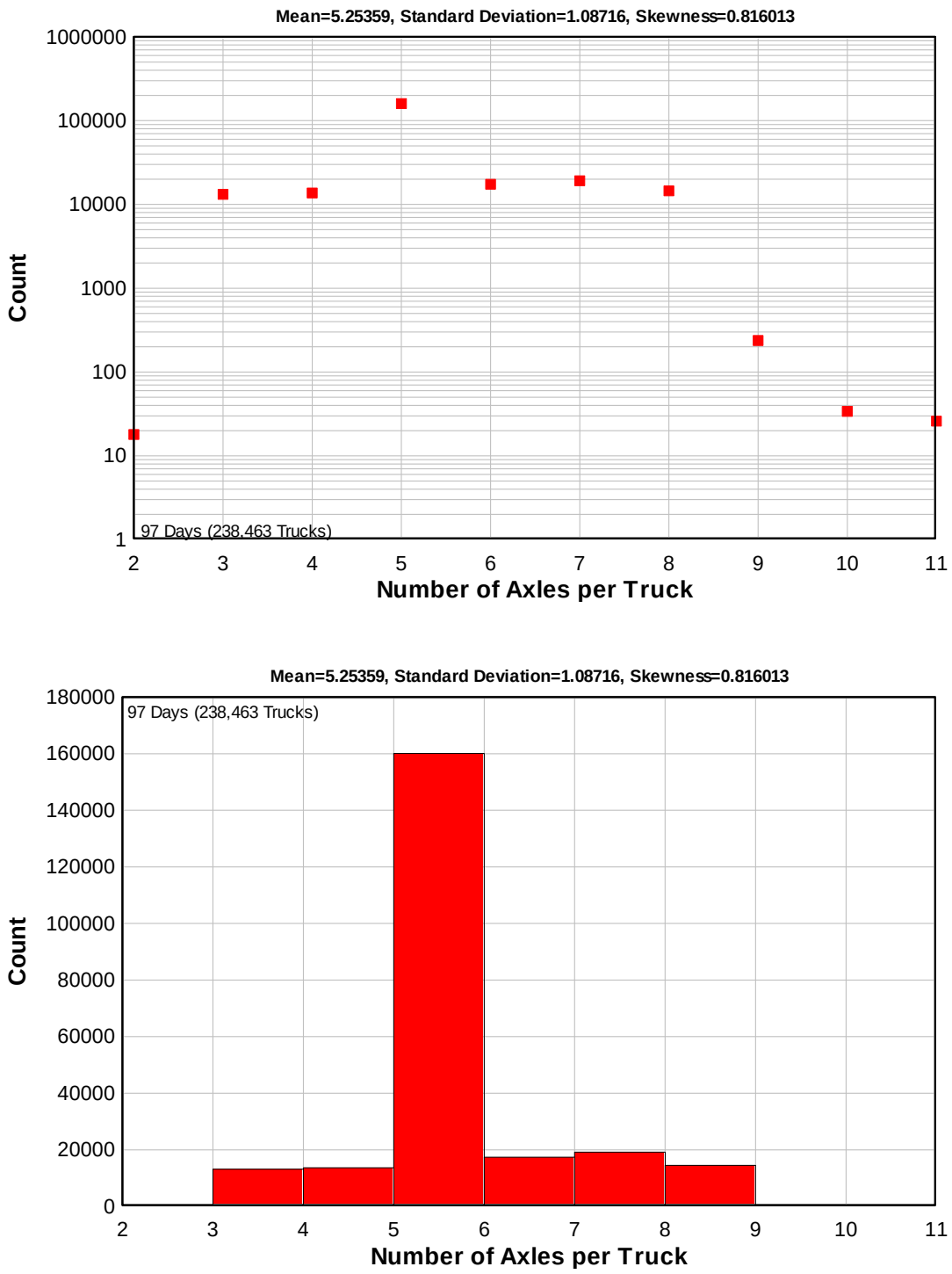

Figure 5.11: Histograms of axle number per vehicle for all trucks captured by Wilbur WIM

The last item collected by WIM is the truck length measured from the steer axle to the rear axle. The histogram for the truck front to rear axle length suggests that the modal truck is 55-60 ft long as shown in Figure 5.12.

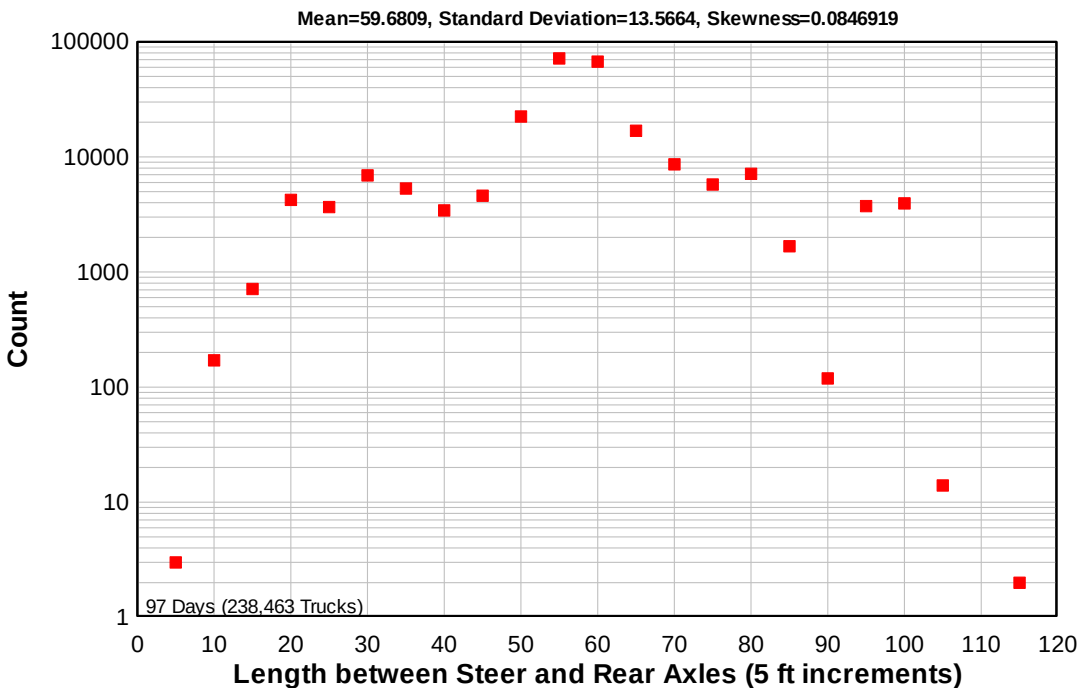

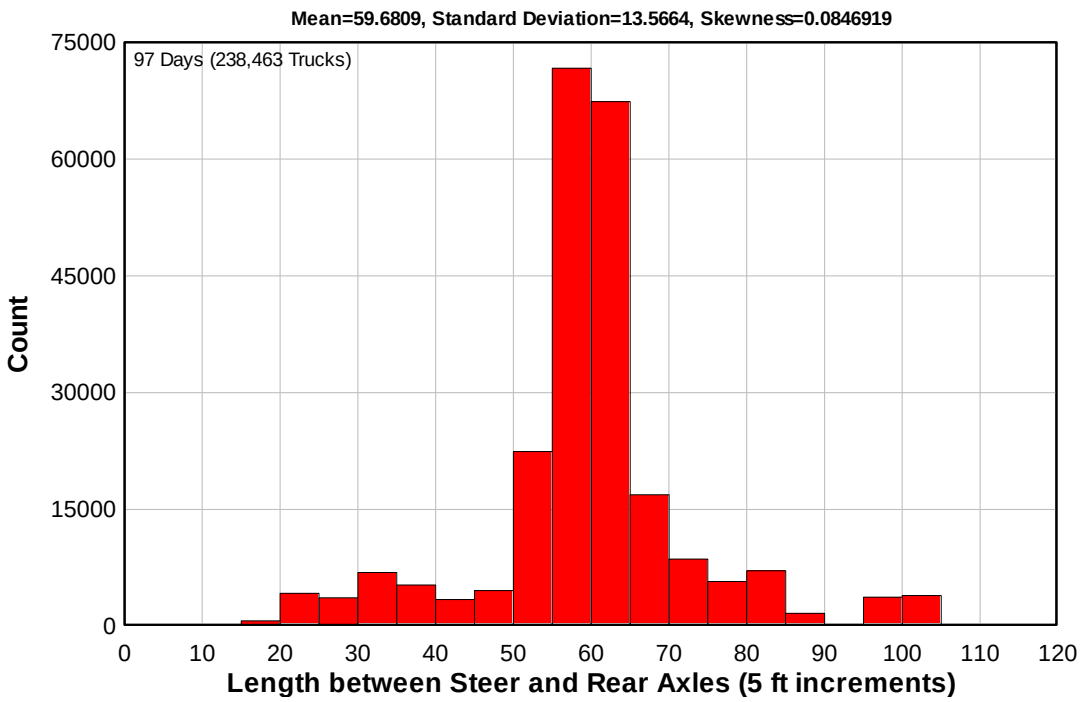

Figure 5.12: Histograms of steer to rear axle length for all trucks captured by Wilbur WIM

The WIM vehicles from the first collection period at Wilbur (97 days) were classified into the permit tables. There are less than 15,000 vehicles of the nearly 240,000 vehicles that fall into Permit Table 3, 4 or 5 as shown in Figure 5.13.

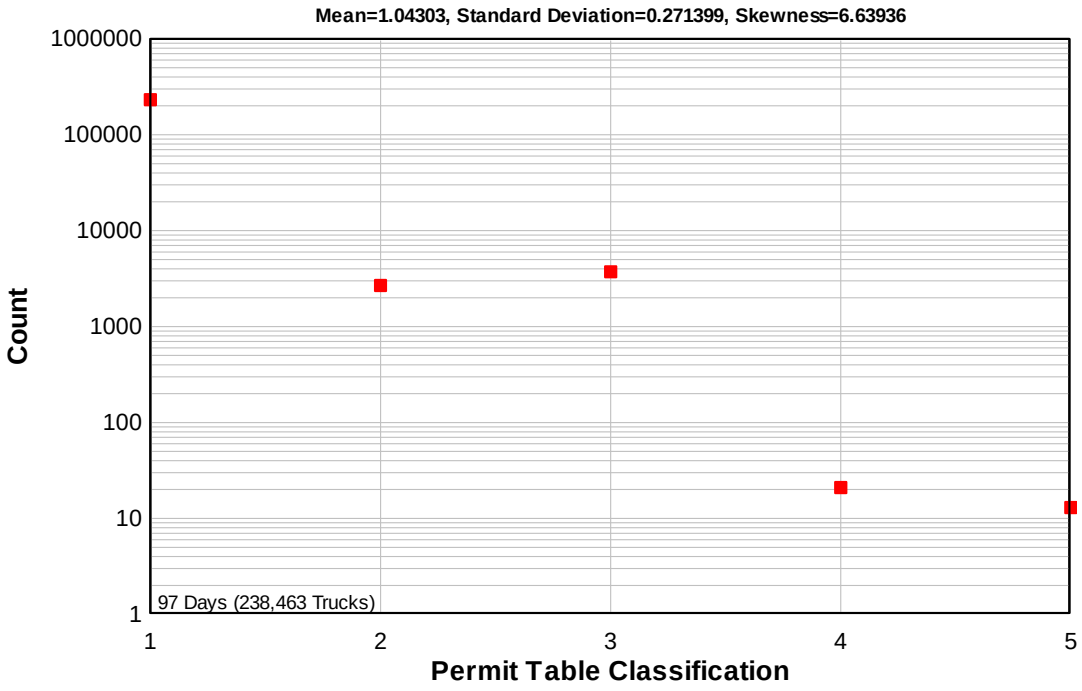

Figure 5.13: Histogram of Permit Table classification for all trucks captured by Wilbur WIM

The vehicles captured at Woodburn POE in one month were also classified by Permit Table for comparison. As foreshadowed by the GVW comparison of the two stations (Figure 4.7), there are in fact more occurrences of vehicles in the higher Permit Tables, during a shorter collection period, at Woodburn POE as shown in Figure 5.14. This indicates that the occurrence rate for large loads may be dependent on location.

The vehicles captured at the Wilbur WIM station from January 2003 to January 2004 are classified into the different permit tables for illustration purposes only, since the program written does not account for any exceptions related to the permit tables. The entire year of Wilbur WIM data was separated into subsets for Permit Tables 3, 4 and 5 and will be used in subsequent figures and evaluations.

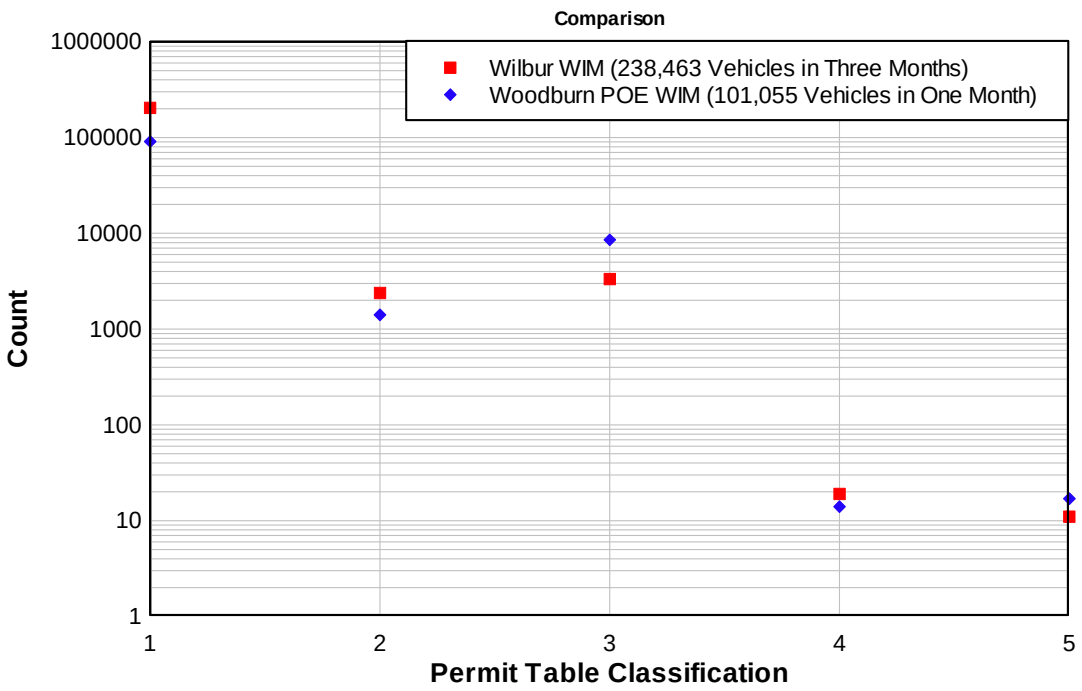

Figure 5.14: Comparison of WIM vehicle permit classifications

5.4.2 Vehicle Load Effects

To determine the effects of truck loadings on a specific bridge, a FORTRAN program based on the slope-deflection method of structural analysis was written where span lengths can be varied. Separate program are used for different bridge indeterminacies. It has been shown that a linear-elastic analysis is adequate for predicting shear forces in directly cracked RCDG bridges under service loads (*Higgins, et al. 2004*). From the database of Oregon's RCDG bridges built between 1947 and 1962, it was found that simply-supported and three-span continuous are the most common bridge configurations. Others occurring much less frequently are two-span, four-span, five-span, and six-span continuous bridges.

The truck data are input into the 2-D linear-elastic model of a particular bridge and the load effects are calculated at points of interest. The truck is moved in a thousand small increments (zeta) across the bridge until the last axle leaves the bridge. The entire history of the load effects is collected as the truck model incrementally moves across the span, and the maximum shear with corresponding moment as well as maximum moment with corresponding shear are extracted.

The load effect history for each vehicle is of interest because as each axle group approaches a section, that axle group dominates the load effect. This is illustrated when the moment and shear are plotted together and when they are plotted separately as illustrated by the two parts of Figure 5.15. The analysis does not account for section changes in the girder, such as horizontal taper or vertical haunch. For bridges with taper or haunch, the geometry changes are typically within a quarter span length from continuous supports.

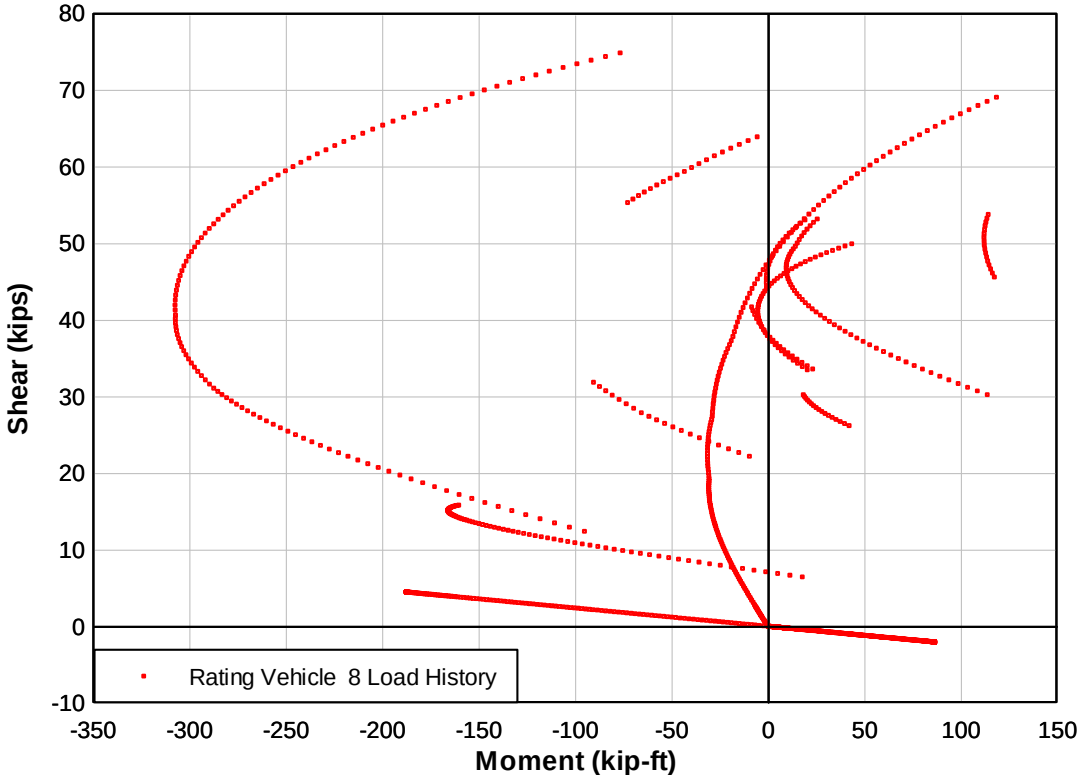

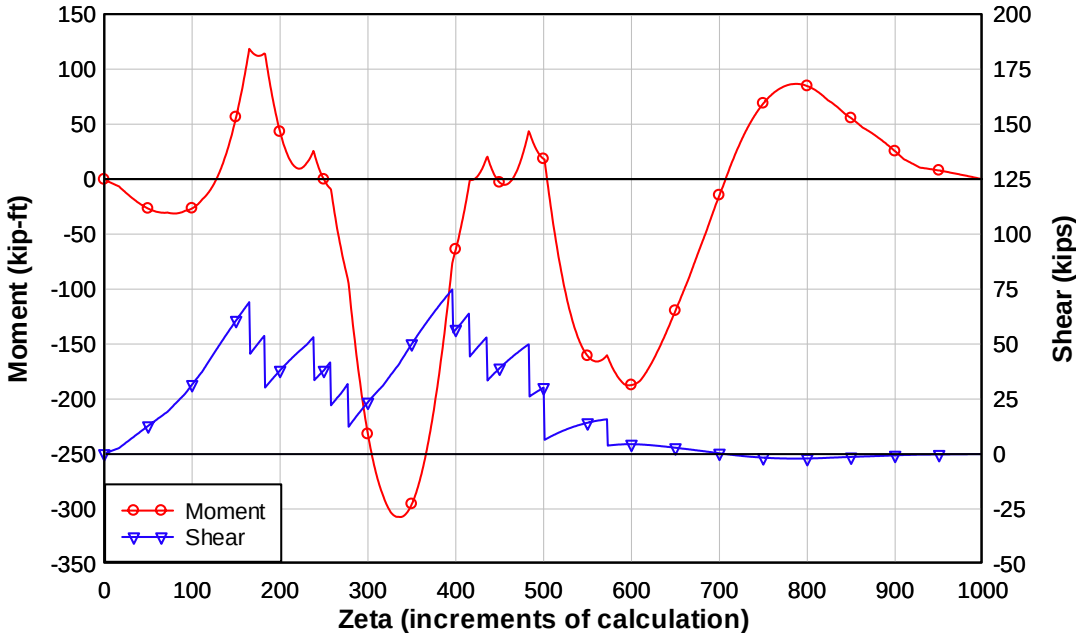

Figure 5.15: Load effect history of Rating Vehicle 8 on three (50 ft) - span continuous bridge

A preliminary investigation (Appendix C1) using SAP 2000 (CSI, 2001) showed that the effect of horizontal taper at supports on the maximum shear is less than 2% and on maximum moment near continuous supports is approximately 15%. Vertical haunch affected the maximum shear and maximum moment near supports by less than 3% and approximately 30%, respectively. The relatively small impact on the maximum shears indicated that uniform prismatic sections, may provide reasonable estimates of combined shear and moment, for assessment of shear dominated response.

5.4.3 Representative Rating Vehicle Load Effects

Currently, the ODOT Bridge Section uses eleven different vehicles when rating bridges. The description of these vehicles is shown in Appendix C2. For simplicity, the vehicles are numbered from one (1) to eleven (11) in this study. In order to assess the load effects produced by the eleven ODOT Rating Vehicles, as compared with actual permitted vehicles, analyses were performed for a range of bridge indeterminacies and span lengths. Results will enable a reduced number of rating vehicles to be used for assessments (specifically for one-time overloads) of RCDG bridges. Using the bridge database (*Higgins, et al. 2004*) as a guide, four indeterminacies were included: simple, two-span continuous, three-span continuous, and four-span continuous. Span lengths ranging from short to long were investigated. End spans resting on abutments were considered simply supported. For the multi-span bridges, all spans were of equal length. The following cases were considered:

- Single-Span simply-supported – 11 ft span and 64 ft span
- Two-Span continuous – 25 ft spans, 50 ft spans and 70 ft spans
- Three-Span continuous – 50 ft spans and 120 ft spans
- Four-Span continuous – 50 ft spans and 70 ft spans

Analysis results were collected at locations corresponding to diagonal cracking damage observed in the field. These included locations of relatively high shear. To simplify the number of locations, the maximum shear (V_{max}) versus corresponding moment (M) at 4 ft from the supports was used for the nine bridges. This corresponds roughly to the girder depth away from the support. Analysis results are shown in Appendix C2. Also shown in these figures is the maximum moment (M_{max}) versus corresponding shear (V) at the same location. These two points characterize the extremes of the load effect history. However, due to the actual shape of the loading history as shown in Figure 5.15, the controlling load effect for capacity may be some intermediate value between these extremes.

The various ODOT Rating Vehicles as described imply representation of actual vehicles falling into specific permit tables. Three example plots are shown in Figures 5.16 to 5.18. Figure 5.16 shows that for a common span length of 50 ft, Rating Vehicles 10, 11, and 8 envelop the Permit Table 3, 4 and 5 WIM vehicles, respectively. Figure 5.17 shows that for long spans, Rating Vehicle 10 is no longer adequate to capture Table 3 load effects; likewise for Rating Vehicle 11 capturing Table 4 effects. Figure 5.18 indicates that for shorter spans, Rating Vehicle 7 is necessary to capture Table 4 and 5 WIM vehicle load effects, whereas Rating Vehicle 5 is needed to capture Table 3.

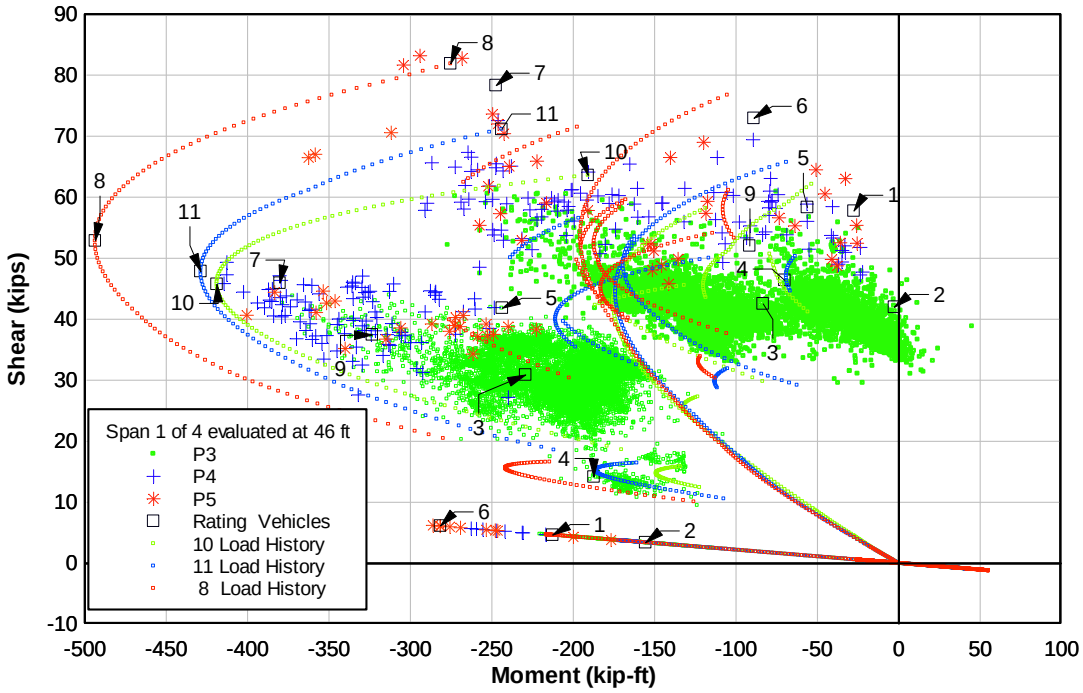

Figure 5.16: Maximum load effects for 1 year of Wilbur WIM permit vehicles (14,510) on a four (50ft) – span continuous bridge

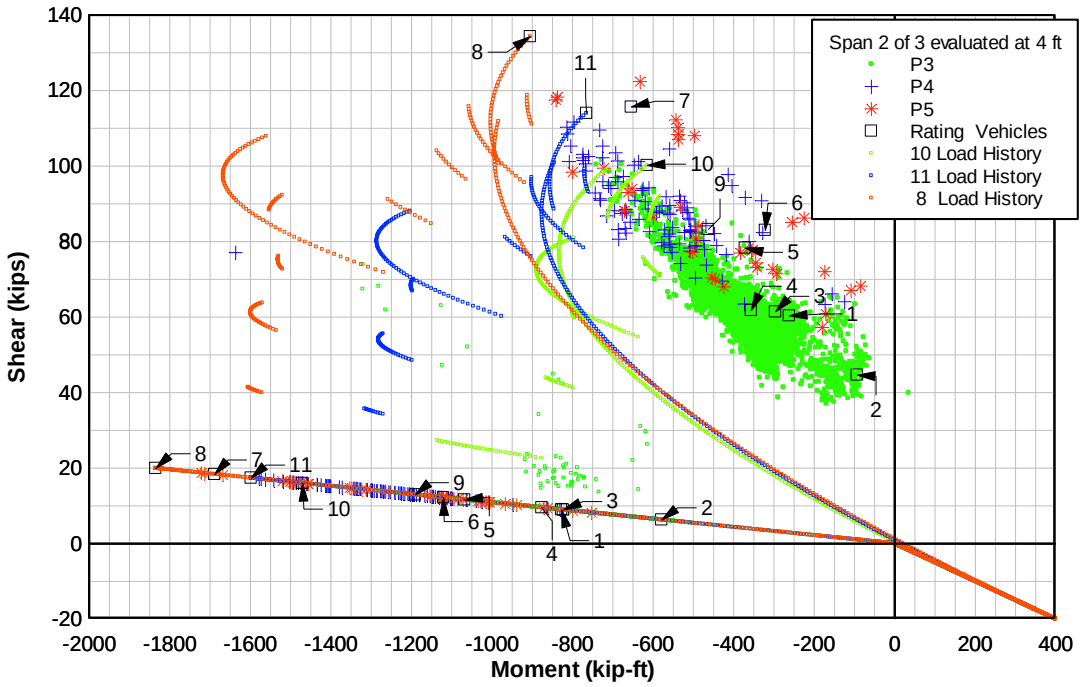

Figure 5.17: Maximum load effects for 1 year of Wilbur WIM permit vehicles (14,510) on a three (120 ft) – span continuous bridge

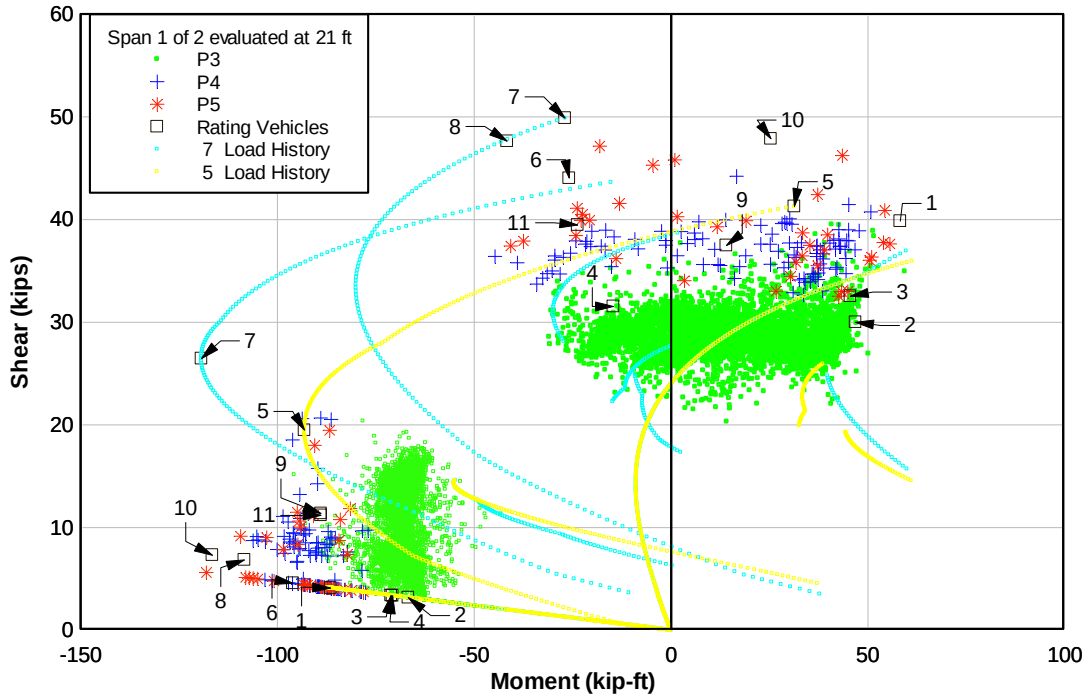

Figure 5.18: Maximum load effects for 1 year of Wilbur WIM vehicles (14,510) on a two (25 ft) – span continuous bridge

Evaluation of the various load effects in Appendix C2 for the rating vehicles and their ability to describe WIM permit classifications is summarized in Table 5.1.

Table 5.1: Correlation between load effects from rating vehicles and WIM permit vehicle classifications

Permit Table	Rating Vehicle Implied to Represent	Rating Vehicle that Represents Load Effects
Table 1 (Legal Loads)	1 thru 4	Not assessed
Table 3 (Continuous Trip)*	5 and 6	10 and 5 (and 11 for long spans)
Table 4 (Single Trip)	7	11 and 7 (and 8 for long spans)
Table 5 (Single Trip)	8	8 and 7

*Table 3 WIM vehicles were not separated into CTP and STP for this evaluation.

Figures 5.16, 5.17 and 5.18 also make it apparent that there is no clear separation in the load effects produced by vehicles classified in Permit Tables 3, 4 and 5. Although Permit Tables imply that Permit Table 5 produces the largest load effects, many instances occur where a WIM vehicle corresponding to Permit Table 5 produces smaller load effects than a WIM vehicle corresponding to Permit Table 3. However, inspection of the WIM vehicles classified as Permit Table 5 (Appendix C2) indicates that trucks commonly reached the higher table classification

because of one heavy axle or axle group, whereas the WIM vehicle classified as Permit Table 3 that produced larger load effects was most likely fully loaded.

5.5 ASSESSMENT METHODOLOGY WITH APPLICATION

The load effects calculated for the WIM vehicles and ODOT Rating Vehicles can be used to evaluate whether or not the capacity of a given section along the span is adequate for the live load effects that are likely to occur during the life of the structure. The load effects were used to evaluate the service level performance and the capacity of an RCDG bridge, considering both one-time overloads and low-cycle fatigue. High cycle fatigue (HCF) was not evaluated, as field and laboratory work indicate that HCF loading, due to the low stress range in the stirrups, is unlikely to cause stirrup fracture.

A flowchart for the application process is illustrated in Figure 5.19. Service level performance evaluation is not included in the figure since it is only being performed in this study to explain the presence of diagonal cracks in the RCDG bridges and is not part of the methodology for assessment. The figure shows how the Oregon load spectrum, field testing, laboratory testing, bridge inspection, and bridge drawings are integrated to evaluate a bridge. The methodology is described and demonstrated using a typical 1950s vintage RCDG bridge with diagonal cracks.

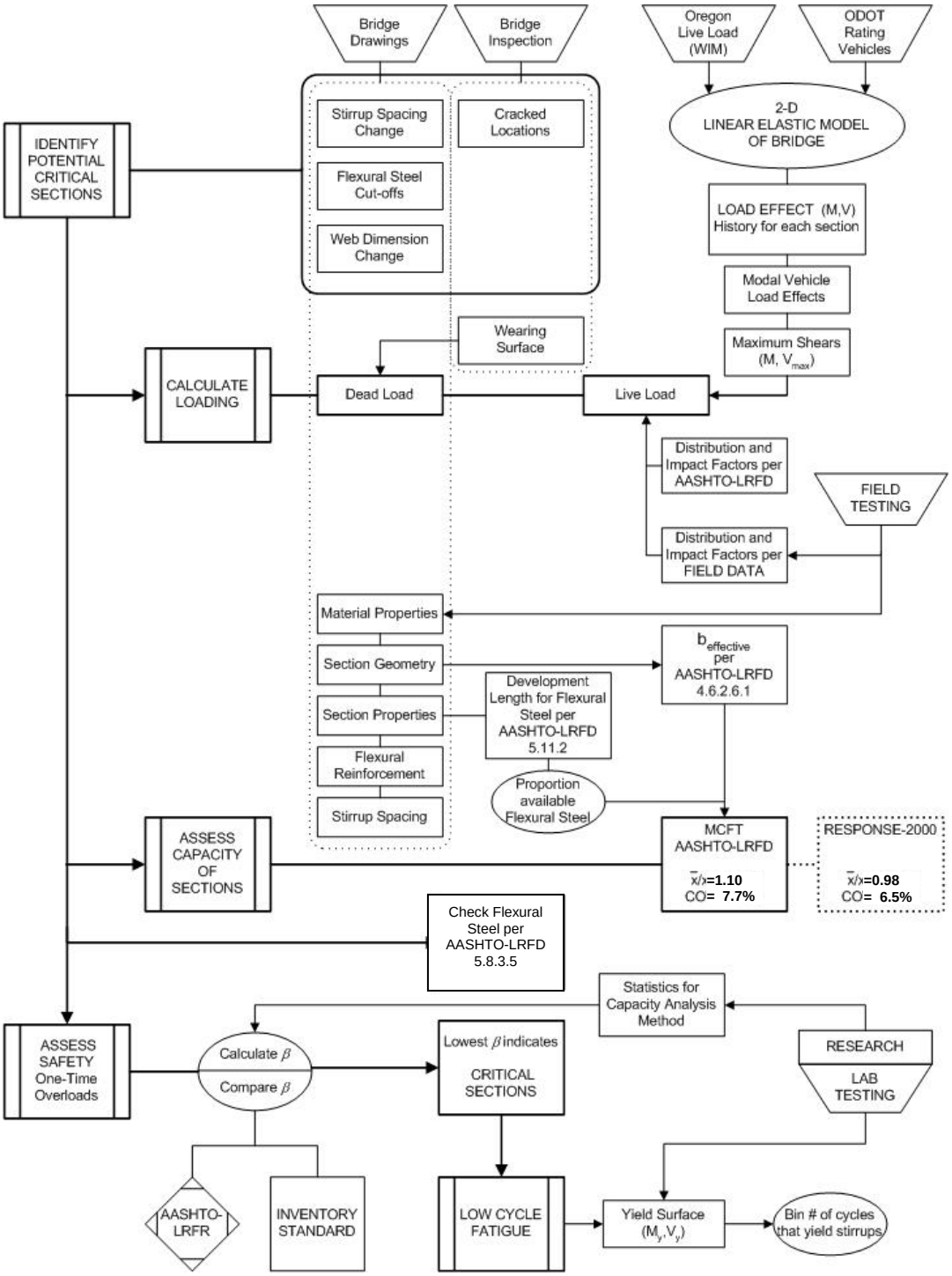

Figure 5.19: Flowchart for safety assessment and low cycle fatigue evaluation

5.5.1 Bridge Description

The McKenzie River Bridge (also called Spores Bridge) (ODOT #08175N and Figure 2.1) on I-5 northbound just north of Eugene, OR was part of the field testing described previously and was identified as crack stage 3 by ODOT. It has a three-span continuous portion with all three spans 50 feet long. The bridge deck cross-section and exterior girder being analyzed are shown in Figure 5.20 and the profile is shown in Figure 5.21. The girder has a horizontally tapered web between the span quarter points on either side of continuous supports. The detailed bridge drawing is shown in Figure 2.1. A digital photograph of diagonal cracking on the exterior girder face is shown in Figure 5.22.

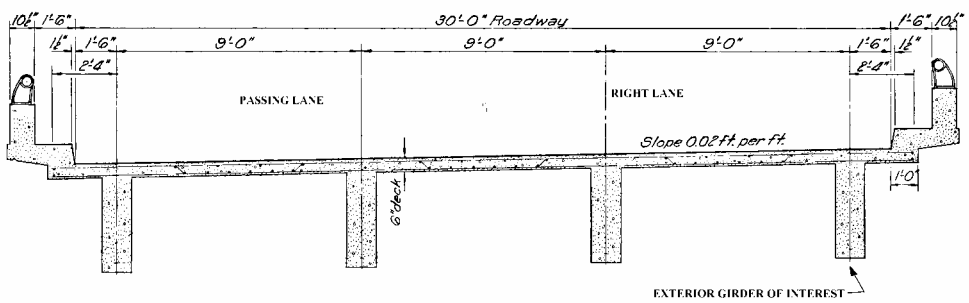

Figure 5.20: McKenzie River bridge deck cross-section

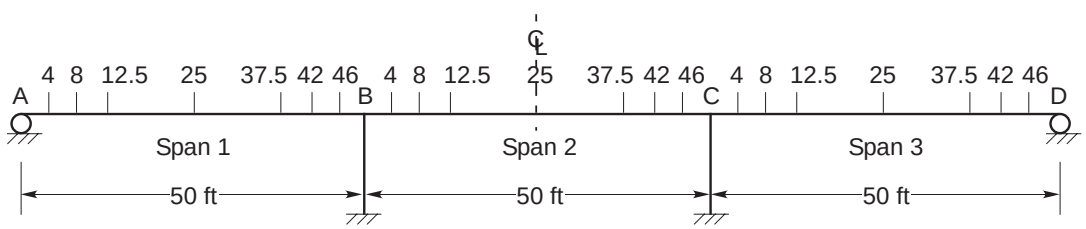

Figure 5.21: Profile view of McKenzie River bridge with cross-section locations (feet)

Figure 5.22: Existing cracks on the McKenzie River bridge exterior girder in span 1 near support B. The first diaphragm framing is 12.5 ft from support B centerline.

5.5.2 Identify Potential Critical Sections

The first step is to identify girder sections that possibly control the capacity of the girder. Two sources for information are the bridge drawings and bridge inspection. The potentially critical sections will likely occur where there is a change in stirrup spacing, flexural reinforcing steel is cut-off, or there is a change in web dimensions. These can be determined from bridge drawings, and field verified as needed. The other indicator for a potential critical section is a diagonal tension crack in the girder, based on field inspection. For example, the exterior girder of the McKenzie River bridge has diagonal cracks at approximately 4 ft, 8 ft, and 12.5 ft from the centerline of support B as shown in Figure 5.22.

The drawings reveal that the tapered web section begins at 12.5 ft from support B and that top and bottom flexural steel are cut-off at that location. There are seven stirrup changes in Span 1. The first is at about 4 ft from support A and another is about 8 ft from Support A. Not all stirrup change locations and flexural bar cut-off locations were evaluated for this example. The potentially critical locations that were assessed are depicted in Figure 5.21.

5.5.3 Calculate Load Effects

Once section locations were determined for evaluation, the next step was calculating the dead load and live load at each section.

5.5.3.1 Dead Load

The permanent loading, referred to as dead load, is the self-weight of the bridge members, deck, wearing surface and other components. The dead load was estimated from the bridge drawings. Additional information can be collected from field investigation such as the thickness of the wearing surface. The weight carried by each girder was taken as the total weight divided by the number of girders, and this is applied as a distributed load along the length of the member. The dead load for components and wearing surfaces were not separated in the example, but they could be if necessary.

5.5.3.2 Vehicle Load

The live load effects on a bridge girder were determined from structural analysis of moving load models to determine the maximums at each section of interest. The static load effects were amplified for dynamic/impact effects using an impact factor. These forces were then assigned to girders by means of a distribution factor. Distribution factors represent how much of each lane load, or load effect of a truck, is distributed to an individual girder. The factor is dependent upon the bridge geometry and truck width as well as the lateral placement of the truck on the bridge.

Equations for live load distribution factors used in the AASHTO-LRFD Bridge Design Specification (*2003*) are dependent on the superstructure cross-section, span length, girder longitudinal stiffness and deck thickness for RCDG bridges. AASHTO-LRFD provides distribution factors for lane loads based on the 6 ft wide HS vehicles (centerline of wheel-group to wheel-group). Observations from weigh station visits at Philomath and Woodburn indicate that actual truck width ranges from about 6’-3” to 7’-0”. Large permit loads can be even wider. The distribution factors become larger as the width narrows. To be slightly conservative, 6 ft is used for the truck width when calculating AASHTO-LRFD distribution factors applied to the WIM vehicle effects.

Distribution and impact factors calculated from AASHTO-LRFD could be overly conservative for a specific bridge. Field data can be collected to more reasonably reflect in-situ distribution and impact factors. Based on instrumented stirrups with strain gages at multiple cracked locations, a distribution factor for shear can be estimated. Using a test vehicle and driving it over the bridge at different speeds, an impact factor was also determined previously.

Since an overly conservative assessment may lead to unnecessary and costly repairs and closures (*Stewart, et al. 2002*), and field data are available for the McKenzie River Bridge, two cases for each of the application examples were calculated. Distribution factors and impact factors were applied to the WIM load spectrum load effects using the AASHTO-LRFD method in the first case. In the second case, distribution factors and impact factors determined from field investigations for the McKenzie River Bridge were used. The distribution and impact factors are summarized in Table 5.2.

Table 5.2: Distribution and impact factors for McKenzie River Bridge exterior girder

Data Source	Impact Factor	Distribution Factors (Lane Fraction) Moment	Shear
AASHTO-LRFD	1.33	$DF_M = 0.867$	$DF_V = 0.884$
Field Study*	1.317	Right Lane = 0.61 Passing Lane = 0.15	Right Lane = 0.61 Passing Lane = 0.15

* Field study factors are based on stirrup strains. Moment and shear are assumed to have same distribution for diagonal crack locations.

A previous study for developing the truck load model used in the AASHTO specification revealed that for two lane bridges, the maximum effects are obtained for two side-by-side identical trucks (i.e., perfect correlation between truck weights) *(Nowak and Hong 1991*). Therefore, the AASHTO distribution factors account for this multiple presence. To simplify this multiple presence situation for the field data case on a two-lane bridge with both lanes traveling in the same direction, the shear load histogram is plotted with arithmetic scale (before distribution and impact factors are applied) to determine the most commonly occurring (modal) shear produced. Figure 5.23 is the histogram for shear at 8 ft away from support B (first continuous support) using the 97 days of Wilbur WIM data described above (Figures 5.5, and 5.8 to 5.13), using the three-span continuous linear-elastic model where all three spans are 50 ft.

It is clearly shown that the modal shear of 32 kips occurs much more often than other shears. Therefore, it is assumed that a vehicle producing this shear can reasonably be found to be concurrent with any other vehicle on the bridge. Moreover, if the vehicle on the bridge produces a smaller shear than the modal shear, the vehicle is assumed to be passing. If the vehicle produces a larger shear than the modal shear, it is assumed to be in the right or driving lane. However, the shear produced by Rating Vehicle 2 is 38.6 kips, and since there is not a Rating Vehicle producing a smaller shear, it was used to represent the modal truck, rather than introduce an additional truck model. Load effects representative of Rating Vehicle 2 occurred over 4,000 times in a three month period, so the likelihood of concurrent vehicles is high (Figure 5.23).

The largest data set is the Wilbur WIM data collected from January 2003-January 2004. Wilbur is also the closest WIM station to the McKenzie River Bridge (approximately 60 miles south), whereas the Woodburn POE is approximately 80 miles north. Since the tail vehicles in the distribution are likely to produce the largest load effects, the year of data has been classified into Permit Tables 3, 4 and 5 to reduce the amount of calculation. To reduce calculation further, the rating vehicles determined to represent the WIM vehicles classified in those tables can be used in the safety assessment.

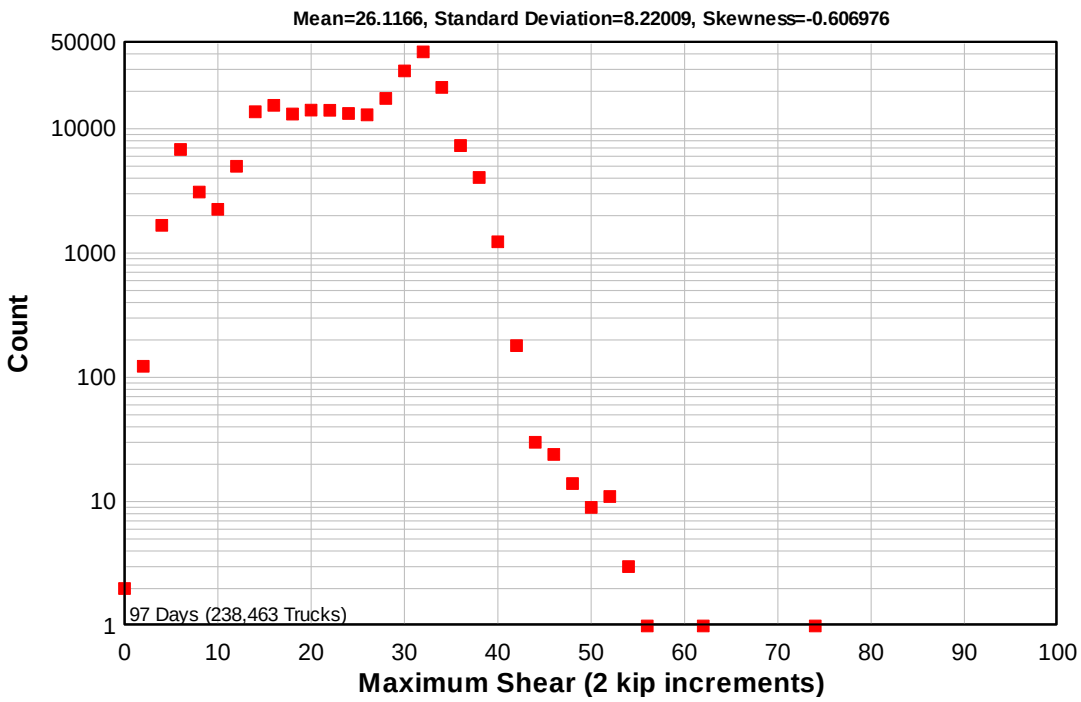

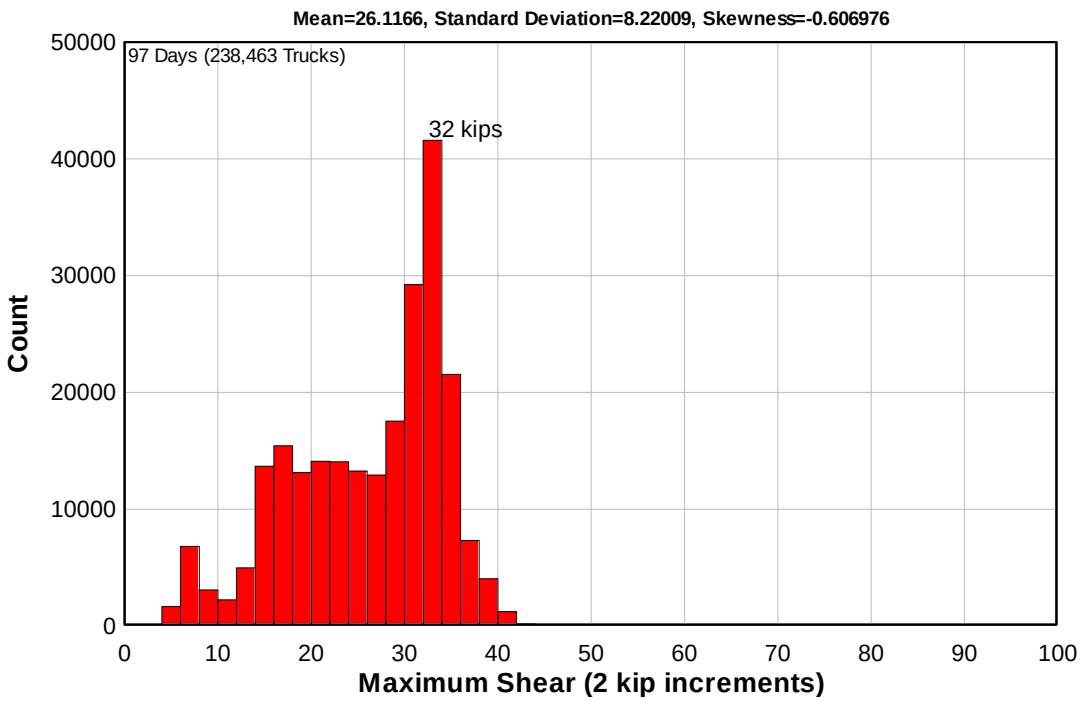

Figure 5.23: Modal shear produced at 42 ft in span 1 of three (50 ft) - span continuous bridge

5.5.4 Prediction of the Load Induced Diagonal Cracking

The initial onset of diagonal-tension cracking was predicted for unfactored live and dead loads. Though not directly part of the safety or life assessment, it identifies the likelihood of diagonal cracking for the bridge. To investigate loads that may initiate diagonal cracking in the bridge, the shear force from load effects was compared with the shear force to cause cracking. In the presence of large moments, for which adequate longitudinal reinforcement is provided, the shear to cause diagonal cracking (V_{cr}) (ACI-ASCE, 1962) is:

$$V_{cr} = 1.9bd\sqrt{f'_c} \qquad \textbf{(5-4)}$$

where b (in) is the beam web width, d (in) is the depth of the shear section and f'_c is the 28-day concrete compressive strength (psi). From laboratory test results of full-scale girders representative of the type used in this bridge, V_{cr} was determined to be an average of 1.4 times $bd_e\sqrt{f'_c}$ where d_e is the depth from the compression face to the centroid of the flexural steel.

The exterior girder section 8 ft away from support face BA (the first interior support) was evaluated and is located in a high moment region. V_{cr} was calculated for the widened section due to horizontal taper near the continuous support locations (b_v=15.5 in. and d_v=41.2 in.) and has been adjusted by subtracting the dead load shear as calculated from the bridge drawings. The service level performance of the exterior girder in Figure 5.24 shows the shear force from each WIM vehicle at 8 ft away from the continuous support using AASHTO-LRFD distribution factors.

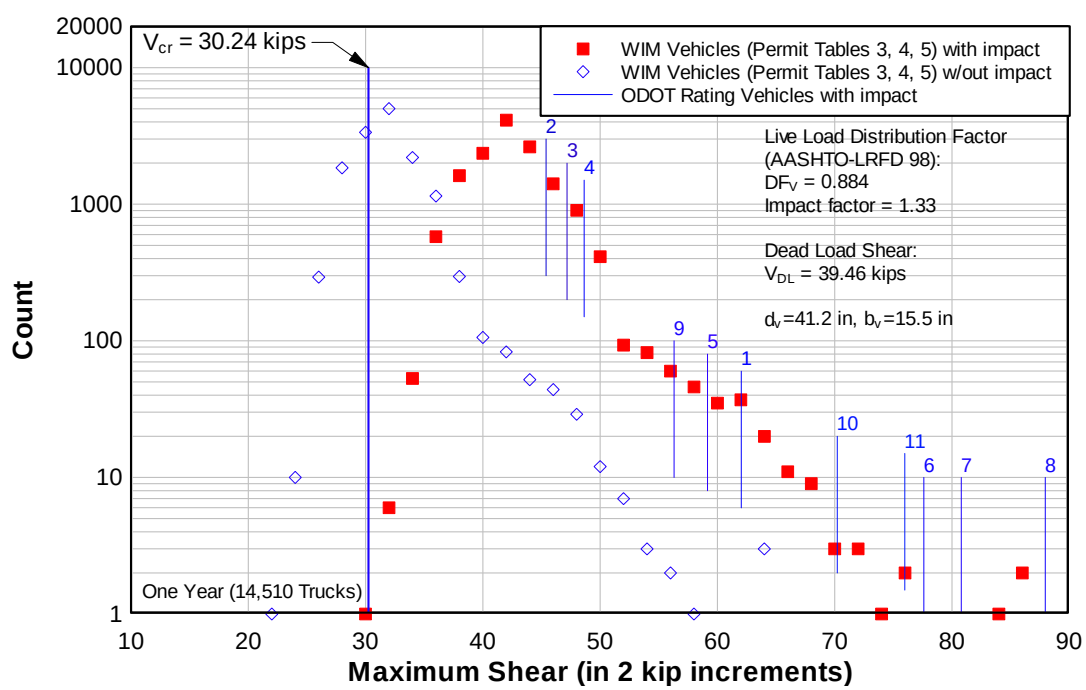

Figure 5.24: Service level performance histogram for diagonal cracking for the McKenzie River bridge at 42 ft. in span 1 (AASHTO-LRFD).

Figure 5.25 shows the shear force from each WIM vehicle on the bridge combined with the vehicle producing the modal shear at 8 ft away from support face BA and distribution factors determined from field study of McKenzie River Bridge. Note that in each case, the shears were determined without impact factors to illustrate that even without dynamic amplification, cracking is likely to occur. The truck count is shown on a logarithmic scale.

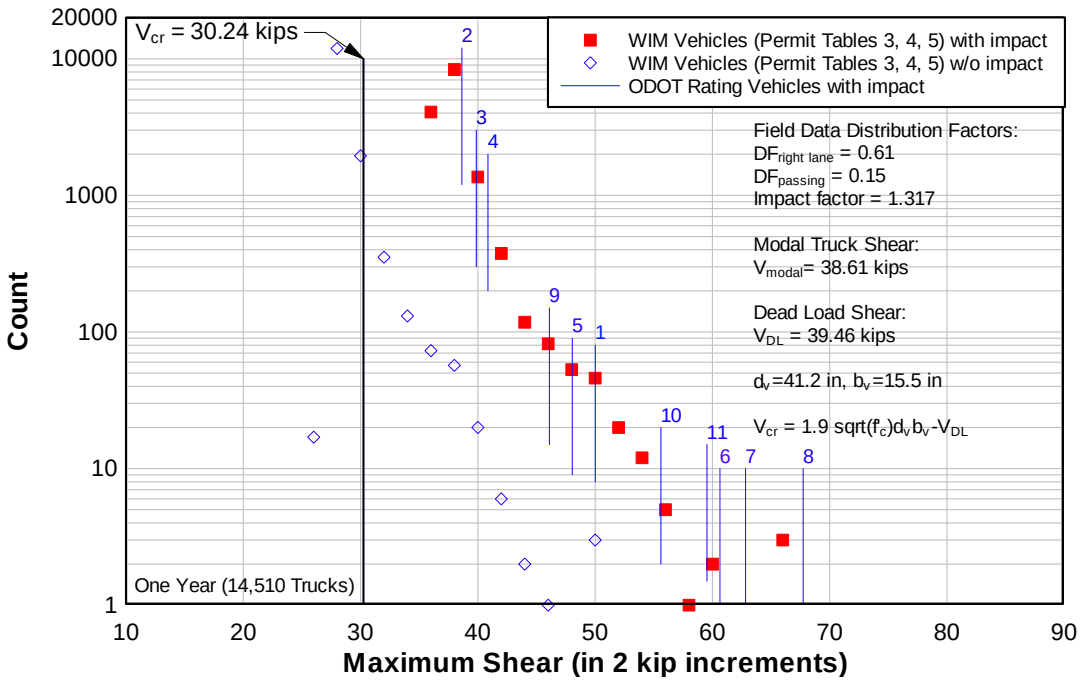

Figure 5.25: Service level performance histogram for diagonal cracking for the McKenzie River bridge at 42 ft. in span 1 (Field data).

Figures 5.24 and 5.25 show that in one year, thousands of WIM vehicles classified as Permit Table 3, 4 and 5 exceeded V_{cr}. Finally, the eleven rating vehicles used by the ODOT Bridge Section when performing bridge ratings are shown as vertical lines for reference. It becomes clear that vehicles from Permit Tables 3, 4, and 5, in both the AASHTO-LRFD case and the field data case, are sufficient to produce diagonal cracking of the girder.

Further, the field case without multiple presence is considered. Calculation of the shear produced by Rating Vehicle 2 multiplied by the field data impact factor and only the right lane distribution factor results in a shear of 30.52 kips, which still exceeds the cracking shear. From this, it is estimated using the logarithmic scale in Figure 5.23, that easily over 10,000 trucks per year produce or exceed the cracking shear for the girder. Based on this assessment, it is apparent that cracking as shown in Figure 5.22 is to be expected for the loading conditions.

5.5.5 Predict Capacity

The next step for assessment is to calculate the capacity of the bridge at sections along the span. An appropriate method to calculate capacity for the structural member is required. For RCDGs the interaction between moment and shear is essential to predicting the capacity. Modified compression field theory (*Vecchio and Collins 1986*) takes into account this interaction, and a simplified form is adopted in the AASHTO-LRFD specification (*AASHTO-LRFD 2003*). The AASHTO-MCFT is more fully described in the AASHTO-LRFD section 5.8.3.4.2 Commentary.

Previous comparisons of results from full-scale laboratory tests of large RC girders (designed to reflect RCDG bridges in Oregon) showed that AASHTO-MCFT provided reasonable capacity prediction. Experimental data from full-scale testing of thirty-one (31) specimens (all specimens except LCF specimens and HCF specimen with stirrup fracture) resulted in an average experimental-to-predicted shear strength ratio of 1.10 with a coefficient of variation (COV) of 7.7%. Figure 5.26 shows the histogram of the predictions using AASHTO-MCFT. A Normal distribution was assumed.

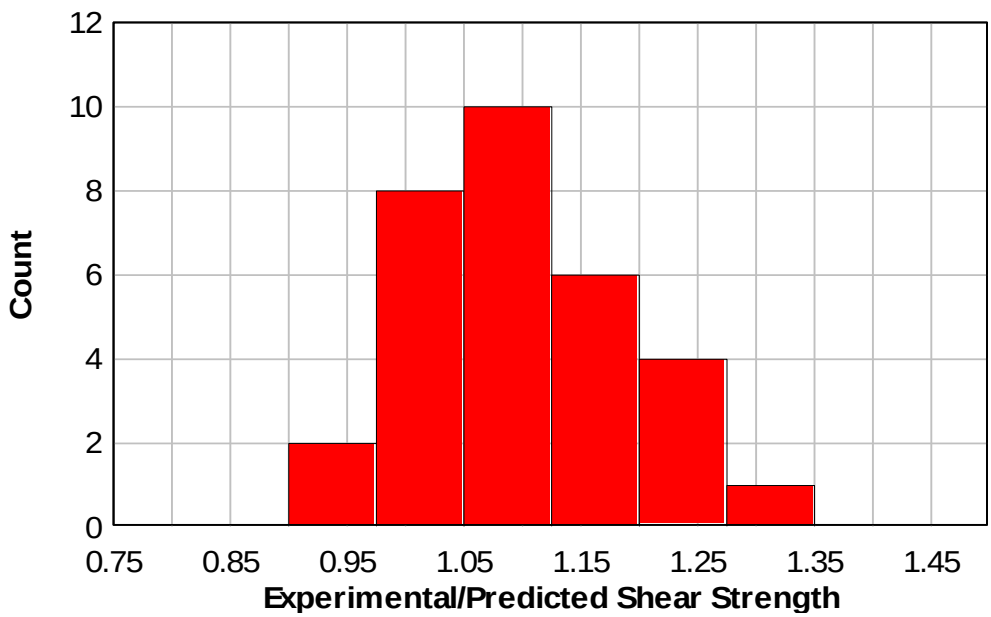

Note: Specimen #s 1, 2, 3, 4, 5, 6, 7, 8, 9, 10, 11, 13, 14, 15, 16, 17, 18, 20, 23, 24, 25, 27, 28, 29, 30, 31, 32, 33, 36, 37, and 40 = all but LCF specimens and HCF specimen with stirrup fracture.

Figure 5.26: Histogram of experimental to AASHTO-MCFT predicted shear capacity from results of 31 full-scale RCDG specimens

Another method for shear capacity prediction developed by Bentz (*2000*) is a specialty analysis program called *Response 2000*™ (R2K) and is also based on MCFT. Laboratory results for the same twenty-three specimens gave an average experimental-to-predicted shear strength ratio of 0.98 with a COV of 6.5%. The statistics for these two methods are summarized in Table 5.3.

Table 5.3: Shear prediction statistics of analysis methods to laboratory results

Analysis Method	Mean Ratio of Experimental to Predicted Shear Strength	COV
Response2000™ (R2K)	0.98	0.065
AASHTO-MCFT	1.10	0.077

Once the section and material properties, geometry, longitudinal reinforcing, and stirrup spacing are known at the location of interest, the program *Response 2000*™ can be used to determine the nominal shear and moment (V_n-M_n) curve for capacity as described by either AASHTO-MCFT or sectional MCFT analysis. Hereafter, results from *Response 2000*™ will be referred to as R2K.

Two parameters for each section for input into *Response 2000*™ require special note: the effective flange width (b_{eff}) and the developed area of steel (A_s). Using the bridge drawings, b_{eff} is calculated using AASHTO-LRFD 4.6.2.6.1. In order to account for shear lag, a linear transition between zero and full b_{eff} was considered in a quarter-span length from the supports (approximately 3*d* away from the support for this example).

Since the flexural reinforcement plays an important role in the shear capacity of a member, the development length becomes of critical importance. Development length required for the flexural steel was calculated per AASHTO-LRFD 5.11.2. It should be noted that the longitudinal steel in the flange of the T-beam (steel to resist negative moment) does not have more than 12 in. of fresh concrete below the steel, because bridges in this study were typically constructed in two casting sequences with a cold joint and shear keys at the flange/web interface. At each cross-section of interest along the girder length, the length of steel available for development is divided by the development length required. This ratio is used to proportion the area of steel at the cross-section that is effective for flexural resistance. This method was also used by Collins (*2003*) for analysis of the laboratory specimens.

As an example, the capacity was calculated using AASHTO-MCFT for the cross-section at 42 ft in span 1. The section has flexural reinforcement located in the deck and base of the web. Due to the cut-off locations of the flexural reinforcement, only four #11 bars were fully developed in the flange and three #11 bars in the bottom of the section. The stirrup spacing was 9 in. and the effective flange width was considered 50 in. to account for shear lag. The web width was 15.5 in. since the section is within the horizontally tapered stem region. The cross-section is shown in Figure 5.27.

Response 2000™ was used to calculate both the AASHTO-MCFT and R2K moment-shear (M-V) interaction curves. It is observed that at this location where the moment is transitioning from positive to negative there is a disconnect in the AASHTO-MCFT capacity curves at zero moment (refer to Figure 5.28). The section was obviously designed for the flexural steel in the flange to be in tension (i.e., negative moment), but moving loads on a bridge can cause moment sign reversal at this location. It is unrealistic for the shear capacity to have two different values at this transition point.

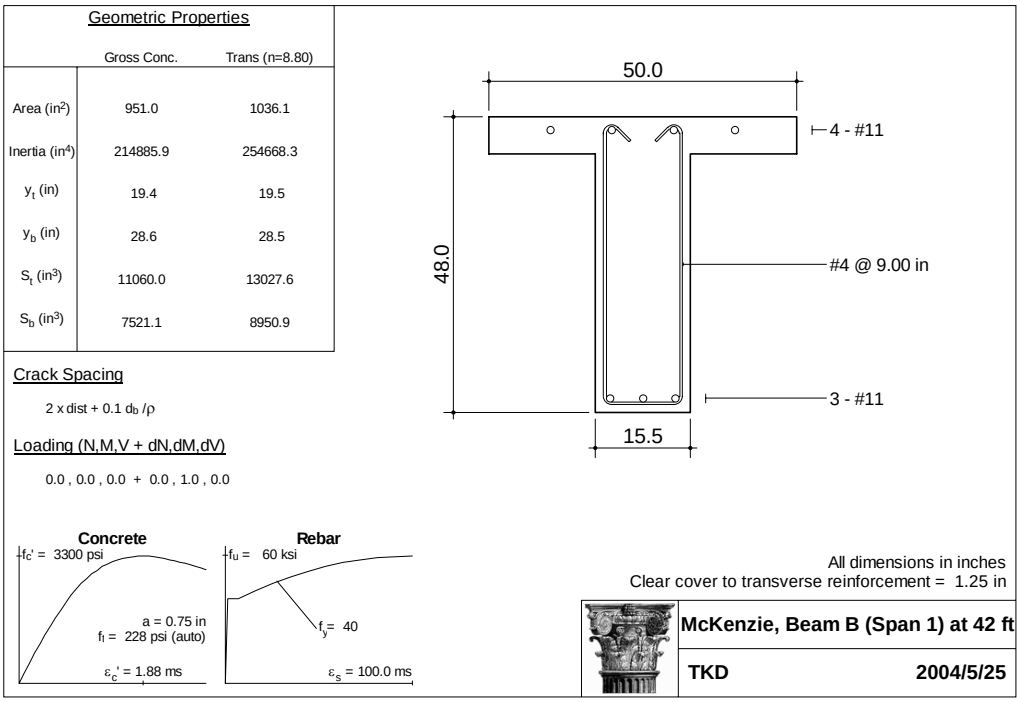

Figure 5.27: Cross-section for McKenzie River Bridge at 42 ft in span 1 (*Response2000*™)

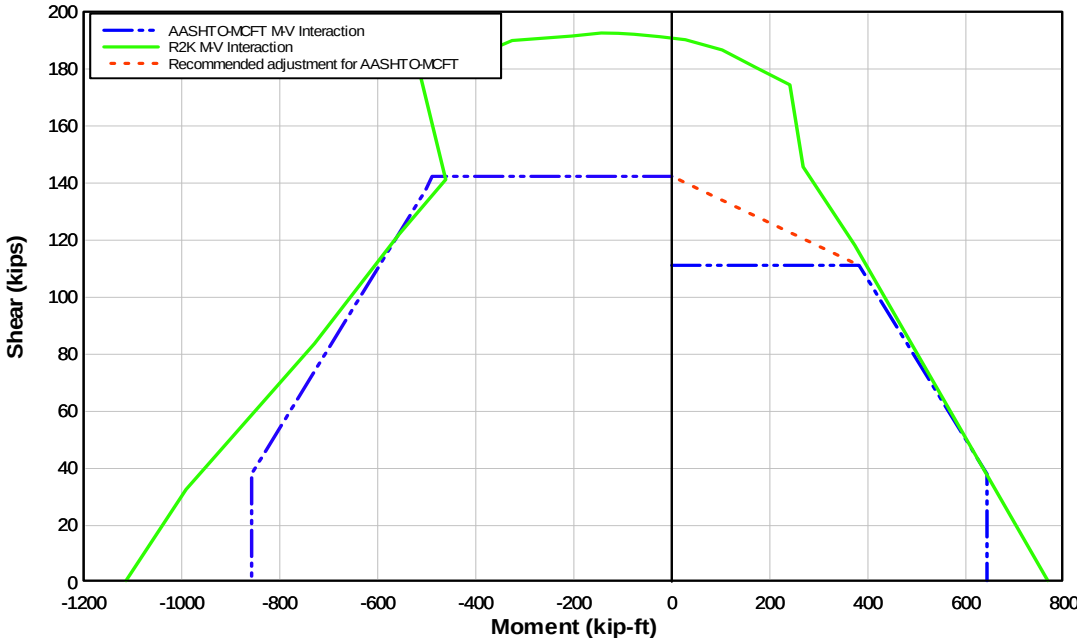

Figure 5.28: Disconnect of AASHTO-MCFT compared to R2K at points of inflection

In contrast, the R2K M-V interaction curve shows continuity through this transition region. Full-scale laboratory testing of RCDGs with a moving load showed that R2K capacity predictions were conservative in this low moment region. Therefore, it is recommended that either R2K be used to predict capacity in this region or that a simple modification to the AASHTO-MCFT M-V curves be made. The modification for AASHTO-MCFT entails changing the shear value at zero moment for the smaller M-V interaction curve to the shear value at zero moment for the larger M-V interaction curve as illustrated by the dashed line in Figure 5.28. Since R2K was found to be conservative near points of inflection (zero moment) and the recommended modification to AASHTO-MCFT is below the R2K prediction, this should provide a viable solution for capacity prediction in situations where the moment changes sign in transition regions due to vehicular loading.

From the experimental statistics for AASHTO-MCFT, assuming normal distributions, the moment-shear interaction curves at the average, and 1, 2, and 3 standard deviations (σ) below the average, were drawn. These were used in the following safety assessment for one-time overloads.

5.5.6 Safety Assessment: One-Time Overloads

An assessment of safety for a bridge girder is performed by comparing the load effects produced at selected cross-sections with the available resistance provided by that section. An effective method for making relative comparisons for safety or reliability is the calculation of the second-moment reliability index (β). For this example, the uncertainty and variability are considered for the resistance (or capacity) while the load (or demand) is considered to be known (deterministic). Figure 5.29 illustrates how β is calculated.

The nominal capacity from AASHTO-MCFT is shown, along with the average and standard deviations at 1σ, 2σ and 3σ, all of which are functions of the statistics described in Table 5.3. Since the distribution for the capacity is assumed Normal, β is simply the number of standard deviations from the coordinate of intersection on the average capacity curve (Mμ, Vμ) to the moment (M) and shear (V) as calculated in Equations 5-5 and 5-6. The entire truck history is shown, but only the controlling moment and shear combination is sketched in Figure 5.29.

The slope *(m)* of the line projected from the controlling load effect coordinate is determined from the ratio of the live load shear (V_{LL}) divided by the live load moment (M_{LL}) as shown in Equation 5-7. This is the slope at which the load effect will increase or decrease if all axle weights in the truck were amplified by a constant value. The y-intercept (V_o) of this projected line is a function of the live load, distribution and impact factors, and the dead load as shown in Equation 5-8.

$$M = M_{LL} DF_M IM + M_{DL} \quad \textbf{(5-5)}$$

$$V = V_{LL} DF_V IM + V_{DL} \quad \textbf{(5-6)}$$

$$m = V_{LL} / M_{LL} \quad \textbf{(5-7)}$$

$$V_o = -mM + V \tag{5-8}$$

where, *IM* is the impact factor and *DF* is the distribution factor for moment and shear as indicated by the subscript.

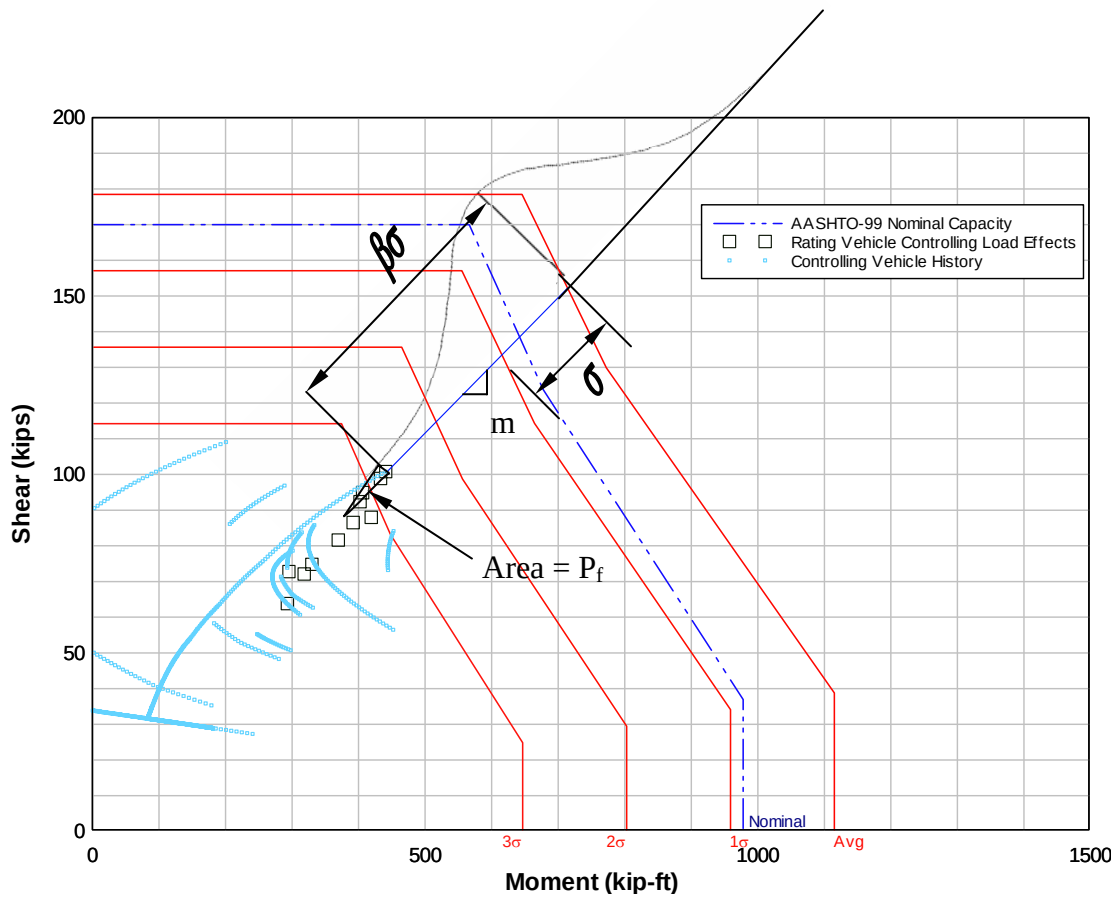

Figure 5.29: Illustration of how the reliability index is calculated.

The probability of failure (p_f) or more suitably in this use, the probability of exceedence, is the area under the normal curve left of the (M, V) coordinate, and is related to β through Equation 5-3. Equation 5-9 is in general probability terms for a discrete value of X,

$$p_f = P(X \le x) = \Phi((x-\mu)/\sigma) \tag{5-9}$$

For this two dimensional case, x is the coordinate (M,V), μ is the coordinate ($M\mu$, $V\mu$), and σ is shown in Figure 5.29.

5.5.7 Calculation of Reliability Index

A FORTRAN program was written to aid in the calculation of p_f and β. This program checks each of the moment and shear pairs produced at the cross-section as the truck models are moved across the bridge and stores the minimum value of β. The smallest β indicates the controlling load effect at the location.

The safety assessment was performed for the McKenzie River bridge at the potential critical locations at 4 ft (~d), 8 ft (~2d), 12.5 ft (quarter-point), 25 ft (mid-span), etc. (refer to Figure 5.21). The tapered web between quarter-points on either side of continuous supports was considered for the resistance calculation. Cross-sections of the girder at each location are shown in Appendix C3. The β values calculated for the eleven ODOT Rating Vehicles are plotted versus the location of the section in Figure 5.30. One critical location is indicated where β dips to the lowest value (~2.5).

The critical location is in the first span, 8 ft from the continuous support (the same section evaluated for cracking). Rating Vehicle 8 produced the smallest β for the section. It produced the smallest β in both the positive and negative moment regions. Three WIM vehicles classified as Permit Table 5 resulted in nearly the same β. For this section, the controlling load effect was V_{max} with corresponding moment.

β at 42 ft in Span 1 was calculated from Figures 5.31 and 5.32 for the AASHTO-LRFD and field data cases, respectively. The comparison of the AASHTO-LRFD and field data cases shows that using distribution values collected for the specific bridge and using loading specific to Oregon will result in higher β values, possibly more representative of in-situ conditions. The AASHTO-MCFT M-V interaction curve has been adjusted to transition the capacity in the disconnected region. It is clear that if the M-V interaction were not adjusted, some rating vehicles would have indicated β less than 1.0 and in some cases exceeded the nominal capacity.

The critical sections occurred where flexural steel is cut-off in both the flange (deck) and the web. The critical section considered for this bridge is at 42 ft from the right abutment, and this section was further evaluated for low-cycle fatigue.

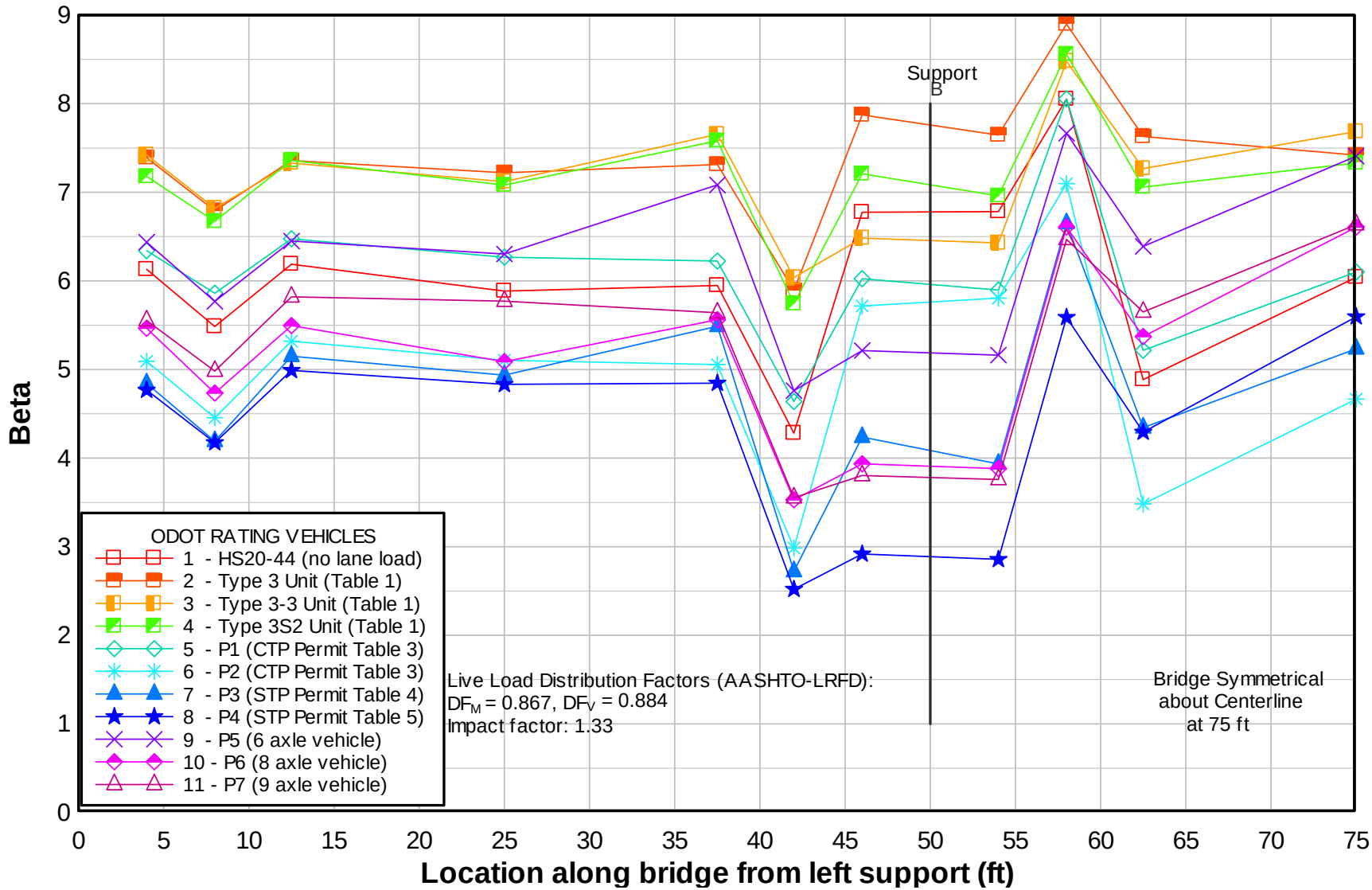

Figure 5.30: Safety assessment for exterior girder of McKenzie River bridge (08175N) using ODOT Rating Vehicles

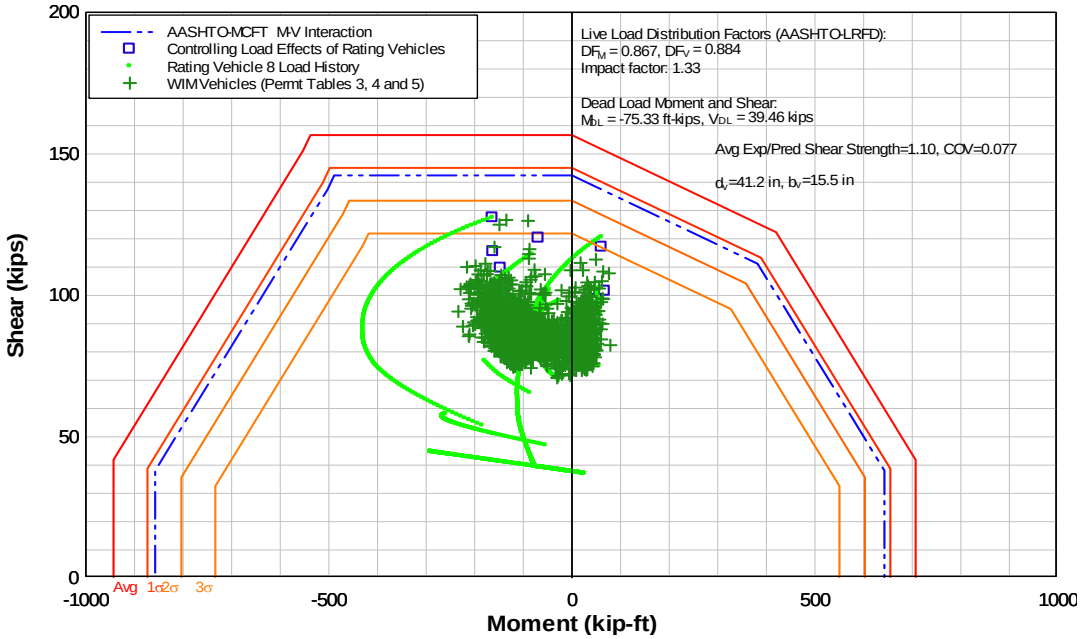

Figure 5.31: Safety assessment for the exterior girder for the cross-section at 42 ft. in span 1. Live load distribution and impact factors from AASHTO-LRFD are applied.

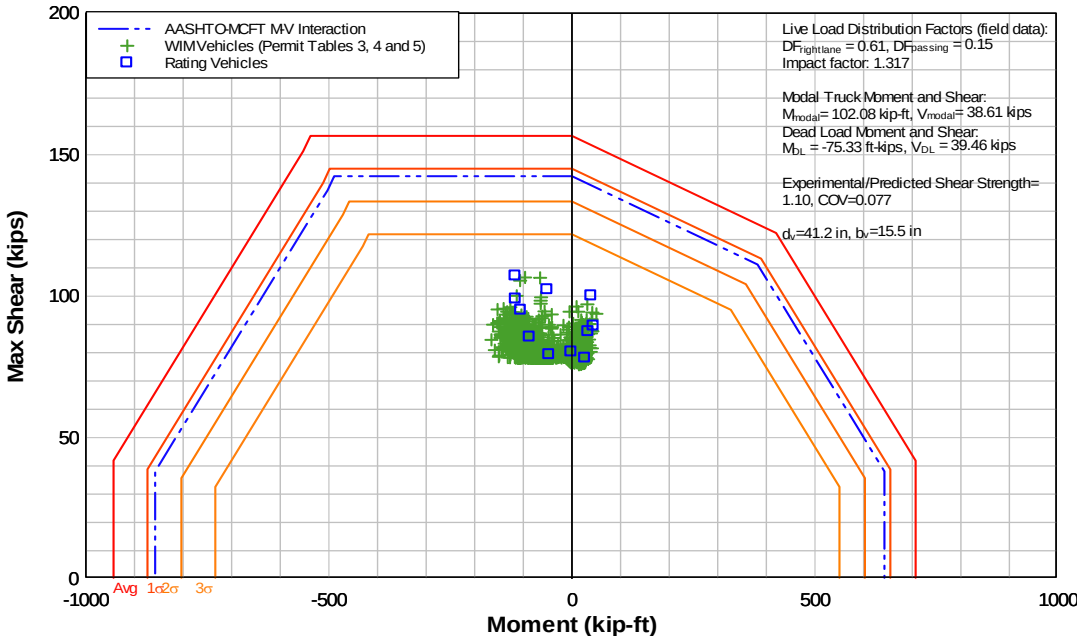

Figure 5.32: Safety assessment for the exterior girder for the cross-section at 42 ft. in span 1. Live load distribution and impact factors from field data are applied.

5.5.8 Comparison of Reliability Indexes

On an individual bridge, the primary use of the reliability index, β, is in locating the critical or controlling sections for strength. The index can also be used for comparison between components and populations of RCDG bridges for ranking. To establish a target reliability index for the bridge inventory, a suite of bridges should be assessed. The suite of bridges should also be rated using the AASHTO 2003 Manual for Condition Evaluation and Load and Resistance Factor Rating of Highway Bridges (LRFR). The LRFR is calibrated for a target reliability index of 2.5. Comparison of the safety assessment to unity in the LRFR will help gauge what index should be selected. Other guiding factors are experience, performance, bridge age, and loading history.

The LRFR provides reliability based rating evaluation in contrast to past practice (Guide Specifications for Strength Evaluation of Steel and Concrete Bridges 1989). The LRFR adopts a target reliability index of 2.5 calibrated to past AASHTO operating level load ratings. The calculations for loads and resistance use many AASHTO-LRFD principles. The main difference is the load and resistance factors are specified for rating based on evaluation.

For comparison, the rating factor for one of the critical sections was calculated using the LRFR. The section at 42 ft for Span 1 was selected. Therefore, the load effects from Rating Vehicle 8 were used. A Permit Load Rating was performed using AASHTO-LRFD distribution and impact factors. The result for checking Rating Vehicle 8 at the critical section gave a Permit Load Rating of 0.83 for Moment and 0.55 for Shear. Since the ratings are less than unity, this vehicle should not be allowed on the bridge. This would indicate that the LRFR β of 2.5 and that of the safety assessment developed here can not be directly compared. It also indicates that a β of 2.5 in the safety assessment may not provide comparable level of safety as that from LRFR. However, it may be possible to compare the service and factored load effects from the HL93, as a reference for the safety indexes.

5.5.9 Evaluate Longitudinal Reinforcement

Adequate capacity of the flexural reinforcing steel must be evaluated in the presence of a diagonal crack. This should be done in accordance with AASHTO-LRFD section 5.8.3.5. This provision checks the demand placed on the flexural steel due to the factored applied shear, factored applied moment, and stirrup force across the crack for a given crack angle. The load case to be considered for this evaluation is the HL93 with LRFR load factors.

For the critical section evaluated above, there was a negligible increase in the flexural steel demand. However, the longitudinal steel intersecting field identified diagonal cracks should be evaluated. Field data for the crack angles and the number of stirrups crossing the crack may be used in this evaluation. Further, load effects from shear and moment should be based on the maximum moment and corresponding shear from moving load analyses. Combining maximum moment and maximum shear may result in overly conservative evaluation.

5.6 EVALUATION OF LOW-CYCLE FATIGUE

Once the critical section (or sections as in this example) is determined, the section can be evaluated for repeated loading. To address the issue of low-cycle fatigue (LCF), it is necessary to identify the number of trucks, when combined with the dead load, to produce load effects sufficient to cause yielding in the stirrups. Further, it is necessary to identify the magnitude of these loads in relation to the nominal capacity. The nominal capacity for AASHTO-MCFT is drawn with a resistance factor (ϕ) of 1.0. The curve is then redrawn at 95%, 90%, 85%, and 80% of ultimate capacity (Figure 5.33).

The yield curve that represents the moment and shear combinations that cause yielding in the stirrups was determined from the cracked sectional analysis method described previously. Due to the nature of the yield surface, only the maximum shears and their corresponding moments need be produced from the load spectrum for this evaluation. Vehicles that fall above yield are binned for each 5%-capacity and are plotted in a histogram for comparison with laboratory testing results for LCF.

Load effects produced by the WIM vehicles in one year as collected at Wilbur and classified as Permit Tables 3, 4 and 5 are calculated for the two critical locations identified by the safety assessment. Two cases for distribution factors and impact factors are presented for each section.

The LCF evaluation for the section at 42 ft in Span 1 of the McKenzie River bridge is illustrated in Figure 5.33 for the AASHTO-LRFD case and Figure 5.34 for the field data case. Of these cases, only the section at 42 ft in Span 1 with AASHTO-LRFD distribution and impact factors applied (Figure 5.33) produced load effects sufficient to yield the stirrups. There were only five events that exceeded the yield threshold; three in the 85% of capacity range and two in the 80% of capacity range.

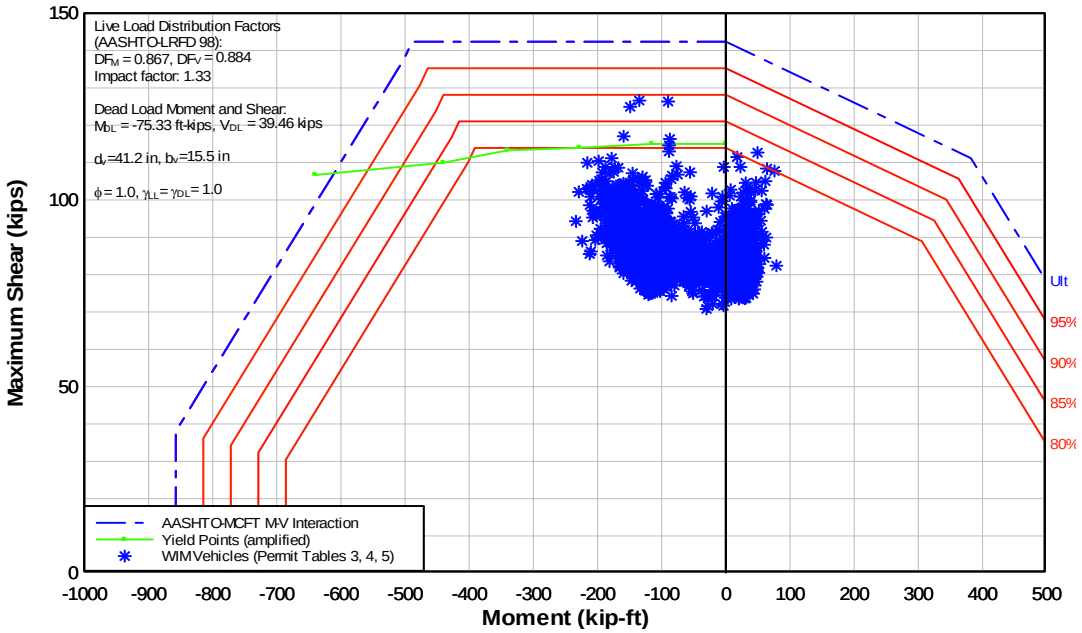

Figure 5.33: Low cycle fatigue evaluation for exterior girder of McKenzie R. bridge at 42 ft. in span 1 (AASHTO-LRFD). One year (14,510) Wilbur WIM permit vehicles

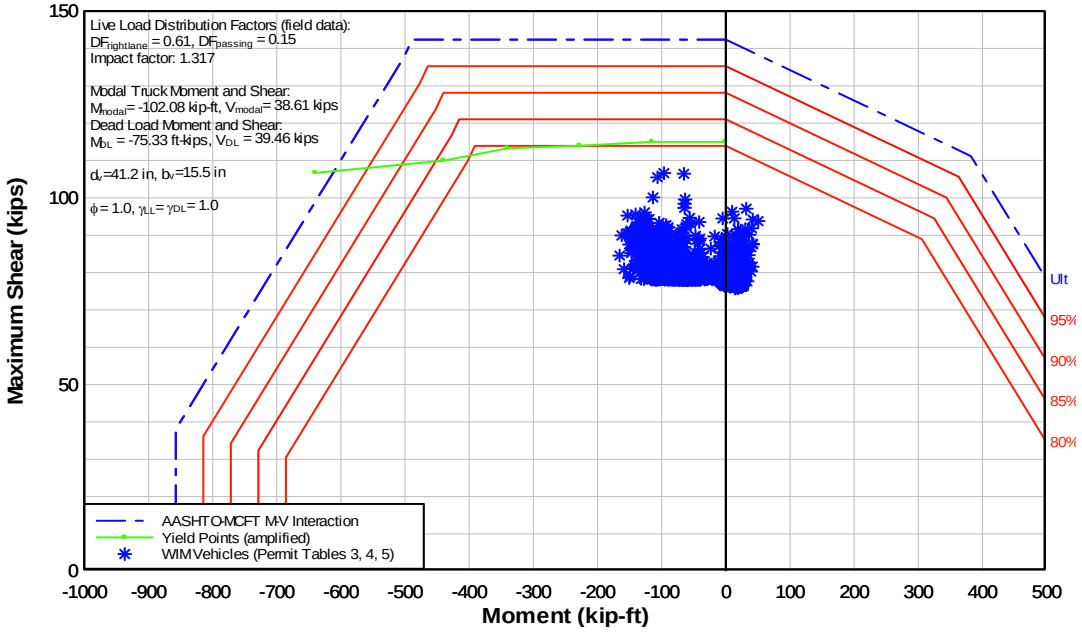

Figure 5.34: Low cycle fatigue evaluation for exterior girder of McKenzie R. bridge at 42 ft. in span 1 (field data). One year (14,510) Wilbur WIM permit vehicles.

The histogram of the results is shown in Figure 5.35. It would be conservative to group the numbers of cycles causing stirrup yielding into a single load ratio based on the largest measured load range.

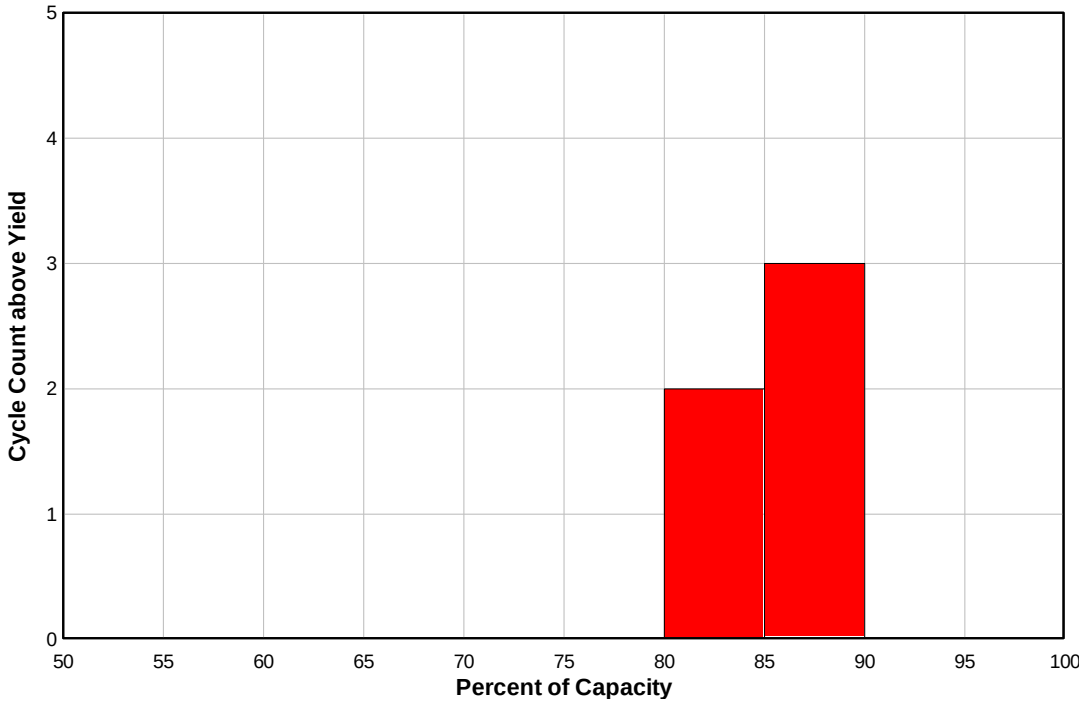

Figure 5.35: Annual cycles with load effects greater than the amplified yield points. Results from low cycle fatigue evaluation at 42 ft. in span 1 for exterior girder of the McKenzie R. Bridge (AASHTO-LRFD).

If it is assumed the annual values for truck load effects are stationary and there is statistical independence, then the annual value of occurrences can be extrapolated to estimate bridge life when compared to the LCF data from full-scale testing in the laboratory. Judgment as to the number of cycles that may already have occurred must be made in order to estimate remaining bridge life. The methodology for estimating life for a given number of overloads causing yielding of the stirrups was described previously in the analysis section.

5.7 CONCLUSIONS

Assessment of an existing bridge is needed when the structure exhibits signs of distress. Assessment practices require refinement in the calculation of loading and resistance, while maintaining an acceptable level of risk, to minimize costs associated with repair, replacement and weight restrictions. The methodology presented integrates full-scale laboratory testing for capacity, which found that the capacity requires assessment of shear and moment capacity simultaneously, and field data, with an Oregon specific truck loading. A live load model (load spectrum) was developed for Oregon, followed by a service level evaluation to explain the presence of diagonal tension cracks in vintage 1950's RCDG bridges. An assessment

methodology was also presented that integrates the vehicular loading specific to Oregon with field data and full-scale laboratory testing findings for evaluation of RCDG bridges.

Investigation of weigh-in-motion data revealed that the rating vehicles used by the ODOT Bridge Section tend to envelop the load effects produced by the WIM data for the suite of bridges considered. It also revealed that there are no clear distinctions between load effects produced by vehicles within the various permit table classifications.

Service level performance evaluation demonstrated that the bridge considered is expected to have diagonal tension cracks. Since this bridge is characteristic of the many bridges in Oregon's inventory, it is anticipated that many of the 1950's vintage RCDG bridges would exhibit this type of cracking.

Phase 1 of the assessment methodology was a safety assessment for one-time overloads at critical sections of a bridge girder. Full-scale laboratory testing of RCDGs revealed that the capacity of a typical girder was reasonably predicted using the AASHTO simplified form of modified compression field theory (MCFT) which accounts for shear and moment interaction. A recommendation was made for section capacity near points of inflection. The statistical characterization for AASHTO-MCFT, based on full-scale testing, was considered for the section capacity and compared to the load effect, which was considered to be deterministic.

A reliability index (β) was calculated to identify critical sections. The section with the smallest reliability index was the most critical. After application of the safety assessment methodology to multiple bridges in the ODOT bridge inventory and comparison to the current load and resistance factor rating specification for highway bridges, a target β can be selected for Oregon's RCDG bridges that will represent an acceptable level of risk to be maintained system-wide.

Phase 2 of the assessment methodology addresses the issue of low-cycle fatigue (LCF). LCF occurs when load effects produce shears and moments sufficient to cause yielding of the stirrups. The most critical section identified in Phase 1 of the methodology is evaluated to determine the number of WIM vehicles (per year) that produces load effects that cause stirrup yielding and at what percentage of the ultimate capacity. If the truck load effects are assumed stationary and to have statistical independence, then the annual number of cycles at the various amplitudes, when compared to the LCF data from full-scale laboratory testing, enables estimation of bridge life.

The assessment methodology can be applied to other structural members (i.e., bent caps and columns) using appropriate capacity models recommended by future research efforts. Once applied to the bridge system, use of both the safety assessment and LCF evaluation will enable engineers to rationally establish load restrictions based on an owner selected target reliability index developed for the bridge inventory, prioritize bridges for replacement or repair (or identify segments of a bridge requiring repair), and evaluate how repeated overload events that cause stirrup yield may reduce the life of a bridge.

5.8 METHODOLOGY SUMMARY

Steps required for implementing the assessment methodology are contained in Appendix C4 along with guidance on field data collection for use in the methodology.

5.9 LIMITATIONS

While the field tests, laboratory experiments, and assessment methods developed for this research program address the major issues associated with 1950's vintage conventionally reinforced deck-girder bridges in Oregon with diagonal cracks, there will be cases and conditions that will be outside the parameters and applicability of the developed assessment methodologies. Some of the cases that may require special attention include the following.

5.9.1 Skew bridges

The bridges investigated as part of the field study were constructed with abutments and intermediate supports perpendicular to girder lines, and laboratory specimens were tested under in-plane loading conditions. Based on a review of data in Higgins, et al. (*2004*), there did not appear to be a strong correlation between the amount of skew and the degree of identified diagonal cracking. The direct impact of skewed supports on bridge or specimen behavior were not investigated. However, it is anticipated that given the recommended use of the AASHTO-LRFD load distribution factors for shear and moment and their conservatism compared with field data, the uncertainty associated with bridge skew will likely be included by using the AASHTO-LRFD skew modification factor for shear amplification on exterior girders per 4.6.2.2.3c.

5.9.2 Bent caps

Bent caps are cross members that support the main girders and are oriented transverse to the direction of traffic. Typical 1950's vintage bent caps are very deep beams that support four to five main girders and are in turn supported on two relatively slender columns. Typical spans range from 21 to 27 ft with main girders, spaced between 7 and 9 ft, framing into the bent caps. The typically slender columns provide relatively small rotational restraint at the ends. Dimensions for bent caps are in the range of 16 in. wide and the depth varies between 5.5 to 9 ft deep.

Bent caps are primarily loaded by reaction forces from the main girders. The girder reactions are more uniformly distributed over the height of the web, instead of being applied directly the the compression face of the member. Consequently, there is little benefit from confinement of the concrete at the load points. Utility holes are commonly located in the bent caps, and the holes typically have diagonal cracks passing through them.

Of particular concern is the anchorage of the flexural steel reinforcement in the bent caps. Vintage details typically contain straight bar anchorages for the flexural steel and cutoff the bars where not required by calculation. These details would be considered inadequate by modern standards which would require that the flexural steel be hooked at the ends for better anchorage.

The presence of diagonal tension cracks at the level of the reinforcing steel increases the stress on the flexural steel and can lead to pullout failure if the bar is not adequately anchored. Failure of a bent cap in such a manner could cause the bridge to collapse, as the bent caps have no redundant load paths.

The leading analysis models for estimating the capacity of RCDGs based on the current research are less accurate as the beam dimensions approach the range of deep beams, which is characteristic of bent caps. Consequently, the suggested analysis methods using MCFT or *Response 2000*™ may not accurately estimate the capacity of bent caps. Indeed, for bent caps the recommended approach for capacity evaluation is the strut-and-tie method (STM), with the flexural anchorage controlling failure for the cases investigated. The STM analysis method does not incorporate assessment of either high or low-cycle fatigue effects, and existing data are not sufficient to evaluate the safety index for these members.

As a result of the significant differences between bent caps and main girders and uncertainty in applying analysis methods developed based on main girder performance, a research project will begin in the summer 2004 to develop methods for assessment of bent caps containing 1950's vintage proportions and reinforcing details. This research will enable ODOT engineers to more reliably evaluate RCDG bridge bent caps with diagonal cracks.

5.9.3 Temperature and shrinkage

The influence of temperature and shrinkage of the capacity of RCDG bridges was investigated previously by elastic finite element analysis (*Higgins, et al. 2004*). Results indicated that stresses induced from temperature changes and shrinkage depend on modeling assumptions at the support conditions. Non-uniform temperature through the height of the section, due to solar heating of the deck surface, tended to increase tensile strains near simple supports, due to uplift restraint provided by the continuous support columns. Shrinkage strains tended to reduce the effect of temperature strains, when both were considered simultaneously.

Temperature and shrinkage strain changes will result in seasonal changes in crack width. This was observed in a bridge near Mitchell Oregon, which had a continuous inspection record of diagonal crack widths (*Pulzone 2003*). During the routine biennial inspection, the diagonal crack width at the simple support location has been measured and recorded on the face of the girder. The first record of the crack was in October of 1989, and the crack widths and inspection dates are shown in Figure 5.36.

The bridge was always inspected in the fall and early winter of the year (September to December). During an out-of-phase inspection that took place while identifying bridges for field investigation (mid-June 2003), the diagonal crack width was measured and indicated two increments of crack growth from the previous inspection performed (November 2002) as measured with the ODOT visual crack comparator card (0.016 to 0.025 in.). This crack motion was attributed to seasonal shrinkage and temperature changes.

Figure 5.36: Digital photograph of bridge near Mitchell Oregon, with 14-year record of diagonal crack width measurements

The impact of temperature shrinkage strains on strength is unclear. The AASHTO-LRFR states in section 6.2.3.6 "temperature effects need not be considered in calculating load ratings for non-segmental bridge components that have been provided with well distributed steel reinforcement to control temperature cracking," and in section 6.2.3.8 states "…shrinkage effects do not need to be considered in calculating load ratings where there is well distributed reinforcement to control cracking in non-segmental, non-prestressed components." It is likely that RCDG of the 1950's would not meet the criteria of well distributed reinforcement, although this is not defined.

The analysis program *Response 2000*™, provides explicit input for analysis of sections with specified temperature and shrinkage strains. Estimation of temperature and shrinkage strains can be performed per AASHTO sections 3.12. and 5.4.2.3. Inclusion of tensile shrinkage and temperature strains reduces the section capacity, but the impact varies depending on the cross-section considered. Only limited studies have been performed, and additional work may be required to provide further guidance for these effects.

5.9.4 Low-Cycle Fatigue

The methodology used to predict remaining life of RCDG bridge girders subject to low-cycle fatigue was based on empirical results for large-scale specimens. The specimens sustained relatively large numbers of cycles even at high loading ratios (V/V_n). Cumulative deformations under low cycle fatigue were above those produced during the control loading tests, and the method for life prediction relies on calculating the cumulative deformations under repeated loads that produce yielding of the stirrups. However, deformation rates in each of the three phases of

damage accumulation were seen to be proportional to the magnitude of the load and specimen dependent. It remains unclear as to how to predict incremental damage in each of the three phases for a generalized specimen. Additional work is planned on component tests in concert with the previously cracked sectional analysis method to produce a more general predictive model.

5.9.5 Girder geometry

The bridges investigated as part of the field study and laboratory specimens were prismatic. Other girder cross-sections existing in the field include bulb shapes and compression flanges, among others. It is anticipated that analysis of these sections using modified compression field theory is appropriate, as the method is applied in practice to conventionally reinforced and prestressed girders of various geometries according to the AASHTO-LRFD specification.

Calculation of load effects for significantly different girder geometry changes may warrant a more detailed linear elastic analysis to calculate moments and shear force effects from rating vehicle load models. For the range of cases considered for haunched or tapered stems, maximum girder shear force effects were reasonably predicted assuming uniform prismatic members, although maximum moments were less well predicted. However, high shear with corresponding moment generally dictates the capacity of the sections.

5.9.6 Stem-flange interface cracks

Some diagonal cracks in the stems of bridge girders were observed to turn horizontal at the deck stem interface along the construction joint between these elements. This condition was also observed in laboratory specimens. The largest horizontal projections observed in the laboratory were approximately 12 in. to 16 in. long. However, there may be cases in the field where these horizontal crack extensions project over a longer length of the girder, and the gap between the stem and flange may be quite wide.

The applicability of the analysis methodologies for the case of a long horizontal projection of a diagonal crack with visible separation between the deck and stem is uncertain. For a significantly cracked condition like this, behavioral theories related to bending and shear likely do not apply. Further, stirrups crossing the horizontal crack plane at the stem-flange interface may not have adequate development to produce yielding. This is particularly true when the deck is in flexural tension. Breakdown of composite action between the deck and girder stem should be of significant concern, and careful attention should be given to these situations.

5.10 RECOMMENDATIONS FOR IMPLEMENTATION

The proposed assessment methodology should be applied to a population of diagonally cracked bridges to determine safety index factors currently accepted in practice. The AASHTO-LRFR approach should be performed concurrently to provide a reference level for the computed safety indexes. After assessments of a representative population of bridges and comparisons of results, consistent safety indexes should be established.

Other structural components, in particular the bent caps, may govern the capacity of a bridge system. The proposed method of reliability assessment will be applicable to bent caps, after better methods to predict capacity are developed and experimental data become available to characterize the statistical variability. Safety assessment for bent caps comparing load effects to the predicting capacity as determined from full-scale testing will be developed as part of a continuing research program.

The ODOT rating vehicle load models appeared to bound the spectrum of WIM vehicle load effects for the suite of bridges and locations considered, although not necessarily for the table classification implied. The initial population of bridges to which the methodology is applied should also include WIM vehicle load effects alongside the ODOT rating vehicles to ensure that peak load effects are adequately captured by the rating vehicles.

The vehicle models should be updated regularly to identify changes in the load spectrum. In addition, the rating vehicles should be compared with vehicle load effects to assure that they reflect in-situ truck traffic. The actual number of rating vehicles used in assessments may be reduced after further investigation.

The WIM data collection format should be modified to eliminate spurious data and unnecessary post-processing to facilitate compilation and integration of new data.

Additional information concerning axle weights and spacing should be collected for all overweight permits issued. This will allow for possible inclusion of additional data in the extreme distribution tails (large load effects with infrequent occurrence) which WIM may not capture.

Available vehicle data for other routes in Oregon should be analyzed, particularly I-84 and US Highway 97 to compare with the load spectrum examined for I-5 in this study.

It may be desirable to characterize the live load effects statistically to permit a single parameter comparison between load effect and resistance. The statistical characterization should account for the variability in the live load, dead load, distribution factors, and impact factors, as all are random variables with variability and uncertainty that result from the phenomena as well as the methods used for measurement and calculation. This may prove untenable, as the shear and moment are not fully correlated near continuous supports, and the controlling load effect (from the truck loading history) varies depending on the shape of the capacity curve.

Comparison of field measured girder distribution values and the load distribution factors computed as recommended in the AASHTO-LRFD specification indicates that the AASHTO distribution values were conservative for the bridges considered. In instances where analysis using the AASHTO distribution factors results in unacceptably low safety index values, it is possible to determine more refined distribution factors for a particular bridge. Two methods that are recommended to develop case specific distribution factors include 1) instrumentation of the bridge and collection of field data to estimate actual distribution as described in this report; or 2) development of a linear-elastic three-dimensional finite element model to estimate distribution, as detailed in Higgins, *et al*. (*2004*).

Based on observations of laboratory test specimens, diagonal cracks became wider as the ultimate capacity was reached. Monitoring of diagonal cracks, either locally or averaged over the beam web appears to be a technique useful for field monitoring of in-service bridges. However, to determine crack changes associated with overloads or bond fatigue, seasonal effects on crack width will have to be identified. This may require relatively long time periods of field data collection to remove seasonal shrinkage and temperature movements from crack displacements. It is recommended that a population of bridges within the ODOT inventory exhibiting significant diagonal cracking and not scheduled for repair or replacement be instrumented. This will permit collection of baseline diagonal crack responses for possible evaluation and analyses necessary in the future. These measurements can further help to identify if cumulative damage is occurring and what phase of damage is occurring for comparison with the proposed assessment methodologies.

6.0 REFERENCES

AASHO, (1941). American Association of State Highway Officials, "Standard Specifications for Highway Bridges," 3th Edition, Washington, D.C.

AASHO, (1944). American Association of State Highway Officials, "Standard Specifications for Highway Bridges," 4th Edition, Washington, D.C.

AASHO, (1949). American Association of State Highway Officials, "Standard Specifications for Highway Bridges," 5th Edition, Washington, D.C.

AASHO, (1953). American Association of State Highway Officials, "Standard Specifications for Highway Bridges," 6th Edition, Washington, D.C.

AASHO, (1957). American Association of State Highway Officials, "Standard Specifications for Highway Bridges," 7th Edition, Washington, D.C.

AASHO, (1961). American Association of State Highway Officials, "Standard Specifications for Highway Bridges," 8th Edition, Washington, D.C.

AASHO, (1965). American Association of State Highway Officials, "Standard Specifications for Highway Bridges," 9th Edition, Washington, D.C.

AASHO, (1969). American Association of State Highway Officials, "Standard Specifications for Highway Bridges," 10th Edition, Washington, D.C.

AASHTO, (1996). American Association of State Highway and Transportation Officials, "Standard Specifications for Highway Bridges," 16th Edition, Washington, D.C.

AASHTO, (2002) American Association of State Highway and Transportation Officials. "Standard Specification for Highway Bridges," 17th Edition," AASHTO, Washington, D. C.

AASHTO LRFD, (2003). American Association of State Highway and Transportation Officials. "LRFD Bridge Design Specifications," 2nd Edition with Interims, AASHTO, Washington, D. C.

AASHTO LRFR, (2003). American Association of State Highway and Transportation Officials. "Manual for Condition Evaluation and Load and Resistance Factor Rating (LRFR) of Highway Bridges," Washington, D. C.

ACI 318-02, (2002). "Building Code Requirements for Structural Concrete," American Concrete Institute, Farmington Hills, Michigan.

ACI 318-63, (1963). American Concrete Institute, "Building Code Requirements for Structural Concrete," American Concrete Institute, Detroit, Michigan.

ASCE-ACI Committee 326, (1962). “Shear and Diagonal Tension,” pt. 2, 326, *J. ACI*, vol. 59, no. 1, pp. 277-333.

Agarwal, A. C., and Wolkowicz, M., (1976). *Interim report on 1975 commercial vehicle survey*. Res. and Dev. Div., Ministry of Transportation, Downsview, Ontario, Canada.

Akgül, F., and Frangopol, D.M., (2004). “Bridge rating and reliability correlation: A comprehensive study for different bridge types,” *J. Struct. Eng*., ASCE, 130(7), pp. 1063-1074.

Akgül, F., and Frangopol, D. M., (2003a). “Rating and Reliability of Existing Bridges in a Network,” *J. Bridge Eng*., ASCE, 8(6), pp. 383-393.

Ang, A. H.-S., and Tang, W. H., (1984). *Probability Concepts in Engineering Planning and Design*, Vol. II, Wiley, New York.

ASCE-ACI Committee 445 on Shear and Torsion, (1998). “Recent Approaches to Shear Design of Structural Concrete,” *J. Struct. Eng.*, ASCE, vol. 124, no. 12, pp. 1375-1417.

ASTM A15-50T, (1950) “Tentative Specifications for Billet-Steel Bars for Concrete Reinforcement,” ASTM, Philadelphia, PA.

ASTM A16-50T, (1950) “Tentative Specifications for Rail Steel Bars for Concrete Reinforcement,” ASTM, Philadelphia, PA.

ASTM A305-50T, (1950). “Tentative Specifications for Minimum Requirements for the Deformations of Deformed Steel Bars Concrete Reinforcement,” ASTM, Philadelphia, PA.

ASTM C39-03, (2003). “Standard Test Method for Compressive Strength of Cylindrical Concrete Specimens,” ASTM International.

ASTM C78-02, (2003). “Standard Test Method for Flexural Strength of Concrete (Using Simple Beam with Third-Point Loading),” ASTM International.

ASTM C496-02, (2003). “Standard Test Method for Splitting Tensile Strength of Cylindrical Concrete Specimens,” ASTM International.

ASTM E8-04, (2003). “Standard Test Methods for Tension Testing of Metallic Materials,” ASTM International.

Balazs, G., (1998). “SP 180-6: Bond under Repeated Loading,” A Tribute to Dr. Peter Gergely, Leon, R. (Editor), American Concrete Institute, Farmington Hills, Michigan, pp. 125-143.

Bannantine, J. A., Comer, J. J., and Handrock, J. L., (1990). *Fundamentals of Metal Fatigue Analysis*, Prentice Hall, Upper Saddle River, New Jersey.

Bentz, E.C., (2000). "Sectional Analysis of Reinforced Concrete Members," PhD Thesis, Department of Civil Engineering, University of Toronto.

Collins, M. P., and Mitchell, D., (1991). *Prestressed Concrete Structures*, Prentice Hall, Englewood Cliffs, NJ.

Collins, M. P., (2003). Personal correspondence with C. Higgins at Oregon State University.

Ellingwood, B., Galambos, T.V., MacGregor, J.G., and Cornell, C.A., (1980). "Development of a Probability Based Load Criterion for American National Standard A58," *NBS Special Publication SP577*, National Bureau of Standards, Washington, D.C.

Estes, A.C., and Frangopol, D.M., (1999). "Repair optimization of highway bridges using a system reliability approach," *J. Struct. Eng*., ASCE, 125(7), pp. 766-775.

Estes, A.C., and Frangopol, D.M., (2003). "Updating Bridge Reliability Based on Bridge Management Systems Visual Inspection Results," *J. Struct. Eng*., ASCE, 8(6), pp 374-382.

Fifer, D., (2002). Personal correspondence with T. Daniels at OSU.

Higgins, C., Yim, S., Miller, T., Robelo, M., and Potisuk, T., (2004). "Remaining Life of Reinforced Concrete Beams with Diagonal-Tension Cracks," *Report No. FHWA-OR-RD-04-12*, Research Unit, Oregon Department of Transportation, Salem, Oregon.

Hognestad, E., (1951). "A Study of Combined Bending and Axial Load in Reinforced Concrete Members," Bulletin 399, University of Illinois Engineering Experiment Station, Urbana, Illinois.

Kawaguchi, M., (1992). "Experiment Relating to Fatigue Strength of Model Reinforced Concrete Beams with Respect to Running Load," *Papers on Structural Engineering*, Vol. 38A, pp. 1265-1274.

Manfredi, G., and Pecce, M., (1997). "Low cycle fatigue of RC beams in NSC and HSC," *Engineering Structures*, Elsevier Science Ltd. Vol. 19, No. 3, pp. 217-223.

MacGregor, J. G., (1997). *Reinforced Concrete: Mechanics and Design*, Prentice Hall, Upper Saddle River, NJ.

Miner, M. A., (1945) "Cumulative Damage in Fatigue," *Journal of Applied Mechanics*, Vol. 12, Trans. ASME Vol. 67, pp. A159-A164.

Mirza S., Hatzinikolas M., and MacGregor J., (1979) "Statistical Descriptions of the Strength of Concrete," Preceedings ASCE, *Journal of the Structural Division*, Vol. 105, No. ST6, June, pp. 1021-1037.

Moses, F., and Ghosn, M., (1985). "A comprehensive study of bridge loads and reliability," *Report No. FHWA/OH-85/005*, Dept. of Civil Engineering, Case Western Reserve University, Cleveland, Ohio.

Nowak, A. S., and Collins, K. R., (2000). *Reliability of Structures*, McGraw-Hill, New York.

Nowak, A.S. and Hong, Y.K., (1991). “Bridge Live Load Models,” *J. Struct. Eng.*, ASCE, 117(9) pp.2757-2767.

Pulzone, M., (2003). Personal correspondence with C. Higgins at Mitchell, OR.

Reineck, Karl-Heinz (Editor), (2002). “SP-208: Examples for the Design of Structural Concrete with Strut-and-Tie Models,” American Concrete Institute, Farmington Hills, Michigan.

Siess, C. P., (1960) “Research, Building Codes, and Engineering Practive,” *ACI Journal*, May, ACI, pp. 1105-1122.

Stewart,M.G., Rosowsky, D.V., and Val, D., (2002). “Reliability-based bridge assessment using risk-ranking decision anlaysis,” *Struct. Safety*, 23(2001), pp. 397-405.

Stewart, M.G., and Val, D., (1999). “Role of load history in reliability-based decision analysis of ageing bridges,” *J. Struct. Eng.*, ASCE, 125(7), pp.776-783.

Stewart, M.G., and Val, D., (2003). “Multiple Limit States and Expected Failure Costs for Deteriorating Reinforced Concrete Bridges,” *J. Struct. Eng*., ASCE, 8(6), pp. 405-415.

Tadashi, A., (2000). “Effects of Running Load on Flexural Load-Carrying Capacity of Reinforced Concrete Beams and Dynamic Effects,” *Transactions of the Japan Concrete Institute*, Vol. 22, pp. 345-352.

Tadashi, A., (1999). “Experimental Research Relating to the Effect of Running Loads on the Flexural Load-Carrying Capacity of Reinforced Concrete Beams,” *Concrete Journal*, Annual Symposium Papers, Vol. 21, No. 3, pp. 211-216.

Todeschini, C. E., Bianchini, A. C. and Kesler, C.E., (1964). “Behavior of Concrete Columns Reinforced with High Strength Steels,” *ACI Journal*, *Proceedings* V. 61, No. 6, pp. 701-716.

Vecchio, F. J., and Collins, M. P., (1986) “The Modified Compression-Field Theory for Reinforced Concrete Elements Subjected to Shear,” *ACI Journal*, March-April, ACI, pp. 219-231.

Vecchio, F. J., and Collins, M. P., (1988) “Predicting the Response of Reinforced Concrete Beams Subjected to Shear using Modified Compression-Field Theory,” *ACI Structural Journal*, May-June, ACI, pp. 258-268.